INDUSTRIAL
PLASMA
ENGINEERING

VOLUME 1
PRINCIPLES

J REECE ROTH

IoP

Industrial Plasma Engineering

Volume 1: Principles

J Reece Roth

Department of Electrical and Computer Engineering
University of Tennessee, Knoxville

Institute of Physics Publishing
Bristol and Philadelphia

Contents   Volume 1: Principles

Projected Contents
Volume 2: Applications

Preface

This two-volume work is intended to provide a description of plasma-related devices and processes which are used industrially. The text assumes that the average student or in-service engineer using it has not recently taken a course in plasma physics, and possesses a background in physics and calculus that ended at the sophomore level. This book is intended to be used as a textbook at the senior or first-year graduate level by students from all engineering and physical science disciplines, and as a reference source by in-service engineers.

Basic information on plasma physics and the physical processes important in industrial plasmas is contained in the first four chapters of Volume 1. Chapters 5 through 7 of Volume 1 describe the sources of ion and electron beams and ionizing radiation which are used in industrial applications. Chapters 8 through 10 of Volume 1 describe the physics and technology of DC electrical discharges, and Chapters 11 through 13 the physics and technology of RF electrical discharges. Chapters 14 through 18 in Volume 2 cover the plasma processing of materials. The last five chapters of Volume 2 describe applications of plasma to various additional industrial devices, processes, or uses. It is anticipated that Volume 2 will be published early in 1997.

This book is intended to be self-contained. Readers who have taken a course in kinetic theory can omit Chapter 2; readers who have had an introductory course in plasma physics should find much of Chapters 3 and 4 useful for review only. This book does not contain derivations from first principles of some of the more advanced material from plasma physics or materials science. Such material can be found in graduate texts, some of which are listed among the references at the end of the individual chapters, or in the annotated bibliography included at the end of Volume 2. SI units have been used throughout the text, except where

conventional usage (e.g., electronvolt, torr) has become so firmly established that non-SI units are more appropriate.

Available technical dictionaries in the fields of physics, chemistry, and electrotechnology generally have an inadequate coverage of the terminology required to discuss the subject of industrial plasma engineering. When an entry can be found in such dictionaries, the definition is too often out of date, incomplete, inaccurate, and/or inconsistent with current usage by professionals in the field. In an attempt to deal with this problem, and to increase the value of this book as a reference source, the technical terminology, jargon and acronyms used in the field of industrial plasma engineering are not only defined and fully discussed but also *italicized* and indexed when they first appear in the text. This practice is intended to assist the student in learning key terminology and concepts, and should provide the in-service engineer or scientist with an equivalent technical glossary until a proper technical dictionary covering the field of industrial plasma engineering becomes available.

In addition to the extensive index, the book is further enhanced as a reference source by several appendices, providing both a comprehensive listing of the mathematical nomenclature and units used throughout the text, and a useful collection of frequently used plasma formulas, physical constants and conversion factors. An annotated bibliography containing over 50 entries from the textbook, monograph, and conference proceedings literature will be included at the end of Volume 2, and should provide an entry into the literature covered by the various chapters of the text.

To facilitate the use of this book for classroom instruction, I have prepared an *Instructor's Manual* for Volume 1, details of which are available from the publisher. This manual includes homework problems and their answers; full-size copies of the figures and tables, from which transparencies can be made; enlarged originals of all the equations in the text for the production of transparencies; and a 42-page topical outline of the text with pagination keyed to the text. A similar manual is proposed to accompany Volume 2.

I would like to express my appreciation to the many individuals whose suggestions and hard work have contributed to the manuscript in its present form. While assuming total responsibility for the contents and correctness of the manuscript myself, I would like to thank my graduate and minicourse students who pointed out errors or opportunities for improvement in early drafts of the manuscript. I especially would like to thank Dr Donald L Smith for his very thorough and helpful review of the final manuscript. I would also like to thank Ms Roberta Campbell who typed the final manuscript and all its drafts, and Ms Jenny Daniel, who drafted nearly all the figures in the text.

Finally, I am especially desirous of establishing contact with the instructors, students, and in-service professionals who use this book, in order to improve it, correct it, and answer any questions. Please feel free to contact me with any corrections or comments at (615) 974-4446 voice, (615) 974-5492 fax; or by e-mail at ROTH@ECE.ENGR.UTK.EDU.

J Reece Roth, PhD
Knoxville, Tennessee, USA
October 28, 1994

Acknowledgments

All figures in this book have been specially drafted for this publication and most are original drawings prepared under the author's supervision. Some figures have been redrawn from other publications and some tables include data from other sources, as indicated in the figure and table captions. The author and publisher gratefully acknowledge permission to reproduce previously published material. They have attempted to trace the copyright holders of all figures reproduced from other sources and apologise to any copyright holders whose prior permission might not have been obtained.

Figure 1.7 is reproduced from Francis (1987), having originally been drawn by Joan Forbes, by permission of *The Christian Science Monitor*; © 1987 TCSPS.

Figures 1.9 and 1.10 are reproduced from Post *et al* (1990) by permission of Sigma Xi, the Scientific Research Society.

Figure 1.11 from McElroy (1988), figure 1.12 from Gribbin (1989), and figure 1.13 from Anon. (1989) are reproduced from *New Scientist* by permission of IPC Magazines.

Figure 4.9 is reproduced from Geller and Hosea (1968) by permission of Association Euratom-CEA.

Tables 4.2 and 4.3 are reproduced from Vidmar (1990) by permission of SRI International, Menlo Park, CA.

Figure 5.8 is reproduced from Poeschel *et al* (1979) by permission of Hughes Research Laboratories, Malibu, CA.

Figure 5.9 from Forrester (1988) and figure 13.22 from Brown (1966) are reproduced by permission of John Wiley and Sons, Inc., New York.

Figures 5.22 and 6.6 are reproduced from Cooper *et al* (1972) by permission of the International Atomic Energy Agency, Vienna.

Figure 8.6 and part of table 8.3 are reproduced from Cobine (1958) by permission of Dover Publications, Inc., New York.

Figures 10.16 and 10.17 are reproduced from Eberhart and Seban (1966) by permission of Elsevier Science Ltd, The Boulevard, Langford Lane, Kidlington OX5 1GB, UK; © 1966.

Figure 13.18 from MacDonald and Brown (1949) and figure 13.23 from MacDonald *et al* (1963) are reproduced by permission of the American Physical Society; © 1949 and 1963.

Full references of all the sources cited above may be found at the ends of corresponding chapters.

The contributions of the author's colleagues and students are acknowledged in the Preface.

About the Author

J Reece Roth obtained a BS in Physics from MIT in 1959, and a
PhD from Cornell University in 1963 with a major in Engineering
Physics. He joined the NASA Lewis Research Center in Cleveland,
Ohio in 1963, where he was Principal Investigator of the Lewis Electric
Field Bumpy Torus Project until 1978. He is currently a Professor of
Electrical Engineering at the University of Tennessee, Knoxville, and
also an Honorary Professor at the University of Electronic Science and
Technology of China, Chengdu, Sichuan Province, People's Republic of
China.

While at NASA, Dr Roth pioneered in the application of
superconducting magnet facilities to high temperature plasma research.
Dr Roth initiated research on the electric field bumpy torus concept,
a magnetoelectric approach to creating a plasma of fusion interest in
which strong radial electric fields are imposed on a bumpy torus plasma.
Among Dr Roth's contributions to the understanding of basic processes in
plasma are his experimental discovery and theoretical description of the
continuity-equation oscillation, and the joint discovery of the geometric
mean plasma frequency, a new mode of electromagnetic emission from
plasma.

Dr Roth is presently engaged in research at the Plasma Science
Laboratory of the University of Tennessee, Knoxville on the interaction
of electromagnetic radiation with electric field dominated plasmas,
corrosion inhibition of metals by plasma ion implantation, and surface
treatment of materials by uniform one atmosphere glow discharge
plasmas.

In the past 30 years, Dr Roth has authored or co-authored more
than 131 plasma-related publications and conference publications. He
is the author of the textbook *Introduction to Fusion Energy*, which also
has been published in a Chinese edition by Tsinghua University Press,

Beijing. Dr Roth is a Fellow of the IEEE, an Associate Fellow of the American Institute of Aeronautics and Astronautics, a Life Member of the AAAS and of Sigma Xi, and a member of the IEEE Nuclear and Plasma Sciences Society, the American Physical Society, and the American Nuclear Society.

1

Introduction

1.1 ORGANIZATION OF TEXT

This work is being published in two volumes, the second of which
will appear approximately two years after the initial publication of the
first. Volume 1, containing Chapters 1 through 13, is concerned with
the principles of industrial plasma engineering; Volume 2, containing
Chapters 14 through 23, is concerned with the application of plasmas to
specific industrial processes or devices.

Chapters 2 through 4 of Volume 1 contain basic physics information
essential to understanding the theory of industrial plasmas, and which
may be unfamiliar to students in some fields of engineering or the exact
sciences. For unusually well prepared students the material in these
chapters will be useful for review only, although some applications are
included which will be new to most students.

The organization of the material in the remainder of Volume 1 is
illustrated by the taxonomy chart in table 1.1. Industrial plasma engineers
are frequently called upon to deal with sources and beams of electrons,
ions, or ionizing radiation. These subjects are covered briefly in Chapters
5 through 7 of Volume 1. Chapters 8 through 10 describe the physics
and technology of DC electrical discharges and plasma sources, while
Chapters 11 through 13, at the end of Volume 1, describe the physics and
technology of RF electrical discharges and plasma sources. This literature
has a long history, some of it going far back into the 19th century. The
approach and much of the vocabulary is entirely different from that used
in fusion research, and essentially all of the material in the last six
chapters should be new to students whose only academic preparation is
in fusion-related plasma theory. Many industrial applications of plasma

have the plasma source as a common feature. These sources are discussed in the last six chapters of Volume 1, so that the information does not have to be repeated in each of the application chapters.

The first five chapters of Volume 2 are concerned with the plasma processing of materials. Chapter 14, on plasma treatment of surfaces, describes how exposure to the active species of a plasma can affect the wettability, printability, adhesion, and charge retention characteristics of materials. Chapters 15 through 17 describe processes which are important in microelectronic circuit fabrication. Chapter 18 describes materials processing with thermal plasma, including plasma flame spraying, plasma torches, and other applications of energetic arcs. Chapter 19 on plasma chemistry describes how plasma is used to produce chemicals of commercial interest.

Finally, Chapters 20 through 23 of Volume 2 describe specific industrial applications of plasma. Chapter 20 is concerned with phenomena that are important in high voltage electrical equipment and in electrical power distribution systems. Chapter 21 is on plasma lighting devices. Chapter 22, on electrohydrodynamics, is concerned with applications such as electrostatic precipitation and paint spraying. Chapter 23 covers research and development plasmas which have not yet found widespread use in industry. This chapter describes some uses of magnetohydrodynamics, the geophysical and space plasmas that affect communications and the operation of large-scale electrical power distribution networks, and space propulsion systems based on the acceleration of matter using plasma-related principles. Finally, the section of Chapter 23 on the military applications of plasma is the most speculative of any in the text.

1.2   LONG-TERM GLOBAL ENERGY ISSUES

The consumption of large amounts of energy is a fundamental characteristic of modern industralized society. Plasma-related industrial processes are, or can be,
related to a significant fraction of the production, conversion, distribution, and consumption of these energy requirements. Plasma-related processes are important not only because they can greatly increase the efficiency of energy-consuming processes, but also because they can make possible new processes and products of industrial interest which would otherwise require very large energy inputs. Some specific examples will be discussed later in this chapter in connection with table 1.2, and in the applications chapters of Volume 2. In this section we review certain aspects of the energy scene which have convinced long-range planners all over the world that the efficient and non-polluting use of energy is a

Table 1.1 Taxonomy chart for sources of energetic matter, radiation, and plasma.

```
                        ┌─────────────────────────┐
                        │  SOURCES OF ENERGETIC    │
                        │  MATTER AND RADIATION    │
                        │  CHAPTERS 5 TO 13        │
                        └─────────────────────────┘
            ┌───────────────────────┼───────────────────────┐
  ┌──────────────────┐   ┌──────────────────┐   ┌──────────────────┐
  │  CHARGED         │   │  SOURCES OF      │   │  PLASMA SOURCES  │
  │  PARTICLE SOURCES│   │  IONIZING        │   │  CHAPTERS 8 TO 13│
  │  CHAPTERS 5 AND 6│   │  RADIATION       │   │                  │
  │                  │   │  CHAPTER 7       │   │                  │
  └──────────────────┘   └──────────────────┘   └──────────────────┘
     ┌──────┴──────┐        ┌──────┴──────┐        ┌──────┴──────┐
┌─────────┐ ┌─────────┐ ┌─────────┐ ┌─────────┐ ┌─────────┐ ┌─────────┐
│ELECTRON │ │ION      │ │PARTICLE │ │PLASMA   │ │DC PLASMA│ │RF PLASMA│
│SOURCES  │ │SOURCES  │ │ACCELER- │ │PINCHES  │ │SOURCES  │ │SOURCES  │
│CHAPTER 5│ │CHAPTER 6│ │ATORS    │ │CHAPTER 7│ │CHAPTERS │ │CHAPTERS │
│         │ │         │ │CHAPTER 7│ │         │ │8 TO 10  │ │11 TO 13 │
└─────────┘ └─────────┘ └─────────┘ └─────────┘ └─────────┘ └─────────┘
```

ELECTRON SOURCES	ION SOURCES	PARTICLE ACCELERATORS	PLASMA PINCHES	DC PLASMA SOURCES	RF PLASMA SOURCES
– THERMIONIC	– VON ARDENNE	– CYCLOTRON	– RESISTIVE	– DARK DISCHARGES	– INDUCTIVE
– PHOTOELECTRIC	– KAUFMAN	– BETATRON	– INDUCTIVE	– GLOW DISCHARGES	– CAPACITIVE
– FIELD EMISSION	– PENNING	– SYNCHROTRON	– PLASMA FOCUS	– ARC DISCHARGES	– MICROWAVE
– HOLLOW CATHODE	– FREEMAN				
– SECONDARY	– SURFACE				
	– OTHER				

ENERGY CONSUMPTION PER PERSON
(MILLION BTU)

1,000

500

200

100

50

20

10

5

2

1

50 100 200 500 1000 2000 5000 10,000
GNP PER PERSON (IN UNINFLATED DOLLARS)

U.S.
NORTH AMERICA
USSR
EASTERN EUROPE
OCEANIA
WESTERN EUROPE
JAPAN
LATIN AMERICA
COMMUNIST ASIA
AFRICA
OTHER ASIA

Figure 1.1 Energy consumption per person as a function of gross national product per person in constant, inflation-compensated dollars for selected industrialized countries and regional groupings of countries. (Perry and Landsberg 1977).

necessary condition for the future existence of our modern industrialized society as we know it.

1.2.1 Energy and Quality of Life

In the past, there has been a strong correlation between the average income of a country and its energy consumption per person. In figure 1.1 are data taken from the U.S. National Research Council's study, *Energy and Climate* (Perry and Landsberg 1977), which show energy consumption per person as a function of the gross national product per person for a few major industrialized countries, and for regional groupings of countries. To a remarkable extent, these data lie along a straight line over a factor of 50 in the two variables.

This correlation is also apparent when one follows the development of a single country over time. In the United States, for example, the average per capita income, in uninflated dollars, was directly proportional to the average per capita energy consumption over an 83-year period prior to 1973. Although one must be cautious about relating average income to
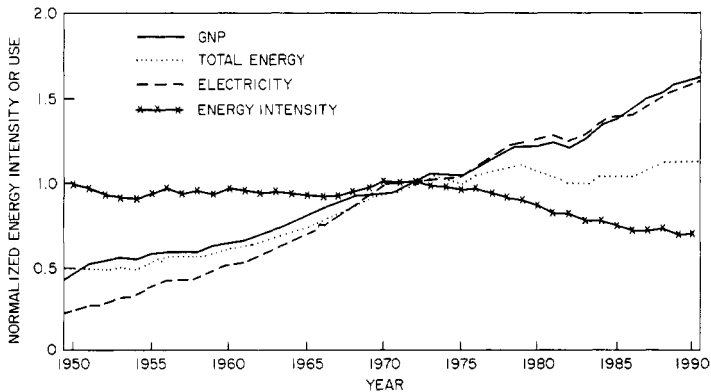
Figure 1.2 The growth of electrical power, total energy consumption, and GNP from 1950 to 1990 (Gibbons and Blair, 1991). The crosses represent the energy intensity, the ratio of total energy used to GNP. All curves have been normalized to 1972 = 1.0.

the quality of life, it is tempting to conclude from such data that there is an underlying, necessary relation between quality of life (or at least average income) and average energy consumption.

Some recent data on this correlation are plotted in figure 1.2, taken from Gibbons and Blair (1991), which shows recent data on the gross national product (GNP), electrical power consumption, and total energy consumption in the United States from the year 1950, normalized to the year 1972. Also plotted in figure 1.2 is the *energy intensity*, the ratio of total energy consumption to GNP. Although the electrical power consumption has remained proportional to GNP, the energy intensity following the OPEC oil embargo of 1973 indicates that the United States reduced its total energy consumption without a proportionate reduction in its total income. In the broad view, however, data such as those in figures 1.1 and 1.2 have led many long-range planners to conclude that not only must global energy consumption increase to bring the non-industrialized countries up to the economic level of the industrialized countries, but also that the efficiency and effectiveness of energy consumption must be improved.

1.2.2 Primary Energy Options

Nearly all energy production discussed above originated with four non-renewable primary energy sources: coal, oil, natural gas, and uranium. In figure 1.3 is shown the distribution of world energy use among these primary sources in 1980, for which actual data are available, and three projections for the year 2020, each originating with a different organization operating on different assumptions (Shepard *et al* 1988).
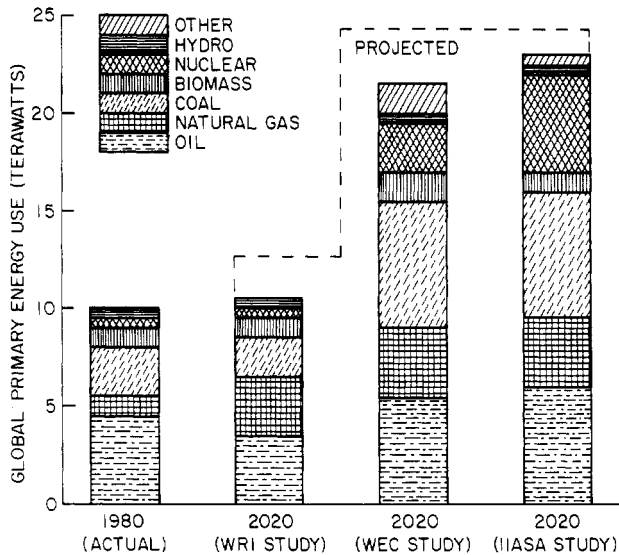
Figure 1.3 Recent and projected energy use according to primary energy source. Projections for the year 2020, based on varying assumptions, are shown from the World Resources Institute (WRI), the World Energy Conference (WEC) and the International Institute for Applied Systems Analysis (IIASA) (Shepard *et al* 1988).

These projections indicate that, even with significant conservation efforts, world energy use will roughly double by the year 2020, with much of the increased supply coming from the burning of coal and the use of nuclear power.

Unfortunately, the reserves of these non-renewable fuels are limited. The availability of each is determined by the amount discovered or brought into production in a given year, and the number of sources depleted or shut down in that same year. The net result over a long period can be described by a gaussian or bell-shaped *depletion curve*, given by equation (1.1),

$$p = p_0 \exp\left(\frac{1}{2}\left[\frac{t - t_0}{\sigma}\right]^2\right). \qquad (1.1)$$

The parameter t is the year of energy production, t_0 is the year of maximum energy production and σ is the standard deviation of the distribution.

Figure 1.4, taken from Perry and Landsberg (1977), shows the idealized depletion curves for U.S. coal, oil, gas, and uranium resources over a 400-year period. As is evident, the United States has already
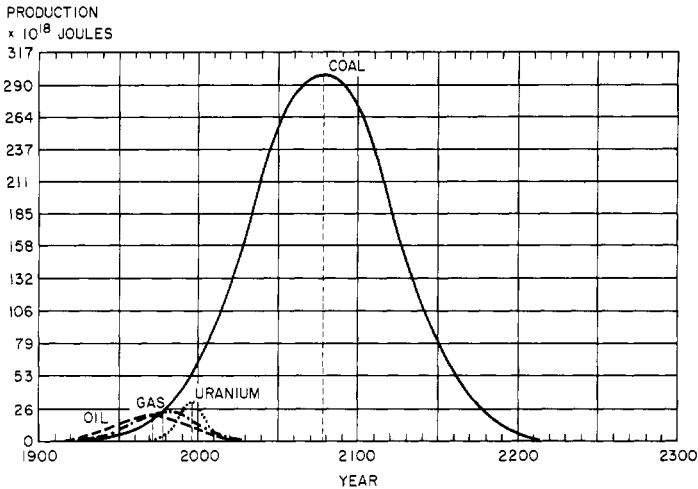
Figure 1.4 Idealized energy depletion curves for coal, uranium, natural gas, and oil in the United States. These curves are described by equation (1.1) (Perry and Landsberg 1977).

passed its maximum availability of oil and natural gas, and is approaching its maximum availability of domestic uranium resources. Only coal appears to offer large resources for future exploitation.

Figure 1.5, also from Perry and Landsberg (1977), shows a similar set of data for the rest of the world, exclusive of the United States, which has not yet reached the maximum of its oil and gas depletion curves. Again, coal appears to be the dominant future energy resource, but even it will be almost depleted by the year 2200 AD. The uranium referred to in figures 1.4 and 1.5 is enriched uranium, which is suitable for burning in light-water fission reactors. If breeder reactor technology became widely available, so that the 99.3% of natural uranium existing as the U-238 isotope could be burned, the total area under the uranium depletion curve would be comparable to or larger than that of coal. All resources represented in figures 1.4 and 1.5 are erratically distributed over the surface of the earth. Although fortunate geographical enclaves may have enough resources to maintain their lifestyles for several hundred more years, this clearly cannot be the case for the world at large.

Sometime after the year 2020, nuclear fusion might contribute to total energy production, but whether this is technically and economically feasible with current approaches remains to be seen. As indicated in figure 1.3, the future contributons of biomass, hydroelectric, solar, tidal, and other sources will be small compared to the total need.
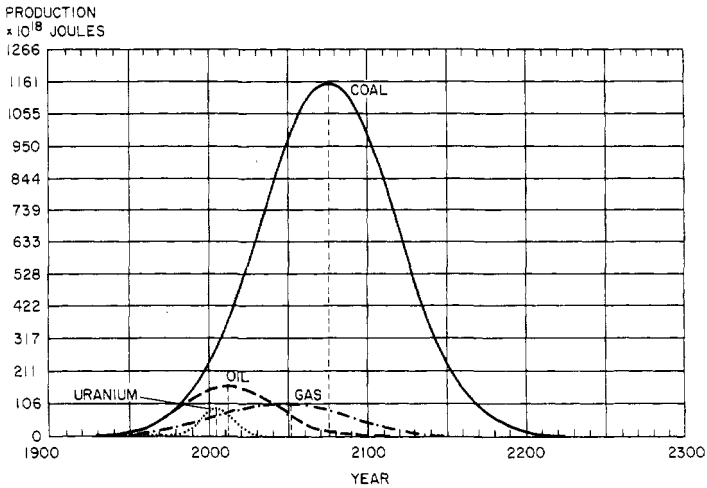
Figure 1.5 Idealized energy depletion curves for coal, oil, natural gas, and uranium in all countries except the United States. These curves are described by equation (1.1) (Perry and Landsberg 1977).

1.2.3 Constraints by Environmental Effects

Plasma-related devices and processes not only achieve many industrially important results more efficiently and effectively than competing non-plasma options; they also can achieve such results while producing few, if any, undesired byproducts, toxic wastes, or environmental pollutants. As one of many possible examples of the magnitude of environmental pollution problems, we look at what is probably the best researched, the environmenal effects of energy production.

In recent years there have been unmistakable indications that the gaseous effluents of our modern, energy intensive lifestyles in the industralized countries are having detrimental effects on the world climate. A major environmental impact is the acid rain which arises from the combustion products of fossil fuels, including sulfur oxides and nitrogen oxides. Figure 1.6, taken from Schwartz (1989), shows sulfur oxide emissions in the upper diagram and nitrogen oxide emissions in the lower diagram, for the United States and Canada, plotted on grids one degree square in latitude and longitude. It is clear that the midwestern United States is a major contributor to emissions of these gases, due to the combustion of high-sulfur fossil fuels, including coal mined in this area. The sulfur and nitrogen oxide emissions from fossil fuel combustion rise in the atmosphere, combine with water vapor, and precipitate as acid rain.

On figure 1.7, taken from Francis (1987), is a contour plot of the acidity (pH) of rainwater in the United States and Canada. Unpolluted
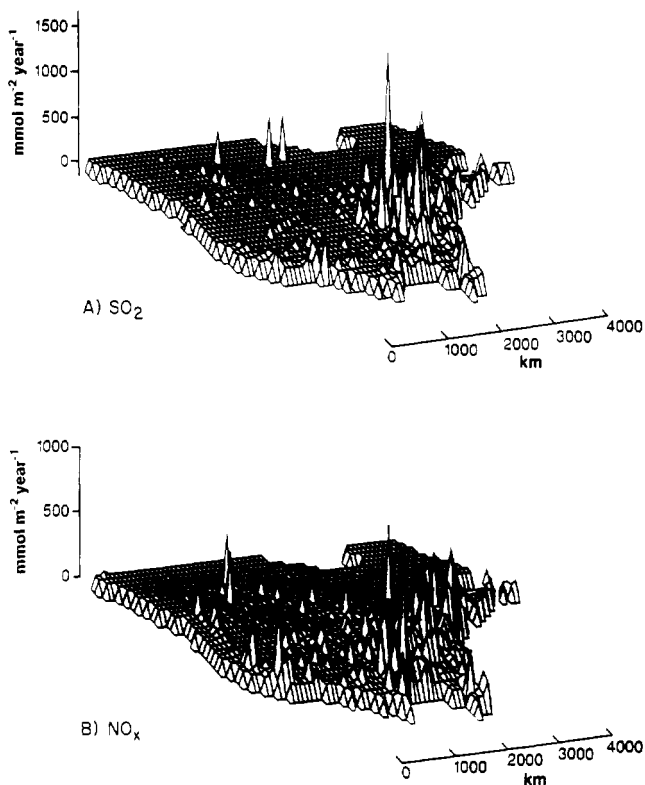
Figure 1.6 Spatial distribution in 1980 of the emissions of (A) sulfur oxides and (B) nitrogen oxides in the United States and Canada south of 60°N, gridded in cells one degree square (Schwartz 1989).

rainfall has a pH level of 5.6, and pure distilled water has a pH of 7.0. Any level below a pH of 5.6 is considered abnormally acidic. The results in figure 1.7 show a major concentration of acid rainfall in eastern Ohio, northern Pennsylvania, and western New York. Acid rain is very detrimental to fish and plant life, and many species of game fish are sensitive to the acidity of the water in which they live. When the water becomes sufficiently acidic, the fish die. There are, by now, thousands of lakes in Scandinavia, the Maritime Provinces of Canada, and northern New York and New England in which the natural population of game fish can no longer survive because of the effects of acid rain.

Acid rain also tends to acidify soil, thus retarding the growth of trees that are incapable of coping with the changed environment, such as some pines. An example of the effects of acid rain in Eastern Tennessee is shown in figure 1.8, taken from Baes and McLaughlin (1984). The upper four graphs show the mean growth rate of short-leaf pine at four sites,
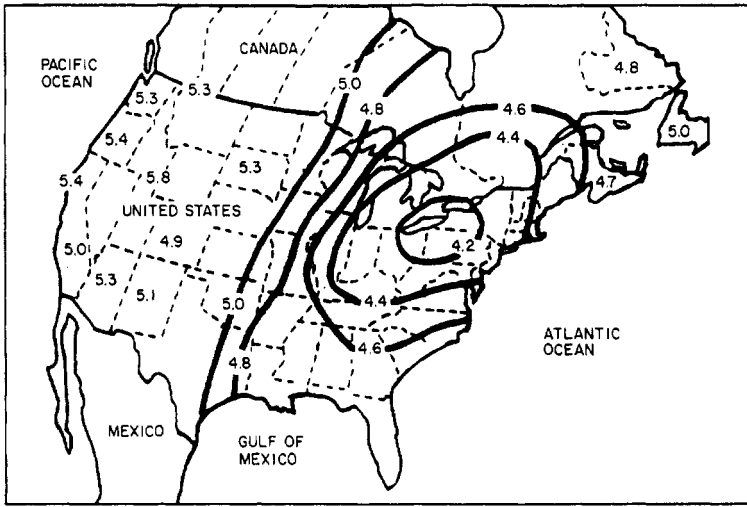
Figure 1.7 Lines of constant rainfall pH in Canada and the United States. Unpolluted rainfall has a pH level of 5.6 (Francis 1987).
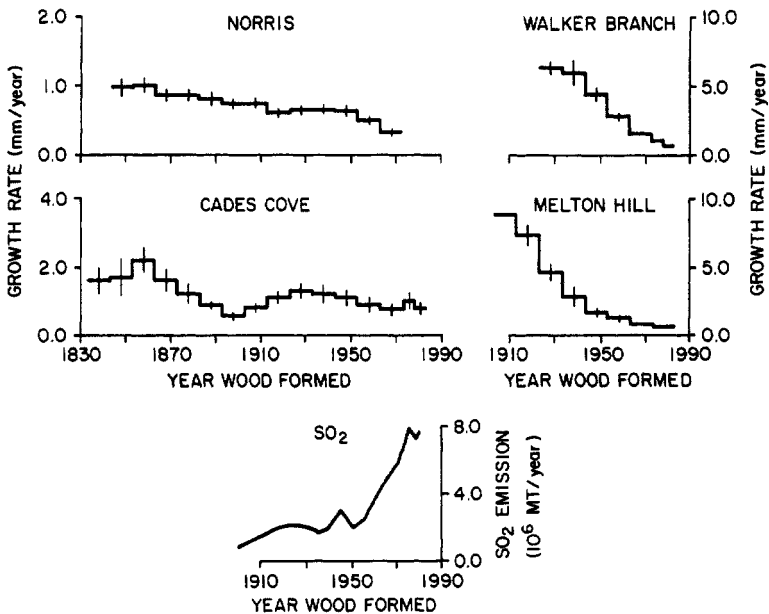
Figure 1.8 Mean growth rate of short-leaf pine at four sites in East Tennessee, and estimated SO_2 emissions upwind from within 900 km southeast–southwest of Cades Cove, Tennessee (Baes and McLaughlin 1984).
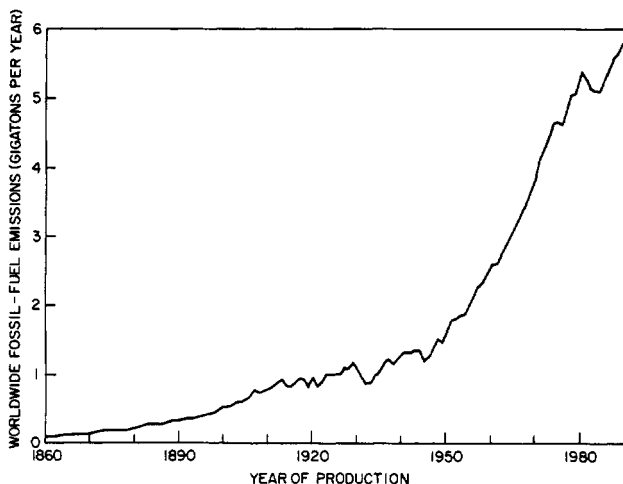
Figure 1.9 Worldwide fossil fuel emissions in gigatons of carbon per year as a function of time, 1860 AD to present (Post *et al* 1990).

as a function of the year in which the wood was formed, going back to 1830. At the bottom center are the estimated SO_2 emissions from within 900 km upwind, southeast–southwest of the area in which the data in the above four graphs were taken, from the year 1910 until recently. There appears to be a definite correlation between the increase in SO_2 production, and the decrease in growth rate of these pines. Where the growth rate has gone to zero at two locations, the trees become vulnerable to insect attack and diseases, and whole forests of these trees are dying.

Another major environmental effect of our energy-intensive lifestyles has been the accumulation in the upper atmosphere of so-called *greenhouse gases*, molecules which interact only weakly with solar radiation as it enters the atmosphere, but strongly with the re-radiated infra-red radiation from the Earth's surface. The effect of these gases is to act like the glass panes in a greenhouse, trapping radiation in the atmosphere and thus warming it. The most important single greenhouse gas is carbon dioxide, the significance of which was first to be recognized.

The SO_2 and NO_x emissions discussed previously are a minor component of the total emissions resulting from fossil fuel combustion, which are dominated by carbon dioxide (CO_2). The total worldwide emissions of fossil fuel combustion are plotted in gigatons per year in figure 1.9, taken from Post *et al* (1990), for the period from 1860 to the present. The enormous growth in fossil fuel emissions from the start of the industrial revolution is evident. These CO_2 emissions are accumulating in the atmosphere, as indicated in figure 1.10, also taken from Post *et al* (1990). This figure shows the atmospheric concentration of CO_2, in parts per million, from the year 1000 AD to the present.
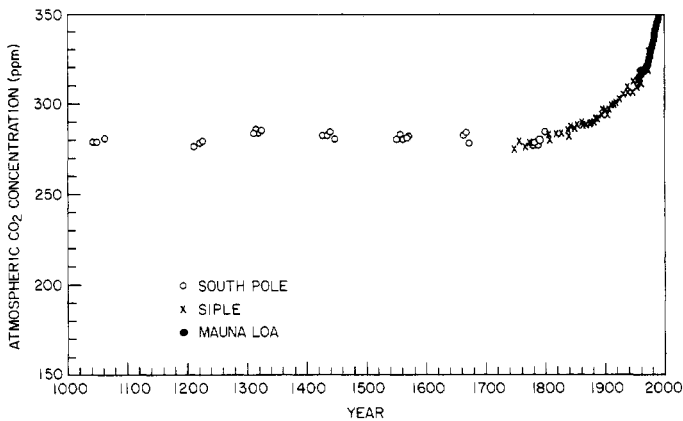
Figure 1.10 The concentration of atmospheric CO_2, in parts per million, from the year 1000 AD to the present. The Mauna Loa data represent direct measurements; the two other data sets are from air trapped in Antarctic ice (Post *et al* 1990).

These data consist of direct measurements at the Mauna Loa observatory in Hawaii after 1957, and measurements of air trapped as bubbles in Antarctic ice cores prior to that time. The 'normal' CO_2 concentration is about 280 parts per million, but is now at 351 ppm and rising.

Carbon dioxide is not the only greenhouse gas. Ozone, methane, nitrous oxide, and chlorofluorocarbons also contribute to global warming. Attempts have been made to assess the effects of these greenhouse gases on the world climate. The atmospheric concentration of these gases, based on known production rates, is assumed as input to computer models. The approximate temperature rise worldwide due to CO_2, and these other greenhouse gases is shown in figure 1.11, taken from McElroy (1988) for present and anticipated levels of these gases.

In figure 1.11, the solid curve running up to the present is the result of a five-year running average of measured data. The three curves projected into the future result from three sets of input assumptions. Scenario A is the consequence of continued growth of greenhouse gas emissons at the current rate. Scenario B assumes that the emissions of greenhouse gases remain at current levels, and scenario C is the result of a massive international effort to curb greenhouse gas emissions starting in the 1990's. The existing climatic models are uncertain, and it is only with great difficulty that the climatic effects of greenhouse gas emissions can be distinguished from natural fluctuations in the yearly average temperature, as is evident on figure 1.11.

There is a lack of agreement as to the quantitative validity of the models that relate greenhouse gas emissions to the temperature rise in
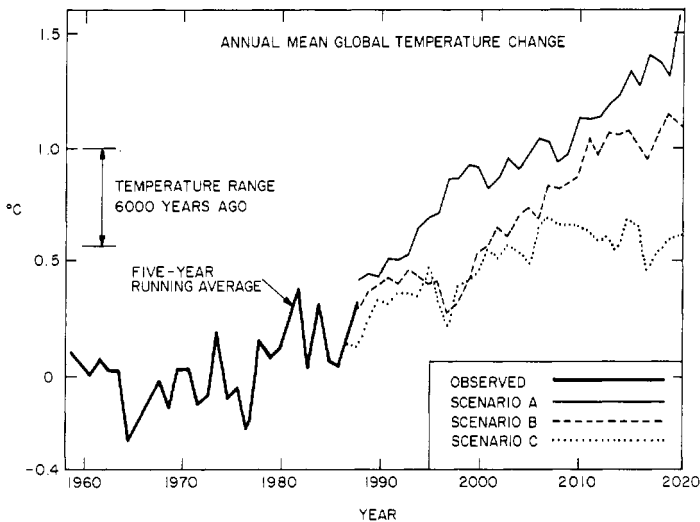
Figure 1.11 Annual mean global temperature change from three computer models: (A) continued growth of greenhouse gas emissions at the current rate; (B) emissions remain at current levels; (C) massive international effort is made to curb pollution in the 1990's (McElroy 1988).

the world's climate. There is further disagreement about the possible significance of a given rise in the average temperature. Perhaps the most valid model for assessing the significance of a rise in the carbon dioxide concentration is the past history of the Earth itself. On figure 1.12 is shown the carbon dioxide concentration and the average temperature for the past 160 000 years. These data are taken from ocean core sediments in a manner described by Gribbin (1989). There has been a very close correlation between the carbon dioxide level and the average temperature over this period of time. Detailed examination of these data indicate that changes in the carbon dioxide level *preceeded* changes in ice cover and temperature, suggesting that the carbon dioxide is a causative agent. It is not reassuring to note that the present carbon dioxide level, indicated on figure 1.12, is off-scale, and is far higher than it has been over the last 150 000 years. Other data indicate that the present level, 351 ppm, is higher than it has been in several million years. There is virtual unanimity among recent climatic models that increasing levels of these greenhouse gases will lead to a warming of the Earth's atmosphere.

The buildup of greenhouse gases in the Earth's atmosphere will have far-reaching effects. In North America, both the temperature and rainfall will increase at high latitudes, but in most of the world's industrialized countries, the climate not only will be hotter but there will be less rainfall in major food-producing areas. The global warming indicated in figure 1.11 will itself have a number of additional effects, including
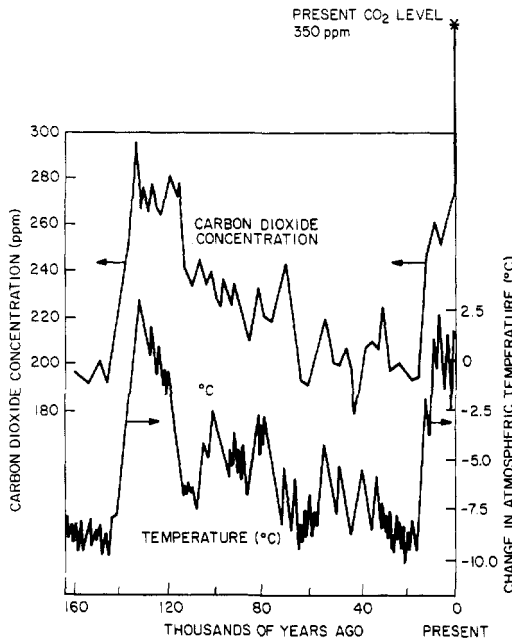
Figure 1.12 Variations of carbon dioxide levels and global temperature over the past 160 000 years. The present CO_2 levels indicated in figure 1.10 are off-scale at the upper right. Changes in carbon dioxide level have preceded corresponding changes in ice cover (Gribbin 1989).

significant increases in sea level. Part of this will be due to thermal expansion of the water column in the oceans, and part will be due to melting of major glaciers and ice fields. On figure 1.13, taken from Anon. (1989), is an indication of the coastal flooding that can be expected in Great Britain during the next century as the result of projected global warming, as an example.

Global warming will also have an effect on the growth of trees. An example is shown in figure 1.14, taken from Roberts (1989). On the left is a map of North America which shows the current range of beech trees, a common deciduous tree in the eastern United States, both at present, and its potential future range as the result of global warming. The range of beech trees will move far to the north, with a relatively limited region of overlap. On the right is a more severe scenario involving more global warming, in which the potential future range of beech trees has been pushed up into northern Canada, and there is almost no overlap with the current range of these trees. For these reasons, one must expect to observe entire forests dying, as the world climate warms up and becomes too hot for trees to thrive where they are located. Moreover, there is some
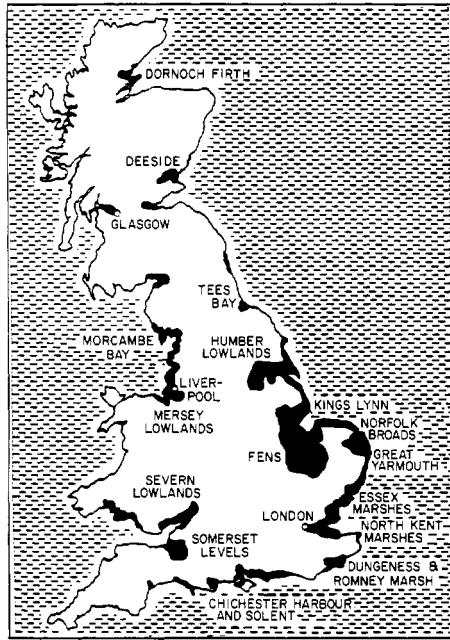
Figure 1.13 The black areas on the coast of Great Britain are likely to be inundated by projected rises in sea level of 0.5 to 1 m (Anon. 1989).
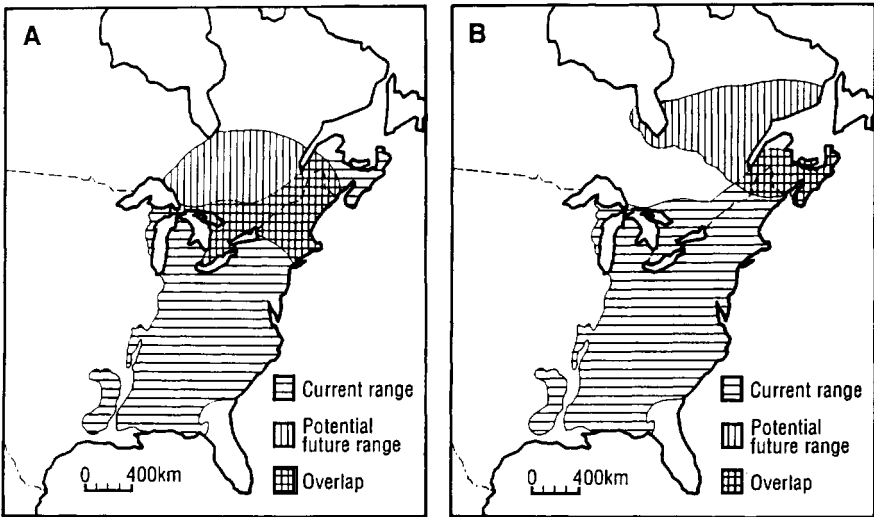
Figure 1.14 Current and future range of beech trees under two greenhouse models: (A) a mild model, (B) a more severe model (Roberts 1989).

concern that slow-growing species will not be able to migrate north fast enough, and may become extinct for this reason.

1.3 THE SOCIAL ROLE OF INDUSTRIAL PLASMA ENGINEERING

It appears that in order to maintain our lifestyles and incomes at their present levels, while sharing the benefits of modern industrialized society with currently non-industrialized countries, the efficiency and effectiveness of our energy consumption must increase on a global scale. Industrial plasma engineering will surely have an important role to play in increasing the efficiency and effectiveness of major energy-consuming processes used in industry.

Plasmas offer two primary characteristics of industrial interest. Plasmas can have temperatures and energy densities higher than can be achieved by chemical or other means; and plasmas can produce energetic *active species* which initiate physical changes or chemical reactions that can occur only with difficulty or not at all in ordinary chemical reactions. Active species can include ultraviolet or visible photons; charged particles, including electrons, ions, and free radicals; and highly reactive neutral species, such as reactive atoms (O, F, etc), excited atomic states, and reactive molecular fragments, such as monomers.

Industrial plasma engineering offers benefits over other industrial processing methods which include the ability to accomplish industrially relevant results more efficiently and cheaply than competing processes; it can perform tasks which can be achieved in no other way; it usually can accomplish results without producing large volumes of unwanted byproducts or waste materials; and it can usually accomplish results with minimal pollution or production of toxic wastes. Some of these applications are indicated on table 1.2.

An excellent example of the reduction in waste production and energy consumption possible by using plasma-related methods is taken from Chapter 14, and has been published by Rakowski (1989). Rakowski compared the resource requirements to achieve the printability of woolen cloth using a conventional chlorination process with an equally effective low pressure plasma treatment. He found that, compared to the conventional chlorination process, the low pressure (2–6 Torr) plasma modification of 120 tonnes/year of wool saves 27 000 m^3 of water, 44 tonnes of sodium hypochlorite, 16 tonnes of sodium bisulphite, 11 tonnes of sulfuric acid, and 685 MWh of electrical energy. When used in the conventional process, these resources produce unwanted or toxic waste products, and occupational hazards to workers. In addition, the comparative energy costs of producing a kilogram of printable woolen cloth are

Table 1.2 The social roles of industrial plasma engineering.

1. More efficient energy utilization
   a) Plasma lighting devices
   b) Plasma chemistry
   c) Materials processing with thermal plasma
2. Accomplishing unique results
   a) Electron, ion, and plasma sources
   b) Circuit interruption
   c) New materials from plasma chemistry
   d) Plasma etching and deposition for microelectronics
   e) Materials processing with thermal plasma
   f) Communications using geophysical plasmas
   g) Space propulsion systems
   h) Electrostatic precipitators and paint spraying
   i) Surface modification of materials
3. Production with minimum waste materials
   a) Plasma chemistry
   b) Plasma etching and deposition for microelectronics
   c) Materials processing with thermal plasma
   d) Surface treatment of materials
   e) Ion implantation of materials
4. Production with minimum toxic wastes
   a) plasma chemistry
   b) plasma etching and deposition for microelectronics
   c) Surface treatment of materials
   d) Ion implantation of materials

7 kWh/kg wool for the conventional chlorination process, and from 0.3 to 0.6 kWh/kg wool for low pressure plasma treatment. Many similar examples abound in the literature of industrial plasma engineering.

1.4 IMPORTANT DEFINITIONS

The scientific study of plasma became possible in 1808 with the development by Sir Humphry Davy of the steady-state DC arc discharge, and with the development of the high voltage DC electrical discharge tube by Michael Faraday and others in the 1830's. Plasma was identified as a fourth state of matter by Sir William Crookes in 1879. In this view, as one adds heat to matter starting at low temperatures, it starts out as a solid, melts to form a liquid, then vaporizes to become a gas. Finally, if still more heat is added, the temperature rises, and the individual atoms break apart into electrons and positively charged ions, thus forming a fourth state of matter. The term *plasma* was introduced by Irving Langmuir in 1928, by which he meant an approximately electrically neutral

Table 1.3 Origin of electrical discharge nomenclature.

Date	Term	Meaning	Originator
Circa 1750	Positive plus	charge excess	B Franklin
Circa 1750	Negative 'minus'	Charge deficit	B Franklin
Circa 1821	Arc	Arched electrical discharge	H Davy
Circa 1834	Electrode	'Electrical road'	M Faraday
	Anode	'Road up'	
	Cathode	'Road down'	
	Ion	'To go'	
	Anion	That which goes to anode	
	Cation	That which goes to cathode	
Circa 1891	Electron	Discrete charge	G T Stoney
Circa 1906	Electron	Particle	H A Lorentz
Circa 1925	Sheath	Plasma boundary layer	I Langmuir
Circa 1928	Plasma	Fourth state of matter	I Langmuir

collection of ions and electrons which may or may not contain a background neutral gas, and which is capable of responding to electric and magnetic fields.

Plasma physics is a division of the discipline of physics concerned with the basic laws and physical processes which govern the behavior of plasma. Two important sub-areas of plasma physics are *magnetohydrodynamics* (MHD), which is concerned with the behavior of electrically conducting fluids (including plasma) in magnetic fields; and *electrohydrodynamics* (EHD), which is concerned with the behavior of electrically charged fluids (or particles) in electric fields.

Plasma chemistry is a branch of the discipline of chemistry that concerns itself with chemical reactions which occur in the presence of a plasma. Such reactions can involve chemical reactions in which only a plasma (including its neutral gas) is a participant, or in which the components of a plasma or plasma–chemical reaction products interact with solid surfaces or liquids.

Plasma science or *plasma engineering* is concerned with the application of plasma to devices or processes. Plasma science can also concern itself with sources of energetic matter and radiation, including particle beam sources, RF and microwave power sources, lasers, plasma light sources, and plasma sources and torches. *Industrial plasma engineering* includes the design or application of industrial devices, processes, or products which utilize plasmas. The origin of some additional nomenclature of plasma science is listed in table 1.3.

1.5 HISTORICAL DEVELOPMENT OF PLASMA PHYSICS AND ENGINEERING

1.5.1 Historical Milestones

Table 1.4 lists some significant events in the historical development of plasma physics and plasma engineering. At the start of the 17th century, Sir William Gilbert introduced some of the basic concepts that we still use to describe electric and magnetic phenomena. The invention of the *Leyden jar* by E G von Kleist in 1745, a primitive capacitor shown in figure 1.15, made it possible to store significant amounts of charge and to achieve high static electric potentials. The Leyden jar allowed Benjamin Franklin to perform experiments in the 1750's which substantiated the single fluid theory of electricity, and to identify lightning as a form of electricity. It was Franklin who introduced the concept of positive and negative polarity. In his original single fluid theory, a positive polarity implied an excess of the positive fluid, and negative polarity implied a deficit of this electrical fluid. Franklin was probably the first electrical engineer, since he invented the lightning rod, thus avoiding much property damage and loss of life.

Rapid progress was made in electrical discharge physics during the 19th century, nearly all of it in a few laboratories in England and Germany. In the early 19th century, Sir Humphry Davy and Michael Faraday worked at the Royal Institution in London with electrical arcs and DC electrical discharge tubes operating at low pressure. They made many discoveries which were described by terminology which was selected by Michael Faraday with the assistance of Greek scholars of the period—terminology which is listed on table 1.3 and is used to this day.

The existence of the electron was suspected for many years before 1895, when Sir Joseph John Thomson made definitive and quantitative observations that are now identified as the formal discovery of the electron. The term *electron* was first introduced by G J Stoney in 1891, who meant by it a massless, photon-like collection of charge but this term did not assume its present meaning until H A Lorentz suggested in 1906 that it be used to describe the particle discovered by J J Thomson in 1897. In the year 1898, Sir William Crookes introduced the term *ionization* to describe the breakup of the neutral atom into an electron and a positive ion. In the 1920's Irving Langmuir introduced the terms *sheath* and *plasma*, which are still in use.

Arc and DC electrical discharge plasmas were extensively researched in scientific laboratories during the 19th century. The only widespread application of plasmas during the 19th century was the use of electrical arcs for illumination, a technology which for a time was competitive with gaslights, but by 1900 lost out to the incandescent lamp because

Table 1.4 Advances in electrical discharge physics.

Date	Contribution/Concept	Originator
Circa 1600	Electricity	W Gilbert
	Magnetic pole	W Gilbert
	Magnetic field line	W Gilbert
1742	Sparks	J T Desagulliers
1745	'Leyden' jar	E G Von Kleist
Circa 1750	Single fluid theory of electricity	B Franklin
Circa 1752	Identifcation of lightning as electricity	B Franklin
1808	Diffusion	J Dalton
	Arc (discharge)	H Davy
1817	Mobility	M Faraday
1836	Moving striations (unpublished)	M Faraday
1848	Moving striations (published)	A Abria
1860	Mean free path	J C Maxwell
1862	Toepler vacuum pump ($\sim 10^{-3}$ Torr)	A Toepler
1876	Cathode rays	E Goldstein
1879	Fourth state of matter	W Crookes
1880	Paschen curve	W de la Rue, H Müller
1889	Maxwell–Boltzmann distribution	W Nernst
1895	X-rays	W C Rontgen
1897	Electron (particle)	J J Thomson
1897	Cyclotron frequency	O Lodge
1898	Ionization	W Crookes
1899	Transport equations	J S Townsend
	Energy gain conditions	H A Lorentz
1901	Townsend coefficients	J S Townsend
1905	Diffusion of charged particles	A Einstein
	Mercury rotary pump ($\sim 10^{-5}$ Torr)	W Gaede
1906	Plasma frequency	Lord Rayleigh
1911	Mercury diffusion pump ($\sim 10^{-5}$ Torr)	W Gaede
1914	Ambipolar diffusion	H Von Seeliger
1921	Ramsauer effect	L W Ramsauer
1925	Sheath	I Langmuir
1928	Plasma	I Langmuir
1929	Debye length	P J W Debye
1935	Velocity distribution functions	W P Allis
	Rotary oil forepump	W Gaede
1955	Oil diffusion pump	
1965	Turbomolecular pump	

of its requirement for high current DC electrical power transmission. Plasma research was stimulated during the 1920's by the development of magnetoionic theory, a major theoretical development in modern plasma
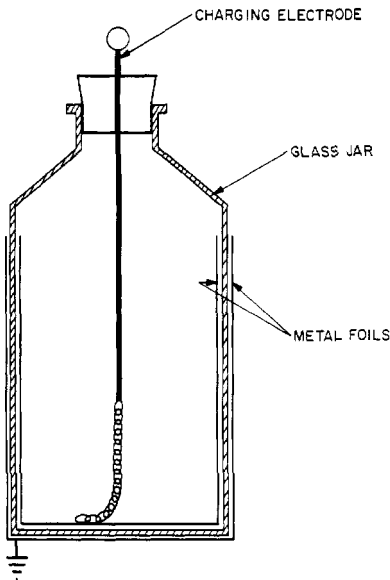
Figure 1.15 The Leyden jar, invented by E G von Kleist, 1745.
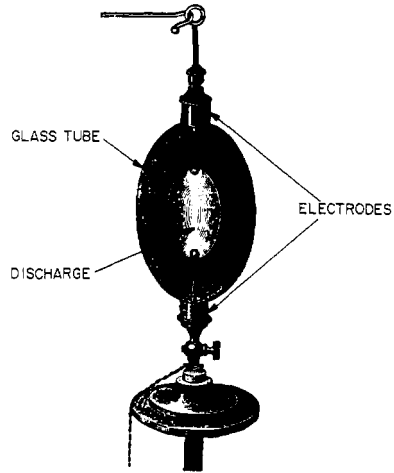
Figure 1.16 The 'Electric Egg' of Crookes, circa 1870, designed to illustrate the influence of pressure on the electrical discharge between two electrodes (Brown 1978).

physics. In the 1930's, commercial research on MHD power generators began in the United States. Plasmas were generated by microwave discharges in the late 1940's, after the development and flourishing of microwave technology for radar during the Second World War.

A major impetus to plasma physics has been controlled fusion research, which began in the major industrialized countries about 1950 and continues to the present day. Most of the current activity in plasma physics at universities and national laboratories originated in the attempt to create and magnetically confine high temperature plasmas of fusion interest. Since 1970, plasmas have been extensively used in the microelectronics industry for the deposition and dry etching processes necessary for the fabrication of microelectronic circuits. Other industrial plasma processing applications have been developed recently and are the subject of later chapters in Volume 2 of this book.

1.5.2 History of Electrical Discharges

The electrical discharges which today find such widespread applications have a long history going back to the origins of modern scientific research. On table 1.4 is a list of major advances or events in electrical
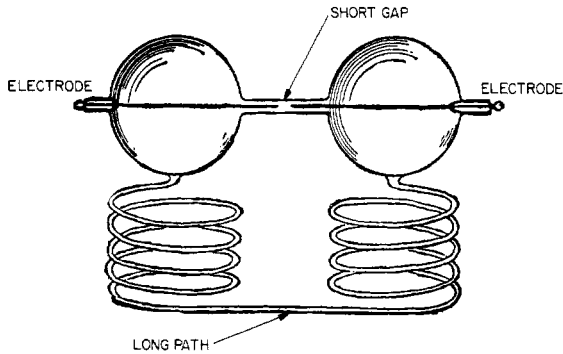
Figure 1.17 Hittorf tube, circa 1884, used to demonstrate the Paschen effect (Brown 1978).
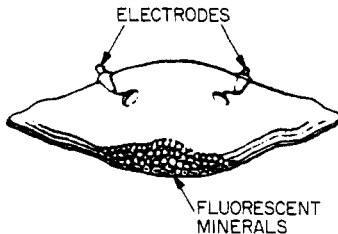
Figure 1.18 A discharge tube to illustrate the fluorescence of chemicals, ores, and rocks when exposed to a low pressure electrical discharge, due to J Plucker, circa 1859 (Brown 1978).

discharge physics. The behavior of low pressure DC electrical discharges in gases was studied by many English and German physicists of the 19th century, who developed various evacuated tubes to illustrate the strange behavior of the 'fourth state of matter'. These investigations have been summarized in a short article by Sanborn C Brown (1978). Most of the illustrations used here are from a lecture by W Crookes (1879).

On figure 1.16 is shown the *electric egg* which was used to demonstrate the effect of lowering the pressure on an electrical discharge at the center. Figure 1.17 shows the *Hittorf tube* of 1884 which demonstrates the *Paschen effect* whereby, at low pressures, the discharge takes place through the long tube and not across the small gap between the metal electrodes.

When an electrical discharge is drawn between two electrodes in an evacuated tube, *cathode rays* cause fluorescence of the glass wall of the vacuum vessel. Cathode rays also cause fluorescence of a large number of chemicals and ores placed inside the tube, as shown in figure
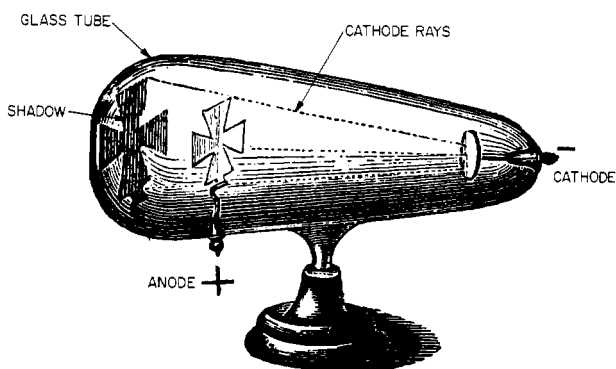
Figure 1.19 An electrical discharge tube designed to illustrate that 'cathode rays' travel in straight lines, and leave a shadow of the anode on the fluorescing wall of the glass tube (Brown 1978).
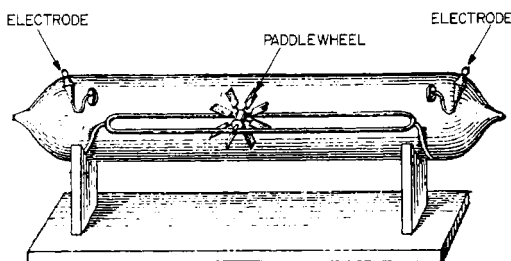
Figure 1.20 The 'railway tube', designed to show that cathode rays were capable of producing a mechanical force on the vanes of a small paddlewheel which moved between the electrodes, from cathode to anode. Due to W Crookes, 1879 (Brown 1978).

1.18, after the investigations carried forward by J Plucker in 1859. Well before the electron was discovered, the phenomenon of cathode rays was established by such experiments as those of J W Hittorf in 1869, shown in figure 1.19. This experiment illustrated that cathode rays, originating at the right, are blocked by an opaque metal anode, which leaves a shadow on the fluorescing glass surface.

The mechanical effects of cathode rays were illustrated by the *railway tube* of W Crookes in 1879, shown in figure 1.20. Cathode rays, originating at the negative electrode, strike the mica vanes of a small paddlewheel, which then is driven to the opposite end of the tube. The cathode rays from a concave cathode were focused on a platinum foil at cathode potential in the Crookes tube shown in figure 1.21, and raised the platinum foil at the focus to incandescence. At about the same time, Thomas Edison noted the *Edison effect*, wherein he was able to
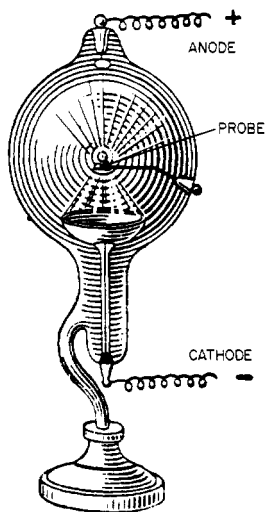
Figure 1.21 A tube designed to show the heating effects of cathode rays which come to a focus and heat a foil to incandescence, due to G H Wiedemann, 1891 (Brown 1978).
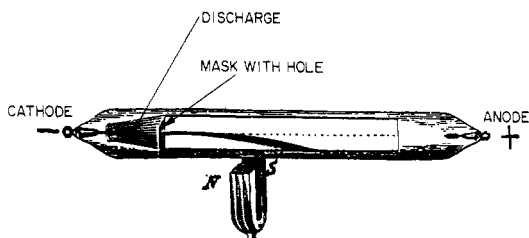
Figure 1.22 An electrical discharge tube designed to illustrate the deflection of cathode rays by a magnetic field, due to J J Thomson, 1897 (Brown 1978).

draw a current between an incandescent cathode filament, and another metallic electrode within the glass envelope. It was found that cathode rays could be deflected by electric and magnetic fields in the manner shown in figure 1.22, which is very similar to the classic experiment of J J Thomson of 1897. Finally, Crookes in the 1890's developed the *focus tube* shown in figure 1.23, in which cathode rays bombard the anode, set at an angle which emits x-rays through the glass wall of the tube to expose photographic plates or cause minerals to fluoresce.
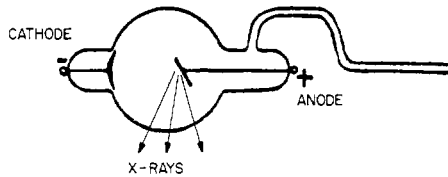
Figure 1.23 A Crookes 'focus tube', circa 1895, of the type Röntgen used in his discovery and investigation of x-rays (Brown 1978).

Other important concepts and discoveries are listed in table 1.4. One of the most important technical advances for DC electrical discharges was the development of adequate vacuum pumps. The mercury-piston pump of August Toepler reached pressures down to approximately 1 mTorr, but had a very slow pumping speed. The field of gaseous discharge physics owes a great debt to the German engineer Wolfgang Gaede, who in 1905 introduced the rotary mercury pump which made what were, for the time, very high pumping speeds possible at base pressures down to 10^{-5} Torr. Gaede later introduced the mercury diffusion pump in 1911, and the modern rotary oil forepump in 1935.

1.6 PLASMA PHYSICS REGIMES AND ISSUES

1.6.1 Density–Temperature Regimes

On figure 1.24 is a two-dimensional representation of the plasma number density and kinetic temperature regimes for various research and industrial applications. The electron kinetic temperature axis is expressed in electronvolts, with one electronvolt (eV) being equal to 11 605 degrees kelvin (K); see equation (2.17). Man-made plasmas range from near room temperature to temperatures comparable to those found in the interior of stars. The range of densities spans more than 20 orders of magnitude, from that characteristic of interplanetary space, to densities approaching that of solids. Most plasmas of industrial significance fall between 1 and 20 eV in kinetic temperature, with electron number densities that range from 10^{12} to 10^{25} electrons/m^3.

1.6.2 Heterogeneous Interactions of Plasma

Plasma can interact with other states of matter individually, or with combinations of solids, liquids, and gases. When electrons and ions interact with neutral gases, the relatively high kinetic temperature of the electrons and ions can cause dissociation, ionization, and plasma
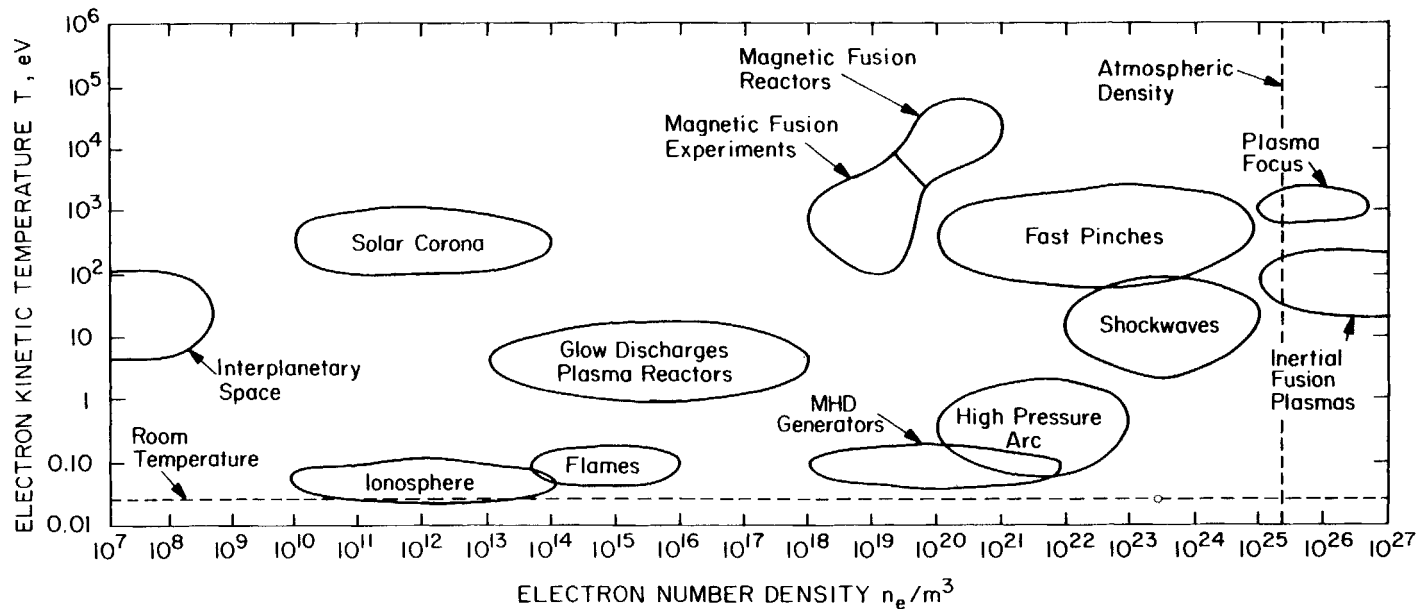
Figure 1.24 Operating regimes of various natural, research, and industrial plasmas (Book 1990, Roth 1986, Cobine 1958).

chemical reactions with the neutral gas. The interaction of plasma with liquids is relatively little studied, but such interactions form bubbles, and fluid dynamic boundary layers as well as sheaths by volatization of the liquid. When plasmas interact directly with solid walls, they form an electrostatic sheath between the plasma and the wall. This sheath is characterized by a rapid, approximately exponential drop in density and a significant electrostatic potential drop which can accelerate ions across the sheath to hit the wall with relatively high energies. This process is widely used in plasma etching for microelectronics, and in coating surfaces with thin films by sputtering.

1.6.3 Approaches to the Study of Plasmas

Three distinct approaches are found in the literature of plasma physics. In the continuum approach, of which magnetohydrodynamics and electrohydrodynamics are examples, a plasma is treated as if it were a continuous fluid. This theoretical approach is a branch of fluid mechanics, and only macroscopic parameters are used to describe the plasma properties. This approach is dominant in the area of thermal plasmas and magnetohydrodynamic power production.

A second major theoretical approach to the study of plasma is to regard it as a collection of individual particles, and its collective behavior as the result of their motion. In this approach, plasma theory becomes a branch of dynamics, and the plasma is described by microscopic variables which are statistically averaged over the particle distribution functions, usually assumed to be Maxwellian. This is the theoretical approach appropriate for most branches of industrial plasma engineering, although many industrial glow discharge plasmas have non-Maxwellian electron energy distribution functions.

A third major approach to the study of plasmas, unfortunately much too common in industrial plasma engineering, is to regard the plasma as a black box with inputs and outputs. The desired output of a plasma-related process is achieved by adjusting inputs until the desired result is achieved. In this approach, no serious attempt is made to understand the plasma-physical processes occuring in the black box. The isolation of workers in many branches of industrial plasma engineering is in part a result of this lack of understanding of the common physical processes which underlie many industrial applications of plasma.

1.6.4 The Challenges of Plasma Physics

The complete description of a fully ionized plasma using the individual particle or microscopic approach is a multi-body problem, because of the long-range Coulomb forces which act between each and every charged particle in the plasma. Attempts to reduce such a multi-body problem

to a mathematically tractable form usually result in approximations which reduce confidence in the results obtained, and sometimes lead to erroneous results.

Another difficulty is that the differential equations which describe the conservation of particles, momentum, and energy in plasmas are often nonlinear. Such nonlinear equations do not, in general, have a finite number of solutions, or closed form solutions expressed as standard mathematical functions. Indeed, even if one is fortunate enough to find a closed form solution to a nonlinear problem, one has no assurance that the plasma will behave as predicted by that particular mathematical solution. The wide prevalence of nonlinear differential equations in the description of plasma contrasts with other fields, like classical electrodynamics, where the basic equations are linear, and unique solutions can be obtained rigorously in closed form.

Other reasons why plasma-related research and development is so challenging is that plasma experiments are usually difficult to set up and interpret. Boundary conditions are often sensitive and critically important determinants of the behavior of the plasma. Plasma behavior is also often governed by a large number of parameters, resulting in a multi-variable problem in which the interpretation of experimental results is complicated by inadequate control of all parameters which affect the results. Because of their high energy density, industrial arc plasmas, for example, are difficult to create and maintain, particularly in the steady state, and usually involve high heat fluxes, high power densities, and extremes of other operating conditions.

Plasma, because of its high kinetic temperature and high energy density, is difficult to diagnose. Perturbing probes inserted into it can be damaged or destroyed. In many cases when a perturbing probe can be maintained in a plasma, it so changes the plasma characteristics that the probe is useless in determining the unperturbed state of the plasma. The subject of plasma diagnostics has gradually evolved in recent decades, and techniques are now available to measure most of the important plasma parameters with non-perturbing methods, although the equipment and methods are often expensive and relatively complex.

Magnetic fusion research has developed a wide variety of plasma diagnostic instruments and methods, many of which could provide useful information about industrially relevant plasmas which operate in the same or similar plasma density and temperature regimes. However, many fusion diagnostic instruments are too expensive for routine application to industrial plasmas (laser Thomson scattering is a good example). Another difficulty is that the different density and temperature regime appropriate to industrial plasmas (as shown on figure 1.24 for example) may move the industrial plasma outside the density and temperature ranges where fusion-relevant diagnostic instruments can produce valid data.

1.7 PROFESSIONAL INTERACTIONS IN PLASMA SCIENCE

1.7.1 The Scientific Journal Literature

The international scientific literature offers a wide range of archival journals in which plasma-related papers may be published. Some of the most widely used archival journal outlets in plasma science are listed in table 1.5. A cross ($\times$) in a particular entry of the table means that that journal publishes, at least occasionally, papers on the aspect of plasma research and development indicated. The first two columns refer to the theoretical and experimental aspects of plasma physics. The third and fourth columns refer, respectively, to the theoretical and experimental aspects of plasma applications. Because of the large amount of effort in the field of fusion research, fusion physics and technology have their own journals, and these are indicated in the fifth and sixth columns of table 1.5. Finally, those journals that publish papers on industrial plasma applications are indicated in the last column.

1.7.2 Scientific Conferences

The archival journals shown in table 1.5 contain a record of completed and reviewed work in the field of plasma science. Researchers in most plasma-related fields also present progress reports of ongoing work, as well as their most recent results at the plasma-related scientific conferences listed on table 1.6, which is confined, for the most part, to conferences held in North America. This table lists the formal name of the conference, the international scientific body or professional society which sponsors it, the frequency with which the conference is held, and finally, in the manner of table 1.5, a listing of which sub-areas of plasma-related research are covered most heavily at these conferences. Other conferences are held regularly in Asia and Europe.

1.7.3 International Scope of Industrial Plasma Engineering

The industrial applications of plasma are part of the infrastructure of all of the major industrialized countries, and is of academic and commercial interest in industrializing countries because of its importance for many high-tech industrial processes. Until the decade of the 1980's, the relatively small number of academic and full time industrial engineers active in this field had few outlets at which they could share results and maintain contact. Prior to 1980, a principal forum for industrial plasma engineering papers was the Gordon Research Conference on Plasma Chemistry, held in the summers of even-numbered years in the United States. This series of conferences terminated in 1992. Other than this,

Table 1.5 Plasma-related archival journal literature.

Journal	Theor. Plasma Physics	Exptl. Plasma Physics	Theor. Plasma Science	Exptl. Plasma Science	Fusion Physics	Fusion Technology	Industrial Plasma Applications
Appl. Phys. Lett.		×	×	×			×
Commun. Plasma Phys.	×				×	×	
Fusion Technology					×	×	
IEEE Trans. Plasma Sci.	×	×	×	×			×
J. Appl. Phys.		×	×	×			×
J. Fusion Energy					×	×	
J. Geophys. Res. A	×	×	×	×			
J. Plasma Phys.	×	×	×	×	×		×
Nuclear Fusion	×				×	×	
Nucl. Instrum. & Methods A		×		×		×	
Physics of Plasmas	×	×	×	×	×		
Phys. Rev. A	×		×				
Phys. Rev. Lett.	×	×	×		×		
Plasma Phys. & Control. Nucl. Fusion	×	×	×	×	×		×
Plasma Sources, Sci. & Technol.		×	×	×			×
Rev. Sci. Instrum.		×		×		×	×
J. Vacuum Sci. & Technol. B		×	×				×
Plasma Chem. & Plasma Proc.	×		×	×			×

Table 1.6 Plasma-related scientific conferences.

Conference	Sponsor	Frequency	Theor. Plasma Physics	Exptl. Plasma Physics	Theor. Plasma Science	Exptl. Plasma Science	Fusion Physics	Fusion Technology	Industrial Plasma Applications
APS Plasma Physics Division Meeting	APS	Annual	×	×	×	×	×	×	
Gaseous Electronics Topical Conference	APS	Annual		×	×	×			×
International Conference on Plasma Science	IEEE	Annual	×	×	×	×			×
International Symposium on Plasma Chemistry	IUPAC	Odd years			×	×			×
Gordon Conference on Plasma Chemistry	AAAS	Even years			×	×			×
International Conference on Phenomena in Ionized Gases	IUPAP	Odd years	×	×	×	×			×
Topical Conference on RF Power in Plasmas	APS	Odd years			×	×	×	×	×
Symposium on Fusion Technology	IEEE	Odd years				×	×	×	
Topical Conference on Fusion Energy	ANS	Even years					×	×	
American Vacuum Society Meetings	AVS	Annual		×	×	×		×	×

papers in this area appeared in very scattered outlets. This situation has changed for the better in recent years, with journals such as the *Review of Scientific Instruments* and several other of the journals and scientific conferences listed above now receptive to papers and reports in the field of industrial plasma engineering.

On a global scale, Europe is probably the leading regional grouping of countries in the field of industrial plasma engineering at this time, both in terms of the amount of research in academic institutions, and active, full time research efforts in industry. The International Union of Pure and Applied Chemistry (IUPAC) recently published an international listing of plasma chemistry laboratories engaged in plasma processing research of a kind covered in Chapters 14 through 18 of this text (Boulos 1993). Europe had far more listings in this directory, 114, than any other regional grouping of countries. After Europe, Japan was in second place, with 45 listings. These listings were approximately equally divided between academic and industrial institutions. The United States was in third place, with 39 listings. While Japan's interest in industrial plasmas is largely focused on microelectronic-related technologies, the interests of Europe and Canada are in thermal plasmas, the subject of Chapter 19.

In the field of industrial plasma engineering, the United States occupies a rank inferior to those of the entities mentioned above. While applications of plasma are found throughout U.S. industry, few industrial laboratories are studying plasmas systematically, or doing plasma-oriented research and development on a full time basis, or with a significant commitment of resources. This situation can be traced to the dominance of fusion research in U.S. universities, unwillingness of industry to enter into research and development in this field, and lack of support for industrial plasma engineering research and development by federal government agencies in the United States. The inadequate state of research and development in the field of industrial plasma engineering was documented in a report entitled 'Plasma Processing of Materials', put out by a panel of the U.S. National Academy of Sciences' National Research Council (Anon. 1991).

REFERENCES

Anon. 1989 East Coast of Britain Will Bear the Brunt of Rising Sea Levels *New Scientist* 1 July 1989 p 38

Anon. 1991 *Plasma Processing of Materials: Scientific Opportunities and Technological Challenges* (Washington DC: National Academy Press) ISBN 0-309-04597-5

Baes C F III and McLaughlin S B 1984 Trace Elements in Tree Rings: Evidence of Recent and Historical Air Pollution *Science* **224** 494–497

Book D L 1990 *NRL Plasma Formulary* NRL Publication 177-4405 (Washington, DC: Naval Research Laboratory) pp 40–41

Boulos M I 1993 *Plasma Chemistry Research Directory, PCRD-93* (Sherbrooke, Canada: IUPAC Subcommittee on Plasma Chemistry)

Brown S C 1978 A Short History of Gaseous Electronics, in: Hirsh M N and Oskam H J (ed) *Gaseous Electronics* vol I (New York: Academic Press) ISBN 0-12-349701-9 ch 1, pp 1–18

Cobine J D 1958 *Gaseous Conductors* (New York: Dover Publications) ch 1

Crookes W 1879 Radiant Matter *Lecture to the British Association for the Advancement of Science (Sheffield, 22 August 1879)*

Francis D R 1987 Canada Acts on Acid Rain, Looks to U.S. *Christian Science Monitor* 6 April 1987 p 11

Gibbons J H and Blair P D 1991 U.S. Energy Transition: On Getting from Here to There *Physics Today* July 1991 pp 22–30

Gribbin J 1989 The End of the Ice Ages? *New Scientist* 17 June 1989 pp 48–52

McElroy M 1988 The Challenge of Global Change *New Scientist* 28 July 1988 pp 34–36

Perry H and Landsberg H H 1977 *Projected World Energy Consumption in Energy and Climate* (Washington, DC: U.S. National Research Council) pp 35–50

Post W M, Peng T-H, Emanuel W R, King A W, Dale V H and DeAngelis D L 1990 The Global Carbon Cycle *American Scientist* **78** 310–326

Rakowski W 1989 Plasma Modification of Wool Under Industrial Conditions *Melliand Textilberichte* **70** 780–785

Roberts L 1989 How Fast Can Trees Migrate? *Science* **243** 735–737

Roth J R 1986 *Introduction to Fusion Energy* (Charlottesville, VA: Ibis Publishing) ISBN 0-935005-07-2 ch 2

Schwartz S E 1989 Acid Deposition: Unraveling a Regional Phenomenon *Science* **243** pp 753–763

Shepard M *et al* 1988 The Politics of Climate *EPRI Journal* **13** (4) 4–15

2

The Kinetic Theory of Gases

It is not possible to fully understand the physical processes which occur in the industrial applications of plasma without a knowledge of the behavior of gases on a *microscopic scale*, i.e. at the level of individual atoms, molecules, and charged particles. The behavior of gases on the microscopic scale is described by a branch of physics called the *kinetic theory of gases*, and the implications of this behavior in the macroscopic world are treated by the subject of *statistical mechanics*. This chapter is intended to survey material which is derived rigorously in textbooks on kinetic theory and statistical mechanics, such as that of Sears and Salinger (1975).

2.1 MEASUREMENT OF HIGH VACUUM

A significant fraction of the equipment and processes which incorporate plasma is operated well below atmospheric densities and/or pressures. It is therefore necessary to be acquainted with the non-SI units which are commonly used to measure pressure or density. Through historical accident, commercial vacuum gauges read in units of pressure, even though the quantity of physical interest is almost always the number density of the neutral background gas in a vacuum system.

In the 19th century, when the first quantitative measurements were made in vacuum systems, the degree of vacuum was measured with mercury manometers which referred the pressure in the vacuum system to that of the atmosphere. Thus, in the older literature the common unit of pressure was the *millimeter of mercury* (mm Hg), in which one *standard atmosphere* (atm), at 0°C, was equal to 760 mm Hg. In the mid-20th century, an international standards committee decided to change the name of the unit of pressure from millimeters of mercury to the

torr, which is, at this time, the unit most frequently found in the North American literature of plasma science. The torr was named in honor of Evangelista Torricelli (1608–1647), an Italian physicist known for his work on barometers. (It is a peculiarity of the protocol of units and symbols that the unit of torr has the symbol Torr when associated with a numerical value.) In industrial applications such as thermal plasma processing and magnetohydrodynamic power generation, the pressures involved are usually at or slightly above 1 atm, and in those fields it is more common to express the pressure in atmospheres. Another non-SI unit which is occasionally seen in the older literature is the *micron*, which also is the *millitorr*, equal to 10^{-3} Torr. Because of the potential for confusion with the unit of length equal to 10^{-6} m, which is widely used in materials science and microelectronic plasma processing, we do not employ the micron as a pressure unit in this book.

After the introduction of the torr, the same international standards committee decided that the official unit of pressure in the SI system of units would henceforward be the *pascal* (symbol Pa), defined as 1 newton per square meter (N/m²). This unit was named in honor of Blaise Pascal (1623–1662), a French scientist remembered, among other things, as the first to take a barometer up a mountain and demonstrate the decrease of pressure with altitude. At least in the United States, the pascal has not been generally accepted as a unit of pressure for measuring vacua, and is only rarely encountered in the literature. (In this book we sometimes preferentially refer to a force per unit area in newtons per square meter rather than the equivalent pressure in pascals.) In the field of industrial plasma engineering, it is still common practice to quote the vacuum pressure in torr, with an increasing tendency to cite the neutral particle densities, rather than background pressures.

The conversion between the pascal and the torr is via the standard atmosphere which is defined as exactly equal to both 760 Torr and 1.01325×10^5 Pa, such that 1 Torr is equal to $1.01325 \times 10^5/760 = 133.32$ Pa (Book 1987). The relationship between the pressure (p') in torr and the pressure (p) in pascals is thus given by

$$p'(\text{Torr}) = \frac{760}{1.0133 \times 10^5} \, p(\text{Pa}). \qquad (2.1)$$

This pressure can be related to the number density in particles per cubic meter by the perfect gas law,

$$p = nkT. \qquad (2.2)$$

where k is Boltzmann's constant. Substituting $p(\text{Pa})$ from equation (2.1) into equation (2.2), and evaluating at the conventional laboratory

temperature of 300 K, one obtains

$$n(\text{particles/m}^3) = \frac{1.0133 \times 10^5}{760 \, kT} p'(\text{Torr}) = 3.220 \times 10^{22} p'(\text{Torr}) \quad (2.3)$$

which is the conversion factor at that temperature between the neutral number density in a vacuum system and the background pressure in torr. One should be mindful that this conversion factor is temperature dependent. Further conversion formulas for vacuum systems may be found in Appendix D. At 1 atm and 300 K, there are approximately 2.447×10^{25} molecules (or atoms) per cubic meter in ordinary gases.

2.2 PARTICLE DISTRIBUTION FUNCTIONS

The individual particles of ordinary gases and plasmas do not all move with the same speed. If these particles are allowed to interact and equilibrate, their velocities and energies become distributed over a range of values described by the *Maxwell–Boltzmann distribution function*.

2.2.1 Velocity Distribution Functions

In Cartesian coordinates (x, y, z), the number of particles dn_x in the velocity interval between v_x and $v_x + dv_x$, where n is the number of particles per unit volume, is given by the one-dimensional Maxwell–Boltzmann distribution function,

$$f(v_x) = \frac{dn_x}{dv_x} = \frac{n}{\pi^{1/2}} \left(\frac{m}{2kT} \right)^{1/2} \exp \left[-\frac{mv_x^2}{2kT} \right]. \quad (2.4)$$

The number of particles in a cubical volume in velocity space with velocities between v_x and $v_x + dv_x$, v_y and $v_y + dv_y$, and v_z and $v_z + dv_z$, is equal to the product of the three velocity components,

$$\frac{d^3 n_{xyz}}{dv_x dv_y dv_z} = \frac{n}{\pi^{3/2}} \left(\frac{m}{2kT} \right)^{3/2} \exp \left[-\frac{mv^2}{2kT} \right]. \quad (2.5)$$

The relation between the velocity components and the speed v is given by

$$v^2 = v_x^2 + v_y^2 + v_z^2 \quad (2.6)$$

where v is the radius vector of a spherical coordinate system in velocity space. The distribution of speeds dn_v between v and $v + dv$ is given by the distribution function for the speed v,

$$f(v) = \frac{dn_v}{dv} = \frac{4n}{\pi^{1/2}} \left(\frac{m}{2kT} \right)^{3/2} v^2 \exp \left[-\frac{mv^2}{2kT} \right]. \quad (2.7)$$

VELOCITY PROBABILITY DENSITY

TOTAL VELOCITY
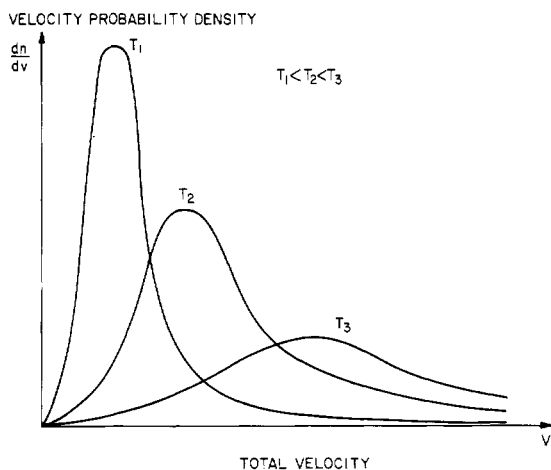
Figure 2.1 Sketch of the Maxwell–Boltzmann velocity distribution function of a gas at progressively higher temperatures, $T_1 < T_2 < T_3$. The area under each of the three curves is the same and is equal to the particle number density.

Figure 2.1 shows schematically the distribution of speeds $f(v)$ from equation (2.7) as a function of the speed v for three kinetic temperatures, $T_1 < T_2 < T_3$. As the kinetic temperature of the gas increases, the distribution function spreads out to higher speeds and therefore to higher energies. The area under the distribution function curves remains constant as long as the gas is confined in a fixed volume. By integrating equation (2.7) over all velocities $0 \leqslant v \leqslant \infty$, one can show that this constant is equal to the gas number density n, in particles per unit volume,

$$\int_0^\infty f(v)\,\mathrm{d}v = n. \tag{2.8}$$

The first three moments of the velocity distribution function have physical significance. The zeroth moment, equal to the area under the distribution function, is given by equation (2.8) above. The first moment of the velocity distribution function is the *arithmetic mean speed*, which is also known as the *mean thermal velocity* $\bar{v}$, given by

$$\bar{v} = \frac{1}{n}\int_0^\infty v f(v)\,\mathrm{d}v = \left(\frac{8kT}{\pi m}\right)^{1/2} \tag{2.9}$$

while the second moment is related to the *root mean square speed* of the particles and is given by

$$v_{\mathrm{rms}} = \frac{1}{n}\left(\int_0^\infty v^2 f(v)\,\mathrm{d}v\right)^{1/2} = \left(\frac{3kT}{m}\right)^{1/2}. \tag{2.10}$$

VELOCITY PROBABILITY DENSITY

$\frac{dn}{dv}$

v_m $\bar{v}$ v_{rms} v
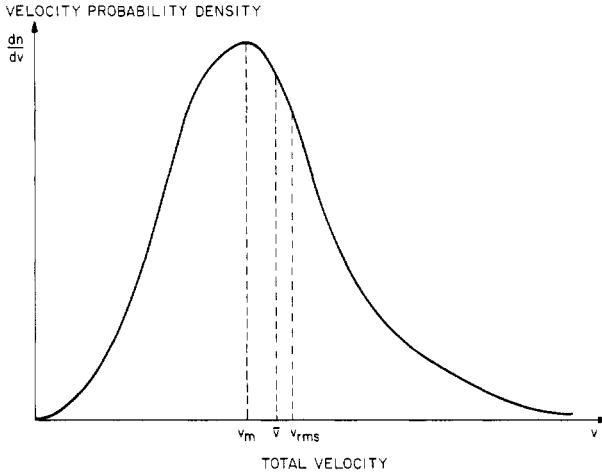
TOTAL VELOCITY

Figure 2.2 Sketch of the Maxwell–Boltzmann velocity distribution function with the most probable velocity v_m, the mean thermal velocity $\bar{v}$, and the second moment, root mean square velocity v_{rms} indicated schematically on the distribution function.

Another characteristic speed is the *most probable speed*, v_m, corresponding to the maximum of the velocity distribution function. This can be found by differentiating the distribution function of equation (2.7) once and setting it equal to zero, to obtain

$$v_m = \left(\frac{2kT}{m}\right)^{1/2}. \qquad (2.11)$$

The relationship of these characteristic speeds to the distribution function is indicated schematically in figure 2.2. When the velocity distribution function is non-Maxwellian, as sometimes happens in industrial plasmas, the zeroth moment (2.8) remains unaffected, but the arithmetic mean, root mean square, and most probable speeds assume values different from those given in equations (2.9) to (2.11). When one wishes to select a characteristic velocity of a Maxwellian distribution, the mean thermal velocity $\bar{v}$ (2.9) is normally used.

2.2.2 Energy Distribution Functions

The energy of individual particles in a gas which is in kinetic or thermodynamic equilibrium also obeys a Maxwell–Boltzmann distribution. If one defines the kinetic energy w in terms of the speed v as

$$w \equiv \frac{1}{2}mv^2 \qquad (2.12)$$

ENERGY PROBABILITY DENSITY
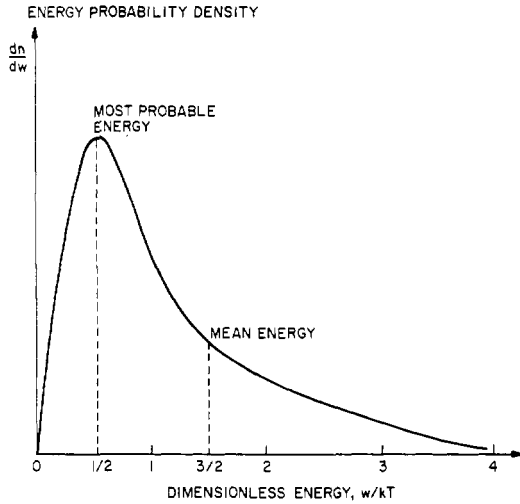
Figure 2.3 Sketch of the Maxwell–Boltzmann energy distribution function. The most probable energy, at the maximum, is $w_m = kT/2$ and the mean energy is $\bar{w} = 3kT/2$. The area under the curve is equal to the particle number density.

then the distribution function of energies between w and $w + \mathrm{d}w$ is

$$f(w) = \frac{\mathrm{d}n_w}{\mathrm{d}w} = \frac{2n}{\pi^{1/2}} \frac{w^{1/2}}{(kT)^{3/2}} \exp\left[-\frac{w}{kT}\right]. \qquad (2.13)$$

A sketch of the energy distribution function of equation (2.13) is shown in figure 2.3, where the energy axis has been normalized to the value kT.

By differentiating equation (2.13) and setting it equal to 0, it can be shown that the *most probable kinetic energy* of a Maxwellian gas is $w_m = kT/2$. The *mean energy*, $\bar{w}$, of a gas with a Maxwellian distribution is given by the first moment of equation (2.13),

$$\bar{w} = \frac{1}{n} \int_0^\infty w f(w) \, \mathrm{d}w. \qquad (2.14)$$

Substituting equation (2.13) into equation (2.14),

$$\bar{w} = \frac{2}{\sqrt{\pi}} \int_0^\infty \left(\frac{w}{kT}\right)^{3/2} \exp\left[-\frac{w}{kT}\right] \mathrm{d}w = \frac{3}{2} kT. \qquad (2.15)$$

Low-pressure glow discharge plasmas of industrial interest often have non-Maxwellian electron energy distribution functions. If the mean

energy $\bar{w}$, in joules per particle, of a gas with a non-Maxwellian distribution is the same as that of a Maxwellian distribution with an effective kinetic temperature T_{eff}, one can define, using equations (2.14) and (2.15),

$$T_{\text{eff}} \equiv \frac{2}{3kn} \int_0^\infty wf(w)\,\mathrm{d}w \ . \tag{2.16}$$

For a Maxwellian distribution, equation (2.16) is just the kinetic temperature T.

The energy distribution function of particles is described by the Maxwell–Boltzmann distribution function if the particles are in either thermodynamic or kinetic equilibrium. *Thermodynamic equilibrium* is by far the most stringent requirement and implies that all energy flows in the gas are insignificant, that the photon mean free paths are much smaller than the dimensions of the gas, and that the gas is radiating like a black body. Thermodynamic equilibrium is a necessary and sufficient condition for the application of the powerful methods of classical thermodynamics to the gas. While this condition is satisfied by some thermal plasmas used for materials processing, such as welding arcs for example, it is not satisfied by most plasmas of industrial interest. *Kinetic equilibrium* is a much less stringent condition, which allows energy flows in the medium and does not require that the medium radiate like a black body. Kinetic equilibrium requires only that the particles have interacted among themselves sufficiently to achieve a Maxwell–Boltzmann distribution of velocities.

The degree kelvin (K) is an inconveniently small unit with which to measure kinetic temperatures in plasmas, and so one expresses the kinetic temperature (T') in electronvolt units (eV) through the relationship

$$kT(\text{K}) \equiv eT'(\text{eV}) \tag{2.17}$$

where T is the kinetic temperature in degrees kelvin, k is Boltzmann's constant and e is the electron charge. Taking the ratio e/k, one finds that 1 eV is equivalent to 11 604 K.

2.3 PARTICLE COLLISIONS

The Maxwell–Boltzmann distribution functions discussed above are maintained by collisions among the individual particles of the gas or plasma. Some of the different kinds of binary or multi-body collisions which can occur among electrons, ions, and neutral atoms or molecules of types A, B, and C are listed in table 2.1. In industrial applications, it is necessary to consider not only binary collisions between two individual charged particles of the plasma, but also interactions of these charged

Table 2.1 Principal kinds of collision.

Electrons

$e + A \rightarrow A^+ + 2e$	Ionization
$e + A \rightarrow e + A^* \rightarrow e + A + h\nu$	Excitation
$e + A^* + B \rightarrow 2e + A + B^+$	Penning ionization
$e + A \rightarrow e + A$	Elastic scattering
$e + AB \rightarrow e + A + B$	Dissociation
$e + AB \rightarrow 2e + A^+ + B$	Dissociative ionization
$e + AB \rightarrow A^- + B$	Dissociative attachment
$e + A^+ + B \rightarrow A + B$	Recombination

Ions

$A^+ + B \rightarrow A + B^+$	Charge exchange
$A^+ + B \rightarrow A^+ + B$	Elastic scattering
$A^+ + B \rightarrow A^+ + B^+ + e$	Ionization
$A^+ + B \rightarrow A^+ + B^* \rightarrow A^+ + B + h\nu$	Excitation
$A^+ + e + B \rightarrow A + B$	Recombination
$A^+ + BC \rightarrow A^+ + B + C$	Dissociation
$A + BC \rightarrow C + AB$	Chemical reaction

particles with other forms of matter including solids, liquids, and the background neutral gas in which it is imbedded.

2.3.1 Elastic Binary Collisions

Binary collisions are collisions involving only two particles in a gas or plasma. *Elastic binary collisions* are those, like the interaction of billiard balls, in which the total kinetic energy of the two particles is conserved, and is the same before and after the collision. *Inelastic binary collisions* are those in which the initial kinetic energy of two colliding particles is greater than the kinetic energy after the collision, as the result of leaving one or both of the particles in an excited state, or of having undergone some other energy-absorbing process.

To a first aproximation, collisions between neutral particles, or one charged and one neutral particle, can be treated as if they were collisions between hard spheres. The effective cross-sectional target area for such collisions is the *cross section* σ, which is measured in square meters in the SI system of units. For collisions between neutral molecules in air, the cross section is somewhat above 10^{-19} m^2. If the two colliding particles are perfectly elastic spheres of radius a, then a collision will occur whenever they come within a distance $2a$ of each other, as shown in figure 2.4. Their effective target area, as indicated by the dashed circle
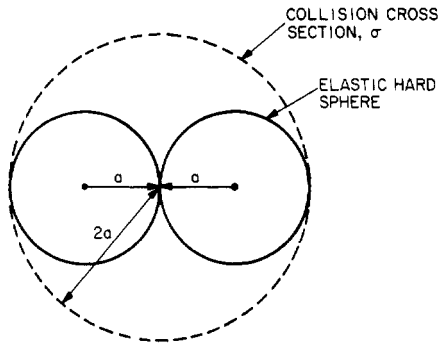
Figure 2.4 Two elastic, hard-sphere atoms of radius a in contact at the moment of collision. The total cross section, σ, for this process is the area of the dotted circle.

in figure 2.4, is the collision *cross section* σ, given by

$$\sigma = \pi(2a)^2 = 4\pi a^2 \qquad (m^2). \qquad (2.18)$$

Very important in fusion research, but almost irrelevant in the industrial applications of plasma, are binary collisions between charged particles, i.e. between two electrons, two positive ions, or ions and electrons. Such *Coulomb collisions* are the dominant collisional process in fully ionized plasmas, and are taken as the basis for the microscopic approach to fusion-related or astrophysical plasmas. Although some recently developed high intensity glow discharges can have an ionization fraction above 10%, in most industrial plasmas the degree of ionization is generally quite low, and binary Coulomb collisions usually play an insignificant role in determining the transport properties and the microscopic behavior of the plasma. The dominant collisional process is between charged particles and the neutral background gas. A gas in such a collisional regime is referred to as a *Lorentzian gas*.

The binary collision of two neutral particles or a neutral and a charged particle require a close approach and physical contact of the kind implied by figure 2.4. *Coulomb collisions*, on the other hand, are the result of two particles interacting through the inverse square Coulomb force, either attractive or repulsive depending on the sign of the charges on the two particles. The long-range Coulomb forces are responsible for the fact that charged particles in a fully ionized plasma simultaneously interact with more than one other particle at a time, so that the transport coefficients are dominated by multiple, small angle collisions, rather than single binary interactions between the charged particles. Further discussion of Coulomb collisions and cross sections may be found in Roth (1986).

2.3.2 Inelastic Binary Collisions

When two particles undergo an inelastic binary collision, their kinetic energy is less after the collision than it was prior to it, as a result of several possible energy-absorbing processes listed in table 2.1. One such process is the *excitation* of a neutral atom by the energetic charged particles of the plasma, in which an orbiting electron is raised to a higher energy state. These excited neutral atoms (or excited high-Z ions) emit line radiation which can represent a significant energy loss in industrial plasmas. If the neutral gas consists of molecules, *dissociation* can occur, in which collisions with an energetic ion or electron break up a molecule into one or more of its constituent parts. Background neutral atoms or molecules may experience an *ionizing collision* with ions or electrons of the plasma, in which one or more electrons is stripped completely away from the atom or molecule. The process of ionization can also lead to a significant energy loss in a partially ionized plasma. A *charge-exchange collision* results in exchanging an electron between a cold neutral atom or molecule and an energetic ion in the plasma. Finally, if a partially ionized plasma is of atmospheric or greater density, significant *recombination* can occur, which is the formation of a neutral atom or molecule from an electron and an ion, in the presence of a third body. Recombination must be a three-body process, in order to conserve kinetic energy, linear momentum, and angular momentum during the recombination process.

2.3.3 Heterogeneous Interactions at Surfaces

Heterogeneous interactions are those which occur between different states of matter. These interactions will be studied in quantitative depth in later chapters where their applications appear. Most of these heterogeneous interactions involve wall bombardment by energetic free radicals, ions, or electrons, which can result in knocking electrons (*secondary electron emission*) or neutral atoms (*sputtering* or *erosion*) from the material of the wall. In addition, when ions and electrons from the plasma reach a surface, they can recombine to form neutral atoms or molecules; or they can promote *catalysis* in which the adsorbed gas undergoes a chemical reaction either with itself, or with the material of the underlying solid surface. Finally, either because of a buildup of particles impinging on the surface from the plasma, or because of *induced chemical reactions* or *polymerization* on the surface, *deposition* and *coating* of thin films can result.

2.3.4 Plasma Collisionality Regimes

In courses on advanced plasma physics, the kinetic parameters and transport coefficients discussed in the next section are derived from the

equations of motion and distribution functions of the individual particles which comprise the plasma. These kinetic approaches are usually separated into three collisionality regimes. The *Lorentzian approach* to plasma theory is based on the *Lorentzian gas*, which is a hypothetical gas in which the electrons are assumed not to interact with each other, and the positive ions are considered to remain at rest. The electrons undergo binary collisions with a neutral background gas which acts as an infinite absorber of energy and momentum from the colliding electron population. A refinement of the Lorentzian gas is the *Krook model*, in which the effective collision time is independent of the particle momentum and energy. This is sometimes a good approximation to the interactions of electrons with noble gases.

Another theoretical approach, most relevant to the fully ionized fusion regime, is the *Boltzmann–Vlasov model*, in which the governing equation describes a high temperature plasma for which the collisional mean free path is much larger than all of the characteristic lengths of the system. This model may be useful in industrial plasmas operated at low pressures, below 1 mTorr, or in some astrophysical or geophysical plasmas. Another important theoretical model in fusion research, but which has limited applicability in industrial plasmas, is the *Fokker–Planck model*, in which the motion of a colliding particle in the velocity space of a fully ionized, highly turbulent, or electric field dominated plasma is determined by the cumulative effect of weak deflections resulting from distant encounters, or fluctuating electric fields. In the Fokker–Planck model, these cumulative effects of weak encounters are more important than the effects of occasional large deflections. In the theoretical developments later in this book, we will rely on the Lorentzian model, sometimes specializing to the Krook model.

2.4 KINETIC CHARACTERISTICS IN THE HARD-SPHERE MODEL

In studying the behavior of plasma, it is necessary to draw heavily on concepts from the kinetic theory of gases. The material covered in this section is derived rigorously in textbooks on kinetic theory, such as that by Sears and Salinger (1975), and those derivations will not be repeated here. Where space allows, rough derivations of the important parameters of kinetic theory are provided to give physical insight, without doing too much violence to quantitative rigor.

2.4.1 Collisional Parameters

Consider a gas consisting of elastic hard spheres of type 1 into which a test particle of type 2 with velocity v is introduced, as in figure 2.5. Both
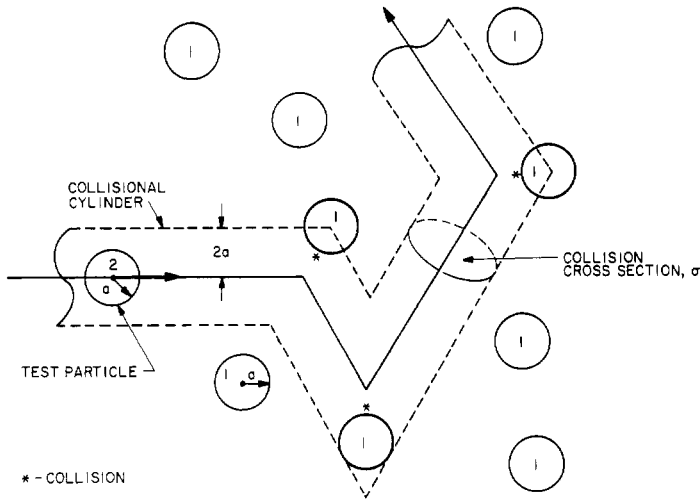
Figure 2.5 A hard-sphere test particle of type 2 interacting elastically with a background of hard-sphere particles of type 1. The test particle will collide with all background atoms of type 1 that lie on a cylinder of radius $2a$ from the test particle trajectory. The area of the cylinder's cross section is σ for the process.

species of particles have the same radius a and the background particles of type 1 are so much slower moving and/or massive that they remain fixed while the test particle of type 2 interacts with them. This assumption will introduce only a small numerical correction of order unity into our results. As the test particle scatters off the background particles, it will move along a random, zigzag path through the gas. The test particle will collide with every background particle of type 1, the center of which lies on a cylinder having a cross-sectional area σ. This cylinder will be irregular, with a kink in its axis wherever the test particle has collided with a background gas atom.

In a time interval t, a test particle with a velocity v covers a distance vt along this irregular, zigzag path and sweeps out a cylindrical volume of length vt and cross section σ as it collides with other particles, the centers of which lie on the surface of this cylindrical volume. If there are n_1 particles of type 1 per unit volume, the number with centers on the cylinder swept out by the test particle is equal to the number of collisions, and is given by the product of this number density and the volume of the cylinder swept out

$$\text{number of collisions} = n_1 \sigma vt. \qquad (2.19)$$

The velocity v in equation (2.19) is usually given by a Maxwellian distribution, and the cross section σ is often velocity dependent. These

velocity dependences are accounted for by defining an energy-dependent *reaction rate coefficient*,

$$\langle \sigma v \rangle = \frac{1}{n} \int_{-\infty}^{\infty} \sigma(v) v f(v) \, dv \qquad (2.20)$$

where $f(v)$ is the Maxwellian distribution given by equation (2.7). The angle brackets in equation (2.20) imply averaging σ over a Maxwellian distribution. The number of collisions per unit time, or *collision frequency* v_c, is

$$v_c = n_1 \langle \sigma v \rangle \qquad \text{(collisions/s)}. \qquad (2.21)$$

The molecules of the air surrounding us each collide with a frequency of approximately 7×10^9 collisions/s.

If one wishes to know the total number of collisions per unit volume between all particles of type 1 and all particles of type 2 in a gas, this total *interaction rate* or *reaction rate* R is given by the product of the number density of 'test' particles of type 2 and the collision frequency of each test particle with the background gas of type 1. This interaction rate is given by

$$R = n_2 v_c = n_1 n_2 \langle \sigma v \rangle \qquad \text{(interactions/m}^3\text{-s)}. \qquad (2.22)$$

The interaction rate of nitrogen molecules in the air surrounding us is approximately 9×10^{34} collisions/m^3-s.

The average distance between collisions is called the *mean free path* and is given the Greek symbol λ. The mean free path is the total distance covered by a test particle of mean velocity $\bar{v}$ in time t, divided by the number of collisions during this time, given by equation (2.19). Therefore,

$$\lambda = \frac{\bar{v}t}{n_1 \langle \sigma v \rangle t} = \frac{\bar{v}}{n_1 \langle \sigma v \rangle} \simeq \frac{1}{n_1 \sigma}. \qquad (2.23)$$

In the air surrounding us, the mean free path between collisions is approximately 6×10^{-8} m, a very small distance. In many low-pressure plasmas of industrial interest, the mean free path between collisions ranges from less than a millimeter to several tens of centimeters.

2.4.2 Particle Flux on a Surface

Another useful result from kinetic theory is the flux of particles on the walls surrounding a confined gas or plasma. The Maxwellian velocity distribution function $f(v)$ given by equation (2.7) describes the number of particles with velocities between v and $v + dv$ in a hemispherical shell above the surface being bombarded. In figure 2.6 is a spherical coordinate
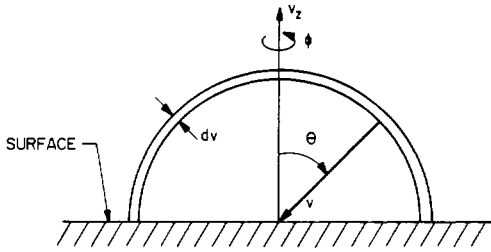
Figure 2.6 The hemisphere above a point of interest on the wall of a container. The vector velocity of an incoming particle is specified by the speed v, and the azimuthal and polar angles ϕ and θ, respectively.

system with its origin on the surface of interest. The number of particles per unit solid angle in a small differential area of the spherical shell of thickness dv is given by

$$dn(v, \theta, \phi) = \frac{f(v) \sin \theta}{4\pi}. \tag{2.24}$$

If the z direction is normal to the surface, then only those particles with velocities pointing toward the surface will hit it. The z component of velocity in the coordinate system of figure 2.6 is given by

$$v_z = v \cos \theta. \tag{2.25}$$

The flux of particles, the number of particles per unit area per unit time hitting the surface, is given by the product of the velocity normal to and toward the surface, given by equation (2.25), and the number of particles approaching the surface in the small differential volume in velocity space between v and $v + dv$, θ and $\theta + d\theta$, and ϕ and $\phi + d\phi$, given by equation (2.24). This differential flux is

$$d\bar{\Gamma}(v, \theta, \phi) = v_z \, dn(v, \theta, \phi) = \frac{vf(v) \sin \theta \cos \theta \, d\phi \, d\theta \, dv}{4\pi}. \tag{2.26}$$

If the particles are isotropic and homogeneous in velocity space and approach the surface from the hemisphere above it, the total flux reaching the surface is given by

$$\bar{\Gamma} = \int_0^\infty vf(v) \, dv \frac{1}{4\pi} \int_0^{2\pi} \int_0^{\pi/2} \sin \theta \cos \theta \, d\theta \, d\phi = \frac{1}{4} \int_0^\infty vf(v) \, dv. \tag{2.27}$$

Substituting equation (2.7) for the velocity distribution function in equation (2.27) and integrating, one obtains

$$\Gamma = n \left(\frac{2kT}{\pi m}\right)^{1/2} \int_0^\infty x^3 e^{-x^2} \, dx = \frac{1}{4} n \left(\frac{8kT}{\pi m}\right)^{1/2}$$

$$= \tfrac{1}{4} n \bar{v} \quad \text{(particles/m}^2\text{-s)}. \tag{2.28}$$

where $\bar{v}$ is the mean thermal velocity of the particles. It is this bombardment of walls by a confined gas which is responsible for the gas exerting pressure on the wall. Under standard conditions, air molecules bombard the walls of a typical room at a rate that results in approximately 3.3×10^{27} collisions/m^2-s.

2.4.3 Power Flux on a Surface

For energetic industrial plasmas in which the wall heat flux may be an issue, it is useful to know not only the rate at which particles bombard the surface, but also the power flux to be expected from a gas or plasma of known number density and kinetic temperature. Equation (2.26) gives the differential flux of particles hitting a surface; if we wish to know the differential power flux, in watts per square meter, we must multiply this differential particle flux by the kinetic energy of each particle,

$$dP(v, \theta, \phi) = \tfrac{1}{2} m v^2 d\Gamma(v, \theta, \phi) . \tag{2.29}$$

Substituting equation (2.26) into equation (2.29) yields

$$dP(v, \theta, \phi) = \frac{mv^3}{2} f(v) \frac{\sin\theta \cos\theta \, d\theta \, d\phi \, dv}{4\pi} . \tag{2.30}$$

If equation (2.7) is substituted into equation (2.30) and integrated over all velocities,

$$P = \frac{m}{8} \int_0^\infty v^3 f(v) \, dv = \frac{nm}{2\sqrt{\pi}} \left(\frac{2kT}{m}\right)^{3/2} \int_0^\infty x^5 e^{-x^2} \, dx \tag{2.31}$$

or

$$P = \frac{mn}{2\sqrt{\pi}} \left(\frac{2kT}{m}\right)^{3/2} = 2kT\bar{\Gamma} \quad \text{(W/m}^2\text{)}. \tag{2.32}$$

This expression for the power flux to a surface is not equal to the product of the particle flux given by equation (2.28) and the mean energy of the particle distribution function given by $\bar{w} = 3kT/2$ (see equation (2.15). Equation (2.32) states that the average energy of a particle hitting the surface is $2kT$, not $3kT/2$ as appropriate to the bulk of the gas. This occurs because the more energetic particles in the distribution function hit the walls more frequently than the slower particles and thereby contribute more than their proportionate share to the power flux on the wall.

2.5 DIRECT TRANSPORT PHENOMENA

Four direct transport mechanisms are familiar from classical kinetic theory and can occur in plasmas as well. The transport of particles, momentum, energy, and charge can result, respectively, from gradients of number density, velocity, temperature, and electrostatic potential. These forms of transport result, respectively, in particle diffusion, viscosity, thermal conductivity, and electrical current. We will not derive here the transport coefficients for these processes in detail; such a derivation may be found in standard texts on kinetic theory and statistical mechanics (Sears and Salinger 1975).

2.5.1 Diffusive Particle Transport

When particles in a gas or an unmagnetized plasma collide they perform a random walk from their initial starting point, the step size of which is equal to the mean free path for collisions. If there exists a density gradient in the gas, and if the gas is not convectively mixed, this random walk will result in more particles moving from a region of high concentration to a region of low concentration than vice versa. This process is called *diffusive transport*.

If the mean free path λ is much shorter than the characteristic *density scale length*, L, such that

$$\frac{\lambda}{n_0}\frac{\partial n}{\partial x} = \frac{\lambda}{L} \ll 1 \qquad (2.33)$$

then *Fick's law of diffusion* can be written in the following form, where v_d is the diffusive velocity of mass transport, and Γ is the diffusive particle flux

$$\Gamma = nv_d = -D\nabla n. \qquad (2.34)$$

The parameter D on the right-hand side is the *diffusion coefficient* and is assumed to be independent of position within the gas. The minus sign is present because the particle flux is down the density gradient, from regions of higher to lower number density.

If the collision frequency of the particles is ν_c, and the average distance traveled between the collisions is Δx, the diffusion coefficient can be approximated as

$$D \sim \nu_c(\Delta x)^2 . \qquad (2.35)$$

From kinetic theory arguments (Sears and Salinger 1975), it can be shown that if equation (2.33) is satisfied, the diffusion coefficient is given by

$$D \approx \tfrac{1}{3}\nu_c\lambda^2 = \tfrac{1}{3}\bar{v}\lambda = \tfrac{1}{3}\bar{v}^2\tau \qquad (2.36)$$
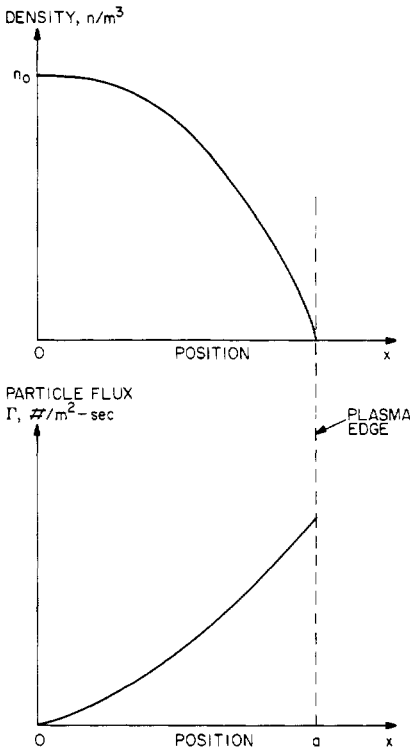
Figure 2.7 Fickian diffusion down a density gradient. Top: density profile; bottom: sketch of particle flux.
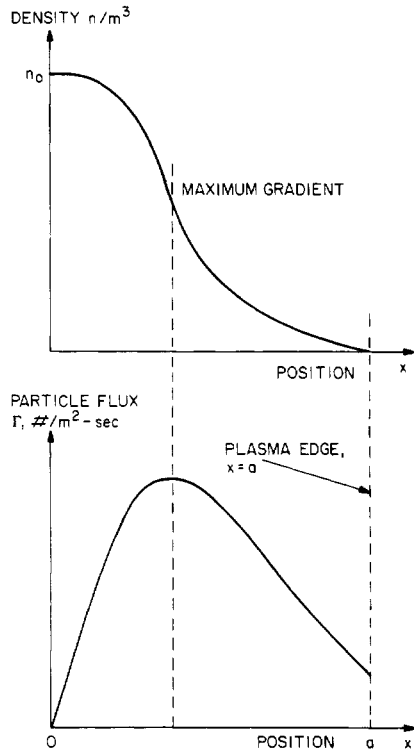
Figure 2.8 Non-Fickian and/or non-diffusive transport down a density gradient. Top: density profile; bottom particle flux, to right. Note the positive second derivative of the density profile near the plasma edge.

where τ is the time between collisions and $\bar{v}$ the mean thermal velocity.

In figure 2.7 is a sketch of a plasma electron number density profile undergoing Fickian diffusion. Such profiles are characteristic of cylindrical DC normal glow discharges, such as fluorescent light tubes. In this density profile, the *second* derivative of $n(x)$ is everywhere *negative*, implying that this process will contribute a *loss* term to the overall particle balance described by the particle conservation (continuity) equation. The profile shown in the upper part of figure 2.7 is often adequately described by a Bessel function or a parabolic distribution in cylindrical plasmas.

In figure 2.8 is sketched a characteristic radial number density profile which can result from a non-Fickian and/or non-diffusive radial transport process. Such profiles are sometimes seen in the outer regions of turbulent industrial plasmas and near the edge of Tokamak plasmas in

fusion research. These profiles are characterized by an inflection point, illustrated in figure 2.8 (top), and a *positive* second derivative in the outer region of the plasma. This positive second derivative contributes an inflowing, *source* term to the continuity equation at the radius r. This in turn implies that transport processes other than diffusion are dominant, and provide the particle losses required to maintain a steady state particle balance. Figure 2.8 (bottom) shows a characteristic profile of particle flux, which is highest at the point of maximum density gradient. The very thin, and much steeper sheath density gradient between the plasma and the wall is not shown in figures 2.7 or 2.8.

2.5.2 Momentum Transport

Viscosity (or *drag*) is a force resulting from the net transport of momentum from one region to another by a velocity gradient, as shown on figure 2.9. Here, a flat plate of area A parallel to a fixed wall is moving through a viscous medium. This motion produces a steady state velocity profile which is zero at the wall, and a maximum at the flat plate. The force per unit area on the plate is given by

$$F' = \eta \frac{\mathrm{d}u}{\mathrm{d}z} \qquad (\mathrm{N/m^2}). \qquad (2.37)$$

This force is proportional to the velocity gradient and is described by a constant *coefficient of viscosity* η. This coefficient of viscosity may be described in terms of the microscopic kinetic parameters by

$$\eta = \frac{1}{3} \frac{m\bar{v}}{\sigma} \qquad (\mathrm{N\,s/m^2}) \qquad (2.38)$$

where $\bar{v}$ is the mean thermal velocity, and σ is the cross section for the binary hard-sphere collisions occuring in the gas (Sears and Salinger 1975).

2.5.3 Energy Transport

Energy transport is described by *thermal* or *heat conduction*, a net transport of energy by non-radiative, collisional means from one region to another due to a gradient in temperature. The heat flow is given by

$$H = -\kappa \frac{\mathrm{d}T}{\mathrm{d}z} \qquad (\mathrm{W/m^2}) \qquad (2.39)$$

where κ is the *coefficient of thermal conductivity*. The heat flow is proportional to the temperature gradient. Equation (2.39) contains a

POSITION ABOVE SURFACE Z, METERS
FLUID VELOCITY μ(y), METERS/SEC

PLATE AREA A m²
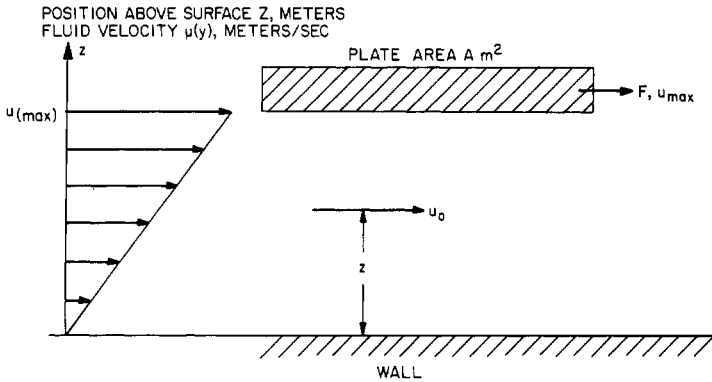
Figure 2.9 Flat plate of area A moving with a constant velocity u_{max} to the right, against the constant force F arising from viscosity in the velocity gradient between it and the wall.

minus sign, since heat flows from high to low temperatures. The thermal conductivity of a medium is described by the heat transfer coefficient κ in equation (2.39). It can be shown from kinetic theory arguments (Sears and Salinger 1975) that the heat transfer coefficient for gases is given by

$$\kappa = \frac{C_v \bar{v}}{3 N_A \sigma} \qquad \text{(W/m-K)} \qquad (2.40)$$

where C_v is the specific heat capacity of the gas (in J/kg-K), $\bar{v}$ is the mean thermal velocity, N_A is Avogadro's number, and σ is the cross section for hard-sphere, binary collisions. Kinetic theory arguments predict that for gases the following relationship between the heat transfer coefficient and coefficient of viscosity holds:

$$\frac{\kappa M}{\eta C_v} = 1.0 \qquad (2.41)$$

where M is the molecular weight of the gas in kg/kmole. In real gases, the ratio of equation (2.41) is approximately 2.0 ± 0.5.

2.5.4 Charge Transport

Electrical conductivity results from the transport of net charge due to an electrical potential gradient, i.e. an electric field. The electrical conductivity will be discussed in Chapter 4.

REFERENCES

Book D L 1987 *NRL Plasma Formulary–1987* NRL Publication 0084-4040 (Washington, DC: Naval Research Laboratory)

Roth J R 1986 *Introduction to Fusion Energy* (Charlottesville, VA: Ibis Publishing) ISBN 0-935005-07-2 ch 2

Sears F W and Salinger G L 1975 *Thermodynamics, Kinetic Theory, and Statistical Thermodynamics* 3rd edn (Reading, MA: Addison-Wesley) ISBN 0-201-06894-X

3

Motion of Charges in Electric and Magnetic Fields

An important difference between plasma and ordinary neutral gases is that plasma responds strongly to imposed electric and magnetic fields, while neutral gases do not. This behavior of plasma is important in many industrial applications. In order to better understand it, we will review the interaction of individual charged particles and space charge of one polarity with electric and magnetic fields, and apply the results to a few important practical applications.

3.1 CHARGED PARTICLE MOTION IN ELECTRIC FIELDS

A uniform electrostatic field can be generated by two plane, parallel electrically conducting plates separated by a distance L, as shown in figure 3.1. Suppose the left-hand plate is at ground potential, and the right-hand plate is maintained at a positive potential V_a. A positive test charge placed between these plates will move to the left, from higher electrostatic potentials to lower, more negative potentials. An electron will move to the right, toward more positive potentials.

By definition, the direction of the electric field, E, between these parallel plates is determined by the direction in which a positive test charge will move. In the SI system of units, the force on a charged particle between these plates is given by

$$F = qE \qquad (\text{N}) \qquad\qquad (3.1)$$

where the charge q is a signed quantity, and the electric field is defined in terms of the electrostatic potential V,

$$E = -\nabla V \quad \text{(V/m)}. \tag{3.2}$$

In general, this force is a function of position and is conservative.

One can apply the principle of conservation of mechanical energy by writing Newton's second law in vector form,

$$F = m\frac{dv}{dt} = qE \quad \text{(N)}. \tag{3.3}$$

The work done on the particle during a small displacement dx between the plates is

$$dW = F \cdot dx = m\frac{dv}{dt} \cdot dx = mv \cdot dv \quad \text{(J)}. \tag{3.4}$$

If the particle moves from an initial position x_1 to a final position x_2, one can use the definition of the electric field (3.2) to write

$$\int_1^2 F \cdot ds = -q\int_1^2 \frac{dV}{dx}dx = q(V_1 - V_2) \tag{3.5}$$

and Newton's law (3.4) to write

$$\int_1^2 F \cdot ds = m\int_1^2 \frac{dv}{dt}dx = m\int_1^2 v\,dv$$
$$= \frac{1}{2}mv_2^2 - \frac{1}{2}mv_1^2 \tag{3.6}$$

where v_1 and v_2 are the speeds of the particle at positions x_1 and x_2, respectively.

From equations (3.5) and (3.6) one obtains

$$qV_1 + \tfrac{1}{2}mv_1^2 = qV_2 + \tfrac{1}{2}mv_2^2 \equiv W = \text{constant.} \tag{3.7}$$

The constant W is the total energy of the motion, a conserved quantity. In this respect it is similar to the motion of a mass in a uniform gravitational field, in which the sum of potential and kinetic energy remains constant as a particle drops from a height. The constant total energy is

$$W = \tfrac{1}{2}mv^2 + qV \quad \text{(J)} \tag{3.8}$$
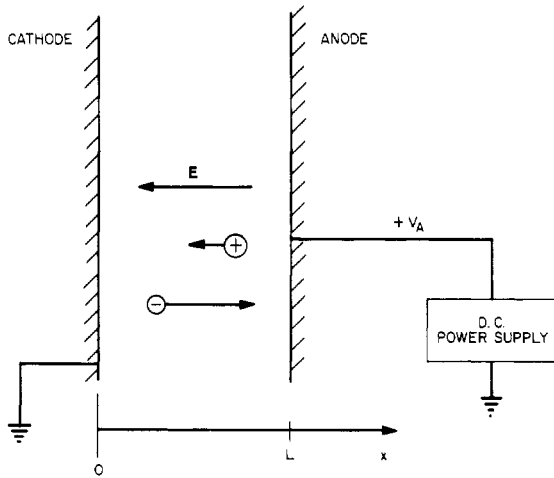
Figure 3.1 The motion of positive and negative charges in a uniform electric field between two plane parallel plates.

for the motion of a particle of charge q in an electrostatic field of potential V. The charge q is negative for electrons and positive for protons and ionized atoms.

In the situation depicted in figure 3.1, an electron emitted with zero initial velocity from the left-hand plate (*cathode*) has a potential energy $q V_a$. The electron acquires kinetic energy at the expense of its potential energy, as it accelerates between the plates and finally hits the positive plate (*anode*) on the right, where all its energy is kinetic.

3.1.1 The electronvolt as an Energy Unit

The usual unit of energy, the joule in SI units, is inconveniently large for many quantitative calculations involving individual particles in the field of plasma science. Consequently, it is useful to introduce a widely used (non-SI) unit of energy, the *electronvolt*. An electronvolt (eV) is the kinetic energy that an electron (or a singly-charged ion), of charge $e = 1.602 \times 10^{-19}$ C, gains when it is accelerated through a potential difference of one volt. The energy $\mathcal{E}$ in joules is related to the energy $\mathcal{E}'$ in electronvolts by

$$\mathcal{E}(\mathrm{J}) = e\mathcal{E}'(\mathrm{eV}) \qquad (3.9)$$

such that 1 eV is equivalent to $1.602 \times 10^{-19} J$.

In the example in figure 3.1, an electron leaving the cathode on the left with zero initial velocity would acquire a kinetic energy of V_A electronvolts upon its arrival at the anode at $x = L$. For elementary

particles carrying the same charge as the electron, the kinetic energy $\mathcal{E}'$ in electronvolts is equal numerically to the voltage required to accelerate the particle from rest. If the charged particle carries an integer multiple of the electronic charge, $q = Ze$, then the kinetic energy in electronvolts of the charge Ze, after acceleration through the potential difference V_A, is just ZV_A, as if each elementary charge on the particle were separately accelerated across that potential. The relation between the energy in joules $\mathcal{E}$, the charge state Z, the accelerating potential V_A, and the energy $\mathcal{E}'$ in electronvolts is

$$\mathcal{E}(\text{J}) = ZeV_A = e\mathcal{E}'(\text{eV}). \tag{3.10}$$

For example, a doubly-charged helium ion (He^{++}) accelerated in figure 3.1 from zero initial velocity at the anode would have a kinetic energy of $2V_A$ eV at the time it hit the cathode on the left.

3.1.2 Van de Graaff Generator

We consider the Van de Graaff Generator as an application of the concepts discussed above. This simple, relatively inexpensive, and widely used device for generating megavolt electrostatic potentials was invented by Robert J Van de Graaff in 1929, and patented by him in 1935 (Van de Graaff 1935). It is used in high energy physics research and other particle accelerator applications to generate high potentials, in the range from 0.5 to 25 MV. These devices can provide high voltage with a stability of about one part in 10^4, thus making them useful, for example, in the accurate determination of nuclear energy levels.

The principle of operation of the Van de Graaff generator is indicated in figure 3.2. The high voltage terminal is typically a hollow spherical shell supported on an insulating column, within which is an insulating belt that runs over two pulleys; one at ground potential at the bottom, and one in the interior of the high voltage terminal. The belt is driven over these pulleys by a motor, which provides the mechanical work which is done on the electrostatic charges on the belt as they are lifted from ground potential to high voltage. At the bottom of the charge-conveying pulley system, electrostatic charges are transferred to or induced on the surface of the insulating belt. When the charges find themselves in the interior of the high voltage terminal, a region of zero electric field, they are removed by a contactor connected to the spherical shell through a small battery. As a result of this process, a charge Q builds up on the high voltage terminal.

If the high voltage terminal is a sphere of radius a, the potential on the sphere due to a total accumulation of Q coulombs of charge is given by

$$V_s = \frac{Q}{4\pi\varepsilon_0 a} \qquad (\text{V}). \tag{3.11}$$
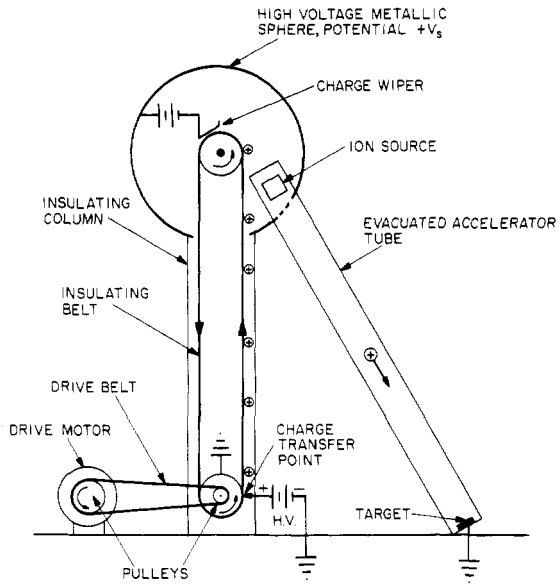
Figure 3.2 Schematic of the operation of a Van de Graaff electrostatic generator and particle acceleration column.

This potential will give rise to an electric field on the surface of the sphere given by

$$E_s = \frac{Q}{4\pi \varepsilon_0 a^2} \leqslant E_b \qquad \text{(V/m)}. \qquad (3.12)$$

When the electric field reaches the breakdown electric field of the surrounding gas, E_b, corona discharges or streamers will form and operation of the device will become unstable. For atmospheric air, the breakdown electric field may be somewhere between 1 and 3 MV/m, depending on humidity. Van de Graaff generators used for research purposes are usually operated in enclosed buildings containing an atmosphere of a highly insulating gas such as sulfur hexafluoride. The required radius of the sphere is related to the breakdown electric field at its surface and to its potential by

$$a = \frac{V_s}{E_b} \qquad \text{(m)}. \qquad (3.13)$$

When the Van de Graaff generator is used as a particle accelerator, an evacuated accelerator tube is attached to the high voltage terminal. An ion source designed to generate the species of interest is operated inside the high voltage terminal, and the ions are accelerated by the electric

field between the high voltage terminal and a target at ground potential. The charges which are accelerated down the tube to the target obey the conservation of energy described by equation (3.8), and hit the target with an energy, in electronvolts, which depends only on their charge state (whether they are singly- or multiply-charged) and the potential on the accelerating column. Thus, the potential energy of the charges at the top of the column is converted into kinetic energy as they are accelerated by the electric field in the evacuated tube. The power requirements of the ion source and other devices inside the high voltage terminal are supplied by a generator driven off the shaft horsepower of the upper pulley. Approximately twice the radius given by equation (3.13) is needed for stable operation.

3.2 CHARGED PARTICLE MOTION IN MAGNETIC FIELDS

The *magnetic field* is a field of force surrounding a current flowing through a conductor. The *magnetic field strength* is given by the symbol H and is measured in amperes per meter in the SI system of units. In the older literature it was called the *magnetic intensity*. The *magnetic flux density* or, alternatively, the *magnetic induction* is given the symbol B. The magnetic induction is measured in tesla (T) and represents the magnetic flux passing through a unit area perpendicular to the magnetic induction vector B. The relationship between the magnetic induction B and the magnetic field strength H is

$$B = \mu H \qquad \text{(T)} \qquad \qquad (3.14)$$

where μ is the *magnetic permeability*.

The reader should be cautioned that these definitions, while correct and generally accepted, are sometimes inconsistent with conversational usage in the field of plasma science. In particular, the magnetic induction B is often referred to as 'the magnetic field' or the 'magnetic field strength'. Plasmas have a permeability equal to that of free space, μ_0, and thus B and H are related by a fixed constant in plasmas.

A *magnetic field line* is mapped out by a large number of small compass needles which are free to move. Maxwell's equations do not predict or require the existence of magnetic field lines, which are a convention useful in visualizing some phenomena that occur in a magnetic field of force, and which do not involve relativistic velocities. The sign convention for the direction of a magnetic field is such that the magnetic induction B points in the direction in which a compass needle would point. The magnetic induction vector points toward a south magnetic pole and out of a north magnetic pole, as shown in figure 3.3.
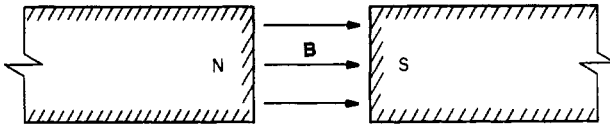
Figure 3.3 Sign convention of the magnetic induction *B* between a north and a south magnetic pole.
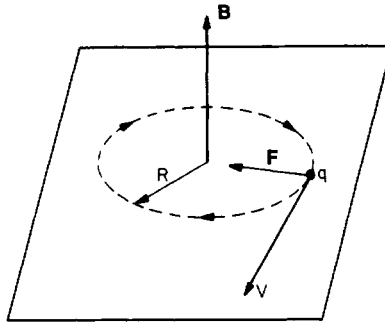
Figure 3.4 The gyration of a positive charge with velocity *v* in a plane perpendicular to the magnetic induction *B*.

3.2.1 Magnetic Particle Dynamics

Consider a particle of mass m and charge q moving in a magnetic field B. The equation of motion is

$$F = q(v \times B) \qquad \text{(N)}. \qquad (3.15)$$

This force is perpendicular to both B and to the velocity v of the particle. Since the force is at right angles to the velocity, this deflecting force cannot change the kinetic energy of the particle, only the direction of its motion. The inability of a static magnetic field to do work on a charged particle, or on a plasma, has important implications. Magnetic containment of a plasma represents a state of thermodynamic disequilibrium because the entropy of the plasma can always increase by expansion. Only by applying electric fields or time-varying magnetic fields can one do work on a plasma, and resist this expansion across a magnetic field.

Suppose a charged particle enters a uniform magnetic field with its velocity v at right angles to the magnetic induction B, as shown in figure 3.4. The speed of the particle will remain constant, since the magnetic field does no work on the particle, and a balance will be reached between the centripetal magnetic force given by equation (3.15) and the centrifugal force,

$$F = qvB = \frac{mv^2}{R} \qquad \text{(N)}. \qquad (3.16)$$
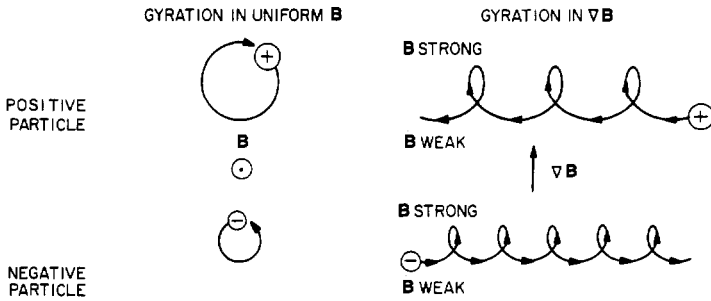
Figure 3.5 The sign convention for the motion of positive and negative charges in a magnetic induction pointing out of the plane of the diagram. At the right is shown the motion of positive and negative charges in a magnetic gradient.

The *radius of gyration*, R, is given by

$$R = \frac{mv}{qB} \qquad \text{(m)} \qquad (3.17)$$

and remains constant in a uniform magnetic field, since v is constant. The trajectory is therefore a circle. The angular velocity, or *gyrofrequency*, of this circular motion is

$$\omega = \frac{v}{R} = \frac{qB}{m} \qquad \text{(rad/s)} \qquad (3.18)$$

and in the classical, non-relativistic limit is independent of the particle energy and the particle speed v. In equation (3.18), as elsewhere in this text, the symbol ω is used to denote a radian frequency, in radians per second, and v to denote the frequency in hertz,

$$v = \frac{\omega}{2\pi} \qquad \text{(Hz)}. \qquad (3.19)$$

3.2.2 Particle Trajectories in Magnetic Fields

The effects of a constant magnetic field and of a magnetic field gradient on charged particles of opposite sign are indicated in figure 3.5. In this figure, the magnetic field points out of the plane of the paper. The symbol $\odot$ is used to designate a vector pointing out of the plane of the paper, and the symbol $\oplus$ a vector pointing into the plane of the paper. Positive particles rotate in a clockwise direction in figure 3.5, and negative particles in a counter-clockwise direction.
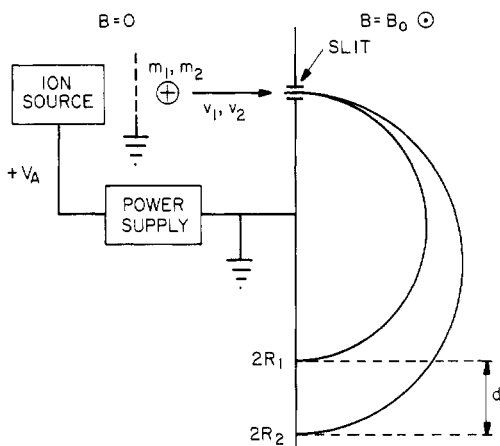
Figure 3.6 Schematic drawing of the Calutron electromagnetic isotope separator. Ions are accelerated to an energy of V_A electronvolts, and allowed to perform half an orbit in an evacuated chamber in which the magnetic induction has a value B_0.

When a gradient of magnetic field exists, as shown on the right, with the magnetic field stronger at the top than at the bottom, particles drift to the right or left, because they have a smaller radius of gyration in the stronger field than they do in the weaker field. Positive and negative charged particles drift in opposite directions when a plasma is subject to a magnetic field gradient, thus leading to plasma polarization.

3.2.3 Electromagnetic Isotope Separation

A device which uses the principles discussed above is the electromagnetic isotope separator, or Calutron. This device has been used for the relatively inefficient separation of the uranium isotopes U-235 and U-238 during the Manhattan Project of World War II, and is still used to separate isotopes for scientific study. A simple form of the Calutron is shown in figure 3.6. Singly-charged positive ions of the isotopes which are to be separated are created in an ion source biased to a potential V_A. For the sake of simplicity, we assume that the element of interest has two isotopes, with masses m_1 and m_2. The ions of both isotopes are accelerated to the potential V_A in a magnetic field-free region shown on the left, and then pass through a small slit into an evacuated region in which a magnetic induction B_0 exists, pointing out of the plane of the paper.

At the entrance slit, both isotopes have the same kinetic energy, given by

$$eV_a = \tfrac{1}{2}m_1 v_1^2 = \tfrac{1}{2}m_2 v_2^2. \tag{3.20}$$

The radii of curvature of the two isotopes are not the same, as a result of their different masses and velocities. The radii of curvature are

$$R_1 = \frac{m_1 v_1}{e B_0} \qquad R_2 = \frac{m_2 v_2}{e B_0}. \qquad (3.21)$$

The two isotopes will accumulate at the positions $2R_1$ and $2R_2$, which are separated by a distance d, equal to

$$d = 2(R_2 - R_1) = \frac{2}{e B_0}(m_2 v_2 - m_1 v_1). \qquad (3.22)$$

The speeds of the two isotopes as they pass through the entrance slit are given by

$$v_1 = \sqrt{\frac{2e V_a}{m_1}} \qquad v_2 = \sqrt{\frac{2e V_a}{m_2}}. \qquad (3.23)$$

Substituting equations (3.23) into equation (3.22), one obtains

$$d = \frac{2}{B_0}\sqrt{\frac{2m_1 V_a}{e}}\left[\sqrt{\frac{m_2}{m_1}} - 1\right]. \qquad (3.24)$$

For the isotopes of uranium and other heavy elements, the masses m_2 and m_1 differ by only a small amount Δm,

$$m_2 = m_1 + \Delta m \qquad (3.25)$$

where

$$\varepsilon \equiv \frac{\Delta m}{m_1} \ll 1 \qquad (3.26)$$

The quantity in square brackets in equation (3.24) may therefore be expanded in terms of the small parameter ε to yield

$$\sqrt{\frac{m_2}{m_1}} = \sqrt{1 + \varepsilon} \approx 1 + \tfrac{1}{2}\varepsilon + \dots \qquad (3.27)$$

The physical distance by which the two isotopes are separated is then

$$d \approx \frac{\varepsilon}{B_0}\sqrt{\frac{2m_1 V_A}{e}} = \frac{\Delta m}{B_0}\sqrt{\frac{2V_a}{e m_1}}. \qquad (3.28)$$

3.3 CHARGED PARTICLE MOTION IN STEADY ELECTRIC AND MAGNETIC FIELDS

Consider the motion of a charged particle in a region where steady, uniform electric and magnetic fields coexist. The *Lorentz equation* (named after Hendrick Lorentz, 1853–1928) describes the force on such a particle and is given by

$$F = q[E + (v \times B)]. \qquad (3.29)$$

3.3.1 Crossed-Field Particle Dynamics

Let us specialize to an important case in electric field dominated plasmas, in which the electric and magnetic fields are at right angles. This is the 'magnetron', or 'crossed fields' case shown in figure 3.7, with the magnetic induction along the z axis, and the electric field at right angles to it along the y axis. In the geophysical literature particularly, the axes are referred to by the names of three magnetoionic theorists of the early twentieth century, as reflected in figure 3.7. The components of equation (3.29) for the crossed-field case shown in figure 3.7 are

$$m\frac{dv_x}{dt} = q(v \times B)_x = qv_y B \qquad (3.30a)$$

$$m\frac{dv_y}{dt} = q[E + (v \times B)]_y = qE - qv_x B \qquad (3.30b)$$

and

$$m\frac{dv_z}{dt} = 0. \qquad (3.30c)$$

Equation (3.30c) states that v_z is constant, so the interesting particle dynamics is confined to the x–y plane. Using the angular frequency of equation (3.18), equation (3.30a) becomes

$$\frac{dv_x}{dt} = \omega v_y = \omega\frac{dy}{dt} \qquad (3.31)$$

and can be integrated directly. If a positive charge starts from rest at the origin of the coordinate system in figure 3.7, this integration gives

$$v_x = \omega y. \qquad (3.32)$$

Putting this value of the x component of velocity into equation (3.30b), one obtains

$$\frac{d^2 y}{dt^2} + \omega^2 y = \frac{Eq}{m}. \qquad (3.33)$$
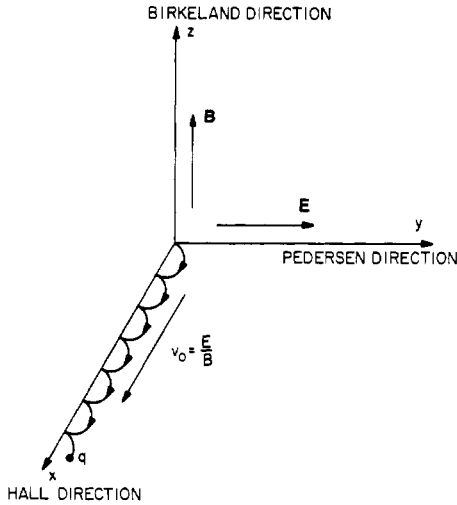
Figure 3.7 The motion of a positive charge in crossed electric and magnetic fields, yielding the average drift velocity E/B.

This is the equation of a simple harmonic oscillator subject to a constant external force. Its solution is, where C_1 and C_2 are arbitrary constants of integration,

$$y = \frac{Eq}{m\omega^2} + C_1 \cos \omega t + C_2 \sin \omega t. \tag{3.34}$$

Differentiating this equation to get the y component of velocity yields

$$v_y = -\omega C_1 \sin \omega t + \omega C_2 \cos \omega t. \tag{3.35}$$

If the initial conditions are a positive charge starting at the origin with zero initial x and y velocities at time $t = 0$, then $C_2 = 0$ and $C_1 = -Eq/m\omega^2$. Equation (3.34) then becomes

$$y = \frac{Eq}{m\omega^2}(1 - \cos \omega t). \tag{3.36}$$

Inserting this value into equation (3.32) and integrating for the x motion yields

$$x = \frac{Eq}{m\omega^2}(\omega t - \sin \omega t). \tag{3.37}$$

Equations (3.36) and (3.37) are parametric for a cycloid, a trajectory of which is shown schematically in figure 3.7 for a positive particle. The

x and y velocities can be obtained from equations (3.36) and (3.37) by differentiating each to obtain

$$v_y = \frac{E}{B} \sin \omega t \qquad (3.38)$$

and

$$v_x = \frac{E}{B}(1 - \cos \omega t). \qquad (3.39)$$

3.3.2 Crossed-Field Drift Velocity

From equations (3.38) and (3.39) it is evident that the average value of v_y is 0, but the average of v_x is not. The average velocity in the x direction is the *crossed-field drift velocity* and is given by

$$v_x = v_d = \frac{E}{B} \qquad \text{(m/s).} \qquad (3.40)$$

This is an important quantity in plasmas confined in the 'magnetron' geometry, with electric and magnetic fields at right angles. It predicts that both ions and electrons will move in the $E \times B$ direction with the same velocity, and this velocity is independent of the sign, mass and kinetic energy of the charge.

If the electric and magnetic fields are parallel, any initial velocity the particle might have perpendicular to the magnetic field will not be changed. The particle will be accelerated along the magnetic field, and the trajectory will look like a spiral of increasing pitch drawn on the surface of a cylinder, the radius of which is equal to the gyroradius of the particle in the magnetic field.

If one considers a configuration more general than that in figure 3.7 in which the electric field has components both parallel and perpendicular to the magnetic field, then equation (3.30c) is equal to qE_z, and the y component of the electric field appears in equation (3.30b). The z component of the motion is then one of constant acceleration, and the motion of the particle in space is the result of the cycloidal motion in the x–y plane and the uniformly-accelerated motion along the z axis.

The sign conventions and qualitative nature of charged particle orbits in crossed electric and magnetic fields are indicated in figure 3.8. This figure shows positive and negative particles gyrating in a magnetic field that points out of the plane of the paper. The electric field points vertically upward. On the upper half of the figure is shown the gyration of positive and negative particles in the absence of an electric field. On the lower part of the figure is shown the motion, with superimposed drift velocity, which results from crossed electric and magnetic fields.

MAGNETIC FIELD ALONE   ELECTRIC FIELD ALONE

CROSSED ELECTRIC AND MAGNETIC FIELDS
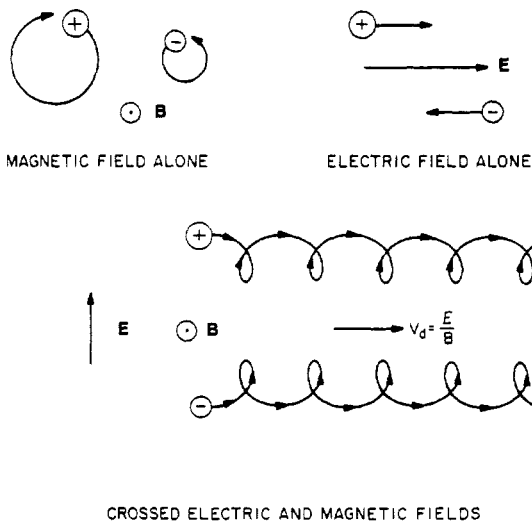
Figure 3.8 The motion of positive and negative charges in electric and magnetic fields separately, and in crossed electric and magnetic fields. The magnetic induction points out of the plane of the diagram. The electric field points vertically upward.

3.3.3 Magnetoelectric Heating

It can be advantageous to apply crossed electric and magnetic fields to a magnetically contained plasma. Usually, the magnetic field provides gross containment, while the electric fields, since they can do work on the plasma, are used to heat it and to improve containment. An example of a magnetoelectrically contained cylindrical plasma is shown in figure 3.9. In this configuration, a cylindrical plasma is in contact with a biased ring electrode which maintains the plasma column at a negative potential with respect to its surroundings.

A negative bias on the plasma results in its becoming a cylindrical potential well for ions. The plasma ions undergo E/B drift. This drift velocity is given by

$$v_{\rm d} = \frac{E_\perp}{B}. \tag{3.41}$$

This velocity is independent of the energy, mass, and sign of the charge species. This drift velocity can be used to raise the plasma constituents to an energy that is given by

$$\mathcal{E} = \frac{1}{2}mv_{\rm d}^2 = \frac{1}{2}m\frac{E_\perp^2}{B^2} \qquad {\rm (J)}. \tag{3.42}$$
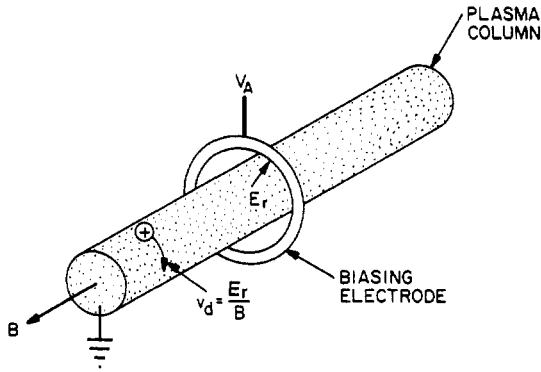
Figure 3.9 An arrangement for applying crossed electric and magnetic fields to a cylindrical plasma column, in order to induce high azimuthal drift velocity in the charged particles of the plasma.

Thus, the energy imparted to the particles by the radial electric field is proportional to their mass.

Plasma biased in the way indicated in figure 3.9 is usually turbulent with associated electrostatic fluctuations. These fluctuations produce radial transport, as well as thermalization of the monoenergetic energies associated with the E/B drift described by equation (3.41). The transport, in this case, is favorable to the confinement of ions; inward-pointing radial electric fields create a cylindrical electrostatic potential well down which ions fall when subject to the stochastic fluctuations of the electric field associated with plasma turbulence (Roth 1983).

3.3.4 The Electromagnetic Flowmeter

A simple application of crossed electric and magnetic fields is the *electromagnetic flowmeter*, a device used to measure the velocity of conducting fluids flowing through a region of constant magnetic field. This device has been used to measure the velocity of liquid metals, and the exhaust velocity of rocket engines (Roth 1957). Consider figure 3.10, a schematic drawing of the latter application. The exhaust jet of a rocket engine passes through two plates, separated by a distance d, which are electrically connected through a high impedance voltmeter that does not load down the charge available from the exhaust jet. A uniform magnetic field B is applied at right angles to the exhaust jet, and also at right angles to the (vertical) axis of the two electrode plates.

The y component of force in the region between the plates is given by equation (3.30b), or

$$F_y = m\ddot{y} = q\left[E_y + (v \times B)_y\right] = q\left(E_y - v_x B\right) . \qquad (3.43)$$
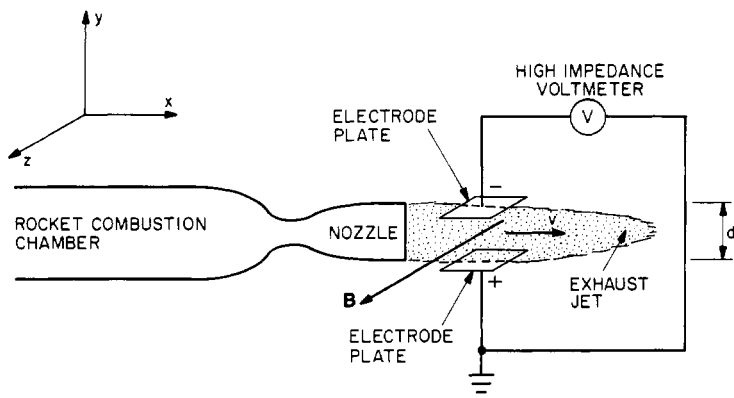
Figure 3.10 Schematic drawing of the electromagnetic flowmeter used to measure the exhaust velocity of a rocket engine.

When the rocket engine is turned on, an electric field builds up between the two plates until the exhaust jet can pass between the plates undeflected. This condition will be reached when $F_y = 0$, or, from equation (3.43),

$$v_x = \frac{E_y}{B} \quad (\text{m/s}). \tag{3.44}$$

The electric field between the plates will be equal to

$$E_y = \frac{V_p}{d} \quad (\text{V/m}) \tag{3.45}$$

provided that the plate separation d is small compared with the plate dimensions. The exhaust velocity in the x direction is found by substituting equation (3.45) into equation (3.44), and is equal to

$$v_x = \frac{V_p}{d\,B} \quad (\text{m/s}). \tag{3.46}$$

The electromagnetic flowmeter is therefore a linear instrument, and produces a voltage which is directly proportional to the velocity one wishes to measure. This voltage depends only on two additional fixed quantities, the separation of the plates and the imposed magnetic field B. The production of a voltage in the above configuration is also known as the *Hall effect*.

3.3.5 Bainbridge Mass Spectrograph

Another application of charged particle motion in crossed electric and magnetic fields is the *Bainbridge mass spectrograph*, which was
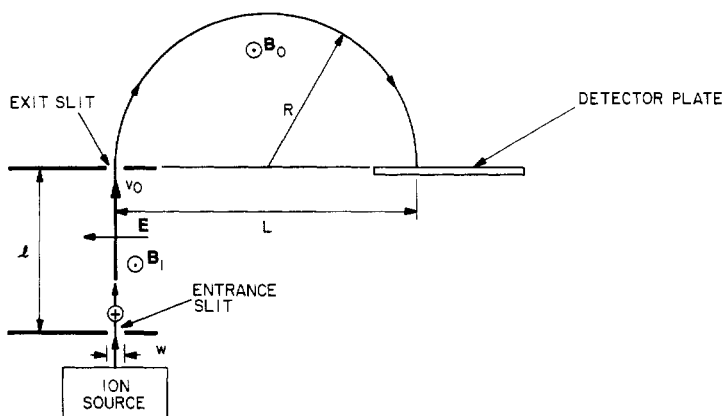
Figure 3.11 A schematic drawing of the Bainbridge mass spectrograph. A source of energetic ions is at the lower left.

originally employed to determine the atomic mass and relative abundance of the isotopes of the elements, and also finds uses in mass spectrometry and ion mass filters. This instrument, a schematic of which is shown in figure 3.11, was developed by Bainbridge just prior to the First World War. A source provides energetic ions for the velocity selector shown in the lower left. In this velocity selector, a transverse electric field acts over a distance ℓ in the presence of a magnetic induction B_1 pointing out of the plane of the diagram. This arrangement will allow only ions with the drift velocity v_0 to leave through the exit slit into a region in which a second magnetic field B_0 is the only force acting on the ions. This drift velocity is given by

$$v_0 = \frac{E}{B_1} \quad \text{(m/s)}. \tag{3.47}$$

In the absence of the electric and magnetic field in the velocity selector, ions of any speed could pass through both the entrance and exit slits if their velocities were correctly aligned. With the fields present, only those ions of speed given by equation (3.47) and normal to the planes of the slits will be undeflected in the region between the slits and will pass through both. When these ions arrive in the magnetic analyzer region in the upper part of the diagram, their trajectories will be deflected in a semi-circle of radius R given by

$$mv_0 = qB_0R = \tfrac{1}{2}qB_0L \tag{3.48}$$

where L is the distance from the exit slit on the velocity selector to the detector plate in the same plane. The relationship between the charge to

mass ratio of the ions and the distance L from the exit slit is therefore given by

$$\frac{q}{m} = \frac{2v_0}{B_0 L} = \frac{2E}{B_1 B_0 L}. \tag{3.49}$$

Since the ions may be multiply charged with $q = Ze$, with Z an integer, the mass of the ions may be determined from the following relation,

$$m = \frac{ZeB_0 B_1}{2E} L. \tag{3.50}$$

Thus, the Bainbridge mass spectrograph is a linear instrument for measuring particle mass, which is directly proportional to the distance from the exit slit. In actual instruments, the magnetic inductions B_0 and B_1 are often the same, and a sensitive detector is put at a fixed distance L from the exit slit. The mass distribution of the ions is then examined by varying the electric field in the velocity selector.

3.4 CHARGED PARTICLE MOTION IN SLOWLY VARYING ELECTRIC OR MAGNETIC FIELDS

'Slowly' varying electric and magnetic fields are those for which the inertia of charged particles is small enough that they can respond freely to the forces exerted by these fields. Two examples of industrial importance will be examined: the radio frequency resonant heating of a plasma in slowly time-varying electric fields; and the magnetic mirror, a method for slowing down and reflecting charged particles in a slowly spatially varying magnetized plasma.

3.4.1 Radio Frequency Resonant Heating

Consider the electrons in a magnetized plasma gyrating in a constant magnetic field which points out of the plane of the diagram of figure 3.12. The applied electromagnetic field is assumed to have a component in the x direction in resonance with the gyrofrequency of the electrons, given by

$$E_x = E_0 \sin(\omega t). \tag{3.51}$$

The electron gyrates in the counterclockwise direction in this diagram. The relation between the gyration frequency, ω, and the phase θ of the electron around its orbit is just $\theta = \omega t$. The electron has a gyroradius equal to r_g. The electric field given by equation (3.51) is said to be in resonance with the motion of the electron because it has a frequency
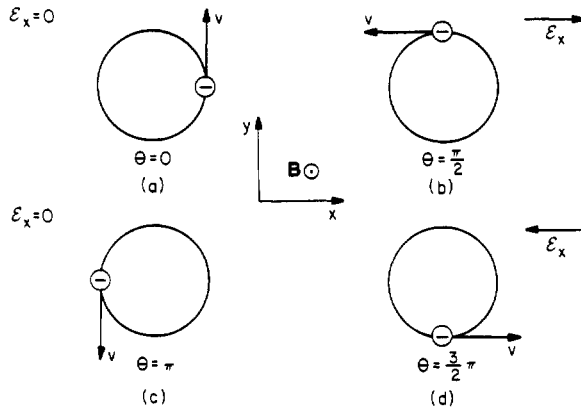
Figure 3.12 The relationship between particle velocity and resonant RF electric field for an electron in phase with the RF heating power.

of oscillation, ω, equal to the electron gyrofrequency, $\omega = \omega_c$, and also because the phase angle is such as to increase the energy of the electron.

Figure 3.12(a) shows the situation when the phase angle $\theta = 0$. At this point, the electric field vector is 0, and the electron is located with its velocity vector pointing in the positive y direction. At a phase angle of $\theta = \pi/2$, shown in figure 3.12(b), the electric field is pointing in the positive x direction, opposite the velocity of the electron. Since the electron is accelerated in the direction of its velocity, the electron acquires energy during this portion of its orbit. When the phase angle is $\theta = \pi$, shown in figure 3.12(c), the velocity vector of the electron is pointing vertically downward, and the electric field is 0. Finally, when the phase angle is $\theta = 3\pi/2$, shown in figure 3.12(d), the electron velocity vector is pointing in the positive x direction, and the electric field is again at its maximum value, pointing in the negative x direction. The x component of the electric field is always in phase and pointing in the opposite direction to the x component of the electron velocity, thus adding energy to the electron during its entire orbit.

The situation depicted in figure 3.12 is that of an electron in resonance with the incident electromagnetic wave. If the position of the electron on its orbit were 180° in advance of that shown in figure 3.12, it would be exactly out of resonance and the electric field would slow down such a particle and extract its energy. It is evident that only those particles in resonance will be effectively heated.

The process of RF resonance heating may be examined quantitatively by a simple argument originally put forward by Glasstone and Lovberg (1960). The work done on the electron shown in figure 3.12 is given by the dot product of the instantaneous force on the charged particle exerted
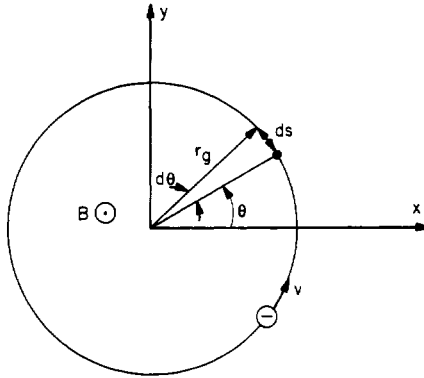
Figure 3.13 The relationship between the gyroradius, r_g, the phase angle θ, and the distance ds traveled around the circumference of an electron's gyro-orbit.

by the electromagnetic wave having an electric field strength E volts per meter, and the differential distance through which it moves in its orbit, shown in figure 3.13. This differential energy increase is given by

$$d\mathcal{E} = -qE \cdot ds = -qE \sin\theta \, ds = -qE_0 \sin^2\theta \, ds \qquad (3.52)$$

where equation (3.51) has been substituted for the polarized electric field in the x direction, and the dot product has been replaced with $\sin\theta$, since energy is added by the electric field only to the x component of the electron velocity. The differential distance along the orbit, ds, is given by

$$ds = r_g \, d\theta. \qquad (3.53)$$

The gyroradius r_g is given by

$$r_g = \frac{mv_\perp}{qB} = \frac{(2m\mathcal{E}_\perp)^{1/2}}{qB} \qquad (3.54)$$

where $\mathcal{E}_\perp$ is the perpendicular component of the electron energy, in joules.

If equation (3.53) is substituted into equation (3.52), one obtains an expression for the differential energy added to the perpendicular component of the electron motion,

$$d\mathcal{E}_\perp = -qE_0 r_g \sin^2\theta \, d\theta. \qquad (3.55)$$

In one rotation of the electron about its gyrocenter, the energy added is given by

$$\Delta\mathcal{E}_\perp = q \oint E \cdot ds = 2qE_0 r_g \int_0^\pi \sin^2\theta \, d\theta = \pi r_g q E_0. \qquad (3.56)$$

Substituting equation (3.54) for the gyroradius into equation (3.56), one obtains for the energy added per rotation,

$$\Delta\mathcal{E}_\perp = \frac{\pi E_0 (2m\mathcal{E}_\perp)^{1/2}}{B}. \tag{3.57}$$

Taking the derivative of the gyroradius, equation (3.54), and converting it into a difference in the gyroradius Δr_g, for an energy increase $\Delta\mathcal{E}$, one obtains

$$\frac{dr_g}{d\mathcal{E}_\perp} \approx \frac{\Delta r_g}{\Delta\mathcal{E}_\perp} = \frac{1}{2qB}\left(\frac{2m}{\mathcal{E}_\perp}\right)^{1/2}. \tag{3.58}$$

If one substitutes equation (3.57) into equation (3.58), the difference in the gyroradius per rotation is

$$\Delta r_g = \frac{\pi m E_0}{q B^2}. \tag{3.59}$$

Thus, the increase in the gyroradius per rotation is independent of the electron energy, and is the same for all gyroradii.

If the electron has an initial gyroradius r_{g0}, an initial energy $\mathcal{E}_{\perp 0}$, and a final energy $\mathcal{E}_\perp$ at a gyroradius r_g, the number of gyrations or orbits required to reach the final energy, N, is just the difference in gyroradii divided by the constant increment in the gyroradius for each orbit given by equation (3.59),

$$N = \frac{r_g - r_{g0}}{\Delta r_g} = \frac{(2m)^{1/2}}{q B \Delta r_g}\left(\mathcal{E}_\perp^{1/2} - \mathcal{E}_{\perp 0}^{1/2}\right). \tag{3.60}$$

Substituting equation (3.59) into equation (3.60), one obtains the total number of turns required to reach the energy $\mathcal{E}_\perp$,

$$N = \frac{B}{\pi E_0}\left(\frac{2}{m}\right)^{1/2}\left(\mathcal{E}_\perp^{1/2} - \mathcal{E}_{\perp 0}^{1/2}\right). \tag{3.61}$$

The gyration frequency, $\omega_c = qB/m$, is a constant independent of the energy, and its inverse multiplied by 2π is just the time for each orbit. The *heating time*, τ_H, required to go from an energy $\mathcal{E}_{\perp 0}$ to the energy $\mathcal{E}_\perp$ is given by

$$\tau_H = \frac{2\pi N}{\omega_c} = \frac{2\pi\left(r_g - r_{g0}\right)}{\omega_c \Delta r_g} \quad \text{(s)} \tag{3.62}$$

where the total number of orbits N, has been taken from equation (3.60). If one substitutes equations (3.59) and (3.61) into equation (3.62),

$$\tau_H = \frac{2(2m)^{1/2}}{qE_0}\left(\mathcal{E}_\perp^{1/2} - \mathcal{E}_{\perp 0}^{1/2}\right) < \tau_c, \tau_0. \tag{3.63}$$

In order for heating to be possible, this heating time must be less than the particle containment time, τ_0, or the particle collision time, τ_c, in the plasma, whichever is smaller. The heating time is independent of the confining magnetic field strength. To minimize the heating time required to achieve a given energy, one must use as strong an electric field as technological limitations will permit. After electrons are heated in this manner to the desired energy $\mathcal{E}_\perp$, their energy is thermalized by collisions or electrostatic turbulence in the plasma to yield a Maxwellian distribution of energies.

If charged particles can make several gyrations between collisions ($\omega\tau \gg 1$), it then becomes possible to use RF fields oscillating at the resonant frequency of gyration to heat plasmas. This can be done at the *ion cyclotron resonance heating* frequency *(ICRH)*, and, as illustrated in figures (3.12) and (3.13), at the *electron cyclotron resonance heating* frequency *(ECR, ECRH)*. Electron cyclotron resonance heating at the microwave oven frequency of 2.45 GHz has been introduced in recent years as a convenient method of heating industrial plasmas.

3.4.2 Magnetic Mirrors and Nozzles

Since many industrial plasmas are very hot, far from thermodynamic equilibrium, and/or require a great deal of energy to create and maintain, it is often helpful to use constant magnetic fields to assist in confining them, or to use magnetic fields instead of material walls as plasma nozzles and diffusers. These applications of a magnetic field work best when the magnetic moment is an approximate constant of the motion. If the spatial gradients of the magnetic field are small, such that the ratio

$$\varepsilon \equiv \frac{R}{Z_0} = \frac{mv_\perp}{eBZ_0} \ll 1 \tag{3.64}$$

then the magnetic moment is approximately constant. R is the gyroradius of the particle, and Z_0 a characteristic scale length of the magnetic field gradient. When condition (3.64) is satisfied, the particle motion in the magnetic field is said to be *adiabatic*.

The *magnetic moment* of a charged particle in a magnetic field is defined as the current flowing around the boundary of the gyro-orbit times the enclosed area of the orbit illustrated in figure 3.4,

$$M = \pi I r^2 \approx \text{constant}. \tag{3.65}$$
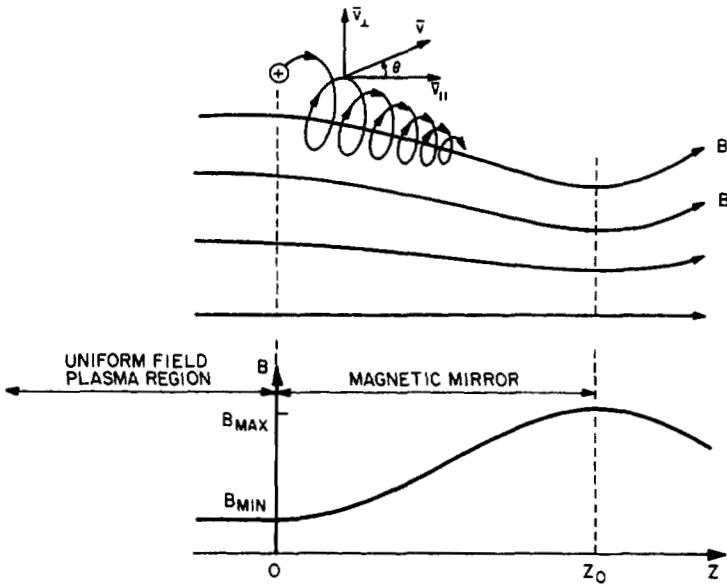
Figure 3.14 The motion of positive charged particles in the magnetic field gradient of a magnetic mirror.

The radius of the orbit is the gyroradius, given by

$$r_g = R \equiv \frac{m v_\perp}{q B} \qquad (3.66)$$

where $v_\perp$ is the velocity perpendicular to the magnetic field. The current associated with a singly-charged gyrating particle is equal to its charge, e, times the frequency with which it gyrates around the gyro-orbit,

$$I = ev = \frac{e\omega}{2\pi} \qquad (A). \qquad (3.67)$$

Substituting equations (3.66) and (3.67) into equation (3.65), one obtains the magnetic moment in terms of the kinetic energy perpendicular to B,

$$M = \frac{m v_\perp^2}{2B} = \frac{\mathcal{E}_\perp}{B} \equiv \mu \qquad (3.68)$$

which is an approximate, but not an exact, constant of the motion.

A *magnetic mirror* configuration is illustrated in figure 3.14 and consists of a strong axisymmetric magnetic barrier with maximum field B_{max} on the right, and a region of weaker magnetic field B_{min} on the left, in which a plasma is confined. In this cylindrical coordinate system,
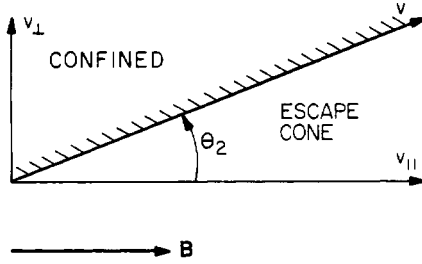
Figure 3.15 Velocity space in the uniform magnetic field region of figure 3.14. Particles within the escape cone will be lost through the magnetic mirror; those in the confined region will be reflected.

the z axis points along the axis of the magnetic field. The distance z_0 separates the minimum value of the magnetic field B_{min}, and the axial position of the maximum magnetic field, B_{max}.

Figure 3.15 illustrates velocity space for particles in the region $0 \leqslant z \leqslant z_0$. The angle θ is the angle between the z direction, and the total velocity vector v, such that

$$v_\perp = v \sin \theta. \tag{3.69}$$

If the confined plasma is free of electric fields, the magnetic moment, given by equation (3.68), will remain constant as the particle moves from the boundary of the uniform plasma region at $z = 0$, to the point of maximum magnetic field at $z = z_0$,

$$\mu(z = 0) = \mu(z = z_0). \tag{3.70}$$

If the particle still has a non-zero parallel velocity at the point $z = z_0$, it will be lost to the right. Thus, the particle that just reaches $z = z_0$ at $B = B_{max}$, and has $v_\parallel = 0$ at that point, is the particle on the verge of confinement. These particles will have $\theta = \pi$ and $v = v_\perp$ at $z = z_0$.

If the magnetic moment remains constant, its value at $z = 0$ and at $z = z_0$ must be the same,

$$\mu = \frac{m v^2 \sin^2 \theta_2}{2 B_{min}} = \frac{m v^2}{2 B_{max}} \tag{3.71}$$

where θ_2 is the *escape cone angle* in velocity space at $z = 0$, illustrated in figure 3.15. Within this angle in velocity space, particles in the uniform plasma region on the left will be lost from containment because they have too much parallel velocity. Outside the escape cone, particles will remain confined for as long as collisions do not knock them from the

confined region into the escape cone. This critical escape cone angle is found from equation (3.71),

$$\sin \theta_2 = \left(\frac{B_{\min}}{B_{\max}} \right)^{1/2} . \qquad (3.72)$$

The fraction of an initially isotropic distribution of particles released in the uniform field region on the left which remains confined can be calculated. If each particle is represented as a point in velocity space, the initial distribution function $f(v)$ is spherically symmetric and hence depends only on the radial coordinate in velocity space, which is the speed, v. The fraction F_T of trapped particles is therefore

$$F_T = \frac{\int_0^\infty v^2 dv \int_{\theta_0}^{\pi - \theta_2} \sin \theta \, d\theta \int_0^{2\pi} f(v) \, d\phi}{\int_0^\infty v^2 dv \int_0^\pi \sin \theta \, d\theta \int_0^{2\pi} f(v) \, d\phi} . \qquad (3.73)$$

The numerator is the number of trapped particles in figure 3.15, and the denominator is the total number of particles in the initial, isotropic distribution. Performing the integrations indicated, and making use of equation (3.72) for the escape cone angle θ_2, one obtains

$$F_T = \cos \theta_2 = \left(1 - \frac{B_{\min}}{B_{\max}} \right)^{1/2} . \qquad (3.74)$$

Magnetic mirrors are an example of open-ended magnetic containment devices in which the field lines leave the containment volume and intersect the walls. This leads to particle losses in a collisional plasma, since a 90° scattering collision anywhere in the containment volume can lead to a particle being deposited in the escape cone. Such a particle will be lost after only one transit time across the length of the plasma.

The *magnetic nozzle* is a related device which is the inverse of the magnetic mirror. Its functioning also depends on the constancy of the magnetic moment, and is found in many industrial applications of plasmas. This device, at first glance, appears to violate the second law of thermodynamics because it is capable of converting a random distribution of velocities into a virtually unidirectional beam through the use of a static magnetic field that cannot do work on the charged particle distribution. In performing this function, the magnetic nozzle acts like an aerodynamic nozzle to convert thermal energy into directed motion, but the physics of the process is entirely different, since the magnetic nozzle relies upon an absence of collisions among the charged particles.

The magnetic field in a characteristic magnetic nozzle is shown in figure 3.16. If the magnetic induction varies slowly over the distance
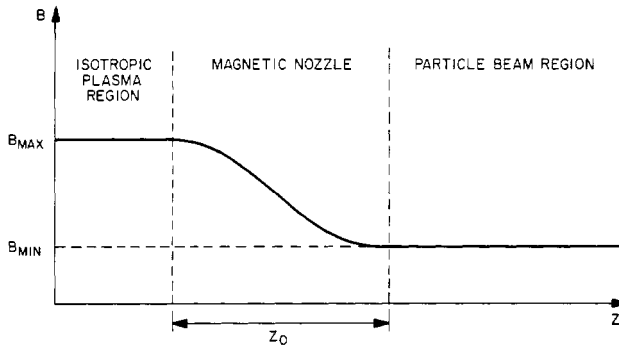
Figure 3.16 A schematic drawing of a magnetic nozzle.

z_0 in the sense described by the inequality of equation (3.64), then the magnetic moment given by equation (3.71) for charged particles moving from the uniform field region on the left into the low field region on the right will remain constant. If the magnetic moment remains constant, as the magnetic induction B decreases in the denominator, then the perpendicular energy, and the perpendicular component of velocity, must also decrease as the particle moves to lower magnetic fields. If the particle motion remains adiabatic, essentially all of the perpendicular energy initially possesed by the particle on the left can be converted into parallel velocity on the right, i.e. the isotropic particle distribution has been converted into a beam. The magnetic nozzle will be discussed further in the next section.

3.4.3 Magnetic Confinement of Industrial Plasmas

The industrial applications of both DC and RF glow discharges can benefit from the application of magnetic fields. Magnetic confinement can increase the power efficiency or the number density of DC or RF glow discharges; a magnetic field also can improve the mass utilization efficiency in contexts where one wishes to ionize as much as possible of the gas flow, as in plasma or ion sources; magnetic fields parallel to a wall can also reduce wall bombardment by charged particles and associated sputtering, and thereby lower impurity concentrations. In certain parameter ranges, magnetic fields can improve the stability of operation of a glow discharge (although it is also possible to destabilize a glow discharge by application of magnetic fields); magnetic fields can be used to manipulate a plasma configuration and improve uniformity of surface interaction; and finally, magnetic fields can be used to focus or increase the perpendicularity of ion bombardment in many plasma processing applications.
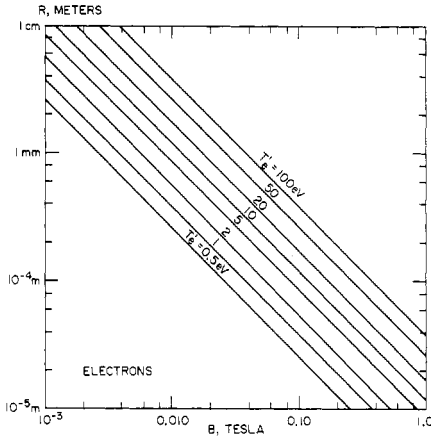
Figure 3.17 Magnetization criteria for electrons. The electron gyroradius is plotted as a function of magnetic induction for various electron kinetic energies.

In order to use magnetic fields effectively, it is necessary that a plasma be *magnetized*, that is, the following two criteria must apply:

$$\omega_c \tau = \frac{eB}{m v_c} \gg 1 \qquad (3.75)$$

and

$$a > R = \frac{mv}{eB}. \qquad (3.76)$$

Equation (3.75) requires that a charged particle perform many gyrations before it collides, and equation (3.76) requires that the radius of gyration, R, of a charged particle be less than the plasma radius, a. An alternative requirement to equation (3.75) is that the particle's mean free path be comparable to or larger than the plasma radius.

On figure 3.17 the electron gyroradius is plotted as a function of the electron kinetic energy and magnetic induction. This figure indicates that magnetic inductions greater than 0.004 T will magnetize a plasma if the background neutral gas pressures are low enough to allow electrons to perform several gyrations between collisions. As a practical matter, if one magnetizes the electrons of a glow discharge, the entire plasma also is magnetized, since the ions cannot leave without setting up very strong electric fields which tend to keep them in place. Thus, magnetizing and containing electrons is equivalent to magnetically containing the entire plasma for most glow discharges.

When one wishes to manipulate the ion population magnetically, however, it is necessary that the ions also meet the magnetization criteria of equations (3.75) and (3.76). The ions are harder to magnetize because of their higher mass, lower gyrofrequency, and larger gyroradius. Figure 3.18 shows ion gyroradii as a function of the ion kinetic energy and magnetic induction for He^+ ions, Ne^+ ions, and A^+ ions. In
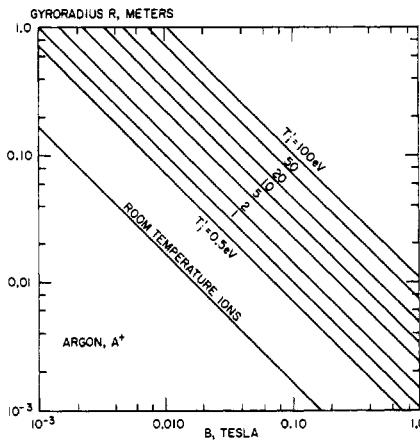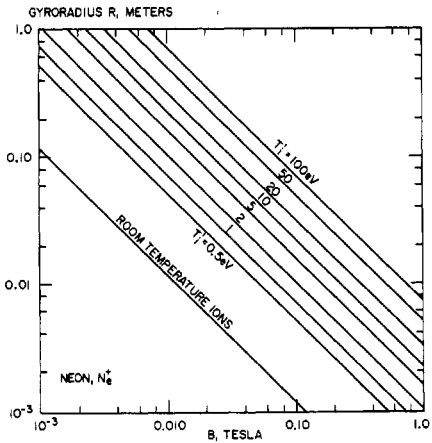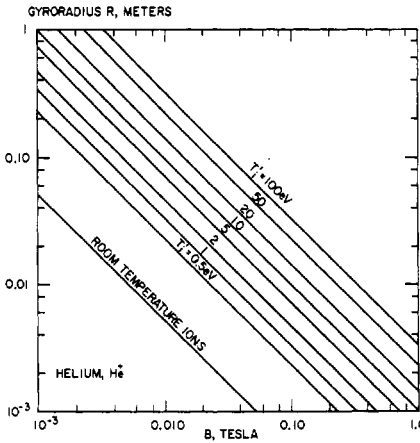
Figure 3.18 Magnetization criteria for selected singly charged ions. The gyroradius is plotted as a function of magnetic induction for several ion kinetic energies, including room temprature ions at 0.025 eV. Data are shown for He$^+$, Ne$^+$, and A$^+$.

many industrial glow discharges, the ions collide so frequently with the neutral background gas that they are essentially at room temperature, $T_i' = 0.025\ eV$. For such ions, the gyroradii are less than the typical plasma dimensions for magnetic inductions greater than 0.01 T. If the ion energies reach 1000 eV, they are relatively hard to magnetize, and might require magnetic inductions of several tenths of a tesla.

In order to manipulate glow discharge ions or electrons magnetically, it is necessary that they be adiabatic in the sense of equation (3.64), as well as being magnetized. Consider the magnetic mirror geometry of figure 3.14. If equation (3.64) is satisfied, the magnetic moment, defined in equation (3.68), is constant, and one can write

$$\mu = \frac{v_\perp^2}{B} = \frac{v^2 \sin^2 \theta_2}{B_{\min}} = \frac{v^2 \sin^2 \theta_1}{B_{\max}} = \text{constant} \qquad (3.77)$$

where θ_2 is the angle of the velocity vector with respect to the magnetic
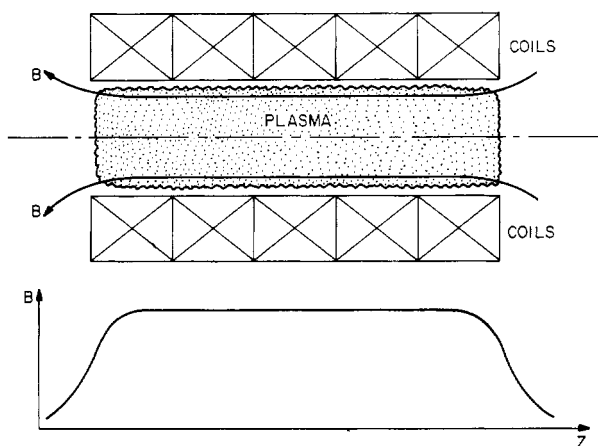
Figure 3.19 Uniform field configuration with plasma trapped in the region of minimum magnetic field.

field in the minimum magnetic field on the left, and θ_1 is the angle of the velocity vector in the maximum magnetic field on the right. The distance z_0 is taken as the distance required to go from B_{min} to B_{max} along the z axis.

The variations of the *magnetic barrier* or *magnetic mirror* shown in figure 3.14 which are used to confine industrial glow discharge plasmas are almost infinite, but most of them attempt to improve the confinement of the plasma by surrounding it with an increasing magnetic field near the walls. The configuration of figure 3.14 can be used to reflect a plasma from a wall, and two such mirrors facing each other can be used to confine a plasma which would otherwise escape along magnetic field lines.

Coaxial magnetic confinement can be accomplished with an axisymmetric array of coils, or with permanent magnets capable of generating an equivalent field. Figure 3.19 illustrates an axisymmetric, uniform magnetized plasma, useful in some plasma ion sources. Such a plasma can interact only weakly with the side walls, but is not confined along the magnetic field lines and is free to escape from the ends. Figure 3.20 illustrates an axisymmetric plasma, confined by two opposing magnetic mirrors, like that shown in figure 3.14, thus trapping all particles whose velocity vectors at the midplane are greater than θ_2. In such a magnetic mirror geometry, loss of confinement can result only when ions or electrons are scattered into the escape cone by collisions.

In the *magnetic mirror*, or *magnetic bottle*, of figure 3.20, the currents in the two coils which generate the mirror configuration flow in the same sense. Figure 3.21 illustrates an axisymmetric *cusp*, in which the plasma is trapped in the low field region between two coils, the currents of
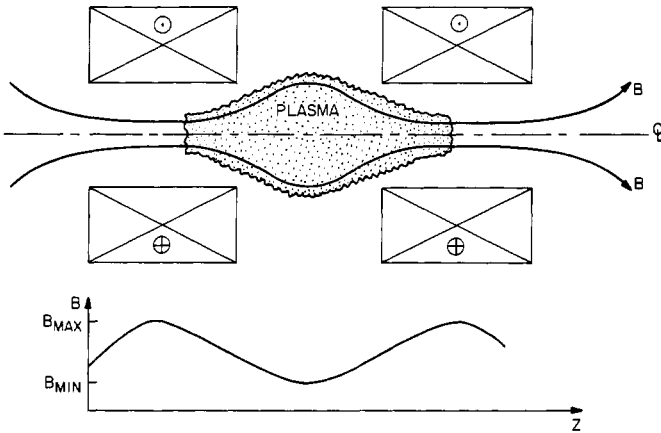
Figure 3.20 Magnetic bottle configuration, in which the plasma is trapped between two regions of increasing magnetic field.
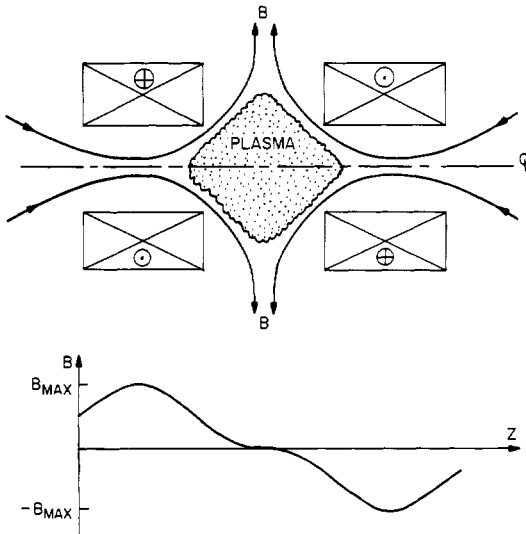
Figure 3.21 Magnetic cusp geometry, formed by two axisymmetric coils with currents flowing in opposite senses. The plasma is confined in the low field region between the two coils.

which flow in opposite senses. The cusp configuration of figure 3.21 is the basis for the *multipolar cusp* confinement widely used in industrial applications.

Figure 3.22 shows how the magnetic confinement configurations discussed above can be produced with permanent magnets. It is now possible to buy, relatively cheaply, permanent magnets which are capable
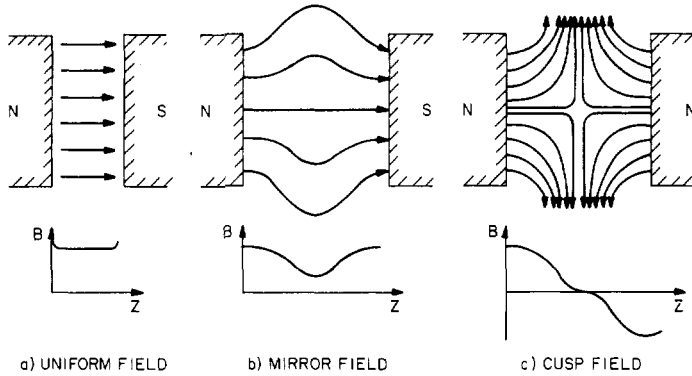
Figure 3.22 Methods of generating a uniform, mirror, and cusp magnetic containment geometry with permanent magnets.
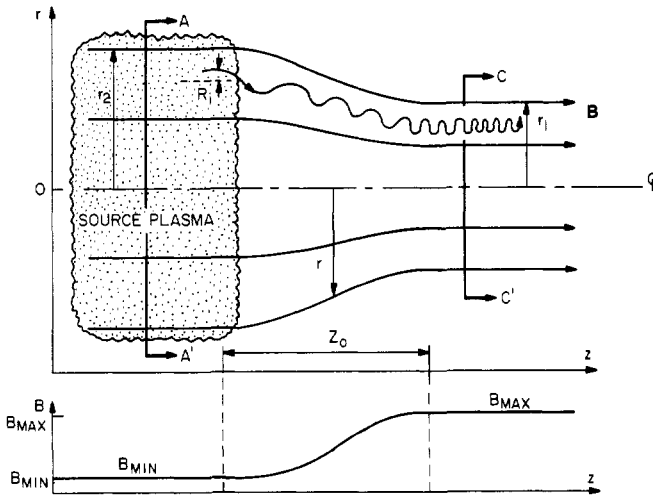
Figure 3.23 The magnetic diffuser, in which an isotropic source of plasma on the left flows into an increasing magnetic field. The particle velocity parallel to the magnetic induction is slowed as a result of the conservation of the adiabatic invariant.

of 0.2 T on their pole face, and 0.1 T at 1 cm above the pole face. Such magnetic inductions are adequate to magnetize electrons and room temperature ions, and thus a properly designed array of such magnets on the walls of vacuum vessels can greatly reduce plasma contact with the walls and improve plasma confinement in the working volume.

In some applications, it is desirable to slow down the parallel velocity and/or decrease the radius of a plasma. To accomplish this, one can use a *magnetic diffuser*, shown on figure 3.23. The magnetic diffuser is also
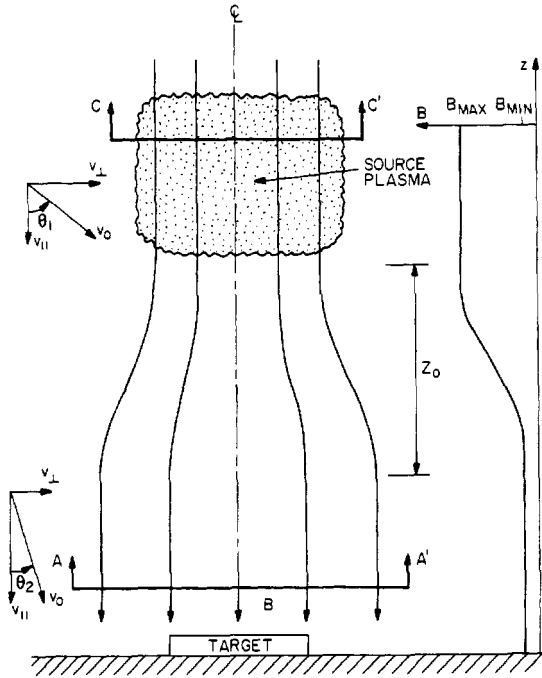
Figure 3.24 The magnetic nozzle, in which an isotropic source of plasma in a strong magnetic induction expands along field lines to a region of weaker magnetic field over the distance z_0.

a magnetic mirror, and its ability to reflect incident charged particles can be a drawback, particularly in applications for which one wishes simply to decrease the diameter of a flowing plasma. The fraction reflected is given by equation (3.74), provided that the particle motion is adiabatic.

The radius of the plasma at the position (r, z) is found from the conservation of magnetic flux along the z axis,

$$\phi = \pi r^2 B = \pi r_2^2 B_{\min} = \pi r_1^2 B_{\max}. \qquad (3.78)$$

Thus, the plasma radius at the position r is given by

$$r = r_2 \sqrt{\frac{B_{\min}}{B}} \qquad (3.79)$$

and the final radius at $B_{\max}$ is given by

$$r_1 = r_2 \sqrt{\frac{B_{\min}}{B_{\max}}}. \qquad (3.80)$$

A related device is the *magnetic nozzle* shown in figure 3.24. This device is used in materials processing, for example, to spread uniformly the plasma (ions) escaping from a source at B_{max}, over a target located downstream in a weaker magnetic field, B_{min}. The magnetic nozzle also is used to reduce the velocity transverse to the magnetic field. Since no particles are lost or reflected in moving from CC' to the position AA' in a magnetic nozzle, the equation of continuity along the z axis may be written

$$n_1 A_1 v_1 = n_2 A_2 v_2 \qquad (3.81)$$

where n are the particle number densities, A the cross-sectional areas of the plasma, and v_1, v_2 the parallel velocities in the strong and weak magnetic inductions, respectively. If the ions moving along the magnetic field are adiabatic, the parallel velocities are given by

$$v_1 = v \cos \theta_1 \qquad (3.82a)$$

and

$$v_2 = v \cos \theta_2. \qquad (3.82b)$$

Substituting equations (3.82a) and (3.82b) into equation (3.81) gives the ion number density, n_2, to be expected at the position AA',

$$n_2 = n_1 \frac{B_{min}}{B_{max}} \frac{\cos \theta_1}{\cos \theta_2} \qquad (3.83)$$

where equation (3.80) was used to eliminate the square of the radii appearing in the area ratio.

From equation (3.77), the constancy of the magnetic moment, one obtains

$$\sin^2 \theta_2 = 1 - \cos^2 \theta_2 = \frac{B_{min}}{B_{max}} \sin^2 \theta_1. \qquad (3.84)$$

Solving equation (3.84) for $\cos \theta_2$, and substituting this into (3.83) yields the number density above the target,

$$n_2 = n_1 \frac{B_{min}}{B_{max}} \frac{\cos \theta_1}{\sqrt{1 - \frac{B_{min}}{B_{max}} \sin^2 \theta_1}}. \qquad (3.85)$$

If the source plasma is isotropic in velocity space, one can obtain the number density at the target by integrating the right-hand side of equation (3.85) over the angles $0 < \theta_1 < \pi/2$, and using the definition of the magnetic mirror ratio,

$$R_m \equiv \frac{B_{min}}{B_{max}}. \qquad (3.86)$$

Equation (3.85) can be written,

$$n_2 = n_1 R_m \int_0^{\pi/2} \frac{\cos\theta \, d\theta}{\sqrt{1 - R_m \sin^2\theta}} = n_1 \sqrt{R_m} \sin^{-1}\sqrt{R_m} \approx n_1 R_m. \quad (3.87)$$

Thus, expanding a plasma in a magnetic nozzle will reduce the source plasma density by a factor approximately equal to the mirror ratio over which the plasma ions remain adiabatic and magnetized.

One industrial variant of figure 3.24 is use of the magnetic nozzle in an *electron cyclotron resonance* (ECR) heated plasma in which the electrons are given a very large perpendicular velocity in the source plasma. The electrons then leave the source region with an angle in velocity space $\theta_1 \approx (\pi/2) - \theta$ where $\theta \ll \theta_1$, so equation (3.85) gives the approximate density fall-off,

$$n_2 \approx n_1 R_m \frac{\theta}{\sqrt{1 - R_m}} \quad (3.88)$$

which is a much smaller density at the workpiece than is produced by the isotropic plasma described by equation (3.87).

In etching applications, the magnetic nozzle is also used to reduce the transverse velocity of ions which hit the target in the region AA', or to get the angle θ_2 as small as possible. From equation (3.77), if the particle motion is adiabatic, one can calculate the decrease in θ of a particle starting out with the angle θ_1,

$$\sin\theta_2 = \sin\theta_1 \sqrt{\frac{B_{min}}{B_{max}}} = \sin\theta_1 \sqrt{R_m}. \quad (3.89)$$

The impact angle θ_2 is plotted as a function of the starting angle θ_1 and of the mirror ratio R_m in figure 3.25. For small angles, one has from equation (3.89)

$$\theta_2 \approx \theta_1 \sqrt{R_m}. \quad (3.90)$$

Thus, the magnetic nozzle can decrease beam divergence and undercutting in etching applications. It should be noted, however, that it is relatively difficult to keep ions both magnetized and adiabatic over small magnetic mirror ratios, $R_m < 0.10$.

Multipolar magnetic cusp confinement is a method for keeping plasma away from the walls of devices using glow discharges. On figure 3.26 is a *picket fence* multipolar cusp configuration, generated by a series of current-carrying wires on the outside of a vacuum vessel wall. Adjacent conductors have equal currents flowing in opposite directions. The picket fence configuration can also be generated (and usually is) by a row of permanent magnets. The confined plasma at the top of figure 3.26 will

IMPACT ANGLE θ_2, DEGREES
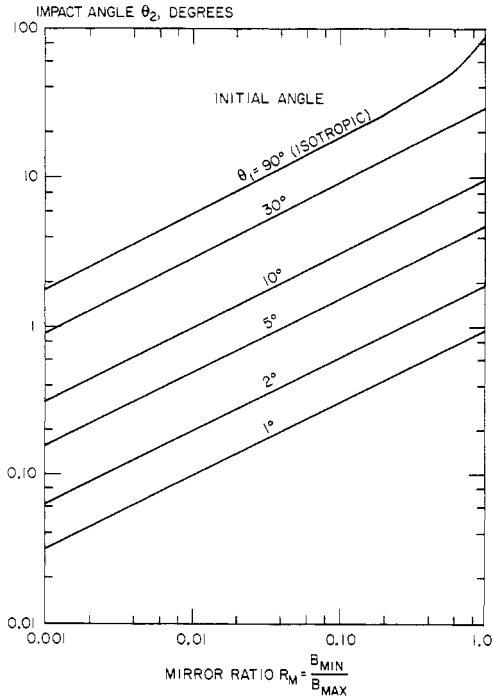
Figure 3.25 The reduction of transverse velocity components by expansion in a magntic nozzle. The impact angle on the target of figure 3.24 is shown as a function of the magnetic mirror ratio for adiabatic expansion with initial angle of the velocity vector θ_1.
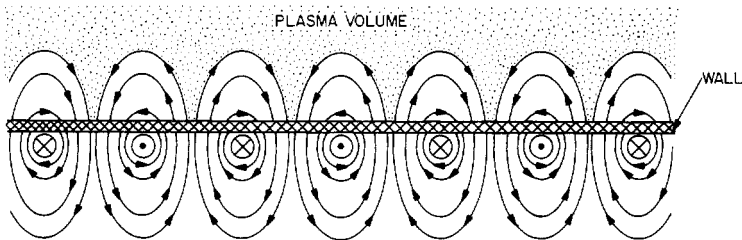
Figure 3.26 The picket fence multipolar magnetic field configuration generated by oppositely flowing currents on the surface of a vacuum vessel.

be kept away from the tank wall by the increasing magnetic field, with some particles lost along the line cusp which contacts the wall halfway between the conductors. In such configurations, it is usual practice to put water cooling lines outside the vacuum vessel halfway between the conductors, where the cusp deposits the plasma constituents with their accompanying heat load.

a) CHECKERBOARD ARRAY

b) AXISYMMETRIC CUSP ARRAY

c) LONGITUDINAL CUSP ARRAY
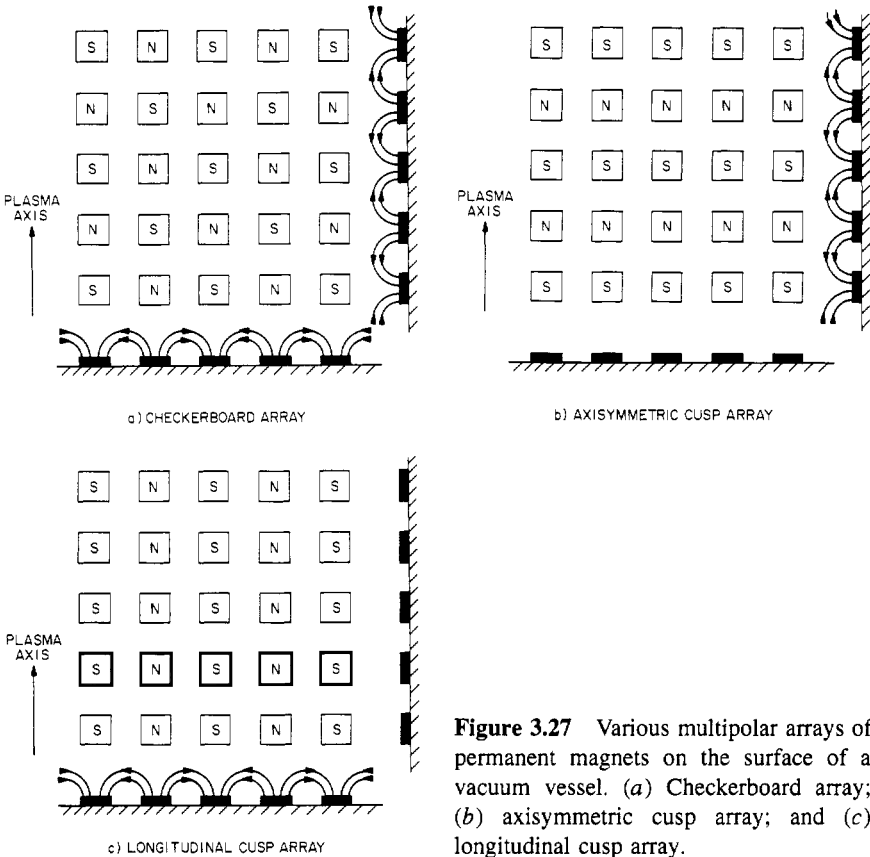
Figure 3.27 Various multipolar arrays of permanent magnets on the surface of a vacuum vessel. (*a*) Checkerboard array; (*b*) axisymmetric cusp array; and (*c*) longitudinal cusp array.

Multipolar cusp confinement by small permanent magnets can be effected in at least three ways. Figure 3.27(*a*) shows the *checkerboard array* which produces cusps both axially and azimuthally, if the plasma axis is pointing vertically upward as indicated. Figure 3.27(*b*) is an *axisymmetric cusp array* which gives a series of axisymmetric cusps along the vertical axis. The cusps look like a series of axisymmetric bands along the axial length of the vacuum tank wall. On figure 3.27(*c*) is the *longitudinal cusp array*, which gives a series of longitudinal cusps which vary in azimuth as one moves around the circumference of the vacuum tank, but with little or no axial variation.

Multipolar cusps can reduce wall losses and increase the density of DC and RF glow discharge plasmas. On figure 3.28 is a plan view of a longitudinal cusp array which was used in the UTK (University of Tennessee, Knoxville) Plasma Science Laboratory to improve confinement in the Microwave Plasma Facility (MPF), a uniform, large volume plasma generated with 2.45 GHz microwave power in a vacuum tank 0.5 m diameter and 1 m high. The multipolar
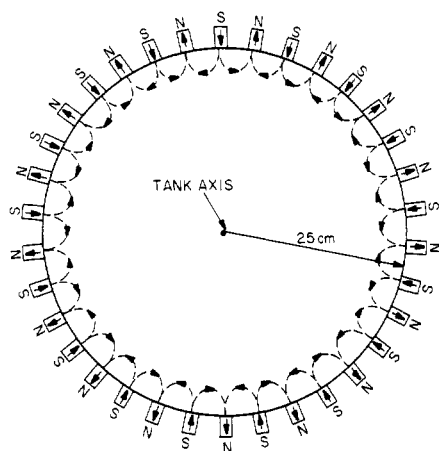
Figure 3.28 Longitudinal cusp array of multipolar magnets used for confinement of a cylindrical microwave plasma.

cusp confinement used consists of 34 parallel rows of permanent magnets which produce a field of 0.03 T a few millimeters above the inner surface of the vacuum tank. In order to assess the confinement effect of these longitudinal cusps, which were located on the exterior periphery of the cylindrical portion of the vacuum tank but not on the end plates, the plasma electron density was measured before and after installing the magnets, under conditions of nitrogen gas pressure and microwave power input as nearly identical as possible. It was found that an electron number density improvement of a factor of 1.7 occurred after the magnets were installed. No magnets were put on the end plates because of the many service and diagnostic ports located there. In a similar unpublished experiment at Berkeley, (M A Lieberman, private communication, 1991), an improvement in electron number density of a factor of 2.0 was seen when multipolar magnets were placed on all surfaces of a smaller plasma experiment. These investigations clearly indicate that the peripheral multipolar cusp considerably improves the confinement of glow discharge plasmas.

3.5 RELATIVISTIC CHARGED PARTICLE MOTION

Einstein's theory of relativity is one of the major accomplishments of 20th century science, and has widespread application to astrophysics and high energy physics research. The energies required to produce relativistic effects are so high that it has not been until recently that these effects have been of interest in industrial applications. There is much industrial involvement in the manufacture of high energy particle
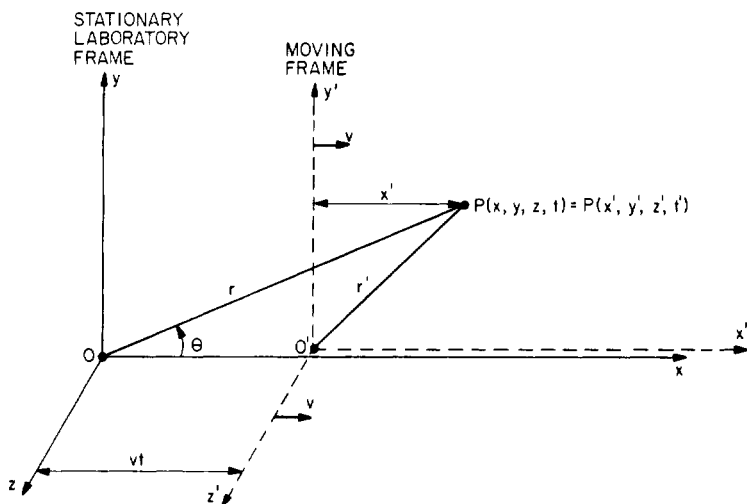
Figure 3.29 Two Cartesian coordinate systems: the laboratory frame of reference O, which remains fixed; and the moving coordinate system O', which moves in the x direction with a velocity v.

accelerators for physics research. Beyond that, high energy accelerators have been applied to the production of energetic particles and radiation for medical therapy, food processing, and radiation for microlithography of microelectronic circuits. The highly precise and accurate measurement of time now possible shows that satellite-borne clocks are affected by relativistic effects. Relativistic effects also are important in many microwave tubes which depend on the relativistic mass increase to provide plasma instabilities which generate high frequency radiation. It is therefore appropriate to review some basic concepts and phenomena related to relativistic charged particle motion.

3.5.1 Galilean Transformation

The question of relative motion in Newtonian or classical mechanics is described by the *Galilean transformation*, named in honor of the Italian physicist Galileo Galilei (1564–1642) who was the first to study particle dynamics quantitatively and experimentally with modern scientific procedures. The Galilean transformation is illustrated in figure 3.29, which shows two Cartesian frames of reference locating an object at the point P. The unprimed Cartesian coordinate system is the stationary, sometimes called the *laboratory frame of reference*. In addition, there is a moving frame of reference, the primed system, which is moving in the x direction with a velocity v. The point P is at a radius r from the origin

O of the laboratory frame, and a distance r' from the origin O' of the moving frame of reference.

In the laboratory frame, the coordinates of the point P are

$$P(r, t) = P(x, y, z, t) \qquad \text{origin O.} \tag{3.91}$$

The coordinates of the point P in the coordinate system moving along the x axis with a velocity v are

$$P(r', t') = P(x', y', z', t') \qquad \text{origin O'.} \tag{3.92}$$

For the Galilean transformation, the relationship between the radius vectors of the point P in the two coordinate systems is

$$r' = r - vt \tag{3.93a}$$
$$t' = t. \tag{3.93b}$$

In Cartesian coordinates, the relationship between the frames of reference is

$$x' = x - vt \tag{3.94a}$$
$$y' = y \tag{3.94b}$$
$$z' = z \tag{3.94c}$$
$$t' = t \tag{3.94d}$$

Note that time is assumed to elapse at the same rate in both the stationary and moving Galilean coordinate systems. In Galilean, also called *inertial coordinate systems*, Newton's law $F = ma$ is valid for all systems moving with constant velocity with respect to each other, and the Galilean transformation described by equations (3.93) and (3.94) holds.

3.5.2 Lorentz Transformation

The *Einstein principle* is the basis of *special relativity*. It states the assumption that the velocity of light in free space is the same for all observers in uniform relative motion, and is therefore independent of the relative motion of source and observer. It follows from the Einstein principle that no experiment in a closed system can detect a uniform translatory motion in space. That is, an observer in a closed box at the point P of figure 3.29 could not tell whether he was moving with respect to the laboratory frame of reference or not. This principle was first stated by Albert Einstein (1879–1956) in 1905.

Since the speed of light in free space plays a fundamental role in the theory of relativity, it is useful to normalize the velocity, v, of a moving frame of reference to the speed of light, as follows:

$$\beta \equiv \frac{v}{c}. \tag{3.95}$$

Because it appears so frequently, the *relativistic parameter* γ is defined,

$$\gamma \equiv \frac{1}{\sqrt{1 - v^2/c^2}} = \frac{1}{\sqrt{1 - \beta^2}}. \tag{3.96}$$

In the theory of special relativity, the coordinate transformation from the stationary to a moving frame of reference is described by the *Lorentz transformation*, named after Hendrick Lorentz (1853–1928), which is given by

$$x' = \frac{1}{\sqrt{1 - \beta^2}}(x - vt) = \gamma(x - vt) \tag{3.97a}$$

$$y' = y \tag{3.97b}$$

$$z' = z \tag{3.97c}$$

$$t' = \frac{1}{\sqrt{1 - \beta^2}}\left(t - \frac{vx}{c^2}\right) = \gamma\left(t - \frac{\beta x}{c}\right). \tag{3.98}$$

Note that in the Lorentz transformation, time elapses at different rates in the stationary and moving frames of reference.

An immediate implication of the Lorentz transformation is that a rod oriented along the x axis of length L' as measured by a moving observer in the moving frame of reference O' has an apparent length in the laboratory frame of reference O given by

$$L = x_2 - x_1 = \frac{x_2' - x_1'}{\gamma} = \sqrt{1 - \beta^2}L'. \tag{3.99}$$

In the laboratory, the rod will appear shorter in the x direction by the factor $\sqrt{1 - \beta^2}$ than it would appear to the observer moving with the rod. This phenomenon is called the *Fitzgerald–Lorentz contraction*.

The behavior of time in the two coordinate systems is also very interesting. The duration of an event T' measured in the moving coordinate system O' appears in the laboratory frame of reference O as a duration T, given by

$$T = t_2 - t_1 = \gamma(t_2' - t_1') = \frac{T'}{\sqrt{1 - \beta^2}} = \gamma T'. \tag{3.100}$$

Thus, time intervals registered by a clock moving with the uniform velocity v appear to be lengthened by the factor γ, so the moving clock will appear slow to an observer in the laboratory frame of reference. This phenomenon is called *time dilation*.

3.5.3 Kinematics in Special Relativity

If the point P in figure 3.29 is moving in both the stationary and moving frames of reference O and O', the velocity seen by an observer in the laboratory frame is

$$v = \dot{x}, \dot{y}, \dot{z} = \frac{\mathrm{d}x}{\mathrm{d}t}, \frac{\mathrm{d}y}{\mathrm{d}t}, \frac{\mathrm{d}z}{\mathrm{d}t} \qquad (3.101)$$

while the velocity of P measured by an observer in the moving frame of reference O' is given by

$$v = \dot{x}', \dot{y}', \dot{z}' = \frac{\mathrm{d}x'}{\mathrm{d}t'}, \frac{\mathrm{d}y'}{\mathrm{d}t'}, \frac{\mathrm{d}z'}{\mathrm{d}t'}. \qquad (3.102)$$

The transformation of velocities between these two coordinate systems is given by

$$\dot{x} = \frac{\dot{x}' + v}{1 + (\beta \dot{x}'/c)} \qquad (3.103)$$

$$\dot{y} = \sqrt{1 - \beta^2} \frac{\dot{y}'}{1 + (\beta \dot{x}'/c)} \qquad (3.104)$$

$$\dot{z} = \sqrt{1 - \beta^2} \frac{\dot{z}'}{1 + (\beta \dot{x}'/c)}. \qquad (3.105)$$

Not only is there a relativistic correction to the velocity in the x direction, but there is also a relativistic correction to the components of velocity perpendicular to the relative velocity of the two coordinate systems.

3.5.4 Lorentz Transformation of Electric and Magnetic Fields

In the two coordinate systems of figure 3.29 moving with a relative velocity v along the x axis, an application of the above transformation equations to Maxwell's equations yield the following transformation equations for the electric field and displacement vector,

$$E'_{\parallel} = E_{\parallel} \qquad (3.106a)$$

$$D'_{\parallel} = D_{\parallel} \qquad (3.106b)$$

parallel to the direction of motion (x axis), with

$$E'_\perp = \gamma(E_\perp + v \times B) \qquad (3.107a)$$

and

$$D'_\perp = \gamma\left(D_\perp + \frac{v \times B}{c^2}\right). \qquad (3.107b)$$

transverse to the direction of motion. The magnetic induction and magnetic field strength parallel to the direction of motion are

$$B'_\parallel = B_\parallel \qquad (3.108a)$$

and

$$H'_\parallel = H_\parallel. \qquad (3.108b)$$

These quantities transverse to the direction of motion are given by

$$B'_\perp = \gamma\left(B_\perp - \frac{v \times E}{c^2}\right) \qquad (3.109a)$$

and

$$H'_\perp = \gamma(H_\perp - v \times D). \qquad (3.109b)$$

The above transformation equations predict a *relativistic Doppler effect*. If a moving object at the point P emits radiation with a frequency ω', as measured on the moving object, it will be seen in the laboratory frame as a frequency ω given by

$$\omega' = \omega\frac{1 + \delta\beta}{\sqrt{1 - \beta^2}} = \gamma\omega(1 + \delta\beta) \qquad (3.110)$$

where the parameter δ is a direction cosine. If the stationary observer were to look in the x direction, he would see a *longitudinal Doppler shift* given by

$$\omega' = \omega\gamma(1 \pm \beta) \qquad (3.111)$$

where the $-$ sign is appropriate to an approaching source and gives a higher frequency, i.e. a *blue shift*, as seen by the stationary observer, who measures frequency ω. The $+$ sign is appropriate to a receding source, and is a *red shift* to lower frequency.

In addition to the longitudinal Doppler shift of equation (3.111), another purely relativistic effect, a *transverse Doppler shift*, occurs when $\delta = 0$, or

$$\omega' = \omega\gamma = \frac{\omega}{\sqrt{1 - \beta^2}}. \qquad (3.112)$$

This equation predicts a red shift of moving sources at right angles to the direction of motion, as seen by a stationary observer, and is a direct result of time dilation.

3.5.5 Dynamics in Special Relativity

In special relativity, the particle momentum is the fundamental dynamical variable. If a charge Q is at rest in the moving coordinate system O′ of figure 3.29, and has mass m', the mass $m' = m_0$ is referred to as the *proper* or *rest mass*. The force on a charge in the laboratory frame of reference O is given by

$$F = \frac{dp}{dt} = \frac{d}{dt}\left(\frac{m_0 v}{\sqrt{1 - \beta^2}}\right) = \frac{d}{dt}(\gamma m_0 v). \qquad (3.113)$$

The *apparent mass* of the particle in the laboratory frame of reference, m, may be written as

$$m = \frac{m_0}{\sqrt{1 - \beta^2}} = \gamma m_0 \qquad (3.114)$$

while the momentum in the laboratory frame of reference O is given by

$$p = mv = \frac{m_0 v}{\sqrt{1 - \beta^2}} = \gamma m_0 v. \qquad (3.115)$$

Equation (3.114) predicts that if a particle moves with relativistic velocities with respect to an observer, the apparent mass of that object will increase by the factor γ. This apparent mass increase is detectable experimentally, and has been seen, for example, in high energy particle accelerators when charged particles are accelerated to relativistic velocities.

3.5.6 Particle Energy in Special Relativity

Power input to a relativistic charged particle in the laboratory frame of reference O may be written

$$P = F \cdot v = \frac{d(mv)}{dt} \cdot v \qquad (W) \qquad (3.116)$$

where the momentum mv is given by equation (3.115). By using the relativistic transformation equations discussed above, it can be shown that the power input may be written

$$P = F \cdot v = \frac{d}{dt}\left(\frac{m_0 c^2}{\sqrt{1 - \beta^2}}\right) = \frac{d}{dt}(mc^2). \qquad (3.117)$$

The *rest energy* of a particle in a coordinate system in which it is at rest is given by

$$U_0 = m'c^2 = m_0 c^2. \tag{3.118}$$

The rest energy of an electron is

$$U_e = \frac{m_e c^2}{e} \approx 0.51 \text{ MeV} \tag{3.119}$$

and the rest energy of protons is

$$U_p = \frac{m_p c^2}{e} \approx 935 \text{ MeV}. \tag{3.120}$$

The *total energy* of the charged particle of equation (3.117) in the laboratory frame of reference O is given by

$$U = mc^2 = \frac{m_0 c^2}{\sqrt{1 - \beta^2}} = \gamma m_0 c^2 = \gamma U_0. \tag{3.121}$$

The relativistic kinetic energy $\mathcal{E}$ in the laboratory frame of reference O is given by

$$\mathcal{E} = U - m_0 c^2 = m_0 c^2 (\gamma - 1). \tag{3.122}$$

For classical, non-relativistic velocities such that v is much less than c, the factor γ in equation (3.122) can be expanded in the small parameter $\beta \ll 1$, recovering the classical result for the kinetic energy,

$$\mathcal{E} \approx \tfrac{1}{2} m_0 v^2. \tag{3.123}$$

The relativistic mass-related energy increase described by equation (3.122) is plotted on figure 3.30 as a function of the relativistic parameter β^2. The classical kinetic energy is shown by the dotted line; the relativistic energy does not depart too far from the classical value for $\beta^2 < 0.2$, but near $\beta = 1.0$ increases very dramatically.

Finally, *the relativistic energy–momentum relation* is

$$\left(mc^2\right)^2 = \left(m_0 c^2\right)^2 + p^2 c^2. \tag{3.124}$$

In cylindrical coordinates, the relativistic centrifugal force on a particle in the laboratory system O is given by

$$mr\dot{\theta}^2 = \frac{m_0 r \dot{\theta}^2}{\sqrt{1 - \beta^2}} = \gamma m_0 r \dot{\theta}^2 \tag{3.125}$$

and the relativistic angular momentum in the laboratory frame of reference O is given by

$$p_\theta = mr^2 \dot{\theta} = \gamma m_0 r^2 \dot{\theta}. \tag{3.126}$$
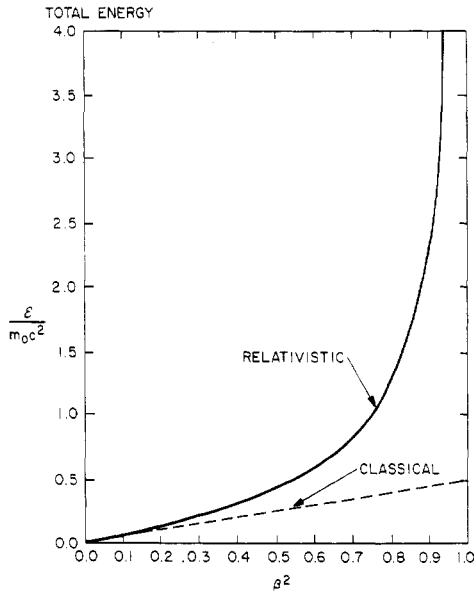
Figure 3.30 The normalized relativistic energy $\mathcal{E}$ as a function of the relativistic velocity ratio β.

3.6 THEORY OF PLANAR DIODES

The theory of planar diodes is fundamental to an understanding of the generation of monoenergetic electron and ion beams, and also to an understanding of the operation and limitations of high power vacuum tubes. In this section we will begin with the theory of non-relativistic, planar diodes.

3.6.1 Characteristics of the Planar Diode

A schematic drawing of the plane, parallel diode is shown in figure 3.31. In such a diode, electrons/ions are emitted from the cathode/anode with zero initial velocity, and are accelerated across a gap of width d, with a potential drop V_0. Figure 3.31 shows a plane parallel diode operating with an electron current. In such a diode, the current density is a constant, independent of the coordinate x:

$$J = n_e e v_e = \text{constant} \qquad (3.127)$$

since there exist no sources or sinks of charge between the electrodes. The potential V_0 is maintained by a DC power supply.

In space-charge limited flow, the cloud of electrons in transit across the diode becomes sufficiently dense that the electric field is reduced near
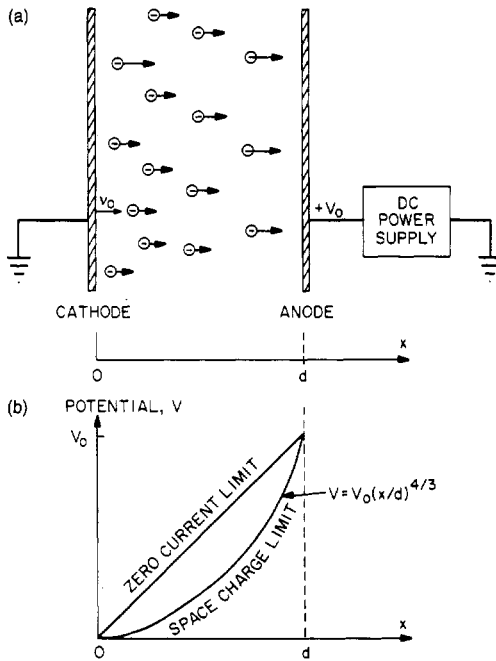
Figure 3.31 Top: schematic of the plane parallel diode. Electrons are emitted from the cathode at $x = 0$, and accelerated to an anode located at $x = d$, maintained at a voltage V_0. Bottom: electrostatic potential as a function of position x for the zero current limit, and for space-charge limited current.

the emission electrode, and is zero at the cathode surface. In figure 3.31 the potential is plotted schematically as a function of distance across the diode. In the zero current limit, when the current density is too small to affect the electric field, the potential is a linear function of the distance across the diode. Under space-charge limited current conditions, the electric field is zero at the cathode surface, and increases with distance according to a power law that will be derived below.

3.6.2 Operation in the Vacuum Limit

In the limit for which the current density and charge density between the electrodes is approximately equal to zero, *Poisson's equation* (one of Maxwell's equations) for the potential between the plates may be written

$$\nabla^2 V = \frac{\mathrm{d}^2 V}{\mathrm{d}x^2} = -\frac{e n_e}{\varepsilon_0} \approx 0. \tag{3.128}$$

Integrating this equation once and applying the boundary conditions on figure 3.31, one finds for the electric field

$$E_0 = \frac{V_0}{d} \quad \text{(V/m)}. \tag{3.129}$$

Integrating this electric field once more, with the boundary condition that the potential is zero at $x = 0$, yields

$$V(x) = V_0 \frac{x}{d} \quad \text{(V)}. \tag{3.130}$$

This linear increase of potential with distance in the zero current limit is shown in figure 3.31.

3.6.3 Space-Charge Limited Current Flow

In the upper limit of *space-charge limited current flow* across the diode, we assume that the cathode freely emits electrons, until the space charge in transit between the plates builds up to the point where the electric field is zero at $x = 0$. At this point, no additional electrons can flow out of the cathode. This condition is the *space-charge limited current density*, J_c. For this condition Poisson's equation is

$$\nabla^2 V = \frac{\mathrm{d}^2 V}{\mathrm{d}x^2} = -\frac{\rho}{\varepsilon_0} = -\frac{en_e}{\varepsilon_0}. \tag{3.131}$$

Since there are no sources or sinks of electrons between the plates, the current density may be written

$$J = -en_e(x)v(x) = \text{constant}. \tag{3.132}$$

If the electrons are emitted with a velocity v_0, conservation of energy as the electron moves between the electrodes requires that

$$\tfrac{1}{2}mv^2 = eV + \tfrac{1}{2}mv_0^2 \tag{3.133}$$

from which we obtain the electron velocity at the position x,

$$v(x) = \sqrt{v_0^2 + \frac{2eV}{m}} \quad \text{(m/s)}. \tag{3.134}$$

Solving equation (3.132) for $n_e(x)$ and substituting it into equation (3.131), we obtain with the help of equation (3.134),

$$\frac{\mathrm{d}^2 V}{\mathrm{d}x^2} = -\frac{en_e(x)}{\varepsilon_0} = \frac{J}{\varepsilon_0 v(x)} = \frac{J}{\varepsilon_0} \left(v_0^2 + \frac{2eV}{m} \right)^{-1/2}. \tag{3.135}$$

This is a second-order nonlinear differential equation which may be integrated once by multiplying both sides by $2\frac{dV}{dx}\,dx$ and using the identity

$$\frac{d}{dx}\left(\frac{dV}{dx}\right)^2 = 2\frac{dV}{dx}\frac{d^2V}{dx^2}. \qquad (3.136)$$

Equation (3.135) becomes

$$2\frac{dV}{dx}\frac{d^2V}{dx^2}dx = \frac{d}{dx}\left(\frac{dV}{dx}\right)^2 dx = \frac{2J}{\varepsilon_0}\left(v_0^2 + \frac{2eV}{m}\right)^{-1/2}dV. \qquad (3.137)$$

If the second and third terms of equation (3.137) are integrated from $x = 0$ to x, equation (3.137) becomes

$$\left(\frac{dV}{dx}\right)^2 - \left(\frac{dV}{dx}\right)_0^2 = \frac{2mJ}{e\varepsilon_0}\left[\sqrt{v_0^2 + \frac{2eV}{m}} - v_0\right]. \qquad (3.138)$$

The second term on the left-hand side of equation (3.138) is zero, since space-charge limited current flow is defined by the requirement that the electric field be zero at $x = 0$.

Equation (3.138) cannot be integrated in elementary form with the initial velocity of the electron v_0 remaining in it as a parameter. However, since the energy of emission is less than a few electronvolts, and V is hundreds of volts or kilovolts in a typical application, it is justified in most respects (except in the calculation of the electron number density as will be seen later) to ignore the initial velocity in equation (3.138). By setting the electric field at the emitting electrode equal to zero and the emission velocity of the electron equal to zero in equation (3.138), one obtains

$$\frac{dV}{dx} = E(x) = \sqrt{\frac{2J}{\varepsilon_0}}\left(\frac{2m}{e}\right)^{1/4}V^{1/4}. \qquad (3.139)$$

Equation (3.139) can be integrated and yields, with the potential set equal to zero at the emitter,

$$\int_0^V \frac{dV}{V^{1/4}} = \left(\frac{8J^2m}{\varepsilon_0^2 e}\right)^{1/4}\int_0^x dx = \frac{4V^{3/4}}{3}. \qquad (3.140)$$

Performing the integration in equation (3.140) and rearranging yields,

$$V(x) = \left(\frac{9J}{4\varepsilon_0}\right)^{2/3}\left(\frac{m}{2e}\right)^{1/3}x^{4/3}. \qquad (3.141)$$

Solving equation (3.141) for the current density, one obtains

$$J = \frac{4\varepsilon_0}{9} \sqrt{\frac{2e}{m}} \frac{[V(x)]^{3/2}}{x^2} \qquad (A/m^2). \qquad (3.142)$$

Equation (3.142) holds all the way across the diode, $0 \leqslant x \leqslant d$, so one may write, at the anode shown on figure 3.31 where $x = d$,

$$J_c = \frac{4\varepsilon_0}{9} \sqrt{\frac{2e}{m}} \frac{V_0^{3/2}}{d^2} \qquad (A/m^2). \qquad (3.143)$$

Equation (3.143) is the *Child space-charge limited flow condition*, first derived by C D Child (1911). This is the maximum possible unipolar current density which can be drawn across a plane parallel diode of separation d with an applied potential V_0 volts between the plates. If the diode is accelerating ions rather than electrons, the ion mass must be substituted in equation (3.143), and if the ion is multiply charged, its charge state must multiply the electronic charge under the square root.

3.6.4 Space-Charge Limited Planar Diodes

Following Forrester (1988), we honor C D Child by defining χ, the '*Child*' for electrons as

$$\chi \equiv \frac{4\varepsilon_0}{9} \sqrt{\frac{2e}{m}} = 2.334 x 10^{-6} \qquad (A/V^{3/2}). \qquad (3.144)$$

Note that this value applies only to electrons. If other species are involved, their charge state and mass must be substituted in equation (3.144), as appropriate. Using equation (3.144), the Child law can be written

$$J_c = \chi \frac{V_0^{3/2}}{d^2} \qquad (A/m^2). \qquad (3.145)$$

If one divides equation (3.141) by the anode conditions, $V(d) = V_0$ at $x = d$, one obtains

$$V(x) = V_0 \left(\frac{x}{d}\right)^{4/3} \qquad (V) \qquad (3.146)$$

which is the power law relationship for the potential as a function of distance shown schematically on figure 3.31. Differentiating equation (3.146) yields the electric field,

$$E(x) = \frac{dV}{dx} = \frac{4}{3} \frac{V_0}{d} \left(\frac{x}{d}\right)^{1/3} = \frac{4E_0}{3} \left(\frac{x}{d}\right)^{1/3} \qquad (3.147)$$
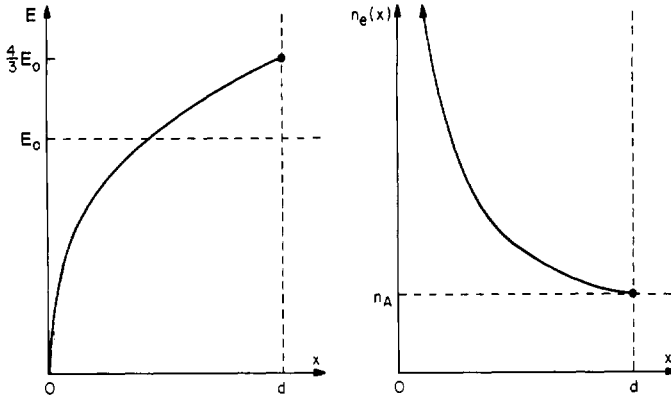
Figure 3.32 A schematic drawing of the electric field (left) and electron number density (right) as a function of position in a space-charge limited diode operating at the Child current density. E_0 is the electric field for the vacuum case; the electron number density becomes infinite as one approaches the cathode at $x = 0$.

where E_0 is the electric field of the vacuum case.

For space-charge limited flow conditions, the electric field between the diode plates ranges over the values

$$0 \leqslant E(x) \leqslant \frac{4}{3} E_0.$$

This relationship for the electric field is shown schematically in figure 3.32. The electron number density between the diode plates may be found from Poisson's equation,

$$\nabla^2 V = \frac{dE}{dx} = -\frac{\rho_e}{\varepsilon_0} = \frac{en_e(x)}{\varepsilon_0} = \frac{4}{9} \frac{V_0}{d^2} \left(\frac{d}{x}\right)^{2/3} \tag{3.148}$$

where the derivative of the electric field in equation (3.147) has been substituted to yield the right-hand term of equation (3.148). From the two right-hand terms of equation (3.148) we can obtain the number density as a function of position,

$$n_e(x) = \frac{4\varepsilon_0 V_0}{9ed^2} \left(\frac{d}{x}\right)^{2/3} \quad \text{(particles/m}^3\text{)}. \tag{3.149}$$

In the vicinity of the cathode, equation (3.149) predicts the aphysical result that the electron number density is infinite at the cathode surface.

This came about because the initial velocity of the electrons was neglected after equation (3.138). At the anode, the electron number density may be written

$$n_e(d) = \frac{4\varepsilon_0 V_0}{9ed^2} = n_A \qquad (3.150)$$

which allows the electron number density as a function of position to be written in terms of the anode number density,

$$n_e(x) = n_A \left(\frac{d}{x}\right)^{2/3}. \qquad (3.151)$$

The qualitative variation of electron number density with position in the space-charge limited diode is sketched in figure 3.32.

The space-charge limited current density across the diode, which is a constant independent of x, can be written with the help of equation (3.127) as

$$J_c = en_e(x)v(x) = en_A v(d) = \text{constant}. \qquad (3.152)$$

From equation (3.134), if the initial velocity is $v_0 = 0$, the conservation of energy requires that

$$v(d) = \sqrt{\frac{2eV_0}{m}}. \qquad (3.153)$$

Substituting equation (3.153) into equation (3.152), one obtains

$$J_c = en_A \sqrt{\frac{2eV_0}{m}} = en_e(x)v(x). \qquad (3.154)$$

Substituting equation (3.151) for the electron number density in the right-hand term of equation (3.154) yields

$$v(x) = \left(\frac{x}{d}\right)^{2/3} \sqrt{\frac{2eV_0}{m}} \qquad \text{(m/s)}. \qquad (3.155)$$

This gives the electron velocity at any position x between the diode plates. If the electrons exit through the anode, as they do in electron guns, their velocity is

$$v(d) = \sqrt{\frac{2eV_0}{m}} \qquad x \geqslant d. \qquad (3.156)$$

Thus, the electrons acquire a velocity appropriate to their potential energy when emitted from the cathode.

The particle flux in electrons per square meter per second at the anode surface for space-charge limited flow is given by

$$\Gamma_c = \frac{J_c}{e} = \frac{\chi}{e}\frac{V_0^{3/2}}{d^2} \qquad \text{(particles/m}^2\text{-s).} \qquad (3.157)$$

For electron guns, the flux Γ_c must be supplied by a hollow cathode or heated filament, the current density of which is greater than or equal to Γ_c.

The power flux in the space-charge limited beam is given by

$$P = J_c V_0 = \chi \frac{V_0^{5/2}}{d^2} \qquad \text{(W/m}^2\text{).} \qquad (3.158)$$

In practical applications, these power fluxes can be quite large, and require active cooling of electrodes or targets on which they impinge.

Space-charge limited diodes are often used in high power radio frequency tubes, in which the electron transit time determines the tube's frequency response. For the vacuum condition with no significant space charge, we get from equation (3.129) Newton's law in the form

$$F = m\frac{\mathrm{d}^2 x}{\mathrm{d}t^2} = eE_0 = \frac{eV_0}{d}. \qquad (3.159)$$

Integrating equation (3.159) twice with the electrons starting out at $x = 0$ with $v_0 = 0$ at $t = 0$, the transit time t_0 may be found from

$$\int_0^d \mathrm{d}x = d = \frac{eV_0}{md}\int_0^v \int_0^{t_0} \mathrm{d}v\,\mathrm{d}t = \frac{eV_0 t_0^2}{2md}. \qquad (3.160)$$

Solving the second and fourth terms of equation (3.160) for the transit time t_0, yields

$$t_0 = d\sqrt{\frac{2m}{eV_0}} \qquad \text{(s).} \qquad (3.161)$$

This transit time places a fundamental limitation on the frequency response of vacuum tubes operating far below the space-charge limited current.

For the space-charge limited case, described by equation (3.155), the velocity as a function of position is given by

$$v(x) = \frac{\mathrm{d}x}{\mathrm{d}t} = \sqrt{\frac{2eV_0}{m}}\left(\frac{x}{d}\right)^{2/3} = \frac{2d^{1/3}}{t_0}x^{2/3}. \qquad (3.162)$$

Rearranging the second and fourth terms of equation (3.162) and integrating both sides, one obtains

$$\int_0^d \frac{dx}{x^{2/3}} = 3d^{1/3} = \frac{2d^{1/3}}{t_0} \int_0^{t_{sc}} dt = 2d^{1/3} \frac{t_{sc}}{t_0} \qquad (3.163)$$

where t_{sc} is the transit time under space-charge limited flow conditions and is equal to

$$t_{sc} = \frac{3}{2}t_0 = \frac{3}{2}d\sqrt{\frac{2m}{eV_0}}. \qquad (3.164)$$

Thus, space-charge limited flow conditions slow the electron transit time by 50%, reducing the frequency response of diodes as they approach the space-charge limit.

3.7 RELATIVISTIC PLANAR DIODE

Relativistic beam-forming diodes like those shown schematically in figure 3.33 have been developed for military applications in the past, and are likely to find future applications in industry for in-depth welding and flash x-ray radiography. Typical requirements for a relativistic beam-forming diode system might include a high voltage energy storage device capable of delivering megajoules of energy at megavolts of potential over very small durations. Such a diode system is controlled by a fast switch, and includes a pulse-forming network designed to deliver the energy at high potential. The electrostatic potential and electric fields involved are high enough that a field-emitting cathode (the process of field emission will be discussed in Chapter 5) can be used to supply the electrons. These electrons are then accelerated across a potential of the order of megavolts.

3.7.1 Characteristics of the Relativistic Diode

In this discussion, we follow the analysis of W L Howes (1966a, b), who obtained closed-form solutions to the relativistic Child law using a relativistically covariant formulation of Poisson's equation. His analysis assumes initial conditions such that the electric field at the emission electrode is zero, and that the initial velocity of the electrons is zero upon emission.

3.7.2 Space-Charge Limited Current Flow

We begin by formulating the non-relativistic Child law of equations (3.144) and (3.145), as applied to the plane parallel geometry of
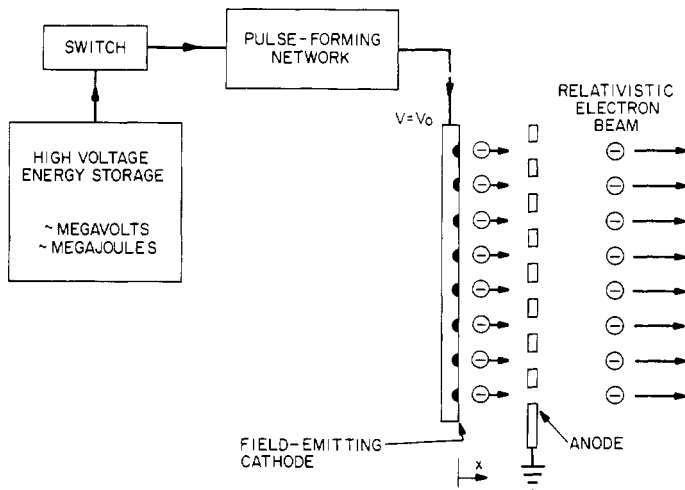
Figure 3.33 Schematic of a pulsed, megavolt relativistic electron beam generator based on a field-emitting cathode.

figures (3.31) and (3.33). In the non-dimensional units adopted by Howes, the following variables characterize the problem:

$$\text{Potential: } \phi \equiv \frac{V}{V_0} \qquad (3.165a)$$

$$\text{Distance: } \xi \equiv \frac{x}{d} \qquad (3.165b)$$

$$\text{Energy: } \varepsilon \equiv \frac{eV_0}{m_0 c^2} \qquad (3.165c)$$

$$\text{Current density: } \mathcal{J} \equiv \frac{J}{J_c} \qquad (3.165d)$$

where m_0 is the rest mass of the electron and J_c is the non-relativistic Child law current given by equations (3.144) and (3.145).

3.7.3 Relativistic Child Law

The relativistic parameter γ is given by

$$\gamma \equiv \frac{1}{\sqrt{1 - (v/c)^2}} \qquad (3.166)$$

where $v(x)$ is the electron velocity. The relativistic equation of continuity is given by

$$\mathcal{J} = ev(x)n_e(x) = \text{constant} \qquad (3.167a)$$

and in the dimensionless form defined by Howes is

$$\mathcal{J} \equiv \frac{J}{J_c} = \frac{ev(x)n_e(x)}{J_c}. \tag{3.167b}$$

The relativistic conservation of energy for an electron moving between the diode plates is given by

$$eV = (\gamma - 1)m_0 c^2 \tag{3.168a}$$

which, in the above dimensionless units may be written

$$\varepsilon\phi = (\gamma - 1). \tag{3.168b}$$

Howes (1966a, b) has shown that the relativistic form of Poisson's equation in dimensionless units is given by

$$\phi'' = \frac{d^2\phi}{d\xi^2} = \frac{4\sqrt{2\varepsilon}}{9} \mathcal{J} \frac{(1 + \varepsilon\phi)}{\sqrt{(1 + \varepsilon\phi)^2 - 1}}. \tag{3.169}$$

Integrating equation (3.169) once, the dimensionless electric field becomes

$$\phi' = \frac{d\phi}{d\xi} \equiv \frac{E}{E_0} = \left[\frac{8\mathcal{J}}{9} \sqrt{\frac{2}{\varepsilon}} \left((1 + \varepsilon\phi)^2 - 1 \right)^{1/2} \right]^{1/2}. \tag{3.170}$$

Equation (3.170) is a nonlinear first-order differential equation, which Howes solved in terms of *Jacobian elliptic functions*. Equation (3.170) can be transformed into integral form by using

$$\xi = \int_0^\xi d\xi = \left(\frac{8\mathcal{J}}{9} \right)^{-1/2} \left(\frac{\varepsilon}{2} \right)^{1/4} g(\phi, \varepsilon) \tag{3.171}$$

where the parameter $g(\phi, \varepsilon)$ is given by

$$g(\phi, e) \equiv \int_0^\phi \frac{d\phi}{[e\phi(2 + e\phi)]^{1/4}}. \tag{3.172}$$

The integral in equation (3.172) can be expressed in the form of Jacobian elliptic functions. At the anode, the dimensionless position is $\xi = 1$, and the dimensionless potential is $\phi = 1$, so equation (3.171) yields the relativistically altered current density,

$$\mathcal{J} = \frac{J}{J_c} = \frac{9}{8} \sqrt{\frac{\varepsilon}{2}} g^2(1, \varepsilon). \tag{3.173}$$

Substituting equation (3.173) back into equation (3.171) yields an implicit expression, independent of current density, for the dimensionless potential ϕ as a function of the dimensionless position ξ,

$$\xi = \frac{g(\phi, \varepsilon)}{g(1, \varepsilon)}. \tag{3.174}$$

The integral in equation (3.172) has a known solution in terms of Jacobian elliptic functions. Define

$$\frac{v}{c} \equiv \tanh \omega. \tag{3.175}$$

If we now use equations (3.165c), (3.166), and (3.168), equation (3.175) can be written in the form

$$\omega = \text{arccosh}(1 + \varepsilon\phi). \tag{3.176}$$

If equation (3.176) is substituted into equation (3.172), the parameter g now becomes

$$g(\omega_1, \varepsilon) = \varepsilon^{-1} \int_0^{\omega_1} \sqrt{\sinh \omega} \, d\omega \tag{3.177}$$

where ω_1 is equation (3.176) evaluated at the upper limit of (3.172). If we now define the parameter

$$\psi \equiv \text{arccosh} \left[\frac{1 - \sinh \omega_1}{1 + \sinh \omega_1} \right]. \tag{3.178}$$

The solution to equation (3.177) can be written as

$$g(\psi, \varepsilon) = \frac{2}{\varepsilon} \left[\frac{\sin \psi \sqrt{1 - \frac{1}{2} \sin^2 \psi}}{(1 + \cos \psi)} + \frac{1}{2} F(\psi, 2^{-1/2}) + E\left(\psi, 2^{-1/2}\right) \right] \tag{3.179}$$

where F and E are incomplete elliptic integrals of the first and second kind. The notation of Byrd and Friedman (1954) has been used. Additional information on elliptic integrals, in different notation, may be found in Abramowitz and Stegun (1964). Outside the tabulated range of $0 \leqslant \phi \leqslant \pi/2$, the incomplete elliptic integrals are given by

$$\pm F(\psi, 2^{-1/2}) = F(n\pi \pm \psi, 2^{-1/2}) - 2nK \tag{3.180a}$$

and

$$\pm E(\psi, 2^{-1/2}) = E(n\pi \pm \psi, 2^{-1/2}) - 2nE \tag{3.180b}$$

where n is an integer, and K and E are complete elliptic integrals of the first and second kinds, respectively.

Using n_A, the non-relativistic electron number density at the anode given by equation (3.150), and writing the dimensionless Poisson equation (3.169) in terms of the dimensionless electron number density, the latter may be written

$$N \equiv \frac{n_e(x)}{n_A} = \mathcal{J}\frac{\sqrt{2}(1 + \varepsilon\phi)}{\sqrt{\phi(2 + \varepsilon\phi)}}. \qquad (3.181)$$

Substituting equation (3.173) for the dimensionless current density $\mathcal{J}$ into equation (3.181) yields

$$n_e(\xi) = \frac{9}{8}\frac{n_A \varepsilon g^2(1, \varepsilon)(1 + \varepsilon\phi)}{\sqrt{\varepsilon\phi(2 + \varepsilon\phi)}}. \qquad (3.182)$$

The electron transit time across the relativistic diode can be derived by substituting equation (3.181) into equation (3.167b), then integrating the velocity $v(x)$ across the diode. If the relativistic transit time is nondimensionlized with respect to the non-relativistic transit time t_{sc} from equation (3.164), the dimensionless relativistic transit time is

$$T \equiv \frac{t_r}{t_{sc}} = \left(\frac{2 + \varepsilon}{2\mathcal{J}^2}\right)^{1/4}. \qquad (3.183)$$

If we now substitute equation (3.173) for $\mathcal{J}$, the relativistic transit time becomes

$$T \equiv \frac{t_r}{t_{sc}} = \frac{2}{3g(1, \varepsilon)}\left[\frac{4(2 + \varepsilon)}{\varepsilon}\right]^{1/4}. \qquad (3.184)$$

As the dimensionless energy goes to 0, one recovers the non-relativistic limit $T \to 1$, and $N \to 1$ at $\xi \to 1$. In general, this transit time is longer than the non-relativistic time, because of the asymptotic approach of the electron velocity to the speed of light.

3.8 THEORY OF CYLINDRICAL DIODES

Most applications of space-charge limited flow theory involve the one-dimensional formation and acceleration of charged particle beams. An important exception are some high power industrial electronic tubes, an application of space-charge limited flow in a cylindrical geometry.
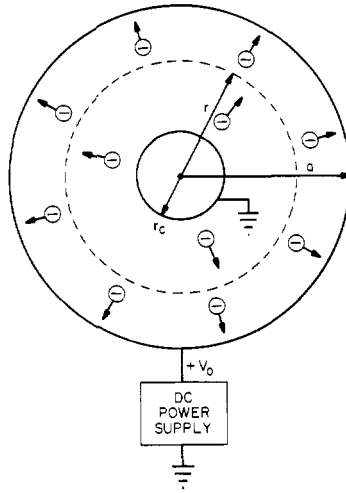
Figure 3.34 Schematic of an axisymmetric, cylindrical space-charge limited diode with a cathode of radius r_c maintained at ground potential $V = 0$, and an anode of radius $r = a$, maintained at a potential $+V_0$.

3.8.1 Characteristics of the Cylindrical Diode

Consider the cylindrical diode geometry shown in figure 3.34, representative of axisymmetric vacuum tubes with a cylindrical, heated, electron-emitting filament. This electron-emitting cathode has a radius r_{sc}, an anode radius $r = a$, and a potential V_0 applied between the cathode and anode. Electrons, once emitted from the cathode with zero initial velocity, are accelerated in the radial direction, and arrive at the anode with an energy equal to the potential V_0 through which they have fallen. Azimuthal and axial variations are ignored.

As in the planar diode, we are interested in two limiting cases; the vacuum case, for which the charge density between the electrodes is zero, and the space-charge limited case. For both cases, the boundary conditions are

$$E(r_c) = 0 \qquad (3.185a)$$
$$v(r_c) = 0 \qquad (3.185b)$$
$$V(r_c) = 0 \qquad (3.185c)$$

and

$$V(a) = V_0. \qquad (3.185d)$$

These conditions are the cylindrical analog of the boundary conditions used for the space-charge limited planar diode, with zero electric field

and a zero initial velocity at the emitting electrode. Since there is no axial or azimuthal variation, Poisson's equation can be written

$$\nabla^2 V = \frac{1}{r}\frac{d}{dr}\left(r\frac{dV}{dr}\right) = -\frac{en_e}{\varepsilon_0} \qquad (3.186)$$

where it is assumed that only electrons exist in the space $r_c \leqslant r \leqslant a$.

3.8.2 Operation in the Vacuum Limit

In the 'vacuum' case for which the electron number density in equation (3.186) is close to zero, a first integration of equation (3.186) yields

$$r\frac{dV}{dr} = C = \text{constant}. \qquad (3.187)$$

Integrating equation (3.187) a second time, and evaluating the constants for the cylindrical boundary conditions of equation (3.185) yields the vacuum dependence for the potential between two concentric cylinders,

$$V = V_0\frac{\ln{(r/r_c)}}{\ln{(a/r_c)}} \qquad \text{(V)}. \qquad (3.188)$$

The vacuum electric field is found by taking the radial derivative of equation (3.188), and is

$$E(r) = \frac{V_0}{r\ln{(a/r_c)}} \qquad \text{(V/m)}. \qquad (3.189)$$

3.8.3 Cylindrical Space-Charge Limited Current Flow

In the cylindrical space-charge limited flow condition, the cloud of electrons in transit from the cathode to the anode reduces the electric field at the cathode surface to zero. The current per unit length, J' at the radius r in figure 3.34 is given by

$$J' = 2\pi r J \qquad \text{(A/m)}. \qquad (3.190)$$

J' cannot be a function of radius, since there are no sources or sinks of electrons between the cathode and anode. Applying the equation of continuity, the relationship between the current density J and the current per unit length J' is given by

$$J = \frac{J'}{2\pi r} = en_e(r)v(r) \qquad \text{(A/m}^2). \qquad (3.191)$$

If electrons are emitted from the cathode with negligible initial velocity, their radial velocity at the radius r can be obtained from the conservation of energy,

$$\tfrac{1}{2}mv^2 = eV(r).$$ (3.192)

Solving equation (3.192) for $v(r)$,

$$v(r) = \sqrt{\frac{2eV(r)}{m}}.$$ (3.193)

Using equation (3.191) to obtain $n_e(r)$ and substituting equation (3.193), one obtains

$$en_e(r) = \frac{J}{v(r)} = \frac{J'}{2\pi r}\sqrt{\frac{m}{2eV}}.$$ (3.194)

Substituting equation (3.194) into Poisson's equation (3.186), yields

$$\frac{\mathrm{d}}{\mathrm{d}r}\left(r\frac{\mathrm{d}V}{\mathrm{d}r}\right) = \frac{J'}{2\pi\varepsilon_0}\sqrt{\frac{m}{2e}}\frac{1}{V^{1/2}}.$$ (3.195)

Equation (3.195) is a second-order, nonlinear differential equation with no (known) exact analytical solutions. To deal with this equation, it is necessary to transform its variables to obtain a more soluble problem. Taking a hint from the vacuum solution (3.188), we define a dimensionless radial variable

$$\rho \equiv \ln\left(\frac{r}{r_c}\right)$$ (3.196a)

for which

$$\frac{\mathrm{d}\rho}{\mathrm{d}r} = \frac{1}{r}.$$ (3.196b)

We also use a dimensionless parameter $\beta(\rho)$, defined to make the cylindrical space-charge current density look as much as possible like the equation for the planar case,

$$J = \frac{J'}{2\pi r} = \frac{4\varepsilon_0}{9}\sqrt{\frac{2e}{m}}\frac{V^{3/2}}{r^2\beta^2} \qquad (\mathrm{A/m^2}).$$ (3.197)

Equation (3.197) is equivalent to defining β as

$$\beta^2 \equiv \frac{8\pi\varepsilon_0}{9J'}\sqrt{\frac{2e}{m}}\frac{V^{3/2}}{r}.$$ (3.198)

Equation (3.195) can now be converted to the two variables, ρ and β. From equation (196b),

$$r \frac{\mathrm{d}V}{\mathrm{d}r} = \frac{\mathrm{d}V}{\mathrm{d}\rho} \qquad (3.199)$$

and the left-hand side of Poisson's equation therefore becomes

$$\frac{\mathrm{d}}{\mathrm{d}r} \left(r \frac{\mathrm{d}V}{\mathrm{d}r} \right) = \frac{1}{r} \frac{\mathrm{d}^2 V}{\mathrm{d}\rho^2}. \qquad (3.200)$$

Substituting equations (3.200) and (3.198) into equation (3.195) yields

$$\frac{\mathrm{d}^2 V}{\mathrm{d}\rho^2} = \frac{4}{9} \frac{V}{\beta^2}. \qquad (3.201)$$

Taking the logarithm of equation (3.198) and differentiating it with respect to ρ, one obtains

$$\frac{\mathrm{d}V}{\mathrm{d}\rho} = \frac{2}{3} V \left(1 + \frac{2}{\beta} \frac{\mathrm{d}\beta}{\mathrm{d}\rho} \right). \qquad (3.202)$$

Differentiating equation (3.202) again with respect to ρ, and using equation (3.202) to eliminate $\mathrm{d}V/\mathrm{d}\rho$ yields

$$\frac{\mathrm{d}^2 V}{\mathrm{d}\rho^2} = \frac{4V}{9} \left[1 + \frac{4}{\beta} \frac{\mathrm{d}\beta}{\mathrm{d}\rho} + \frac{1}{\beta^2} \left(\frac{\mathrm{d}\beta}{\mathrm{d}\rho} \right)^2 + \frac{3}{\beta} \frac{\mathrm{d}^2\beta}{2\rho^2} \right]. \qquad (3.203)$$

Substituting equation (3.203) into equation (3.201) yields the equivalent differential equation

$$3\beta \frac{\mathrm{d}^2\beta}{\mathrm{d}\rho^2} + \left(\frac{\mathrm{d}\beta}{\mathrm{d}\rho} \right)^2 + 4\beta \frac{\mathrm{d}\beta}{\mathrm{d}\rho} + \beta^2 = 1. \qquad (3.204)$$

Equation (3.204) does not appear at first glance to be much of an improvement over equation (3.195), but it has the important characteristic that it contains no parameter other than ρ and β, so a solution for ρ versus β^2, will be universal, whereas a solution to equation (3.195) would require a family of curves, with J' as a parameter.

For large values of r/r_e, the following approximation was obtained by Langmuir and Compton who neglected the $(\mathrm{d}\beta/\mathrm{d}\rho)^2$ term, to yield the approximation

$$\beta \approx 1 + 0.9769 \left(\frac{r_\mathrm{c}}{r} \right)^{2/3} \sin \left[1.0854 \log_{10} \left(\frac{r}{11.93 r_\mathrm{c}} \right) \right]. \qquad (3.205)$$
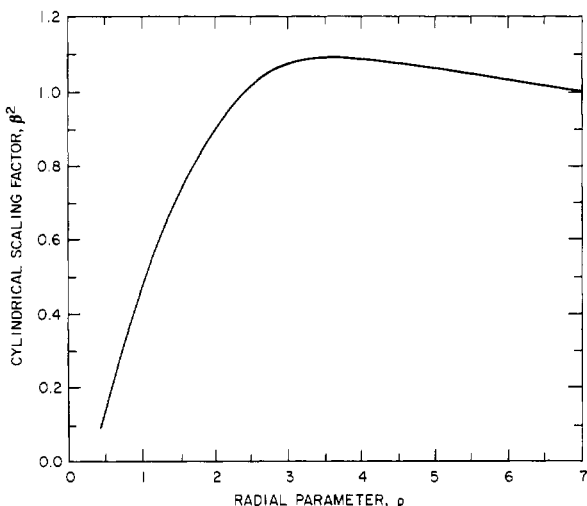
Figure 3.35 A universal solution to equation (3.204) for the parameter β^2 as a function of the dimensionless radius ρ. An approximation to this solution is given by equation (3.205).

This approximation may be used to 0.1%, for $r/r_c \leqslant 50$. An exact numerical solution to equation (3.197) is plotted in figure 3.35.

3.8.4 Operation of Cylindrical Diodes

The anode current density, J_A, at $r = a$ can be calculated from equation (3.197),

$$J_A = \frac{4\varepsilon_0}{9}\sqrt{\frac{2e}{m}}\frac{V_0^{3/2}}{a^2\beta_A^2} \qquad (\text{A/m}^2). \qquad (3.206)$$

where β_A is found from figure 3.35 for the value of ρ at the anode,

$$\rho_A = \ln\left(\frac{a}{r_c}\right). \qquad (3.207)$$

The current density at a radius r between the anode and cathode is found by using equation (3.196a) and figure 3.35 to obtain this corresponding value of β^2 at the radius r.

The radial potential profile $V(r)$ may be found from the constancy of J', and from equations (3.144), (3.190) and (3.197), which yield

$$J' = 2\pi\chi\frac{(V(r))^{3/2}}{r\beta^2} = 2\pi\chi\frac{V_0^{3/2}}{a\beta_A^2} \qquad (\text{A/m}). \qquad (3.208)$$

One can solve equation (3.208) for the radial variation of potential,

$$V(r) = V_0 \left(\frac{r}{a}\right)^{2/3} \left(\frac{\beta}{\beta_A}\right)^{4/3}. \tag{3.209}$$

This dependence replaces the logrithmic relationship appropriate to the vacuum solution to Poisson's equation.

REFERENCES

Abramowitz M and Stegun I A (ed) 1964 *Handbook of Mathematical Functions (National Bureau of Standards Applied Mathematics Series, No. 55)* (Washington, DC: U.S. Govt. Printing Office) LCCCN 64-60036

Byrd P F and Friedman M D 1954 *Handbook of Elliptic Integrals for Engineers and Physicists* (Berlin: Springer) pp 184 ff

Child C D 1911 Discharge from Hot CaO *Phys. Rev.* ser I **32** 492–511

Cobine J D 1958 *Gaseous Conductors* (New York: Dover Publications) pp 553 ff

Forrester A T 1988 *Large Ion Beams—Fundamentals of Generation and Propagation* (New York: John Wiley) ISBN 0-471-62557-4

Glasstone S and Lovberg R H 1960 *Controlled Thermonuclear Reactions* (New York: D Van Nostrand) p 139

Howes W L 1966a One-Dimensional Space-Charge Theory. I Generalization *J. Appl. Phys.* **37** 437–8.

—— 1966b One-Dimensional Space-Charge Theory. II Relativistic Child Law *J. Appl. Phys.* **37** 438–9

Roth J R 1957 An Application of Particle Dynamics to the Measurement of Rocket Exhaust Velocity *American Rocket Society Annual Meeting (6 December 1957)* paper ARS S-57 (available through the AIAA)

—— 1983 Ion Heating and Containment in an Electric Field Bumpy Torus (EFBT) Plasma *Nucl. Instrum. Methods* **207** 271–99

Van de Graaff R J 1935 US Patent #1,991,236

4

Characteristics of Plasma

In Chapter 2 we studied the behavior of ordinary gases on the microscopic or atomic scale, where individual particles of the gas interact through elastic hard-sphere collisions. In Chapter 3 we studied the individual and collective motions of charged particles of one polarity in electric and magnetic fields. In this chapter we will combine the previous information to study *plasma*, an approximately electrically neutral collection of positive and negative charges that, in most applications of industrial interest, interacts strongly with a background neutral gas. The presence of charged particles in plasma also makes it strongly responsive to both electric and magnetic fields. Large electromagnetic body forces can be exerted on plasma, a medium without any intrinsic tensile or compressive strength whatever. Because of this, the behavior of plasma is fundamentally different from that of solids, liquids, or gases. In this chapter we will discuss some of the characteristics of plasma which are important in industrial applications, and provide simple derivations which are designed to make clear the physical processes involved. More extensive discussions of plasma fundamentals may be found in Chen (1990), Kettani and Hoyaux (1973) and Roth (1986).

4.1 BULK PROPERTIES OF PLASMA

The bulk properties of plasma, or any other electrical conductor, can be discussed in terms of figure 4.1. This figure illustrates a conducting rectangular slab with a cross-sectional area A, and a length L. A voltage V is maintained across the axial length of this slab, causing a current I to flow, and giving a total resistance R between the ends of the slab.
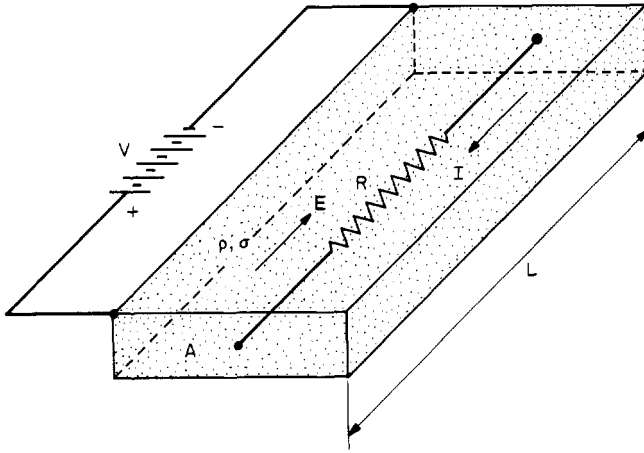
Figure 4.1 Relationship between bulk and specific electrical properties of a rectangular, electrically conducting slab of cross section A and length L.

4.1.1 Electrical Resistivity and Conductivity

The *current density* flowing in the slab of figure 4.1 is given by

$$J = \frac{I}{A} \quad (\text{A/m}^2) \tag{4.1}$$

and is the current flowing along the axis of this slab divided by its cross-sectional area. The electrical *bulk resistivity* ρ is related to the total resistance R of the slab in ohms, and its cross-sectional area A by

$$\rho = \frac{RA}{L} \quad (\Omega\text{-m}). \tag{4.2}$$

The *bulk resistivity* given by equation (4.2) is a property of the material comprising the slab, and not its geometry. The units of electrical resistivity are ohm meters (Ω-m) in the SI system of units. The *electrical conductivity* is the inverse of the electrical resistivity, and is given by

$$\sigma = \frac{1}{\rho} = \frac{L}{RA}. \tag{4.3}$$

The units of electrical conductivity in the SI system are siemens per meter (S/m) where the siemens is an inverse ohm (or mho).

In a plasma, the electrical current of figure 4.1 is carried by both ions and electrons, which move in opposite directions in a background electric field, as shown in figure 4.2. This figure shows a low pressure
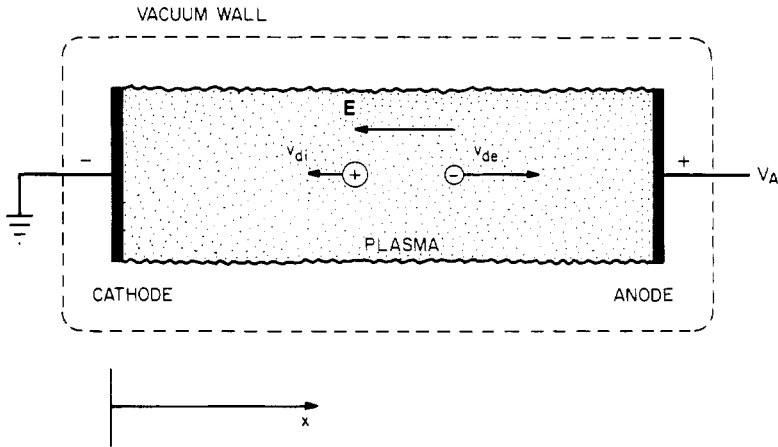
Figure 4.2 The motion of ions and electrons in a DC low pressure electrical discharge tube.

DC electrical discharge tube with a cathode on the left, and an anode on the right. In such a plasma, both ions and electrons collide with the neutral background gas, and reach steady-state drift velocities along the axis of the tube. The electric field in figure 4.2 points to the left, causing electrons to move toward the right. Because their mass is much greater, ions move with much smaller drift velocities to the left, in the direction of the electric field. The ions make only a small contribution to the axial current because of their small drift velocity. The *current density* of either species is given by

$$J = e\Gamma \qquad (\text{A/m}^2) \qquad (4.4)$$

where the *particle flux* Γ is given by the number density of the species in question times its average drift velocity v_d, to yield a current density

$$J = env_d \qquad (\text{A/m}^2). \qquad (4.5)$$

Thus, the current density in a plasma is proportional to the average drift velocity of the species carrying the current, and to the number density of the species itself.

Ohm's law in the unmagnetized plasma shown in figure 4.2 is given by

$$J = \sigma E \qquad (4.6)$$

where σ is the electrical conductivity given by equation (4.3) above. Substituting equation (4.5) into equation (4.6), and solving for the electron drift velocity yields

$$v_{de} = \frac{\sigma}{en_e} E \qquad (\text{m/s}) \qquad (4.7)$$

demonstrating a direct proportionality between the electron drift velocity and the axial electric field, or the electrical conductivity of the plasma.

The equation of motion for an electron in the plasma of figure 4.2 may be written

$$m_e \frac{\mathrm{d}v_x}{\mathrm{d}t} = eE \qquad \text{(N)}. \qquad (4.8)$$

If equation (4.8) is integrated once, the time-dependent velocity along the axis of the plasma is given by

$$v_x = C + \frac{eE}{m_e} t. \qquad (4.9)$$

In a Lorentzian plasma, the electrons in figure 4.2 are accelerated toward the right and will collide repeatedly with the neutral background gas. For purposes of this derivation, an average time between collisions, t_c, or *collision time*, is defined in terms of the average collision, which is sufficient to cause the electron to lose its average drift velocity v_{de} *in the x direction* each time it collides. This momentum appears primarily in directions perpendicular to the electric field, and to a lesser extent is transferred to the much heavier neutral gas atoms (*Lorentzian collisions*). If the electron did not shed its average drift velocity in an average collision, then it would be accelerated from one end of the tube to the other, contrary to observation.

From equation (4.9), the electron velocity just after a collision at $t = 0$ is given by

$$v_x(t = 0) = C. \qquad (4.10a)$$

Just before a collision at the time t_c the drift velocity is given by

$$v_x(t = t_c) = C + \frac{eE}{m_e} t_c. \qquad (4.10b)$$

Since the electron has to lose its entire drift velocity in an average collision, the axial velocity change in an average collision time is given by

$$\Delta v_x = v_x(t = t_c) - v_x(t = 0) = v_{de} = \frac{eE}{m_e} t_c \qquad (4.11)$$

which relates the average drift velocity to the collision time of the electrons in the plasma. The *average drift velocity* may be calculated from equation (4.9) by integrating over the collision time t_c

$$v_{de} = \frac{1}{t_c} \int_0^{t_c} v_x(t) \, \mathrm{d}t. \qquad (4.12)$$

Performing the integration, and using the right-hand member of equation (4.11),

$$v_{de} = C + \frac{eE}{2m_e}t_c = C + \frac{1}{2}v_{de} \qquad (4.13)$$

which yields the constant of integration,

$$C = \frac{1}{2}v_{de}. \qquad (4.14)$$

Substituting equation (4.14) into (4.9) yields the time-dependent velocity between collisions,

$$v_x(t) = \frac{1}{2}v_{de} + \frac{eE}{m_e}t \qquad 0 \leqslant t \leqslant t_c. \qquad (4.15)$$

Therefore, the velocity just after a collision is given by

$$v_x(t = 0) = \frac{1}{2}v_{de} \qquad (4.16a)$$

and just prior to the next collision is equal to

$$v_x(t = t_c) = \frac{3}{2}v_{de}. \qquad (4.16b)$$

This velocity is plotted in figure 4.3 as a function of time. An electron, having just collided at $t = 0$, will have, on the average, a velocity of half the mean drift velocity in the x direction. The electron will be accelerated by the electric field (assumed to be independent of x), and the velocity will increase linearly until it reaches a value of 3/2 times the average drift velocity, v_{de}. At the time $t = t_c$, it will collide, losing its average drift velocity, and start over with a drift velocity one half its average value, and increase as before. The situation shown in figure 4.3 is obviously highly idealized. In a real plasma neither the time between collisions nor the increment of drift velocity lost would be uniform from one collision to the next.

By comparing equation (4.7) with equation (4.11), we may write

$$v_{de} = \frac{eEt_c}{m_e} = \frac{e}{m_e v_{ce}}E = \frac{\sigma}{en_e}E \qquad (m/s) \qquad (4.17)$$

which allows us to obtain the electrical conductivity σ in terms of the microscopic parameters of the plasma,

$$\sigma = \frac{e^2 n_e}{m_e v_{ce}} = \frac{1}{\rho}. \qquad (4.18)$$
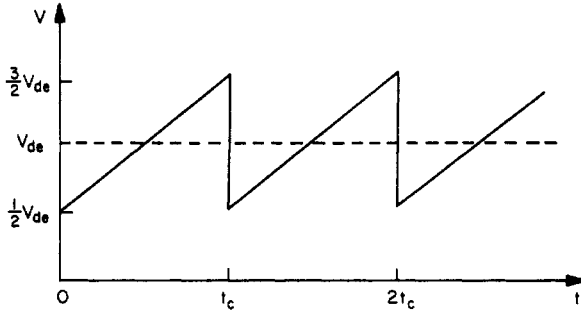
Figure 4.3 The idealized electron drift velocity in the electrical discharge tube of figure 4.2 over several collision times, as described by equation (4.15).

This equation gives the bulk electrical conductivity of a plasma in terms of the electron number density and the electron collision frequency ν_{ce}, where we have used in equation (4.17) the fact that the collision time, t_c, is equal to the inverse of the collision frequency.

Equation (4.18) is appropriate to *Lorentzian plasmas*, in which electron collisions with the neutral background gas predominate. Industrial plasmas are almost always Lorentzian. In those cases for which electrons collide only with charged particles, each of which has a charge state Z, the bulk electrical conductivity is given by the *Spitzer conductivity*, σ_S, named after the Princeton physicist Lyman Spitzer, given by

$$\sigma_s = \frac{51.6\varepsilon_0^2}{e^2 Z}\left(\frac{\pi}{m_e}\right)^{1/2}\frac{(kT_e)^{3/2}}{\ln\Lambda}. \qquad \text{(S/m)} \qquad (4.19)$$

The factor $\ln\Lambda$ in the denominator is the *Coulomb logarithm*,

$$\ln\Lambda = \ln\left(\frac{12\pi(\varepsilon_0 kT_e)^{3/2}}{Z^2 e^3 n_e^{1/2}}\right). \qquad (4.20)$$

Equation (4.20) is a very slowly varying function of plasma properties, and is of the order of 14 for most industrial plasmas. If electron–electron Coulomb collisions predominate in a plasma, a situation which can occur in fusion research and some astrophysical plasmas, the Spitzer conductivity for such electron–electron collisions is given by

$$\sigma_{se} = \frac{Z\sigma_s}{2} \qquad \text{(S/m)} \qquad (4.21)$$

in terms of the Spitzer conductivity for ions given by equation (4.19).

4.1.2 Mobility

From equation (4.17), the average drift velocity of either species in a plasma may be written

$$v_d = \frac{e}{m v_c} E = \frac{\sigma}{e n_e} E = \mu E \qquad (4.22)$$

where the quantity μ is the *mobility*, defined as

$$\mu \equiv \frac{e}{m v_c} \qquad \text{(C-s/kg)}. \qquad (4.23)$$

The mobility of a species is a function of the collision frequency and remains approximately constant at a given pressure of the neutral background gas in most plasmas of industrial interest. The mobility therefore allows one to write the drift velocity in a form that is directly proportional to the electric field. The mobility must be assigned a sign appropriate to the sign of the charge, and the direction of the drift velocity in the electric field. By using the last two members of equation (4.22), the electrical conductivity can be related to the mobility as follows,

$$\sigma = e n_e \mu. \qquad \text{(S/m)} \qquad (4.24)$$

4.1.3 Ohmic Heating of Plasmas

The electrons in the plasma shown in figure 4.2 acquire energy from the electric field, which is maintained by external power supplies. This energy is dissipated in inelastic collisions, including the ionization events which maintain the plasma, and excitation collisions which lead to photon emission that makes the plasma visible (a 'glow' discharge). The electron energy is also dissipated in elastic collisions with the background neutral gas, thus heating the gas through ohmic dissipation. The *power density* resulting from this process is given by

$$p = \rho J^2 = \frac{J^2}{\sigma} = \sigma E^2 \qquad \text{(W/m}^3\text{)}. \qquad (4.25)$$

Substituting equation (4.18) into equation (4.25) yields for a Lorentzian plasma,

$$p_c = \frac{m_e v_{ce}}{e^2 n_e} J^2 = \frac{e^2 n_e}{m_e v_{ce}} E^2 \qquad \text{(W/m}^3\text{)} \qquad (4.26)$$

which is an expression that can be applied to most plasmas of industrial interest.

In plasmas dominated by Coulomb collisions, the Spitzer conductivity is appropriate in equation (4.25), yielding a power density

$$p_s = \frac{e^2}{51.6\varepsilon_0^2} \left(\frac{m_e}{\pi}\right)^{1/2} \frac{J^2 \ln \Lambda}{(kT_e)^{3/2}} \qquad (\text{W/m}^3). \qquad (4.27)$$

Equation (4.27) illustrates the somewhat suprising result that for high temperature astrophysical or fusion plasmas dominated by Coulomb collisions, the power density due to ohmic heating is inversely proportional to the 3/2 power of the electron kinetic temperature. Industrial plasmas almost never reach this regime, however.

4.1.4 Energy Transfer Frequency

The electrical conductivity σ and the electrical resistivity ρ were originally introduced to describe uniform media such as solid electrical conductors and liquid metals. In such media, σ and ρ are constants, independent of position, and they appear only as constant coefficients in the differential equations describing the transport properties of the medium. In plasma, σ and ρ are almost always functions of position. It is clear from equation (4.18) that σ and ρ are functions of electron number density, electron kinetic temperature, and neutral number density, all of which can, and usually do, vary with position in plasmas of industrial interest. Under such conditions, σ and ρ lose much of their utility, since the differential equations for continuity, momentum, and energy flow now have variable, usually nonlinear, coefficients. If one assumes that σ and ρ are constant in plasmas, the concepts of electrical conductivity and resistivity can become obstacles to understanding the behavior of plasma. In addition to this problem of spatial variation, the relevance of σ to RF plasmas is hard to visualize and has often caused confusion on the part of students of the subject.

As a result of the above concerns, a new parameter, the *energy transfer frequency*, is introduced as follows. The right-hand member of equation (4.26) for the power density of a plasma may be written as

$$p = \sigma E^2 = \frac{e^2 n_e}{m_e \nu_{ec}} E^2 = \frac{\varepsilon_0}{2} E^2 x \frac{e^2 n_e}{\varepsilon_0 m_e} x \frac{2}{\nu_{ec}}$$

$$= \frac{1}{2}\varepsilon_0 E^2 \frac{2\omega_{pe}^2}{\nu_{ec}} = \frac{1}{2}\varepsilon_0 E^2 \nu_* \qquad (\text{W/m}^3). \qquad (4.28)$$

The power dissipated by ohmic heating in the plasma is now written as the product of the electrostatic energy density of the electric field, $\varepsilon_0 E^2/2$, and the energy transfer frequency ν_*, given by

$$\nu_* \equiv \frac{2\omega_{pe}^2}{\nu_{ec}} = \frac{2e^2 n_e}{\varepsilon_0 m_e \nu_{ec}} = \frac{2\sigma}{\varepsilon_0} \qquad (\text{Hz}). \qquad (4.29)$$

The energy transfer frequency is the frequency with which the electrostatic energy density provided by external power supplies is transferred to the plasma.

4.1.5 Ohm's Law and Body Forces in Magnetized Plasmas

The *current density* in a magnetized plasma may be written in the form of a generalized Ohm's law,

$$J = \sigma[E + (v \times B)] \qquad (\text{A/m}^2) \qquad (4.30)$$

where the velocity v is the total *macroscopic drift velocity* of the charged particles comprising the plasma. The *body force* acting on a plasma is given by

$$F = J \times B \qquad (\text{N/m}^3). \qquad (4.31)$$

These forces are at right angles to the magnetic induction and the current density given by equation (4.30). Substituting equation (4.30) into (4.31) and applying a vector identity yields the body force

$$F = \sigma(E \times B) - \sigma B^2 v + \sigma(B \cdot v)B \qquad (4.32)$$

Thus, the body force acting on a plasma will have components at right angles to the electric and magnetic fields, along the drift velocity, and along the magnetic induction itself.

4.2 QUASI-NEUTRALITY OF PLASMA

If left to itself, a plasma exhibits a very strong tendency to become electrically neutral so that the charge density of ions and electrons is approximately equal. This condition, referred to as *quasi-neutrality*, is a consequence of the strong electrical forces that exist between opposite charge species. Charge separation in a plasma can be maintained only by externally imposed electric fields or the *internal energy* (thermal energy) of the plasma itself. The maximum deviation from charge neutrality that can be supported by the kinetic temperature of the plasma will now be estimated.

Let us consider an energetic plasma consisting of electrons and singly-charged, positive ions of almost equal density, n_0 particles per cubic meter, as illustrated in figure 4.4. In a small spherical region of the plasma of radius r, the electrostatic energy associated with this volume depends on the excess charge that it contains (assumed to be negative). The electrostatic potential at the surface of this sphere is given by

$$V = \frac{Q}{4\pi \varepsilon_0 r} \qquad (\text{V}) \qquad (4.33)$$
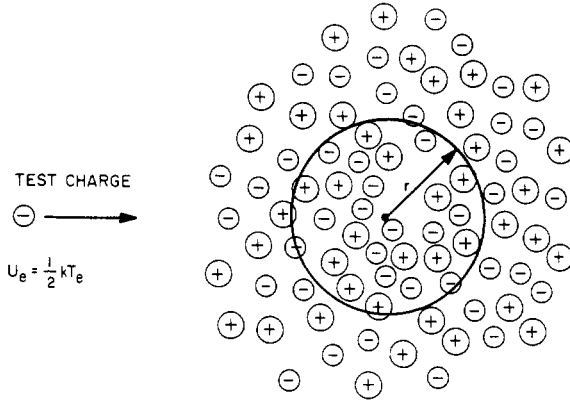
Figure 4.4 The quasi-neutrality of a sphere of radius r in a plasma with electron kinetic temperature T_e. A single electron approaches the center of the sphere from the left with an energy $kT_e/2$.

where Q is the net charge within the sphere. This charge is given by the volume of the sphere times the excess charge, $e\delta n$, where e is the charge on the electron, and δn is the difference between the electron and (possibly multiply-charged) ion number densities in the sphere,

$$\delta n = n_e - Zn_i \ll n_0. \tag{4.34}$$

The electrostatic potential on the surface of the sphere is

$$V = \frac{\frac{4}{3}\pi r^3 e\delta n}{4\pi\varepsilon_0 r} = \frac{r^2 e\delta n}{3\varepsilon_0} \quad \text{(V)}. \tag{4.35}$$

The energy that an electron gains upon being pushed into this region against the net negative charge within it is given by the electrostatic potential of equation (4.35) times the electronic charge, or

$$U_e = eV = \frac{r^2 e^2 \delta n}{3\varepsilon_0}. \tag{4.36}$$

This energy can come only from the kinetic energy that the electron has as a result of its finite kinetic temperature, T. The radial degree of freedom of the electron motion has associated with it a characteristic thermal energy given by

$$U_e = \tfrac{1}{2}kT = \tfrac{1}{2}eT' \tag{4.37}$$

where k is Boltzmann's constant. Substituting equation (4.37) into (4.36), one can solve for the relative departure from charge neutrality,

$$\frac{\delta n}{n_0} = \frac{3T'\varepsilon_0}{2er^2 n_0} = 8.3 \times 10^7 \frac{T'}{n_0 r^2} \tag{4.38}$$

where T' is the kinetic temperature in electronvolts.

Plasmas of industrial interest will have number densities of approximately 10^{16} particles/m^3, and $T' \approx 10$ eV. Such plasmas with a characterstic dimension of 0.05 m will have a departure from charge equality of a few parts in 10^5. Thus, any significant volume of plasma will contain almost exactly the same quantity of positive and negative charge. This assumption is called *quasi-neutrality*, and allows one to assume that $Zn_i \simeq n_e$, so that in many calculations it is unnecessary to consider the ion or electron population separately.

4.3 ELECTROSTATIC BOLTZMANN (BAROMETRIC) EQUATION

A plasma in kinetic equilibrium eventually finds its way to the bottom of an electrostatic potential well and forms an 'atmosphere' with the highest densities at the bottom of the well, and an exponentially decreasing number density as one moves to higher levels of electrostatic potential energy. This is analogous to what happens to the atmosphere in the Earth's gravitational potential well. When plasmas are confined by insulating walls, they lose the faster-moving and more mobile electrons to the walls until a surface charge builds up which attracts enough ions from the plasma to establish an ambipolar, equal flow of ions and electrons in a steady state.

Consider the situation in figure 4.5, with an insulating wall at an ambipolar negative potential V_0 and an electric field pointing out of the plasma. If one considers a small pillbox at the surface of the plasma of cross-sectional area dA and height dZ, the individual charges within the pillbox each have a force on them given by

$$f = qE \qquad \text{(N)}. \qquad (4.39)$$

The total force acting on all of the charged particles of one sign within the pillbox is given by

$$F = nf \, dA \, dZ = nqE \, dA \, dZ \qquad \text{(N)}. \qquad (4.40)$$

The kinetic pressure exerted on the top surface of the pillbox by all of the negative charges above it is given by

$$p_1 = \frac{dF}{dA} = n_1 kT \qquad \text{(N/m}^2) \qquad (4.41)$$

where the right-hand member of equation (4.41) is a statement of the perfect gas law.
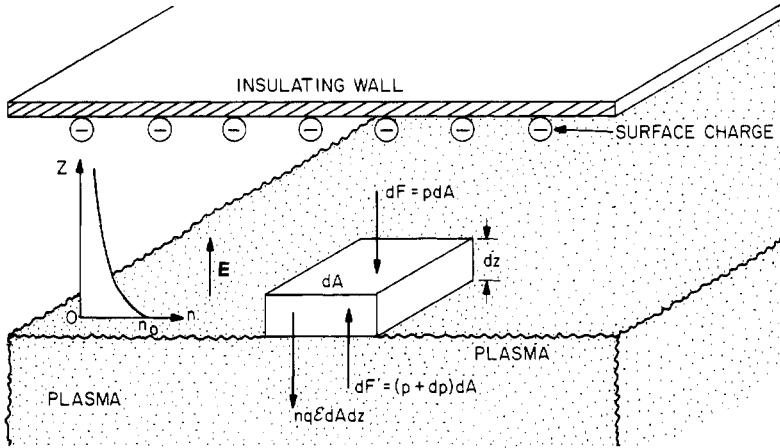
Figure 4.5 The sheath between a plasma and an insulating wall. The body forces on charged particles in the pillbox are the sum of the electric field forces, and the kinetic pressure of particles above and below the pillbox.

In kinetic equilibrium, the forces on the pillbox will be in balance, such that

$$(p + dp)\,dA = p\,dA + nqE\,dA\,dZ. \tag{4.42}$$

The force on the left-hand side of equation (4.42) is the upward force provided by the kinetic pressure of the plasma on the bottom of the pillbox. On the right-hand side of equation (4.42) is the kinetic pressure due to the electrons above the top surface of the pillbox and the body force acting on the charges in the pillbox due to the electric field. Equation (4.42) may be written

$$dp = nqE\,dZ. \tag{4.43}$$

The right-hand member of equation (4.41) can be substituted into equation (4.43) and rearranged to obtain

$$\frac{dp}{p} = \frac{qE}{kT}\,dZ. \tag{4.44}$$

Equation (4.44) can be integrated from the top surface of the plasma, where $Z = 0$, $p = p_0$, and $V = V_0$ to the position Z within the pillbox to obtain

$$\int_{p_0}^{p} \frac{dp}{p} = \ln p \Big|_{p_0}^{p} = \frac{q}{kT} \int_{0}^{Z} E\,dZ. \tag{4.45}$$

The electric field can be written as the gradient of the potential V,

$$E = -|\nabla V| = -\frac{dV}{dZ} \qquad (V/m) \tag{4.46}$$

and the kinetic temperature T' in electronvolts can be written as

$$kT = eT'. \tag{4.47}$$

Substituting equations (4.46) and (4.47) into equation (4.45) yields

$$\ln \frac{p}{p_0} = -\frac{q}{kT} \int_{V_0}^{V} dV = \frac{V_0 - V}{T'}. \tag{4.48}$$

Thus, the *kinetic pressure* of a plasma in an electrostatic potential well may be written

$$p = p_0 \exp\left(\frac{V_0 - V}{T'}\right). \tag{4.49}$$

Equation (4.49) states that the kinetic pressure (and hence the number density of an isothermal plasma) increases toward the bottom of an electrostatic potential well. In figure 4.5, the electric field will push electrons away from the wall and into the plasma. The plasma therefore is surrounded by an atmosphere of electrons that falls off exponentially in number density or kinetic pressure as the wall is approached. The finite kinetic temperature of the electrons allows some of them to get part way up the potential well for part of the time, and the net effect is the exponential atmosphere described by equation (4.49). This characteristic of electrostatic trapping is important in plasma-related lighting devices such as fluorescent light tubes and in plasma reactors where the electric fields between the plasma and wall are maintained by external power supplies.

4.4 SIMPLE ELECTROSTATIC PLASMA SHEATHS

An electrode or wall in contact with a plasma will usually affect only its immediate surroundings in a plasma. Unless large currents flow in the plasma, or unless it is highly turbulent, a plasma will tend to form a surface sheath to shield itself from applied electric fields. The characteristic *shielding distance* is approximately equal to the thickness of the *sheath* that forms between a plasma and a surrounding wall, similar to that illustrated in figure 4.5.

Starting with Poisson's equation, one obtains for static electric fields in the sheath region,

$$\nabla \cdot E = \frac{\rho}{\varepsilon_0}. \tag{4.50}$$

If equation (4.46) is used for the definition of electric field, equation (4.50) becomes for a plasma of singly-charged ions,

$$\nabla^2 V = \frac{d^2 V}{dZ^2} = -\frac{\rho}{\varepsilon_0} = +\frac{e(n_i - n_e)}{\varepsilon_0}. \tag{4.51}$$

The one-dimensional case considered in figure 4.5 will be used, with the potential V a function of Z only. Here, because of their much greater mass, the ions are considered to be rigidly fixed in place, to provide a constant background $n_i \approx n_0$. The potential is taken to be $V_0 = 0$ at the bottom of the pillbox in figure 4.5, and the electrons of density n_e are assumed to be able to move freely among the fixed population of more massive ions. Equation 4.51 therefore becomes

$$\frac{d^2V}{dZ^2} \approx \frac{e}{\varepsilon_0}(n_0 - n_e). \tag{4.52}$$

From the previous discussion of quasi-neutrality, it is apparent that n_e cannot depart far from the average ion density, n_0, and can do so only when driven by the electron kinetic temperature. From equation (4.49), with $V_0 = 0$,

$$n_e = n_0 \exp\left(-\frac{eV}{kT}\right) \tag{4.53}$$

which, when substituted into equation (4.52), yields

$$\frac{d^2V}{dZ^2} \approx -\frac{n_0 e}{\varepsilon_0}\left[\exp\left(-\frac{eV}{kT}\right) - 1\right]. \tag{4.54}$$

In the vicinity of $Z = 0$, where the potential V is small, the exponential can be expanded to obtain

$$\frac{d^2V}{dZ^2} \approx -\frac{n_0 e}{\varepsilon_0}\left(1 - \frac{eV}{kT} - 1\right) = \frac{n_0 e^2}{\varepsilon_0 kT}V. \tag{4.55}$$

Equation 4.55 has the solution

$$V = V_0 \exp\left(\pm\frac{Z}{\lambda_d}\right). \tag{4.56}$$

Thus, a plasma will be shielded by an exponential sheath, with a characteristic e-folding or shielding distance λ_d given by

$$\lambda_d = \left(\frac{kT_e \varepsilon_0}{n_e e^2}\right)^{1/2} \quad (\text{m}). \tag{4.57}$$

The parameter λ_d is called the *Debye shielding distance* after the physical chemist Peter J W Debye (1884–1966) who first described it during his studies of electrolytes. If the kinetic temperature T' is expressed

in electron volts, and the number density in electrons per cubic meter, equation (4.57) is numerically

$$\lambda_d \approx 7434 \left(\frac{T'}{n_e} \right)^{1/2} \qquad \text{(m)}. \qquad (4.58)$$

The Debye shielding distance is the characteristic thickness of sheaths which form between a plasma and an electrode, or a plasma and a wall. Equation 4.58 predicts a Debye shielding distance of approximately 0.17 mm for plasmas of industrial interest with a kinetic temperature of 5 eV and a number density of 10^{16} particles/m^3. In relatively quiescent plasmas in which most free energy reservoirs have been exhausted, sheaths as thin as predicted by equation (4.58) might occur; however, in magnetized plasmas with gyroradii larger than the Debye shielding distance, or in unmagnetized plasmas that carry electrical currents or are highly turbulent, the characteristic sheath thickness may be greater.

4.5 PLASMA FREQUENCY

Consider the plasma polarized between two plane parallel plates in figure 4.6. The left-hand plate is grounded, and the right-hand plate is connected through a fast switch to a potential $+V_a$. The plasma will become polarized and its surface covered with electrons on the right side and the heavy, positive ions will remain behind on the left side. If the potential V_a is turned off with the switch, the electrons, since they are much lighter than the ions, will be attracted to the left, and will oscillate among the cloud of relatively immobile positive ions until their oscillatory motion is damped by collisions. This frequency is now calculated.

Consider the small pillbox on the right-hand surface of the plasma, shown in detail in figure 4.6. The Z coordinate is taken normal to the plane of this pillbox, with its origin at the surface of the plasma, where the surface charge of electrons resides when the plasma is polarized. The electric field points toward the left, the direction in which a positive test charge would move. The surface charge density, σ, (not to be confused with the cross section or the electrical conductivity) on this pillbox is

$$\sigma = neZ \qquad \text{(C/m}^2). \qquad (4.59)$$

The electric field at the surface is related to the surface charge density by

$$E = \frac{\sigma}{\varepsilon_0} = \frac{neZ}{\varepsilon_0} \qquad \text{(V/m)} \qquad (4.60)$$
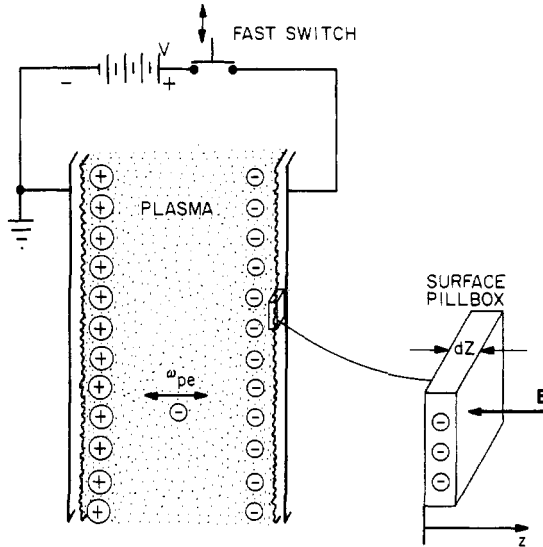
Figure 4.6 A polarized plasma slab between two plane parallel electrodes, maintained at a voltage V_a, which can be disconnected by a fast switch. A small pillbox at the plasma surface with a negative surface charge is shown to the lower right.

where the right-hand member of equation (4.60) has incorporated equation (4.59). This polarization electric field will be equal and opposite to the applied electric field. The equation of motion of one electron of mass m is given by

$$m\frac{d^2Z}{dt^2} = -eE = -\frac{ne^2Z}{\varepsilon_0}. \tag{4.61}$$

The minus sign occurs in equation (4.61) because the force on an electron is toward the $-Z$ direction. This equation can be written

$$\frac{d^2Z}{dt^2} = -\left(\frac{ne^2}{m\varepsilon_0}\right)Z. \tag{4.62}$$

This differential equation describes simple harmonic motion, the frequency of which is

$$\omega_{pe} = \left(\frac{ne^2}{m\varepsilon_0}\right)^{1/2} \qquad (rad/s). \tag{4.63}$$

Equation 4.63 is the *electron plasma frequency*, the frequency with which electrons oscillate among the heavier, immobile ions when the

electron population is disturbed. In rare cases, the electrons are the immobile species (having been immobilized perhaps by strong magnetic fields) and the ions will oscillate among the background of fixed electrons. In such a case, the appropriate frequency is the *ion plasma frequency*, which is identical with equation (4.63), but contains the ion rather than the electron mass and the ionic charge number in the numerator. Numerically, the electron plasma frequency based on the electron number density in particles per cubic meter is given by

$$v_{pe} = 8.980 n_e^{1/2} \qquad \text{(Hz)}. \qquad (4.64)$$

For plasmas of industrial interest, a characteristic number density is $n_e \approx 10^{16}$ particles/m^3, and $v_{pe} \approx 0.898$ GHz.

The electron plasma frequency given by equation (4.63) is critical to the propagation of electromagnetic radiation in plasmas. Consider the plasma slab shown in figure 4.7. A source of radiation at the lower left launches electromagnetic radiation with the frequency ω toward the slab. This radiation will be mostly reflected or transmitted, depending upon the relationship of the source frequency ω to the electron plasma frequency, ω_{pe}. If electromagnetic radiation with a frequency below ω_{pe} is incident on the slab, the electrons in the plasma respond to the electric field in the electromagnetic wave and extract energy from it. If there are collisions or other dissipative processes in the plasma, the electromagnetic wave is damped, as wave energy is converted into kinetic energy of the plasma constituents. Another consequence of incident radation below the electron plasma frequency is that individual electrons near the surface of the plasma will act like miniature dipoles and re-radiate the incident radiation, reflecting it from the plasma. This is an important effect, and is responsible for the reflection of low frequency AM band radiation from the Earth's ionosphere, thus facilitating long distance communication at frequencies below the ionosphere's electron plasma frequency.

If the incident electromagnetic radiation shown in figure 4.7 has a frequency above the electron plasma frequency, the electrons have too much inertia to respond to the electric field of the wave, and the radiation is able to propagate through the plasma without significant reflection or attenuation. This happens in the Earth's ionosphere to signals in the FM and TV bands above 90 MHz. This phenomenon also is important to fusion-related plasmas, because if it is desired to probe the plasma for diagnostic purposes, or to heat the plasma by electron cyclotron resonance heating, the incident radiation must be above the electron plasma frequency if it is not to be reflected or attenuated.

If a plasma is irradiated with electromagnetic radiation of frequency ω, as indicated in figure 4.7, there is a critical electron number density, below which the electromagnetic radiation will be transmitted through
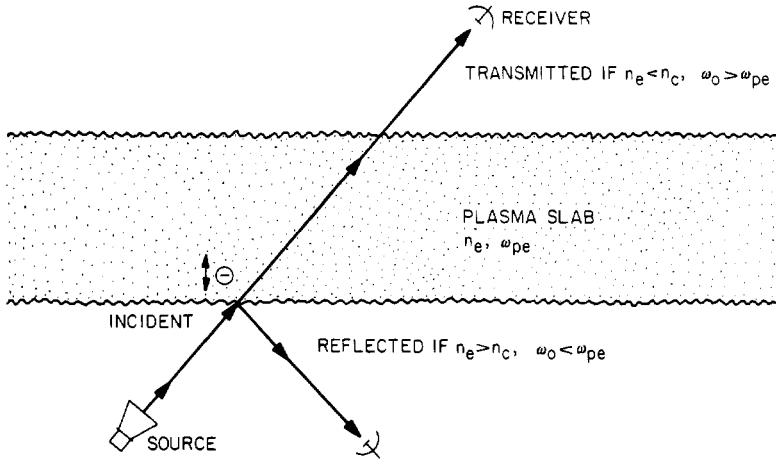
Figure 4.7 Electromagnetic radiation from a source with frequency $\omega = \omega_0$ incident on plasma slab with number density n_e, and electron plasma frequency ω_{pe}. The incident radiation will be reflected from, or transmitted through this slab, depending on the relation of the incident frequency to the electron plasma frequency in the slab.

the slab. If the electron number density is above this critical density, the electromagnetic radiation will be reflected. This critical number density is the threshold for which the incident frequency is equal to the electron plasma frequency given by equation (4.63). Making this substitution, and solving equation (4.63) for the *critical number density* yields

$$n_c = \frac{\omega^2 m_e \varepsilon_0}{e^2} = \frac{4\pi^2 m_e \varepsilon_0}{e^2} \nu^2 \qquad (\text{electrons/m}^3). \qquad (4.65)$$

Substituting for the natural constants in equation (4.65) gives the critical number density as a function of the incident frequency (in hertz),

$$n_c = 1.2404 \times 10^{-2} \nu^2 \qquad (\text{electrons/m}^3). \qquad (4.66)$$

At the microwave power frequency of 2.45 GHz, used in commercial and domestic microwave ovens, equation (4.66) predicts a critical electron number density of 7.45×10^{16} electrons/m^3. When the electron number density exceeds this value, microwave radiation will not penetrate to the interior of a plasma, and may heat only a narrow annulus on its outer surface.

In some plasma processing applications, it is simple and relatively efficient to create and maintain a plasma with electron cyclotron resonant heating. In order to heat a magnetized plasma with the extraordinary mode of electromagnetic radiation, in which the electric field vector is

perpendicular to the confining magnetic field, incident radiation at the electron gyrofrequency must be above the electron plasma frequency in order to penetrate the plasma and heat it throughout its volume. For electron cyclotron resonance heating (ECRH), this required condition is

$$\omega_{ce} = \frac{eB}{m_e} \geqslant \omega_{pe} = \left(\frac{e^2 n_e}{\varepsilon_0 m_e}\right)^{1/2}. \tag{4.67}$$

If both sides of equation (4.67) are squared, one finds that the electron number density must be below a value that is a function of only the magnetic field, B (in teslas),

$$n_e \leqslant \frac{\varepsilon_0 B^2}{m_e} = 9.72 \times 10^{18} B^2 \qquad (\text{electrons/m}^3). \tag{4.68}$$

Equation (4.68) may be regarded as a constraint on the magnetic induction required to apply ECRH to a plasma of number density n_e.

4.6   THE SAHA EQUATION

In fusion research and many astrophysical situations, a fully ionized plasma can exist without significantly interacting with other states of matter. In industrial applications, however, it is usual for the charged particles of the plasma to interact strongly with the neutral background gas, with solid boundaries, and sometimes even with liquids. As thermal energy is added to a gas, it will become more and more highly ionized. In many low pressure gases, the ions, electrons, and neutral gas are each at different kinetic temperatures, and the mixture is far from thermodynamic equilibrium, a requirement for which is that all species be at a common temperature. In such plasmas, one must calculate the ionization fraction from the microscopic dynamics.

Some industrial plasmas, including many DC arcs and RF plasma torches operating at one atmosphere, are in or close to thermodynamic equilibrium, in which state the temperature of the electrons, ions, and neutral gas is the same. Under these conditions, the transition from a neutral gas to the fully ionized plasma state can be described by the *Saha equation*, derived by the Indian astrophysicist Meghnad Saha (1893–1956). This relation states that the relationship between the electron, ion and neutral number densities (neutral number density n_0) is given by

$$\frac{n_e n_i}{n_0} = \frac{(2\pi m_e kT)^{3/2}}{h^3} \frac{2g_i}{g_0} \exp\left(\frac{-eE_i'}{kT}\right) \tag{4.69}$$

Table 4.1 Parameters for the Saha equation for selected gases.

Species	Ionization potential	Statistical weights	
	E_i', eV	g_0	g_i
Li	5.39	2	1
Na	5.14	2	1
K	4.34	2	1
Cs	3.89	2	1
He	24.58	1	2
Ne	21.56	1	6
A	15.76	1	6
0_2	12.05	3	4
N_2	15.6	1	2
NO	9.26	8	1
CO	14.1	1	2

where h is Planck's constant, T is the common thermodynamic temperature of the three species, E_i' is the ionization potential of the atoms, g_i is the statistical weight of the ground state of the ion, and g_0 is the statistical weight of the ground state of the neutral atom. The ratio to g_i/g_0 is 0.50 for alkali metal plasmas, and of order unity for other gases. The ionization potential and statistical weights for selected gases are listed in table 4.1. Since most plasmas of industrial interest are quasi-neutral, n_i is equal to n_e, and the *ionization fraction* F may be written

$$F \equiv \frac{n_e}{n_0}. \tag{4.70}$$

We can substitute for the neutral gas number density n_0 the pressure of the neutral gas and its kinetic temperature through the perfect gas law,

$$p_0 = n_0 kT. \tag{4.71}$$

Substituting equations (4.70) and (4.71) into equation (4.69) yields the ionization fraction F as a function of kinetic temperature,

$$F^2 = \frac{(2\pi m_e)^{3/2} (kT)^{5/2}}{p_0 h^3} \frac{2g_i}{g_0} \exp\left(\frac{-eE_i'}{kT}\right). \tag{4.72}$$

4.7 DIFFUSIVE TRANSPORT IN PLASMAS

Because industrial plasmas are so much hotter than their surroundings, their effective containment within a restricted volume is required in order

to generate and maintain them efficiently and with reasonable inputs of power. In this section, we consider diffusive transport mechanisms for plasma.

4.7.1 Fick's Law of Diffusion

As in ordinary fluids and neutral gases, *Fick's law of diffusion*,

$$\Gamma = n v_d = -D\nabla n \qquad (2.34)$$

can be used to describe the transport of ions and electrons down a density gradient in partially ionized plasmas. It is usually assumed that the diffusion coefficient D is independent of position, and that the mean free path of the particles diffusing is much smaller than the characteristic scale length of the density gradient. This latter assumption may not be valid in industrial plasmas operating at pressures below 1 Torr.

4.7.2 Containment Time in a Diffusion-Dominated Plasma

Consider the particle continuity equation without sources or sinks in a cylindrically-symmetric plasma with no gradients along the Z axis (figure 4.8), in which only simple Fickian diffusion occurs, and in which the relationship of the mean free path and the density gradient scale length satisfies equation (2.33). In such a plasma, we have

$$\nabla \cdot \Gamma = \frac{\partial n(r, t)}{\partial t}. \qquad (4.73)$$

It can be shown by a separation of time and radial variables that the number density decays in time by simple Fickian diffusion, given by equation (2.34), according to an exponential law,

$$n(r, t) = n(r)e^{-t/\tau}. \qquad (4.74)$$

One can obtain from equation (4.73) the continuity equation

$$\nabla \cdot [D\nabla n(r)] = -\frac{n(r)}{\tau} \qquad (4.75)$$

where the characteristic time $\tau = \tau_p$ is the *particle containment time* in the plasma.

If the diffusion coefficient, D, is independent of position, and if the plasma is an axisymmetric cylinder of radius a, the equation of continuity may be written

$$\frac{1}{r}\frac{\partial}{\partial r}\left(r\frac{\partial n}{\partial r}\right) + \frac{n}{\tau D} = 0. \qquad (4.76)$$
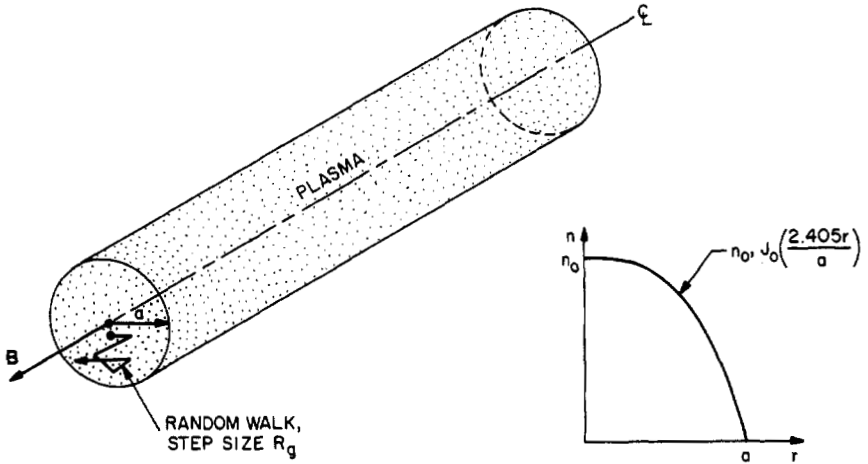
Figure 4.8 Radial diffusion of a cylindrical plasma. In unmagnetized plasma the step size is equal to the mean free path; in magnetized plasmas, the radial step size is equal to the particle gyroradius in the magnetic field.

This is a form of Bessel's equation. If the density is equal to n_0 on the axis, and if $n(a) = 0$, the radial number density profile is given by

$$n(r, t) = n_0 J_0 \left(\frac{2.405r}{a} \right) e^{-t/\tau} \qquad (4.77)$$

where J_0 is the zero-order Bessel function, and the particle containment time is given by

$$\tau = \tau_p = \frac{a^2}{D(2.405)^2}. \qquad (4.78)$$

4.7.3 Diffusion Coefficient in an Unmagnetized Plasma

In an unmagnetized plasma, the diffusion of electrons and ions from regions of high concentration to regions of low concentration is usually assumed to be driven by binary collisions with a background neutral gas which acts as an infinite absorber of energy and momentum from the colliding particle species (a *Lorentzian gas*) or, further, from Lorentzian collisions in which the effective collision time, τ, is independent of the particle momentum and energy (the *Krook model*).

Diffusive transport in an unmagnetized plasma is a random walk, the step size of which is equal to the mean free path. If the collision frequency of the particles is ν_c, and if the average distance travelled between the collisions is Δx, the diffusion coefficient can be approximated as

$$D \sim \nu_c (\Delta x)^2. \qquad (4.79)$$

In unmagnetized plasmas the distance Δx can be identified with the mean free path, λ. If this mean free path is much smaller than the density gradient, it can be shown from kinetic theory arguments (Sears and Salinger, 1975) that the diffusion coefficient D is given by

$$D = \tfrac{1}{3}\nu_c\lambda^2 = \tfrac{1}{3}\bar{v}\lambda = \tfrac{1}{3}\bar{v}^2\tau_c \qquad (4.80)$$

where τ is the time between collisions, and $\bar{v}$ is the mean thermal velocity.

4.7.4 Classical Diffusion in a Magnetized Plasma

The radial transport process just discussed is an example of *ordinary diffusion*. *Classical diffusion* across a magnetic field, however, is a random walk, the step size of which is equal to the gyroradius. Classical diffusion possesses some theoretical interest, since it represents the slowest rate at which particles can be transported across a static magnetic field and down a density gradient in the absence of electric fields. Any other process that affects the radial transport rate of a plasma confined by magnetic fields alone will lead to a radial transport rate higher than the classical value.

In classical diffusive transport across a magnetic field, the particle moves one gyroradius per collision on the average, and hence the radial distance travelled across the magnetic field between collisions, Δx of equation (4.79), is equal to the gyroradius,

$$\Delta x \approx R_g = \frac{m\bar{v}}{eB} = \frac{\bar{v}}{\omega_c} \qquad (4.81)$$

where ω_c is the gyrofrequency. The diffusion coefficient perpendicular to the magnetic field is then given by

$$D_\perp \approx \frac{\bar{v}^2}{\omega_c^2\tau} = \frac{m^2\bar{v}^2}{e^2B^2\tau} \qquad (4.82)$$

where τ is the time between collisions.

A more detailed analysis based on the Krook model of a Lorentzian gas yields a tensor diffusion coefficient in a magnetic field which may be written

$$\mathbf{D} = D_0\mathbf{T} \qquad (4.83)$$

where $\mathbf{T}$ is the *transport matrix*, defined by

$$\mathbf{T} = \begin{vmatrix} \dfrac{1}{1+\omega_c^2\tau^2} & -\dfrac{\omega_c\tau}{1+\omega_c^2\tau^2} & 0 \\[3mm] \dfrac{\omega_c\tau}{1+\omega_c^2\tau^2} & \dfrac{1}{1+\omega_c^2\tau^2} & 0 \\[3mm] 0 & 0 & 1 \end{vmatrix}. \qquad (4.84)$$

Here ω_c is the gyrofrequency, positive for ions and negative for electrons, and τ is the effective time between binary collisions. The components of the *diffusion matrix* are then

$$\mathbf{D} = \begin{vmatrix} D_\perp & -D_H & 0 \\ D_H & D_\perp & 0 \\ 0 & 0 & D_\| \end{vmatrix} \tag{4.85}$$

where D_H is the Hall contribution. The components of this diffusion matrix are given by:

Coefficient	ω finite	$\omega_c\tau \to 0$	$\omega_c\tau \to \infty$	
$D_\| =$	$\dfrac{v^2\tau}{3} = D_0$	D_0	D_0	(4.86a)
$D_\perp =$	$\dfrac{D_0}{1 + \omega_c^2\tau^2}$	D_0	$\dfrac{D_0}{\omega_c^2\tau^2}$	(4.86b)
$D_H =$	$\dfrac{D_0\omega_c\tau}{1 + \omega_c^2\gamma^2}$	0	$\dfrac{D_0}{\omega_c\tau}$	(4.86c)

The next to last column of equations (4.86) is the *collisional limit*, in which $\omega_c\tau \to 0$, and the particle makes less than one gyro-orbit between collisions. The last column in equations (4.86), is the *collisionless limit* in which $\omega_c\tau \to \infty$, and the particle makes many gyro-orbits between binary collisions. In the collisionless limit, the diffusion coefficient perpendicular to the magnetic field may be written

$$D_\perp \approx \frac{D_0}{\omega^2\tau^2} = \frac{\bar{v}^2 m^2}{\tau e^2 B^2} \approx \frac{R_g^2}{\tau} \tag{4.87}$$

and the diffusion coefficient for the Hall term is given by

$$D_H \approx \frac{D_0}{\omega_c\tau} = \frac{\bar{v}^2 m}{eB} \approx R_g\bar{v}. \tag{4.88}$$

A collisionless plasma in a strong magnetic field contains both ions and electrons, which move across the magnetic field at different rates. In industrial, Lorentzian plasma, the electrons have larger cross-field diffusion coefficients and diffusion rates than the ions. Thus, within the context of classical diffusion theory, the electrons control the rate at which the plasma as a whole moves across a magnetic field. This leads to the classical diffusion coefficient,

$$D_{cl} \approx \frac{m_e k T_e}{e^2 B^2 \tau_c} \tag{4.89}$$

where τ_c is the electron–neutral collision time.

If this diffusion coefficient is substituted into equation (4.78), one obtains the particle containment time for classical diffusion,

$$\tau_{cl} = \frac{a^2}{D_{cl}(2.405)^2} = \frac{e^2 B^2 a^2 \tau_c}{m_e k T_e (2.405)^2}. \tag{4.90}$$

4.7.5 Mobility in a Magnetized Plasma

An important non-diffusive radial transport process is *mobility*, in which charged particles are caused to move across or along magnetic field lines by applied electric fields. The *mobility flux*, in particles per square meter per second, is given by

$$\Gamma_{mob} = n v_{mob} = n \mu \cdot E \tag{4.91}$$

where v_{mob} is the drift velocity due to mobility, and μ is the *mobility tensor*. The mobility tensor can be written in terms of the transport matrix of equation (4.84),

$$\Gamma_{mob} = n \mu_0 \mathbf{T} \cdot E \tag{4.92}$$

where the mobility coefficient μ_0 is given by

$$\mu_0 = \frac{q\tau}{m} \tag{4.93}$$

and τ is the time between collisions. The mobility coefficient of equation (4.93) is a signed quantity, negative for electrons and positive for ions.

The total flux of one species in a plasma is given by the sum of the mobility and diffusional fluxes,

$$\Gamma = n\mu \cdot E - \mathbf{D} \cdot \nabla n = n\mu_0 \mathbf{T} \cdot E - D_0 \mathbf{T} \cdot \nabla n \tag{4.94}$$

where both components have been written in terms of the transport matrix, equation (4.84). It is an interesting observation that, for one charge species, an applied radial electric field can bring to a halt the outward diffusive flux driven by the density gradient. The application of radial electric fields by external biasing, which are capable of doing work on the plasma, can act as a mechanism to assist in keeping the ions or the electrons of a plasma well confined. In unmagnetized plasmas, the electric field in the sheath often plays a similar role, leading to ambipolar diffusion, discussed below.

4.7.6 Einstein's Relation

For Maxwellian gases and unmagnetized plasmas, a relation between the diffusion coefficient of equation (4.80) and the mobility of equation (4.93) may be obtained by solving both for the collision time,

$$\tau_c = \frac{3D}{\bar{v}^2} = \frac{m\mu}{q}. \qquad (4.95)$$

Solving equation (4.95) for the diffusion coefficient, and using equation (2.9) for the mean thermal velocity, $\bar{v}$, yields

$$D = \frac{m\bar{v}^2}{3q}\mu = \frac{8kT}{3\pi q}\mu. \qquad (4.96)$$

Equation (4.96) is known as (Albert) *Einstein's relationship*, and predicts that the ratio of the diffusion coefficient to the mobility is a linear function of the kinetic temperature.

4.7.7 Bohm Diffusion Coefficient

During the Second World War, the physicist David Bohm put forward an empirically-derived diffusion coefficient which appeared to describe the radial diffusion of plasma in certain electrical arcs. This *Bohm diffusion coefficient* is

$$D_B = \frac{1}{16}\frac{kT_e}{eB}. \qquad (4.97)$$

It contains no dependence on collision frequency or particle number density, and the magnetic field dependence is weaker than that of classical diffusion, given by equation (4.89). When substituted into equation (4.78), this diffusion coefficient yields a confinement time

$$\tau_B = \frac{a^2}{D_B(2.405)^2} = \frac{16eBa^2}{(2.405)^2kT_e} = 2.77\frac{Ba^2}{T_e'(\text{eV})} \quad \text{(s)}. \qquad (4.98)$$

4.7.8 Ambipolar Diffusion

In lighting devices and other situations frequently encountered in industrial applications, the plasma is contained by an insulating wall, in the manner of a fluorescent light tube, as illustrated schematically in figure 4.5. As equation (4.93) implies, the mobility of the electrons is much greater than that of the ions because of their smaller mass. When a plasma is initially created within insulating walls, the more

mobile electrons reach the surface and build up a negative charge. This buildup of negative charge cannot go on indefinitely, and as time evolves, the negative charge on the wall becomes sufficiently great to attract an oppositely charged flux of ions from the plasma. Only when the flux of electrons and ions to an insulating wall is equal, can the plasma achieve a steady state. The diffusion coefficient describing this steady state, the *ambipolar diffusion coefficient*, can be found as follows.

In the simple one-dimensional geometry of figure 4.5, equation (4.94) gives for the flux of electrons normal to the surface,

$$\Gamma_e = -n_e \mu_e E - D_e \nabla n_e \tag{4.99}$$

and the equal flux of ions reaching the surface is given by

$$\Gamma_i = +n_i \mu_i E - D_i \nabla n_i. \tag{4.100}$$

In a steady state, $\Gamma_e = \Gamma_i$, and quasi-neutrality allows us to assume that the electron and ion number densities are approximately equal, $n_e = Zn_i = n$. Subtracting equation (4.99) from equation (4.100) yields the *ambipolar electric field* which maintains the steady state,

$$E = \frac{D_i - D_e}{\mu_i + \mu_e} \frac{\nabla n}{n}. \tag{4.101}$$

Substituting this ambipolar electric field into equation (4.99) yields an expression for the particle flux to the wall,

$$\Gamma_e = \Gamma_i = \Gamma = -\frac{D_i \mu_e + D_e \mu_i}{\mu_e + \mu_i} \nabla n = -D_a \nabla n \tag{4.102}$$

where D_a is defined as the *ambipolar diffusion coefficient*, given by

$$D_a \equiv \frac{D_i \mu_e + D_e \mu_i}{\mu_e + \mu_i}. \tag{4.103}$$

In a steady state, a plasma confined by insulating walls will have an effective diffusion coefficient given by equation (4.103). Since the electron mobility dominates, $\mu_e \gg \mu_i$, we can neglect the ion mobility in the denominator of equation (4.103), and make use of Einstein's relation, equation (4.96), to obtain a relationship between the ambipolar diffusion coefficient and the ion diffusion coefficient,

$$D_a \approx D_i \left(1 + \frac{D_e}{D_i} \frac{\mu_i}{\mu_e}\right) = D_i \left(1 + \frac{T_e}{T_i}\right). \tag{4.104}$$

In most plasmas of industrial interest, the electron temperatures are much greater than the ion kinetic temperatures, thus yielding an ambipolar diffusion coefficient much larger than the diffusion coefficient for the ion population.

4.8 ELECTRON COLLISION FREQUENCY

In the partially ionized plasmas prevalent in industrial applications, the particle, momentum, energy, and charge transport properties of the plasma are determined by electron–neutral collisions. We have seen in the above discussion that the electron collision frequency ν_c plays an essential role in determining the power dissipation in the plasma; the energy transfer frequency; and all of the transport coefficients, including the diffusion coefficient, the mobility, the viscosity, the thermal conductivity, and the electrical conductivity. Since ν_c plays such a fundamental role in the transport properties of plasma, it is useful to survey the literature describing the binary electron-neutral collisions which dominate Lorentzian gases.

4.8.1 Classification of Gases

It is useful to classify gases according to the characteristics of their electron collision frequency, as follows:

Gases for which ν_c is independent of energy. A restricted class of gases, some of them of industrial importance, possess electron collision frequencies which are independent of energy over the electron kinetic temperature range likely to be encountered, from approximately 3 to 30 eV. These gases allow (and generally produce good) comparisons between theory and experiment. Such gases include hydrogen, spectroscopically pure helium, and the gas known as Heg, which is helium with a small admixture of mercury. Heg gas is such that the electron population does not lose energy to inelastic excitation, only to the first ionization state of the mercury atoms.

Noble gases. These gases include neon, argon, xenon, and krypton. They can be purified relatively easily, do not usually undergo plasma–chemical reactions or dissociation, and therefore undergo fewer physical processes that might affect measurements made in them. Because of these properties, there is by now a large body of literature on their transport properties, and comparisons of theory and experiment using these gases.

Air. The transport properties and behavior of air plasmas have been widely studied because of its importance to a wide variety of military and industrial applications. Data involving air may be affected by plasma–chemical reactions producing nitrogen oxides or ozone, as well as dissociation of the oxygen and nitrogen molecules. In spite of the problem of assuring reproducibility of results in the face of plasma–chemical reactions and dissociation, air has been widely studied and its transport properties are available in the literature.

Other Gases. Probably more than 95% of the published data on electron collision frequencies and the transport properties of gases have used the gases listed above. Data on other gases are relatively sparse, usually not cross-checked by different investigators, and the reported data are often complicated by the effects of plasma–chemical reactions among contaminants or mixtures, or plasma–surface interactions.

4.8.2 Tabulated Data

There is a relatively large body of data on the electron collision frequency in various gases, but this literature can be a minefield for those who are not acquainted with the atomic physics literature in depth, and simply need some data for a particular application. A common problem with the older literature on electron–neutral collisions is that, prior to the mid 1950's, most experimental vacuum systems were seriously contaminated by mercury vapor. This contaminant originated either from mercury diffusion pumps or McLeod gauges, which were used to measure the vacuum pressure. The presence of even small amounts of mercury vapor in the gas under investigation could result in errors ranging from a factor of 2 to several orders of magnitude in the transport properties.
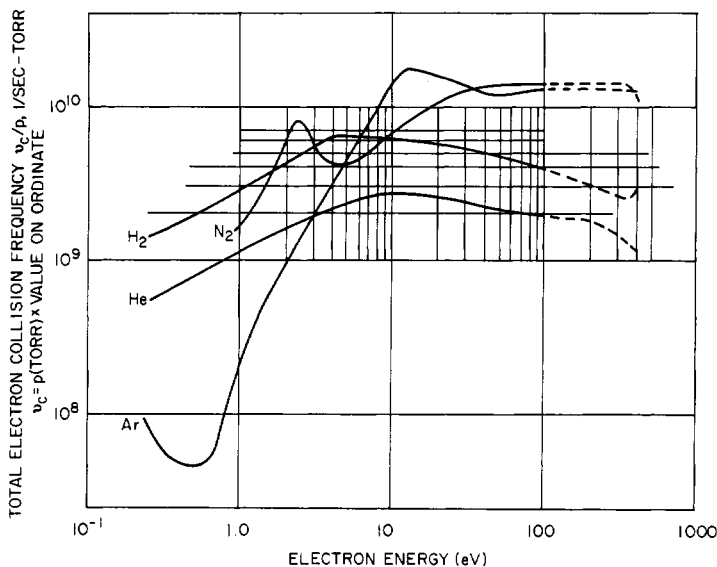

Figure 4.9 The effective collision frequency, in collisions per second-torr, for various gases, taken from Geller and Hosea (1968). Note the Ramsauer minimum in argon gas below 1 eV.

Table 4.2 Momentum transfer collision rates for various gas species at low background neutral gas temperatures. Data taken from Vidmar (1990).

Gas Species	$\nu/N [10^{-14} \text{ m}^3\text{s}^{-1}]$		
	$T = 300$ K	500 K	1000 K
N_2	0.594	0.959	1.77
O_2	0.286	0.437	0.804
CO_2	10.05	9.68	7.48
H_2O	77.90	56.25	34.6
He	0.763	1.01	1.50
Ne	0.07	0.118	0.217
Ar	0.220	0.146	0.094
Kr	1.775	1.315	0.713
Xe	5.29	3.81	1.90
Dry Air	0.529	0.845	1.550

Data: N is gas density in m^{-3}.

A good discussion of the physics of the collision processes responsible for electron–neutral interactions is given in McDaniel's classic book *Collision Phenomena in Ionized Gases* (McDaniel 1964). This book also has a very good critical discussion of the experimental data available up to the time of publication. Other compilations of electron–neutral cross sections may be found in the books by Sanborn C Brown (1967), and by MacDonald (1966).

A useful compilation of the electron–neutral collision frequency in argon, helium, hydrogen, and nitrogen is shown in figure 4.9, from an unpublished laboratory report by Geller and Hosea (1968). One obtains the collision frequency of the gases shown by multiplying the value on the ordinate by the background gas pressure measured in torr. Another tabulation of useful data is shown on tables 4.2 and 4.3, from a recent publication by Vidmar (1990). Table 4.2 shows the momentum transfer collision rate for various gas species at and slightly above room temperature. These data show the very low collision frequencies at low electron kinetic temperatures of the noble gases due to the Ramsauer effect, and the data in this table also illustrate the very large cross section for electron scattering by the water molecule. On table 4.3 is shown the electron collision rate in air as a function of altitude above sea level, and for very low electron kinetic temperatures such as one might encounter in the atmosphere at the altitudes indicated.

An important phenomenon occuring at low electron kinetic temperatures is the *Ramsauer effect*, whereby the collision cross section of certain gases drops to extremely low levels at low electron kinetic temperatures as the result of quantum mechanical effects. The Ramsauer

Table 4.3 collision rate in air as a function of altitude above the Earth's surface, for three background gas temperatures. Data taken from Vidmar (1990).

Altitude (km)	Pressure(torr)	Momentum transfer, collision/s		
		$T = 300$ K	500 K	1000 K
0	760	466×10^9	417×10^9	425×10^9
3.44	500	103	121	180
10	200	23.6	37.6	72.0
14.5	100	12.1	19.3	37.1
18.9	50	6.07	9.70	18.6
24.8	20	2.38	3.00	7.27
29.4	10	1.18	1.87	3.57
34	5	0.584	0.914	1.73
40.7	2	0.272	0.382	0.672
45.9	1	0.215	0.248	0.365
51.5	500×10^{-3}	122×10^6	134×10^6	189×10^6
58.6	200	26.7	37.8	67.1
63.7	100	11.8	18.3	34.4
68.7	50	5.92	9.42	18.0
74.7	20	2.49	3.98	7.64
77.3	10	1.27	2.03	3.89
83.5	5	0.662	1.06	2.03
88.7	2	0.257	0.411	0.789
91.4	1.32	0.161	0.258	0.494

effect is illustrated by argon in figure 4.9, which shows very low electron–neutral collision cross sections at approximately 0.5 eV. Although the Ramsauer effect is normally associated with the heavier noble gases, it can also become evident in some molecular gases, including the nitrogen oxides.

On figure 4.10 is shown the pressure in torr as a function of altitude, shown in kilometers on the abscissa. The nearly straight line reflects the fact that the Earth's atmosphere is almost isothermal up to very high altitudes. The relationship between the neutral number density and pressure in torr (as given in Appendix D) at the conventional laboratory temperature of 300 K is given by

$$n_0 = 3.220 \times 10^{22} p(\text{Torr}) \qquad (\text{atoms/m}^3). \qquad (4.105)$$
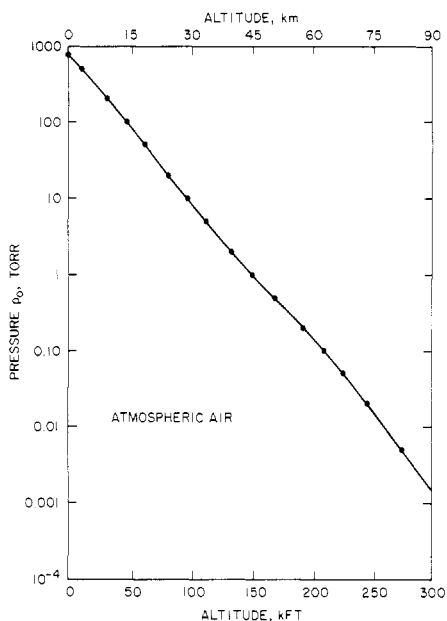
Figure 4.10 The pressure of atmospheric air in torr as a function of altitude in the Earth's atmosphere.

4.9 LOW PRESSURE ELECTRICAL DISCHARGE

4.9.1 Classical Geometry

Most early research on electrical discharge physics was performed on the classical low pressure electrical discharge tube illustrated in figure 4.11. This arrangement was the prototype of the 'neon' advertising sign and the fluorescent light tube. It consists of an evacuated glass tube, with circular disk electrodes at either end, connected to a high voltage DC power supply. By adjusting the ballast resistor R, one can sweep out a voltage–current characteristic which is highly nonlinear. In the plasma, electrons migrate toward the anode, and positive ions toward the cathode, both of them frequently colliding with the neutral background gas.

4.9.2 Voltage–Current Characteristic

The voltage–current regimes of a DC low pressure electrical discharge are listed in table 4.4, and can be illustrated schematically by the voltage–current diagram shown in figure 4.12. If one takes a low pressure electrical discharge tube like that illustrated in figure 4.11, and raises the voltage V, while measuring the current I flowing through the discharge, the discharge will trace out the highly nonlinear voltage–current curve
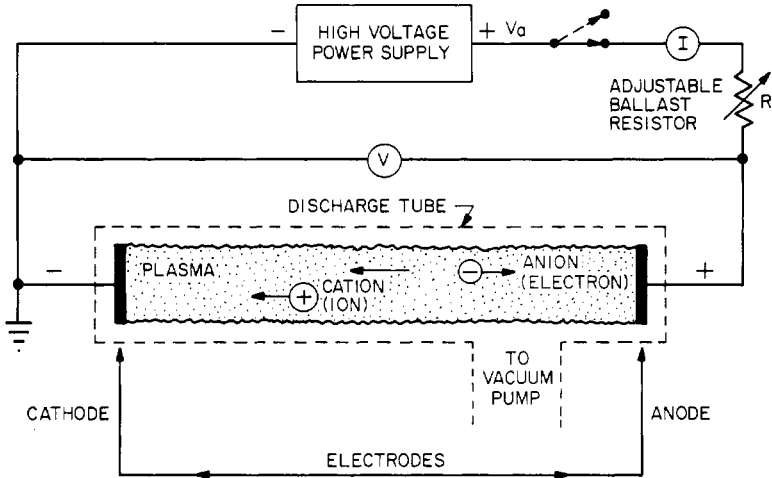
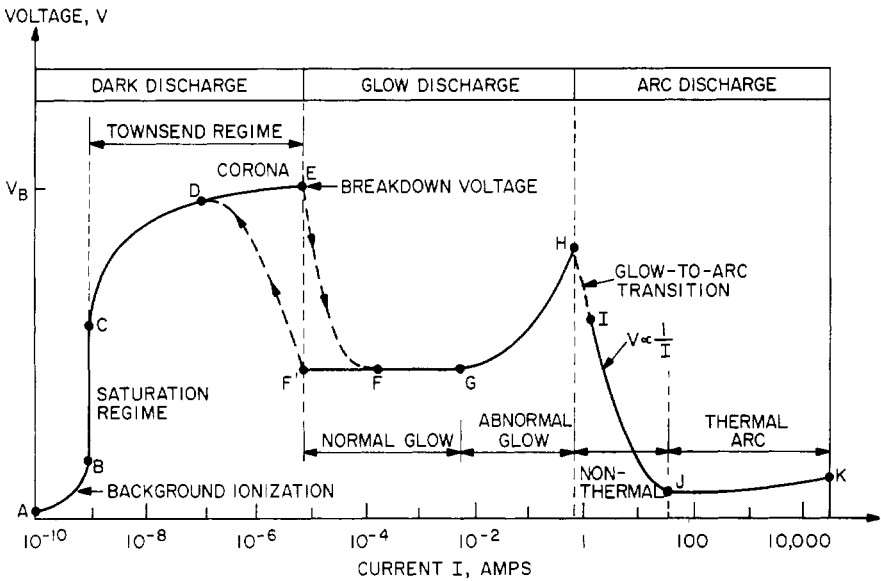**Figure 4.11** Schematic of the low pressure electrical discharge tube.

Figure 4.12 Voltage–current characteristic of the DC low pressure electrical discharge tube.

shown schematically in figure 4.12. Starting at a very low voltage at the lower left, the region between A and B on the curve is the *background ionization regime*, in which the increasing voltage sweeps out an increasingly large fraction of the individual ions and electrons created by cosmic rays and other forms of ionizing background radiation.

Table 4.4 Voltage–current regimes of low pressure DC electrical discharges.

(1)	Dark discharges
	(A) Background ionization
	(B) The saturation regime
	(C) The Townsend regime
	(D) Corona discharges
	(E) Electrical breakdown
(2)	Glow discharges
	(A) The normal glow discharge
	(B) The ahnormal glow discharge
(3)	Arc discharges
	(A) The glow-to-arc transition
	(B) Nonthermal arcs
	(C) Thermal arcs

In the *saturation regime* between B and C, all of the ions and electrons produced by background radiation are removed from the discharge volume, and the electrons do not possess enough energy to create new ionization. In the region from C through E, the *Townsend regime*, the electrons in the discharge volume acquire sufficient energy from the electric field that they ionize some of the neutral background gas, leading to a very rapid, exponentially increasing current as a function of voltage. In the region between D and E, unipolar *corona discharges* will occur, as the result of local electric field concentrations on the surface of the electrodes at sharp points, sharp edges, or asperities. These strong local electric fields exceed the breakdown strength of the surrounding neutral gas. When the voltage is increased further to the voltage V_B, at the point E, electrical breakdown will occur. The regime between A and E on the voltage–current characteristic is termed a *dark discharge* because, except for the corona discharges and the electrical breakdown spark itself, the discharge remains invisible to the eye.

Once electrical breakdown occurs at point E, the discharge makes a transition to the *glow discharge* regime, in which the current is high enough, and the amount of excitation of the neutral background gas great enough, that the plasma is visible to the eye. After a discontinuous transition from the point E to F, one is then in the *normal glow* region of the voltage–current characteristic, in which the voltage across the discharge is almost independent of the current over several orders of magnitude in the discharge current. As the current is increased from F to G, the fraction of the cathode occupied by the plasma increases, until the plasma covers the entire cathode surface at the point G. At that point, the discharge enters the *abnormal glow* regime from G through

H, in which the voltage is an increasing function of the current. If one were to start at point G of the curve and move to the left, one normally would see a form of hysteresis in the voltage–current characteristic, when, instead of retracing the voltage–current characteristic from F to E, the discharge would maintain itself in the normal glow regime to the point F′, at considerably lower currents and current densities than F, and only then make a transition back to the Townsend regime.

At the point H, the current density on the cathode can become great enough to heat the cathode to incandescence, thus triggering a discontinuous *glow-to-arc transition*, shown by the dotted line between H and I. After this transition, the discharge settles down at some point between I and K which depends upon the internal resistance of the DC power supply. The *arc regime*, from I through K, is one in which the discharge voltage decreases as the current increases, until large currents are achieved at the point J, after which the voltage once again increases slowly with increasing current. The regime of falling voltage with increasing current between I and J is the *non-thermal arc regime*, in which the electron, ion, and gas temperatures are unequal. The portion with positive slope between J and K is the *thermal arc regime*, in which the plasma is close to thermodynamic equilibrium and the temperatures of all species are approximately equal.

4.10   PLASMA POWER SUPPLIES

Direct current (DC), alternating current (AC), or radio frequency (RF) power are used to generate the plasmas used industrially. These applications include DC and AC line frequencies, as well as assigned frequency bands across the entire electromagnetic spectrum from 1 kHz to 10 GHz. The essential components of a generic plasma reactor are shown in figure 4.13. The DC and AC plasma reactors have a power supply connected directly to the reactor. Thus, all additional components required for RF operation between the DC power supply (which usually operates at kilovolt voltages in both cases) and the reactor represent an additional expense and additional sources of operational and reliability problems, compared to DC and AC plasma reactors.

The additional cost and complexity of RF power supplies and plasma reactors must be justified in terms of their operational advantages. Such advantages have been identified for many industrial applications, and include the following:

(1) The RF power deposited in the plasma is transferred by displacement, not real currents. This implies less electron and ion bombardment of the electrodes; easier coupling of power through the vacuum wall; less electrode heating; no, or much weaker, electrode jets of a kind discussed
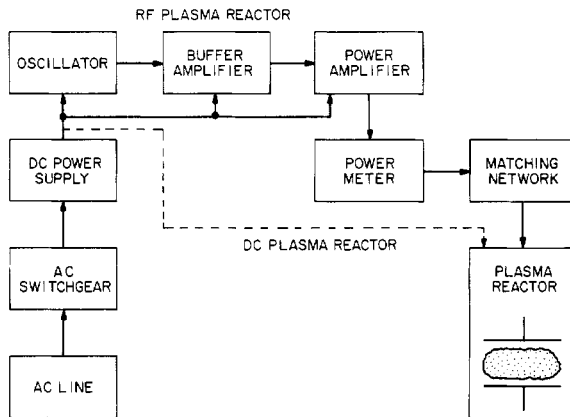
Figure 4.13 Power supplies for a parallel plate glow discharge plasma reactor. The dotted line shows the power flow for DC glow discharge plasmas; the solid arrows indicate the power flows for RF glow discharge production.

in connection with DC arcs; and lower losses and wall recombination, since there is one less mechanism for losing electrons and ions from the plasma containment volume.

(2) In general, it has been found that RF-generated plasmas offer greater stability of operation than an equivalent DC or AC plasma, particularly with respect to electrode effects, and the ability to function without mode transitions of the kind present in some DC or AC discharges.

(3) RF plasmas provide a higher electron kinetic temperature than an equivalent DC or AC plasma source of the same electron number density, and this can be beneficial in applications where it is desired to increase the number of free radicals, plasma–chemical reactions, or dissociation and ionization reactions.

(4) RF generated plasmas often tend to have higher electrical efficiency than equivalent DC or AC plasma sources of the same volume and number density, partly because they have much lower electrode losses.

4.10.1 Power Supply Frequency Regimes

The standard frequency/wavelength bands designated by the International Telecommunications Union (ITU) are shown in table 4.5 (Book 1987). Significant industrial plasma engineering applications (as opposed to communications applications) occur from 1 kHz to at least 3 GHz. The availability of radio frequency power is indicated very schematically on figure 4.14. Along the top are the ITU designated frequency bands. Below approximately 200 W, there are few important industrial applications, other than lighting devices and electronic test equipment.
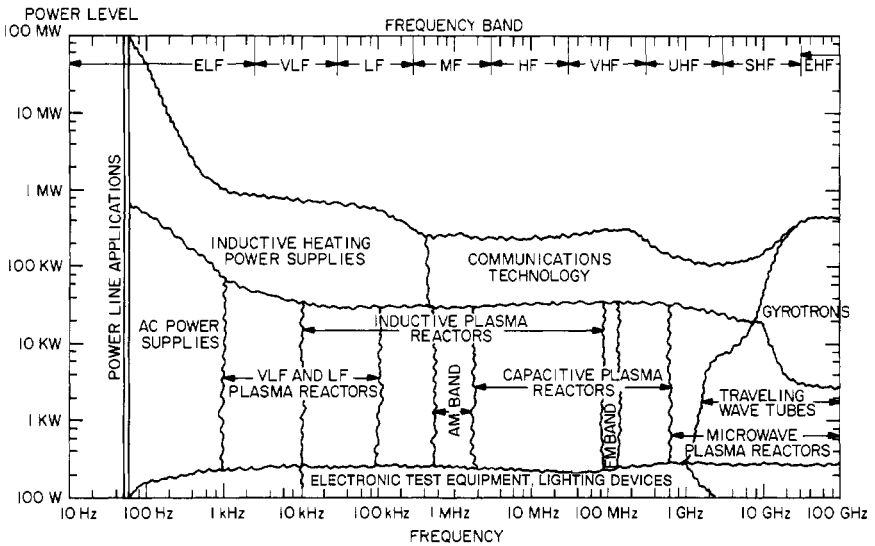
Figure 4.14 Availability of radio frequency power. This shows the approximate availability of off-the-shelf RF power sources as a function of their power output level and frequency.

4.10.2 Power Supply Availability

The power levels of interest industrially range approximately from a minimum of 200 W, up to perhaps 50 kW, although some industrial applications require power supplies up to 1 MW. The enclosed area in figure 4.14 includes off-the-shelf technology readily available in the current marketplace. Above 50 kW, off-the-shelf units are available in most frequency bands, but are often intended for communications applications rather than industrial plasma generation. The division of industrial RF power applications is arbitrary, but for the sake of definiteness, and because they tend to be distinguished by somewhat different technology, we distinguish here the following frequency regimes, indicated in table 4.6, along with the most prominent assigned frequencies. The AC, VLF, LF, and microwave regimes are characterized by their frequency ranges indicated in table 4.5; the inductive and capacitive plasma reactor regimes are characterized by the power coupling technology only, and both span a relatively wide range of frequencies, including part or all of several bands listed in table 4.5.

4.10.3 Power Supply Technology

The block diagram of a typical RF plasma reactor shown in figure 4.13 contains several elements that are not necessary in DC plasma reactor

Table 4.5 Designation of electromagnetic frequency/wavelength bands, after ITU standards (Book 1987).

Designation	Frequency range		Wavelength range	
	Lower	Upper	Lower	Upper
ULF[a]		10 Hz	3 Mm	
ELF[a]	10 Hz	3 kHz	100 km	3 Mm
VLF	3 kHz	30 kHz	10 km	100 km
LF	30 kHz	300 kHz	1 km	10 km
MF	300 kHz	3 MHz	100 m	1 km
HF	3 MHz	30 MHz	10 m	100 m
VHF	30 MHz	300 MHz	1 m	10 m
UHF	300 MHz	3 GHz	10 cm	1 m
SHF[b]	3 GHz	30 GHz	1 cm	10 cm
S	2.6	3.95	7.6	11.5
G	3.95	5.85	5.1	7.6
J	5.3	8.2	3.7	5.7
H	7.05	10.0	3.0	4.25
X	8.2	12.4	2.4	3.7
M	10.0	15.0	2.0	3.0
P	12.4	18.0	1.67	2.4
K	18.0	26.5	1.1	1.67
R	26.5	40.0	0.75	1.1
EHF	30 GHz	300 GHz	1 mm	1 cm
Submillimeter	300 GHz	3 THz	100 nm	1 mm
Infrared	3 THz	430 THz	700 nm	100 mm
Visible	430 THz	750 THz	400 nm	700 nm
Ultraviolet	750 THz	30 PHz	10 nm	400 nm
x-ray	30 PHz	3 EHz	100 pm	10 nm
Gamma Ray	3 EHz	—	—	100 pm

[a] The boundary between ULF and ELF is variously defined.
[b] The SHF (microwave) band is further subdivided as shown.

systems. The oscillator–amplifier must maintain an assigned frequency in the face of a variable output power and variable load impedance. In some frequency bands this can be technically difficult and/or expensive, and is a principal distinction between industrial plasma and communications applications. In the latter applications, the RF power supply normally works into a constant impedance such as a fixed antenna, at a constant power output.

Because a plasma reactor is usually a variable load, an impedance matching network is necessary. To see why, consider the circuit of figure 4.15, in which the source and load are purely resistive (both, in fact, usually have complex impedances, but this has little effect on
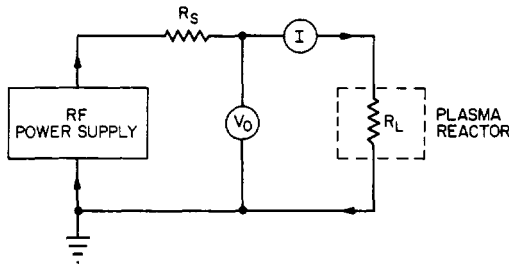
Figure 4.15 Impedance matching of a simple circuit with purely resistive source and plasma reactor impedances.

the discussion below). The power absorbed by the load in figure 4.15 is given by

$$P_L = I^2 R_L = \frac{V_0^2 R_L}{(R_L + R_S)^2} \quad \text{(W)}. \qquad (4.106)$$

If the source resistance, R_S, and output voltage V_0 are fixed, the usual situation with off-the-shelf equipment, the power transferred to the load is maximized by adjusting the load resistance R_L, such that

$$\frac{dP_L}{dR_L} = 0 = \frac{2V_0^2(R_S - R_L)}{(R_S + R_L)^3}. \qquad (4.107)$$

Equation (4.107 is satisfied when

$$R_S = R_L \quad (\Omega) \qquad (4.108)$$

at which point, from equation (4.106), the maximum power delivered to the load is

$$P_L = \frac{V_0^2}{4R_L} \quad \text{(W)}. \qquad (4.109)$$

Table 4.7 Approximate cost (in dollars per watt) of RF power in various regimes of frequency and for various kinds of plasma reactor.

Regime	Approximate cost ($/W)
(1) DC	0.20–1.00
(2) Powerline AC	0.05–0.50
(3) VLF and LF plasma reactors	0.20–1.00
(4) Inductive plasma reactors	0.50–3.00
(5) Capacitive plasma reactors	1.00–3.00
(6) Microwave plasma reactors	0.50–3.00

In figure 4.15, the plasma reactor includes not only the plasma-generating load, but also the impedance matching network, which is variable, thus justifying the minimization procedure contained in equation (4.107).

One can compare this maximum power transfer of equation (4.109) with a fictitious 'perfect' power supply (like a large battery bank) for which $R_S = 0$. From equation (4.106), with $R_S = 0$,

$$P_L = \frac{V_0^2}{R_L} \quad \text{(W)}. \tag{4.110}$$

Thus, the best impedance match into a purely resistive DC plasma reactor can deliver only 25% of the power of an ideal power supply. Impedence matching in real circuits with complex impedances can greatly improve upon this factor of 0.25, but usually one ends up paying for more power supply capacity than can be transferred to the load, even by optimum impedance matching. Commercial power supplies are usually designed to a standard load of $R_S = 50\ \Omega$, although other impedances, not too far from this value, are also available.

4.10.4 Relative Cost of Input Power

A rough estimate from a limited range of catalog quotations of the cost of DC, AC, and RF power in various frequency bands is summarized on table 4.7. Note that, per watt, RF power is 5 to 10 times as expensive as DC, and its use must be justified in terms of operational or product quality advantages. Some of these advantages have been discussed previously.

4.10.5 Operational Constraints

Only limited frequency bands are available for high power industrial use. In the United States, the Federal Communications Commission (FCC)
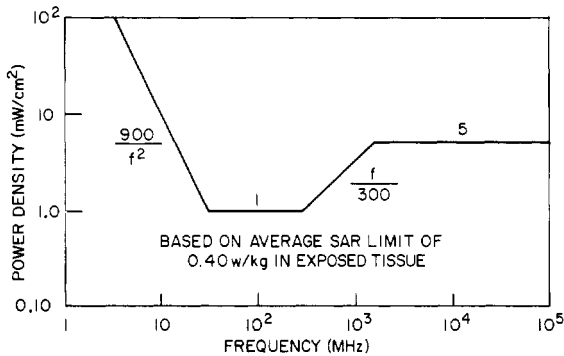
Figure 4.16 American National Standards Institute C95.1, 1982 RF radiation exposure limits.

has reserved certain frequencies for high power industrial use, and many of these are also an international standard. Some of these frequencies are 400 kHz, 450 kHz, 3.0 MHz, 13.56 MHz, 27.12 MHz, 0.915 GHz and 2.45 GHz but this does not represent an inclusive list. These are the frequencies at which most high power industrial RF power supplies are available.

In addition to these assigned frequencies, the use of RF power supplies brings into play a number of regulatory constraints associated with occupational and public safety. The use of high voltage, high power RF excitation raises the following safety issues.

(1) *RF arcs*, particularly at low frequencies of the order of 10 kHz: RF arcs can strike and be maintained over much greater distances than a DC arc at the same applied voltage. For example, at 10 kHz, an arc more than 15 cm in length from a source with only 5 kV rms can be maintained in the steady state.

(2) *High voltage RF shielding* is required, since some RF plasma reactors can act like radio antennas, and induce dangerously high voltages on electrical conductors in the near radiation field of the source.

(3) *Harmonic production and frequency drifts* must not produce radio frequency interference (RFI) which interferes with other uses of the electromagnetic spectrum at frequencies other than the assigned frequency. If frequency drift or harmonics are problems, adequate shielding is required.

(4) *Occupational exposure* of staff to RF power flux. This area of occupational safety standards is a very vexed question, since the United States standards for this occupational hazard are a factor 100 or more higher than that of many other countries. The current U.S. standard, dating from 1982, is shown in figure 4.16. At 2.45 GHz, the microwave oven frequency, this *occupational* standard calls for 5 mW/cm^2; at

frequencies in the vicinity of 100 MHz, this standard is 1 mW/cm^2. These standards are under review, and it is likely that the occupational safety limit, as well as the limit for public exposure, will in the future be set at or below 1 mW/cm^2.

REFERENCES

Book D L 1987 *NRL Plasma Formulary–1987* NRL Publication 0084-4040 (Washington, DC: Naval Research Laboratory)

Brown S C 1967 *Basic Data of Plasma Physics, 1966* (Cambridge, MA: MIT Press) LCCCN 67-15601

Chen F F 1974 *Introduction to Plasma Physics and Controlled Fusion* vol I *Plasma Physics* 2nd edn (New York: Plenum)

Geller R and Hosea J 1968 *Electron Collision Frequencies* Report EUR-CEA-FC-495, Grenoble

Kettani M A and Hoyaux M F 1973 *Plasma Engineering* (New York: John Wiley) ISBN 0-470-47330-4

MacDonald A D 1966 *Microwave Breakdown in Gases* (New York: John Wiley) LCCCN 66-22841

McDaniel E W 1964 *Collision Phenomena in Ionized Gases* (New York: John Wiley) LCCCN 64-13219, p 19

Roth J R 1986 *Introduction to Fusion Energy* (Charlottesville, VA: Ibis Publishing) ISBN 0-935005-07-2

Sears F W and Salinger G L 1975 *Thermodynamics, Kinetic Theory, and Statistical Thermodynamics* 3rd edn (Reading, MA: Addison-Wesley) ISBN 0-201-06894-X

Vidmar R J 1990 *Plasma Cloaking Air Chemistry, Broadband Absorption, and Plasma Generation* Final Report, SRI Project 8656 (Menlo Park, CA: SRI International)

5

Electron Sources and Beams

The previous four chapters included an introduction to the field of industrial plasma engineering, and a review of basic concepts from kinetic theory, charged particle dynamics, and plasma physics which are fundamental to the industrial applications of plasma. In the remaining nine chapters of Volume 1, these principles will be applied to industrial plasma sources and reactors according to the taxonomy outlined in table 1.1. This chapter will cover electron sources and beams, and the next chapter ion sources and beams. Chapter 7 will be devoted to a brief coverage of sources of ionizing radiation. Chapters 8 through 10 discuss DC plasma sources and reactors, and the final three chapters are devoted to RF plasma sources and reactors.

5.1 THERMIONIC EMISSION SOURCES

Vacuum tubes and many other vacuum-electronic devices require electron emission from a cathode with current densities up to the Child law limit. Electron sources include heated filaments, photoelectric emission, field emission, hollow cathodes, and secondary electron emission. Heated filaments and hollow cathode sources are the most widely used electron sources. Ions, as well as electrons, can be emitted from hot, refractory metal surfaces. Surface ion emission is discussed by Forrester (1988), but here we discuss only the *thermionic emission* of electrons from heated filaments made of refractory metals.

5.1.1 Physics of Thermionic Emission

The electrons in a metal are trapped in a potential well, shown schematically in figure 5.1. The depth of this potential well is equal
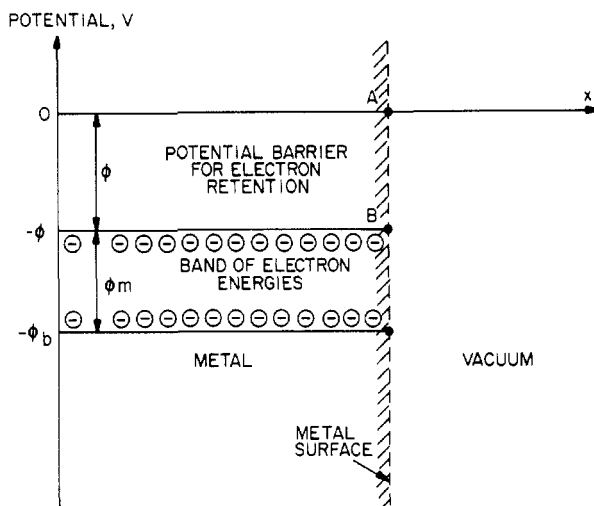
Figure 5.1 The potential–distance diagram for electrons near the surface of a metal, indicated by the hatched line. The potential ϕ is the work function, the potential which an electron must acquire, from thermal energy or other sources, to leave the metal.

to the *work function*, ϕ. The band of mobile electrons in the metal has a width ϕ_m, giving a total *band depth* $\phi_b = \phi + \phi_m$. In figure 5.1 the metal surface is at the position indicated by the hatched line. In order for an electron to escape the metal, it has to overcome a potential barrier of ϕ eV. At room temperature, this does not happen to any significant extent. At high temperature, in excess of 1000 K, electrons in the metal acquire enough thermal energy so that the more energetic of them reach the potential ϕ and can escape from the metal.

5.1.2 Richardson Equation

It is a result from statistical mechanics that at the temperature T, the emission of electrons from surfaces is given by the *Richardson equation* (Richardson and Young 1925),

$$ J = A \, T^2 \exp\left(-\frac{e\phi}{kT}\right) \qquad (\text{A/m}^2) \qquad (5.1) $$

where T is the temperature of the surface, the parameter A is the *emission constant*, and the work function ϕ is the minimum energy, in electronvolts, which must be added to an electron in a metal at $T = 0$ K in order for it to escape the metal. When electrons are emitted from a cathode surface according to the Richardson equation, it is said
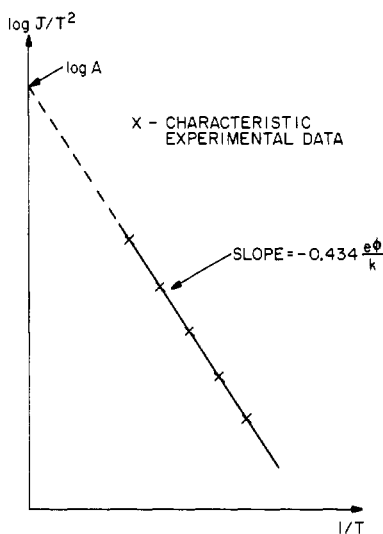
Figure 5.2 A Richardson plot, showing the current density divided by the square of the temperature, plotted logarithmically on the ordinate, as a function of the parameter $1/T$. The intersection of a straight line drawn through the experimental data with the vertical axis yields the constant A in the Richardson equation, and the slope yields the work function for the material.

to be *thermionically emitting*. The constants A and ϕ are determined experimentally by measuring the current density J, emitted from a metallic surface at several values of the temperature T, then plotting J/T^2 as a function of $1/T$ on a semi-logarithmic *Richardson plot*, illustrated in figure 5.2. The work function ϕ is found from the slope of the straight line on this graph, and the constant A from the vertical axis intercept.

Statistical mechanical theory predicts that for all metals the parameter A appearing in the Richardson equation is given by

$$A = \frac{4\pi m e k^2}{h^3} = 1.2 \times 10^6 \text{ A/m}^2\text{-K}^2. \tag{5.2}$$

This universal, constant value of A is inconsistent with experiment, since some metals have a value about half this great. Characteristic values of the parameter A are shown in table 5.1, taken from Forrester (1988), and values for the work function have been taken from the *Handbook of Chemistry and Physics* (Weast *et al* 1988). For a range of clean refractory metals, the value of the parameter A can range over the values $30 \times 10^4 < A < 200 \times 10^4$ A/m^2-K^2. Special thermionic

Table 5.1 Representative thermionic emission data.

Metal	A (A/m^2-K^2)	ϕ (V)
W	70.0×10^4	4.55
Ta	55.0×10^4	4.25
Ni	30.0×10^4	5.15
Cs	160.0×10^4	2.14
Pt	32.0×10^4	5.65
Cr	48.0×10^4	4.50
Ba on W	1.5×10^4	1.56
Cs on W	3.2×10^4	1.36
C	—	5.0

emitters include barium-impregnated tungsten for low work function, and thoriated iridium for low work function plus oxidation resistance.

In a space-charge limited diode with a thermionically emitting cathode, the current of electrons can be limited to less than the Child law value by operating the cathode at a temperature such that less than the space-charge limited current density J_c is emitted and available. This is illustrated on figure 5.3, where T_1, T_2, and T_3 are successively higher cathode temperatures, and the straight line relating the current density to the voltage V_0 across the diode is the Child law current.

As electron emitters, heated filaments have the advantage of being a well known technology, they are simple to construct, and they do not require a gas flow to maintain their operation. Among the disadvantages of heated filaments as electron sources are a relatively short lifetime, since the refractory materials of which filaments are made are subject to chemical attack, and high power consumption, leading to cooling problems.

5.2 PHOTOELECTRIC EMISSION SOURCES

5.2.1 Photoelectric Effect

A second method by which electrons can be emitted from solids is through the *photoelectric effect*, illustrated in figure 5.4, in which electrons acquire enough energy from the photons associated with incident electromagnetic radiation to overcome the work function, ϕ, of the solid material. For this process to happen, the frequency of the incident radiation must be above the *photoelectric threshold*, ν_{min}, given by

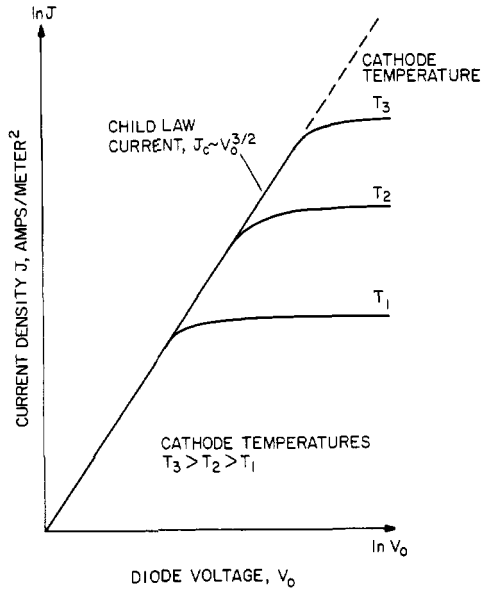$$\nu_{min} = \frac{e\phi}{h} \quad \text{(Hz)}. \tag{5.3}$$

Figure 5.3 The logarithm of the current density flowing in a space-charge limited diode with a thermionically emitting cathode, as a function of the voltage applied across the diode V_0, for three successively increasing cathode temperatures, T_1, T_2 and T_3.
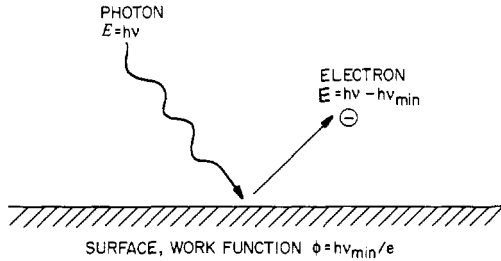

Figure 5.4 Emission of a photoelectron from a surface with work function ϕ.

For the alkali metals shown in table 5.1, ν_{min} is in the visible part of the spectrum, putting significant electron emission within reach of intense sources of visible light. For nearly all other metals and insulators, $4\,\text{eV} < \phi < 5\,\text{eV}$, thus requiring intense sources of ultraviolet radiation in order to observe the photoelectric effect. The energy of electrons emitted from a surface is given by *(Albert) Einstein's photoelectric equation*,

$$\mathcal{E} = h(\nu - \nu_{min}) \qquad \text{(J)}. \qquad (5.4)$$

5.2.2 Photoelectron Current Densities

An upper bound on the electron current density possible by photoelectric emission can be calculated on the assumption that the incident radiation has a frequency $\nu = \nu_{\min}$, and a power flux S W/m^2, to give a flux of photoelectrons

$$\Gamma_e = \frac{S}{e\mathcal{E}'_{\min}} = \frac{S}{h\nu_{\min}} = \frac{S}{e\phi} \qquad \text{(electrons/m}^2\text{-s)}. \qquad (5.5)$$

The current density of these electrons is

$$J_e = e\Gamma_e = \frac{S}{\phi} \qquad \text{(A/m}^2\text{)}. \qquad (5.6)$$

For ordinary levels of illumination, exemplified by the solar constant $S = 1338$ W/m^2, and a characteristic work function of $\phi = 1.5$ eV, the electron current density would be $J_e \approx 93$ mA/cm^2. If one had an intense ultraviolet source with $S = 10^8$ W/m^2 and a surface with a work function $\phi = 4.5$ eV, the electron current density would be as high as 2200 A/cm^2.

5.2.3 Applications

Practical limitations on the intensity of ultraviolet sources have restricted use of the photoelectric effect to stabilizing dark discharges in the Townsend regime, stabilizing glow discharges, and to initiating electrical breakdown between electrodes. As UV lasers become available for industrial plasma applications, photoelectric emission may become a useful alternative to thermionic or field emission in applications where hot cathodes or strong electric fields are inconvenient. Also, a photo-emitting cathode can be operated at room temperature, an advantage in many applications.

5.3 FIELD EMISSION SOURCES

Field emission sources operate by placing such a high electric field on a metal (or insulator) that electrons are pulled out of the surface by electrostatic forces. Consider a small hemispherical point of radius R raised to the potential V_0, shown in figure 5.5. The electric field at the surface of the tip is given by

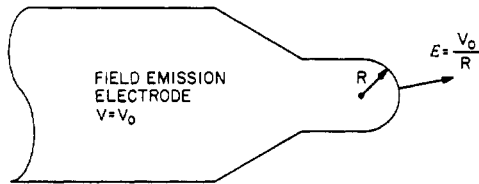$$E = \frac{V_0}{R} \qquad \text{(V/m)}. \qquad (5.7)$$

Figure 5.5 Field emission of electrons from a microscopic fine point of radius R, and negative potential V_0. The surface electric field is given by the applied voltage divided by the effective radius of the tip.
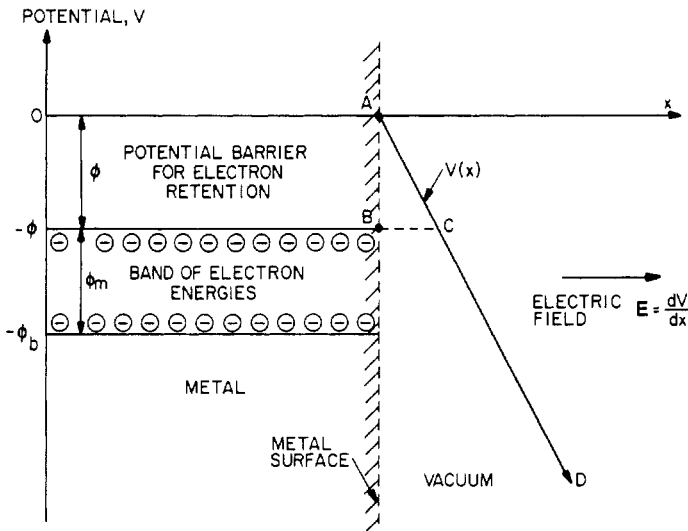

Figure 5.6 Potential–distance diagram at the surface of a metal, given by the hatched line, subject to a very strong electric field. The potential as a function of distance above the surface is shown by the sloping line AD. If the electric field is strong enough, and the distance CD small enough, electrons in the conduction band can tunnel through the potential barrier BAC and be pulled out of the solid material by the strong electric field.

It is not too difficult to apply potentials of $V_0 = 10$ kV to sharp points, the radius of curvature of which is $R = 10^{-6}$ m. Electric fields at the tip can therefore reach magnitudes of 10^{10} V/m, a value high enough that field emission can occur.

5.3.1 Physics of Field Emission

If the electric field given by equation (5.7) is high enough, electrons can be pulled out of the surface by *field emission*, the physical mechanism of which is illustrated in figure 5.6. This figure shows a schematic energy

level diagram for electrons in a metal or insulator, in which the band of electron energies is depressed by the work function ϕ below the reference potential. Imposition of a strong electric field results in a potential as a function of distance above the surface of the metal given by the line ACD. Beyond the point C, an electron outside the metal would have a potential lower than its value inside the metal; this provides a driving force for quantum mechanical tunneling of electrons from B to C, through the potential barrier immediately above the surface of the material. This process was studied by Fowler and Nordheim (1928) and by Fowler (1933), who derived the field emission current density,

$$J_f = CE^2 \exp\left(-\frac{D}{E}\right) \qquad (A/m^2). \qquad (5.8)$$

For ϕ in eV, the constant C is given by

$$C = \frac{e^2 \phi_m^{1/2}}{2\pi h \phi_b \phi^{1/2}} = 6.16 \times 10^{-6} \times \frac{1}{\phi_b}\sqrt{\frac{\phi_m}{\phi}} \; A/V^2 \qquad (5.9)$$

and the constant D by

$$D = \frac{8\pi}{3h}(2me)^{1/2}\phi^{3/2} = 6.83 \times 10^9 \phi^{3/2} \; V/m. \qquad (5.10)$$

From figure 5.6,

$$\phi_b = \phi + \phi_m \qquad (5.11)$$

where ϕ is the work function of the metal, and ϕ_m is the band potential. An estimate of the band potential ϕ_m is given by

$$\phi_m = \frac{h^2}{2me}\left(\frac{3N}{8\pi}\right)^{2/3} = 3.65 \times 10^{-19} N^{2/3} \; eV \qquad (5.12)$$

where N is the number density in electrons per cubic meter in the metal, typically one electron per atom in electrical conductors.

As an example, consider tungsten, for which $\phi = 4.5$ eV, $\phi_m = 9.0$ eV, and $\phi_b = 13.5$ eV. For these values, using equations (5.8) and 5.9, one obtains $C = 6.45 \times 10^{-7}$ A/V^2, and $D = 6.52 \times 10^{10}$ V/m. These values, substituted into equation (5.8), yield the field emission current densities, J_f, as a function of the electric field E, as listed in table 5.2. This table indicates the enormous capability of field emission to emit electrons from materials, provided only that the electric field at the surface be above approximately 5 GV/m. Although such electric fields may appear very large, they can be produced by potentials of the order of tens of kilovolts,

Table 5.2 Field emission characteristics of tungsten.

E (V/m)	J_f (A/m^2)
10^9	3×10^{-17}
5×10^9	3.5×10^7
10^{10}	9.5×10^{12}

applied to fine points or asperities with characteristic dimensions of the order of 1 μm.

The advantages of field emission include a relatively small power consumption, operation at room temperature, not being space-charge limited, and a relatively long lifetime. Disadvantages of field emission as an electron source include the facts that, to avoid electrical breakdown, these sources are usually operated in a pulsed mode only; that very high potentials and/or electric fields are required to exhibit the phenomenon of field emission; and that sputter erosion of the emitting tip can reduce the high electric fields required to exhibit the phenomenon of field emission.

5.4 HOLLOW CATHODE SOURCES

Hollow cathode sources have been extensively developed since 1965, and have come into widespread use because of their several advantages over other electron sources, such as the thermionic filament. Applications of this source have proliferated without an adequate analytical theory of the physical processes by which they operate.

5.4.1 Alternative Configurations

The geometry of the *Lidsky hollow cathode*, which was historically among the first of this kind, is shown in figure 5.7(a). In this source, a hollow tube constricting in diameter to a capillary-like nozzle is operated with gas flowing axially through the tube and into the plasma chamber on the right. The Lidsky cathode is maintained at a negative potential with respect to the surrounding plasma, so that ion bombardment heats the small capillary tube, maintaining a plasma inside. Large electron currents, with greater than Child law current densities, can be drawn from this plasma. The gas flow is needed to maintain the capillary plasma in the small tube, from which the electrons are drawn.

This arrangement is hard to initiate and maintain in the steady state, so a later modification included a cylindrical heater to raise the cathode to incandescence. Among the many modifications developed over the
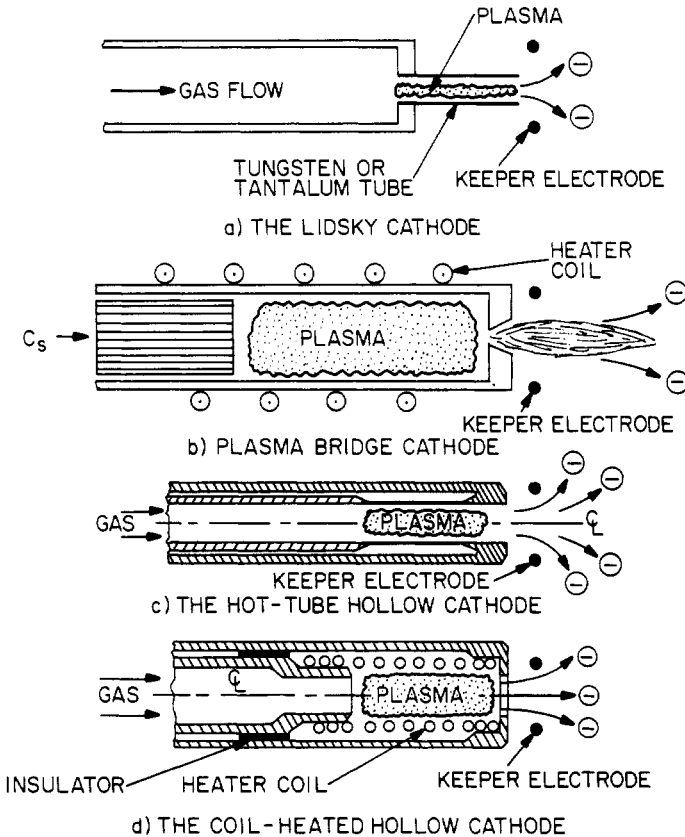
PLASMA

GAS FLOW

TUNGSTEN OR
TANTALUM TUBE   KEEPER ELECTRODE

a) THE LIDSKY CATHODE

HEATER
COIL

C_s PLASMA

KEEPER ELECTRODE
b) PLASMA BRIDGE CATHODE

GAS   PLASMA

KEEPER ELECTRODE
c) THE HOT-TUBE HOLLOW CATHODE

GAS   PLASMA

INSULATOR   HEATER COIL   KEEPER ELECTRODE

d) THE COIL-HEATED HOLLOW CATHODE

Figure 5.7 Various designs of hollow cathodes, with a gas flow entering from the left to maintain the plasma. (*a*) Lidsky capillary, consisting of a plasma formed in a refractory metal capillary heated to incandescence. (*b*) Plasma bridge cathode, heated to incandescence by a heater coil and operated with alkali metal vapor. (*c*) The hot-tube hollow cathode, in which the thin walled portion of the tube is heated to incandescence by electrical current flowing between the inner and outer tubes. (*d*) The coil-heated hollow cathode, in which a helical filament is heated to incandescence, maintaining a plasma on the axis.

years, many of them for electrostatic ion engines intended for space propulsion, are the *plasma bridge cathode* shown in figure 5.7(*b*); the *hot-tube hollow cathode* in figure 5.7(*c*), in which the side wall is heated by electrical currents flowing through concentric tubes to the thin annular side wall surrounding the plasma; and the *coil-heated hollow cathode*, shown in figure 5.7(*d*), in which electrical currents flow axially along concentric tubes, and heat a coiled electrical filament which surrounds the
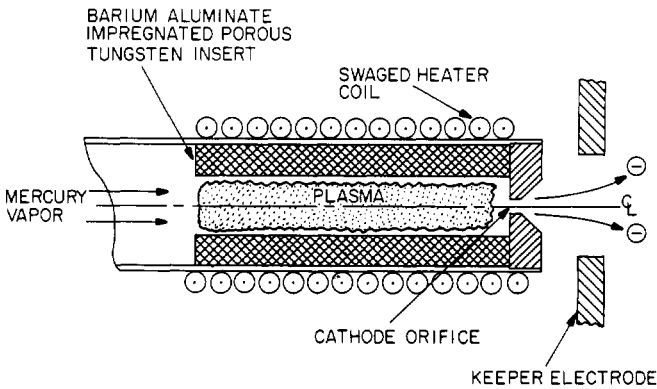
Figure 5.8 A hollow cathode designed for mercury vapor, used in space propulsion applications, and capable of operating without degradation for thousands of hours. (From Poeschel *et al* 1979.)

hollow cathode plasma. Hollow cathodes are usually run with a 'keeper' electrode about 1 cm downstream of the capillary nozzle, which draws a small current that maintains and stabilizes the plasma in the hollow cathode.

5.4.2 Foil-Enhanced Hollow Cathodes

Two highly evolved versions of the hollow cathode include that developed for space applications by Poeschel *et al* (1979) shown in figure 5.8, and the *tungsten foil hollow cathode*, illustrated in figure 5.9 and discussed by Forrester (1988). These sources were intended to operate with mercury vapor, the propellant of ion engines for space applications. Hollow cathode sources of these designs were capable of operating for 10 000 hours or more; they both featured a concentric keeper electrode a few millimeters downstream of the exit of the hollow cathode; they were approximately 4 mm in diameter; and they were capable of emitting several amperes of electron current.

Hollow cathodes have come into relatively widespread use as electron sources in the last two decades, after having been extensively developed for the space program by NASA. Advantages of the hollow cathode include its long lifetime, measured in the best cases in tens of thousands of hours; small size; small power consumption, relative to thermionic filaments; and the further advantage that they can ionize almost any working gas which flows axially through them. Their disadvantages include a relatively complex design in which optimum operation depends on proprietary materials and unpublished lore. The operation of hollow cathodes is difficult to derive from first principles, and a basic understanding of the physical processes operating in the devices is
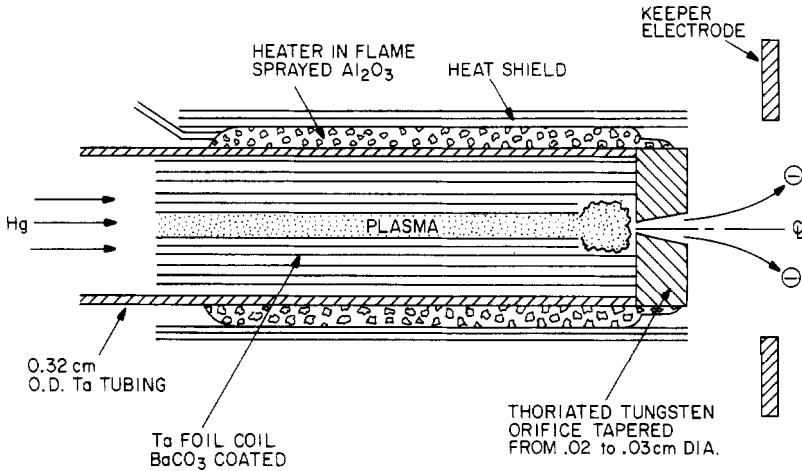
Figure 5.9 Tungsten foil hollow cathode design for space propulsion applications, also intended to operate on mercury. (From Forrester 1988.)

lacking. Hollow cathodes have a major disadvantage in that they require a gas flow for their operation, to maintain the intense plasma in the final nozzle from which the electrons are drawn. This gas throughput can be an advantage when one needs to ionize the working gas, but it can be a disadvantage in an application for which only electron current is desired.

5.5 SECONDARY ELECTRON EMISSION SOURCES

Secondary electron emission from the cathodes plays a key role in maintaining the currents which flow in the Townsend regime and in glow discharges. Because the current densities available from secondary electron emission are relatively small compared to the current densities available from the electron sources discussed above, electron sources based on secondary electron emission are relatively infrequently used.

Secondary electron emission sources, like that shown schematically in figure 5.10, are based on the secondary emission of electrons by ion impact. This process is characterized by the *secondary electron emission coefficient*,

$$\gamma_e = \frac{\text{\# of electrons emitted}}{\text{\# of ions incident on surface}}.$$

For ions impacting the cathode with keV energies, the secondary electron emission coefficient can be greater than one. Secondary electrons may also be emitted by energetic electron impact on an anode. The importance of secondary electron emission as an electron source is most frequently manifested in the transient initial build-up phases of normal glow or arc
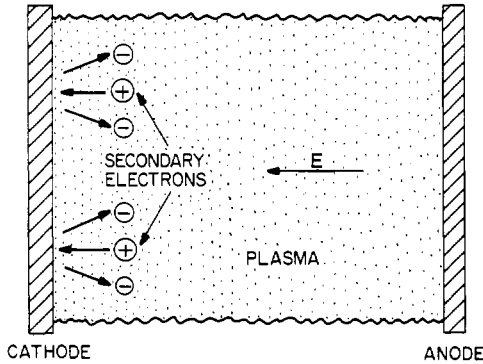
discharges. In these regimes, secondary electrons provide a current until the electron–neutral ionization process can provide a volumetric source of electrons which maintains a plasma in the steady state.

5.6 SOURCE AND BEAM CHARACTERISTICS

Many military, aerospace, and plasma processing applications require the generation of a beam of energetic ions or electrons. If beam focusing and a monoenergetic energy distribution are not critical requirements, one or more of the electron sources discussed in this chapter are often adequate. However, if an application demands a parallel or well-focused electron trajectory, or a monoenergetic energy distribution, then the electron source of choice is usually based on a system of plane parallel grids, operating at, or just below, the space-charge limited current. In this section, we discuss some of the parameters used to characterize electron beams, and the figures of merit by which electron sources may be characterized.

5.6.1 Beam Parameters

In a unidirectional beam, such as might be produced by one of the sources discussed above, the velocity reached by a particle of mass m as the result of being accelerated across a potential V_0 is given by the beam velocity,

$$v_b = \sqrt{\frac{2eV_0}{m}} \qquad (m/s). \qquad (5.13)$$

The number density of the charges in a space-charge limited beam is equal to that at the acceleration electrode, given by equation (3.150),

$$n_b = n_a = \frac{4\varepsilon_0 V_0}{9ed^2} \qquad \text{(electrons/m}^3\text{)}. \qquad (5.14)$$

The particle flux in the space-charge limited beam of figure 5.11 is given by combining the above two equations,

$$\Gamma_b = \frac{J_c}{e} = v_b n_b = \frac{4\varepsilon_0}{9e}\sqrt{\frac{2e}{m}}\frac{V_0^{3/2}}{d^2} \qquad \text{(electrons/m}^2\text{s)} \qquad (5.15)$$

where d is the separation of the two grids across which the potential V_0 appears. This expression is, of course, the Child law.

The beam power flux is given by the product of the accelerating voltage and the space-charge limited current density flowing between the grids,

$$P_b = J_c V_0 = \frac{4\varepsilon_0}{9}\sqrt{\frac{2e}{m}}\frac{V_0^{5/2}}{d^2} \qquad \text{(W/m}^2\text{)}. \qquad (5.16)$$

It should be noted that because of the very large difference between ion and electron masses, the power flux carried by electron beams is far higher than that carried by space-charge limited ion beams, thus making it necessary to avoid impingement of electron beams on accelerating grids, and to provide adequate cooling of the target on which an electron beam is collected.

5.6.2 Figures of Merit for Electron Sources

Referring to figure 5.11, the total beam current is given by

$$I_b = \frac{\pi D^2}{4} J \qquad \text{(A)} \qquad (5.17)$$

where D is the diameter of the beam, and J is the current density, the upper limit of which is the Child law current. A source with an extraction voltage V_0 and an initial beam cross sectional area $A = \pi D^2/4$ will have a *perveance* $\mathcal{P}$

$$\mathcal{P} \equiv \frac{I_b}{V_0^{3/2}} = \frac{J\pi D^2}{4V_0^{3/2}} \qquad \text{(A/V}^{3/2}\text{)} \qquad (5.18)$$

where equation (5.17) has been substituted for the total current. The perveance allows one to compare the performance of a specific, actual design to an idealized Child law diode with no webbing in the accelerator grids, no beam divergence, etc. For an electron source with fixed cross-sectional area, $\mathcal{P}$ depends only on the geometry of the extractor and
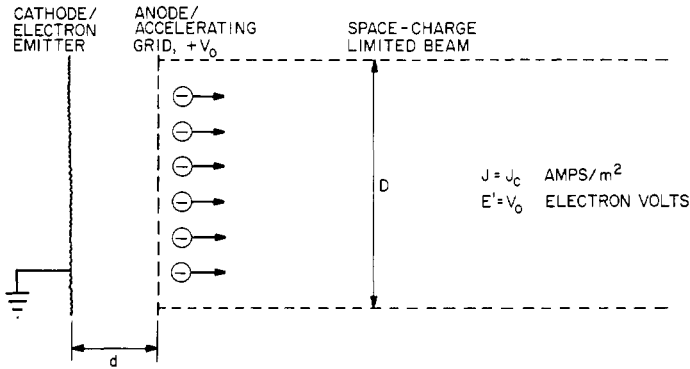
Figure 5.11 Schematic drawing of a space-charge limited beam of diameter D, with an ion-emitting beam neutralizer at the beam edge.

accelerating grids. The larger is the perveance, the better the source design.

The power required to produce an electron beam is composed of the beam power P_b of equation (5.16), and the power required to operate the source, P_s. The source power may be written

$$P_s = P_d + P_f + P_0 = I_b V^* \quad \text{(W)} \tag{5.19}$$

where P_d is the power required to maintain a source discharge (such as a hollow cathode), P_f is the power required to supply filaments or cathodes, and P_0 is other power drain required to maintain the source, I_b is the beam current, and V^* is the eV per beam electron required in the source to produce each electron. For electron sources, the minimum value of V^* is the work function of the cathode, shown for selected materials in table 5.1.

The total power required by the source is given by

$$P_t = P_b + P_s = I_b(V_0 + V^*) \quad \text{(W)}. \tag{5.20}$$

The *electrical efficiency* of the source, η_E, is the ratio of the beam to the total power, given by

$$\eta_E \equiv \frac{P_b}{P_t} = \frac{V_0 I_b}{I_b(V_0 + V^*)} = \frac{V_0}{V_0 + V^*}. \tag{5.21}$$

Equation (5.21) can be written
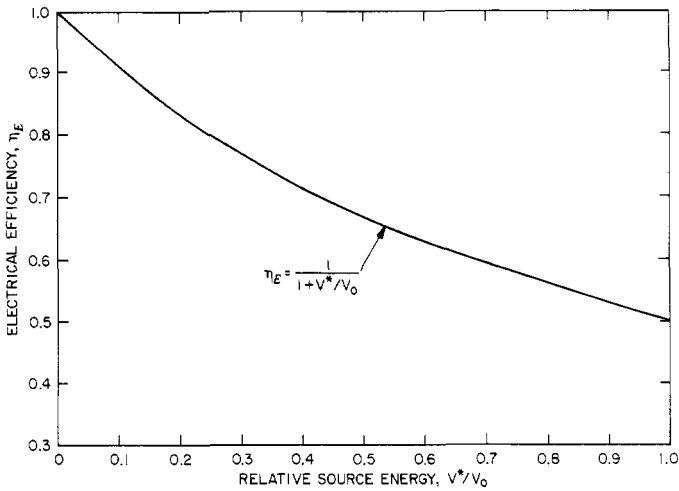
$$\eta_E = \frac{1}{1 + (V^*/V_0)}. \tag{5.22}$$

Figure 5.12 The electrical efficiency η_E, given by equation (5.22), as a function of V^*, the eV per ion, and the accelerating potential V_0.

The electrical efficiency is plotted as a function of the ratio V^*/V_0 on figure 5.12. By making a calorimetric measurement of the beam power, and measuring the total electrical energy into the source, η_E can be calculated and V^* found from figure 5.12.

5.7 CHARGED PARTICLE BEAM TRANSPORT

Most industrial applications of charged particle beams require that they be deflected, focused, or kept parallel in order to be transported and effectively utilized. The subject of beam transport includes electron (or ion) optics, by analogy with visible light. This section will briefly review some methods for ion and/or electron beam transport. More extensive discussions of these methods may be found in Brown (1989), Dearnaley et al (1973), Forrester (1988), Humphries (1990), Pierce (1949), and Wilson and Brewer (1973).

5.7.1 Source Requirements

For an electron beam with current I and diameter D, the flux required of the source and in the beam may be written

$$\Gamma_b = \frac{4I}{\pi e D^2} \qquad \text{(electrons/m}^2\text{-s)}. \qquad (5.23)$$

If the source is space-charge limited, we can use equation (3.145) to write the *beam flux* in the form

$$\Gamma_b = \frac{J_c}{e} = \frac{\chi}{e} \frac{V_0^{3/2}}{d^2} \qquad \text{(electrons/m}^2\text{-s)} \qquad (5.24)$$

where χ is the Child, defined in equation (3.144). This electron flux must be provided by the electrode surface which is part of the electron source.

If the source is other than space-charge limited, the beam number density may be obtained from its current density,

$$J = \frac{I}{A} = \frac{4I}{\pi D^2} = e n_b v_b \qquad \text{(A/m}^2\text{)} \qquad (5.25)$$

where v_b is the beam velocity obtained from conservation of energy in equation (3.156). Substituting equation (3.156) into equation (5.25) and solving for the beam number density yields

$$n_b = \frac{4I}{\pi e D^2} \sqrt{\frac{m}{2eV_0}} \qquad \text{(electrons/m}^3\text{)}. \qquad (5.26)$$

If the source is space-charge limited, the electron number density at the exit and in the beam is given using equation (3.150),

$$n_b = \frac{4\varepsilon_0 V_0}{9 e d^2} \qquad \text{(electrons/m}^3\text{)}. \qquad (5.27)$$

5.7.2 Current Density Enhancement

To enhance the current density above the Child law limit, at least two possibilities exist. One is the *bipolar diode* shown in figure 5.13, in which one maintains a potential V_0 across a gap of width $x = d$. The effect of the space-charge cloud between the electrodes is reduced by emitting electrons or negative ions from the cathode, and positive ions from the anode. It has been shown by Howes (1965) that this partial neutralization of the space charge between the electrodes will allow higher than Child law currents to flow, but such an arrangement is difficult to set up in practice.

A second method of current density enhancement is shown schematically on figure 5.14 and is known as the *accel–decel configuration*. Suppose one wishes to create an electron beam with energy V_0 (eV). If one accomplishes this with a standard Child law diode with a gap d, the current density is

$$J_c = \chi \frac{V_0^{3/2}}{d^2} \qquad \text{(A/m}^2\text{)}. \qquad (5.28)$$
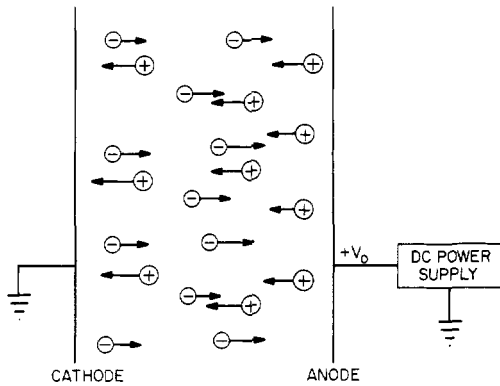
Figure 5.13 Schematic drawing of the bipolar diode, in which electrons or negative ions are emitted from the cathode, and positive ions are emitted from the anode. The partial cancellation of space charge allows higher than Child law currents to flow.
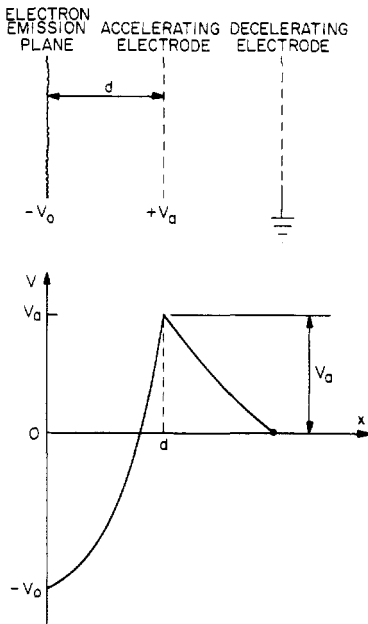

Figure 5.14 Schematic drawing of the geometry and potential distribution in the accel–decel configuration. Electrons are accelerated through a potential difference $V_0 + V_a$ between the first two electrodes, providing a Child law current for that potential drop, and then decelerated between the second pair of electrodes through a potential drop V_a.

If one uses the accel–decel configuration shown schematically in figure 5.14, an electron is first accelerated across the potential $V = V_0 + V_a$ in the gap d, then decelerated through a potential V_a. The electron leaves with an energy V_0, and a current density given by

$$J_e = \chi \frac{(V_0 + V_a)^{3/2}}{d^2} \qquad (\text{A/m}^2). \qquad (5.29)$$

The current density enhancement is found by dividing equation (5.29) by equation (5.28), to yield

$$\frac{J_e}{J_c} = \left(\frac{V_0 + V_a}{V_0}\right)^{3/2} = \left(1 + \frac{V_a}{V_0}\right)^{3/2}. \tag{5.30}$$

Significant enhancement of the current density is possible using this method, but this configuration may defocus the beam, and the higher electric field between the first two electrodes in figure 5.14 may lead to excessive sparking or breakdown. As in all space-charge limited beams, electron optics may become a problem above about 85% of the Child law current.
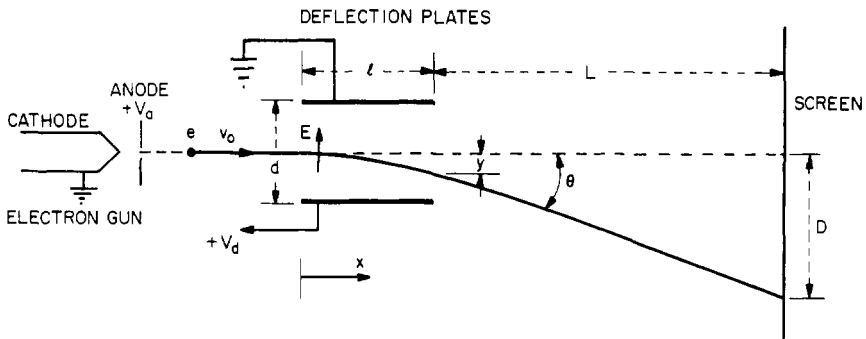

Figure 5.15 Schematic drawing of an electrostatically deflected cathode ray tube.

5.7.3 Electrostatic Beam Deflection

Many situations arise in which it is desirable to electrostatically deflect beams of charged particles. Probably the most important and widely used device incorporating these principles is the electrostatically deflected cathode ray (electron beam) tube, found in all oscilloscopes. The oscilloscope was invented in the year 1897 by the German physicist Ferdinand Braun (1850–1912).

The functioning of an *electrostatically deflected cathode ray tube* is shown on the diagram in figure 5.15. On the left, an electron gun accelerates electrons through a potential V_a and forms a small, cylindrical, well-focused electron beam which travels to the right between two flat metal deflection plates of length ℓ and separation d. When no deflection potential V_d is applied between the deflection plates, the electron beam travels in a straight line along the x axis and impinges at the center of

the screen on the right. When a positive deflection voltage V_d is applied to the lower plate, the resulting electric field deflects the electron beam by an angle θ, and the beam impinges on the screen a distance D from the center.

If the deflection plates are plane and parallel, the electric field between them can be written in terms of the deflection voltage and separation as

$$E = \frac{V_d}{d} \qquad \text{(V/m)}. \qquad (5.31)$$

While the electron is between the deflection plates, the equation of motion in the plane of the diagram may be written

$$F_y = m_e \frac{d^2 y}{dt^2} = eE = \frac{eV_d}{d} \qquad (5.32)$$

and

$$F_x = 0 = m_e \frac{d^2 x}{dt^2}. \qquad (5.33)$$

Integrating the equation of motion for the y direction once, one obtains

$$\frac{dy}{dt} = v_y = \frac{eV_d}{md} t \qquad (5.34)$$

if the electron enters the deflection region at $y = 0$ and at time $t = 0$. Integrating equation (5.34) again, one obtains the y deflection of the electron as a function of time while it remains between the deflection plates,

$$y = \frac{eV_d}{2md} t^2 \qquad (5.35)$$

since the y velocity is 0 when the beam enters the region between the deflection plates.

In the x direction, integration of equation (5.33) yields

$$\frac{dx}{dt} = v_0 = \text{constant}. \qquad (5.36)$$

Thus, the electric field in the y direction does not affect the energy or velocity of the particle in the x direction orthogonal to it. The constant x velocity of the electron as it moves between the plates is determined by the conservation of energy in the electron gun at the left,

$$\frac{1}{2} m v_0^2 = eV_a. \qquad (5.37)$$

Because the x velocity is constant, the time-of-flight of the electron between the deflection plates is given by

$$t_f = \frac{\ell}{v_0} = \ell\sqrt{\frac{m}{2eV_a}}. \tag{5.38}$$

Substituting this time-of-flight into equation (5.34) yields the y velocity at the time the electron leaves the deflecting region,

$$v_{yf} = \frac{eV_d\ell}{mdv_0}. \tag{5.39}$$

This velocity, when substituted into equation (5.35), yields the vertical deflection of the electrons as they leave the deflection region,

$$y_f = \frac{eV_d\ell^2}{2mv_0^2 d} = \frac{V_d\ell^2}{4V_a d} \tag{5.40}$$

where equation (5.37) has been used to eliminate v_0.

If we ignore the effect of fringing fields, the electrons will have no forces acting on them after they leave the deflection region between the plates, so the tangent of the deflection angle is given by the ratio of the y and x velocities as the electron leaves the deflection region,

$$\tan\theta = \frac{v_{yf}}{v_0} = \frac{eV_d\ell}{mdv_0^2} = \frac{V_d\ell}{2V_a d}. \tag{5.41}$$

Equations (5.37) and (5.39) have been used to get the right-hand member of equations (5.41). From the trigonometry of figure 5.15, the final deflection D on the screen is given by

$$D = y_f + L\tan\theta. \tag{5.42}$$

Substituting equations (5.40) and (5.41) into (5.42) yields the following expression for the y deflection on the oscilloscope screen,

$$D = \left(\frac{\ell^2}{4d} + \frac{\ell L}{2d}\right)\frac{V_d}{V_a} = \frac{\ell}{2dV_a}\left(L + \frac{\ell}{2}\right)V_d$$
$$= \text{constant} \times V_d. \tag{5.43}$$

The deflection angle and deflection distance on the screen are independent of the mass and charge of the particle beam being deflected, and depend only on the geometry and the initial energy of the particles. Of great practical importance is the fact that the deflection on the screen is directly

proportional to the deflection voltage V_d, so that the oscilloscope is a linear instrument for measuring voltages. In actual oscilloscope tubes, a second set of deflecting plates, at right angles to those shown in figure 5.15, deflects the electron beam in and out of the plane of the figure, thus providing a time base for the measurement of time-varying electrostatic potentials.

5.7.4 Magnetic Beam Deflection

A second method to deflect a charged particle beam is the use of a static magnetic field. Since the magnetic force $q(v \times B)$ is perpendicular to the velocity at all times, magnetic deflection does not add energy to the deflected particles. As an example of magnetic deflection, we will use the *magnetically deflected cathode ray tube*, illustrated in figure 5.16.

In this figure, a uniform magnetic induction B is applied in a region of width ℓ with sharp boundaries at $x = 0$ and $x = \ell$. Electrons are accelerated through a potential V_a in an electron gun to the left, and impinge on the deflection region, within which they move with a constant radius of curvature R given by

$$R = \frac{mv_0}{eB} = \frac{m}{eB}\sqrt{\frac{2V_a}{m_e}} = \frac{1}{B}\sqrt{\frac{2mV_a}{e}}. \tag{5.44}$$

After being deflected by an angle θ, the electrons exit the deflection region at $x = \ell$, at a distance y below the x axis. Applying the Pythagorean theorem, one obtains

$$R^2 = \ell^2 + (R - y)^2. \tag{5.45}$$

Simplifying, this is equivalent to

$$y^2 - 2Ry + \ell^2 = 0 \tag{5.46}$$

from which the final deflection distance y may be obtained using the quadratic formula,

$$y = R\left[1 - \left(1 - \frac{\ell^2}{R^2}\right)^{1/2}\right]. \tag{5.47}$$

From the geometry of the figure, the deflection angle θ of the electron beam may be written

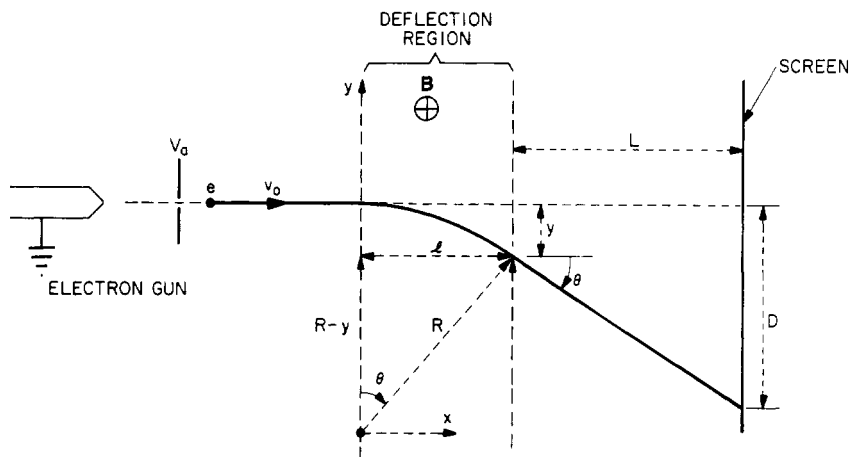$$\tan\theta = \frac{\ell}{R - y} \tag{5.48}$$

Figure 5.16 Schematic drawing of the magnetically deflected cathode ray tube. Electrons are accelerated to an energy of V_a eV in a gun at the left.

and the total deflection D on the screen is given by

$$D = y + L \tan \theta. \qquad (5.49)$$

Substituting equations (5.47) and (5.48) into equation (5.49) yields for the total deflection D,

$$
\begin{aligned}
D &= y + \frac{\ell L}{R - y} \\
&= R \left[1 - \left(1 - \frac{\ell^2}{R^2} \right)^{1/2} \right] + \frac{\ell L}{R} \left(1 - \frac{\ell^2}{R^2} \right)^{-1/2}. \qquad (5.50)
\end{aligned}
$$

If the width of the deflection region is much smaller than the radius of gyration of the electrons in the magnetic induction B, the usual situation, the expressions involving this small quantity in equation (5.50) may be simplified using

$$\left(1 - \frac{\ell^2}{R^2} \right)^{1/2} \approx 1 - \frac{\ell^2}{2R^2} \qquad \text{if} \quad \ell^2 \ll R^2. \qquad (5.51)$$

Substituting equation (5.51) into equation (5.50), and neglecting all terms higher than second-order in ℓ/R, the deflection on the screen may be written with the help of equation (5.44) as

$$D \approx \frac{\ell^2}{2R} + \frac{\ell L}{R} = \frac{\ell}{R} \left(L + \frac{\ell}{2} \right) = \ell \left(L + \frac{\ell}{2} \right) \left(\frac{e}{2 m_e V_a} \right)^{1/2} B. \qquad (5.52)$$

The deflection of an electron beam on the screen of a magnetically deflected cathode ray tube is thus proportional to the magnetic induction B. The induction B is generated by two coils, one each above and below the plane of the diagram of figure 5.16. This magnetic induction is proportional to the current flowing in these coils and thus, for small deflection angles θ, the magnetically deflected cathode ray tube is a linear instrument for measuring current, in contrast to the electrostatically deflected cathode ray tube, which is a linear instrument for measuring voltage. In actual tubes, a second pair of coils deflects the beam in and out of the plane of the diagram in figure 5.16, providing a time base.
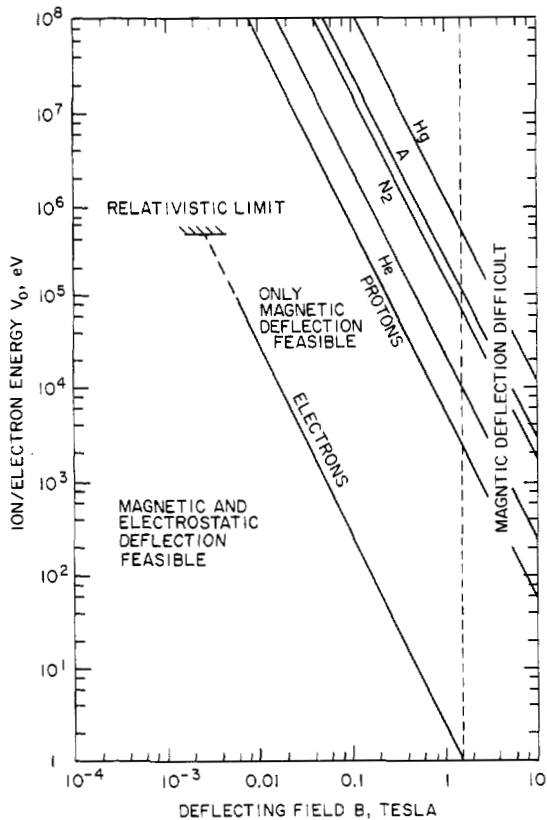

Figure 5.17 Comparison of electrostatic and magnetic deflection of electron beams. For singly-charged ions of particles with the masses indicated, both magnetic and electrostatic deflection is feasible below and to the left of the lines shown. Above and to the right of the lines, magnetic deflection is the method of choice, although even this becomes difficult beyond magnetic inductions of 1.5 T.

5.7.5 Comparative Deflection Capabilities

Sometimes it is not obvious whether electric or magnetic beam deflection is the method of choice. If equations (5.41) and (5.48) are used to examine the relative beam deflection capabilities of electric and magnetic fields for the same small deflection angle, $\theta \approx \sin\theta \approx \tan\theta$, then equations (5.41) and (5.48) yield

$$\sin\theta \approx \frac{\ell}{R} = \ell B \sqrt{\frac{e}{2mV_a}} \approx \tan\theta = \frac{E\ell}{2V_a}. \qquad (5.53)$$

This equation allows us to relate the electric field and magnetic induction required to produce the same small deflection angle of a charged particle beam. Solving equation (5.53) for the electric field, one obtains

$$E = \frac{2V_a}{R} = B\sqrt{\frac{2eV_a}{m}} = v_b B \qquad \text{(V/m)}. \qquad (5.54)$$

Thus, the electric and magnetic fields required for the same deflection angle are related by the beam velocity, v_b.

In the presence of a plasma or other source of ultraviolet radiation, it is difficult to maintain electric fields higher than approximately 1 MV/m. With this as an upper limit, equation (5.54) becomes

$$B \leqslant 7.226 \times 10^{-5} E \sqrt{\frac{A}{V_a}} = 72.26 \sqrt{\frac{A}{V_a}} \qquad \text{(T)} \qquad (5.55)$$

where A is the atomic mass number of the species being deflected. The relationship represented by the equality in equation (5.55) is plotted on figure 5.17. For a given particle energy V_a, both electrostatic and magnetic deflection are feasible below the curves; from the curves to $B = 1.5$ T, magnetic deflection is feasible, and beyond 1.5 T, even magnetic deflection becomes technically difficult, usually requiring superconducting magnets.

If the beam current density is so high that its space-charge shields against electrostatic deflection, magnetic fields may be the deflection mechanism of choice. Another consideration is that beam deflection with electric fields is not mass selective, but magnetic deflection is. Thus, if a source produces a spread of isotopic masses which one wishes to maintain in a beam, electric field deflection can accomplish this, while magnetic deflection would not.

Finally, because a static magnetic induction cannot do work on a charged particle, magnetic deflection does not add energy to the deflected
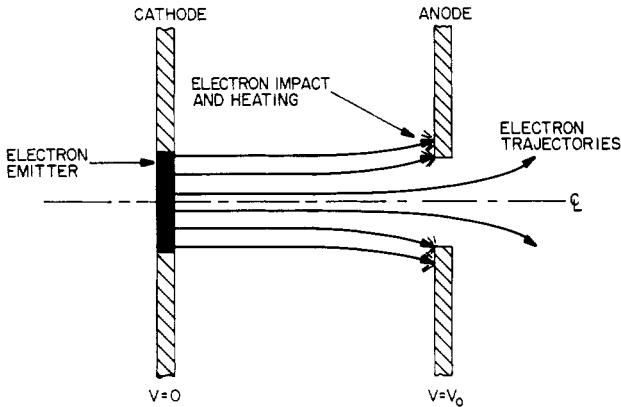
CATHODE ANODE

ELECTRON IMPACT
AND HEATING

ELECTRON
TRAJECTORIES

ELECTRON
EMITTER

℄

V=0   V=V₀

Figure 5.18 Illustration of direct ion impact on an accelerating grid due to improper design of the grid.

particle, while electrostatic deflection adds, from equation (5.39), an amount of energy given by

$$\mathcal{E} = \frac{1}{2}mv_{yb}^2 = \frac{m}{2}\frac{e^2E^2\ell^2}{m^2v_0^2} = \frac{eE^2\ell^2}{4V_a} \qquad \text{(J)}. \qquad (5.56)$$

This energy added by the electric field can be substantial, and is often undesirable.

5.7.6 Paraxial Beam Transport

If an accelerating electrode configuration is not properly designed, electrode impingement, illustrated in figure 5.18, and beam divergence, illustrated in figure 5.19, can result. Electrode impingement leads to a parasitic drain on the source power supply and a requirement for electrode cooling; beam divergence is undesirable in many applications. To maintain a parallel beam of charged particles through accelerating electrodes, consider the section between two plane parallel electrodes indicated schematically by the dotted lines on figure 5.20(a). If one wishes to create a beam equal to the width of the dotted lines in figure 5.20(a), one must ask what configuration of electrodes is required to 'make up' for the missing electrons outside the beam which maintain parallel trajectories. The answer is the (Pierce) configuration, orginally suggested by Pierce (1940, 1949) and shown in figure 5.20(b), which maintains electric field lines parallel to the beam, and gives rise to trajectories which do not intersect the electrodes. Such impacts, if they should occur, lead to parasitic power losses, electrode heating, and electrode erosion. Calculation of the electrode shape which yields a
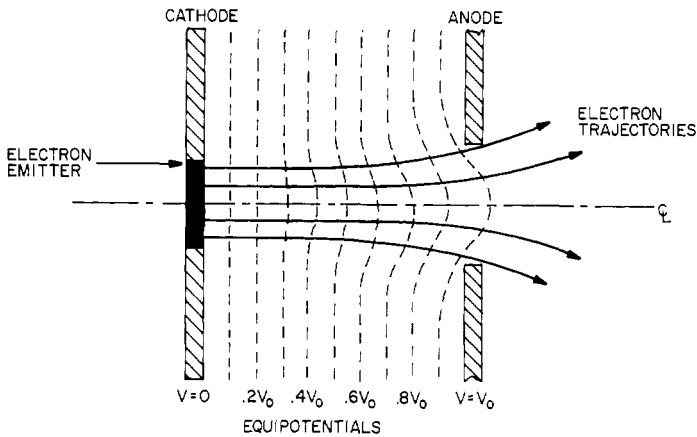
Figure 5.19 An illustration of the defocusing of an ion beam by the bulging of equipotential lines near the gap of an accelerating grid.
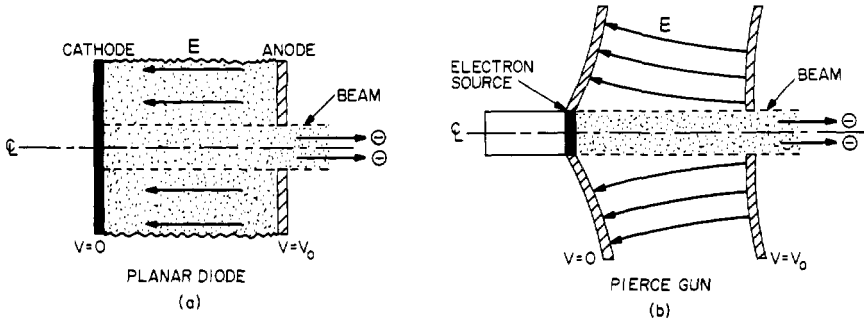

Figure 5.20 (a) Electrode geometry for the production of parallel beams. The dotted lines show the beam diameter of an equivalent infinite, plane parallel space-charge limited diode. (b) The Pierce electron gun geometry, in which the electrode shape keeps the electric field parallel to the boundary of the beam, and the electron trajectories parallel to the axis of the beam line.

parallel beam is best done with conformal mapping or computer modeling techniques.

A calculation for a cylindrical Pierce geometry, originally published by Pierce (1940), is shown in figure 5.21. The equipotential curves may be replaced by electrodes at these potentials, with the shapes indicated in the figure. In figure 5.21, the units shown for the radial and axial dimensions are normalized with respect to the beam radius.

The equipotentials of a three-electrode ion-accelerating configuration studied by Cooper *et al* (1972) are shown in figure 5.22. This is an accel–decel configuration with $V = V_0$ on the source, $V = -0.1V_0$ on the accelerating electrode, and $V = 0$ on the final electrode, to ensure that the beam is at ground potential when it leaves the source. The geometry
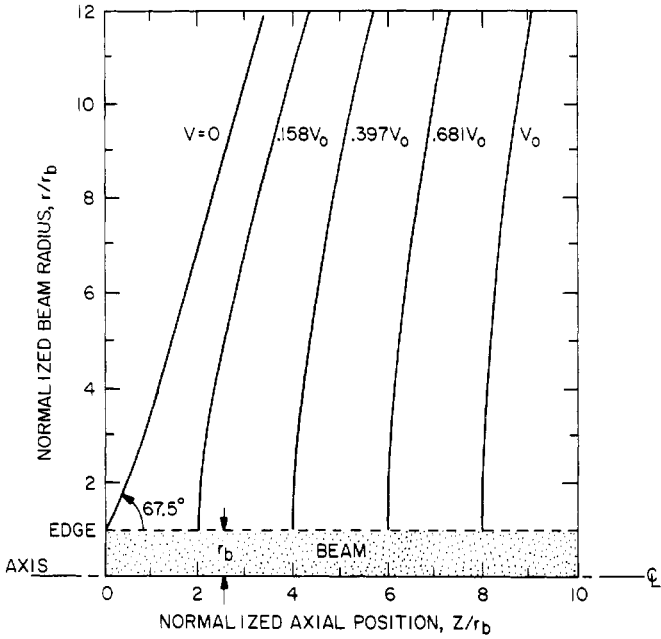
Figure 5.21 Equipotentials and electrode shapes for an axisymmetric, parallel beam, Pierce-type geometry, normalized to the beam radius (Pierce 1940).
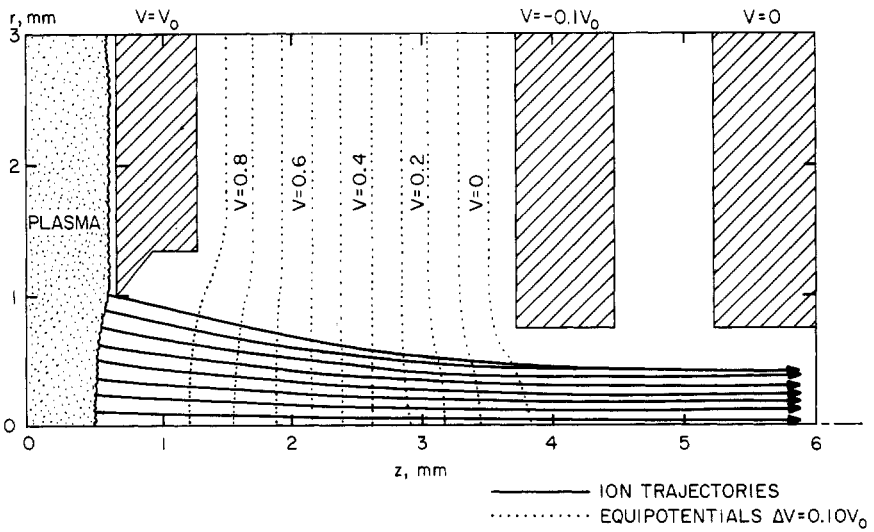

Figure 5.22 Focused trajectories and equipotentials from an axisymmetric, three-electrode geometry, as reported by Cooper *et al* (1972).
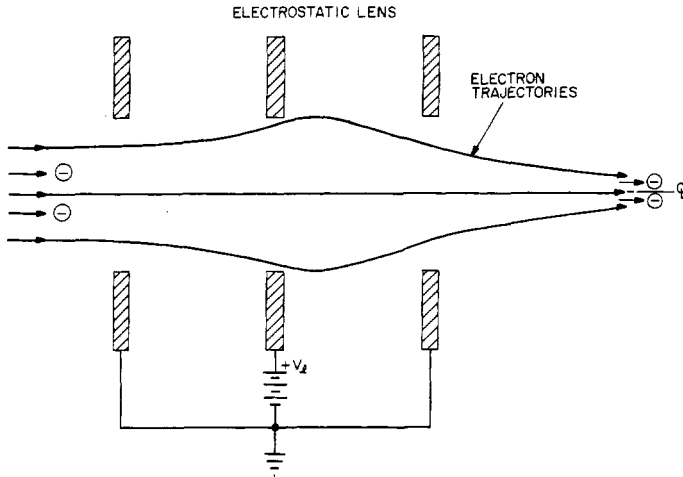
ELECTROSTATIC LENS

Figure 5.23 A schematic illustration of an electrostatic lens. By adjusting the potential on the middle electrode, V_ℓ, an initially parallel ion beam entering from the left can be made to focus at a point on the right.

of this source has been optimized so that ion trajectories do not intersect the electrodes. The equipotentials between the source electrode on the left and the accel electrode in the middle are indicated by the dotted lines.

5.7.7 Beam Focusing

If one has a well collimated, parallel beam at its source, like those discussed in the previous section, it can be brought to a focus (or defocused) with an electrostatic lens like that shown schematically on figure 5.23. Adjusting the voltage V_ℓ adjusts the focal length of this configuration.

REFERENCES

Brown I G (ed) 1989 *The Physics and Technology of Ion Sources* (New York: John Wiley) ISBN 0-471-85708-4

Cooper W S, Berkner H H and Pyle R V 1972 Multiple-Aperture Extractor Design for Producing Intense Ion and Neutral Beams *Nucl. Fusion* **12** 263–265

Dearnaley G, Freeman J H, Nelson R S and Stephen J 1973 *Ion Implantation* (Amsterdam: Elsevier) ISBN 0-444-10488-7

Forrester A T 1988 *Large Ion Beams—Fundamentals of Generation and Propagation* (New York: John Wiley) ISBN 0-471-62557-4

Fowler R H 1933 Notes on Some Electronic Properties of Conductors and Insulators *Proc. R. Soc. London* A **141** 56–71

Fowler R H and Nordheim L 1928 Electron Emission in Intense Electric Fields *Proc. R. Soc. London* A **119** 173–181

Howes W L 1965 Effect of Initial Velocity on One-Dimensional, Bipolar, Space-Charge Currents *J. Appl. Phys.* **36** 2039–2045

Humphries S Jr 1990 *Charged Particle Beams* (New York: John Wiley) ISBN 0-471-60014-8

Pierce J R 1940 Rectilinear Electron Flow in Beams *J. Appl. Phys.* **11** 548–554

—— 1949 *Theory and Design of Electron Beams* (New York: Van Nostrand)

Poeschel R L, Beattle J R, Robinson P A and Ward J W 1979 3-cm Mercury Ion Thruster Technology *AIAA/DGLR 14th Int. Electric Propulsion Conf. (Princeton, NJ, Oct. 30–Nov. 1 1979)* paper 79-2052

Richardson O W and Young A F A 1925 The Thermionic Work-Functions and Photoelectric Thresholds of the Alkali Metals *Proc. R. Soc. London* A **107** 377–410

Weast R C *et al* (ed) 1988 *CRC Handbook of Chemistry and Physics* 69th edn (Boca Raton, FL: CRC Press) ISBN 0-8493-0469-5

Wilson R G and Brewer G R 1973 *Ion Beams—With Applications to Ion Implantation* (New York: John Wiley) ISBN 0-471-95000-9

6

Ion Sources and Beams

In this chapter we discuss ion sources, many of which owe their origins to the experimental necessity of producing ion beams of gaseous, rare, or refractory elements. Some of these sources, like the von Ardenne, Zinn, and Penning sources, originated with atomic and nuclear physics research, while others, like the Kaufman and surface ionization sources, were developed in the 1960's for space propulsion applications. Other ion sources had their origins in ion implantation for microelectronic applications. In this chapter we briefly survey some of the more widely used and most useful ion sources; a more complete discussion of ion sources and beam optics may be found in several of the monographs listed at the end of this chapter, including Brown (1989), Dearnaley *et al* (1973), Forrester (1988), Humphries (1990), and Wilson and Brewer (1973).

6.1 CHARACTERISTICS OF ION SOURCES

The variety of electron sources is limited by the relatively few physical processes which produce free electrons. These include thermionic, photoelectric, secondary electron, and field emission; and extraction from a hollow cathode plasma. Ion sources, on the contrary, exist in a profusion of forms because of the requirements of a wide variety of industrial and research applications; because of the necessity of generating ions from solids, liquids, or gases; and because of the many ways of generating the DC glow discharge or arc plasmas from which the ions are extracted. A generalized ion source is shown in figure 6.1. Since the purpose of any ion source is to produce a more or less unidirectional, monoenergetic ion
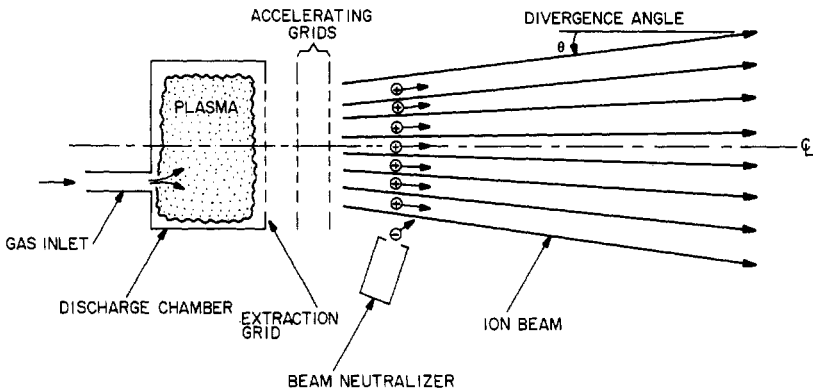
Figure 6.1 Schematic drawing of a generalized ion source.

beam, such sources are operated in vacuum systems at pressures below 1 mTorr, low enough that the ion mean free paths are longer than the distance between the source and its target.

6.1.1 Ionization Source

The ionization source must have a provision for introducing and metering the material from which the ions are formed. This is usually accomplished with consumable electrodes or rods for solid materials; fine capillaries for liquids; and conventional gas flow and metering systems for gases. In all cases, the material to be ionized must be supplied at a rate equal to the flow carried away by the beam, plus any losses in the source.

Once introduced to the ion source, the material must be ionized. This is usually done in a low pressure DC glow discharge plasma, from which the desired ionic species is extracted through a grid. The discharge plasma can be generated by a wide variety of processes which include magnetized or unmagnetized operation, and a wide range of (sub-atmospheric) neutral gas pressures. The mechanism for generating the plasma discharge is the principal distinguishing characteristic among ion sources, and has been used to organize the material later in this chapter.

An infrequently used ionization mechanism is *surface contact ionization*, in which atoms of the material to be ionized come into contact with a hot, refractory metal. If the ionization potential of the atom is less than the work function of the refractory metal, the incident atom will be ionized on the surface. This requirement is met only for alkali metals, such as sodium, potassium, rubidium, thallium, and cesium. Refractory metals used in such sources include tungsten and molybdenum.

6.1.2 Accelerating Grids

After ions are generated in a glow discharge plasma and extracted, it is usually desired to form them into a unidirectional, monoenergetic beam. This is done with a set of *accelerating grids*, indicated on figure 6.1. These grids may be designed for near space charge limited flow at the Child law limit, or for lower current density beams. The ion optics of the accelerating grids is designed to reduce the beam *divergence angle* to its required value.

6.1.3 Ion Beam and Neutralization

Upon exiting the ion source in figure 6.1, the beam will diverge with an angle θ, the value of which will depend on the design of the extraction and accelerating grids. In some applications, the ion beam is neutralized by electron emission from a *hollow cathode beam neutralizer*. This prevents a spacecraft from charging up in space applications, possible plasma instabilities, or *beam 'blow-up'* due to mutual repulsion of ions in the beam.

6.2 FIGURES OF MERIT OF ION SOURCES

6.2.1 Perveance

The *perveance* of an ion or electron source with fixed cross-sectional beam area is given by equation (5.18),

$$\mathcal{P} \equiv \frac{I_b}{V_0^{3/2}} = \frac{J\pi D^2}{4V_0^{3/2}} \qquad (\text{A}/\text{V}^{3/2}) \tag{6.1}$$

where D is the *initial* beam diameter on figure 6.1, and J the current density. The perveance of an ion source with fixed cross-sectional area is a function only of the charge state and mass of the ions, and the source geometry. The geometric factors include the thickness and spacing of the extractor and accelerating grids, the diameter of the extractor holes, and the ratio of open area to total cross-sectional area of the grids. The perveance increases, for example, as the ratio of open area to webbing area of the grids increases.

An ideal ion source with planar accelerating grids separated by the distance d, with no webbing between the extractor holes in the grids, and an extraction voltage V_0 across the accelerating gap d would operate at the space-charge limited Child law current density given by

$$J_c = \frac{4\varepsilon_o}{9} \sqrt{\frac{2eZ}{M}} \frac{V_0^{3/2}}{d^2} \qquad (\text{A}/\text{m}^2) \tag{6.2}$$

where M is the ion mass, and Z its charge state. Such an ideal ion source would operate at the maximum perveance,

$$\mathcal{P}_{max} = \frac{J_c \pi D^2}{4 V_0^{3/2}} = \frac{\pi \varepsilon_0}{9} \sqrt{\frac{2eZ}{M}} \left(\frac{D}{d}\right)^2 \qquad (\text{A/V}^{3/2}). \qquad (6.3)$$

The closer a source is to this value, the better its design.

6.2.2 Source Energy Cost

The power required to produce an ion beam is composed of the beam power P_b,

$$P_b = I_b V_0 \qquad (\text{W}) \qquad (6.4)$$

and the power required to operate the source, P_s. The source power may include the following contributions:

(1) P_m – power to electromagnets,
(2) P_d – power to maintain the source discharge,
(3) P_f – power to supply filaments or cathodes,
(4) P_o – other power drains to maintain the source.

The source power may be therefore be written

$$P_s = P_m + P_d + P_f + P_o = I_b V^* \qquad (\text{W}) \qquad (6.5)$$

where I_b is the beam current, and V^* is the eV per beam ion required by the source to produce the ion.

For ion sources, one can make the following observations about V^*:

(1) The absolute minimum value of V^* is the ionization potential of the gas used.
(2) For space-related ion engines prior to 1975, $170 < V^* < 250$ eV/ion.
(3) For current state-of-the-art in ion engine technology, $90 < V^* < 190$ eV/ion.
(4) In fusion and non-optimized industrial ion sources, V^* is usually much greater than these values.
(5) From the gas discharge physics of Chapter 8, the best one should hope for is $(\eta_{min})^{-1}$, in volts per ion–electron pair. This value is $V^* = 50$ eV/ion for a mercury plasma.

6.2.3 Efficiency of Ion Sources

The total power required by the source is given by

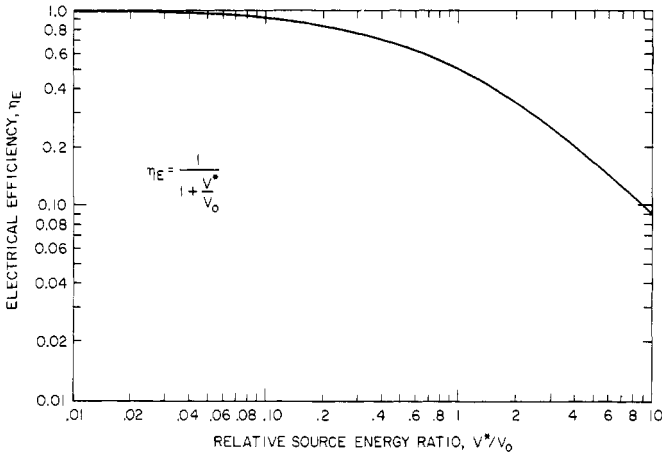$$P_t = P_b + P_s = I_b(V_0 + V^*) \qquad (\text{W}). \qquad (6.6)$$

Figure 6.2 The electrical efficiency η_E as a function of V^* (eV/ion) and the accelerating potential V_0.

The *electrical efficiency* of the source, η_E, is the ratio of the beam to the total power, given by

$$\eta_E \equiv \frac{P_b}{P_t} = \frac{V_0 I_b}{I_b(V_0 + V^*)} = \frac{V_0}{V_0 + V^*}. \tag{6.7}$$

For space-related ion engines, values of $\eta_E > 0.95$ have been achieved. Equation (6.7) can be written as

$$\eta_E = \frac{1}{1 + (V^*/V_0)}. \tag{6.8}$$

The electrical efficiency is plotted as a function of the ratio V^*/V_0 on figure 6.2. By making a calorimetric measurement of the beam power, and the total electrical energy into the source, η_E can be calculated, and V^* can be obtained from figure 6.2.

Another important figure of merit for ion sources is how fully the source uses the input neutral gas flow to produce ions. If too little of the gas is ionized, the source becomes a heavy load on the vacuum system. The *gas (propellant) utilization efficiency* η_g is defined as

$$\eta_g = \frac{\text{flow of ions from source}}{\text{flow of neutrals into source}} = \frac{S_i}{S_n} = \frac{I_b}{eS_n}. \tag{6.9}$$

In space propulsion applications, values of $\eta_g > 0.90$ are routinely achieved. In such applications, the conservation of propellent mass is imperative on long space missions, but many industrial applications

involving radioactive, precious, or rare atomic species can benefit from a high gas utilization efficiency, aside from the desirability of reducing the gas load on the vacuum system. Some recently developed electrodeless, high density plasma sources also have a high mass utilization efficiency, because of their high ionization fraction.

A comprehensive figure of merit for an ion source is the *overall efficiency* η_o,

$$\eta_o \equiv \eta_g \eta_e. \tag{6.10}$$

Values of $\eta_o > 0.85$ have been achieved for Kaufman ion engines; MPD and other plasmadynamic sources used industrially rarely have $\eta_o > 0.50$.

6.3 ION SOURCE PERFORMANCE PARAMETERS

In this section, we will discuss performance parameters which are particulary important in applications of ion sources. Some of these are specializations to ion beams of the electron beam parameters discussed in Chapter 5, between equations (5.23) and (5.27).

6.3.1 Required Gas Flow Rate

Ion sources must be provided with ionizable neutral gas, at a flow rate implied from equation (6.9), which is

$$S_n = \frac{I_b}{Ze\eta_g} \qquad \text{(neutral atoms/s).} \tag{6.11}$$

At background pressures below 1 mTorr, (0.13 Pa), this represents a significant pumping load on most industrial vacuum systems. For example, an ion source producing 1 A of singly-charged ions from a source with gas utilization efficiency $\eta_g = 0.50$ will require a gas flow of 1.25×10^{19} atoms/s. At a pressure of $p = 10^{-4}$ Torr of argon, this would equal the flux of room temperature argon atoms impinging on a circular opening in the vacuum system wall 18.5 cm in diameter—the size of a moderately large diffusion or turbomolecular pump.

6.3.2 Ion Flux in Beam

For an ion beam with total current I and diameter D, the flux in the beam may be written

$$\Gamma_b = \frac{4I}{\pi e Z D^2} \qquad \text{(ions/m}^2\text{-s).} \tag{6.12}$$

If the source is space-charge limited, we can use equation (3.145) to write the beam flux in the form

$$\Gamma_b = \frac{J_c}{Ze} = \frac{\chi}{Ze} \frac{V_0^{3/2}}{d^2} \quad \text{(ions/m}^2\text{-s)} \tag{6.13}$$

where χ is the Child, discussed in Chapter 3. Note that χ is a function of ion mass. This ion flux must be provided by the discharge plasma which is part of the ion source.

6.3.3 Beam Number Density

If the source is other than space-charge limited, the beam number density may be obtained from

$$J = \frac{I}{A} = \frac{4I}{\pi D^2} = Zen_b v_b \quad \text{(A/m}^2\text{)} \tag{6.14}$$

where v_b is the velocity of the beam ions, obtained from conservation of energy in equation (3.156). Substituting equation (3.156) into equation (6.14) and solving for the beam number density yields

$$n_b = \frac{4I}{\pi e Z D^2} \sqrt{\frac{M}{2eZV_0}} \quad \text{(ions/m}^3\text{)}. \tag{6.15}$$

If the source is space-charge limited, the number density at the exit and in the beam is given by equation (3.150),

$$n_b = \frac{4\varepsilon_0 V_0}{9eZd^2} \quad \text{(ions/m}^3\text{)}. \tag{6.16}$$

This density is independent of the mass of the ions.

6.4 ION SOURCE DESIGN

6.4.1 Electrode Lifetime Limits

Important to the lifetime of ion sources is the reduction of particle bombardment of the accelerating electrodes of a kind shown in figures 6.3 and 6.4. Figure 6.3 shows ion impingement due to an inappropriately designed electrode geometry; figure 6.4 illustrates the defocusing effect of operating at other than the designed extraction voltage. Figure 6.4(a) shows non-intersecting trajectories at the design point; figure 6.4(b)
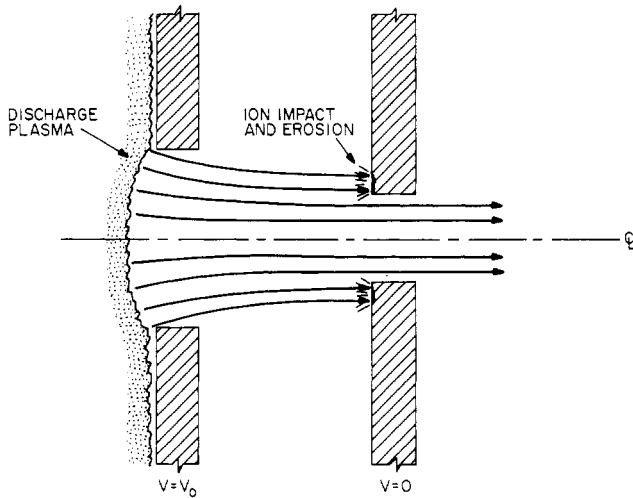
Figure 6.3 Illustration of direct ion impact on an accelerating grid due to improper design of the grid.

shows ion impact on an electrode due to the defocusing resulting from a lower than designed extraction voltage. Eliminating ion impact from these or any other causes reduces parasitic power drains, reduces electrode erosion by ion sputtering, increases the electrode lifetime, and improves mass utilization and electrical efficiency. One therefore must design ion sources to eliminate direct ion impact on the electrodes. Not quite so obvious is the fact that one must also eliminate the possibility of charge-exchange neutral impact with the electrodes, where the charge-exchange neutrals can originate anywhere along the ion trajectories.

In figure 6.5, above the centerline, is shown an optimum ion trajectory, for which neither ions nor charge-exchange neutrals formed along the ion trajectory will intersect the electrodes. Below the centerline is shown an over-focused trajectory, some charge-exchange neutrals of which will hit the electrodes as a result of the straight-line trajectory followed by such neutrals after charge exchange occurs. Ion and charge-exchange neutral impact occur with high enough energy that significant sputtering of the electrode material can occur, shortening the lifetime of the electrodes. With properly developed ion optics, common in the field of space propulsion, electrodes can be made to operate for tens of thousands of hours without significant sputtering-induced erosion.

6.4.2 Power Deposition Limits

The power deposited on electrodes by radiation, and by parasitic ion, electron, and neutral fluxes must be removed either by radiation or with a flowing coolant. In many ion sources, the accelerating electrodes are
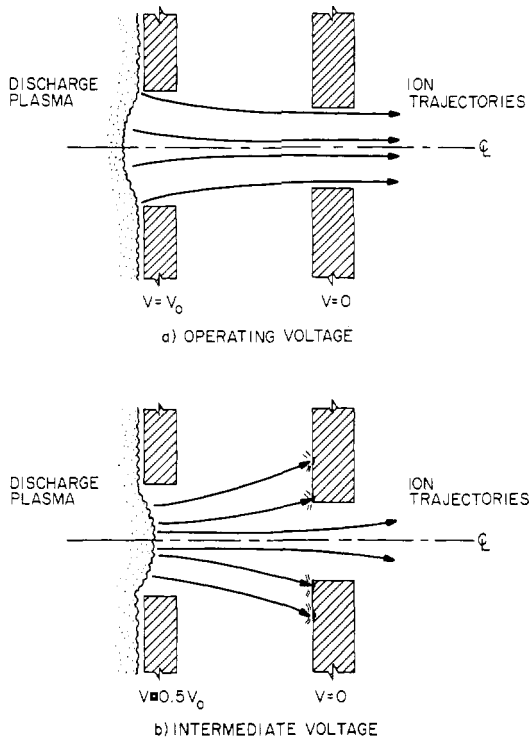
a) OPERATING VOLTAGE

b) INTERMEDIATE VOLTAGE

Figure 6.4 The defocusing of an ion beam as the result of off-optimum operating conditions. (a) Properly optimized ion trajectories at the operating voltage. All ion trajectories, including those at the edge of the beam, pass through the gap in the accelerating electrode. (b) Off-optimum operating voltage, which results in ion trajectories that intersect the accelerating electrode.

made of sheet metal, and cannot be cooled except by radiation. If the parasitic power flux to an electrode surface is ϕ_p watts per square meter, this can be set equal to the radiated power, from the Stefan–Boltzmann radiation law,

$$\phi_p = \varepsilon \sigma T^4 \qquad (\text{W/m}^2) \qquad (6.17)$$

where ε is the emissivity, and σ is the Stefan–Boltzmann constant, $\sigma = 5.671 \times 10^{-8}$ W/m²-K⁴.

The maximum power which uncooled sheet metal electrodes can radiate is found at the melting temperature of the electrode material, T_m, and at ε_m, the emissivity of the electrode material at its melting point. For aluminum, $(\phi_p)_{max} \approx 0.82$ W/cm², a relatively low value, indicating the importance of reducing to an absolute minimum the incident power flux on uncooled electrode surfaces.
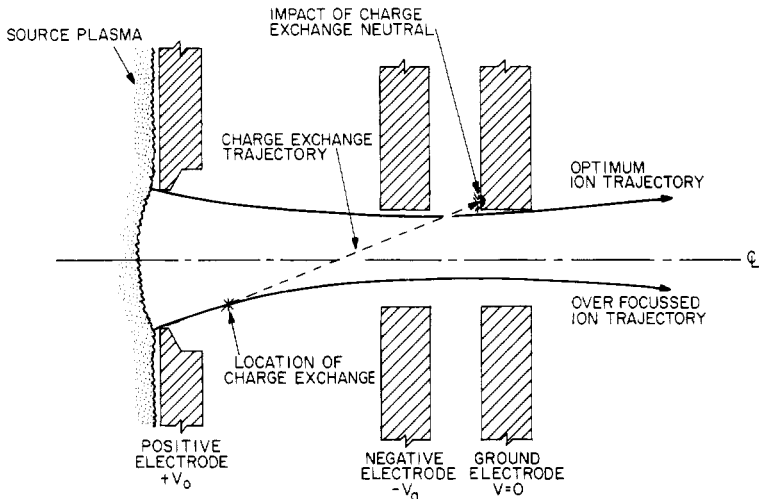
Figure 6.5 Illustration of an optimum ion trajectory, above the centerline, for a three-electrode ion accelerating grid system; and below the centerline, illustration of an overfocused ion trajectory, which allows charge-exchange neutrals formed along the early portions of the ion trajectory to impact the accelerating grid, thus reducing its lifetime.

If active cooling with a flowing coolant is necessary, heat fluxes as high as 5 kW/cm^2 can be accommodated with the most advanced aerospace-related methods. Such high fluxes, however, shorten the lifetime of materials so cooled, by thermal stress-induced cracking, leading to an unacceptable failure mode for equipment which must be operated in a vacuum system.

6.4.3 Design Optimization

The geometry of an ion source must be optimized to assure unobstructed ion trajectories through the electrode system at or near space-charge limited current conditions. In figure 6.6(a), Coupland *et al* (1973) have optimized the electrode thicknesses t, the distance between electrodes d, and the electrode radii r, as well as the accelerating potential V_0 and the decelerating potential $-V_a$ to obtain the non-intersecting ion trajectories shown. These trajectories also have the characteristic that their tangents (the trajectory of charge-exchange neutrals) also do not intersect the electrodes. The presence of the inset in the positive extraction electrode was found by these authors to facilitate the design of optimum, non-intersecting ion trajectories.

The equipotentials of a three-electrode configuration studied by Cooper *et al* (1972) are shown in figure 6.6(b). This is an accel-decel configuration with $V = V_0$ on the source, $V = -0.1V_0$ on the
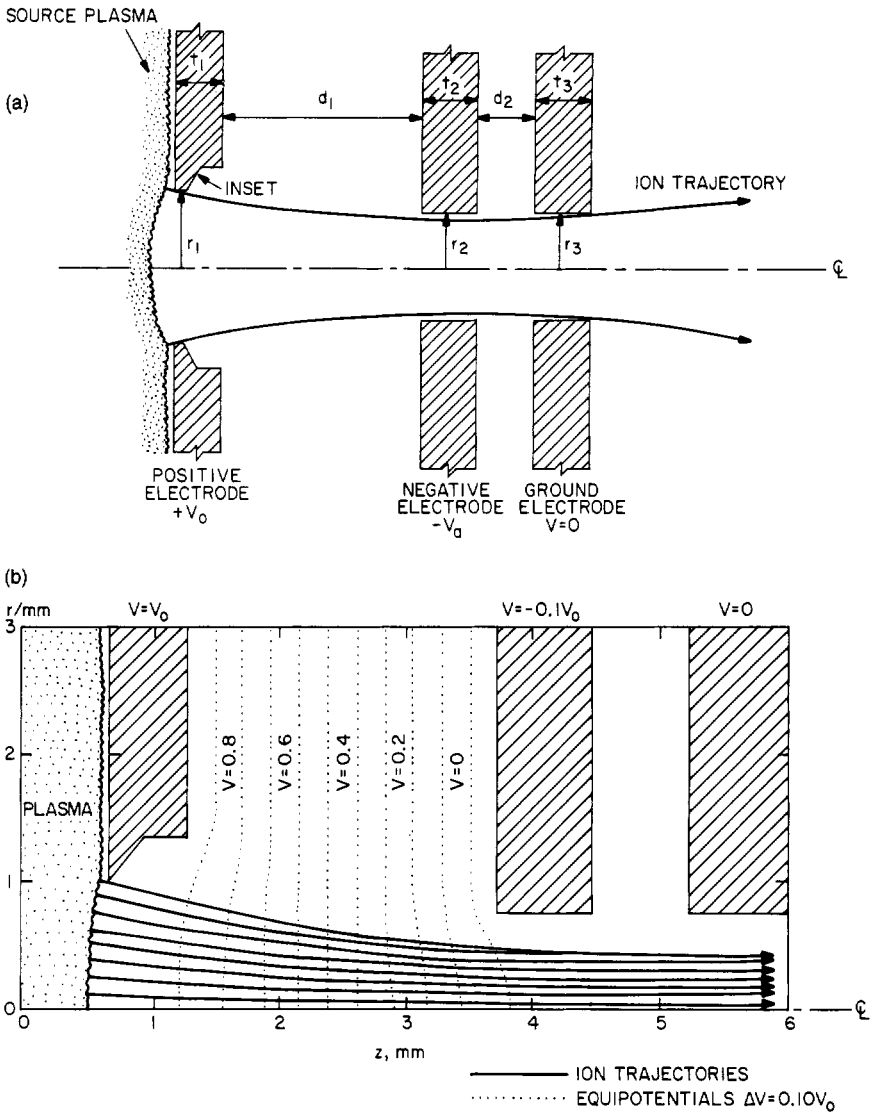
Figure 6.6 Optimization of ion trajectories in an accel–decel three-electrode source. (a) A schematic illustration of the parameters which must be optimized to ensure proper focusing of the ion trajectories: the electrode thicknesses, t; electrode separations, d; and electrode radii, r. (b) Focused ion trajectories and equipotentials from an axisymmetric, three-electrode geometry. From Cooper *et al* (1972).

accelerating electrode, and $V = 0$ on the final electrode, to ensure that the beam is at ground potential when it leaves the source. The geometry of this source has been optimized so that ion trajectories and their tangents
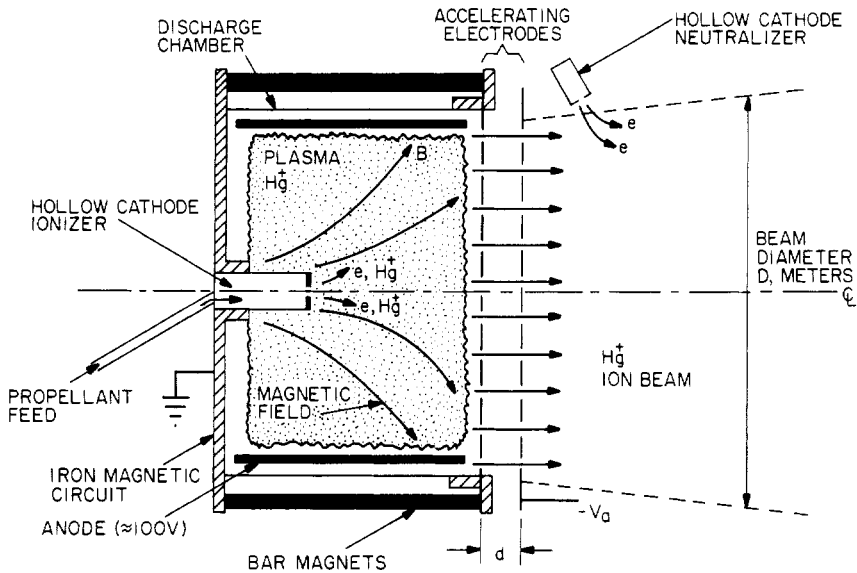
Figure 6.7 The Kaufman ion source, also known as the electron bombardment ion source. This space-charge limited source was developed for space propulsion applications.

do not intersect the electrodes. The equipotentials between the source electrode on the left and the accel electrode in the middle are indicated by the dotted lines.

6.5 KAUFMAN ION SOURCE

This source was developed by Harold L Kaufman (1961, 1963) and colleagues at the NASA Lewis Research Center for space applications over a period of several decades following 1958. Also known as the *Kaufman ion engine* or the *electron bombardment ion source*, this source achieved very high mass utilization and electrical efficiencies, higher than 0.9 and 0.95 respectively. It also demonstrated extremely long lifetimes, exceeding ten thousand hours in actual orbital applications as an electrostatic thruster.

6.5.1 Basic Configuration

A characteristic Kaufman source is shown in figure 6.7, incorporating many of the advances in ion engine technology of the 1960's and 1970's. In this axisymmetric source, ions are produced in a *discharge chamber* by a DC glow discharge operating below 1 mTorr. The discharge chamber is
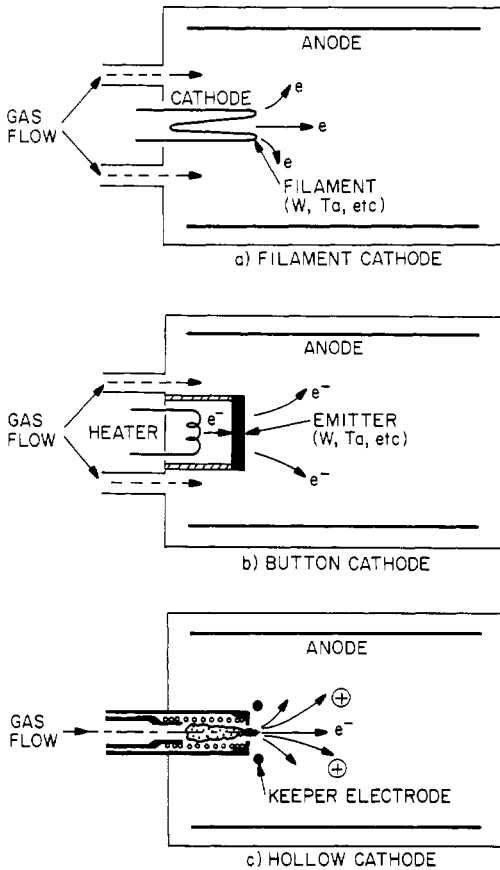
Figure 6.8 Various cathode configurations for the Kaufman ion source. Early sources of this type, and sources for which lifetime considerations are not important, use: (a) one or more hairpin filaments as the electron source, with independent neutral gas feed into the discharge chamber, or (b) the button cathode configuration with independent gas feed and a heater coil which raises a button electron emitter to incandescence, from which the electrons are emitted. (c) The hollow cathode, which acts as an electron source, and ionizes the gas flow before it reaches the discharge chamber.

permeated by a weak magnetic field, between 5 and 12 mT, enough to magnetize the electrons but not the ions. The glow discharge is maintained by a few hundred volts across the gap from the hollow cathode ionizer to the axisymmetric anode at the outer circumference of the discharge chamber.

The Kaufman ion source uses a hollow cathode to ionize the working gas, and as an electron emitter. Since neutralization of the ion beam is required in space applications, a second hollow cathode neutralizer emits
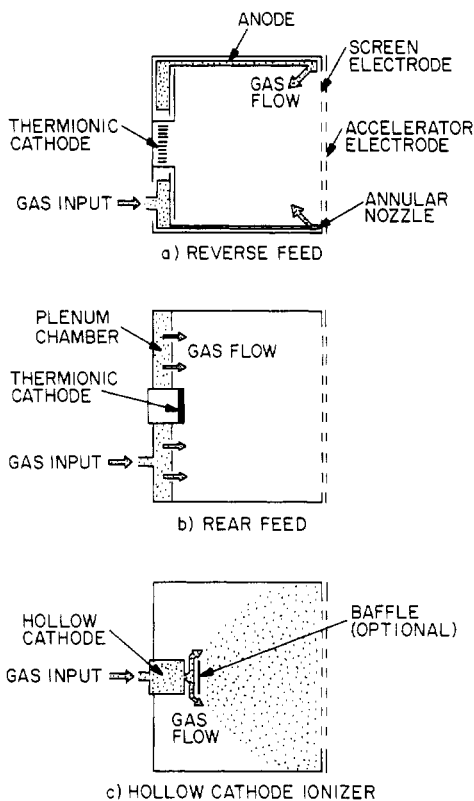
Figure 6.9 Gas feed mechanisms for the Kaufman ion source. (*a*) Reverse feed of neutral gas, in which gas is injected toward the rear of the discharge chamber. (*b*) Rear feed, in which the gas flow is distributed by a plenum at the rear of the chamber, and escapes into the discharge chamber through a large number of small holes. (*c*) The hollow cathode ionizer, in which the neutral gas flows through the hollow cathode, where it is ionized and contributes to the electron emitting plasma formed in the neutralizer.

electrons into the beam to provide neutralization. In space applications, the Kaufman source shown in figure 6.7 was optimized for operation with mercury and xenon gas. These engines had lifetimes greater than ten thousand hours, and current densities between 80 and 90% of the Child law current.

6.5.2 Alternative Configurations

During the decade of the 1960's, many configurations of the Kaufman source were tested, some of which may have unique advantages for certain gases or specialized industrial applications. On figure 6.8 are shown various cathode configurations, including the hairpin filament in figure 6.8(*a*), an incandescent refractory emitter, shown in figure 6.8(*b*), and the hollow cathode in figure 6.8(*c*), which is the preferred arrangement for space and many other applications.

On figure 6.9 are shown some of the gas feed arrangements which have been tested. Figure 6.9(*a*) shows a reverse feed of neutral gas into the discharge chamber. Figure 6.9(*b*) shows the 'shower head' feed of neutral gas from many small holes in a plenum at the rear of the
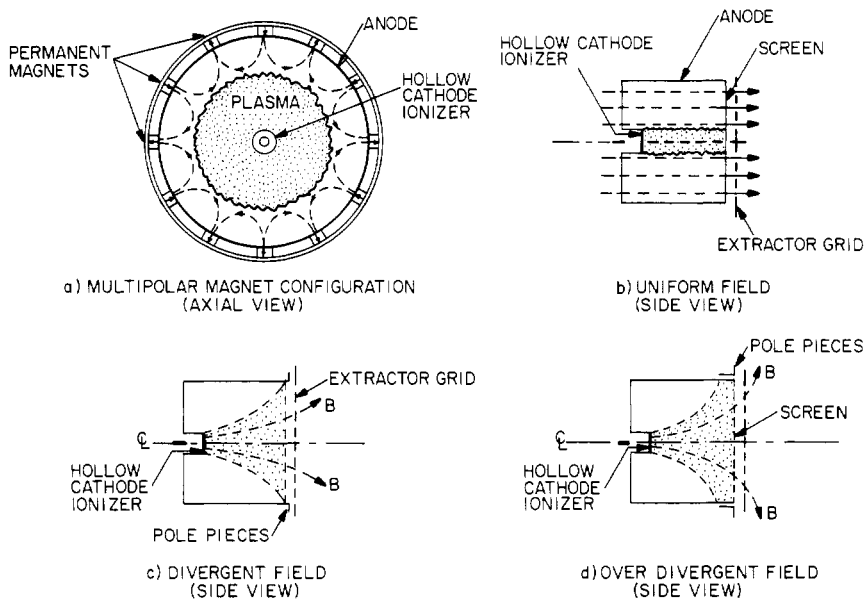
Figure 6.10 Magnetic field configurations for the Kaufman ion source. (*a*) Cross sectional view of the multipolar magnetic configuration, in which small permanent magnets are placed axially along the outside surface of the discharge chamber, providing a multipolar cusp. (*b*) Axial cross section of a discharge chamber with a uniform magnetic field through the discharge chamber. (*c*) Axial cross section of the divergent field configuration, which leads to a more uniform radial distribution of plasma. (*d*) Axial cross section of an over-divergent magnetic field configuration, in which the efficiency of the discharge chamber is impaired by direct current flow along field lines from the cathode to the cylindrical anode.

discharge chamber. In the hollow cathode shown in figure 6.9(*c*), the gas flows through the hollow cathode and is ionized in the process. All of these gas feed configurations are capable of producing a high overall gas utilization efficiency, probably because at the low pressures at which Kaufman sources are operated, the gas distributes itself evenly in the chamber regardless of how it is injected.

The magnetic field configurations which have been used to improve the electrical efficiency of the discharge chamber of Kaufman ion sources include the multipolar configuation shown in figure 6.10(*a*), viewed along the axis. This is a relatively recent development, in which permanent magnets with opposite polarities are placed around the circumference of the discharge chamber. These multipolar magnets create a magnetic field-free plasma in the center of the discharge chamber, the transport of which to the anode is retarded by the increasing magnetic field (magnetic mirror) as the plasma approaches the anode.

The least useful axisymmetric magnetic field configuration is the uniform field along the axis of the discharge chamber shown in figure 6.10(*b*). Here, the plasma tends to be constrained to the field lines in contact with the hollow cathode surface. The most efficient of the axisymmetric magnetic field configuations is that shown in figure 6.10(*c*), in which the magnetic field diverges from the hollow cathode ionizer to the accelerating grid, with the magnetic field line connecting the edge of the hollow cathode just touching the end of the discharge chamber. This arrangement spreads the plasma relatively uniformly over the surface of the accelerating grid. Finally, the over-divergent field, shown in figure 6.10(*d*), is less efficient, because of the direct transport of ions along the magnetic field lines from the cathode to the anode.

6.5.3 Operating Characteristics

The Kaufman ion source developed for space applications had accelerating voltages ranging from 1 to 10 kV, total beam currents ranging from 0.05 to 10 A, current densities that ranged from 0.70 to 0.95 of the space-charge limited values, and beam diameters that ranged from 10 cm to 1.5 m (Kaufman 1965, Poeschel *et al* 1979). The lifetime of sources of this type which were intended for space applications could exceed 10 000 hours. The Kaufman ion source was by far the most extensively developed of any ion source during the period from 1958 to the present and has been widely applied industrially to ion beam sputtering and ion milling of surfaces.

6.6 PENNING DISCHARGE SOURCES

The Penning discharge was developed by Frans Michel Penning (1894–1953) in the 1930's (Penning 1936, Penning and Moubis 1937), and was modified into an ion source by R G Meyerand and S C Brown (1959).

6.6.1 Penning Configuration

A *Penning ion source* similar to that developed by Meyerand and Brown is shown schematically in figure 6.11. The Penning ion source consists of a magnetoelectrically confined plasma discharge, in which gross confinement of electrons is provided by an axial magnetic field and an axial electrostatic potential well. Electrons are electrostatically trapped axially, and magnetically trapped radially until they collide and ionize, enabling the plasma to be maintained at background neutral gas pressures as low as 10^{-7} Torr (1.33×10^{-5} Pa). The electron–neutral ionizations avalanche until the ionization and loss processes reach a steady state. Starting electrons for the Penning plasma can be provided
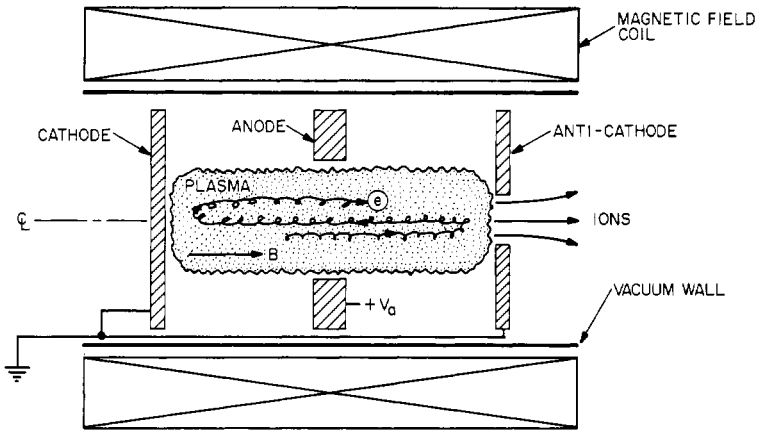
Figure 6.11 The Penning ion source, with a cylindrical anode ring at the center and two cathodes at either end. A small hole on the axis of one cathode allows a beam of ions to escape.

by volume ionization from background radiation, secondary emission from cold cathodes, a hot filament as shown in figure 6.12, or a hollow cathode.

Although the axial electrostatic potential distribution is a potential well for electrons, it repels ions produced between the anode and cathode. If a hole is opened up in one or both cathodes, ions, instead of impacting the cathode, will pass through, producing a relatively intense beam of ions, as noted by Meyerand and Brown (1959). Penning ion sources can be operated at gas pressures between 10^{-7} Torr $(1.33 \times 10^{-5}$ Pa$)$ and 100 mTorr, (13.3 Pa), magnetic inductions from 0.01 to 3 T, anode voltages from 100 to 50 000 V, currents from 10^{-7} to 20 A, electron kinetic temperatures from 2 to 15 eV, and the ion energies produced can range from less than 1 eV to several keV.

6.6.2 Ion Heating in Penning Sources

It is an interesting property of the Penning discharge as an ion source that it can produce a beam of ions with kilovolt kinetic energies, far higher than the kinetic temperature of the background electrons (Meyerand and Brown 1959, Roth 1966, 1973a, b). The high ion energies associated with Penning sources result from the circumstance that Penning discharges can have radial electric fields in excess of 1 kV/cm between the plasma and the anode. This leads to magnetoelectric heating by E/B drift in the azimuthal direction, with a velocity

$$v_{\mathrm{d}} = \frac{E \times B}{B^2} = \frac{E_{\mathrm{r}}}{B}. \qquad (6.18)$$

The kinetic energy corresponding to this drift velocity is given by

$$\mathcal{E} = \frac{1}{2}mv_d^2 = \frac{m}{2}\frac{E_r^2}{B^2}. \tag{6.19}$$

Thus, in Penning discharges, the particle energy is proportional to mass, and this is why ions in low pressure Penning discharges are often more energetic than the electrons.

At pressures below 30 μTorr, and at magnetic fields above 0.2 T, Penning discharges become very turbulent, and can provide a Maxwellian distribution of ions with kinetic temperatures up to several keV (Roth 1973a, b). One can also adjust the operating parameters to achieve a uniform distribution function of ion energies over the range $0 < E < E_{max}$, where E_{max} is given by equation (6.19). At higher gas pressures, above 100 μTorr, nearly monoenergetic ion energy distributions at the Penning anode voltage are observed. These ions acquire high energies by falling down the electrostatic potential gradient between the anode and cathode.
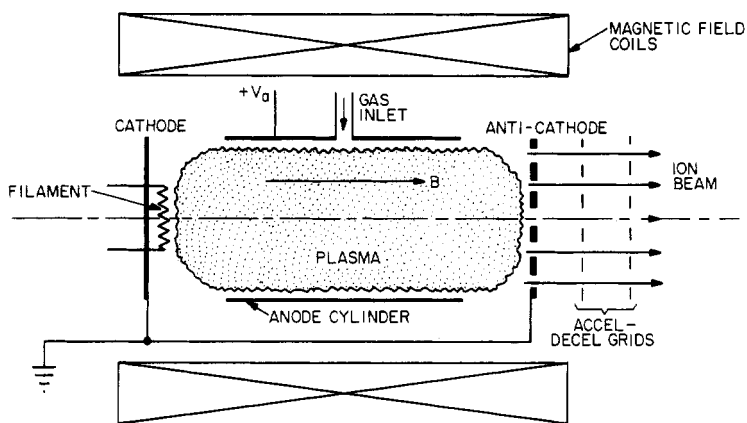
Figure 6.12 A Penning ion source in the duoPIGatron configuration, in which electrons are emitted from a filament or a hollow cathode on the left-hand surface, and generate a Penning plasma between the cathode and anticathode. In the duoPIGatron, the working gas is injected radially into the anode cylinder and ions are extracted through holes in the anti-cathode, which may be replaced by an accelerating grid.

6.6.3 Other Penning Configurations

Penning ion sources can be operated in the *duoPIGatron* configuration, which was developed as a fusion-related ion source at the Oak Ridge National Laboratory by Stirling, Morgan *et al*. This modification of the
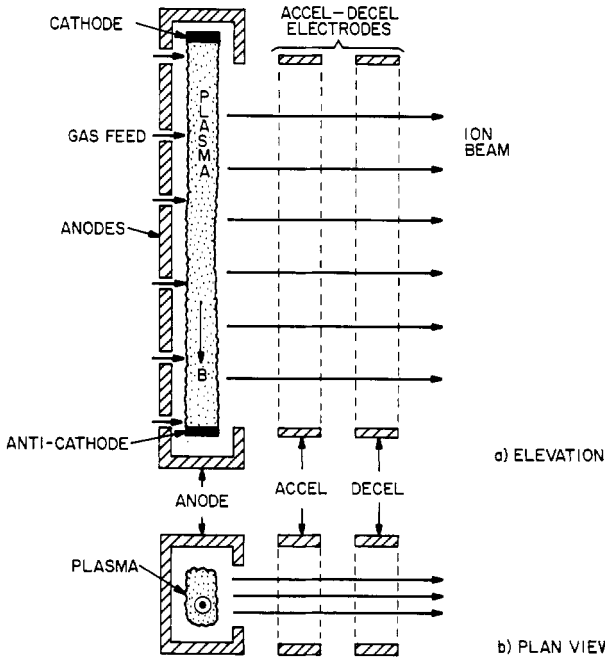
Figure 6.13 A Penning ion source in the Calutron configuration, in which a long, narrow beam of ions is produced. The ions are created in a Penning discharge, shown in the elevation view, which has a uniform magnetic induction along its axis. Ions are extracted along the length of this plasma and accelerated by an accel–decel electrode configuration.

Figure 6.14 The sputtering ion source, a Penning discharge in which the left-hand cathode is biased to attract ions, and after being heated to incandescence, boils off neutral atoms which are ionized in the discharge, and extracted through the anti-cathode to form an ion beam.

Penning discharge is shown in figure 6.12, in which the Penning ion source provides ions to an accel–decel configuration.

The *Calutron* is a Penning discharge with ions drawn normal to the axis of a long, thin Penning discharge, as shown in figure 6.13. The Calutron was originally used for electromagnetic separation of isotopes, where a long, thin beam of ions was required.
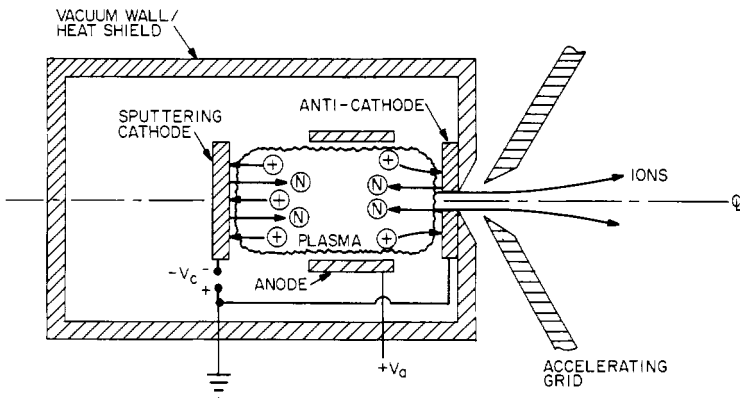
The *sputtering ion source* is a Penning ion source in which atoms of refractory materials are ionized in the Penning discharge plasma to form an ion beam, in the manner indicated schematically in figure 6.14. In this source, ions bombard the Penning cathodes, which are made of the refractory material which it is desired to form into an ion beam. The cathodes are heated to the point at which neutral atoms of the cathode material either sputter or evaporate from the surface, become ionized in the Penning plasma, and are then accelerated through the cathode on the left, to form an ion beam.

6.7 BEAM-PLASMA ION SOURCES

The *beam-plasma ion sources* have in common the use of an electron beam or linear DC arc discharge between a cathode, usually a heated filament, and an anode. The interaction of the electron beam with a gas of the
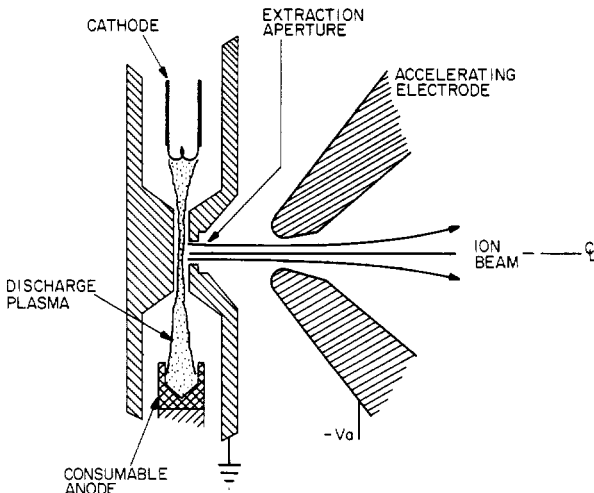

Figure 6.15 The capillary arc source. This consists of an arc drawn between a cathode, and an anode shown on the left. The capillary arc terminates on an anode which is heated and the material of which is vaporized. Atoms vaporized from the anode are ionized and extracted radially through a small hole in the capillary where they are accelerated into an ion beam.

species of interest produces a plasma, from which the ions are extracted. Separate electrodes then accelerate the ions to the desired energy.

6.7.1 Capillary Arc Source

The *capillary arc source* shown in figure 6.15 was developed for high energy physics applications, where it is sometimes desirable to generate an ion beam from radioactive, rare or precious solid materials. In this source, an arc is drawn between a cathode and an anode through a small capillary opening on the left. The capillary arc terminates on a heated anode, which vaporizes and emits atoms into the arc. These atoms are ionized and become available for extraction through a small hole normal to the axis of the arc. These extracted ions are then accelerated to form a beam.

6.7.2 Perpendicular Beam-Plasma Ion Source

Another ion source, useful for atomic species that are available as a gas, is the *perpendicular beam-plasma ion source* shown in figure 6.16. This source resembles the Calutron, but uses an electron beam to ionize the
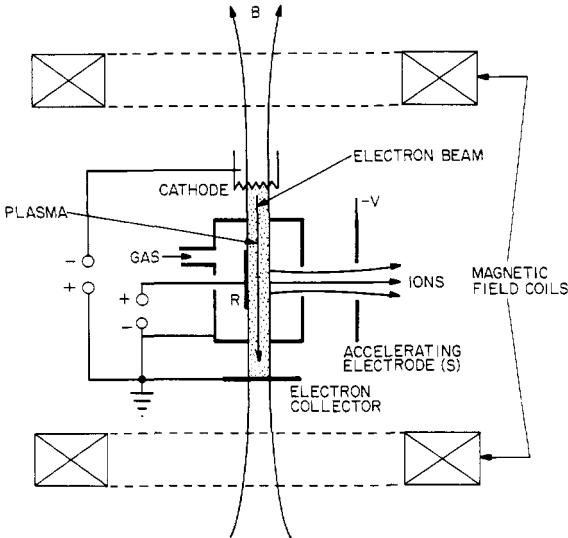

Figure 6.16 The perpendicular beam-plasma source, in which an electron beam travels along a magnetic field between a cathode and the electron collector. This electron beam creates a plasma in a small chamber, from which ions are extracted at right angles to the magnetic field and accelerated by an external system of electrodes.

working gas, instead of a Penning discharge plasma. In this source, a magnetic field transverse to the ion beam is imposed by the coils shown, and a high current electron beam is drawn between a cathode and an anode along the magnetic field lines. This electron beam interacts with the working gas in an isolated chamber, producing ions of the working gas, some of which are extracted perpendicular to the electron beam and are accelerated by a series of grids to form a beam.

6.7.3 Parallel Beam-Plasma Ion Source

A related device is the *parallel beam-plasma ion source* shown in figure 6.17. In this configuration, the working gas is ionized by an electron beam as in the previous source, but the ions are extracted axially along the magnetic field and accelerated to form a monoenergetic ion beam.

6.8 VON ARDENNE ION SOURCES

These sources were originally described by M von Ardenne (1956). Related sources were developed by other authors for applications to atomic and nuclear physics research.
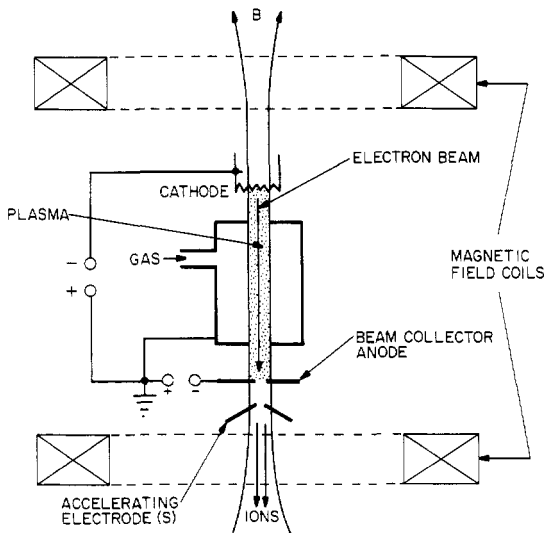

Figure 6.17 The parallel beam-plasma ion source. This source is similar to that shown in figure 6.16, but here the ions are extracted axially along the magnetic field where they are accelerated and form a beam.
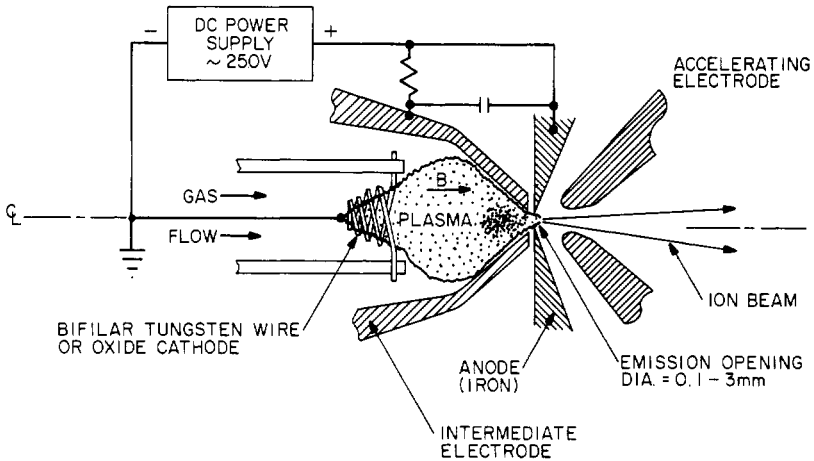
Figure 6.18 The von Ardenne ion source, consisting of an axisymmetric combination of a source to the left, and a set of accelerating electrodes on the right. Ions are produced in a discharge plasma formed by flowing gas through a hot filament, and creating a dense plasma on the interior of the extraction electrode orifice.

6.8.1 Von Ardenne Source

A characteristic *von Ardenne source* is shown in figure 6.18. This source is typically an axisymmetric geometry, is relatively small in physical size, and operates much like a hollow cathode electron source, but with extraction electrodes which suppress electron emission and instead extract ions from the dense, concentrated plasma which is located between the filament and the intermediate electrode. A strong magnetic field is created by using iron for the accelerating electrodes, and shaping the magnetic field to achieve the desired ion optics.

Like the hollow cathode electron source, the von Ardenne ion source requires an axial gas flow, a keeper electrode for stable operation, and usually has accelerating electrodes to produce a monoenergetic axial beam of the desired ions. The gas flowing through the source consists of the atomic species which one wishes to ionize to form the beam. Because some versions of this source use a hot filament for its operation, the von Ardenne source is subject to chemical attack. Some modified versions of the von Ardenne source use a hollow cathode instead of a filament as an electron source, and/or dispense with the axial magnetic field.

6.8.2 Capillaritron Ion Source

A related ion source is the *capillaritron ion source* shown in figure 6.19. This source resembles the von Ardenne ion source, but is usually much
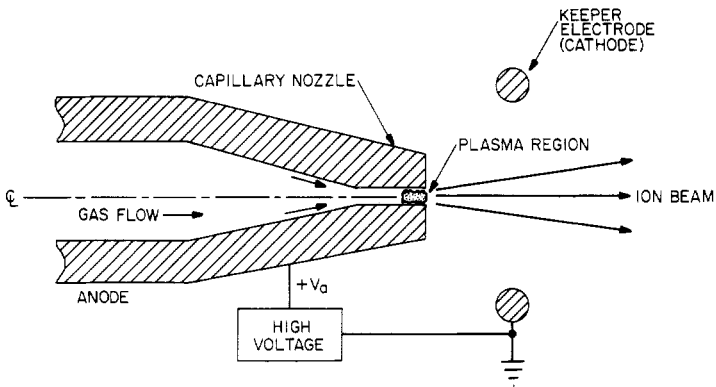
Figure 6.19 The capillaritron ion source. This ion source resembles the Lidsky hollow cathode, in that it has a gas flow passing through a region of dense plasma in the opening of a small capillary nozzle. A high voltage is maintained between a keeper electrode and the capillary nozzle, thus extracting ions from the plasma region.

smaller in size. The capillaritron ion source, unlike the von Ardenne source, has no externally heated cathode, and a keeper electrode is used instead to stabilize its operation. It operates in the steady state, requires an axial gas flow, and is good for the production of low currents at the level of milliamps and below.

6.8.3 Zinn Ion Source

The *Zinn ion source* (Zinn 1937) shown in figure 6.20 is also similar to the von Ardenne ion source, but instead draws an arc between a ring cathode and an anode. The arc terminates on a coaxial anode, after making a right angle turn through an annular space. Ions formed in the dense plasma between the end of the anode and the intermediate electrode may be accelerated by an extraction electrode, to form an ion beam. Ions can be formed from a working gas flowing coaxially, or by vaporization or sputtering of the solid anode material.

6.8.4 Electron Heated Vaporization Source

In some applications it is desired to form an ion beam from solid or even refractory materials. One option is to use the *electron heated vaporization source* shown in figure 6.21. The material of which it is desired to make an ion beam is incorporated in the consumable axial electrode. It operates in some respects like the Zinn source, but relies on heating the axial anode to incandescence, thus vaporizing the electrode material and making it available for ionization by the intense plasma that forms between the
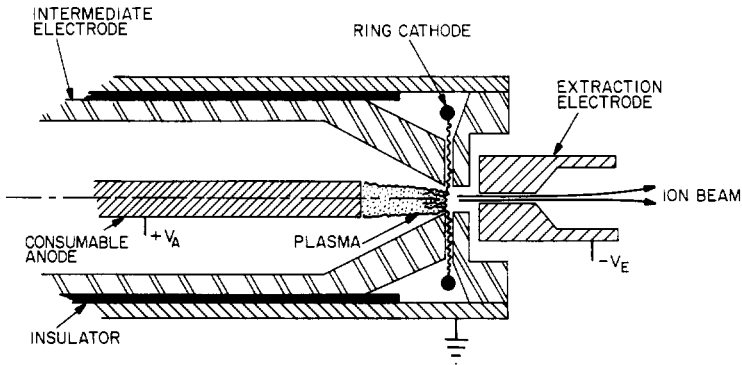
Figure 6.20 The Zinn ion source. In this source, an arc is struck between the axial anode on the left, and radially through a small opening to a ring cathode. Ions are extracted from the plasma formed in this region and accelerated by the extraction electrode at the right to form an ion beam.
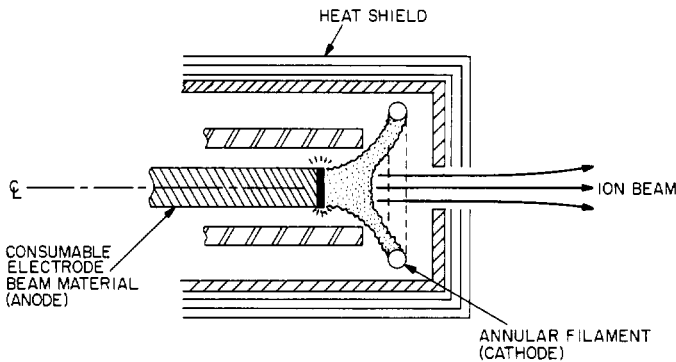
Figure 6.21 The electron heated vaporization source operates in a manner similar to that of the Zinn source. A consumable axial electrode is used to draw an arc to an annular filament. As the material of the electrode vaporizes, it forms ions which are extracted to form an ion beam.

anode and the annular filament cathode. Such sources usually operate above 1000 K. To reduce power requirements, heat shields are usually employed around the source as shown in figure 6.21.

6.8.5 Hollow Cathode von Ardenne Source

A smaller version of the von Ardenne source, utilizing a hollow cathode electron source instead of hot filaments, is shown in figure 6.22. This configuration can be made small in size, and is useful when only small currents of extremely rare or radioactive materials are required.
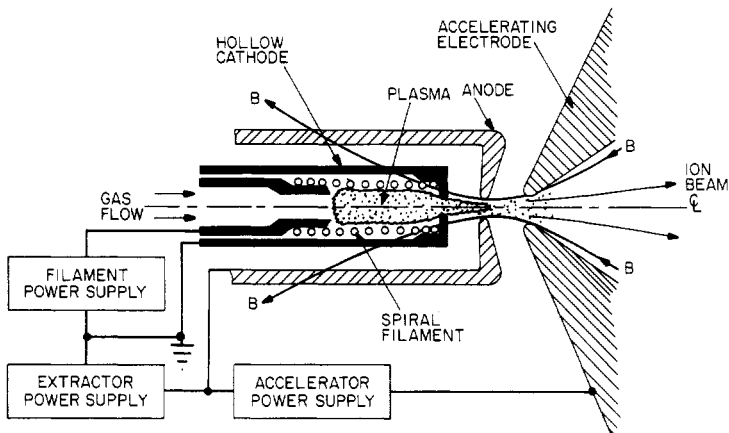
Figure 6.22 The magnetized hollow cathode ion source is similar to the von Ardenne source, with the addition of a hollow cathode to improve the efficiency of ion extraction.

6.9 FREEMAN ION SOURCE

A more recently developed ion source is that described by J H Freeman (1963) and shown schematically in figure 6.23. Its geometry is a long, narrow slit configuration resembling the Calutron. Gas or vapor is fed into a discharge chamber containing an anode which is operated at a few hundred volts above the filament and discharge casing. A plasma is generated by electron bombardment behind the extraction slit, with electrons emitted from a massive filament parallel to and just behind the extraction slit. This massive filament is the characteristic feature of the Freeman source. Ions are extracted from the discharge plasma and accelerated by an accel–decel electrode configuration, the ion optics of which is designed to promote beam uniformity and focusing. A weak vertical magnetic field, typically 15 mT, is sufficient to magnetize and confine electrons in the plasma around the filament, but not the ions.

Many of the ion sources discussed above, including the Penning, beam-plasma, and the von Ardenne sources utilize or require electron beams and/or strong local electric and magnetic fields. These give rise to ion heating or plasma instabilities, the effect of which is usually to defocus the ion beam and impair the ion optics. The above-mentioned sources and their variants must usually be painstakingly tuned up to reach a stable operating regime for the discharge plasma, without the 'hash', or plasma instabilities that lead to beam defocusing. In electromagnetic isotope separation and in many microelectronic ion implantation applications, the ion optics must be well focused to achieve the desired result.

The Freeman ion source is capable of stable operation because of
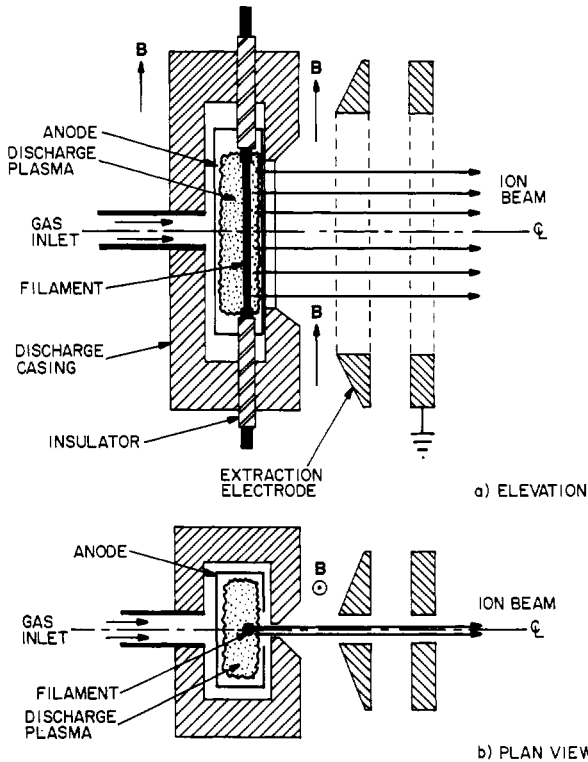
Figure 6.23 The Freeman ion source in elevation and plan views. A filament is operated immediately behind the vertical extraction slit. A weak vertical magnetic field traps electrons in the vicinity of the filament.

its low electric and magnetic fields in the discharge region, and its lack of electron beams to drive plasma instabilities. For this reason, it has become widely used in ion beam implantation for microelectronic and other applications. A modification of the Freeman source for such applications has been described by Aitken (in Aitken 1987 and in Chapter 9 of Brown 1989).

6.10 MISCELLANEOUS ION SOURCES

6.10.1 Canal Ray Ion Source

The *canal ray ion source* shown on figure 6.24 is historically significant because it represented the first experimental observation of ion beams in the mid-19th century, although it was not until circa 1900 that the nature of the 'canal rays' was understood to be an ion beam. The original canal
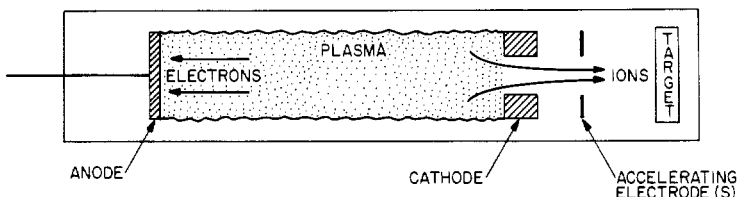
Figure 6.24 The 'canal ray' source. This primitive ion source consists of a DC glow discharge, in which a small hole is opened in the cathode, allowing ions to escape and be accelerated to form an ion beam.
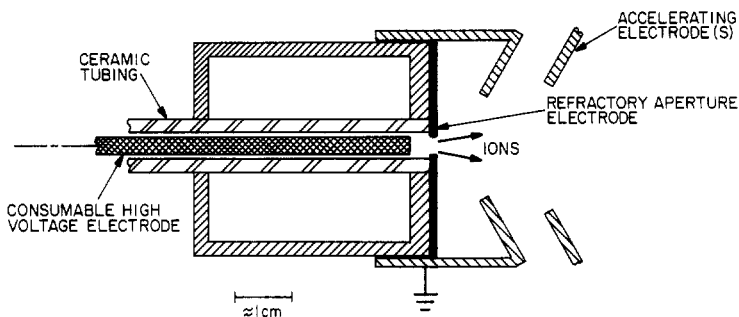
Figure 6.25 The pulsed spark ion source. In this source, a consumable high voltage electrode is fed in axially, and a spark drawn between this electrode and a refractory aperture electrode. The pulsed arcs produce a dense cloud of plasma, ions from which are accelerated by the external electrode.

ray source consisted of a DC glow discharge on the left, with an opening in the cathode, through which ions escaped from the plasma. Beyond the cathode, a series of electrodes could be placed to accelerate ions to high energies.

6.10.2 Pulsed Spark Sources

For some applications, a high density, pulsed plasma is desired. In the *pulsed spark ion source*, shown in figure 6.25, a pulsed high voltage is applied between the consumable high voltage electrode on the axis, and the refractory aperture electrode which is part of the grounded casing of the source. The high voltage draws an arc between the axial electrode and the aperture electrode. Ions are formed from the axial electrode material or, if the axial electrode is loaded with gas such as hydrogen or deuterium, the plasma can be formed from the gas absorbed in the electrode. A pulsed source similar to figure 6.25 is the *Marshall ion*
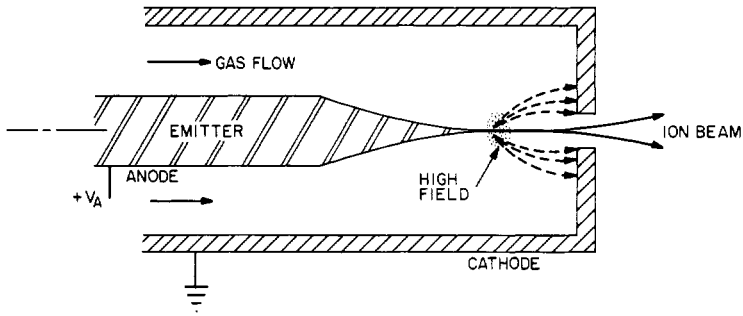
Figure 6.26 The field emission ion source with gas feed, in which an emitter at a high potential maintains a very strong electric field at the tip. Gas flowing past this tip becomes ionized, and is then accelerated by the electric field through a hole in the cathode, to form an ion beam.
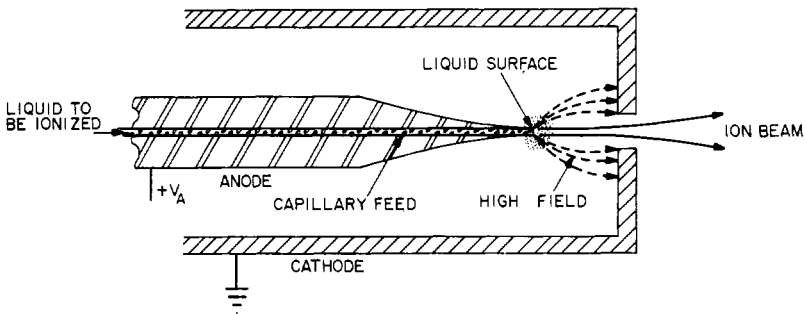
Figure 6.27 The field emission ion source with liquid feed. This source consists of an anode with a small capillary along the axis in which the liquid to be ionized is drawn by capillary action to a liquid surface at the tip. A high electric field at this tip ionizes the liquid at the surface, and the ions so formed are accelerated along the axis to form an ion beam.

gun, which produces its plasma between two adjacent electrodes, across which a pulsed arc is drawn.

6.10.3 Field Emission Ion Sources

An entirely different approach to forming ion beams at the microamp level is the *field emission ion source* shown in figure 6.26. In the source, an emitter electrode is drawn to a very fine point, and maintained at a high positive potential. The strong electric field at the tip of the emitter is capable of ionizing the working gas which flows around it. Ions formed in the region of high electric field are accelerated by the electric field between the emitter and the grounded cathode structure. An ion beam is

then formed from axially escaping ions as shown on the left-hand side of figure 6.26.

Figure 6.26 shows a field emission ion source using gas and in figure 6.27 is a related field emission ion source with a liquid feed. In the latter source, a coaxial anode with a fine capillary along its axis is maintained at high positive potential. The liquid to be ionized is fed along the capillary to the tip, where strong electric fields ionize the molecules comprising the liquid as the liquid evaporates into the vacuum. The positive ions so produced are accelerated by the electric fields between the anode and the surrounding structure and form a beam. A disadvantage of field emission ion sources is that they do not in general produce monoenergetic or monatomic ions.

6.11 SURFACE IONIZATION SOURCES

During the decade of the 1960s, surface ionization sources were developed as ion engines for space propulsion applications, and as
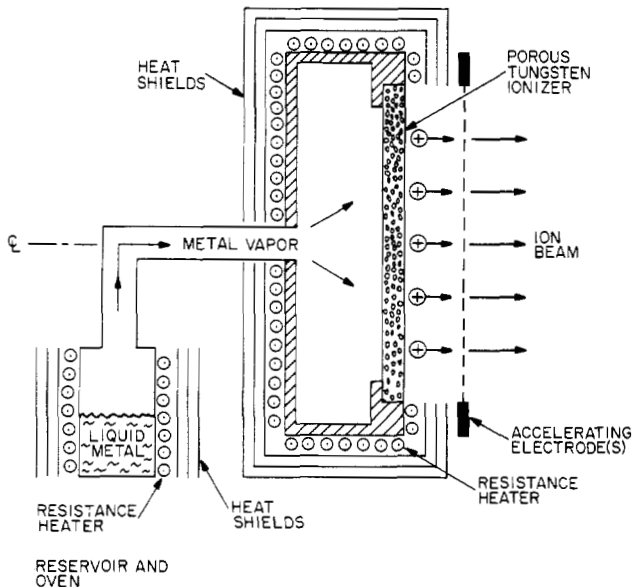
Figure 6.28 The porous tungsten surface ionization source. In this source, an incandescent plate of porous tungsten is permeated by an akali metal vapor which is fed from the rear. Upon leaving the front surface of the ionizer plate, alkali metal atoms are ionized, then accelerated to form a space-charge limited beam.
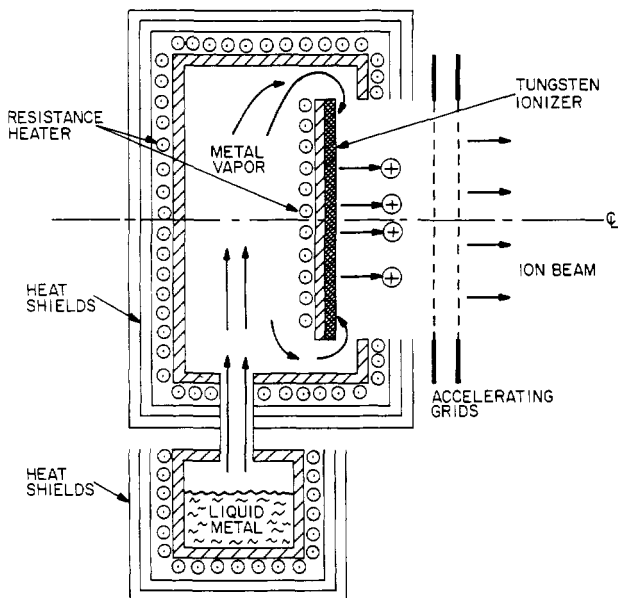
Figure 6.29 A surface ionization source in which alkali metal vapor is fed on the front surface of an incandescent tungsten or iridium ionizer plate, where atoms are converted to ions and accelerated to form an ion beam.

sources of quiescent (Q-machine) plasmas for basic research on the radial transport of plasma across a magnetic field. *Surface ionization sources* are used to produce beams of ions of alkali metals. These sources rely on the fact that when an alkali metal or other element with a low ionization potential leaves the surface of an incandescent refractory material like tungsten or molybdenum, it may leave the surface in an ionized state if the ionization potential of the atom is less than the work function of the surface, the latter being 4.55 V for tungsten.

6.11.1 Forrester Porus Plate Ion Source

The *Forrester porus plate ion source* was originally developed by A Theodore Forrester (Forrester *et al* 1963, Forrester 1965, 1988) and is shown schematically in figure 6.28. This source operates by forming an alkali metal vapor in a reservoir at the lower left. The metal vapor is fed behind a porous tungsten ionizer plate which is maintained at temperatures above 1000 K by a resistance heater and heat shields, which perform a second function of preventing condensation of the vapor. The alkali metal vapor permeates through fine capillary passages in the porous tungsten plate, and emerges from the front surface in an

ionized state (Forrester 1965). The ions are accelerated by a system of grids, usually an accel–decel combination in space applications, and this permits a space-charge limited ion beam to be formed. This source has not found widespread application for at least two reasons: one was the large energy losses associated with keeping the porous tungsten ionizer in an incandescent state; and the second problem was that over long periods of time (hundreds of hours), the capillaries in the porous tungsten ionizer plate tended to sinter together, thus progressively blocking the flow of the alkali metal through the tungsten plate.

6.11.2 Surface Contact Ion Source

A modification of the porus plate ionization source designed to eliminate the problem of decreasing ionizer plate porosity is the *surface contact ion source*, shown in figure 6.29. In this design, alkali metal vapor, formed in a heated oven, is fed around the sides of a tungsten or iridium ionizer plate, and is ionized when it contacts the surface. The ions produced at the surface are drawn off by the accelerating electric field of a grid structure, which forms the ion beam. This approach to the surface ionization source has the disadvantage that it is difficult to provide a uniform beam over a large ionizer surface area, and is useful only for the formation of relatively small diameter beams.
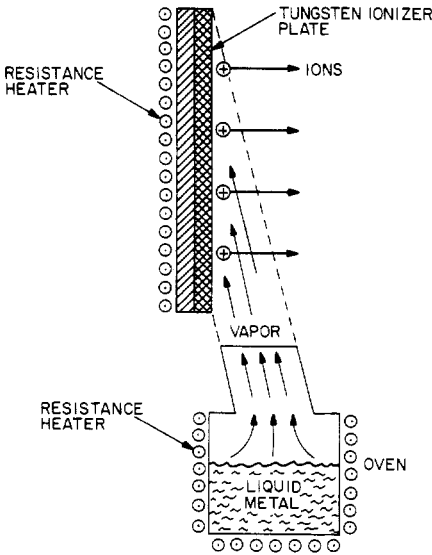

Figure 6.30 A modification of the surface ionization source in which an alkali metal vapor is formed in an oven and directed at an angle to an iridium or tungsten ionization plate.

6.11.3 Atomic Beam Ion Source

A second modification of the surface ionization source is the *atomic beam ion source*, shown in figure 6.30. This arrangement is used in atomic physics and plasma research when it is desired to produce a quiescent alkali metal plasma, and the gas utilization efficiency is not a factor. In this arrangement, a relatively large diameter beam is formed by evaporating a liquid metal from an oven through a collimating duct which effuses or distributes the alkali metal vapor uniformly over the surface of a hot refractory metal ionizing plate. If the ionization potential of the alkali metal is below the work function of the refractory metal, the vapor will be ionized, producing an extended surface source of alkali metal ions.

A potential shortcoming of this type of source, which caused much embarrassment to the plasma physics experimental community in the late 1960s, is that the beam uniformity is very sensitive to the temperature of the ionizing plate. Many alkali metal plasma experiments in the mid and late 1960s produced worthless data because it was not understood that many of the phenomena being observed were due to beam nonuniformities and radial electric fields induced by ionizer plate temperature gradients. A truly quiescent plasma was produced only when great care was taken to uniformly heat the ionizer plate and maintain it at a uniform temperature.

REFERENCES

Aitken D 1987 The Precision Implant 9000 Beam Line *Nucl. Instrum. Methods Phys. Res.* B **21** 274–279

von Ardenne M 1956 New Developments in Applied Ion and Nuclear Physics *Atomkernenergie* **1** 121–126

Brown I G (ed) 1989 *The Physics and Technology of Ion Sources* (New York: John Wiley) ISBN 0-471-85708-4 (see chap 9 for Aitken)

Cooper W S, Berkner H H, and Pyle R V 1972 Multiple-Aperture Extractor Design for Producing Intense Ion and Neutral Beams *Nucl. Fusion* **12** 263–265

Coupland J R, Green T S, Hammond D P and Riviere A C 1973 A Study of the Ion Beam Intensity and Divergence Obtained from a Single Aperture Three Electrode Extraction System *Rev. Sci. Instrum.* **44** 1258–1270

Dearnaley G, Freeman J H, Nelson R S and Stephen J 1973 *Ion Implantation* (Amsterdam: Elsevier) ISBN 0-444-10488-7

Forrester A T, Kuskevics G and Marchant B 1963 Ionization of Cesium on Porous Tungsten *Proc. 14th Int. Astronautical Congress (Paris, 1963)* p 447

Forrester A T 1965 Analysis of the Ionization of Cesium in Tungsten Capillaries *J. Chem. Phys.* **42** 972–890

—— 1988 *Large Ion Beams—Fundamentals of Generation and Propagation* (New York: John Wiley) ISBN 0-471-62557-4

Freeman J H 1963 A New Ion Source for Electromagnetic Isotope Separation *Nucl. Instrum. Methods* **22** 306–316

Humphries S 1990 *Charged Particle Beams* (New York: John Wiley) ISBN 0-471-60014-8

Kaufman H R 1961 An Ion Rocket with an Electron-Bombardment Ion Source *NASA Technical Note TND-585* January 1961

—— 1963 The Electron-Bombardment Ion Rocket *Advanced Propulsion Concepts* vol I (*Proc. 3rd Symp., October 1962*) (New York: Gordon and Breach)

—— 1965 Performance Correlation for Electron-Bombardment Ion Sources, *NASA Technical Note TND-3041* October 1965

Meyerand R G and Brown S C 1959 High Current Ion Source *Rev. Sci. Instrum.* **30** 110–111

Penning F M 1936 Glow Discharge at Low Pressure Between Coaxial Cylinders in an Axial Magnetic Field *Physica* **3** 873–894

—— 1937 A New Manometer for Low Gas Pressures Between 10^{-3} and 10^{-5} Torr *Physica* **4** 71–75

Penning F M and Moubis J H A 1937 A Neutron Source Without Pumping *Physica* **4** 1190–1199

Poeschel R L, Beattie J R, Robinson P A and Ward J W 1979 3-cm Mercury Ion Thruster Technology *AIAA/DGLR 14th Int. Electric Propulsion Conf. (Princeton, NJ, Oct. 30–Nov. 1 1979)* paper 79-2052

Roth J R 1966 Modification of Penning Discharge Useful in Plasma Physics Experiments *Rev. Sci. Instrum.* **37** 1100–1101

—— 1973a Hot Ion Production in a Modified Penning Discharge *IEEE Trans. on Plasma Sci.* **1** 34–45

—— 1973b Energy Distribution Functions of Kilovolt Ions in a Modified Penning Discharge *Plasma Phys.* **15** 995–1005

Wilson R G and Brewer G R 1973 *Ion Beams—With Applications to Ion Implantation* (New York: John Wiley) ISBN 0-471-95000-9

Zinn W H 1937 Low Voltage Positive Ion Source *Phys. Rev.* **52** 655–657

7

Ionizing Radiation Sources

Many sources of high-energy ionizing radiation are either plasma-related or plasma-based. Such sources are finding increasing industrial uses for ion implantation above 300 keV, plasma diagnostics, and the production of intense beams for welding, military weapons, and fusion research. Intense beams and sources of x-rays or neutrons have potential applications for industrial radiography, x-ray lithography, and thickness measurement. In this chapter, we will discuss the principles of operation of some of the conventional and plasma-related ionizing radiation sources which are likely to be encountered in industrial plasma research. The Van de Graaff generator has been discussed in Chapter 3, and will not be repeated here. The 'conventional' particle accelerators of high energy physics will be discussed first, followed by the inductive and resistive spherical plasma pinches, and finally by the plasma focus as an x-ray and neutron source.

7.1 NON-RELATIVISTIC CYCLOTRON

A *cyclotron* includes a large electromagnet, with two large pole-pieces of radius R_{max}. The opening between the pole-pieces forms a large, thin disc perpendicular to which is a magnetic induction B, that can range up to the saturation value of iron, approximately 2.0 T. In this disc-shaped space between the pole pieces is inserted two D-shaped structures, appropriately called 'dees', which are enclosed in a vacuum system. The configuration of these dees is shown in figure 7.1. They consist of two metallic electrodes, each of which forms a semicircular disc cavity, electrically isolated from each other.

In figure 7.1 the cross section XX' shows the plane of a charged particle orbit gyrating in the magnetic field in the hollow cavity formed
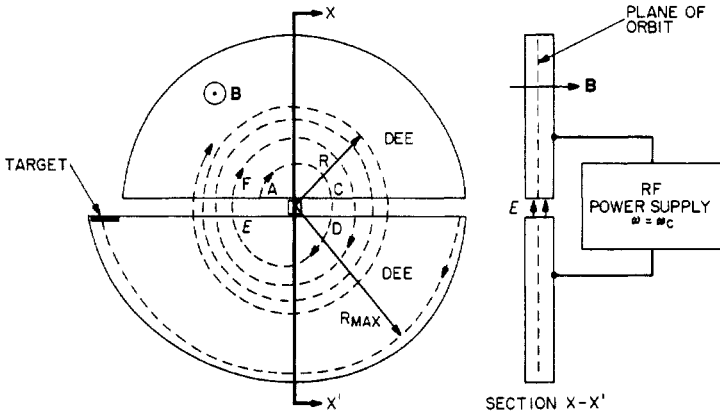
Figure 7.1 The principle of operation of the cyclotron. Two hollow RF electrodes, the dees, are connected to an RF power supply oscillating at the gyrofrequency of the ions in the magnetic induction B.

by the two dees. To the left is a plan view showing as a dotted line the orbit of a resonant ion being accelerated in the cyclotron. The two dees are connected to an RF source which oscillates at the gyrofrequency of the ion in the magnetic field, given by

$$\omega = \frac{qB}{m_0} \qquad \text{(rad/s)}. \qquad (7.1)$$

An ion might start out at position A in figure 7.1, and over half a cycle gyrate from A to C. If the ion is in *resonance*, when it reaches the point C it will find an electric field between the two dees which will accelerate it across the gap CD, thus acquiring an energy equal to the peak RF voltage applied by the power supply. Once the ion reaches the point D, it will again be in an electric field free region, and will gyrate with a constant radius from D to E. Since the ion is in resonance, and has now arrived at the point E half a cycle later, the electric field imposed by the RF power supply will have reversed. Thus, the ion will again be accelerated as it travels from E to F. The resonant ion will acquire an amount of energy equal to twice the peak RF voltage during each cycle of gyration between the dees. Ions which are out of phase with the applied RF voltage will acquire less energy per gyration.

To make this resonance happen, the driving RF electric field should have a frequency

$$\nu = \frac{\omega}{2\pi} = \frac{qB}{2\pi m_0} \qquad \text{(Hz)}. \qquad (7.2)$$

The relationship between the radius and momentum of the ion is given by

$$R = \frac{mv}{qB} = \frac{p}{qB}. \tag{7.3}$$

If the cyclotron is operating at energies low enough to be non-relativistic, one can substitute the rest mass in the center term of equation (7.3). In such a cyclotron, an ion at the radius R will have a non-relativistic kinetic energy given by

$$\mathcal{E} = \frac{1}{2}m_0 v^2 = \frac{p^2}{2m_0} = \frac{q^2 B^2 R^2}{2m_0}. \tag{7.4}$$

The maximum energy which an ion may have is found by substituting the maximum radius of the dees into the right-hand term of equation (7.4). The non-relativistic cyclotron was invented by E O Lawrence and S Livingston circa 1930, and has formed the basis for subsequent developments in high energy physics and accelerator technology.

7.2 RELATIVISTIC CYCLOTRON

The rest energy of a proton is 938 MeV, so as one accelerates protons above approximately 100 MeV, one must take into account relativistic effects. Because of the relativistic mass increase, the RF driving frequency indicated in equation (7.2) must be reduced to keep pace with the gyrofrequency, given by

$$\omega = \frac{qB}{m} = \frac{qB}{m_0}\sqrt{1 - \beta^2} \tag{7.5}$$

where m_0 is the rest mass of the particle. Equation (7.5) may also be written

$$\omega = \frac{qBc^2}{mc^2} = \frac{qBc^2}{m_0 c^2 + \mathcal{E}} \tag{7.6}$$

where $\mathcal{E}$ is the kinetic energy of the particle in joules. Equation (7.6) states that the frequency of a relativistic cyclotron must decrease as the particle acquires energy. This requires pulsed or cyclic operation of such cyclotrons, resulting in bunches of particles arriving at the target.

From equation (7.6), the period of revolution is

$$T = \frac{2\pi}{\omega} = \frac{2\pi}{qBc^2}(m_0 c^2 + \mathcal{E}) \qquad \text{(s)} \tag{7.7}$$

where the *relativistic kinetic energy* is given by

$$\mathcal{E} = \sqrt{(m_0 c^2)^2 + p^2 c^2} - m_0 c^2$$
$$= \sqrt{(m_0 c^2)^2 + (qBRc)^2} - m_0 c^2 \qquad \text{(J)}. \tag{7.8}$$
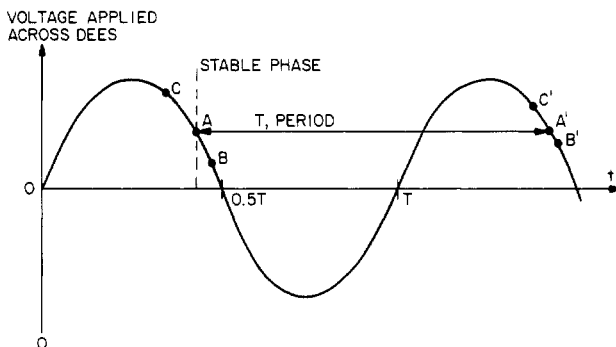
Figure 7.2 An illustration of the principle of phase stability. The sinusoidal voltage applied between the dees is shown as a function of time. If A–A′ is the stable phase, then relativistic effects will cause a particle at the point C to become heavier and slow down to the phase at point C′. A particle at B, which is leading in phase, will acquire less energy as it crosses the gap, and will speed up relative to the other particles.

The relativistic cyclotron is also known as the *FM* (frequency modulated) *cyclotron* or the *synchrocyclotron*. In operation, these devices produce protons up to at least 450 MeV, with a pulsed repetition rate that is typically 60 Hz.

The *principle of phase stability* is very important to the operation of the relativistic cyclotron. Equation (7.7) for the period of an ion in a relativistic cyclotron indicates that as the kinetic energy $\mathcal{E}$ increases, the period also increases. This relativistic increase in period allows the ions being accelerated to bunch up in phase, and stay that way.

The principle of phase stability is illustrated in figure 7.2, where the sinusoidal RF voltage applied across the dees of a relativistic cyclotron is plotted as a function of time. If the stable phase of operation is at the region A–A′ on the waveform, an ion that lags in phase at the point C will experience a higher accelerating gap voltage and will therefore acquire more energy than the ions in the stable phase at point A. Since the ion at C acquires more energy, it will have a longer period due to the relativistic mass increase, landing it at the position C′ after one revolution, closer to the ions in the stable phase at A′. After several revolutions, the ion starting out at point C will asymptotically approach the point of stable phase at A.

If an ion is lagging the stable phase at the point B initially, it will acquire less energy because of the lower accelerating voltage between the dees, thus leading to a shorter period than the stable phase at A′. This shorter period will continue over several cycles, so the ions starting out at point B will asymptotically approach the stable phase A from
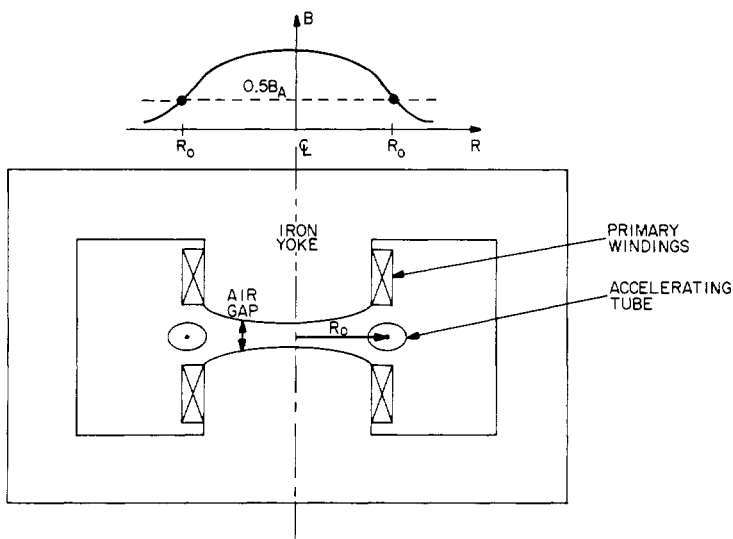
Figure 7.3 Cross section of a betatron. An evacuated accelerating tube of radius R_0 is located just outside the gap of an iron electromagnet, where the average magnetic induction is B_{av}.

below. The principle of phase stability illustrates how relativistic effects bunch particles in a stable phase in a relativistic cyclotron. As one approaches the non-relativistic limit, the stable phase approaches the maximum voltage applied between the dees, V_{max}.

7.3   THE BETATRON

The *betatron* is so-called because it is used to accelerate electrons (beta particles), by an inductive principle different from that of the cyclotron. The configuration of a betatron is shown in figure 7.3. Like the cyclotron, it consists of an electromagnet with an iron yoke, and two pole pieces with an air gap. Unlike the cyclotron, the electrons in a betatron are accelerated in an evacuated tube of constant radius R_0. Energy is transferred to the electrons by a changing magnetic field, rather than a changing RF electric field as in the cyclotron.

At the constant radius R_0, the following relationship must hold between the relativistic momentum p of the electrons, and the magnetic induction B,

$$R_0 = \frac{p}{qB}. \tag{7.9}$$

To keep the radius constant, the magnetic induction B must increase as p increases. The relativistic momentum p is given by

$$p^2c^2 = (mc^2)^2 - (m_0c^2)^2 \tag{7.10}$$

where m_0 is the rest mass. Combining equations (7.9) and 7.10 and solving for the constant radius R_0, one obtains

$$R_0 = \frac{\sqrt{(mc^2)^2 - (m_0c^2)^2}}{qBc}. \tag{7.11}$$

The induced electric field E_θ is given by

$$\oint E \cdot ds = 2\pi R_0 E_\theta = -\frac{\partial \phi}{\partial t} \tag{7.12}$$

where the time-varying magnetic flux is shown on the right-hand side of equation (7.12). The relationship of the magnetic flux at the radius R_0 to the average magnetic field inside the radius R_0 is given by

$$\phi_0 = \int_0^{R_0} 2\pi r B \, dr = \pi R_0^2 B_{av}. \tag{7.13}$$

The angular frequency of electrons circulating in the betatron is given by

$$\omega = \frac{eB_0}{m} \tag{7.14}$$

where the magnetic induction B_0 at the radius R_0 and the average magnetic induction B_{av} are both functions of time, $B_0 = B_0(t)$ and $B_{av} = B_{av}(t)$.

The *betatron condition* for the magnetic induction at the radius R_0 is given by

$$B_0 = \frac{\phi_0}{2\pi R_0^2} = \frac{\pi R_0^2 B_{av}}{2\pi R_0^2} = \frac{B_{av}}{2} \tag{7.15}$$

where equation (7.13) has been inserted for the magnetic flux at the orbital radius R_0. This condition requires that, to maintain the electrons at a constant radius during the acceleration process, the average magnetic induction at the acceleration radius R_0 be equal to one-half the average magnetic induction across the entire orbit of radius R_0. For this reason, the accelerating tube is put slightly outside the pole pieces, where the condition of equation (7.15) can be met. The angular frequency of the electron as it acquires energy is given by substituting equations (7.9) and (7.10) into equation (7.14), and evaluating at the radius R_0,

$$\omega = \frac{c/R_0}{\sqrt{1 + (m_0c/eB_0R_0)^2}}. \tag{7.16}$$

As the magnetic induction B_0 increases, the angular frequency asymptotically approaches a value which is equal to the speed of light divided by the orbital radius.

The electron momentum is given by

$$p = m\omega R_0 = eB_0R_0 \tag{7.17}$$

and the kinetic energy of the electrons in the betatron is given by the relativistic expression

$$\mathcal{E} = \sqrt{(m_0c^2)^2 + (eB_0R_0c)^2} - m_0c^2. \tag{7.18}$$

For very high energies such that $eB_0R_0c \gg m_0c^2$,

$$\mathcal{E} \approx eB_0R_0c \qquad \text{(J)}. \tag{7.19}$$

This expression for the asymptotic energy holds true for all relativistic particle accelerators, and indicates why, if one desires extremely high energies, it is necessary to have either strong magnetic inductions, or very large radii for the machines. Since the value of magnetic induction B_0 is limited by the saturation of iron to about 2 T, and by superconducting magnetic technology to perhaps 6 T, the production of particles of very high energies must be done in machines of very large size, some of which have R_0 on the order of kilometers. Betatrons are never this large, however, as they are used to produce electrons with energies up to approximately 300 MeV.

In betatrons, it is necessary that the electron orbits in the accelerating tube be stable in both the R and Z directions (z normal to the plane of the orbit). In order to assure such stability, the vertical magnetic induction must vary with radius as

$$B(r) = \frac{1}{2}B_{\text{av}}\left(\frac{r}{R_0}\right)^{-n} \qquad r \approx R_0 \tag{7.20}$$

where the parameter n must lie within the range $0 < n < 1.0$. This is a requirement that the magnetic induction decrease with increasing radius in a very specific way, usually accomplished by appropriate shaping of the pole pieces.

7.4 THE SYNCHROTRON

The principle of operation of the *synchrotron* is indicated in figure 7.4. In this device, an accelerating tube of constant radius R_0 contains the
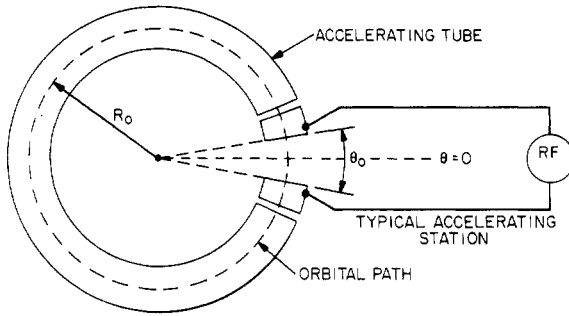
Figure 7.4 Principle of operation of the synchrotron, where electrodes on either side of the gap in the accelerating tube of radius R_0 are driven by the RF frequency ω.

ions to be accelerated, which receive energy from electric fields which appear across one or more gaps, each with an angular extent θ_0, as shown in figure 7.4. An electric field with a variable RF frequency ω is imposed across this gap, with a phase which adds energy to the ions being accelerated. In the synchrotron, it is not necessary to fill the area enclosed by the accelerating tube with magnetic induction, resulting in a significant saving in the cost of these devices, relative to the betatron or the cyclotron. Sufficient vertical magnetic induction, B_0, is provided to balance the centrifugal forces.

If the ion energy in a synchrotron is so high that the velocity is approximately that of light, then the frequency imposed by the RF source is equal to

$$\omega \approx \frac{c}{R_0} = \frac{eB_0}{m} = \frac{eB_0c^2}{(m_0c^2 + \mathcal{E})}. \tag{7.21}$$

This frequency must be reduced as the particle energy $\mathcal{E}$ increases. Like the betatron at high energies, the kinetic energy of ions in the synchrotron is given approximately by

$$\mathcal{E} \approx B_0 e c R_0 \quad \text{(J)}. \tag{7.22}$$

The advantages of the synchrotron are that the betatron condition is not required; there is no magnetic field inside the orbit, making its cost far less than a cyclotron or betatron producing particles of the same energy; and that any loss of energy by radiation, which is very important when accelerating electrons, may be made up by the RF source. Indeed, the limiting energy of electrons can be established by their so-called synchrotron radiation, which arises from the centrifugal acceleration which the electrons experience in their circular orbit.

The kinetic energy of particles in a synchrotron may be written

$$\frac{\mathcal{E}}{m_0 c^2} = \sqrt{1 + \left(\frac{e B_0 R_0}{m_0 c}\right)^2} - 1 \qquad (7.23)$$

and the frequency which must be imposed across the gap is given by

$$\omega = \frac{e B_0/m_0}{\sqrt{1 + (e B_0 R_0/m_0 c)^2}} \qquad (7.24)$$

where B_0 is the vertical magnetic field at the orbit. This magnetic induction must be modulated in a cyclic manner to compensate for the relativistic mass increase, in order to accelerate successive bunches of particles. The synchrotron is capable of accelerating ions or electrons up to energies of GeV.

7.5   INDUCTIVE SPHERICAL PINCH

The *inductive spherical pinch* has been developed by Panarella (1980), and is an outgrowth of inertial magnetic fusion energy research. The plasma generated by the inductive spherical pinch is capable of generating x-rays for soft x-ray lithography of microelectronic circuits and industrial radiography.

A schematic of the inductive spherical pinch is shown in figure 7.5. The plasma is generated in a spherical chamber approximately 10 cm in diameter, which contains either openings for laser irradiation, or two plasma formation electrodes inserted along opposite ends of a diameter. A hot, dense primary plasma is generated by either laser irradiation, or by discharging a capacitor bank across these electrodes through a gas at relatively high pressure. This primary plasma then expands to fill a significant volume of the spherical cavity. Before the expansion of this primary plasma proceeds too far, a second capacitor bank is discharged through an array of zonal conductors on a spherical shell outside the plasma volume, like the geometry shown in figure 7.6. The fast-rising currents in this spherical shell induce large image currents on the outer surface of the primary plasma, producing spherical shock waves which converge radially inward, compressing and further heating the primary plasma. After this secondary shock heating and compression, the plasma is suffcently hot and dense to produce an intense source of x-rays, until the plasma re-expands and cools.

The driving circuit for the inductive spherical pinch is based on capacitive energy storage at high voltage. A schematic of the driving
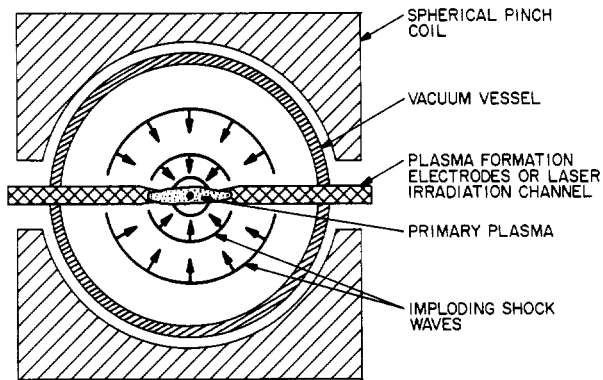
Figure 7.5 Operation of the inductive spherical pinch. A hot, dense plasma is created by an intense arc between the plasma formation electrodes. After an appropriate delay, large currents flow in the spherical pinch coil, inducing spherical shock formation at the outer surface of the plasma. The imploding shock waves heat and compress the pre-formed plasma.
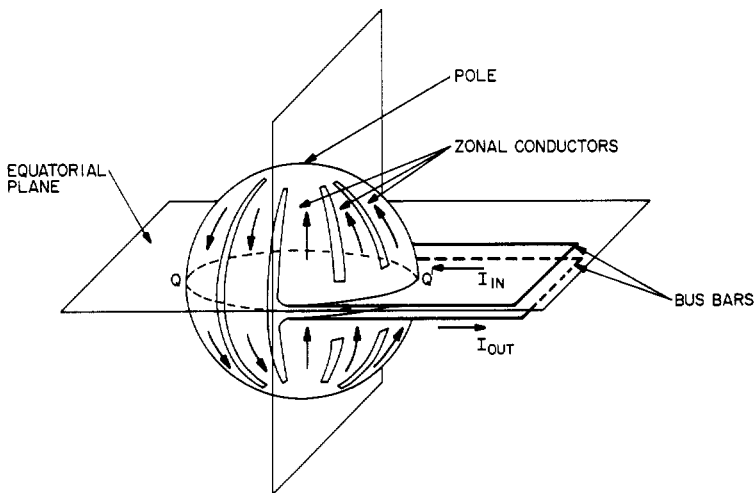
Figure 7.6 The inductive theta pinch, in which a rapidly rising current pulse in the zonal conductors located on a spherical surface induce currents on the surface of a spherical plasma. This results in heating and compression to conditions which produce x-rays.

circuit for the primary arc-formed plasma is shown in figure 7.7. Proper timing of the implosion circuit with respect to the plasma formation arc or laser is crucial to the successful operation of the inductive spherical pinch (Panarella 1980, Panarella and Savic 1983, Gupta *et al* 1982).
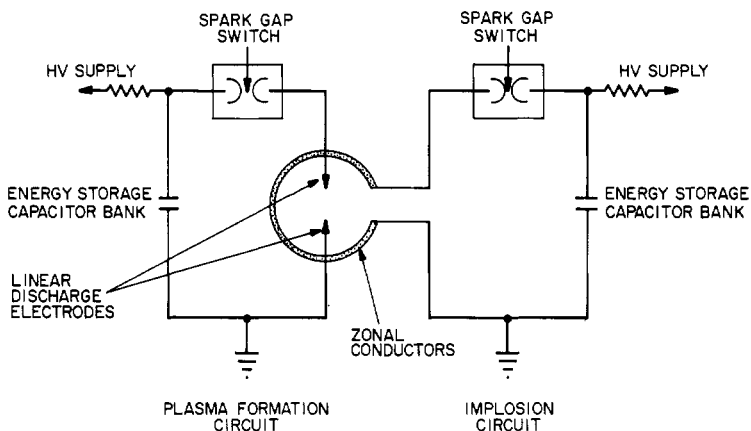
Figure 7.7 Firing circuit for the inductive spherical pinch plasma. A dense plasma is pre-formed with the pulsed arc discharge powered by the circuit on the left; an inductively created shock wave is generated by the circuit on the right, further heating and compressing the pre-formed plasma.

By adjusting the type of gas used to form the plasma, the background pressure, the delay between the formation of the primary plasma and the compression, and the profile of the current pulse compressing the plasma, one may obtain x-ray pulses of various durations, spectral widths, and intensities. The inductive spherical pinch has been used as the basis for a soft x-ray source.

7.6 RESISTIVE SPHERICAL PINCH

A device related to the inductive spherical pinch is the *resistive spherical pinch*, a schematic of which is shown in figure 7.8. The plasma generated by the resistive spherical pinch is capable of generating neutrons from appropriate fusionable gases, for application to industrial neutron radiography, nuclear weapons simulation, and scientific applications.

The resistive spherical pinch plasma shown in figure 7.8 is generated in a spherical chamber approximately 10 cm in diameter, which has numerous resistive arc electrodes spaced over its surface, as shown in figure 7.9, and two plasma formation electrodes inserted along a radius of the sphere. A hot deuterium primary plasma is generated by discharging a capacitor bank across these electrodes at relatively low pressures of deuterium gas, using the circuit shown in figure 7.10.

Before the primary plasma expands too far, a second capacitor bank is discharged across pairs of arc electrodes located at the outer surface of the spherical cavity. The sudden energy addition on the plasma
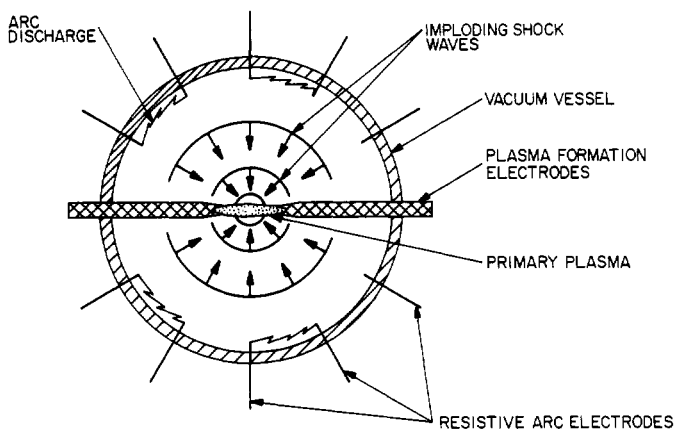
Figure 7.8 Operation of the resistive spherical pinch. A preformed plasma is generated by a linear arc between two plasma formation electrodes. This plasma is further compressed and heated by spherically converging shock waves, generated by arcs across multiple pairs of electrodes.
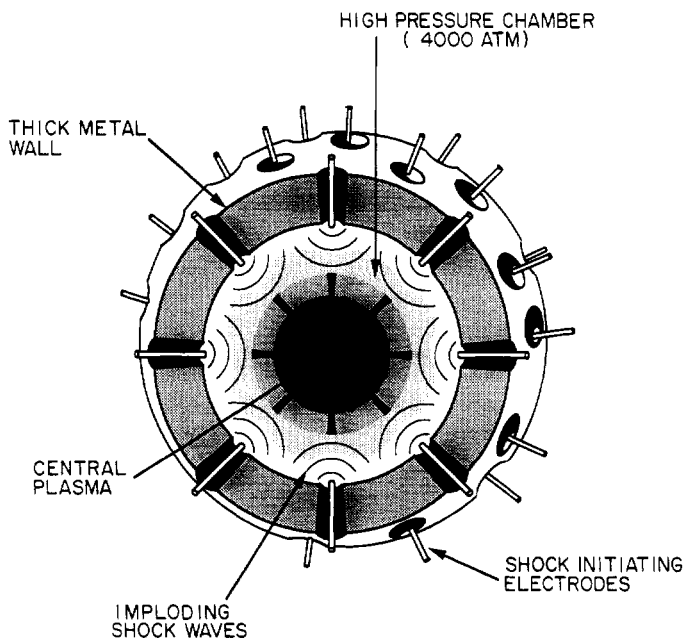
Figure 7.9 The resistive spherical pinch, in which arcs simultaneously struck across a large number of electrodes located on a spherical surface initiate a radially imploding shock wave that heats and compresses deuterium to the point where fusion reactions occur.
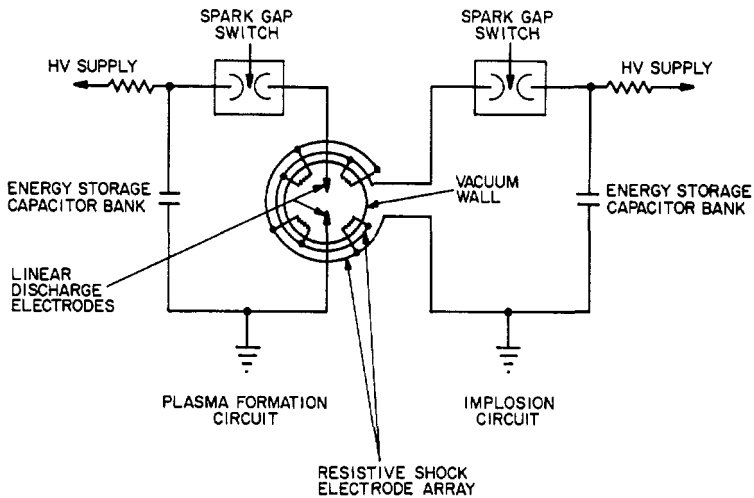
Figure 7.10 Firing circuit for the resistive spherical pinch. A pre-formed plasma is created by discharging the plasma formation circuit on the left across two electrodes. This plasma is further compressed and heated by converging spherical shock waves generated by arc discharges between multiple pairs of electrodes on a spherical surface.

surface induces a spherical shock wave which converges radially inward, compressing and further heating the primary plasma. If the initial gas is deuterium at relatively low pressures (relative to the inductive spherical pinch), a fusion-grade plasma is formed which is capable of producing intense pulses of 2.45 MeV neutrons.

Like the inductive spherical pinch, the driving circuit of the resistive spherical pinch is based on two capacitor banks, one to generate the primary deuterium plasma, and one to compress it. The timing of the resistive compression shock relative to the primary plasma formation discharge is crucial to the proper operation of the resistive spherical pinch.

The inductive and resistive spherical pinches differ in at least two fundamental ways from the cylindrical theta pinch from which they evolved. One significant difference is their spherical geometry, which precludes the axial end losses of the theta pinch. A second significant difference is the flexibility to adjust the time delay between forming the primary plasma and the shock heating and compression in the spherical pinch. In the classical theta pinch, plasma formation, heating, and compression are done in one unitary process, without the flexibility to adjust their relative timing.
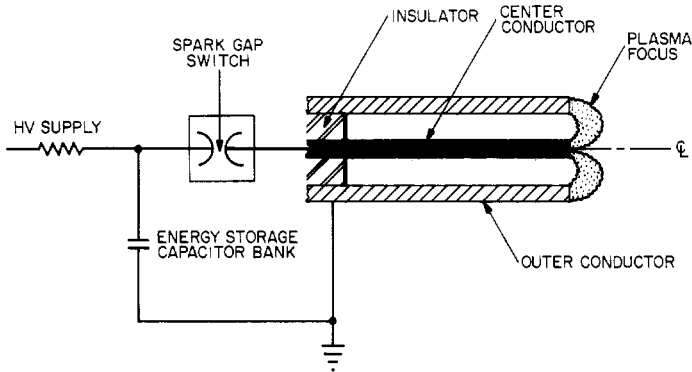
Figure 7.11 The plasma focus x-ray/neutron source. High voltage switched on between coaxial electrodes forms an axisymmetric arc, which is pinched down to high densities and temperatures by large currents to form a plasma focus.

7.7 PLASMA FOCUS

The plasma focus was originally developed as a pulsed source of intense x-rays with potential applications to weapons simulation. A schematic of the plasma focus is shown in figure 7.11. The plasma focus is formed at the end of coaxial electrodes which are connected to a high voltage capacitor bank by a spark gap switch. When the high voltage appears across the gap at the end of the electrodes, an umbrella-shaped axisymmetric plasma is formed from the electrode material, or from gases absorbed in the electrodes. The large currents between the electrodes first cause the plasma to expand as a result of ohmic plasma heating, and then to collapse into a very small volume immediately in front of the center electrode as a result of a Bennett pinch-like mechanism. This dense plasma focus is capable of producing MeV x-rays, energies hundreds of times greater than typical voltages applied between the electrodes. If the electrodes are doped with a fusionable species such as deuterium, the plasma focus can produce an intense burst of neutrons from DD reactions.

REFERENCES

Gupta R P, Panarella E and Silvester P 1982 A Finite Element Analysis of the Plasma Pinched In Three Dimensions, in: Gallagher R H, Norrie D H, Oden J T and Zienkiewicz O C (ed) *Finite Elements in Fluids* vol 4 (New York: John Wiley) ch 25, pp 551–572

Panarella E 1980 Quasi-Spherical Compression of a Spark-Channel Plasma *Can. J. Phys.* **58** 983–999

Panarella E and Savic P 1983 Scaling Laws For Spherical Pinch Experiments *J. Fusion Energy* **3** 199–213

8

Dark Electrical Discharges in Gases

In this and the following two chapters, we will proceed to examine the operating regimes of the DC electrical discharge illustrated in figure 4.12 and listed on table 4.4, starting with the dark discharge on the left and moving toward the arc discharge on the right. The *dark discharge* receives its name from the fact that, with the exception of the more energetic corona discharges, it does not emit enough light to be seen by a human observer. The number density of excited species is so small in this regime that what little excitation light is emitted is not visible. The dark discharge regime shown in figure 4.12 is shown separately on figure 8.1. Dark discharges have five phenomenological divisions. They are, in order of increasing current density: *background ionization; the saturation region; the Townsend discharge; corona discharges; and sparking or electrical breakdown*.

8.1 BACKGROUND IONIZATION

The dominant physical process in the *background ionization* division from A to B in figure 8.1 is the sweeping out, by the electric field along the axis of the discharge tube, of ions and electrons created by ionization from background radiation. Such radiation, from cosmic rays, radioactive minerals in the surroundings, or other sources, is capable of producing a constant and measurable degree of ionization in air at atmospheric pressure.

   The existence of this ionization can be demonstrated by a classic experiment with a gold-leaf electroscope, shown in figure 8.2. This is an instrument containing two flexible pieces of gold foil which are undisturbed by air currents inside a glass jar, as shown in figure 8.2(*a*). When the electroscope is charged by bringing a positively charged wand
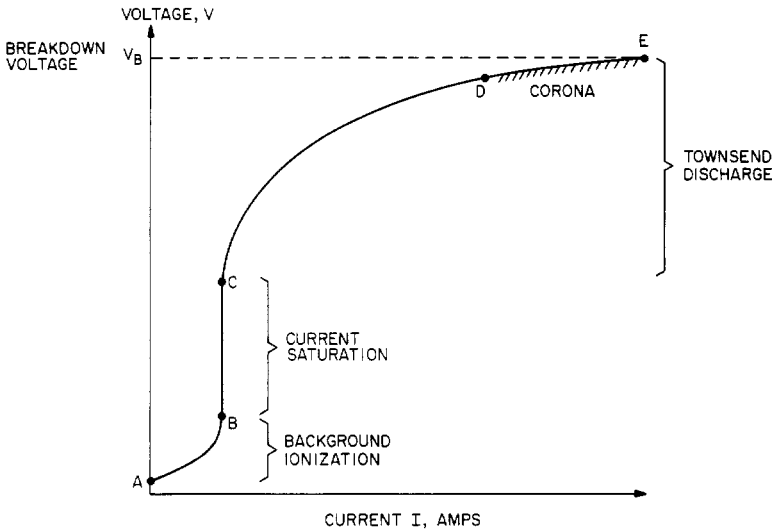
Figure 8.1 Regions of the dark discharge regime.

in contact with the center conductor, the charges on the two pieces of gold foil repel each other, spreading the foils apart by an angle which is proportional to the charge on the surface. After a length of time, which is measured in minutes or hours, ions and electrons generated by background radiation in the atmospheric air surrounding the gold foils will migrate to the foils and neutralize the surface charges on them until the electroscope is discharged, as shown in figure 8.2(*b*). This same ionization process is active in a classical DC low pressure dark discharge like that shown in figure 8.3. When an electric field is imposed along the axis of such a cylindrical discharge tube, the ion and electron pairs formed by ionizing radiation migrate to the electrodes in the imposed electric field, giving the weak current illustrated from A to B in figure 8.1.

8.2 SATURATION REGIME

If the voltage between the electrodes on the DC low pressure discharge tube of figure 8.3 is increased far enough, eventually all the available ions and electrons produced in the volume between the electrodes will be collected, leading to saturation of the current between the points B and C on figure 8.1. In this saturation region, the current remains constant while the voltage is increased. If the volumetric source of ions and electrons from ionizing radiation is given by the *source strength*, *S*, it can be written

$$S = \frac{dn}{dt} \quad \text{(electrons or ions/m}^3\text{-s)}. \quad (8.1)$$
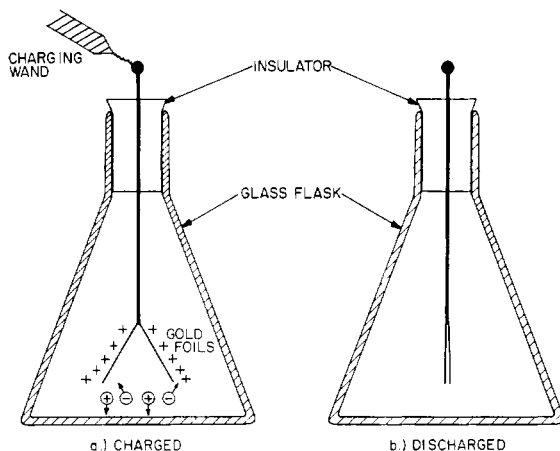
Figure 8.2 Discharge of a gold-leaf electroscope, designed to illustrate the ionization of air by cosmic rays and background radiation.
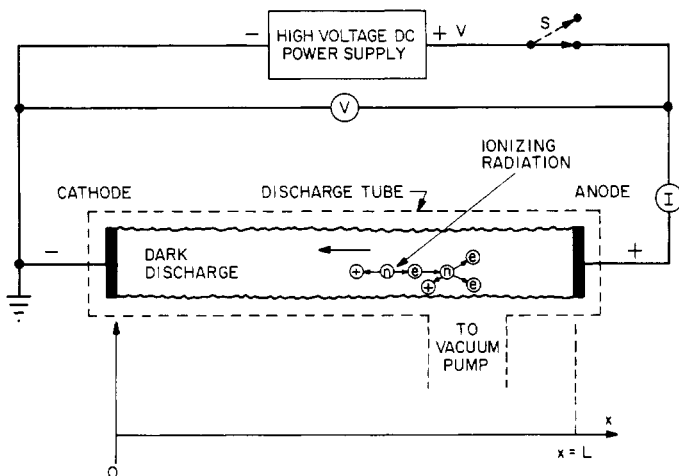
Figure 8.3 Schematic of a classical DC low pressure dark discharge configuration.

The saturation current is given by

$$I_S = AdeS \quad (A) \tag{8.2}$$

where A is the cross-sectional area of the discharge, and $d = L$ is the length of the discharge shown on figure 8.3. The total currents involved in equation (8.2) are typically of the order of picoamperes or nanoamperes. These currents are independent of the applied voltage, but

linearly dependent on the radiation source strength, S, a regime useful in some radiation counters. The saturation current density J_s is given by

$$J_S = \frac{I_S}{A} = edS \qquad (\text{A/m}^2). \qquad (8.3)$$

8.3   TOWNSEND DISCHARGE

Processes of industrial importance occur in the *Townsend discharge* (John Sealy Edward Townsend (1865–1957)), including corona and the electrical breakdown of dielectric gases, and for this reason we will study it at length. Consider an analysis for which the electric field E is constant along the axis of the low pressure discharge tube shown on figure 8.3. In such a discharge, consisting of two parallel plates with a uniform electric field between them, additional electrons can arise from photo- or secondary electron emission from the cathode, with a flux given by

$$\Gamma_{e0} \qquad (\text{electrons/m}^2\text{-s}). \qquad (8.4)$$

A second, volume ionization source can be present, due to ionization of the background gas by energetic electrons accelerated in the electric field. This volume source may be written

$$S_e = R_e = n_e n_0 \langle \sigma v \rangle_{ne} \qquad (\text{electrons or ions/m}^3\text{-s}) \qquad (8.5)$$

where n_0 is the neutral number density, and $\langle \sigma v \rangle_{ne}$ is the Maxwellian-averaged reaction rate coefficient for electron–neutral impact ionization.

8.3.1   Current Growth

If the voltage across the low pressure discharge tube of figure 8.3 is increased beyond point C on figure 8.1, the current will rise exponentially. The physical process responsible for this is indicated in figure 8.3. The electrons initially produced in the creation of ion–electron pairs by ionizing radiation or from other sources are accelerated in the electric field of the discharge tube. If the electric field is high enough, the electrons can acquire sufficient energy before reaching the anode to ionize another neutral atom. As the electric field becomes stronger, these secondary electrons may themselves ionize a third neutral atom, thus leading to a chain reaction, or *avalanche* of electron and ion production. This region of exponentially increasing current between C and E on figure 8.1 is called the *Townsend discharge*.

8.3.2 Townsend's First Ionization Coefficient

We analyze the Townsend discharge with a time-honored formalism, based on *Townsend's first ionization coefficient*, α, which is the number of ionizing collisions made on the average by an electron as it travels one meter along the electric field. The parameter α has the units of ion–electron pairs per meter, and in terms of kinetic theory parameters, is related to the mean free path for ionization as follows:

$$\alpha \sim \frac{1}{\lambda_i} = \frac{\nu_{ei}}{\bar{v}_e} = \frac{n_0 \langle \sigma v \rangle_{ne}}{\bar{v}_e}. \tag{8.6}$$

A situation of great practical importance is that in which initiating electrons are emitted from the cathode, with no significant contribution by volume ionization. In the geometry of figure 8.3, at a distance x from a cathode emitting Γ_{e0} electrons per square meter per second, the differential electron flux resulting from the impact of electrons between x and $x + dx$ is given in terms of Townsend's first ionization coefficient as

$$d\Gamma_e = \alpha \Gamma_e \, dx. \tag{8.7}$$

If no recombination or loss of electrons occurs as they move along the axis, we can obtain the total electron flux by integrating from $x = 0$ to x,

$$\int_{\Gamma_{e0}}^{\Gamma_e} \frac{d\Gamma_e}{\Gamma_e} = \int_0^x \alpha \, dx. \tag{8.8}$$

Usually the mean free path for ionization is not a function of x, so α is independent of x, allowing equation (8.8) to be integrated directly, to yield

$$\Gamma_e = \Gamma_{e0} e^{\alpha x} \qquad \text{(electrons/m}^2\text{-s)}. \tag{8.9}$$

The electrons from the cathode which initiate the exponential build-up of current along the discharge are *primary electrons*, and Γ_{e0} is the *primary electron flux*. The current density in the discharge is found by multiplying both sides of equation (8.9) by the electronic charge, to yield

$$J_e = e\Gamma_e = J_{e0} e^{\alpha x} \qquad \text{(A/m}^2\text{)}. \tag{8.10}$$

The total electron current is found by multiplying equation (8.10) by the cross-sectional area of the discharge, A,

$$I_e = I_{e0} e^{\alpha x} = A J_{e0} e^{\alpha x} \qquad \text{(A)}. \tag{8.11}$$

Equation (8.11) indicates that the current flowing between two parallel plates with an applied voltage across them will increase exponentially

as the distance between the plates is increased. This is experimentally observed, and is used to measure the coefficient α.

If there is a significant volume source of electrons throughout the discharge volume, S_e electrons per cubic meter per second, with no cathode emission, then the increase in electron flux between x and $x + dx$ is the sum of two processes; electrons produced by ionization in the electric field as before, and the volume source. These two processes can be expressed in the form

$$d\Gamma_e = \alpha \Gamma_e dx + S_e dx \qquad (8.12)$$

where it has been assumed that $\Gamma_{e0} = 0$ at $x = 0$, because there is no cathode emission. Rearranging, and integrating from the cathode to the point x, one obtains

$$\int_0^{\Gamma_e} \frac{d\Gamma_e}{\alpha \Gamma_e + S_e} = \int_0^x dx = \left. \frac{\ln(\alpha \Gamma_e + S_e)}{\alpha} \right|_0^{\Gamma_e}. \qquad (8.13)$$

The resulting electron flux is

$$\Gamma_e = \frac{S_e}{\alpha}(e^{\alpha x} - 1) \qquad \text{(electrons/m}^2\text{-s)}. \qquad (8.14)$$

and the electron current density becomes

$$J_e = e\Gamma_e = \frac{eS_e}{\alpha}(e^{\alpha x} - 1) \qquad \text{(A/m}^2\text{)}. \qquad (8.15)$$

Writing this equation in terms of the saturation current of equation (8.3) yields

$$J_e = \frac{J_S}{\alpha d}(e^{\alpha x} - 1) \qquad \text{(A/m}^2\text{)}. \qquad (8.16)$$

The coefficient in equation (8.16) can be written with the help of equation (8.5) as

$$\frac{J_S}{\alpha d} = \frac{eS_e}{\alpha}. \qquad (8.17)$$

We will next derive an analytical expression for Townsend's first ionization coefficient, which has proven very useful in describing the characteristics of electrical discharges. Townsend's first ionization coefficient is equal to the number of ionizing mean free paths per meter and is therefore related to the probability of an electron traveling an axial distance greater than the *ionizing distance* x_i. If the electrons have

an ionizing mean free path λ_i, with $\lambda_i d = L$, the discharge length, the number of mean free paths per meter is given by

$$\# \text{ mean free paths/meter} = \frac{1}{\lambda_i}. \tag{8.18}$$

The primary electrons, initially of number density n_{e0}, will be exponentially attenuated as they move through the gas, giving the probability of an electron having an ionization distance x greater than a length x_i given by

$$\frac{n_e(x)}{n_{e0}} = \exp\left(-\frac{x_i}{\lambda_i}\right). \tag{8.19}$$

Townsend's first ionization coefficient, α, is the probable number of ionizing collisions per meter of travel, or, using equations (8.18) and (8.19), the product of the number of mean free paths per meter, and the probability of an electron having a free path greater than x_i,

$$\alpha = \frac{1}{\lambda_i}\frac{n_e(x)}{n_{e0}} = \frac{1}{\lambda_i}\exp\left(-\frac{x_i}{\lambda_i}\right). \tag{8.20}$$

Using equation (8.6), we can write

$$\frac{1}{\lambda_i} = \frac{n_0\langle\sigma v\rangle_i}{\bar{v}_e} = Ap \tag{8.21}$$

where A is a constant which depends on the electron kinetic temperature and the type of gas and p is the pressure in newtons per square meter. Substituting equation (8.21) into equation (8.20) yields

$$\alpha = Ap\exp(-Apx_i). \tag{8.22}$$

In the distance x_i, an electron can gain enough energy from the electric field E to ionize the background gas with an *effective ionization potential* $V^* > V_i$, where V_i is the actual ionization potential. The effective ionization potential is greater than the actual ionization potential because an electron will lose energy by elastic and inelastic (excitation) collisions, as well as ionization. If an electron travels the distance x_i in making this ionization,

$$x_i \approx \frac{V^*}{E}. \tag{8.23}$$

Substituting equation (8.23) into equation (8.22) yields

$$\frac{\alpha}{p} = A\exp\left(-\frac{AV^*}{E/p}\right) = A\exp\left(-\frac{C}{E/p}\right). \tag{8.24}$$

Table 8.1 Phenomenological constants A and C of Townsend's first ionization coefficient for selected gases, as given by equation (8.24) for the range of validity $C/2 \leqslant E/p \leqslant 3C$.

Gas	A ion pairs/m-Torr	C V/m-Torr
A	1200	20 000
Air	1220	36 500
CO_2	2000*	46 600
H_2	1060	35 000
HCl	2500*	38 000
He	182	5 000
Hg	2000	37 000
H_2O	1290*	28 900
Kr	1450	22 000
N_2	1060	34 200
Ne	400	10 000
Xe	2220	31 000

* These values may be high by as much as a factor of two.

We have followed the existing literature in combining the product AV^* into the parameter C. Equation (8.24) is the canonical form of *Townsend's first ionization coefficient*. Note that the ratio on the left, α/p, is a function only of the ratio of the electric field and the pressure,

$$\frac{\alpha}{p} = f\left(\frac{E}{p}\right) \qquad \text{(ion–electron pairs/m-Torr)} \qquad (8.25)$$

a result first derived by Townsend. The parameter C is related to A and the effective ionization potential V^* by the relation

$$C \equiv AV^*. \qquad (8.26)$$

The parameters A and C must be experimentally determined. In general, these parameters hold only over a limited range of the plasma parameters and are different for each gas. These parameters, taken from references in which the gases probably were not contaminated by mercury vapor, are shown in table 8.1. Also indicated is their general range of validity, approximately $C/2 \leqslant E/p \leqslant 3C$.

8.3.3 Measurement of α/p and E/p

The experimental measurement of the constants in table 8.1, and of the ratio α/p as a function of the ratio E/p, is based upon equation (8.11),
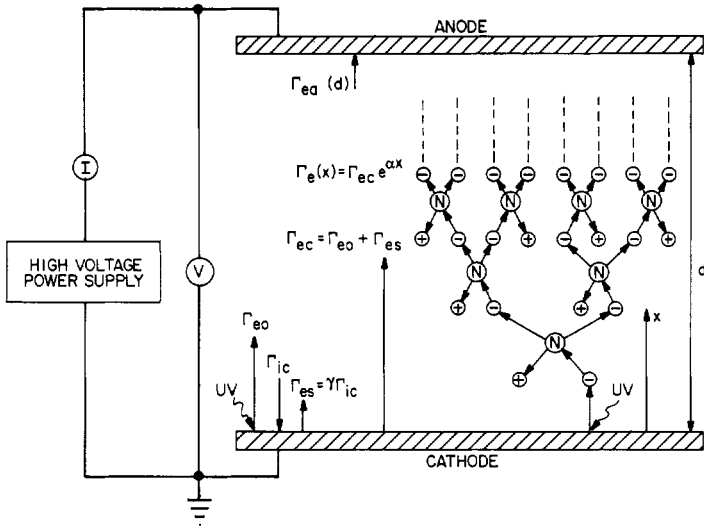
Figure 8.4 A parallel plate configuration in the dark discharge regime.

which predicts that in a geometry like that shown in figure 8.4, the current flowing between the plates will increase exponentially as the separation of the plates increases. Equation (8.25) implies that such a measurement should be made at a constant electric field, and this is therefore the procedure for experimental measurements of α/p as a function of E/p. In the geometry of figure 8.4, the voltage across the plates is adjusted to maintain a constant electric field, while the current I is monitored as the separation of the plates increases. This will produce a straight line on a semilogarithmic plot of the data, the slope of which is a function of the electric field between the plates. This procedure is repeated for a range of pressures and electric fields, to produce experimental data for a particular gas. Many early experiments (prior to 1960) used vacuum pumps and/or vacuum gauges based on liquid mercury, and the gases were therefore seriously contaminated by mercury vapor. This contamination invalidated many of these early measurements.

Figure 8.5 shows schematically the straight lines on a semilogarithmic plot which result from the type of experiment just described for two values of E/p. The straight line relation on such a graph, reflecting the functional dependence of equation (8.11), usually breaks down at high values of the electrode separation or discharge current for one of two reasons. The production of *secondary electrons* from the cathode surface will increase the current above the levels arising from the gas itself, leading to the increase indicated by the curves labeled A in figure 8.5. A contrary process is the *attachment* of electrons, the removal of electrons from the exponentially increasing cascade of current by attachment
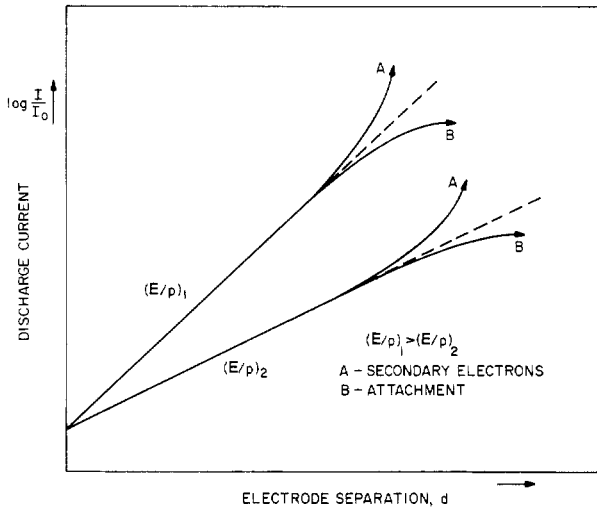
Figure 8.5 A schematic showing the current drawn between parallel electrodes like those illustrated in figure 8.4, as a function of electrode separation, for two different values of the ratio E/p. Departures from linearity result from: (A) secondary electron emission from electrodes, and (B) attachment processes in the gas which take free electrons out of circulation.

to background atoms or molecules in the gas. When such attachment occurs, the current between the plates falls below the values predicted by equation (8.11), as shown on the curves labeled B in figure 8.5.

Some experimental data for the ratio of α/p as a function of E/p for various gases is shown in figure 8.6. These data have been taken from various sources, and all appear to be free of mercury contamination in the original experiments which produced them.

8.3.4 Stoletow Point

In 1890, Stoletow found that, in an experiment of the kind shown on figure 8.4, if the electric field between the plates remained constant, then there is a pressure in the Townsend discharge where the current is a maximum. As will be shown later, this pressure is related to the electrical breakdown of the gas, and has great practical importance. In his experiments on air, Stoletow found that the pressure for maximum current is

$$p_{max} = \frac{E}{37\,200} \text{ Torr} \tag{8.27}$$

where the electric field E is in volts per meter. This pressure has been designated the *Stoletow point*.
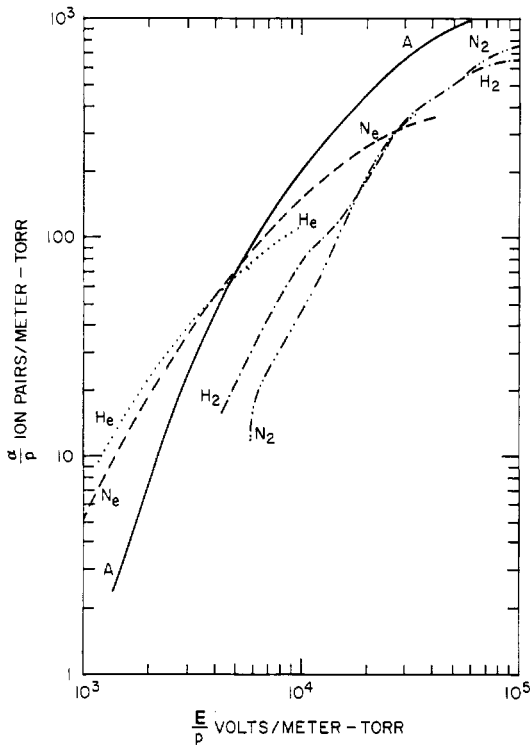
Figure 8.6 Townsend's first ionization coefficient α/p as a function of E/p for selected gases and from data sets which should not be contaminated by mercury vapor, from Cobine (1958).

Townsend discharge theory allows this pressure for maximum current to be predicted. If the separation, d, between the plates is fixed, equation (8.11) predicts that the current is a maximum when Townsend's first ionization coefficient α is a maximum. Differentiating equation (8.25) to find this point yields

$$\frac{d\alpha}{dp} = \frac{d}{dp}\left[pf\left(\frac{E}{p}\right)\right] = 0. \tag{8.28}$$

Performing the differentiation on the right, one obtains

$$f\left(\frac{E}{p}\right) - \frac{E}{p}f'\left(\frac{E}{p}\right) = \frac{\alpha}{p} - \frac{E}{p}f'\left(\frac{E}{p}\right) = 0. \tag{8.29}$$

This can be arranged to yield the condition for the maximum value of α as a function of pressure,

$$\left(\frac{\alpha/p}{E/p}\right) = f'\left(\frac{E}{p}\right) = \tan\theta. \tag{8.30}$$
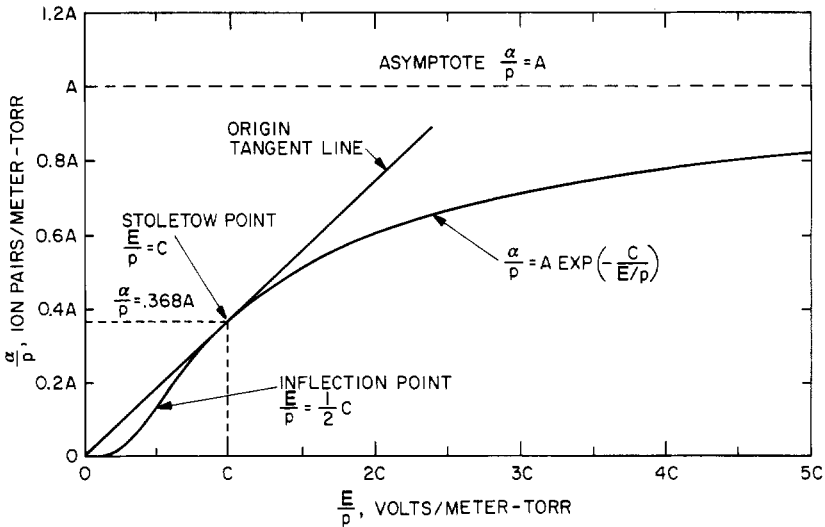
Figure 8.7 The theoretical expression for Townsend's first ionization coefficient, given by equation (8.24), plotted against the normalized value E/p with major features of the curve indicated.

Equation (8.30) predicts that where the tangent to the α/p versus E/p curve intersects the origin, the current will be a maximum. This is the Stoletow point, which can be found by graphical construction, as will be illustrated shortly.

Using Townsend's relation for Townsend's first ionization coefficient, equation (8.24) can be rewritten in the form

$$\alpha = pA \exp\left(-\frac{Cp}{E}\right). \qquad (8.31)$$

To find the value of the pressure at which α is a maximum, we differentiate equation (8.31), to obtain

$$\frac{d\alpha}{dp} = A\left[1 - \frac{pC}{E}\right]\exp\left(\frac{-Cp}{E}\right) = 0 \qquad (8.32)$$

so the maximum value of α occurs when the expression in the square bracket is zero,

$$p_{max} = \frac{E}{C} = \frac{E}{36\,500} \qquad (8.33)$$

using the value of C for air in table 8.1. This result is in excellent agreement with Stoletow's empirical result given in equation (8.27). The Stoletow point is the minimum of the Paschen breakdown curve for gases, discussed at the end of this chapter.

Table 8.2 Stoletow constants of selected gases.

Gas	$(E/p)_{\text{opt}} = C$ (V/m-Torr)	$(\alpha/p)_{\text{opt}}$ (ion pairs/ m-Torr)	η_{min} (eV/ion –electron pair)	$V^* = C/A$ (eV/ion –electron pair)	V_i (eV)
A	20 000	443	45	16.7	15.7
Air	36 500	449	81	30	—
CO_2	46 600	736	63	23	13.7
H_2	35 000	390	90	33	15.4
HCl	38 000	920	41	15	—
He	5 000	67	75	28	24.5
Hg	37 000	736	50	19	10.4
H_2O	28 900	475	61	22	12.6
Kr	22 000	532	41	15.2	14
N_2	34 200	390	88	32	15.5
Ne	10 000	147	68	25	21.5
Xe	31 000	818	38	14	12.1

The physical significance of the Stoletow point described by equation (8.30) or by equation (8.33) may be illustrated with the aid of a plot of Townsend's first ionization coefficient, described by equation (8.24) and plotted in dimensionless units of A and C in figure 8.7. On this figure it is apparent that the tangent to α/p which goes through the origin, described mathematically by equation (8.30), is tangent at the point where E/p equals C, the Stoletow point. Other characteristic features of equation (8.24) for Townsend's first ionization coefficient are that the value of α/p approaches the value A asymptotically for very large values of E/p; and that the relationship for α/p has an inflection point at $E/p = C/2$, a relationship which can be verified by setting the second derivative of equation (8.24) equal to zero. In addition, the Stoletow point occurs at a value of $\alpha/p = e^{-1}A = 0.368A$.

The Stoletow constants have been determined for many gases, a few of the more reliable values of which are shown in table 8.2. Shown on this table for each gas are the optimum value of $E/p = C$, the value of α/p at which the Stoletow point occurs; and the inverse of equation (8.30), given by

$$\left(\frac{E}{\alpha}\right)_{\text{max}} = \cot\theta = \eta \qquad \text{(eV/ion–electron pair)} \qquad (8.34)$$

where η is the *energy cost* of generating an ion–electron pair in the gas. From equation (8.34), it is clear that the Stoletow point occurs when the cost in energy of generating an ion–electron pair is a minimum. This is

Figure 8.8 Townsend's first ionization coefficient as a function of E/p for argon gas. The solid line is based on equation (8.24) and the constants of table 8.1; the crosses are experimental data taken from Loeb (1961), page 692.
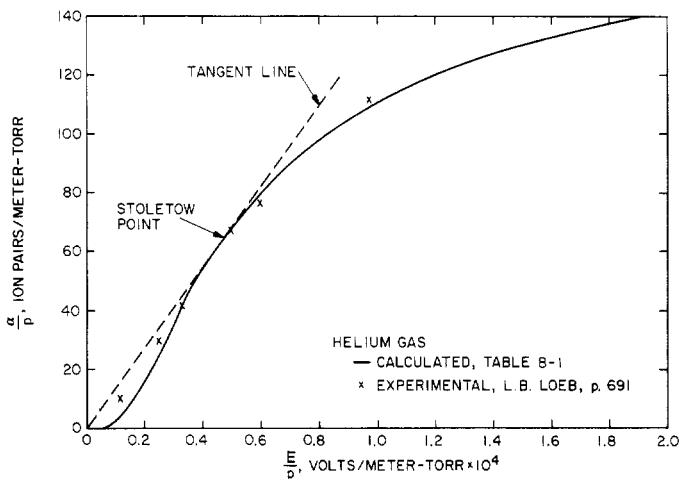
Figure 8.9 Townsend's first ionization coefficient as a function of E/p for helium gas. The solid line is the theoretical expression from equation (8.24) using the constants from table 8.1. The crosses are experimental data from Loeb (1961), page 696.

compared in table 8.2 with V^*, the effective ionization potential, which is equal to the ratio C/A. In the last column of table 8.2 is the actual ionization potential of the gas in question. As might be expected, the
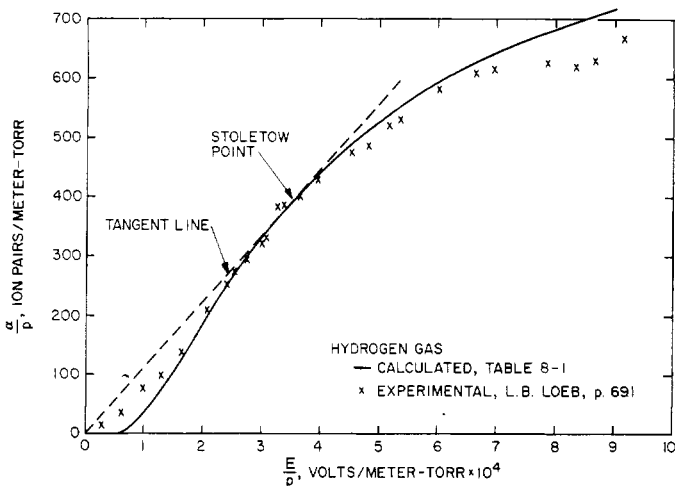
Figure 8.10 Townsend's first ionization coefficient as a function of E/p for hydrogen gas. The solid line is the value calculated from equation (8.24), using the constants from table 8.1. The crosses are experimental data taken from Loeb (1961), page 691.

number of electronvolts required to produce an ion–electron pair at the Stoletow point is in all cases larger than either the effective or the actual ionization potential of the gas, since the latter quantities are the energy cost of a single collisional event.

On figures 8.8 through 8.12 are experimental data for five different gases in which the experimentally measured values of α/p are plotted against the experimentally determined value of E/p, represented by the crosses. These experimental data have been taken from Loeb (1961). Also plotted on these graphs are the 'theoretical' values of α/p, given by equation (8.24), using the values of the constants A and C from table 8.1. These experimental curves all display a general functional dependence consistent with equation (8.24), but for some gases, the experimental values away from the Stoletow point diverge from the theoretically predicted values. Whether this is a real effect, or a result of contamination of the gases used in the original experiments, is not clear.

8.4 CORONA DISCHARGES

Corona, sometimes referred to as a *unipolar discharge*, is a phenomenon characteristic of Townsend dark discharges which occurs in regions of high electric field near sharp points, edges, or wires in electrically stressed gases prior to the point of electrical breakdown (Bartnikas and McMahon 1979, Loeb 1965). If the coronal currents are relatively high, corona can
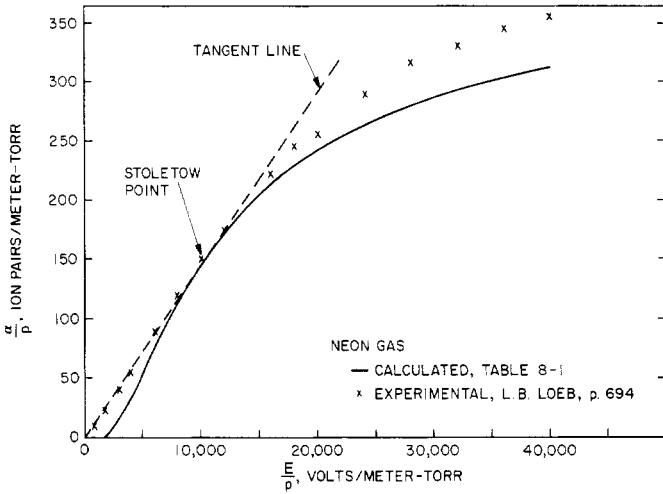
Figure 8.11 Townsend's first ionization coefficient as a function of E/p for neon gas. The solid line is calculated from equation (5.24) using the constants in table 8.1. The crosses are experimental data taken from Loeb (1961), page 694.
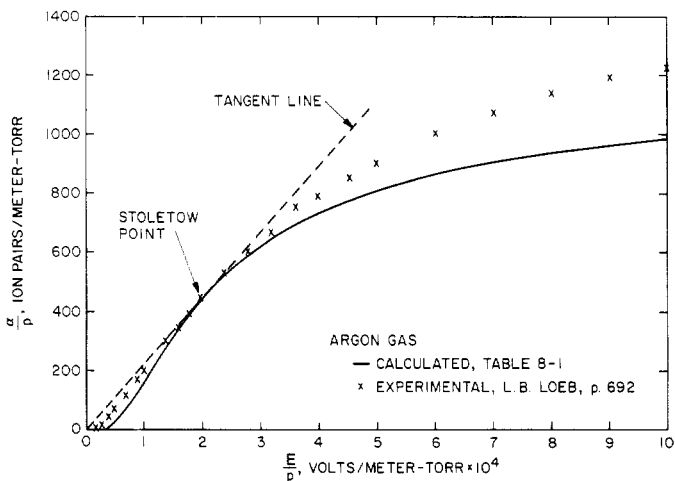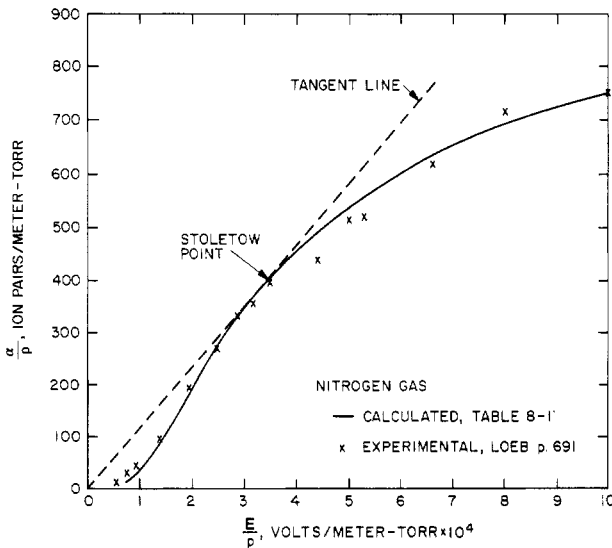

Figure 8.12 Townsend's first ionization coefficient as a function of E/p for nitrogen gas. The solid line is calculated from equation (8.24), with the constants in table 8.1; the crosses are experimental data taken from Loeb (1961), page 691.
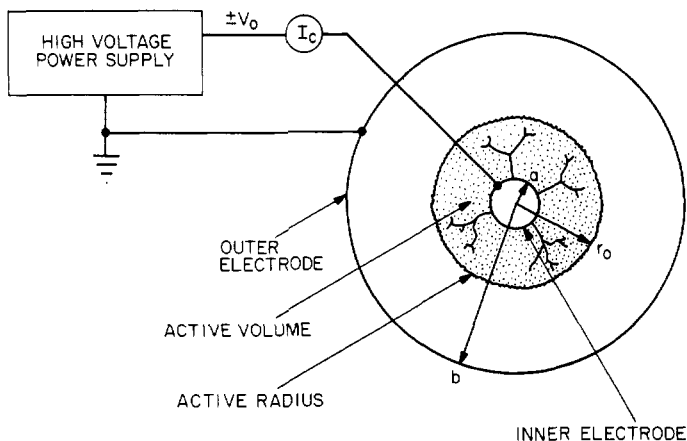
Figure 8.13 Phenomenology of corona generated by a fine wire of radius *a* located on the axis of a grounded cylinder of radius *b*.

be technically a 'glow discharge', visible to the eye. For low currents, the entire corona is dark, appropriate to the dark discharges with which we classify it. Related phenomena include the *silent electrical discharge*, an inaudible form of the filamentary discharge, and the *brush discharge*, a luminous discharge in a non-uniform electric field, in which many corona discharges are active simultaneously and form streamers which penetrate the highly electrically stressed gas surrounding the point of initiation.

8.4.1 Phenomenology of Corona

The phenomenology of corona may be understood with the assistance of figure 8.13. Here, we show corona generated around a fine wire of radius *a*, which is located on the axis of a large grounded cylinder of radius *b*. The point of *corona initiation* is that point at which the voltage on the inner conductor of radius *a* is high enough that corona is just detectable, usually by becoming visible, or by the onset of a coronal current, when the discharge is not visible. Corona should not be confused with sparking, or electrical breakdown, which will be discussed later in this chapter. Sparking or electrical breakdown is usually a transient, localized, high current discharge, while corona is a very low current, continuous phenomenon, the currents of which are orders of magnitude smaller than those that flow during electrical breakdown.

The *breakdown voltage* in kilovolts at standard temperature and pressure of dry air is given by

$$V_B = 3000d + 1.35 \text{ kV} \tag{8.35}$$

for plane, parallel electrodes separated by the distance d, in meters (Cobine 1958). The *breakdown electric field* is found by dividing equation (8.35) by the gap width d, to obtain

$$E_B = \frac{V_B}{d} = 3000 + \frac{1.35}{d} \text{ kV/m}. \tag{8.36}$$

Thus, the breakdown electric field for dry air at standard atmospheric conditions is about 3 MV/m, or 30 kV/cm. When the local electric field around points or fine wires exceeds the breakdown field given by equation (8.36), corona results. Around a sharp point or a fine wire like that shown in figure 8.13, the electric field will be a maximum at the surface of the inner conductor, and will decrease with radius and reach a minimum value at the outer electrode.

When the applied voltage, V_0, is higher than necessary to initiate corona, the electric field will drop off to the breakdown value given by equation (8.35) at a radius r_0 called the *active radius*. The active radius is usually associated with the visible radius of the coronal discharge, and it is within this *active volume* that most corona-initiated plasma chemistry occurs. At pressures near one atmosphere, electrons attach to oxygen quite readily, and therefore the electrical current between the active radius and the outer electrode is carried by either negative or positive ions, depending on the polarity of the voltage applied to the inner electrode.

A continuous or intermittent current, usually of the order of microamperes to milliamperes per decimeter of length, will flow to the power supply, with positive polarity resulting in a continuous, DC electrical current, and negative polarity usually resulting in a pulsed or intermittent current. Electrons may participate in the current in the active volume, but in air and other gases are quickly attached to form negative ion species.

Corona can occur for both positive and negative polarity, with little difference in their initiation voltages or coronal current. This is shown in figure 8.14, which schematically illustrates that the coronal current which completes the electrical circuit is carried by positive ions when the inner conductor is positive, and by negative ions when the inner conductor is negative. Corona can initiate on sharp points at potentials as low as 5 kV. On a fine wire, corona can manifest itself as a cylindrical glow (positive polarity), or a string of approximately equally spaced beads on a polished wire (negative polarity). Corona can initiate from sharp points, fine wires, sharp edges, asperities, scratches, or anything which creates a localized electric field greater than the breakdown electric field of the medium surrounding it.

a) POSITIVE CORONA, POSITIVE ION
CURRENT

b) NEGATIVE CORONA, NEGATIVE ION
CURRENT
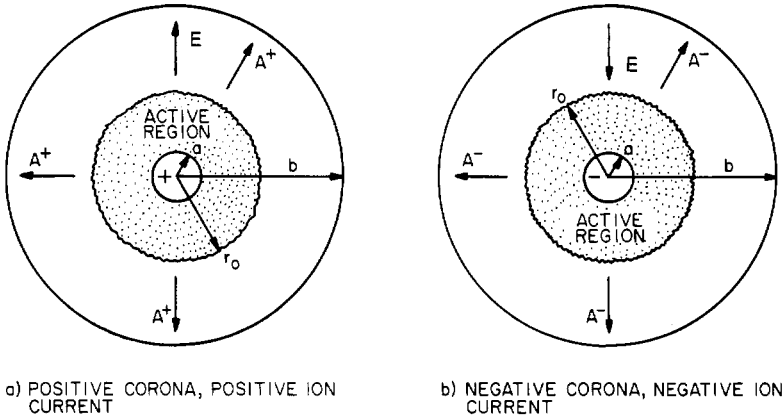
Figure 8.14 Phenomenology of positive and negative corona generated by fine wires.

8.4.2 Applications of Corona

Corona has many important industrial applications, including electrostatic precipitators, which are treated in Chapter 22 (Oglesby and Nicholls 1978). Another important application of corona is in xerography, also discussed in Chapter 22. Corona is used in the modification of surfaces to alter their wettability or adhesive properties, as in the treatment of polymer films to take paints or printing ink. These applications are also discussed in Chapter 14. Corona is used industrially for antistatic applications, in which materials such as photographic film and plastic sheet have surface charge neutralized by exposure to corona. This can be extremely important in materials like stacked sheets of plastic film, where static electrical forces can be strong enough to preclude the practicable manipulation of the sheets. Static control is also important in photographic film, since untreated film in moving through a camera can cause visible electric discharges which expose the film. Antistatic applications of corona are discussed in Chapter 14.

There are many large-scale applications of corona and corona- like filamentary discharges to plasma chemistry, probably the largest scale of which is the commercial production of ozone in Europe for use in treating public water supplies. Many other chemical compounds of industrial importance can be created in a coronal discharge. These plasma–chemical applications are discussed in Chapter 19. A common feature of most of these industrial applications is that they are based on coronal discharges around fine wires, so it is particularly important that this configuration be well understood theoretically.

8.4.3   Detrimental Effects of Corona

In addition to the commercial applications discussed above, corona has a variety of effects which must be dealt with or eliminated. Some of these effects include power line loss, in which coronal losses from high voltage overland transmission lines can exceed the resistive losses, particularly in humid or snowy conditions. Power line loss will be discussed in Chapter 20. When corona occurs on an electrical conductor, it is capable of forming detrimental chemical species in air, including ozone, NO_2, and nitric acid in the presence of water vapor. These species can attack the electrical conductor itself as well as surrounding insulators. The fomation of chemical species by corona is discussed in Chapter 19.

When the voltage on an electrical conductor exceeds approximately 20 kV, x-rays may be produced by corona, which become progressively more penetrating as the voltage increases. This phenomenon apparently has not led to commercially useful x-ray sources, but it can be a serious personnel hazard in high voltage equipment. Corona is capable of significant radio frequency interference, particularly in the AM band around 1 MHz. It is frequently necessary to eliminate corona or shield high voltage equipment in order to avoid interference with the operation of sensitive RF equipment. Finally, corona is capable of producing audible noise when it occurs, for example, on high voltage transmission lines. Under the proper atmospheric conditions, coronal noise can exceed accepted standards for the exposure of residential communities.

The detrimental effects of corona discussed above are mostly the result of coronal discharges from fine points. Thus, in order to minimize or eliminate these effects of corona, it is necessary to understand theoretically the generation of corona around fine points and sharp edges of a kind that produce corona on high voltage equipment.

8.5   CORONA SOURCES

8.5.1   Corona From a Sharp Point

As was remarked above, in order to eliminate the detrimental effects of corona, it is usually necessary to understand the generation of corona by a sharp point. Consider a sharp point with a spherical radius $r = a$ at a potential V_0 in the center of a spherical cavity wall with radius $r = b$ and potential $V = 0$. Both the sharp point and the surrounding grounded cavity wall are electrically conducting. The breakdown of the surrounding air and the visible corona illustrated in figure 8.15 extend out to the active radius $r = r_0$.

The radial electric field and potential distribution for low coronal currents, i.e. $\rho(r) \approx 0$, will now be calculated. For this zero charge
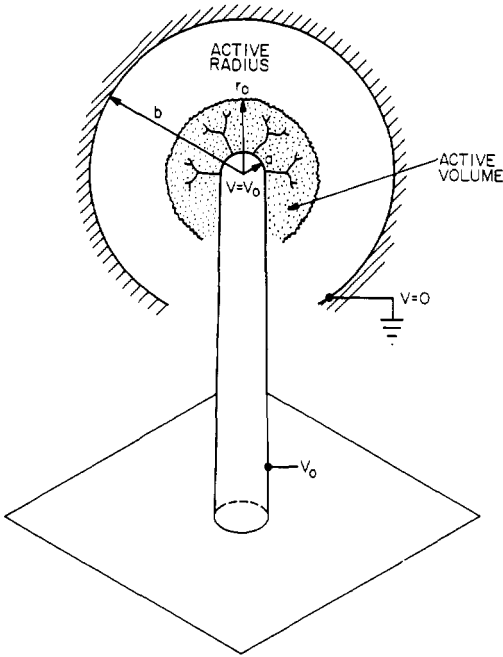
Figure 8.15 Corona from a sharp point in the form of a hemisphere of radius a, located at the center of a grounded spherical electrode of radius b.

density limit, Poisson's equation becomes, for a spherically symmetric point in a spherically symmetric cavity,

$$\nabla \cdot E = \frac{1}{r^2} \frac{\mathrm{d}}{\mathrm{d}r}(r^2 E) = -\frac{\rho}{\varepsilon_0} \approx 0. \qquad (8.37)$$

Since we have assumed spherical symmetry, the potential and electric fields are functions of radius only. From equation (8.37), it follows that

$$r^2 E(r) = \text{constant}. \qquad (8.38)$$

Using equation (8.38), we can write

$$r^2 E = a^2 E_S = r_0^2 E_B = b^2 E_w \qquad (8.39)$$

where E_S, E_B, and E_w are the electric field strengths at the surface of the point; the active radius, where it is equal to the breakdown electric field; and at the wall, respectively. Using the two left-hand terms of equation (8.39), we may write

$$E = -\frac{\mathrm{d}V}{\mathrm{d}r} = \frac{a^2 E_S}{r^2} \qquad \text{(V/m)}. \qquad (8.40)$$

Integrating both sides of equation (8.40) between the limits $a \leqslant r' \leqslant r$, one obtains

$$-\int_{V_0}^{V} dV = V_0 - V(r) = \int_{a}^{r} \frac{a^2 E_S \, dr'}{r'^2} = -\frac{a^2 E_S}{r'}\bigg|_{a}^{r} \qquad (8.41)$$

which gives the electrostatic potential

$$V(r) = V_0 + a^2 E_S \left(\frac{1}{r} - \frac{1}{a} \right) \qquad (\text{V}). \qquad (8.42)$$

We evaluate the electric field at the surface of the point, where $E = E_S$, by setting $V(r) = 0$ at the radius $r = b$, to obtain

$$V_0 = a E_S \left(1 - \frac{a}{b} \right) \qquad (\text{V}). \qquad (8.43)$$

Solving for the electric field E_S, we obtain from equation (8.43)

$$E_S = \frac{V_0}{a} \frac{1}{[1 - (a/b)]}. \qquad (8.44)$$

Substituting equation (8.44) into equation (8.40), the radial electric field at the radius r, we obtain

$$E(r) = \frac{ab V_0}{r^2(b - a)} \qquad (\text{V/m}). \qquad (8.45)$$

If we substitute equation (8.44) into equation (8.42), the radial potential profile for the low coronal current case is obtained,

$$V(r) = V_0 \left(1 - \frac{b}{r} \frac{(r - a)}{(b - a)} \right) = V_0 \frac{a(b - r)}{r(b - a)}. \qquad (8.46)$$

If the coronal current is significant, so that the coronal charge density cannot be neglected, the coronal current can be written in terms of the current density,

$$I_c = \text{constant} = 4\pi r^2 J(r) \qquad (\text{A}). \qquad (8.47)$$

The total coronal current flowing between the point and the surrounding spherical electrode is not a function of radius. The current density appearing in equation (8.47) can be written as

$$J(r) = \rho(r) v_d(r) \qquad (\text{A/m}^2) \qquad (8.48)$$

where the radial drift velocity v_d can be written in terms of the ionic mobility μ_i and the radial electric field,

$$v_d(r) = \mu_i E(r) \qquad (\text{m/s}).\qquad (8.49)$$

Substituting equations (8.49) and (8.48) into equation (8.47), and solving for the charge density yields

$$\rho(r) = \frac{I_c}{4\pi r^2 \mu_i E} \qquad (\text{C/m}^3).\qquad (8.50)$$

Substituting this ionic charge density into Poisson's equation, equation (8.37), yields for the spherical geometry

$$\nabla \cdot E = \frac{1}{r^2}\frac{d}{dr}(r^2 E) = -\frac{\rho}{\varepsilon_0} = -\frac{I_c}{4\pi r^2 \varepsilon_0 \mu_i E}.\qquad (8.51)$$

Rearranging equation (8.51) yields Poisson's equation in the form

$$r^2 E \frac{d(r^2 E)}{dr} = \frac{1}{2}\frac{d}{dr}(r^2 E)^2 = -\frac{I_c r^2}{4\pi \varepsilon_0 \mu_i}.\qquad (8.52)$$

Integrating both sides of equation (8.52), one obtains

$$(r^2 E)^2\Big|_{a,E_S}^{r,E} = -\frac{I_c}{2\pi \mu_i \varepsilon_0}\int_a^r r^2\,dr = -\frac{I_c r^3}{6\pi \mu_i \varepsilon_0}\Big|_a^r \qquad (8.53)$$

where E_S is the electric field at the surface of the point, where $r = a$. Equation (8.53) allows us to solve for the radial electric field at the point r, which is given by

$$E(r) = \left\{ E_S^2\left(\frac{a}{r}\right)^4 - \frac{I_c}{6\pi \mu_i \varepsilon_0 r}\left[1 - \left(\frac{a}{r}\right)^3\right]\right\}^{1/2}.\qquad (8.54)$$

We can relate the voltage on the point, V_0, to the surface electric field, E_S, by integrating the potential from V_0, at $r = a$, to the potential $V = 0$, at $r = b$:

$$E(r) = -\frac{dV}{dr} = \frac{1}{r^2}\left[A - Cr^3\right]^{1/2}\qquad (8.55)$$

where the constants A and C are given by

$$A \equiv a^4 E_S^2 + \frac{I_c a^3}{6\pi \mu_i \varepsilon_0} \qquad C \equiv \frac{I_c}{6\pi \mu_i \varepsilon_0}.\qquad (8.56)$$

Integrating equation (8.55), the potential V_0 is given by

$$-\int_{V_0}^{0} dV = V_0 = \int_{a}^{b} \frac{\sqrt{A - Cr^3}}{r^2} dr. \tag{8.57}$$

This integral does not appear in standard tables. This equation relates the surface electric field on the sharp point to the applied potential V_0.

One can obtain an expression for the radial potential profile. Returning to equation (8.52), the potential $V(r)$ is a solution of the differential equation resulting from Poisson's equation,

$$\frac{d}{dr} \left(r^2 \frac{dV}{dr} \right)^2 + \frac{I_c}{2\pi \mu_i \varepsilon_0} r^2 = 0. \tag{8.58}$$

The potential distribution $V(r)$ is a solution to the nonlinear second-order differential equation,

$$r^2 \frac{dV}{dr} \frac{d^2 V}{dr^2} + 2r \left(\frac{dV}{dr} \right)^2 + \frac{I_c}{4\pi \mu_i \varepsilon_0} = 0. \tag{8.59}$$

Here again, closed form solutions for $V(r)$ do not appear to be available.

8.5.2 Corona From a Fine Wire or Edge

Consider the geometry of a fine wire, shown on figure 8.16, in which a wire of radius a is located on the axis of a coaxial, grounded cylinder of radius b. A related geometry is the sharp edge, shown in figure 8.17. Both are assumed to have an axial length L, and to have no variation of the electrostatic potential or electric field along the axis. In both geometries, the active region extends out to $r = r_0$, where the electric field is equal to the breakdown electric field given by equation (8.36).

Poisson's equation for an axisymmetric cylindrical geometry with no axial variation gives for the radial dependence,

$$\nabla \cdot \mathbf{E} = \frac{1}{r} \frac{d}{dr} (rE) = -\frac{\rho}{\varepsilon_0} = 0. \tag{8.60}$$

As a result, this low corona current case with negligible ionic charge density gives

$$rE = aE_S = r_0 E_B = bE_w = \text{constant} \tag{8.61}$$

where the radii and electric fields have the same significance as previously. From the first two terms of equation (8.61), we may write

$$E(r) = -\frac{dV}{dr} = \frac{E_S a}{r}. \tag{8.62}$$
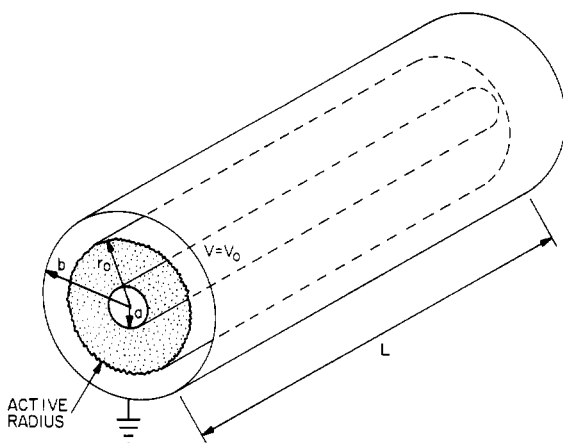
Figure 8.16 Corona in a cylindrical geometry, consisting of an axial fine wire of radius a, and a grounded cylindrical electrode of radius b and length L. The wire is maintained at a potential V_0 with respect to the grounded electrode.
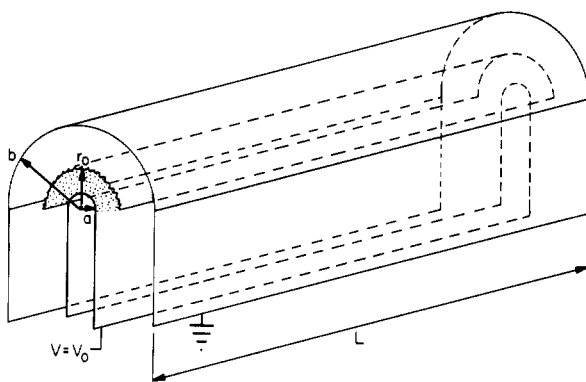
Figure 8.17 Corona generated by a sharp edge consisting of a hemicylindrical surface of radius a, surrounded by a grounded hemicylindrical electrode of radius b and length L.

Integrating equation (8.62) from the surface of the wire at $r = a$, and potential V_0, to a radial position between the electrodes yields

$$-\int_{V_0}^{V} dV = V_0 - V(r) = \int_a^r E_s a \frac{dr}{r} = E_s a \ln r \Big|_a^r. \qquad (8.63)$$

Rearranging equation (8.63) to exhibit the radial potential variation yields

$$V(r) = V_0 - E_s a \ln \left(\frac{r}{a} \right). \qquad (8.64)$$

At the outer electrode, where $r = b$ and the potential $V(b) = 0$, one obtains an expression for the surface electric field,

$$E_S = \frac{V_0}{a \ln(b/a)} \tag{8.65}$$

which relates the surface electric field on the wire to the applied potential and the characteristics of the coaxial geometry. Substituting equation (8.65) into (8.62) yields the radial electric field

$$E(r) = \frac{E_S a}{r} = \frac{V_0}{r \ln(b/a)}. \tag{8.66}$$

By substituting equation (8.65) into equation (8.64), the radial potential variation may be written

$$V(r) = V_0 \left(1 - \frac{\ln(r/a)}{\ln(b/a)} \right) = V_0 \frac{\ln(r/b)}{\ln(a/b)}. \tag{8.67}$$

In cylindrical geometry, the coronal current I_c will be a constant, independent of radius between the wire and the outer coaxial electrode,

$$I_c = \text{constant} = 2\pi r L J(r) = 2\pi r L \rho(r) v(r). \tag{8.68}$$

Substituting equation (8.49) for the radial drift velocity of the ionic charge carriers yields

$$I_c = 2\pi r L \rho(r) \mu_i E(r). \tag{8.69}$$

The radial profile of charge density may be obtained from equation (8.69), and is

$$\rho(r) = \frac{I_c}{2\pi r L \mu_i E}. \tag{8.70}$$

Substituting equation (8.70) into the cylindrical Poisson's equation (8.60) yields

$$\frac{1}{r} \frac{d}{dr}(rE) = -\frac{\rho}{\varepsilon_0} = -\frac{I_c}{2\pi r L \mu_i \varepsilon_0 E}. \tag{8.71}$$

Rearranging equation (8.71), and integrating from the surface of the wire to the position r,

$$d(rE)^2 \Big|_{a, E_S}^{r, E} = -\frac{I_c}{\pi L \mu_i \varepsilon_0} \int_a^r r \, dr \tag{8.72}$$

yields

$$[E(r)]^2 = E_S^2 \frac{a^2}{r^2} - \frac{I_c(r^2 - a^2)}{2\pi r^2 L \mu_i \varepsilon_0}. \tag{8.73}$$

Here, the electric field is modified from the vacuum value, represented by the first term on the right-hand side, by the charge density of the coronal current, represented by the second term. Note that the coronal current I_c and the ionic mobility μ_i are signed quantities, and play a role in determining the sign that appears in front of the coronal current term in equation (8.73).

One may obtain the radial potential variation by writing equation (8.38) in the form

$$E(r) = -\frac{dV}{dr} = \frac{1}{r}\sqrt{a^2 E_s^2 + \frac{I_c a^2}{2\pi L \mu_i \varepsilon_0} - \frac{I_c r^2}{2\pi L \mu_i \varepsilon_0}}. \qquad (8.74)$$

For compactness, we now define the constants

$$B \equiv a^2 E_s^2 + \frac{I_c a^2}{2\pi L \mu_i \varepsilon_0} \qquad (8.75a)$$

$$D \equiv \frac{I_c}{2\pi L \mu_i \varepsilon_0} \ll E_s^2 \qquad (8.75b)$$

where the inequality in (8.75b) holds for the low coronal currents of interest in practically all applied situations. Equation (8.74) can be integrated between the limits $a < r < b$ to relate the applied potential V_0 to the surface electric field on the wire, E_s,

$$-\int_{V_0}^{0} dV = V_0 = \int_a^b \frac{\sqrt{B - Dr^2}}{r} \, dr. \qquad (8.76)$$

Performing the integration, one has

$$V_0 = \sqrt{B - Db^2} - \sqrt{B - Da^2} + \sqrt{B} \ln \frac{a}{b} \left(\frac{\sqrt{B - Db^2} - \sqrt{B}}{\sqrt{B - Da^2} - \sqrt{B}} \right). \qquad (8.77)$$

Expanding the square roots in equation (8.77) in the small parameters $Db^2/B \ll 1$, $Da^2/B \ll 1$, relation (8.77) becomes

$$V_0 \approx \sqrt{B} \left[\frac{D}{2B}(a^2 - b^2) + \ln\left(\frac{b}{a}\right) \right]. \qquad (8.78)$$

Substituting equations (8.75a) and (8.75b) into equation (8.78), and applying the approximation in (8.75b),

$$E_s^2 \gg \frac{I_c}{2\pi L \mu_i \varepsilon_0} \qquad (8.79)$$

one obtains

$$V_0 \approx a E_{\mathrm{S}} \ln \left(\frac{b}{a} \right) + \frac{I_{\mathrm{c}}}{4 \pi L \mu_i \varepsilon_0 a E_{\mathrm{S}}} (a^2 - b^2). \qquad (8.80)$$

The first term on the right-hand side of equation (8.80) is the dominant, vacuum contribution to the potential, and the second term is the first-order modification of the potential due to the presence of the coronal space charge. Equation (8.80) makes it possible to obtain the surface electric field on the wire, E_{S}, from a knowledge of the coronal current I_0, the applied potential V_0, and the geometric parameters of the coaxial configuration.

If equation (8.74) is used to approximate the radial electric field, with $Dr^2/B \ll 1$, one obtains

$$E(r) = \frac{1}{r} - \sqrt{B - Dr^2} \approx \frac{\sqrt{B}}{r} \left(1 - \frac{Dr^2}{2B} \right). \qquad (8.81)$$

Using equation (8.78) to eliminate $\sqrt{B}$, the radial electric field may be written as

$$E(r) \approx \frac{V_0}{r} \frac{[1 - (Dr^2/2B)]}{[D(a^2 - b^2)/2B + \ln(b/a)]} \approx \frac{V_0}{r \ln(b/a)} \left(1 - \frac{Dr^2}{2B} \right) \\ (8.82)$$

which is the vacuum radial electric field modified by the coronal charge density.

To obtain the radial potential profile, one integrates equation (8.76) over the limits $r \leqslant r' \leqslant b$, in which the small expansion of equation (8.78) is given by

$$V(r) = V_0 - \sqrt{B} \left[\frac{D}{2B} (a^2 - r^2) + \ln \left(\frac{r}{a} \right) \right]. \qquad (8.83)$$

Substituting equation (8.78) for the potential V_0, and simpifying, one obtains

$$V(r) = \sqrt{B} \left[\frac{D}{2B} (r^2 - b^2) + \ln \left(\frac{b}{r} \right) \right]. \qquad (8.84)$$

Using equation (8.78) to eliminate $\sqrt{B}$ as a parameter, one obtains the expression for the radial variation of potential,

$$V(r) = V_0 \left[\frac{D(r^2 - b^2)/2B + \ln(b/r)}{D(a^2 - b^2)/2B + \ln(b/a)} \right] \qquad (8.85)$$
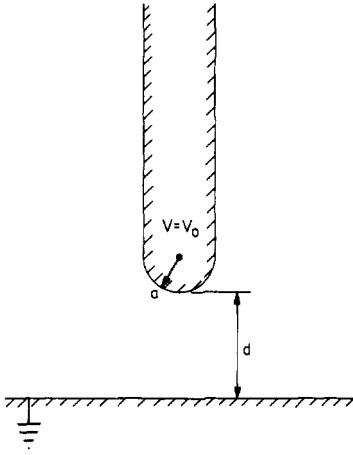
Figure 8.18 Point and plane geometry, with a hemispherical sharp point with radius a located a distance b above an infinite grounded plane.
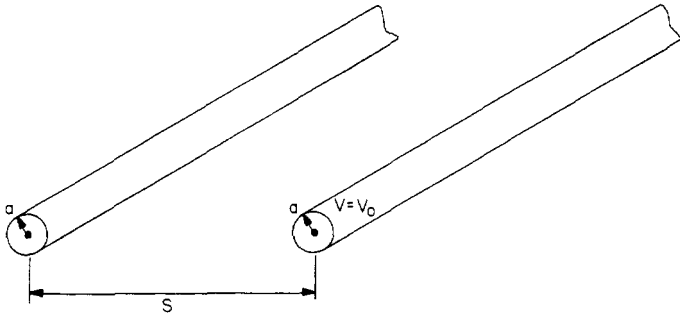
Figure 8.19 Bifilar powerline conductors, each of radius a and with separation S. These wires have an rms voltage V_0 with respect to each other.

which is the desired expression for the potential profile in the presence of coronal charge.

8.5.3 Corona Generating Configurations

To generate corona in industrial applications, the geometric configurations shown in figures 8.18, 8.19, and 8.20 are most frequently used. Near a fine wire or sharp point, the electric field, potential, and radius of the point are related by

$$E_S = \frac{V_0}{aF} \quad \text{(V/m)} \quad (8.86)$$

where F is the *form factor*.
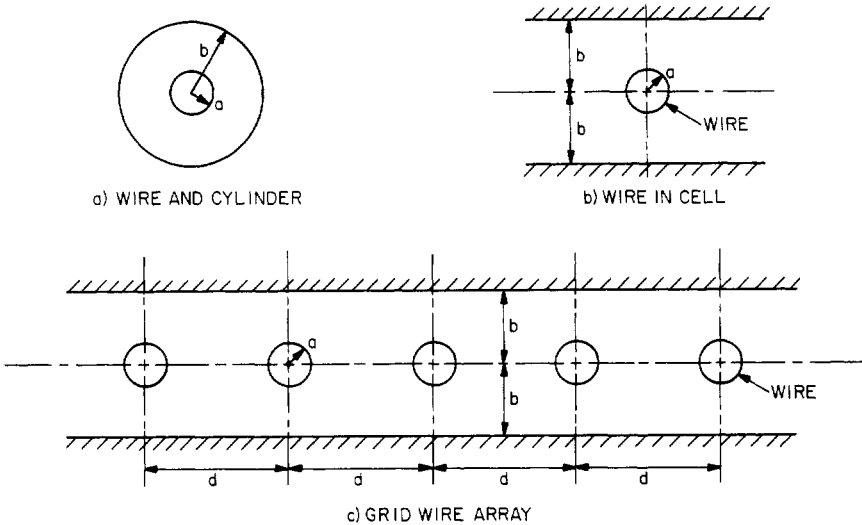
Figure 8.20 Various grid wire geometries used industrially. (*a*) wire and cylinder geometry; (*b*) wire in cell with the wire midway between two planes separated by a distance $2b$; and (*c*) grid wire array, in which an array of wires separated by a distance d from each other is located midway between two planes separated by a distance $2b$.

Figure 8.18 illustrates a sharp point above a grounded plane located a distance d away. For this configuration, we take $d \approx b$, and from equation (8.44), the surface electric field may be approximated as

$$E_S = \frac{V_0}{aF} \approx \frac{V_0}{a[1 - (a/d)]}. \tag{8.87}$$

The form factor is, for the point and plane,

$$F_1 \equiv 1 - (a/d). \tag{8.88}$$

For two cylindrical power line conductors, each of radius a and separated by a distance S, as shown in figure 8.19, Cobine (1958) and Peek (1929) give the form factor for the geometry of figure 8.19 as

$$F_2 \equiv \sqrt{\frac{S - 2a}{S + 2a}} + \ln\left(\frac{S}{2a} + \sqrt{\frac{S^2}{(2a)^2} - 1}\right). \tag{8.89}$$

If the separation of the conductors is much greater than the conductor radius, $S \gg a$, which is the usual case, the form factor in equation (8.89) may be approximated

$$F_2 \approx \ln\left(\frac{S}{a}\right). \tag{8.90}$$

From equation (8.65), the form factor for a coaxial wire in a cylindrical geometry is given by

$$F_3 \equiv \ln\left(\frac{b}{a}\right). \tag{8.91}$$

It has been shown by Bohm (1982) that the form factor for the wire-in-cell configuration of figure 8.20(b) is given by

$$F_4 \equiv \ln\left(\frac{4b}{\pi a}\right) \tag{8.92}$$

where the wire is located midway between two flat grounded plates, each a distance b away. The wire grid assembly illustrated in figure 8.20(c) is often used in commercial electrostatic precipitators, and consists of equally spaced fine wires, each at a high voltage V_0, with radii a, midway between two flat plates located a distance b away, and with a spacing between wires that is equal to d, comparable to the distance b. For the single row wire grid array of figure 8.20(c), Bohm (1982) gives the form factor

$$F_5 \equiv \ln\frac{4b}{\pi a} + \sum_{k=1}^{n} \ln\left[\frac{\cosh\left(\frac{1}{2}k\pi\delta\right) + 1}{\cosh\left(\frac{1}{2}k\pi\delta\right) - 1}\right] \tag{8.93}$$

where δ is given by

$$\delta \equiv d/b \tag{8.94}$$

and the array consists of $k = n$ grid wires.

We now look at the volume in which corona can be generated, since maximizing this active volume is a desirable objective in most industrial applications. The active volume occurs between the conductor radius a and the active radius r_0, $a \leqslant r \leqslant r_0$. Recall that the *active radius* is the point where the electric field has fallen to the value $E(r) = E_B$, the breakdown electric field. Using equation (8.45) to relate the active radius, r_0, to the breakdown electric field E_B of a sharp point yields

$$E_B = \frac{abV_0}{r_0^2(b-a)}. \tag{8.95}$$

In the limit of a large outer radius, $b \gg a$, the active radius is approximately

$$r_{0p} \approx \sqrt{\frac{aV_0}{E_B}} \tag{8.96}$$

for a sharp point. Around a fine wire, the active radius may be found from equation (8.66),

$$E(r_0) = E_B = \frac{V_0}{r_0 \ln(b/a)} \tag{8.97}$$
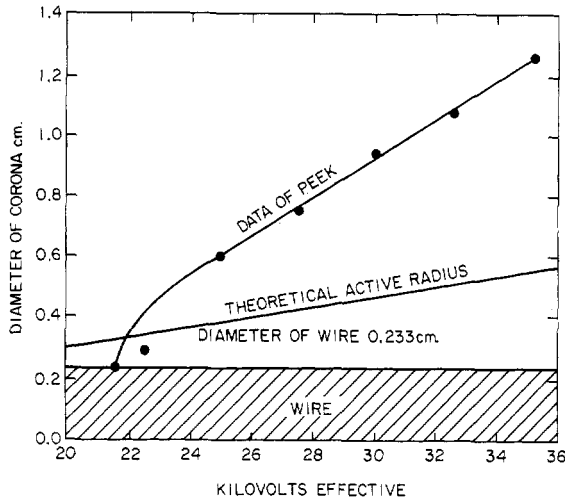
Figure 8.21 Data taken from Peek (1929), showing the visible diameter of corona as a function of the applied voltage on a wire 2.33 mm in diameter. Also shown plotted is the theoretical curve given by equation (8.98), with the breakdown electric field for air taken as 30 kV/cm.

which gives an active radius for a wire,

$$r_{0w} = \frac{V_0}{E_B \ln(b/a)}. \tag{8.98}$$

The theoretical expression for the active radius around a fine wire, given by equation (8.98) may be compared with some data on the visible diameter of corona, from Peek (1929), which is shown in figure 8.21. Here the wire diameter is $2a = 0.233$ cm, the outer radius of the concentric cylinder is $b = 9.3$ cm, the logrithmic factor $\ln(b/a) = 4.38$, and the breakdown electric field is taken as $E_b \approx 3$ MV/m. Equation (8.98) predicts for the coronal diameter, if one identifies the active radius with the visible radius,

$$d \approx \frac{2V_0}{E_B \ln(b/a)} = 1.52 \times 10^{-7} V_0. \quad \text{(m)} \tag{8.99}$$

This expression is drawn in figure 8.21 as the theoretical line, and shows a smaller predicted active radius than the visible radius.

The relative active radii of a wire and a sharp point can be found from equations (8.98) and 8.96, from which the ratio is

$$\frac{r_{0w}}{r_{0p}} = \frac{1}{\ln(b/a)} \sqrt{\frac{V_0}{a E_b}} = \frac{r_{0p}}{a \ln(b/a)}. \tag{8.100}$$
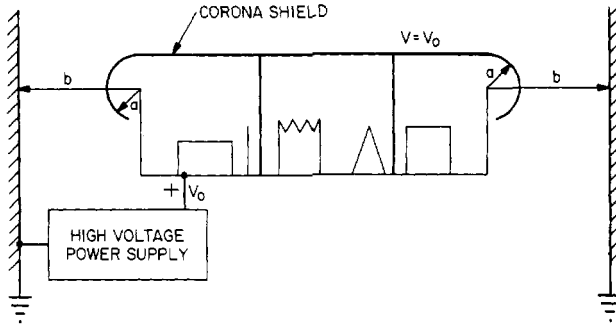
Figure 8.22 A schematic drawing of the critical dimensions for the design of corona shielding. The corona shielding has a radius of curvature a, and is located a distance b from a nearby grounded wall.

This ratio is typically between 1 and 10, thus indicating the superiority of a wire over a sharp point for generating large volumes of corona.

8.5.4 Corona Shielding

In practice, one often wishes to suppress corona from an apparatus which contains sharp corners and edges, by placing a *corona shield* over it, as shown in the schematic drawing in figure 8.22. This illustration shows a piece of high voltage equipment at the potential V_0, which may consist of circuit boards, sheet metal, and other elements with sharp points or edges capable of giving rise to corona. The electric fields in the vicinity of the high voltage components may be reduced to very low values by placing the components in a equipotential box, with rounded edges having a radius of curvature $r = a$, located a distance b away from surrounding grounded walls. Here, we determine the radius, a, required to avoid corona and use equation (8.65) as a cylindrical approximation to the situation in figure 8.22. The electric field at the surface is given by

$$E_S = \frac{V_0}{a \ln(b/a)} = \frac{b V_0}{ab \ln(b/a)}. \tag{8.101}$$

Defining the parameter

$$\alpha \equiv \frac{b}{a} \tag{8.102}$$

and taking $E_S = E_i$, the electric field at the surface for corona initiation, the right-hand term of equation (8.101) may be written as

$$\frac{E_i b}{V_0} = \frac{\alpha}{\ln \alpha}. \tag{8.103}$$
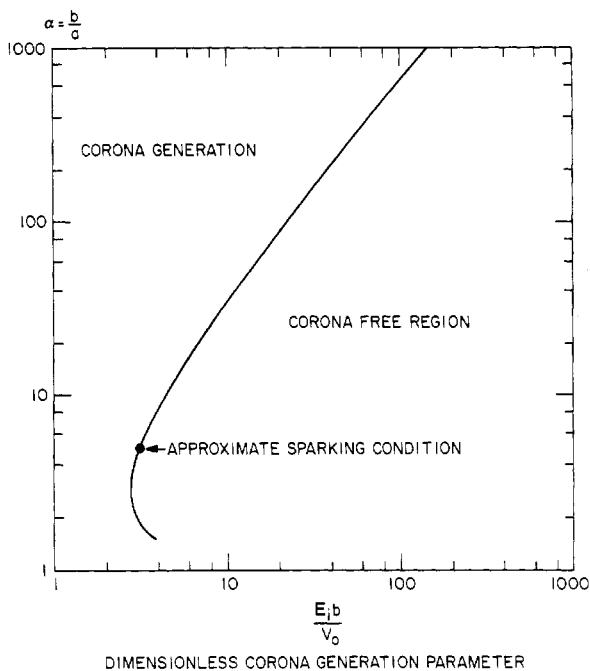
Figure 8.23 A design curve for corona shield design based on equation (8.103).

This equation is plotted in figure 8.23, where corona generation may be expected to the left of the curve, and a corona-free design should exist below and to the right of the line. The further that one is below and to the right of the line, the larger the safety factor against corona generation.

In performing a corona shielding calculation, one starts with the corona initiating electric field E_i, the distance b of the apparatus from the nearest grounded surface, and the maximum operating potential V_0 for the situation of interest, then calculates the left-hand side of equation (8.103). By utilizing figure 8.23, the parameter α can be determined, and this specifies the *maximum* radius of curvature $r = a$ for corona initiation. As an example, consider a laboratory apparatus in which the distance $b = 0.5$ m, $V_0 = 50$ kV, and the initiating electric field $E_i \approx E_B \approx 3$ MV/m. For this case,

$$\frac{E_B b}{V_0} = \frac{3 \times 10^6 \times 0.5}{5 \times 10^4} = 30 = \frac{\alpha}{\ln \alpha}. \tag{8.104}$$

Figure 8.23 yields $\alpha \approx 150$, so equation (8.102) for $b = 0.5$ m predicts that corona should not initiate when the radius of curvature of the corona shield is greater than $a = 0.33$ mm. Thus, everything sharper than this,

which would normally include screw threads and edges of sheet metal, will produce corona, and one then should design for the corona-free region to the lower right of figure 8.23.

8.5.5 Electrical Characteristics of Corona

In the point and plane geometry illustrated in figure 8.18, extensive measurements have been made to obtain a relationship for the corona initiation voltage at the surface of a point of radius a. This initiating electric field has been found to be, for the geometry of figure 8.18, (Cobine 1958, p 262),

$$E_{Sc} = \frac{1.8 \times 10^5}{\sqrt{a}} \text{ V/m.} \tag{8.105}$$

In this empirical expression, the distance between the point and the plane does not enter as a parameter. If the point is a distance d above the plane, as shown in figure 8.18, the initiating voltage is

$$V_c \approx \frac{1.8 \times 10^5 d}{\sqrt{a}} \text{ V} = \frac{180d}{\sqrt{a}} \text{ kV.} \tag{8.106}$$

For AC corona generated around wires of radius a and separated by a distance S, shown in figure 8.19, Peek (1929) gives for the corona initiating electic field at the surface of the wire the empirical relation

$$E_{Sc} = 3.1m\delta \left(1 + \frac{0.0308}{\sqrt{\delta a}} \right) \text{ (MV/m)} \tag{8.107}$$

where m is an empirical *surface roughness factor*, and δ is here the *relative atmospheric density factor*, given by

$$\delta \equiv \frac{298p}{T} \tag{8.108}$$

where p is the pressure in atmospheres, and T is the ambient temperature in kelvin. The empirical surface roughness factor m is given by Cobine (1958) for various situations listed in table 8.3. Note that for $T = 298$ K and $p = 1$ atm, the atmospheric density factor is $\delta = 1.0$. This correction, however, can be significant at high altitude.

The initiation voltage for corona between coaxial cylinders of radii a and b is given by

$$V_c = E_{Sc}a \ln(b/a) \quad \text{(MV)} \tag{8.109}$$

Table 8.3 Corona surface roughness factor m_0, from Cobine (1958) and Peek (1929).

Condition of conductor	m_0
New, unwashed	0.67–0.74
Washed with grease solvent	0.91–0.93
Scratch-brushed	0.88
Buffed	1.00
Dragged and dusty	0.72–0.75
Weathered (5 months)	0.95
Weathered at low humidity	0.92
For general design	0.87–0.90
7-strand concentric lay cable	0.83–0.87
19-, 37- and 61-strand concentric lay cable	0.80-0.85

where the corona-initiating electric field E_{Sc} is given by equation (8.107), and is the maximum value during the AC cycle. For parallel wires separated by the distance S, as shown in figure 8.19, an empirical relation for the maximum corona-initiating surface electric field during the AC cycle is given by Peek (1929),

$$E_{Sc} = 3.0m\delta \left(1 + \frac{0.0301}{\sqrt{\delta a}} \right) \ (\text{MV/m}) \tag{8.110}$$

and the corresponding maximum corona initiating voltage during the AC cycle is given by

$$V_c = E_{Sc} a \ln \left(\frac{S}{a} \right). \tag{8.111}$$

As one can see by comparing equation (8.107) for concentric cylinders and equation (8.110) for parallel conductors, there is not a large difference in the corona-initiating electric fields.

As one gets far away from a sharp point, $r \gg a$, the coronal current is associated with a limiting radial electric field. This may be found from equation (8.54),

$$E_{\text{lim,p}} \approx \sqrt{\frac{-I_c}{6\pi \mu_i \varepsilon_0 r}} \quad (\text{V/m}) \tag{8.112}$$

far from a sharp point. The sign conventions of the ionic coronal current I_c and the ionic mobility μ_i are such that the argument under the square root sign is always positive.

For a wire in a concentric cylinder, the limiting electric field at radii far from the wire, $r \gg a$, can be found from equation (8.74). This limiting electric field is

$$E_{\text{lim,w}} \approx \sqrt{\frac{-I_c}{2\pi L \mu_i \varepsilon_0}} \qquad \text{(V/m)} \qquad r \gg a. \qquad (8.113)$$

In cylindrical geometry, the limiting electric field at large distances from the wire is independent of radius.

The limiting electric fields obtained above make it possible to calculate the charge density far from the wire or point. For the sharp point, substituting equation (8.112) into equation (8.50) gives the limiting charge density at distances far from the point,

$$\rho(r)_{\text{lim}} = \frac{1}{r^{3/2}} \sqrt{\frac{-3 I_c \varepsilon_0}{8\pi \mu_i}} \qquad \text{(C/m}^3\text{)}. \qquad (8.114)$$

The charge density around a point falls off as $r^{-3/2}$ at large distances. In a similar manner, one can obtain the limiting charge density around a wire by substituting equation (8.113) into equation (8.70) to get the charge density far from a wire,

$$\rho(r)_{\text{lim}} = \frac{1}{r} \sqrt{\frac{-I_c \varepsilon_0}{2\pi L \mu_i}} \qquad \text{(C/m}^3\text{)}. \qquad (8.115)$$

In this case, the ionic charge density around the wire falls off as $1/r$. In view of these results, it is perhaps surprising that some authors who analyze corona generation and the operation of electrostatic precipitators use a constant charge density model, in which the charge density is independent of radius.

We now calculate the *coronal current*. For the sharp point, our inability to integrate equation (8.57), or solve equation (8.59) to obtain the radial variation of potential, makes it impractical to derive the coronal current from first principles. However, an empirical relation is available in the literature for the coronal current from a sharp point (Cobine 1958, p 261), which is

$$I_c = C V_0 (V_0 - V_c). \qquad (8.116)$$

In equation (8.116), V_0 is the voltage on the conductor, and V_c is the corona-initiation voltage, given by equation (8.106). This relationship results in a parabolic increase of coronal current with the applied voltage, which has been seen in the experimental data on which equation (8.116)

is based. Further discussion of this empirical relationship may be found in Cobine (1958) or Peek (1929).

For a fine wire, a more rigorous derivation from first principles is possible. Using equation (8.84), the potential at the active radius $r = r_0$, is approximately equal to the corona-initiation voltage V_c, as given by

$$V(r_0) = V_c = \sqrt{B} \left[\frac{D}{2B} \left(r_0^2 - b^2 \right) + \ln \left(\frac{b}{r_0} \right) \right] \qquad (8.117)$$

If we make the following set of approximations to equation (8.117),

$$\sqrt{B} \approx aE_S \qquad r_0 \ll b \qquad \ln \left(\frac{b}{r_0} \right) \approx \ln \left(\frac{b}{a} \right) \qquad (8.118)$$

and use these in equation (8.117), the latter becomes

$$V_c \approx -\frac{Db^2}{2aE_S} + aE_S \ln \left(\frac{b}{a} \right). \qquad (8.119)$$

Using equation (8.75b), and the vacuum approximation to the applied potential V_0 given by equation (8.65),

$$V_0 = aE_S \ln \left(\frac{b}{a} \right). \qquad (8.120)$$

Equation (8.119) becomes

$$V_c \approx -\frac{I_c b^2 \ln (b/a)}{4\pi L \mu_i \varepsilon_0 V_0} + V_0. \qquad (8.121)$$

Solving equation (8.121) for the coronal current I_c gives the coronal current in the form

$$I_c = \frac{4\pi L \mu_i \varepsilon_0}{b^2 \ln (b/a)} V_0 (V_0 - V_c) \qquad (8.122)$$

which gives a parabolic dependence on voltage, consistent with the empirical expressions that have been reported in the literature (see Peek 1929). The expression in equation (8.122) is one half the value reported by Cobine in his equation (8.131).

The power lost to corona can be written for a wire in terms of the coronal current of equation (8.122) and the applied voltage V_0,

$$P_c = V_0 I_c = \frac{4\pi L \mu_i \varepsilon_0}{b^2 \ln(b/a)} (V_0 - V_c) V_0^2 \qquad (8.123)$$

with a similar expression for the power lost by corona from a sharp point. Equation (8.123) predicts a coronal power loss cubic in the applied potential V_0, which is in apparent disagreement with empirical power loss expressions (see Cobine 1958, equation (8.135)), which describe a parabolic dependence on the parameter $(V_0 - V_c) V_0$.

8.6 ELECTRICAL BREAKDOWN

Many industrial applications of plasma involve high voltage, so the phenomenon of electrical breakdown is of great importance, both to initiate it when desired, and to prevent it when necessary. Consider the classical dark discharge configuration shown in figure 8.3. We will examine the Townsend discharge with the emission of a current of secondary electrons from the cathode on the left, due to ion or photon impact. This is also pertinent to the parallel plate geometry shown in figure 8.4, which is widely used in electrical breakdown studies.

8.6.1 Current in the Townsend Discharge

Define a *secondary electron emission coefficient* γ,

$$\gamma \equiv \frac{\text{# of electrons emitted}}{\text{# of incident ions or photons}} \qquad (8.124)$$

which is the number of electrons emitted from the cathode per incident ion or photon. In classical electrical discharge tubes in the Townsend region, the ion energies are generally low, and values of γ are characteristically of the order of 10^{-2} or less. From equation (8.9), the flux of electrons on the anode is given by

$$\Gamma_{ea} = \Gamma_{ec} e^{\alpha d} \qquad (8.125)$$

where d is the separation of the anode and cathode, α is Townsend's first ionization coefficient, and Γ_{ea} is equal to the electron flux at the anode from all sources. The quantity Γ_{ec} is the total electron emission from the cathode, and is equal to

$$\Gamma_{ec} = \Gamma_{es} + \Gamma_{eo} \qquad (8.126)$$

where Γ_{ec} is the flux of electrons from the cathode by secondary electron emission, and Γ_{eo} is the electron flux from the cathode due to photoemission, background radiation, or other processes.

In the steady state, the ion flux arriving at the cathode must equal the difference between the electron flux arriving at the anode, and the electron flux emitted from the cathode,

$$\Gamma_{ea} - \Gamma_{ec} = \frac{\Gamma_{es}}{\gamma} = \Gamma_{ic}. \qquad (8.127)$$

Substituting equation (8.125) into equation (8.127) and re-arranging, one obtains the cathode flux of electrons due to secondary emission,

$$\Gamma_{es} = \gamma \Gamma_{ec}(e^{\alpha d} - 1). \qquad (8.128)$$

Making a further substitution of equation (8.128) into equation (8.126), the total electron flux from the cathode is

$$\Gamma_{ec} = \Gamma_{es} + \Gamma_{eo} = \gamma \Gamma_{ec}(e^{\alpha d} - 1) + \Gamma_{eo}. \qquad (8.129)$$

Solving for the electron flux from the cathode,

$$\Gamma_{ec} = \frac{\Gamma_{eo}}{1 - \gamma(e^{\alpha d} - 1)}. \qquad (8.130)$$

Substituting equation (8.130) into equation (8.125), the electron flux to the anode is

$$\Gamma_{ea} = \Gamma_{eo}\frac{e^{\alpha d}}{1 - \gamma(e^{\alpha d} - 1)} \qquad \text{(electrons/m}^2\text{-s)}. \qquad (8.131)$$

By multiplying both sides by the electronic charge and the electron number density, one can write equation (8.131) in terms of the current density in a plane parallel to the electrode surfaces,

$$J = J_0\frac{e^{\alpha d}}{1 - \gamma(e^{\alpha d} - 1)} \qquad \text{(A/m}^2\text{)}. \qquad (8.132)$$

8.6.2   Townsend's Second Ionization Coefficient

It is possible for the parameter γ to describe a process entirely distinct from secondary electron emission from the cathode. Examples might be a volumetric process of electron production such as that by ionizing radiation, by ion neutral impact ionization, or by a surface process such as photoemission due to incident ultraviolet photons. Under such conditions, one may define *Townsend's second ionization coefficient*, β, which is

$$\beta \equiv \gamma\alpha. \qquad (8.133)$$

This parameter has fallen out of use in the recent literature. When such additional processes are present in the Townsend regime, equation (8.11) for the current as a function of plate separation no longer holds, as illustrated in figure 8.5. The straight line resulting from equation (8.11) holds up to the point where these additional electron-generating processes occur, after which the current increases more rapidly than predicted by equation (8.11).

   Another process which can deplete electrons between two plane parallel plates is the attachment of electrons to molecules of the gas. Attachment takes electrons out of the gas by processes such as

$$e + O_2 \rightarrow O_2^- \qquad \text{etc.} \qquad (8.134)$$
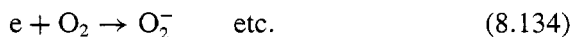
Such attachment processes lead to a reduction of current flowing to the electrodes, an effect important in switchgear and at high pressures. The effect of removing electrons from the gas is shown schematically by the curves labeled B in figure 8.5. These processes occur for all electric fields, becoming more significant as the ratio of E/p increases, also shown schematically on figure 8.5. In switchgear, highly attaching gases such as sulfur hexafluoride are used to promote the extinction of arcs and sparks.

8.6.3 Townsend Criterion

The electrical breakdown of gases is studied in a geometry shown previously in figure 8.4. At the *breakdown*, or *sparking potential* V_b, the current might increase by a factor of 10^4 to 10^8, and is usually limited only by the internal resistance of the power supply connected between the plates. If photo- or secondary electron emission from the cathode is the dominant process, the *Townsend criterion* is obtained from the condition for which the current between the two plates increases without limit. This occurs when the denominator of equation (8.132) goes to zero, or

$$1 - \gamma(e^{\alpha d} - 1) = 0. \tag{8.135}$$

This can be written in the form

$$\gamma e^{\alpha d} = \gamma + 1. \tag{8.136}$$

and is known as the *Townsend criterion*. The left side of equation (8.136) is the number of secondary electrons emitted by $e^{\alpha d}$ positive ions or photons. Equation (8.136) is the criterion for breakdown, and for advancing to a self-sustaining glow discharge.

At the point of electrical breakdown, we can find the breakdown voltage according to the following procedure. If we take the natural logarithm of the Townsend criterion, equation (8.136), we obtain

$$\ln\left(1 + \frac{1}{\gamma}\right) = \alpha d. \tag{8.137}$$

Here we define the breakdown voltage to be V_b and the breakdown electric field will then be, for the plane parallel geometry of equation (8.19),

$$E_b = \frac{V_b}{d}. \tag{8.138}$$

Substituting equations (8.138) and (8.24) for Townsend's first ionization coefficient into equation (8.137) yields

$$Apd \exp\left[-\frac{Cpd}{V_b}\right] = \ln\left(1 + \frac{1}{\gamma}\right). \tag{8.139}$$
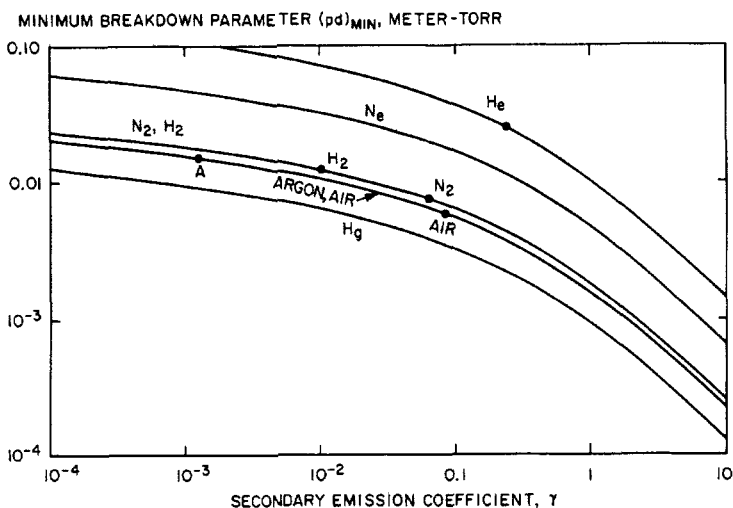
Figure 8.24 The minimum breakdown parameter, $(pd)_{\min}$ for the Paschen curves of several gases, as a function of the secondary electron emission coefficient of the cathode.

Taking the natural logarithm of both sides of equation (8.139), and solving for the breakdown voltage V_b, one obtains

$$V_b = \frac{Cpd}{\ln\left(Apd/\ln[1 + (1/\gamma)]\right)} = f(pd). \qquad (8.140)$$

The observation that the breakdown voltage for a particular gas depends only on the product pd is known as *Paschen's law* (1889) after Friedrich Paschen (1865–1947).

8.6.4 Minimum Breakdown Potential

By differentiating the expression for the breakdown voltage in equation (8.140) with respect to the product of pd and setting this derivative equal to zero, one can show that the value of pd at which the minimum breakdown voltage occurs is given by

$$(pd)_{\min} = \frac{e^1}{A} \ln\left(1 + \frac{1}{\gamma}\right) = \frac{2.718}{A} \ln\left(1 + \frac{1}{\gamma}\right) \qquad (8.141)$$

where the parameter A is listed on table 8.1 for several gases. The minimum value of pd as a function of the secondary emission coefficient γ is plotted on figure 8.24, for several of the gases shown in table 8.1.
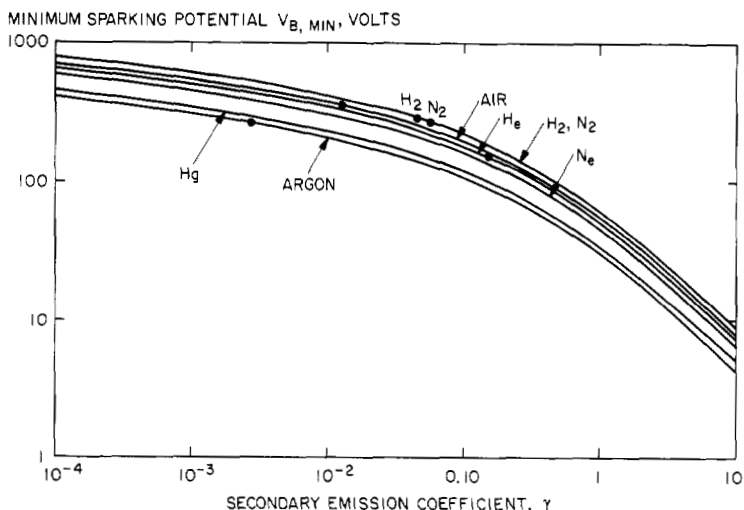
Figure 8.25 The minimum sparking potential of the Paschen curve, $V_{b,min}$, as a function of the secondary electron emission coefficient, γ, for several gases.

The minimum voltage obtained by the differentiation described above can be found by substituting equation (8.141) into equation (8.140), to obtain

$$V_{b,min} = e^1 \frac{C}{A} \ln\left(1 + \frac{1}{\gamma}\right) = 2.718 \frac{C}{A} \ln\left(1 + \frac{1}{\gamma}\right). \qquad (8.142)$$

Equation (8.142) contains the constants C and A from table 8.1, and is plotted for several of the gases in this table in figure 8.25. $V_{b,min}$ is the minimum breakdown voltage which occurs as the product pd is varied, and is called the *minimum sparking potential*, the minimum voltage at which an electrical breakdown can occur in a gas.

8.6.5 A Universal Paschen Curve

If one non-dimensionalizes the product pd, and the breakdown voltage V_b with respect to the minimum values given by equations (8.141) and (8.142), one has, for the dimensionless value of pd,

$$X \equiv \frac{pd}{(pd)_{min}}. \qquad (8.143a)$$

The dimensionless value of the breakdown voltage is given by

$$Y \equiv \frac{V_b}{V_{b,min}}. \qquad (8.143b)$$

RELATIVE SPARKING POTENTIAL $Y = \dfrac{V_B}{V_{B\,MIN}}$

ASYMPTOTIC AT x=0.368

THEORETICAL

AIR, EXPERIMENTAL

AIR

RELATIVE BREAKDOWN PARAMETER $X = \dfrac{(pd)}{(pd)_{MIN}}$
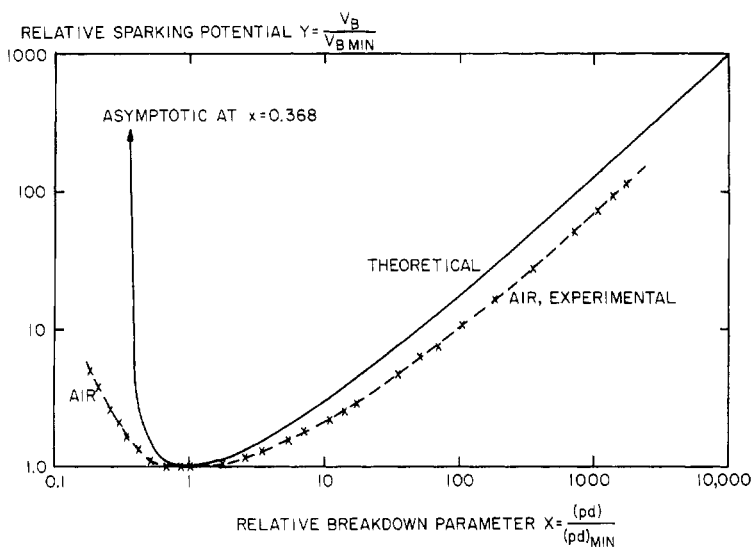
Figure 8.26 A universal Paschen curve from equation (8.144), showing the relative sparking potential as a function of the relative breakdown parameter at the Paschen minimum.

Substituting equations (8.143a) and (8.143b) into equation (8.140) yields a universal breakdown curve given by

$$Y = \frac{V_b}{V_{b,min}} = \frac{X}{1 + \ln X}. \qquad (8.144)$$

This *universal Paschen curve* for gases is plotted as the solid line in figure 8.26. This curve is asymptotic to infinity on the left, when $\ln X = -1$; reaches a minimum at $X = 1$; and increases somewhat slower than linearly on the right, due to the logarithmic term in the denominator.

The universal Paschen curve of figure 8.26 has a characteristic minimum, with a rising breakdown voltage for values of the parameter *pd* smaller and larger than the minimum value. The breakdown voltage increases at small values of *pd* because there are insufficiently many neutral atoms to provide ionizing collisions over the separation *d*; too few mean free paths for ionization exist between the plates to lead to breakdown. Above the Paschen minimum on figure 8.26, the breakdown voltage rises because electron collisions become increasingly frequent as the parameter *pd* increases, removing energy from the electrons, so that stronger electric fields are needed as one goes to higher values of *pd* in order to provide the same degree of ionization. The minimum of the Paschen curve corresponds to the Stoletow point, discussed previously, the pressure at which the volumetric ionization rate is a maximum.

Table 8.4 Minimum sparking constants for selected gases.

Gas	Cathode	$V_{b,min}$ (V)	$(pd)_{min}$ (10^{-3} Torr m)	Reference
A	Fe	265	15	Cobine (1958)
Air	—	360	5.7	Brown (1966)
CO_2	—	420	5.0	Cobine (1958)
H_2	Pt	295	12.5	Cobine (1958)
He	Fe	150	25	Cobine (1958)
Hg	W	425	18	Cobine (1958)
Hg	Fe	520	20	Cobine (1958)
N_2	Fe	275	7.5	Cobine (1958)
N_2O	—	418	5.0	Brown (1966)
O_2	Fe	450	7.0	Cobine (1958)
SO_2	—	457	3.3	Brown (1966)

Some minimum sparking constants for various gases and cathode materials are shown in table 8.4 (Cobine 1958, Brown 1966). The type of cathode material is relevant, because it determines the value of the secondary electron emission coefficient γ, plotted in figures 8.24 and 8.25. These values may be useful to obtain an approximate estimate of the breakdown voltage when substituted into equations (8.143a), (8.143b) and (8.144).

The universal Paschen curve predicts that the breakdown voltage will be infinite when $\ln X = -1$, an important value in practical situations, given by

$$pd = 0.3679(pd)_{min}. \qquad (8.145)$$

Equation (8.145) predicts that electrical breakdown will not occur at values of pd less than 37% of the minimum value. The actual breakdown strength of real gases tends to depart from the universal curve described by equation (8.144). Also plotted on figure 8.26 are experimental points for air, which are about a factor of 1.7 smaller than the universal curve at large values of X. These data also show that electrical breakdown can occur at values of pd less than half the value suggested by the universal curve, equation (8.145).

8.6.6 Breakdown at High Pressures

At high pressures, above about 100 Torr, the mechanism of electrical breakdown often involves streamer formation from the anode. The breakdown voltage for dry atmospheric air in a uniform electric field over limited distances of approximately 1 mm is given by the formula

$$V_b = 3000d + 1.35 \text{ kV}. \qquad (8.146)$$

This predicts an electric field for breakdown of dry atmospheric air of

$$E_b \approx \frac{dV}{dx} \approx 30 \text{ kV/cm}. \qquad (8.147)$$

At these high pressures, Paschen's law and the universal Paschen curve of figure 8.26 are no longer obeyed. Corona or streamers often form when the electric field is greater than the value predicted in figure 8.26 or by equation (8.146), and this process is often present before actual breakdown of the gas occurs.

REFERENCES

Bartnikas R and McMahon E J (ed) 1979 *Engineering Dielectrics* vol I *Corona Measurement and Interpretation (ASTM Special Technical Publication No. 669)* (Philadelphia, PA: ASTM) LCCCN 78.72477, ISBN 04-669000-21

Bohm J 1982 *Electrostatic Precipitators* (Amsterdam: Elsevier North-Holland) ISBN 0-444-99764-4

Brown S C 1966 *Introduction to Electrical Discharges in Gases* (New York: John Wiley)

Cobine J D 1958 *Gaseous Conductors* (New York: Dover Publications)

Loeb L B 1961 *Basic Processes of Gaseous Electronics* 2nd edn (Berkeley and Los Angeles, CA: University of California Press) LCCCN 55-5196

Loeb L B 1965 *Electrical Coronas—Their Basic Physical Mechanisms* (Berkeley and Los Angeles, CA: University of California Press) LCCCN 64-18642

Oglesby S, Jr. and Nichols G B 1978 *Electrostatic Precipitation* (New York: Marcel Dekker) ISBN 0-8247-6649-0

Peek F W, Jr 1929 *Dielectric Phenomena in High Voltage Engineering* 3rd edn (New York: McGraw-Hill)

Von A Engel 1965 *Ionized Gases* 2nd edn (Oxford: Oxford University Press) ch 7

9

DC Electrical Glow Discharges in Gases

The *glow discharge regime* owes its name to the fact that the plasma is luminous. This luminosity arises because the electron energy and number density are high enough to generate visible light by excitation collisions. The glow discharge regime finds widespread industrial applications in lighting devices such as the classical electrical discharge tube used in fluorescent lights; DC parallel-plate plasma reactors; 'magnetron' discharges used for depositing thin films; and electron-bombardment plasma sources. Some of these industrially important configurations of the glow discharge are sketched in figure 9.1.
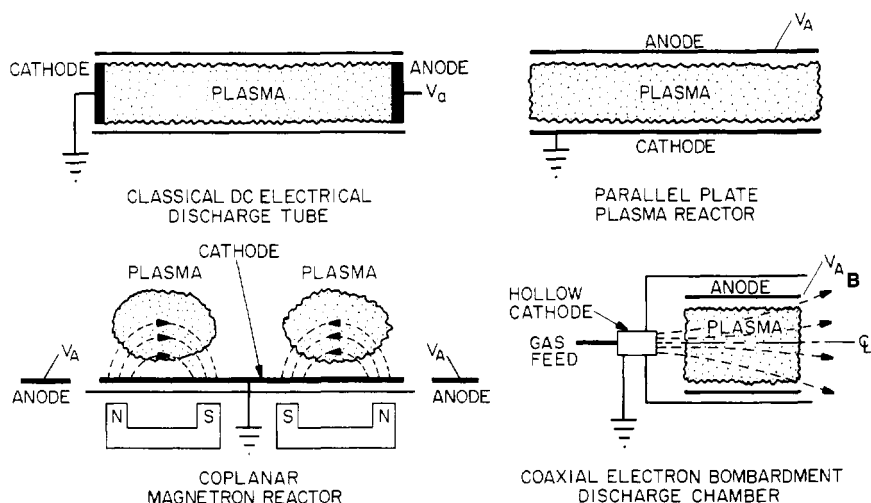

Figure 9.1 Various forms of the DC glow discharge.

9.1 PHENOMENOLOGY OF DC GLOW DISCHARGES

As the voltage across the classical DC low pressure electrical discharge tube, discussed in Chapter 4 in connection with figure 4.12, is increased through the dark discharge regime shown in figure 8.1, the current increases exponentially in the Townsend discharge. As one approaches the breakdown voltage at the point E in figure 8.1, one of two things may happen, depending upon the internal resistance of the power supply. If the internal resistance of the power supply is very high, such that it can deliver only extremely small currents, the discharge tube cannot draw enough current to break down the gas, and the tube will remain in the corona regime with small corona points or brush discharges being evident on the electrodes. If, however, the internal resistance of the power supply is relatively low, then the gas will break down at the voltage V_b, and the discharge tube will move from the dark discharge regime into the low pressure *normal glow discharge* regime, indicated in figure 4.12.

9.1.1 Low Pressure Normal Glow Discharge

The *glow discharge regime* of figure 4.12 is shown in greater detail in figure 9.2. The left-hand plot shows a schematic voltage–current diagram, with total discharge currents on the abscissa which are intended to be characteristic in magnitude. On the right is a corresponding plot of the electrode current density as a function of the total current for the glow discharge regime. After electrical breakdown, a low pressure electrical discharge tube connected to a power supply with a low internal resistance will make a discontinuous transition, on the current–voltage diagram, from the breakdown point E to the point F. The region to the right of point F is almost flat and the voltage across the discharge tube rises only slightly while the current varies over several orders of magnitude.

The region from F to G in figure 9.2 is called the *normal glow discharge*. In this regime, not only is the voltage relatively independent of the total current flowing in the discharge tube, but also the current density reaching the electrodes is relatively independent of the total current. This means that, in the normal glow discharge regime, the plasma is in contact with only a small part of the cathode surface at low currents. As the current increases, the contact surface fills more and more of the total cross section, until at the point G, the boundary of the *abnormal glow*, the plasma covers the entire surface of the cathode, in order to deliver the required total current at a constant current density.

In the abnormal glow above point G, the voltage increases significantly with increasing total current in order to force the cathode current density above its natural value and provide the desired current. At point H,
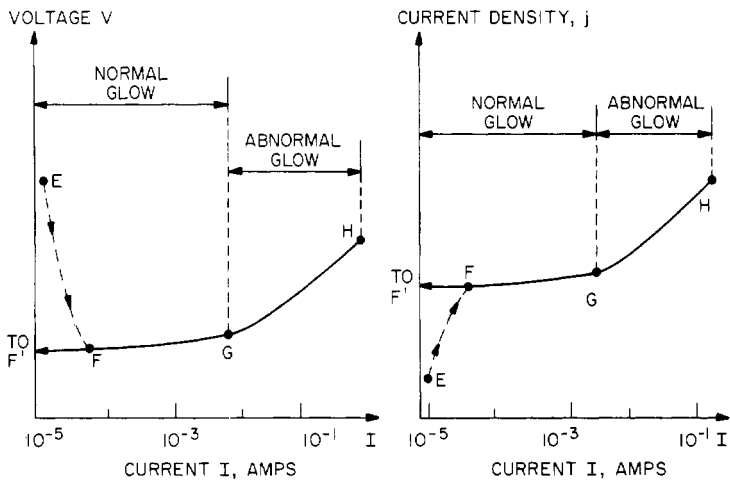
Figure 9.2 The voltage and current density as a function of total current drawn by DC glow discharges.

Table 9.1 Characteristic parameter ranges of DC glow discharges.

Parameter	Low value	Characteristic value	High value
Neutral gas pressure (Torr)	10^{-6}	0.5	760
Electrode voltage (V)	100	1000	50 000
Electrode current (A)	10^{-4}	0.5	20
Number density (electrons/m^3)	10^{14}	5×10^{15}	6×10^{18}
Electron kinetic temperature (eV)	1	2	5
Power level (W)	10^{-2}	200	250 000
Plasma volume (liters)	10^{-6}	0.1	100

the electrodes become sufficiently hot that the cathode emits electrons thermionically. If the DC power supply has a sufficiently low internal resistance, the discharge will undergo a glow-to-arc transition. A rough characterization of the parameter ranges of glow discharges, both normal and abnormal, are summarized in table 9.1. The 'characteristic' values listed are intended to be representative of the DC glow discharges used in industrial plasma processing.

9.1.2 Regions of the Normal Glow Discharge

The plasma which forms in a classical DC low pressure electrical discharge in the normal glow regime can have an appearance like that shown in the idealized sketch of figure 9.3. These structures were

Figure 9.3 A schematic drawing of the visible regions of the normal glow discharge.

first observed in the 1830's by Michael Faraday, and later by such early investigators of the low pressure electrical discharge tube as M Abria (1848). These structures appear over a wide range of operating conditions, and are so characteristic of the normal glow discharge regime that they received individual names, often in honor of the 19th century investigators who were among the first to observe or investigate them. The density of the shading of figure 9.3 is intended to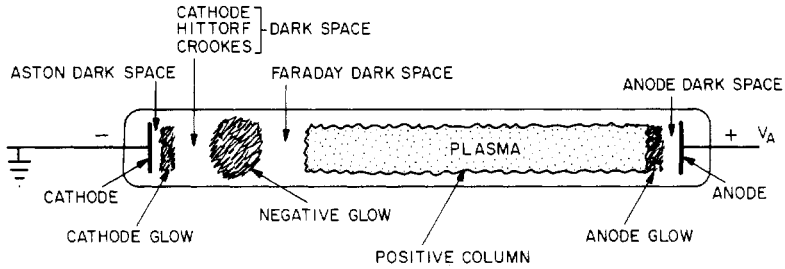 represent the luminous intensity of the structures represented. A characteristic set of operating conditions for the normal glow discharge shown in figure 9.3 might be an anode voltage V_A of one or two kilovolts, a total current of 0.1 A, and air or argon gas at a pressure of a few torr.

Characteristic axial profiles of the light intensity, plasma potential, electric field, and net charge density are indicated schematically on figure 9.4, with the visible structures to which they correspond indicated by the diagram at the top of the figure. The characteristics of the low pressure DC normal glow electrical discharge have been intensively studied in the hundred-year period prior to 1940, and an enormous body of literature is available on its phenomenology. We will now summarize some of these observations by describing the major structures shown in figure 9.3, starting with the cathode on the left, and proceeding right toward the anode.

Cathode. The cathode is made of an electrically conducting metal, the secondary electron emission coefficient, γ, of which has a significant effect on the operation of the discharge tube. The cathode of the classical discharge tube is usually a circular disc, and operates cold; that is, it does not rely on thermionic electron emission to sustain the discharge. The importance of the secondary emission coefficient is implied by equation (8.132) for the current density described by the Townsend theory. In order to attempt a quantitative prediction of the behavior of a normal glow discharge, one needs to know the type of cathode material used, and have some knowledge of the value of its secondary electron emission coefficient. One sometimes uses a *hollow cathode* in which the
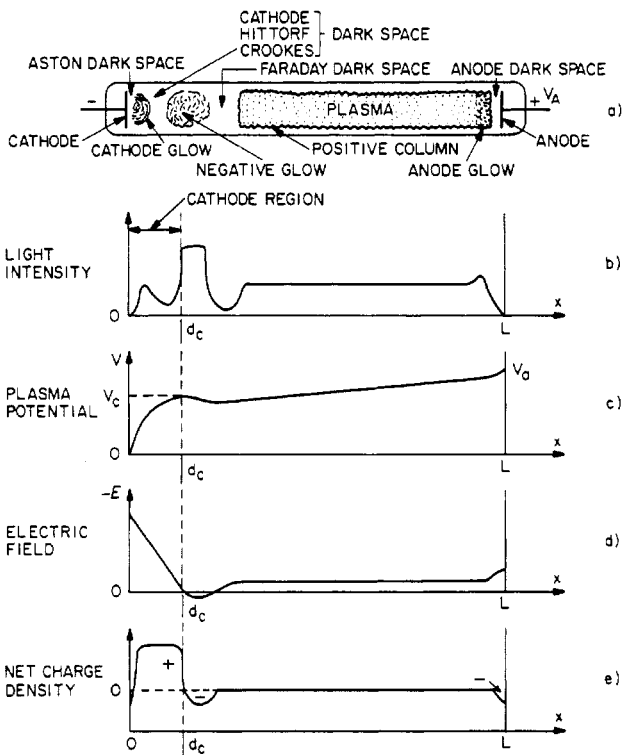
Figure 9.4 Axial variation of the characteristics of the normal glow discharge.

plasma terminates in a cavity, or inside a cylindrical cathode structure, the purpose of which is to conserve particles and photons which lead to ionization and/or emission. An example of a hollow cathode is illustrated in figure 5.8.

Aston dark space. Immediately to the right of the cathode is the Aston dark space, a thin region with a strong electric field and a negative space charge, which contains slow electrons which are in the process of accelerating from the cathode. In this region, the electrons are of too low a density and/or energy to excite the gas, so it appears dark.

Cathode glow. The next structure to the right in figure 9.4 is the cathode glow, which in air is often a reddish or orange color due to emission by excited atoms sputtered off the cathode surface, or incoming positive ions which are moving toward the cathode. The cathode glow has a relatively high ion number density. The axial length of the cathode glow depends on the type of gas and the gas pressure. The cathode glow sometimes clings to the cathode and masks the Aston dark space.

Cathode (Crookes, Hittorf) dark space. This relatively dark region to the right of the cathode glow is referred to as the Crookes dark space in the English literature, and the Hittorf dark space in the early German literature of electrical discharges. It has a moderate electric field, a positive space charge, and a relatively high ion density.

Cathode region. Most of the voltage drop across the discharge tube appears between the cathode and the boundary between the cathode dark space and the negative glow. This region is called the cathode region. It is of length d_c, from the cathode surface ($x = 0$) to the boundary of the negative glow ($x = d_c$). The voltage drop is known as the *cathode fall*, of V_c volts. Most of the power dissipation in a glow discharge occurs in the cathode region. In this region, electrons are accelerated to energies high enough to produce ionization and avalanching in the negative glow, and in regions to the right of the negative glow.

   A low pressure glow discharge will adjust the axial length of its cathode region, d_c, so that a minimum value of the product $d_c p$ is established,

$$d_c p \approx (dp)_{\text{min}} \qquad (9.1)$$

where this product is the *Paschen minimum* of equation (8.141). At the Paschen minimum, the discharge maintains itself under conditions of a minimum cathode fall voltage and power dissipation. In the normal glow discharge, the current density flowing to the cathode remains approximately constant as the total current varies, as the area of the discharge plasma in contact with the cathode increases with total current. Typical values in air at a pressure of 1 Torr might be a current density of 0.3 mA/cm^2, $d_c \approx 0.5$ cm, and a cathode fall voltage ranging between 100 and 300 V.

Negative glow. Immediately to the right of the cathode dark space is the negative glow, the brightest light intensity in the entire discharge. The negative glow has a relatively low electric field, is usually long compared to the cathode glow, and is most intense on the cathode side. Electrons carry almost the entire current in the negative glow region. Electrons which have been accelerated in the cathode region produce ionization and intense excitation in the negative glow, hence the bright light output observed. As these electrons are slowed down, energy for excitation is no longer available and the Faraday dark space begins. The electron number density in the negative glow is characteristically about 10^{16} electrons/m^3.

Faraday dark space. This region is found to the immediate right of the negative glow, and in it the electron energy is low as a result of ionization and excitation interactions in the negative glow. In the Faraday dark space the electron number density decreases by recombination and radial

diffusion, the net space charge is very low, and the axial electric field is relatively small.

Positive column. The positive column is quasi-neutral, and is what Irving Langmuir had in mind when he defined plasma. In the positive column, the electric field is small, typically 1 V/cm. The electric field is just large enough to maintain the required degree of ionization at its cathode end. The electron number density is typically 10^{15} to 10^{16} electrons/m^3 in the positive column, with an electron kinetic temperature of 1 to 2 eV. In air the positive column plasma is pinkish to blue. As the length of the discharge tube is increased at constant pressure, the length of the cathode structures remains constant (pd_c = constant), and the positive column lengthens. The positive column is a long, uniform glow, except when standing or moving striations are triggered spontaneously, or ionization waves are triggered by a disturbance.

Anode glow. The anode glow is a bright region at the anode end of the positive column, slightly more intense than the positive column, and not always present. This is the boundary of the anode sheath.

Anode dark space. The anode dark space, between the anode glow and the anode itself, is the *anode sheath* which has a negative space charge due to electrons traveling from the positive column to the anode, and a higher electric field than the positive column. The anode pulls electrons out of the positive column and acts like a Langmuir probe in electron saturation in this respect.

9.1.3 Striated Discharges

Moving or *standing striations* are, respectively, traveling waves or stationary perturbations in the electron number density which occur in partially ionized gases, including the positive columns of DC normal glow discharge tubes (Garscadden (1978), in Hirsh and Oskam (1978)). In their most usual form, *moving striations* are propagating luminous bands which appear in positive columns, and, depending on operating conditions, can propagate either to the anode (*negative striations*) or toward the cathode (*positive striations*). When observed at a particular point on the axis, moving striations typically have frequencies from a few hertz up to several tens of kilohertz. Moving striations were first observered by Michael Faraday in the 1830's and recorded in his laboratory notebooks, but these observations were never published. The first published description of moving striations appears to be by M Abria (1848). Unless their velocity is low enough to be resolvable by the eye, the observation of moving striations requires phase sensitive stroboscopic methods. Standing striations, however, can be easily photographed. A classic photograph of standing striations taken in a variety of gases and
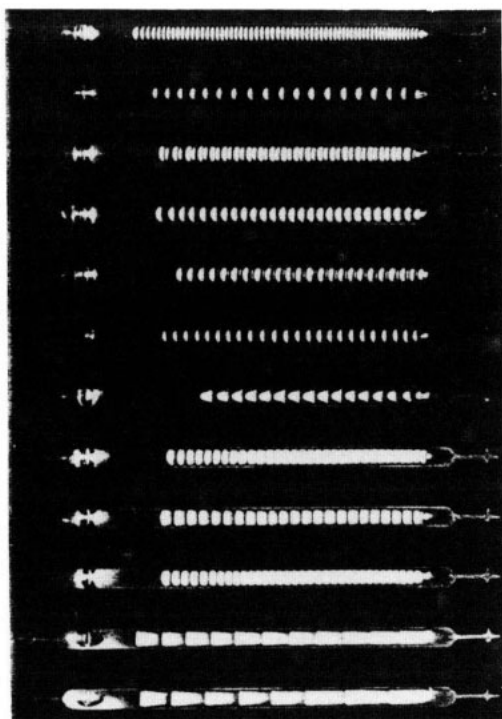
Figure 9.5 Photographs of standing striations in a DC low pressure normal glow electrical discharge tube, published by W de la Rue and H W Muller in 1878 (see Hirsh and Oskam 1978, Chapter 1).

over a range of pressures is shown on figure 9.5. This photograph was originally published by W de la Rue and H W Muller in 1878: the cathode is on the left, the anode on the right, and the standing striations are the bands of luminosity appearing in the positive column.

Many apparently homogeneous, steady-state partially ionized gases and positive columns in reality have moving striations propagating through them, but the waves are out of phase and randomized in such a way that the gas has the overall appearance of uniformity. Standing and slowly moving striations can sometimes be seen in faulty fluorescent light tubes. Striations have an effect, usually undesirable, on partially ionized plasmas used in a variety of industrial applications. Striations can occur in the lasing medium of plasma-pumped lasers, where they modulate the output; they also occur in lighting devices, and standing striations are undesirable in DC parallel plate plasma reactors, where uniformity is required.

9.1.4 Abnormal Glow Discharges

As one increases the current in the classical DC low pressure electrical discharge tube, the voltage initially will rise very slowly in the normal glow region, but finally, when one reaches the point G on the current–voltage curve in figure 9.2, the voltage will increase more rapidly. This increase comes about when the plasma completely covers the surface of the cathode. The only way the total current can increase further is to drive more current through the cathode region by increasing the voltage, and moving away from the Paschen minimum in the cathode region. Except for being more intensely luminous, the *abnormal glow discharge* looks much like the normal glow discharge, but sometimes the structures near the cathode merge into one another, to provide a more or less uniform luminous intensity along the entire discharge between the cathode and anode. As the current and voltage increase, the cathode current density also increases, ultimately to the point where heating of the cathode surface will raise it to incandescence. If the cathode gets hot enough to emit electrons thermionically, the discharge will make a transition into the arc regime, if the internal impedance of the power supply is sufficiently low.

9.1.5 Obstructed Discharges

If the length L of a glow discharge is less than d_c at the Paschen minimum given by Equation (9.1), the cathode fall voltage rises above the Paschen minimum value, $V_{c,min}$. This configuration is known as an *obstructed DC glow discharge*. The obstructed glow discharge finds many uses in industry, where the high electron number densities generated by such discharges are desired.

In some abnormal glow discharges, the distance between the electrodes is shorter than the cathode region dimension required to operate at the Paschen minimum, such that

$$pd_c < (pd_c)_{min} \qquad (9.2)$$

Such an *obstructed abnormal glow discharge* will operate with a higher anode voltage than it would if equation (9.2) were an equality, but this is desired in some plasma processing applications in order to get a large voltage drop across the sheath. Such high voltage drops are sometimes desirable to accelerate ions into a wafer for deposition or etching purposes. A characteristic obstructed abnormal glow discharge used as a DC parallel plate plasma reactor is shown in figure 9.6.
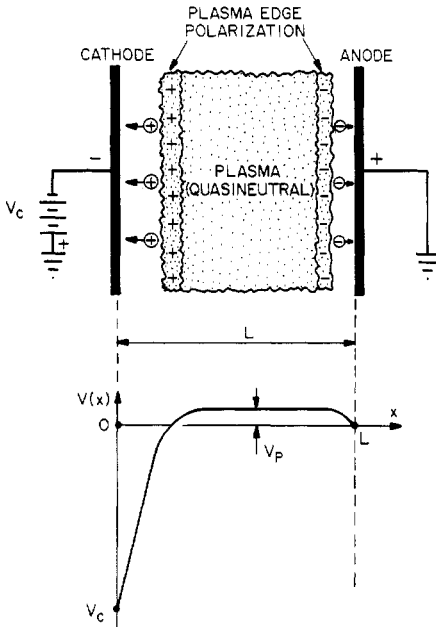
Figure 9.6 A parallel plate reactor operated as an obstructed DC abnormal glow discharge.

9.2 THEORY OF DC GLOW DISCHARGES

In this section we will study some physical processes which relate the major independent and dependent variables of DC glow discharge plasmas. These relationships are often useful in understanding the otherwise surprising behavior of DC glow discharges, even though the utility of these relationships is sometimes more on a qualitative level than for exact quantitative prediction.

9.2.1 Townsend Theory of Cathode Region

The history of research on glow discharges in classical electrical discharge tubes has shown that the theory of the Townsend discharge developed after equation (8.124) can be applied to the cathode region of the normal glow discharge, if only qualitative or rough quantitative understanding is sufficient. In this application, the parameter d_c is the length of the cathode region in meters, and V_c is the cathode fall voltage in volts. To a good approximation, the plasma parameters of the normal glow discharge adjust themselves such that equation (9.1) holds,

$$d_c p \approx (dp)_{\min} \tag{9.1}$$

the minimum breakdown parameter of the Paschen curve, where the cathode fall voltage is given by

$$V_c \approx V_{b,\min} \tag{9.3}$$

and $V_{b,min}$ is the breakdown voltage at the minimum of the Paschen curve. Typically, the minimum cathode fall breakdown parameter pd_c ranges from 5 to 25×10^{-3} Torr m, and the minimum cathode fall voltage, V_c for most gases can range between approximately 150 V and 450 V for a range of common gases and cathode materials. Further data on these parameters are given in Cobine (1958), tables 8.2 and 8.3, but these represent old data in which the gases involved were almost certainly contaminated by mercury vapor. These data may not apply to modern, clean vacuum systems.

In early investigations of the cathode region, F W Aston (1911) reported that the electric field in the cathode region is approximately linear,

$$E = C(d_c - x). \tag{9.4}$$

By integrating this, the cathode voltage at the axial position x can be obtained,

$$V(x) = \int_0^x E \, dx = \int_0^x C(d_c - x) \, dx = C\left(xd_c - \frac{x^2}{2}\right). \tag{9.5}$$

Applying the boundary conditions

$$x = d_c \tag{9.6a}$$

at

$$V(d_c) = V_c \tag{9.6b}$$

to equation (9.5), the constant of integration C may be written

$$C = 2V_c/d_c^2 \tag{9.7}$$

which, when substituted into equation (9.5), yields an expression for the potential along the axis of a normal glow discharge in the cathode region,

$$V(x) = \frac{V_c x(2d_c - x)}{d_c^2}. \tag{9.8}$$

Differentiating equation (9.8) yields the electric field in the cathode fall region,

$$E = \frac{dV}{dx} = \frac{2V_c(d_c - x)}{d_c^2} \tag{9.9}$$

which recovers the linear relation of Aston.

In the cathode region one can obtain the net charge density from Poisson's equation by defining a net charge number density

$$\delta n = Zn_i - n_e. \tag{9.10}$$
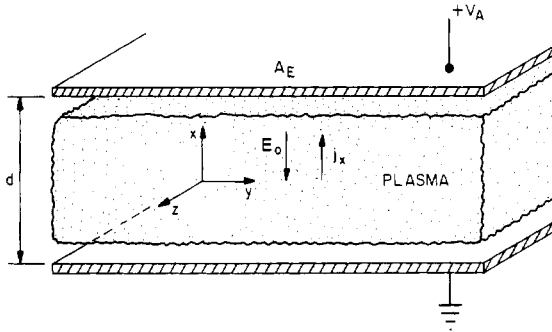
Figure 9.7 A parallel plate reactor with parameters for calculating the power input into an unmagnetized normal glow discharge.

Poisson's equation for the axial dimension of the normal glow discharge may be written

$$\frac{d^2 V}{dx^2} = -\frac{e\delta n}{\varepsilon_0} = -\frac{2V_c}{d_c^2} \qquad (9.11)$$

where the second derivative of equation (9.8) has been substituted to obtain the right-hand member of equation (9.11). Solving equation (9.11) for the net charge density yields

$$\delta n = \frac{2\varepsilon_0 V_c}{e d_c^2} \qquad \text{(particles/m}^3) \qquad (9.12)$$

which is a constant, positive net ion number density in the cathode region of the normal glow discharge. These functional dependences are indicated schematically in figure 9.4.

9.2.2 Unmagnetized Lorentzian Plasmas

We now derive, on a microscopic level, the power input into an unmagnetized DC glow discharge, using the parallel plate geometry shown in figure 9.7. Consider a glow discharge plasma described by a Lorentzian model, in which electrons lose their momentum to the neutral background gas with the collision frequency ν_c. In the geometry of figure 9.7, the equation of motion for individual electrons is given by

$$F = m_e a = m_e \frac{dv}{dt} = -\nu_c m_e v + eE. \qquad (9.13)$$

In a DC electric field, equation (9.13) becomes

$$\frac{dv}{dt} + \nu_c v - \frac{eE_0}{m_e} = 0. \qquad (9.14)$$

If we assume initial conditions for the electron (keeping in mind that this is a steady state discharge),

$$v(t) = v_0 \qquad \text{at } t = 0. \tag{9.15}$$

With this initial condition, the solution to equation (9.14) is

$$v(t) = \frac{eE_0}{\nu_c m_e} + \left(v_0 - \frac{eE_0}{\nu_c m_e} \right) e^{-\nu_c t}. \tag{9.16}$$

The second term in equation (9.16) is a starting transient, which dies out, leaving the constant drift velocity in the steady state,

$$v_d = \frac{eE_0}{\nu_c m_e} \equiv \mu_e E_0 \tag{9.17}$$

where μ_e is the *electron mobility*.

The work done on the electron by the electric field is

$$dW = \boldsymbol{F} \cdot d\boldsymbol{x} = eE_0 \, dx \qquad \text{(J)}. \tag{9.18}$$

The power absorbed by one electron is given by

$$p = \frac{dW}{dt} = eE_0 \frac{dx}{dt} = eE_0 v_d \qquad \text{(W)}. \tag{9.19}$$

Substituting equation (9.17) into equation (9.19) gives the power absorbed by one electron,

$$p = \frac{e^2 E_0^2}{\nu_c m_e} \qquad \text{(W/electron)}. \tag{9.20}$$

If the normal glow discharge has an electron number density n_e, the total power absorbed per unit volume is given by

$$P = n_e p = \frac{n_e e^2 E_0^2}{\nu_c m_e} \qquad \text{(W/m}^3\text{)}. \tag{9.21}$$

Here, we have ignored collective plasma effects which might shield a plasma from an externally imposed electric field.

We can express the power dissipation in terms of the energy density of the electrostatic field,

$$U_{\max} = \frac{1}{2} \varepsilon_0 E_0^2 \qquad \text{(J/m}^3\text{)} \tag{9.22}$$

and the electron plasma frequency,

$$\omega_{pe}^2 = \frac{n_e e^2}{\varepsilon_0 m_e}.$$ (9.23)

Equation 9.21 can be written in terms of equations (9.22) and (9.23) as follows,

$$P = \frac{1}{2}\varepsilon_0 E_0^2 \frac{n_e e^2}{\varepsilon_0 m_e} \frac{2}{\nu_c}.$$ (9.24)

Equation 9.24 then becomes

$$P = U_{max}\frac{2\omega_{pe}^2}{\nu_c} = U_{max}\nu_* \qquad (\mathrm{W/m}^3)$$ (9.25)

where the parameter ν_* is the *energy transfer frequency* which is the frequency, in hertz, with which the electrostatic energy density provided by the external power supply is transferred to a unit volume of the plasma. For this unmagnetized plasma the energy transfer frequency is

$$\nu_* = \frac{2\omega_{pe}^2}{\nu_c} \qquad (\mathrm{Hz}).$$ (9.26)

This frequency, which is fundamental to the transfer of energy into the plasma, is a function of electron number density, electron kinetic temperature, the type of gas, and the neutral background gas pressure.

9.2.3 Magnetized Lorentzian Plasmas

In some situations, it is desired to modify the characteristics of DC glow discharges by applying a magnetic field parallel to the electrodes of a parallel plate reactor, as shown in figure 9.8. There would be relatively little point to applying the magnetic field normal to the planes of the electrodes, since, as was shown in Chapter 4, the transport properties of the plasma along the magnetic field are identical with those in an unmagnetized plasma. Such a geometry might reduce edge losses and improve uniformity across the discharge, however.

If the magnetic field is applied as shown in figure 9.8, the individual ions and electrons will perform an E/B drift in the $+y$ (Hall) direction. An electron, shown to the right, will also perform a slow drift across the magnetic field lines in the $+x$ (Pedersen) direction, in response to the upward force on it by the applied electric field.

For a Lorentzian gas, the force on an individual electron in the parallel plate plasma reactor of figure 9.8 is given by

$$F = ma = q[E + (v \times B)] - m\nu_c v.$$ (9.27)
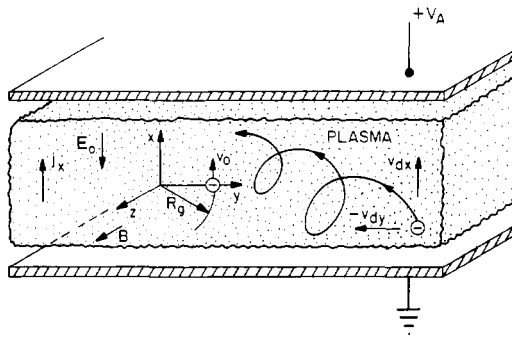
Figure 9.8 A schematic of a parallel plate reactor with a magnetized normal glow discharge plasma, the magnetic field pointing along the z axis.

In this configuration, the electric and magnetic fields and the charge on an electron are given by

$$E = (-E_0, 0, 0) \qquad (9.28a)$$

$$B = (0, 0, B_0) \qquad (9.28b)$$

and

$$q = -e. \qquad (9.28c)$$

As indicated on the left of figure 9.8, the initial conditions at $t = 0$ are

$$y = R_g = \frac{v_0}{\omega_c} \qquad (9.29a)$$

and

$$\frac{dy}{dt} = -v_{d,y} \qquad \text{at } t = 0. \qquad (9.29b)$$

The electron in this case is starting one gyroradius from the origin of the coordinate system at the time $t = 0$, where it is drifting in the y direction due to E/B drift. Also at $t = 0$,

$$x = 0 \qquad (9.30a)$$

and

$$\frac{dx}{dt} = +v_{d,x} + v_0. \qquad (9.30b)$$

The initial position is $x = 0$, and the velocity in the x direction is the gyro velocity v_0, added to the drift velocity in the direction of the electric field.

From equation (9.27), the equation of motion for an electron in the reactor of figure 9.8 is given for the x direction by

$$m\frac{d^2x}{dt^2} + mv_c\frac{dx}{dt} + eE_0 + eB_0\frac{dy}{dt} = 0 \tag{9.31}$$

and for the y direction by

$$m\frac{d^2y}{dt^2} - eB_0\frac{dx}{dt} + mv_c\frac{dy}{dt} = 0. \tag{9.32}$$

Rewriting equations (9.31) and (9.32), the equations of motion are

$$\frac{d^2x}{dt^2} + \omega_c\frac{dy}{dt} + v_c\frac{dx}{dt} + \frac{eE_0}{m} = 0 \tag{9.33}$$

and

$$\frac{d^2y}{dt^2} + v_c\frac{dy}{dt} - \omega_c\frac{dx}{dt} = 0 \tag{9.34}$$

where ω_c is the electron gyrofrequency. The solutions for the position of the electron as a function of time are given by

$$x(t) = -v_{d,x}t - \frac{v_0 v_c}{(v_c^2 + \omega_c^2)}$$
$$- \frac{v_0 e^{-v_c t}}{(v_c^2 + \omega_c^2)}(-v_c \cos\omega_c t + \omega_c \sin\omega_c t) \tag{9.35a}$$

and

$$y(t) = R_g - v_{dy}t - \frac{v_0 \omega_c}{(v_c^2 + \omega_c^2)}$$
$$+ \frac{v_0 e^{-v_c t}}{(v_c^2 + \omega_c^2)}(v_c \sin\omega_c t + \omega_c \cos\omega_c t) \tag{9.35b}$$

where the drift velocities are given by

$$v_{d,y} \equiv \frac{E_0}{B_0}\frac{\omega_c^2}{(v_c^2 + \omega_c^2)} \tag{9.36a}$$

and

$$v_{d,x} \equiv \frac{E_0}{B_0}\frac{\omega_c v_c}{(v_c^2 + \omega_c^2)}. \tag{9.36b}$$

The velocity components of the electron are given by differentiating equations (9.35a) and (9.35b) and applying the boundary conditions of equations (9.29) and (9.30), to obtain

$$\frac{dy}{dt} = -v_{dy} - v_0 e^{-v_c t} \sin \omega_c t \qquad (9.37a)$$

and

$$\frac{dx}{dt} = -v_{d,x} - v_0 e^{-v_c t} \cos \omega_c t. \qquad (9.37b)$$

The current density flowing in the x (Pedersen) direction is

$$J_x = en_e \frac{dx}{dt} \qquad (A/m^2). \qquad (9.38)$$

Using equation (9.37b), and neglecting the time-dependent transient term, equation (9.38) gives for the current density in the x direction,

$$J_x = -\frac{en_e E_0}{B_0} \frac{\omega_c v_c}{(v_c^2 + \omega_c^2)} = -en_e E_0 \mu_P \qquad (9.39)$$

where μ_P is the mobility in the Pederson direction. The Pederson mobility μ_P may be written in terms of the electron mobility in an unmagnetized plasma, μ_0, as

$$\mu_P \equiv \frac{\mu_0 v_c^2}{\omega_c^2 + v_c^2} \qquad (C\text{-}s/kg). \qquad (9.40)$$

One can obtain the current density in the y (Hall) direction by using equation (9.37a), and neglecting the transient terms, to obtain

$$J_y = en_e \frac{dy}{dt} = -en_e v_{dy} = -\frac{e^2 n_e E_0}{m v_c} \frac{\omega_c v_c}{(v_c^2 + \omega_c^2)}. \qquad (9.41)$$

The current density in the y direction can then be written in terms of the *Hall mobility* μ_H,

$$J_y = -en_e E_0 \frac{\mu_0 \omega_c v_c}{(\omega_c^2 + v_c^2)} = -en_e E_0 \mu_H \qquad (9.42)$$

where the Hall mobility is

$$\mu_H \equiv \frac{\mu_0 \omega_c v_c}{(\omega_c^2 + v_c^2)} \qquad (C\text{-}s/kg). \qquad (9.43)$$

It should be noted that the presence of a magnetic field decreases the mobility along the electric field, thus leading to 'magnetic confinement', while increasing the Hall mobility of equation (9.43), which is zero in the absence of a magnetic field.

The power dissipated by the electric field is given by

$$P = n_e F \cdot v \qquad (\text{W/m}^3) \qquad (9.44)$$

where the force exerted by the electric field is given by

$$F = (eE_0, 0, 0) \qquad (\text{N}). \qquad (9.45)$$

Substituting equation (9.37b) into equation (9.44) gives the total power transferred to the plasma by the electric field, neglecting the time dependent transient terms,

$$P = -en_e E_0 \frac{\mathrm{d}x}{\mathrm{d}t} = -\frac{n_e E_0^2}{B_0} \frac{\omega_c \nu_c}{(\nu_c^2 + \omega_c^2)} \qquad (\text{W/m}^3). \qquad (9.46)$$

The right-hand member of equation (9.46) may be factored into the electrostatic energy density, U, of the electric field provided by the power supply; the electron plasma frequency; and the energy transfer frequency, ν_*, as follows,

$$
\begin{aligned}
P &= \frac{1}{2}\varepsilon_0 E_0^2 \frac{e^2 n_e}{m\varepsilon_0} \frac{2\nu_c}{(\omega_c^2 + \nu_c^2)} \\
&= U \frac{2\omega_{pe}^2 \nu_c}{(\omega_c^2 + \nu_c^2)} = U\nu_*. \qquad (9.47)
\end{aligned}
$$

The energy transfer frequency in the magnetized Lorentzian discharge is a measure of the rate at which energy is transferred from the power supply to the plasma, and may be written in terms of the energy transfer frequency for the unmagnetized discharge, ν_{*0}, as follows,

$$\nu_* \equiv \frac{2\omega_{pe}^2}{\nu_c} \frac{\nu_c^2}{(\omega_c^2 + \nu_c^2)} = \nu_{*0} \frac{\nu_c^2}{(\omega_c^2 + \nu_c^2)}. \qquad (9.48)$$

The effect of a magnetic field perpendicular to the DC electric field is always to decrease the energy transfer frequency, and hence the power input into a magnetized DC glow discharge. If this reduction in power is not accompanied by a reduction in number density or other desired discharge properties, it can be of practical advantage.

If the neutral gas pressure (and hence the collision frequency ν_c) is held constant while the magnetic induction (and hence ω_c) is varied,

equation (9.48) implies that the energy transfer frequency ν_* is a maximum when $\omega_c = 0$, i.e. for an unmagnetized plasma. If, on the other hand, ω_c is fixed and the gas pressure (and hence ν_c) is varied, the energy transfer frequency will be a maximum when

$$\frac{\mathrm{d}\nu_*}{\mathrm{d}\nu_c} = \frac{2\omega_{pe}^2}{\left(\omega_c^2 + \nu_c^2\right)^2} \left(\omega_c^2 - \nu_c^2\right) = 0 \qquad (9.49)$$

i.e. when

$$\omega_c = \nu_c. \qquad (9.50)$$

The value of the energy transfer frequency at this point is

$$\nu_* = \frac{\omega_{pe}^2}{\nu_c} = \frac{1}{2}\nu_{*0} \qquad (9.51)$$

i.e. half the energy transfer frequency of an unmagnetized plasma.

9.2.4 Schottky Condition

Schottky (1924) was able to show that the electron kinetic temperature of a cylindrical positive column in a normal glow discharge is determined by the constraint that the electron number density go to zero at the outer radius of the plasma, $r = a$. In the steady state, the equation of continuity for electrons can be written

$$\frac{1}{r}\frac{\mathrm{d}}{\mathrm{d}r}\left(r\Gamma_{er}\right) = S_i = n_e n_0 \langle \sigma v \rangle_{ne}. \qquad (9.52)$$

From Fick's law of diffusion, the radial electron flux Γ_{er} can be written as

$$\Gamma_{er} = -D_e \frac{\mathrm{d}n_e}{\mathrm{d}r}. \qquad (9.53)$$

The radial electron diffusion coefficient D_e may be a weak function of the electron kinetic temperature. Substituting equation (9.53) into equation (9.52) yields

$$\frac{D_e}{r}\frac{\mathrm{d}}{\mathrm{d}r}\left(r\frac{\mathrm{d}n_e}{\mathrm{d}r}\right) + n_e n_0 \langle \sigma v \rangle_{ne} = 0 \qquad (9.54)$$

provided that D_e is not a function of radius. If we use the electron temperature-dependent ionization frequency

$$\nu_i = n_0 \langle \sigma v \rangle_{ne} = f(T_e) \qquad (9.55)$$

to simplify equation (9.54), we obtain Bessel's equation. By substituting equation (9.55) into (9.54), we obtain

$$\frac{1}{r}\frac{\mathrm{d}}{\mathrm{d}r}\left(r\frac{\mathrm{d}n_e}{\mathrm{d}r}\right) + \frac{\nu_i n_e}{D_e} = 0. \tag{9.56}$$

For the boundary conditions $n_e(a) = 0$ and $n_e(0) = n_{e0}$, equation (9.56) has the solution

$$n_e(r) = n_{e0} J_0\left(\frac{2.405r}{a}\right). \tag{9.57}$$

In cylindrical positive column normal glow discharges, the boundary condition that the electron number density goes to zero at $r = a$, the positive column radius, implies that

$$\frac{\nu_i(T_e)}{D_e(T_e)} = \left(\frac{2.405}{a}\right)^2. \tag{9.58}$$

Equation (9.58) is known as the *Schottky condition*, and it places a constraint on the electron kinetic temperature, T_e, required to maintain the positive column in the steady state. This is usually interpreted to imply that the electron kinetic temperature of the positive column is determined by its radius.

9.2.5 T_e from Conservation of Particles

Consider the plane parallel plasma reactor shown in figure 9.7, which contains a glow discharge. This geometry is very common in industrial applications, and in this section we will show that the breakdown parameter, the product of pd, is a function only of the electron temperature of such plasmas.

In figure 9.7 the current density flowing between the electrodes in the x direction may be written as

$$J_x = en_e v_{d,x} = en_e \mu_e E_0 \quad (\mathrm{A/m^2}) \tag{9.59}$$

where μ_e is the electron mobility given by

$$\mu_e = \frac{e}{m_e \nu_c} = \mu_e(T_e). \tag{9.60}$$

The mobility is, in general, a function of the electron kinetic temperature. The total current collected by the electrode is the product of the area of the electrode A_E times the current density,

$$I_e = A_E J_x = en_e \mu_e E_0 A_E \quad (\mathrm{A}). \tag{9.61}$$

We can now compare the current drawn by the power supply, given by equation (9.61), with the rate at which charges are created inside the plasma. The number of ionizations per cubic meter per second in a glow discharge is given by the ionization (reaction) rate,

$$R = n_e n_0 \langle \sigma v \rangle_{ne} \quad \text{(ionizations/m}^3\text{-s)} \quad (9.62)$$

where the ionization rate coefficient is given by

$$\langle \sigma v \rangle_{ne} = \langle \sigma v \rangle_{ne}(T_e) \quad \text{(m}^3\text{/s)} \quad (9.63)$$

which is also a function of the electron kinetic temperature. The ionization rate coefficient is usually a function of electron temperature between about 1 and 5 eV, the operating range of most DC glow discharges. If there is no recombination in the plasma volume, and if all ionizations are single ionizations, the total current in coulombs per second (amperes) collected by the electrode is given by equation (9.62), multiplied by the single electronic charge on each electron or ion produced by the ionization; and by the volume of the discharge which, for the plane parallel reactor, is just the electrode area A_E times the electrode separation d,

$$I_e = e V_p R = e A_E d R \quad \text{(A)}. \quad (9.64)$$

Equating the source of electrons created by ionization in equation (9.64) to the current flowing to the electrodes in equation (9.61) yields the following relationship,

$$\mu_e E_0 = d n_0 \langle \sigma v \rangle_{ne}. \quad (9.65)$$

Equation 9.65 can be rearranged, keeping in mind that the neutral number density n_0 is proportional to the gas pressure, as follows:

$$\frac{1}{pd} \sim \frac{1}{n_0 d} = \frac{\langle \sigma v \rangle_{ne}}{E_0 \mu_e} = f(T_e). \quad (9.66)$$

The normal glow discharge operates in a regime where the voltage across the discharge is almost independent of current. Because $E_0 = V_A/d$, the electric field appearing in the denominator is approximately constant for a normal glow discharge. Equation 9.66 then implies that the breakdown parameter pd, the product of pressure and electrode separation of a glow discharge, is determined by the electron temperature. This is a result similar to the Schottky relationship of equation (9.58), but is based on the axial plasma parameters, rather than the radial particle balance, which is a more specialized condition.

9.2.6 n_e from Conservation of Energy

Having shown that the breakdown parameter pd in normal glow discharges is determined by the electron kinetic temperature, we will now show that the electron number density in DC glow discharges is related to the total power dissipated in the discharge.

The total power dissipated in the normal glow discharge of figure 9.7 is given by

$$P_{\text{tot}} = V_a I_a \qquad \text{(W)} \qquad (9.67)$$

and is simply the product of the anode voltage and the total current flowing to the power supply. Since the discharge is in the steady state, the flux of ions and electrons to the anode and cathode are equal,

$$\Gamma_e = \Gamma_i \qquad \text{(particles/m}^2\text{-s).} \qquad (9.68)$$

Were this relationship not true, a charge would build up in the plasma, violating the initial assumption of a DC discharge, and of quasi-neutrality.

If power lost by line radiation, charge exchange, and recombination are ignored, all of which are normally not large in normal glow DC electrical discharges, the power carried by the electron flux to the anode is given by

$$P_e = e\Gamma_e A \left(\mathcal{E}'_* + \mathcal{E}'_e \right) \qquad \text{(W)} \qquad (9.69)$$

where A is the cross-sectional area of the discharge, and

$$\mathcal{E}'_* = \text{eV/electron–ion pair} = f(T_e). \qquad (9.70)$$

The parameter $\mathcal{E}'_*$ is the number of electronvolts required to produce each electron–ion pair, and is a function of the electron kinetic temperature of the discharge. This parameter is also related to the Stoletow parameters of table 8.2, and is typically from 40 to 90 eV/electron–ion pair. From equation (2.32), in our discussion of kinetic theory, the energy of particles hitting a surface is given by

$$\mathcal{E}'_e = 2T'_e. \qquad (9.71)$$

The bombarding energy is higher than the mean energy of the gas by a factor of 4/3, since the particles which hit the surface have higher average velocities than those that remain in the discharge.

The power carried by the ion flux to the cathode is given by

$$P_i = e\Gamma_i A \mathcal{E}'_i = e\Gamma_e A \mathcal{E}'_i \qquad (9.72)$$

where $\mathcal{E}'_i$ is the ion bombarding energy in eV, and depends on the sheath and discharge characteristics. This may range from a few electronvolts

to several hundred electronvolts, depending on the discharge operating parameters. If the plasma is quasi-neutral, normally an excellent assumption, then the equality of the two fluxes implies

$$\Gamma_e = \Gamma_i = n_e v_{de} = n_e \mu_e E_0. \tag{9.73}$$

Equating the total power delivered to the discharge given by equation (9.67) to the total power carried by the ions and electrons to the electrodes yields, with the help of equations (9.69) and (9.72),

$$P_{tot} = V_a I_a = P_e + P_i = e A n_e \mu_e E_0 (2T_e' + \mathcal{E}_*' + \mathcal{E}_i'). \tag{9.74}$$

Equation 9.74 can be rearranged to solve explicitly for the average electron number density in the normal glow discharge,

$$n_e = \frac{V_a I_a}{e A \mu_e E_0 (2T_e' + \mathcal{E}_*' + \mathcal{E}_i')} \qquad \text{(electrons/m}^3\text{)}. \tag{9.75}$$

Because this is a normal glow discharge, the electric field in the positive column will remain approximately constant while the plasma parameters change. If the plasma operating conditions are not changed too radically, the electron number density is linearly proportional to the power input to the glow discharge, and inversely proportional to a weak function of the electron kinetic temperature. The denominator of equation (9.75) is at most a linear function of electron temperature, and the electron temperature itself tends to be a rather slowly varying function of the input power. Thus, equation (9.75) implies that the electron number density is a linear function of the input power to the discharge, a useful relationship in many practical applications.

9.2.7 Power Distribution in DC Glow Discharges

The power distribution in DC glow discharges is important, especially when they are used as lighting devices where efficiency is a major factor. The power density may be written in terms of the electric field and the energy transfer frequency using equations (9.22) and (9.25),

$$p = \frac{\varepsilon_0 v_*}{2} E^2 \qquad \text{(W/m}^3\text{)} \tag{9.76}$$

where v_* is in hertz, and E is the electric field in volts per meter. From figure 9.4 it is evident that most of the power dissipation in a normal glow discharge occurs in the cathode region, between 0 and $x = d_c$, where the electric field is highest. Thus, in the normal glow discharge, the cathode structures represent fixed losses, and the plasma of the positive column is
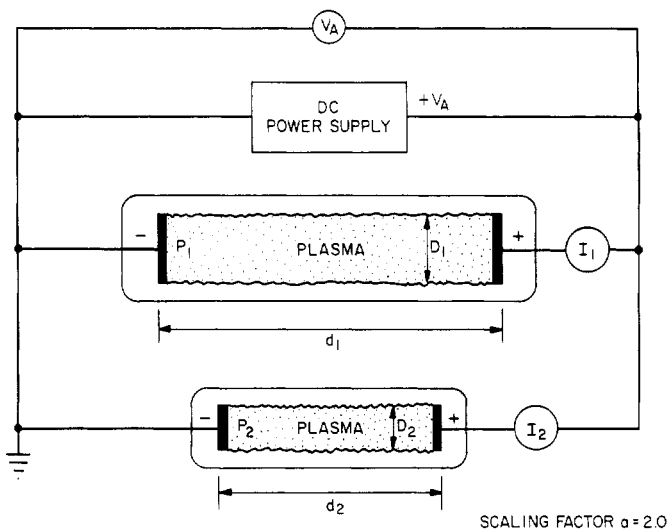
Figure 9.9 Two similar electrical discharge tubes, with dimensions that differ by a factor of two.

almost 'free' in terms of its energy cost. For this reason lighting devices such as fluorescent light tubes, which depend on the positive column, should be as long as possible.

9.2.8 Similarity Relations

A problem which often arises in the design of DC glow discharge plasma reactors, or in electrical lighting devices based on glow discharges, is the scaling in size of a glow discharge from a size which is known to work satisfactorily, to a larger or smaller size. Two glow discharges like those illustrated in figure 9.9 with the same voltage drop V_A across their electrodes, and drawing the same total current in amperes are said to be *similar* if their axial dimensions are related by

$$d_1 = ad_2 \qquad (9.77)$$

and their diameters by

$$D_1 = aD_2. \qquad (9.78)$$

In addition, *similar discharges* have pressures related by

$$p_2 = ap_1. \qquad (9.79)$$

Figure 9.9 shows two similar DC electrical discharge tubes, both connected in parallel to the same power supply and drawing the same

current, $I_1 = I_2$. In similar discharges, the pressures and *all* the dimensions of the discharge are decreased/increased by the same factor, a, which is taken in figure 9.9 to be a factor of 2. It is a characteristic of similar discharges that they draw the same power from the power supply, even though their dimensions and other characteristics differ. This facilitates the design of lighting devices, which are driven by the same voltage, and in which one usually wants the same luminous power output.

In similar discharges, the kinetic and plasma parameters of the discharge scale in a prescribed way. The mean free paths in the two discharges of figure 9.9 are related by

$$\lambda_1 = a\lambda_2 \tag{9.80}$$

and the electric fields are related by

$$E_2 = aE_1. \tag{9.81}$$

The fact that the two discharges draw the same total current in amperes gives the scaling of the current densities,

$$J_2 = a^2 J_1 \tag{9.82}$$

and from this follows the scaling of the electron number densities in the two discharges,

$$n_{e2} = a^2 n_{e1}. \tag{9.83}$$

The utility of similar discharge scaling becomes apparent in the way in which it conserves tabulated experimental data on the behavior of electrical discharges in gases. In similar discharges, the breakdown parameter dp is the same,

$$d_1 p_1 = d_2 p_2 = \text{constant} \tag{9.84}$$

while Townsend's first ionization coefficient scales as

$$\alpha_1 = a\alpha_2. \tag{9.85}$$

The parameter α/p is constant for similar discharges,

$$\frac{\alpha_1}{p_1} = \frac{\alpha_2}{p_2} = \text{constant} \tag{9.86}$$

as is the ratio of the electric field to pressure,

$$\frac{E_1}{p_1} = \frac{E_2}{p_2} = \text{constant}. \tag{9.87}$$

Equations (9.84), (9.86), and (9.87) imply that by scaling a discharge according to the above similarity conditions, one can continue to use known, and presumably reliable, experimental data on Townsend's first ionization coefficient and other related plasma characteristics.
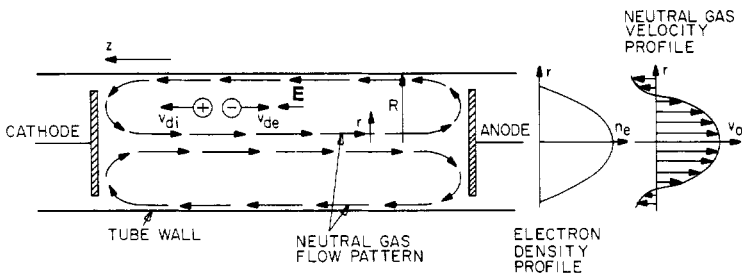
Figure 9.10 Circulation of neutral gas in a DC normal glow electrical discharge tube.

9.3 THEORY OF MOVING STRIATIONS

Moving striations occur at low pressures, where the ionizing mean free paths are long, and Fick's law may not be valid because these mean free paths are comparable to or larger than the density gradient scale length in the gas. Moving striations arise as the result of finite time delays which occur as electrons and neutrals collide and ionize in a low pressure Lorentzian plasma.

9.3.1 Discharge Characteristics

Consider the low pressure electrical discharge tube shown in figure 9.10. This illustrates a DC normal glow discharge, in which there is a convective flow of neutral gas on the axis, driven by the momentum imparted by electron–neutral impacts. Such a flow is common in electrical discharge tubes, and the velocities, particularly at low pressures (on the order of millitorr) can approach the speed of sound. This momentum transfer by the electron population is responsible for the behavior of the classical 'railway tube' discussed in Chapter 1. The electron and ion number densities are assumed to have a Bessel function radial profile, with the neutral number density being constant across the diameter of the discharge.

9.3.2 Equations of Continuity

The continuity equations for neutrals, electrons, and ions in a partially ionized gas are given, respectively, by equations (9.88) through (9.90),

$$\frac{dn}{dt} = -\nabla \cdot \Gamma_n - n_e n \langle \sigma v \rangle_{ne} \tag{9.88}$$

$$\frac{dn_e}{dt} = -\nabla \cdot \Gamma_e + n_e n \langle \sigma v \rangle_{ne} \tag{9.89}$$

and

$$\frac{dn_i}{dt} = -\nabla \cdot \Gamma_i + n_e n \langle \sigma v \rangle_{ne}. \tag{9.90}$$

When the mean free paths of all three species are small compared to the plasma radius, Fick's law of diffusion is valid, and, if quasi-neutrality holds, the electron and ion number densities will have an approximate Bessel function dependence, discussed previously in connection with the Schottky condition.

In this small mean free path limit, the divergence terms of the above equations have the form

$$\nabla \cdot \Gamma \to \frac{2.405^2 D_\perp}{a^2} n_{e,i} - \frac{\partial \phi}{\partial z} \tag{9.91}$$

where the second term on the right is the convective term along the axis, and the first term on the right accounts for Fickian radial diffusion. If the plasma is axisymmetric, the continuity equations in the Fickian limit become

$$\frac{dn}{dt} = -\frac{\partial \Gamma_n}{\partial z} - n_e n \langle \sigma v \rangle_{ne} \tag{9.92}$$

$$\frac{dn_e}{dt} = -\frac{\partial \Gamma_e}{\partial z} - \frac{2.405^2 D_{\perp e}}{a^2} n_e + n_e n \langle \sigma v \rangle_{ne} \tag{9.93}$$

$$\frac{dn_i}{dt} = -\frac{\partial \Gamma_i}{\partial z} - \frac{2.405^2 D_{\perp i}}{a^2} n_i + n_e n \langle \sigma v \rangle_{ne}. \tag{9.94}$$

In general, these equations may be oscillatory and damped, but are not periodic.

When the neutral gas pressure is below 1 Torr, the ionization mean free paths of the electrons and the collisional mean free paths of the neutrals can become comparable to the plasma radius and to the characteristic dimension of the density gradients. In such plasmas the requirement that the mean free path be smaller than the characteristic dimension of the density gradient is no longer met, and Fick's law of diffusion is no longer valid. In this long mean free path limit, the divergence terms of the particle continuity equation must be regarded as the net particle flux across the surface of a small sphere centered at the point of interest, as shown in figure 9.11. The outward flux across this sphere depends on the particle number density within the sphere at the time of observation, t; the inward flux, because of the long mean free paths, depends instead on the particle density one mean free time in the past, $t - t_0$, at a distance of one mean free path from the point of interest. This dependence of
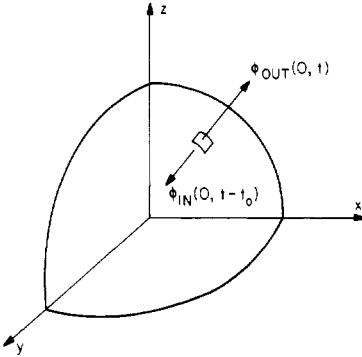
Figure 9.11 The relationship between particle fluxes and time delays across an infinitesimal sphere in a plasma not satisfying Fick's law of diffusion.

the net flux across a small sphere on the mean free time, t_0, between collisions introduces a time delay into the equations of continuity. Like similar situations in control theory, the introduction of a time delay into the system is destabilizing, and leads to propagating waves of electron number density in the plasma.

This time delay, which appears in the divergence term, yields a divergence term for the neutral particle continuity equation in the long mean free path limit given by Roth (1967, 1969b, d)

$$-\nabla_z \cdot \Gamma_n \approx -q v_0 \frac{dn}{dz} + n(z, t) \hat{n}_e \langle \sigma v \rangle_{ne} \qquad (9.95)$$

where $\hat{n}_e$ is the time- and space-averaged electron number density, and the first term on the right is the convective term for neutral gas with the drift velocity v_0 along the axis of the discharge. The parameter q is ± 1 depending on whether the gas is flowing to (+) or from (−) the anode. The z component of the net electron and ion fluxes, which appear in the electron and ion continuity equations, is included in the electron divergence term given by

$$-\nabla_z \cdot \Gamma_e \approx v_{de} \frac{dn_e}{dz} - \hat{n} \langle \sigma v \rangle_{ne} n_e(z, t) \qquad (9.96)$$

where $\hat{n}$ is the time- and space-averaged neutral number density. The first term of equation (9.96) is the convective term describing the electron drift velocity along the axis of the discharge, and the second term is the non-Fickian contribution due to the time delay introduced by the long mean free paths in the discharge. An equation similar to equation (9.96) may be written for the non-Fickian ion contribution to the divergence term in the ion continuity equation (Roth 1969b, d).

Utilizing equations (9.95) and (9.96) at low presures in the non-Fickian limit, the continuity equations for the discharge tube of figure 9.10 may be written as

$$\frac{dn}{dt} = -qv_0\frac{dn}{dz} + \hat{n}_e n\langle\sigma v\rangle_{ne} - n_e n\langle\sigma v\rangle_{ne} \qquad (9.97)$$

$$\frac{dn_e}{dt} = v_{de}\frac{dn_e}{dz} - \alpha_e\hat{n}n_e\langle\sigma v\rangle_{ne} - \frac{2.405^2 D_\perp}{a^2}n_e + n_e n\langle\sigma v\rangle_{ne} \qquad (9.98)$$

$$\frac{dn_i}{dt} = -sv_{di}\frac{dn_i}{dz} - \alpha_i\hat{n}n_e\langle\sigma v\rangle_{ne} - \frac{2.405^2 D_\perp}{a^2}n_i + n_e n\langle\sigma v\rangle_{ne} \qquad (9.99)$$

for neutrals, electrons and ions, respectively. The parameters q and s are direction indices, -1 for flow *to* the cathode, and $+1$ for flow *from* the cathode. These indices are introduced to show explicitly the effects of oppositely directed neutral (q) and ion (s) drift velocities. The parameters α_e and α_i appearing in the second terms of equations (9.98) and (9.99) arise from the fact that $(1 - \alpha_e)$ and $(1 - \alpha_i)$ are the net radial time- and space-averaged electron and ion efflux, respectively. Equation 9.97 can represent metastables, if they are the species being ionized.

The neutral drift velocity v_0 has been observed to play a crucial role in determining the dispersive properties of moving striations. The neutral drift velocity is driven by the momentum transfer to the neutral gas from the electrons which drift along the axis, and is proportional to the current density. The neutral number density is higher at the anode than at the cathode, and this axial pressure gradient leads to a reflux of neutral gas along the edges of the discharge. In the steady state, the gas recirculates in the manner shown in figure 9.10.

The electron and ion drift velocities, v_{de} and v_{di}, are the effective values in the positive column. The terms containing the diffusion coefficients account for the radial loss of ions and electrons. It is assumed that electron–neutral impact ionization with the rate coefficient $\langle\sigma v\rangle_{ne}$ is the only ionization process. The second terms on the right-hand side of equations (9.98) and (9.99) follow from the divergence of the net flux of the ionized species under low pressure conditions when transit time effects are important, and these terms are consequently larger than the usual axial diffusion terms which they replace. The fourth terms of equations (9.98) and (9.99) result from the fact that ions and electrons are created in pairs. We further assume that the plasma is quasi-neutral, so $n_i \approx n_e$.

Equations (9.97) to (9.99) may be non-dimensionalized in the following way. If the number densities of neutrals, electrons and ions are modulated in a sinusoidal manner, one may write for all three species

$$n = n_0 + n_1\sin\theta \qquad (9.100)$$

where the traveling wave argument is given by

$$\theta = kz - \omega t. \tag{9.101}$$

We now define a dimensionless wave number K in terms of the electron drift velocity,

$$K \equiv \frac{v_{de}k}{\omega_0} = \frac{2\pi v_{de}}{\lambda \omega_0}. \tag{9.102}$$

and a dimensionless frequency W, defined by

$$W \equiv \frac{\omega}{\omega_0}. \tag{9.103}$$

The normalizing frequency ω_0 appearing in equations (9.102) and (9.103) is given by

$$\omega_0 = \sqrt{\hat{n}_e n_1} \langle \sigma v \rangle_{ne}. \tag{9.104}$$

Equation (9.104) contains the time- and space-averaged electron and neutral number densities under the square root. If the electron number density at $t = 0$ is written

$$n_e(t = 0) = n_{e0} \tag{9.105}$$

we can define an average neutral density parameter,

$$n_1 = \begin{cases} n_{1e} & \text{in the electron equation} \\ n_{1i} & \text{in the ion equation} \end{cases} \tag{9.106}$$

The neutral density parameter n_{1e} appearing in the electron equation is given by

$$n_{1e} \equiv \alpha_e \hat{n} + \frac{(2.405)^2 D_{\perp e}}{a^2 \langle \sigma v \rangle_{ne}} \tag{9.107}$$

and the neutral density parameter, n_{1i}, which appears in the ion equation, is given by

$$n_{1i} \equiv \alpha_i \hat{n} + \frac{(2.405)^2 D_{\perp i}}{a^2 \langle \sigma v \rangle_{ne}}. \tag{9.108}$$

We further define a dimensionless electron number density, y, given by

$$y \equiv \frac{n_e}{n_{e0}} \tag{9.109}$$

a dimensionless neutral number density, x, given by

$$x \equiv \frac{n}{n_1} \tag{9.110}$$

an ionization fraction, δ, given by

$$\delta \equiv \frac{\hat{n}_e}{n_1} \tag{9.111}$$

and an amplitude modulation factor, η, given by

$$\eta \equiv \frac{\hat{n}_e}{n_{e0}}. \tag{9.112}$$

We finally define a dimensionless neutral gas drift velocity, γ,

$$\gamma \equiv \frac{v_0}{v_{de}} \tag{9.113}$$

and a dimensionless ion drift velocity, β,

$$\beta \equiv \frac{v_{di}}{v_{de}}. \tag{9.114}$$

Substituting these dimensionless parameters into equations (9.97) through (9.99) yields, with $n_i = n_e$ from quasi-neutrality,

$$\frac{dx}{d\theta} = \frac{\delta^{1/2} x(y - \eta)}{(W - q\gamma K)\eta} \qquad \text{for neutrals, metastables} \tag{9.115}$$

$$\frac{dy}{d\theta} = \frac{\delta^{-1/2} y(1 - x)}{(W + K)} \qquad \text{for electrons} \tag{9.116}$$

$$\frac{dy}{d\theta} = \frac{\delta^{-1/2} y(1 - x)}{(W - s\beta K)} \qquad \text{for ions.} \tag{9.117}$$

The left-hand sides of equations (9.116) and (9.117) are not actually equal, but differ by a small term determined by Poisson's equation and the axial electric field. The density parameter given by equation (9.107) is used when equations (9.115) and (9.116) are considered, and the neutral density parameter given by equation (9.108) is used when equations (9.115) and (9.117) are considered. Equations (9.115) and (9.116), and (9.115) and (9.117), considered as pairs, are Lotka–Volterra equations and can have periodic solutions.
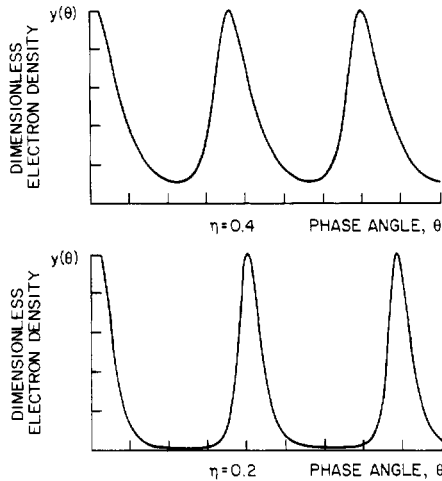
Figure 9.12 Two calculated waveforms of the electron number density of moving striations, for two ratios of maximum to minimum values.

A numerical solution to equations (9.115) and (9.116) is shown in figure 9.12. These two examples plot the normalized electron number density as a function of phase angle for two conditions of operation. Like actual striation waveforms, these examples have a steep initial slope, followed by an approximately exponential dropoff after the maximum of electron number density. The lower example is one in which there are sharp narrow peaks between broad, flat minima.

9.3.3 Dispersion Relation for Moving Striations

If a linearized, small perturbation analysis of these pairs of equations is performed, based on equation (9.100), equations (9.115) and (9.116) yield a dispersion relation

$$(W + K)(W - q\gamma K) = 1. \tag{9.118}$$

This relation describes a pair of dispersion curves for electron–neutral striations, the dominant phenomenon in most DC electrical discharge tubes, given by

$$W_{e\pm} = \frac{1}{2}\left[-(1 - q\gamma)K \pm \sqrt{(1 + q\gamma)^2 K^2 + 4}\right]. \tag{9.119}$$

From equations (9.115) and (9.117) one obtains a second dispersion relation

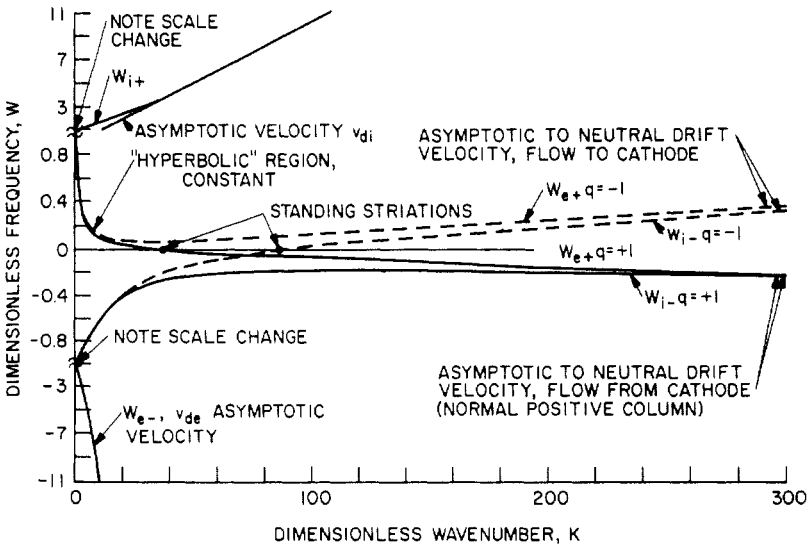$$(W - s\beta K)(W - q\gamma K) = 1 \tag{9.120}$$

Figure 9.13 The complete dispersion curves for moving striations in DC normal glow electrical discharge tubes like those illustrated in figure 9.10.

which yields a second pair of dispersion curves for ion–neutral striations,

$$W_{i\pm} = \frac{1}{2}\left[(s\beta + q\gamma)K \pm \sqrt{(s\beta - q\gamma)^2 K^2 + 4} \right].$$ (9.121)

The striations described by equation (9.121) are usually heavily damped and are seldom observed in electrical discharge tubes.

The shape of the four dispersion curves is illustrated on figure 9.13. The solid curves are for $q = +1$, which should hold for conventional positive columns, and the dotted curves for $q = -1$, the physically unlikely case of neutral gas flow to the cathode. A dispersion curve for electron–neutral striations is shown in figure 9.14. As $K \rightarrow 0$, all four curves become asymptotic to $W = \pm 1$, the asymptotic frequency of equation (9.104). At the opposite limit for which $K \rightarrow \infty$, the dispersion curves become asymptotic to straight lines representing the neutral gas drift velocity.

Another feature of the dispersion curve of figure 9.13 is that standing striations, of a kind shown in the photograph of figure 9.5, occur when equations (9.119) and (9.121) are equal to zero, or

$$K_{se}^2 = -\frac{1}{q\gamma}$$ (9.122a)

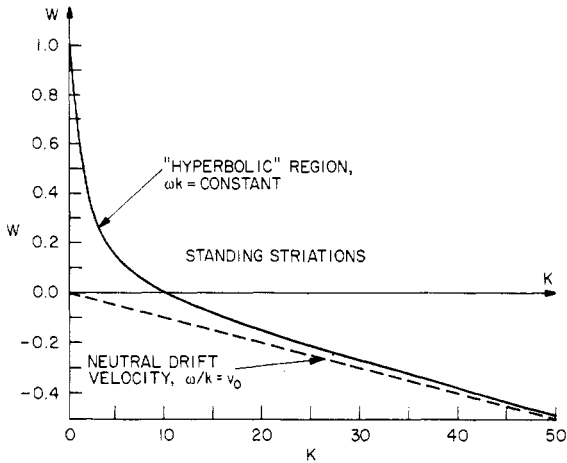$$K_{si}^2 = \frac{1}{qs\gamma\beta}.$$ (9.122b)

Figure 9.14 A dispersion curve for the principal branch of moving striations, most commonly observed, showing the hyperbolic region, standing striations, and the asymptotic convergence to the drift velocity of the neutral gas along the axis of the discharge tube, as $K \to \infty$.

These standing striations are not a standing wave in the discharge tube; they result from the propagation of the moving striation with a velocity that is exactly equal, but opposite, to the neutral gas drift velocity.

The choice of non-dimensionalizing parameters is such that $K > 1$ for typical positive columns, so that the 'hyperbolic' branches of equations (9.119) and (9.121) can be approximated by

$$W_{e+} \approx K \left[\frac{1}{K^2(1 + q\gamma)} + q\gamma \right] \qquad (9.123a)$$

$$W_{i-} \approx K \left[\frac{1}{K^2(q\gamma - s\beta)} + q\gamma \right]. \qquad (9.123b)$$

When the second terms are small, one obtains for positive striations a dispersion relation of the form $\omega k = $ constant, consistent with the dispersion curve observed experimentally. A dispersion curve very much like that shown on figure 9.14 has been observed in neon gas by Barrett and Little (1965) in the data shown in figure 9.15.

As one goes to lower and lower neutral gas pressures, the dimensionless wave number $K \to 0$, and the entire discharge then oscillates in unison, with a single phase and frequency. When these continuity equation oscillations occur coherently, rather than incoherently as is normally the case, an undesirable modulation of the plasma number density can result. As an example of this, consider a quasi-neutral plasma in which all of the drift velocities are zero, and in which there is no radial
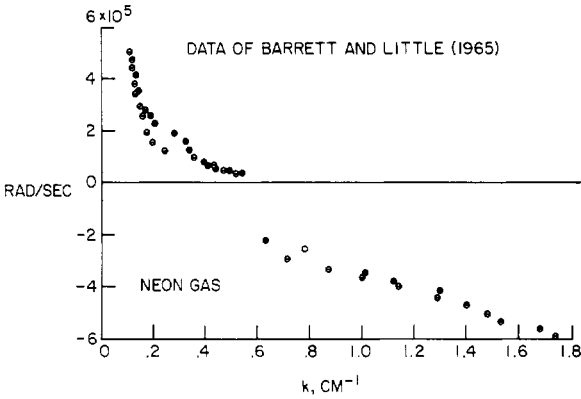
Figure 9.15 Measured dispersion characteristics of moving striations in neon gas as measured by Barrett and Little (1965), compared with the theoretical dispersion curve of figure 9.14.

dependence of the electron or ion number density. In such a plasma, equations (9.97) and (9.98) become

$$\frac{\partial n}{\partial t} = n\hat{n}_e \langle \sigma v \rangle_{ne} - n n_e \langle \sigma v \rangle_{ne} \qquad (9.124)$$

$$\frac{\partial n_e}{\partial t} = -\hat{n} n_e \langle \sigma v \rangle_{ne} + n n_e \langle \sigma v \rangle_{ne}. \qquad (9.125)$$

where $\hat{n}_e$ and $\hat{n}$ are the time- and space-averaged electron and neutral number density, respectively.

This pair of coupled, nonlinear first-order differential equations is of Lotka–Volterra form, and has periodic solutions (Roth 1967, 1969a).
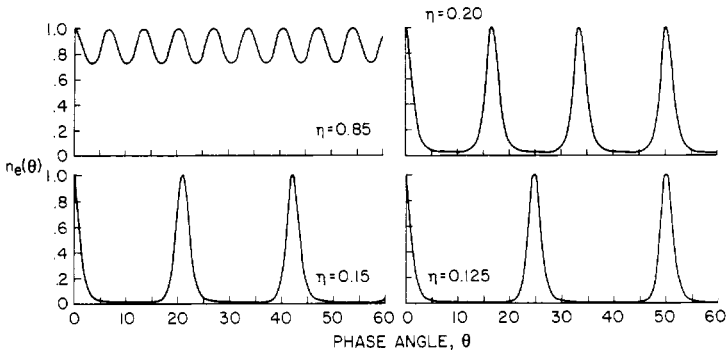

Figure 9.16 Relative electron number density in standing striations as a function of the peak-to-peak amplitude of the electron number density fluctuations.

$\longleftarrow$ t

20 μSEC / CM, $p_T = 8.1 \times 10^{-6}$ TORR

20 μSEC / CM, $p_T = 1.2 \times 10^{-5}$ TORR

10 μSEC / CM, $p_T = 1.7 \times 10^{-5}$ TORR

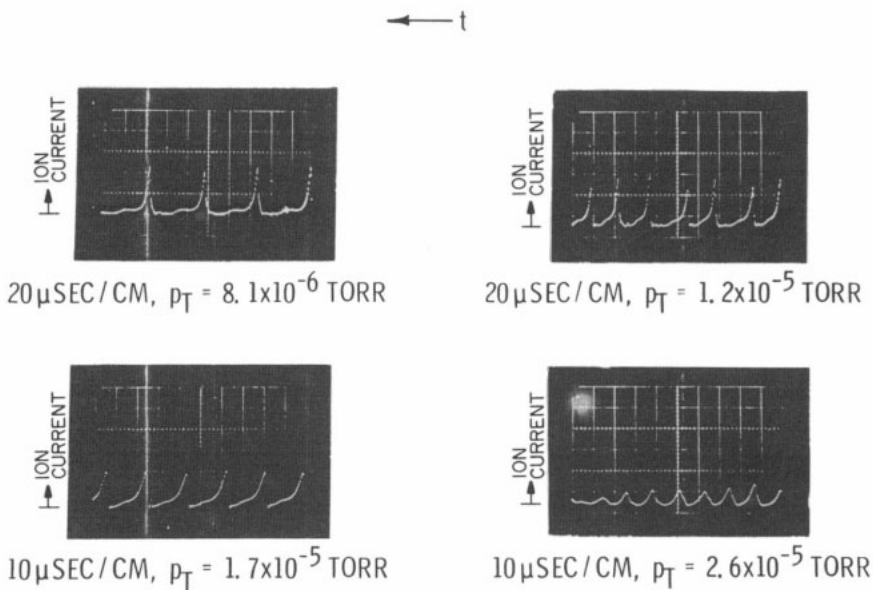10 μSEC / CM, $p_T = 2.6 \times 10^{-5}$ TORR

Figure 9.17 The ion efflux from a low pressure plasma experiment as a function of time, illustrating ion density waveforms similar to those of figure 9.16. Time increases to the left.

An example of some computer solutions to these equations is shown in figure 9.16. When the electron number density is only weakly modulated, as in the upper left, the waveform is approximately sinusoidal. As the peak-to-peak amplitude becomes comparable to the total amplitude, the waveform of this oscillation is described approximately by Jacobian elliptic functions (Roth 1969c), with sharp narrow peaks between broad, flat minima.

An experimental example of these oscillations is shown on figure 9.17, in which the efflux of ions from a low pressure partially ionized Penning discharge was plotted as a function of time, with time increasing toward the left. These exhibit the sharp, narrow peaks between broad, flat minima characteristic of the solutions to equations (9.124) and (9.125). The predicted frequency of this continuity equation oscillation is given by

$$\nu \approx \frac{\sqrt{\widehat{n_e \hat{n}}} \langle \sigma v \rangle_{ne}}{2\pi} \quad \text{(Hz)}. \tag{9.126}$$

This frequency is proportional to the geometric mean of the time- and space-averaged electron and neutral number densities. An experimental confirmation of this relationship is shown on figure 9.18, in which the oscillations shown on figure 9.17 were followed over frequencies from about 400 Hz to approximately 70 kHz. The frequency was proportional
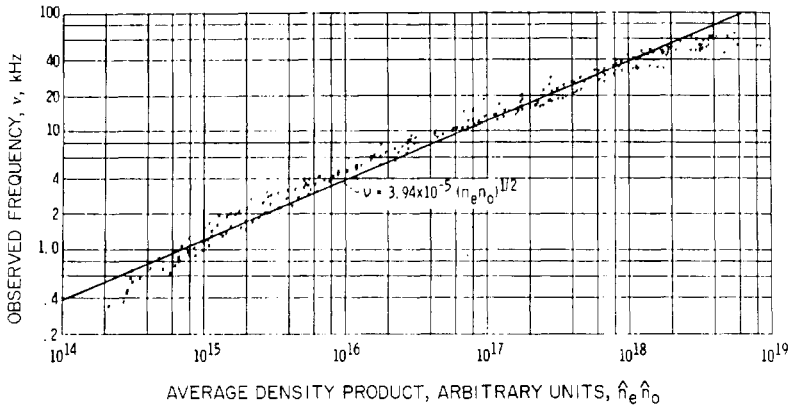
Figure 9.18 The observed frequency of uniform, in-phase oscillations for K = 0 in an experiment, as a function of the product of the electron and neutral number densities. The theoretically predicted square root dependence agrees well with the experimental data.

to the square root of this average density product, as predicted by equation (9.126) (Roth 1969a).

9.4 THEORY OF DC PLASMA SHEATHS

All plasmas are separated from the walls surrounding them by a *sheath*, the properties of which determine the energy and flux of the ions and/or electrons which bombard the wall. The subject of plasma sheaths is not well understood, and thus a variety of models have been put forward to describe the behavior, energy, and number density of the ions and electrons in the sheath between the plasma and the wall.

9.4.1 Low Voltage DC Sheath Approximation

The classical picture of the sheath between the plasma and the wall is drawn schematically in figure 9.19. In this model, the ion number density is constant across the sheath thickness, with the electron number density falling off exponentially in conformity to the electrostatic Boltzmann equation. The higher energies and much higher velocities of the electron population in most plasmas result in their bombarding the wall far more frequently than the ions in the absence of a sheath electric field. If these electrons are drawn off by an electrode, or build up a surface charge, or recombine on a surface, the slower ions which remain behind in the plasma build up a positive *plasma potential* with respect to the wall, the magnitude of which is of the order of the electron kinetic temperature, in
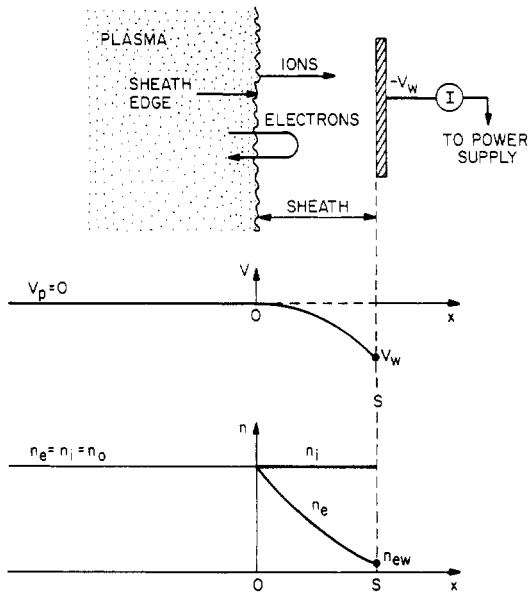
Figure 9.19 The behavior of electrons and plasma parameters in a sheath between a negatively biased wall and a plasma at zero potential. A schematic of the potential and charged particle number density profile in the sheath are indicated.

units of electronvolts. The relative negative polarity of the wall results in essentially all ions which leave the plasma through the sheath being collected on the wall-electrode, and drawn off by an external circuit as a current I, shown at the top of figure 9.19. Because the wall is negative with respect to the plasma, all but the most energetic of the electrons are reflected.

If the wall is electrically conducting and connected to an external circuit, one may vary the wall potential with respect to the plasma in the manner of a Langmuir probe, and a current–voltage trace like that shown on figure 9.20 will result. At high negative potentials, all of the electrons will be repelled back into the plasma and only ions will be collected. This is the *ion saturation regime*, in which the wall flux of ions is given by

$$\Gamma_i = \frac{1}{4}n_0\bar{v}_i = \frac{n_0}{4}\sqrt{\frac{8eT_e'}{\pi m}} \qquad \text{(ions/m}^2\text{-s)}. \qquad (9.127)$$

As one approaches zero current on figure 9.20, equal numbers of ions and electrons strike the wall, and the wall will then be at the *floating potential*, V_f. As one proceeds to more positive applied wall potentials,
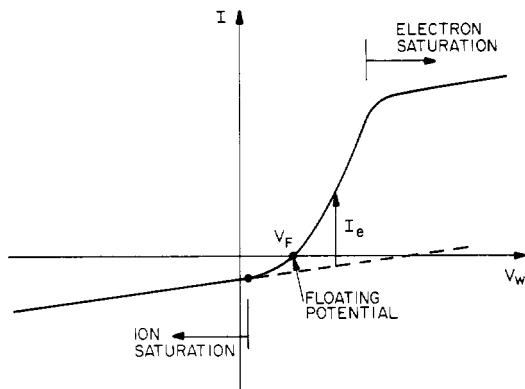
Figure 9.20 The 'Langmuir probe' current-voltage characteristic of a biased wall (probe) at the edge of a quasi-neutral plasma.

the electron current will increase exponentially, and finally, if the electron collecting area is not too great, saturate at a point at which all electrons that reach the edge of the sheath shown in figure 9.19 are collected on the wall. This is the *electron saturation regime*.

As shown at the bottom of figure 9.19, the electron number density at the position $x = S$, will have decreased in response to the electrostatic Boltzmann equation in the electron satuation regime to a value given by

$$n_{ew}(x = S) = n_0 \exp\left(\frac{-V_w}{T_e'}\right). \tag{9.128}$$

We now consider the configuration of figure 9.19 in which the wall is allowed to float at the potential V_w. Under this condition, the electron number density at the wall is given by equation (9.128), and the electron flux at the wall is given by

$$\Gamma_e = \frac{1}{4} n_{ew} \bar{v}_e = \frac{n_0}{4} \sqrt{\frac{8eT_e'}{\pi m}} \exp\left(\frac{-V_w}{T_e'}\right) \tag{9.129}$$

where equation (9.128) has been substituted for the electron number density at the wall. Since the wall is at the floating potential, $V_f = V_w$, no net current flows to it, implying

$$I = eA(\Gamma_i - \Gamma_e) = 0 \tag{9.130}$$

where A is the area of the collecting electrode. Substituting equations (9.127) and (9.129) into equation (9.130) and solving leads to

$$\frac{1}{2} \ln\left(\frac{mT_i'}{MT_e'}\right) = \frac{V_f}{T_e'}. \tag{9.131}$$

Using equation (9.131), the floating potential can be written in terms of the electron kinetic temperature as follows,

$$V_f = -\frac{1}{2}T_e' \ln\left(\frac{MT_e'}{mT_i'}\right).$$ (9.132)

In many normal glow discharges of industrial interest, the electron kinetic temperature is a few electronvolts, and the ion kinetic temperature might be at room temperature, $T_i' = 1/40$ eV. This equation implies that for argon in a fluorescent light tube, where the electron kinetic temperature is about 1.5 eV and the ions are at room temperature, the floating potential would be about 7.6 times the electron kinetic temperature.

9.4.2 Bohm Sheath Model

The above analysis is very approximate, among other reasons because the acceleration of ions in the sheath was neglected. Furthermore, the sheath boundary is not a sharp one, as implied by figure 9.19, and there is a quasi-neutral region between the plasma proper and the sheath edge which has been called the *presheath*. This presheath, a part of the *Bohm sheath model*, is sketched crudely on figure 9.21. In this model, the plasma potential is V_P, falling off to a potential of 0 at the sheath–presheath boundary, and falling off still further in the sheath to the (negative) wall potential V_w. The electron number density in the presheath falls off over a large distance, perhaps 100 electron Debye lengths. In the presheath region, the electron and ion number densities are approximately equal, a quasi-neutral region. In the sheath proper, the ion number density is higher than the electron number density, due in part to the reflection of many of the electrons by the more negative potential at the wall. The sheath proper, near the wall, is only a few electron Debye lengths thick near the anode, but may be thicker and given by the Child law sheath model (discussed below) near the cathode.

The Bohm sheath model is based on the model of plasma potential and electron number density variation sketched in figure 9.21. In the sheath proper, between $x = 0$ and $x = S$, it is assumed that no ionizations occur in the sheath, so the continuity equation for ions may be written

$$n_i(x)v_i(x) = n_s v_s.$$ (9.133)

The parameter n_S is the ion and electron number density and v_S is the velocity at $x = 0$, the left-hand sheath boundary. The velocity v_S may be found from the conservation of energy,

$$\frac{1}{2}mv_s^2 = \frac{1}{2}eT_i' + eV_P \qquad x = 0.$$ (9.134)
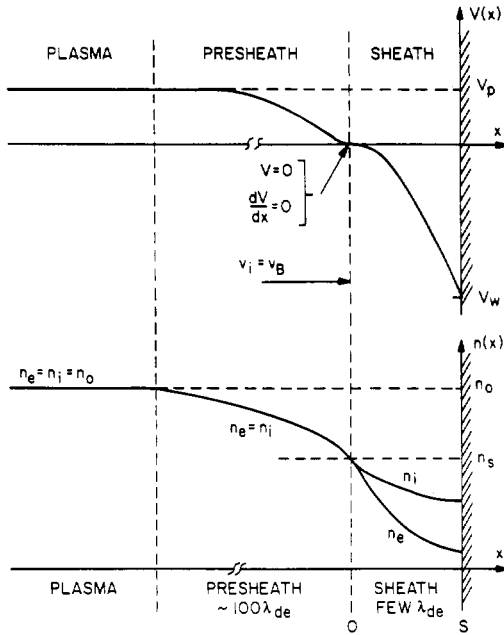
Figure 9.21 A schematic of the potential and charged particle number density across the presheath and sheath of a quasi-neutral plasma. Ions leave the presheath with the Bohm velocity v_b.

Since the plasma potential V_P is generally much larger than the ion kinetic temperature T_i', the velocity v_S may be written

$$v_S \approx \left(\frac{2eV_P}{M} \right)^{1/2}. \tag{9.135}$$

Using the analog of equation (9.135) for velocity, where the potential is $V(x)$, one can write the ion velocity at the position x in the sheath,

$$v_i(x) = \left[\frac{2e(V_P - V)}{M} \right]^{1/2}. \tag{9.136}$$

Substituting equations (9.135) and (9.136) into equation (9.133) yields the ion number density at the position x, in terms of the ion and electron number density at $x = 0$,

$$n_i(x) = n_S \left(\frac{V_P}{V_P - V} \right)^{1/2}. \tag{9.137}$$

The electron number density at the position x is given by the electrostatic Boltzmann equation,

$$n_e(x) = n_S \exp\left(\frac{V}{T_e'}\right).$$

(9.138)

If equations (9.137) and (9.138) are substituted into Poisson's equation, we obtain

$$\frac{d^2 V}{dx^2} = -\frac{e}{\varepsilon_0}[n_i(x) - n_e(x)]$$

$$= -\frac{en_S}{\varepsilon_0}\left[\left(\frac{V_P}{V_P - V}\right)^{1/2} - \exp\left(\frac{V}{T_e'}\right)\right].$$

(9.139)

By using the identity

$$\frac{d}{dx}\left(\frac{1}{2}E^2\right) = \frac{dV}{dx}\frac{d^2 V}{dx^2}$$

(9.140)

substituting equation (9.140) into equation (9.139), and integrating between $x = 0$ and x, where the potential is $V_P = 0$ at $x = 0$, and V at the position x, equation (9.139) becomes

$$d\left(\frac{1}{2}E^2\right)\Big|_0^x = -\frac{en_S}{\varepsilon_0}\int_0^V\left[\left(\frac{V_P}{V_P - V}\right)^{1/2} - \exp\left(\frac{V}{T_e'}\right)\right]dV.$$

(9.141)

Performing the integration, using the fact that the potential is $V = 0$ at $x = 0$, and assuming further that the electric field is zero at $x = 0$, (probably a questionable assumption), one obtains for the electric field in the sheath

$$E^2 = \frac{2en_S}{\varepsilon_0}\left\{2V_P\left[\left(1 - \frac{V}{V_P}\right)^{1/2} - 1\right] + T_e'\left[\exp\left(\frac{V}{T_e'}\right) - 1\right]\right\}.$$

(9.142)

Expanding the square root and exponential to second order, while assuming that the potential is much smaller than both the plasma potential and the electron kinetic temperature (another questionable assumption) one obtains

$$E^2 \approx \frac{en_S V^2}{\varepsilon_0}\left[\frac{1}{T_e'} - \frac{1}{2V_P}\right].$$

(9.143)

In order to have a real solution to equation (9.143) for the electric field, one must have

$$V_P \geqslant \frac{T_e'}{2}.$$

(9.144)

Because the expansion of equation (9.142) assumed that the ratio of the electrostatic potential to the plasma potential and the electron kinetic temperature was a small parameter in figure 9.21, the *Bohm sheath criterion* is taken as the equality in equation (9.144),

$$V_P = \frac{T'_e}{2}.$$ (9.145)

When this is substituted back into equation (9.135) for the ion velocity at the left-hand boundary of the sheath at $x = 0$, one obtains the *Bohm velocity*, v_b, given by

$$v_S = \left(\frac{2eV_P}{M}\right)^{1/2} = \left(\frac{eT'_e}{M}\right)^{1/2} = v_b.$$ (9.146)

It should be noted that the Bohm velocity involves the electron kinetic temperature, but the *ion* mass.

The Bohm sheath criterion also allows one to estimate the relationship of the sheath density at $x = 0$, to the central plasma density n_0. By applying the electrostatic Boltzmann equation to the presheath, one obtains

$$n_S = n_0 \exp\left(-\frac{V}{T'_e}\right) = n_0 e^{-1/2} = 0.61 n_0.$$ (9.147)

Thus, Bohm sheath theory predicts a number density at the sheath–presheath boundary which has fallen to 61% of the central density.

We can now use the presumably more accurate Bohm sheath model to go back and estimate the corrected floating potential. If the plasma is positive with respect to the wall, in the steady state the ion flux at the wall must be equal to the ion flux at the sheath boundary since none of them are reflected and no ionization occurs,

$$\Gamma_i = n_S v_b.$$ (9.148)

A number of the electrons are reflected by the more negative potential before they reach the wall, so the electron flux at the wall must be found in terms of the number density at $x = 0$ by using the electrostatic Boltzmann equation,

$$\Gamma_e = \frac{1}{4} n_{e0} \bar{v}_e = \frac{1}{4} n_S \bar{v}_e \exp\left(\frac{V_f}{T'_e}\right).$$ (9.149)

If there is zero net current at the wall, as before, establishing a floating potential V_f, then

$$\Gamma_e = \Gamma_i.$$ (9.150)

Substituting equations (9.148) and 9.149 into equation (9.150) yields

$$v_b = \frac{\bar{v}_e}{4} \exp\left(\frac{V_f}{T'_e}\right).$$

(9.151)

Writing out explicitly the expression (9.146) for the Bohm velocity and the electron thermal velocity yields

$$\left(\frac{2\pi m}{M}\right)^{1/2} = \exp\left(\frac{V_f}{T'_e}\right).$$

(9.152)

Solving equation (9.152) for the floating potential yields

$$V_f = -\frac{T'_e}{2} \ln\left(\frac{M}{2\pi m}\right).$$

(9.153)

For the same conditions discussed above for equation (9.132), equation (9.153) gives, for the floating potential of an argon plasma with an electron kinetic temperature $T'_e = 1.5$ eV, a floating potential about 4.7 times the electron kinetic temperature. This compares to a ratio of 7.6 for the low voltage sheath approximation. This is not a large difference in the predicted floating potential from two very different models, and is one of the reasons why controversies about the relative merits of various sheath models have not been settled to date.

9.4.3 High Voltage Sheaths

In many DC abnormal glow discharge plasma reactors used industrially, a very deep sheath appears on the cathode, as illustrated in figure 9.22. For these 'high voltage' sheaths, the electron number densities become insignificant, as predicted by the electrostatic Boltzmann equation,

$$n_e = n_0 \exp\left(\frac{-V_w}{T'_e}\right) \to 0.$$

(9.154)

The sheath shown schematically in figure 9.22 is like those in front of a Langmuir probe very deep in ion saturation, in which positive space charge predominates in the sheath.

9.4.4 Transient 'Matrix' Sheaths

A situation which arises in many transient plasma applications, including those used for plasma ion implantation, is the *matrix sheath*, shown on figure 9.23. In this case, a plasma is formed between two plane parallel
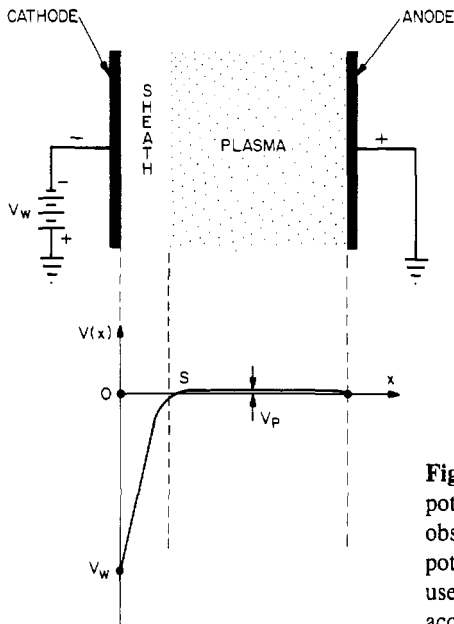
Figure 9.22 A schematic drawing of the potential profile across the sheath of an obstructed DC glow discharge. The negative potential drop V_w across the sheath is often used in plasma processing applications to accelerate ions into the surface of the cathode.

plates, and then a very large negative voltage, shown on the voltage–time diagram, is imposed between the two electrodes at $t = 0$. The voltage involved would be on the order of many kilovolts, and the effect of this high voltage is to draw the mobile electrons out of the matrix of slower, virtually immobile ions. On a time scale short compared to the ion transit time across the sheath width S, the electrons have been removed, leaving behind a matrix of positive ions.

In this matrix sheath, Poisson's equation for a positive ion plasma may be written in the form

$$\frac{\mathrm{d}E}{\mathrm{d}x} = \frac{en_0}{\varepsilon_0}. \tag{9.155}$$

Integrating once, with $E = 0$ at $x = 0$ yields

$$E = \frac{en_0}{\varepsilon_0}x = \frac{\mathrm{d}V}{\mathrm{d}x}. \tag{9.156}$$

The electric field is linear in x, and has its maximum value at $x = S$,

$$E(x = S) = \frac{en_0 S}{\varepsilon_0} \qquad \text{(V/m)}. \tag{9.157}$$

Integrating the electric field of equation (9.156) once more, and applying the boundary condition that $V = 0$ at $x = 0$ yields

$$V(x) = -\frac{en_0 S^2}{2\varepsilon_0}\left(\frac{x}{S}\right)^2 \qquad \text{(V)}. \tag{9.158}$$
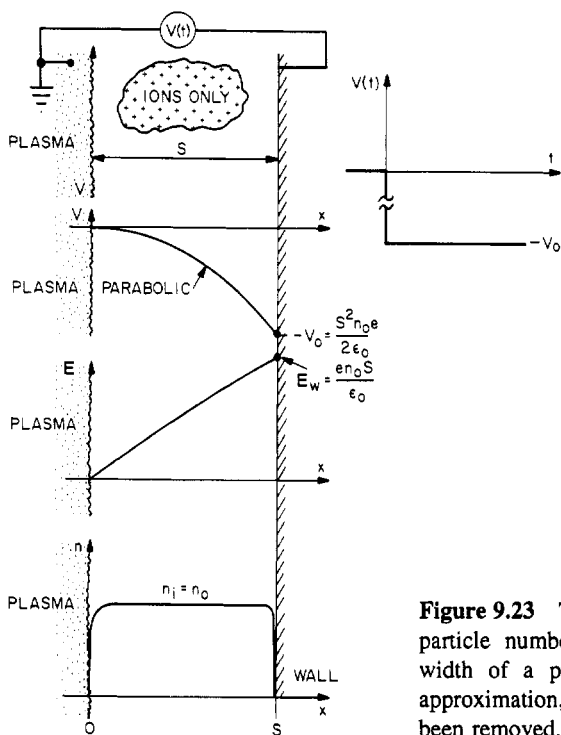
Figure 9.23 The potential, electric field, and particle number density profiles across the width of a plasma in the 'matrix' sheath approximation, in which all electrons have been removed.

The electrostatic potential is parabolic in the distance across the matrix sheath. The thickness of the matrix sheath can be calculated by identifying the electrode at the left, at $x = 0$, with the boundary of a larger plasma, and the sheath of thickness S as the remaining sheath thickness from which electrons have been driven away. The thickness of this matrix sheath is given by using the boundary condition that $V = -V_0$ at $x = S$, in equation (9.158), yielding the matrix sheath thickness

$$S_m = \left(\frac{2\varepsilon_0 V_0}{en_0} \right)^{1/2} \quad \text{(m)}. \tag{9.159}$$

This states that the sheath thickness is proportional to the square root of the voltage applied across it, and inversely proportional to the square root of the ion density. From figure 9.23 it is clear that the matrix sheath model has a constant number density of ions across the sheath, since the time scales of interest are too short for them to flow to the cathode or anode. The electric field is linear across the sheath, and the electrostatic potential is parabolic, reaching a high negative applied potential on the electrode surface.

9.4.5 Child Law Sheath

After an initial time comparable to the sheath thickness divided by the Bohm velocity has elasped in the matrix sheath of figure 9.23, the further development of a high voltage sheath is assumed to be described by a solution to Poisson's equation, which yields the Child law space-charge limited current density,

$$J_0 = \frac{4}{9}\varepsilon_0 \left(\frac{2e}{M}\right)^{1/2} \frac{V_0^{3/2}}{S^2} \qquad (\text{A/m}^2). \qquad (9.160)$$

This equation gives the current density flowing across a diode in which there are no electrons, and a flow of ions, in our case from left to right, to the highly negative wall at a negative potential $-V_0$ on the left-hand side. In this model, the plasma is assumed to extend to the left of $x = 0$, and the boundary of the plasma to remain fixed with a total sheath thickness S which does not change with time. This is probably the least satisfactory aspect of the Child law high voltage sheath theory. The potential across the Child law sheath is assumed to be several hundred volts to several kilovolts, much greater than the electron kinetic temperature of the plasma.

The current density entering the sheath can be written, using the Bohm sheath model, as follows:

$$J_0 = en_0 v_b = en_0 \left(\frac{eT_e'}{M}\right)^{1/2} \qquad (9.161)$$

where n_0 is the ion number density at the sheath boundary, and v_b is the Bohm velocity. Equating equations (9.160) and (9.161) yields an expression for the sheath thickness, S_C, of the Child law space-charge limited sheath,

$$S_C^2 = \frac{4\varepsilon_0}{9en_0} \left(\frac{2}{T_e'}\right)^{1/2} V_0^{3/2}. \qquad (9.162)$$

This can be compared to the thickness of the transient matrix sheath,

$$\left(\frac{S_C}{S_m}\right)^2 = \frac{2\sqrt{2}}{9}\left(\frac{V_0}{T_e'}\right)^{1/2} = 0.31 \left(\frac{V_0}{T_e'}\right)^{1/2}. \qquad (9.163)$$

Thus, the ratio of the two sheath thicknesses is a function of the applied potential V_0, and the electron kinetic temperature in the bulk of the plasma.

The Child law of equation (9.160) was derived on the assumption that there is no significant population of electrons in the sheath, and that the

initial velocity of the ions at $x = 0$ was zero, rather than the Bohm velocity. With these assumptions for the Child law, the potential across the sheath is given by

$$V(x) = -V_0 \left(\frac{x}{S}\right)^{4/3} . \qquad (9.164)$$

Its derivative, the electric field, is given by

$$E(x) = \frac{4V_0}{3S} \left(\frac{x}{S}\right)^{1/3} \qquad (9.165)$$

and finally, the ion number density as a function of position is found by substituting equation (9.164) into Poisson's equation, which yields

$$n(x) = \frac{4\varepsilon_0 V_0}{9S^2} \left(\frac{S}{x}\right)^{2/3} . \qquad (9.166)$$

These quantities are shown schematically in figure 9.24. Equation (9.166) above predicts an infinite number density at $x = 0$, an aphysical result which arises from neglect of the initial velocity. The Child theory can be corrected for an initial ion velocity equal to the Bohm velocity, but this leads to nonlinear differential equations, which are best solved with Jacobian elliptic functions.

9.5   DC GLOW DISCHARGE PLASMA SOURCES

Six configurations of DC glow discharge plasma sources probably account for more than 90% of industrial applications of DC glow discharges. Here we briefly survey these configurations.

9.5.1   Cylindrical Glow Discharge Sources

Figure 9.25 illustrates the *cylindrical normal glow discharge* tube, discussed earlier in this chapter. DC glow discharge plasma sources have been described extensively by Brown (1966), Cobine (1958), Hirsh and Oskam (1978), Howatson (1976), and Loeb (1961). This configuration is used in lighting devices, such as fluorescent lights and neon advertising signs. This discharge is sometimes operated in the abnormal glow regime, and, when it is used for other than lighting applications, is operated in the obstructed mode when high electric fields near the cathode are required.

The cylindrical normal glow discharge tube is only rarely operated with a confining magnetic field, since an axial magnetic induction would
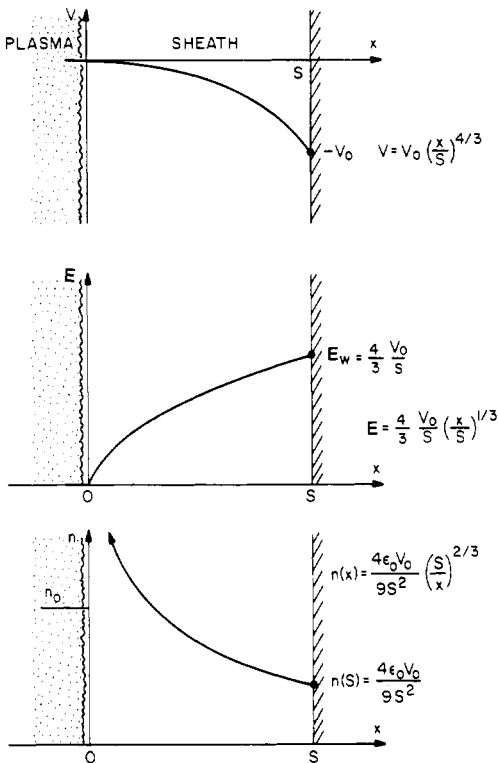
Figure 9.24 A schematic of the potential, electric field, and electron number density profiles across a Child law sheath.

$$V = V_0 \left(\frac{x}{s}\right)^{4/3}$$

$$E_w = \frac{4}{3}\frac{V_0}{s}$$

$$E = \frac{4}{3}\frac{V_0}{s}\left(\frac{x}{s}\right)^{1/3}$$

$$n(x) = \frac{4\epsilon_0 V_0}{9s^2}\left(\frac{s}{x}\right)^{2/3}$$

$$n(S) = \frac{4\epsilon_0 V_0}{9s^2}$$

Figure 9.25 The normal glow cylindrical discharge tube.

have little influence beyond altering the radial transport and possibly slightly lowering the electron kinetic temperature. In practice, the many interesting structures discussed earlier in this chapter are rarely all visible at the same time, under a single set of operating conditions. The positive

Figure 9.26 The normal glow DC parallel plate reactor. (*a*) unobstructed operation with a positive column plasma; (*b*) obstructed operation with only a negative glow and a large cathode voltage drop.

column is sometimes absent, or, in unobstructed configurations, it is sometimes dark.

9.5.2 Parallel Plate Sources

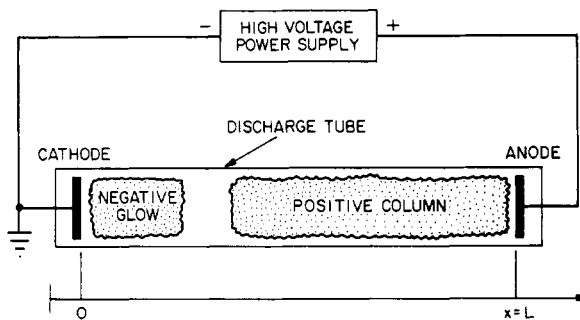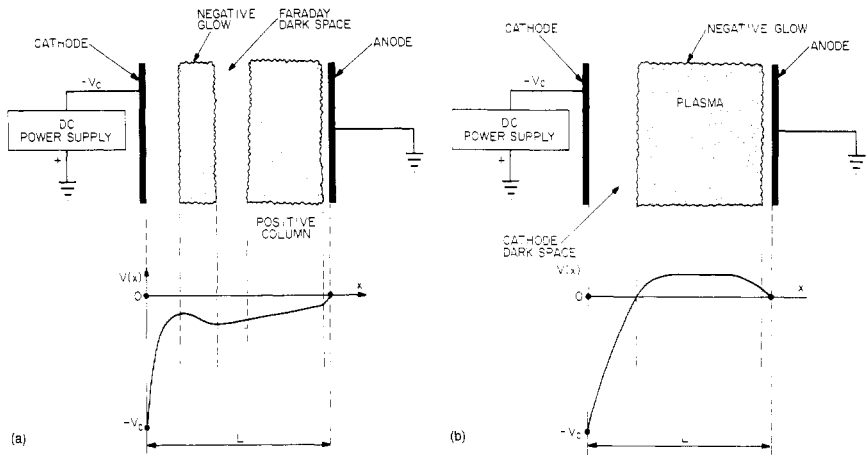The *parallel plate plasma reactors* of figures 9.26(*a*) and 9.26(*b*) are widely used for plasma processing and plasma chemistry applications. These sources have been discussed in Boenig (1988), Sugano (1985) and Vossen and Kern (1978). Figure 9.26(*a*) shows unobstructed operation, with a well-defined negative glow and positive column. This configuration is sometimes useful for plasma–chemical studies, because of the large volume of the positive column. The obstructed configuration of figure 9.26(*b*) is used for plasma processing, where high ion energies bombarding the cathode, over large areas and at vertical incidence, are desired. Wafers or other targets are mounted on the cathode. The sheath potential drop can range over values from $10 < V_C < 200$ V. Magnetic fields along the axis are sometimes employed to enhance power efficiency and prevent edge losses; a magnetic field parallel to the electrodes may be used to apply electron cyclotron resonant (ECR) heating, in the manner described in Chapter 13.

9.5.3 Beam-Plasma Sources

Beam-plasma discharges are sometimes used in ion sources, or to generate high density transient or steady-state plasmas. Figure 9.27(*a*) is
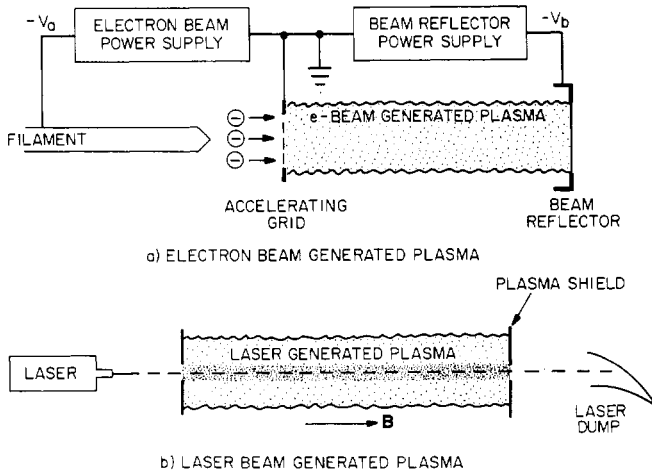
Figure 9.27 Beam generated plasmas: (a) electron beam generated plasma, (b) laser beam generated plasma.

an electron beam generated plasma which provides a plasma made up of a desired ionic species after the neutral gas is ionized. The electron number densities possible with the configuration shown in figure 9.27(a) are higher than other normal glow discharges, and very high power densities are possible with sufficient accelerating voltage for the electron beam power supply.

A high density transient plasma can be generated by the laser beam configuration shown in figure 9.27(b). Sometimes an axial magnetic field is applied to improve plasma confinement. The laser beam can be dumped externally; used to vaporize material from the plasma shield thus providing a desired ionic species; or, if it is desired to operate the configuration in the steady state or at low number densities, the plasma can be incorporated into the lasing cavity, thus avoiding the inefficiencies associated with a single pass of the laser radiation through the plasma.

9.5.4 Electron Bombardment Plasma Sources

The *electron bombardment plasma source* was discussed in connection with the Kaufman ion source in Chapter 6, and is shown in figure 9.28. This source was developed to a high state of efficiency for space applications by Kaufman (1961, 1963) and his colleagues at the NASA Lewis Research Center, where much basic research on the discharge physics of this configuration was done (Kaufman, 1965). In Chapter 6, some of the different configurations of gas feed, magnetic field, and cathodes were discussed. The electron bombardment plasma source provides a cylindrically symmetric glow discharge, with electrons
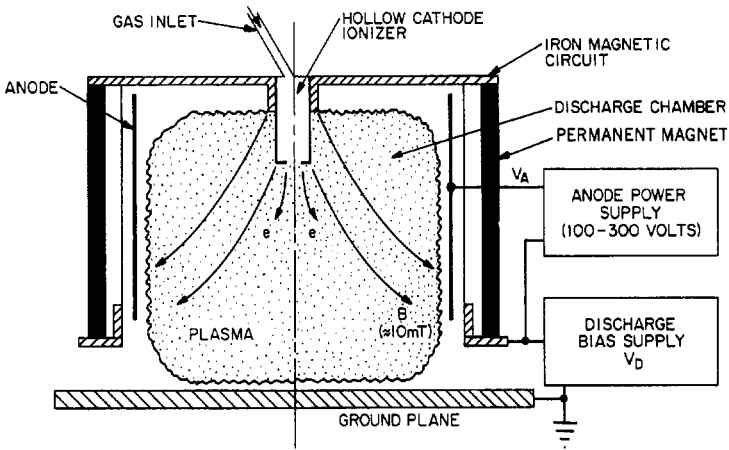
Figure 9.28 The electron bombardment plasma source.

magnetized by a diverging magnetic field, the magnitude of which is approximately 5 to 15 mT.

This plasma source is operated at low pressures, generally below 10 mTorr, and when used for sputtering or plasma processing applications, usually has a sheath between the source and the ground plane, on which the plasma processing target is located. The electron bombardment plasma source is the product of an extensive development program for space applications, much of which is relevent to its industrial applications. This off-the-shelf technology is available in the public domain, and has been carried to the point where the demonstrated mass utilization and power efficiencies are above 90%, far higher than those of most other glow discharge sources.

9.5.5 Penning Discharge Plasma Sources

Penning discharges (Penning 1936, 1937, Penning and Moubis 1937, Roth 1966) have not been widely used in industrial applications, partly because of a lack of industrial familiarity with their characteristics, and partly also because of their requirement for a relatively high axial magnetic field (several tenths of a tesla), which is required to magnetize the ion population for proper operation. Penning discharges are capable of producing energetic ions or a plasma discharge of any material that can be gassified. The classical configuration of a Penning discharge is shown in figure 9.29. It consists of a background magnetic field which can range from $0.05 \leqslant B \leqslant 0.2$ T, an anode voltage that can range from $0.5 \leqslant V_A \leqslant 5$ kV, and neutral gas pressures which range from $10^{-6} \leqslant p \leqslant 10^{-2}$ Torr.
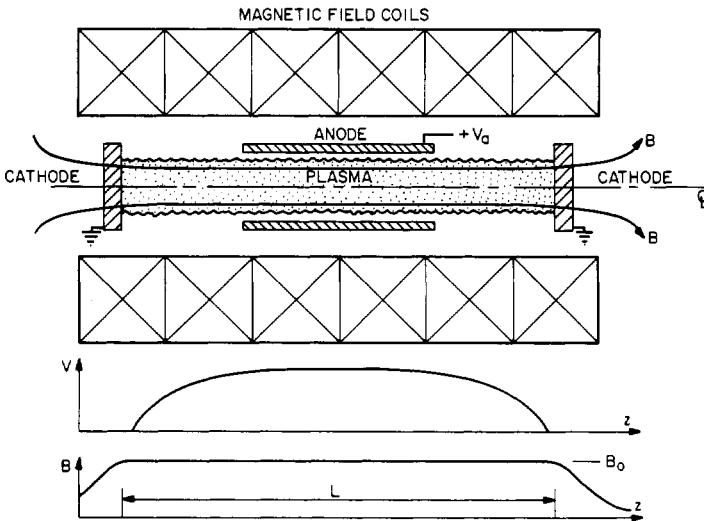
Figure 9.29 The classical Penning discharge with uniform magnetic induction and electrostatic trapping of electrons.

Penning discharges can produce a dense plasma at pressures far below those at which most other glow discharges operate, as a result of trapping of the ionizing electron population in an axial electrostatic potential well. Electrons in the *classical Penning discharge* have very long ionization mean free paths, greater than the discharge length L, at the low pressures at which these discharges are operated. Multiple reflections of the electrons along the axis, between opposing cathodes, result from their being trapped on magnetic field lines and prevented from intercepting the anode by the strong axial magnetic field. The electrons are reflected from the cathodes by axial electric fields.

In various versions of the Penning discharge, electrons are supplied by secondary emission from the cathodes, which result from ion bombardment; by avalanching of ionizing collisions in the plasma volume; or by thermionically emitting filaments located at the cathodes. In the classical Penning discharge configuration, energetic ions hit the cathodes, causing much sputtering. Ion energies ranging from tens of electronvolts to several kiloelectronvolts can be routinely produced. The cathode ion flux might be useful for etching and materials processing applications, but Penning discharges have not been widely used for this application, if at all.

If both electrons and ions in a Penning discharge are magnetized, they can acquire high energies from E/B azimuthal drift, as discussed in Chapter 3 in connection with magnetoelectric heating. From equation (3.42), the energy acquired by a particle as a result of E/B

drift is given by

$$\mathcal{E} = \frac{1}{2}mv_d^2 = \frac{1}{2}m\frac{E_r^2}{B^2} \qquad \text{(J)}. \qquad (9.167)$$

Since the particle energy is proportional to mass, this leads to the interesting circumstance that in magnetized Penning discharges, the ions are hotter than the electrons. In practice, the electron and ion energies do not differ by as much as the mass ratio, but a factor of 10 to 50 difference in the ion and electron kinetic temperatures is not uncommon, with the ions being the hotter species (Roth 1973a, b).

On figure 9.30 are shown alternative *classical Penning discharge* configurations, where 'classical' in this context implies the use of a uniform magnetic field. Figure 9.30(a) is a configuration with a single water-cooled anode ring at the midplane of the discharge and solid grounded cathodes at either end. Figure 9.30(b) is an alternative configuration with a split anode, with anode rings located a short distance from the cathode at either end of the discharge, leaving a large uniform plasma region in the middle of the discharge. The alternative configuration shown in figure 9.30(c) consists of a long anode cylinder and ring cathodes, which allow the plasma and escaping ions to leave along the magnetic field to the right and left. Finally, the alternative configuration in figure 9.30(d) utilizes an incandescent thermionically emitting cathode instead of a cold cathode, and has a ring cathode at the right, allowing a beam of energetic ions or plasma to bombard surfaces at the cathode potential, to the right.
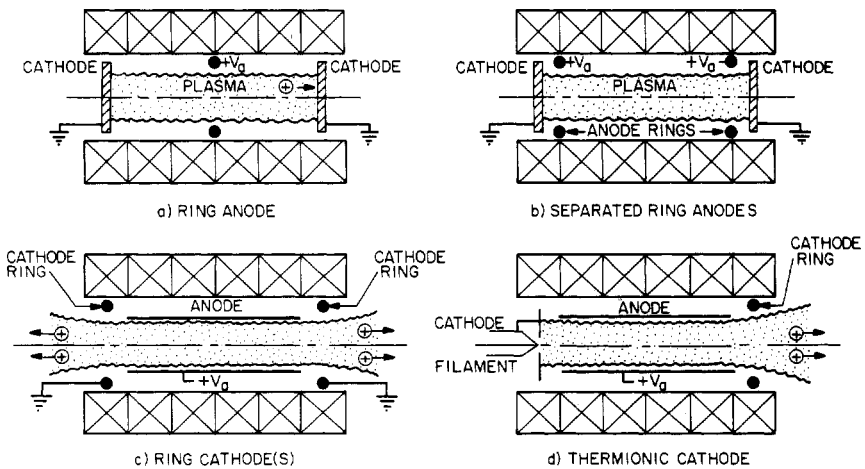

Figure 9.30 Alternative configurations of the classical Penning discharge. (a) ring anode at the midplane, uniform magnetic field; (b) separated ring anodes; (c) ring cathodes with escaping ion beam; and (d) thermionic cathode, with axially escaping ion beam.
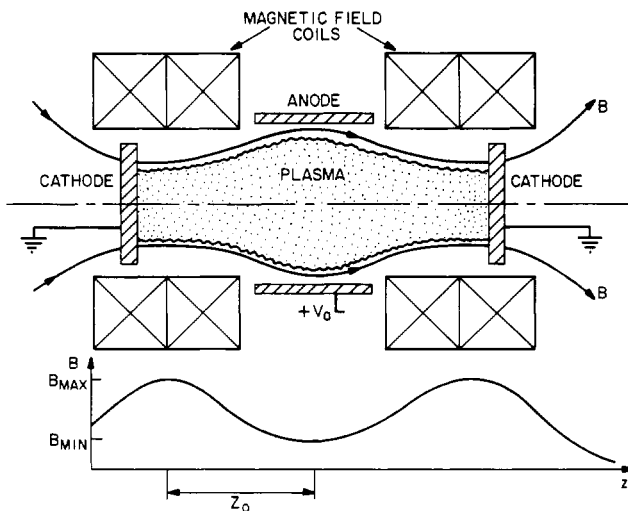
Figure 9.31 The modified Penning discharge, operating in a magnetic mirror geometry. Ions and electrons are trapped in the vicinity of the midplane.

Figure 9.31 shows the *modified Penning discharge*, a Penning discharge operating in a mirror magnetic field (Roth 1966). The presence of magnetic mirrors on either side of the anode traps some ions which would otherwise be lost along the axis to the cathode, and makes it possible to further increase the plasma confinement effect of the axial electrostatic potential well for electrons. If the ions are magnetized, E/B drift can raise the ions to kilovolt energies. The energy distribution function of ions in a modified Penning discharge can be adjusted from nearly monoenergetic to Maxwellian by varying the plasma conditions. For example, in the UTK Plasma Science Laboratory it has been found that a Maxwellianized beam of helium ions can be produced if the magnetic induction $B_{min} > 0.1$ T, if the anode voltage $V_A > 3$ kV, and if the operating pressure of helium gas is below 6×10^{-5} Torr. The modified Penning discharge is one of the very few plasma sources capable of producing a Maxwellianized beam of kilovolt ions (Roth 1973a, b).

9.5.6 Magnetron Plasma Sources

The so-called *magnetron plasma source* configurations are used primarily for plasma-assisted sputtering and deposition. A parallel plate magnetron geometry of a kind used for sputtering applications is shown in figure 9.32. When several hundred volts are applied between the parallel plates, a glow discharge will form, with a negative glow plasma trapped in the magnetic mirrors above the magnet pole pieces. The positive
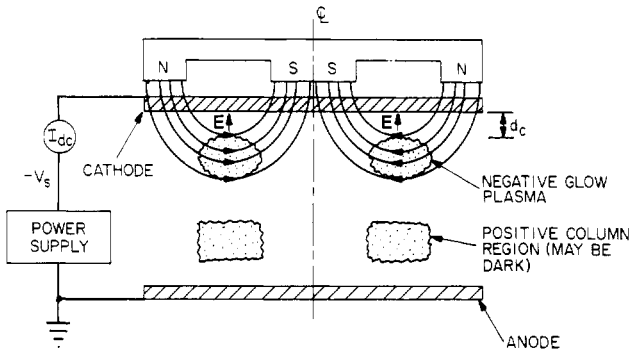
Figure 9.32 Glow discharge plasma formation in the parallel plate magnetron. The negative glow plasma is trapped in the magnetic mirror formed by the magnetron magnets.
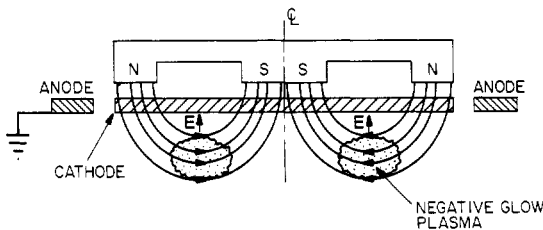
Figure 9.33 The glow discharge plasma in the co-planar magnetron configuration. Only the negative glow plasma, trapped in the magnetic pole pieces, is normally visible in this configuration.

column region may be absent or dark. Relatively strong electric fields exist between the negative glow plasma and the cathode, and these accelerate ions into the cathode, where they sputter the cathode material. If the background pressure is sufficiently low that the mean free paths of the sputtered atoms are comparable to or greater than the distance between the parallel plates, then the sputtered atoms will coat targets located on the grounded anode. In these configurations, it is usual that only the electrons are magnetized, by magnetic inductions in the range of 5 to 50 mT. The plasma may be linear, axisymmetric, or racetrack shaped. E/B drift will cause the plasma to drift around the closed plasma configuration, making the plasma uniform along its length.

Sometimes the anode plate is in the way of the work or is inconvenient for a particular application, in which case the *coplanar magnetron geometry* shown in figure 9.33 is used. In this geometry, the anode is coplanar with the cathode, and the negative glow plasma is again trapped in the magnetic mirrors formed by the permanent magnets. The
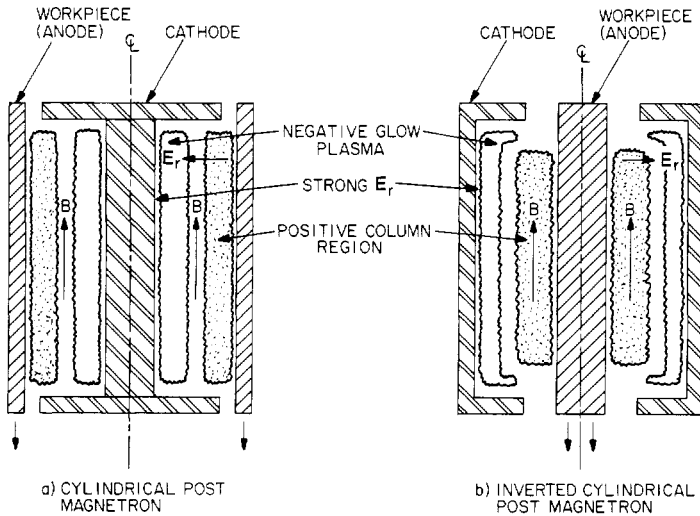
Figure 9.34 Cylindrical glow discharge plasmas formed by the cylindrical post magnetron.

sputtered atoms from the cathode are free to shower down on work pieces located below the negative glow plasma.

The *normal* and *inverted cylindrical post magnetrons* shown in figure 9.34 contain a cylindrical normal glow discharge, with the negative glow plasma forming a cylinder immediately above the cathode, and the positive column plasma forming a cylinder between the negative glow and the anode, when it is present at all. In the cylindrical post magnetron, an axial magnetic field promotes E/B drift around the axis of the configuration, leading to axisymmetric uniformity of the sputtered material on the anode.

Figure 9.35 shows the *normal* and *inverted* configuration of the *cylindrical multipolar magnetron*, in which a ring of negative glow plasma forms in the multipolar magnetic mirrors located above the cathode surface. Here also, E/B drift in the crossed radial electric field and multipolar magnetic field lead to drift around the axis of the configuration, thus promoting axisymmetric uniformity of sputtering effect on the anode surface.

In figure 9.36 are shown two variants of the *sputter-gun* configuration, in which a ring of negative glow plasma is trapped in the magnetic mirrors above a cathode. Neutral atoms sputtered from the cathode surface by ions accelerated by the electric field between the negative glow and the cathode are used in both cases to sputter or to provide sputter deposition on a work piece located vertically at the top, or on the anode surface.
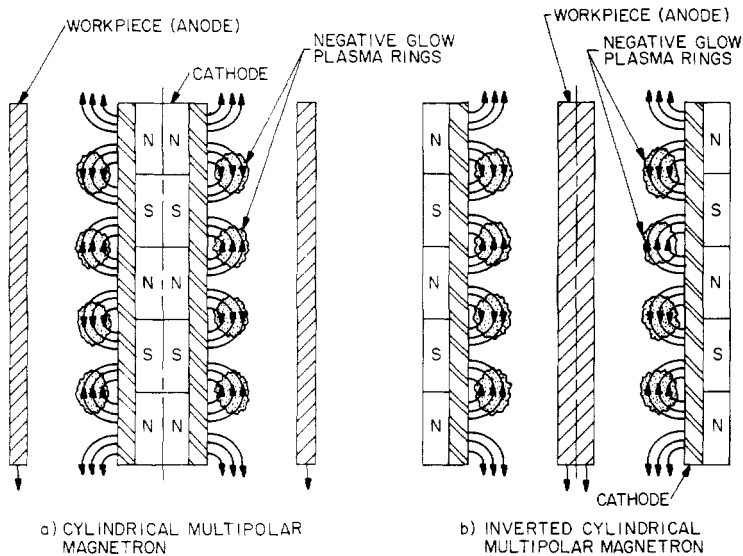
Figure 9.35 Negative glow plasma rings formed in the cylindrical multipolar magnetron geometry.
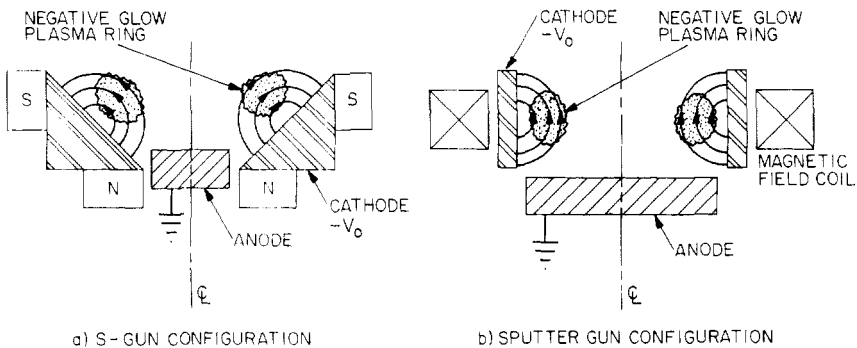
Figure 9.36 Negative glow plasma ring formed in the axisymmetric sputter gun magnetron configuration.

9.6 CHARACTERISTICS OF GLOW DISCHARGE REACTORS

9.6.1 Comparative Operating Characteristics

The comparative operating characteristics of the six plasma source configurations discussed above are shown in very approximate form in table 9.2. In many cases, detailed experimental studies which would justify generalizations about the plasma parameters of these configurations have not been funded or undertaken. Where data are

not available, or generalizations are difficult, a question mark has been entered in the table. For all of these except the Penning discharge, the energy distribution functions and kinetic temperatures of the ion population in the plasma are virtually unknown, although in some cases physical arguments suggest that the ions probably are near room temperature.

Relatively recent literature is available on the plasma parameters of both the electron bombardment sources and Penning discharges, and these plasma properties have been measured with up-to-date plasma diagnostic techniques. The cylindrical discharge tube has an extensive 'classical' literature, and a great deal is known about the plasma parameters of this configuration, although it probably could benefit by application of up-to-date plasma diagnostic methods. In spite of its industrial importance, research on the parallel plate plasma reactor is poorly developed by comparison, although this situation is changing as a result of recent research on the GEC (Gaseous Electronics Conference) reference reactor configuration.

9.6.2 Control Variables for Glow Discharges

In industrial applications of glow discharges, there is rarely if ever an ensemble of plasma diagnostic instruments sufficient to measure all of the plasma parameters listed in table 9.2. In industrial applications, the plasma is often treated like a black box, the external parameters or control variables of which are adjusted for a desired effect. Some of these control variables are:

- Operating voltage,
- Power level,
- Gas pressure,
- Gas type,
- Magnetic induction,
- Electric field geometry,
- Cathode characteristics,
- Gas flow rate.

These control variables are, at best, only a first approximation to attaining reproducible and uniform results in the plasma processing of materials. In addition to the control variables listed, contaminants, impurities, surface conditions, and other hidden variables may be influential even when the control variables are apparently the same. Only if all the plasma parameters are the same can one expect with any confidence to reproduce plasma-related effects after long periods of time or in different types of apparatus.

The operating voltage of a glow discharge affects the axial and radial electric fields, and hence the energy of charged particles in the plasma.

Table 9.2 Comparative plasma source characteristics.

Plasma source configuration	T_e' (eV)	T_i' (eV)	Maxwellian distribution	Neutral pressure p_0 (Torr)	Power level (W)	Number density (particles/m^3)	Efficiency of plasma production	Comments
Cylindrical discharge tube	1.5–5	1/40–0.1	e – two temp. ions – ?	10^{-3}–10	1–500	10^{13}–10^{17}	0.20(?)	Extensive 'classical' literature
Parallel plate reactor	2–5	1/40–0.5(?)	e – yes ions – ?	10^{-3}–10	10–500	10^{14}–10^{17}	0.10–0.50(?)	Parameters poorly diagnosed
Beam-plasma sources	2–10(?)	?	e – yes ions – ?	10^{-3}–10^{-2}	50–10^3	10^{16}–10^{19}	< 0.01(?)	Parameters poorly diagnosed
Electron bombardment sources	1.5–4	1/40(?)	e – two temp. ions – ?	10^{-5}–10^{-2}	10–10^4	10^{14}–10^{16}	> 0.90	Extensively developed for space applications
Penning discharges	2–15	10–1000	e – yes ions – possible	10^{-7}–10^{-2}	1–2.5 × 10^5	10^{13}–6 × 10^{18}	≈ 0.50	Ions heated preferentially
Magnetron geometries	1.5–4	1/40(?)	e – two temp. ? ions – ?	10^{-3}–10	10–500	10^{14}–10^{16}	≈ 0.20(?)	Poorly diagnosed

The power level controls the number of ionizations per unit volume per second, and hence is an approximate control variable for the plasma number density, and it is also a possible control variable for the energy of the plasma constituents. The gas pressure in glow discharges controls the electron collision frequency and the mean free paths of all the plasma constituents. The type of gas controls the ionization potential, and the number of electronvolts required to produce an ion–electron pair in the plasma. The magnetic induction can control transport of the plasma in directions perpendicular to the magnetic field vector, and it can also alter the ion and electron energies in fully magnetized Penning discharges that are heated by magnetoelectric heating. The magnetic induction has little effect on plasma operation in the direction parallel to a magnetic field. The geometry of a glow discharge can affect the energy input by altering the electric field, through changing the geometry of the anode–cathode configuration. Finally, the cathode characteristics, such as its secondary electron emission coefficient or capability of thermionic emission, can also affect glow discharge characteristics.

Industrial plasma engineers of the future have much work ahead of them to investigate and determine the physical processes which relate the control variables listed on page 341 to the plasma parameters listed in table 9.2. The basic knowledge required to do at least some of this is already in place, but in other areas, including elastic scattering, excitation, and ionization cross sections and plasma transport across magnetic fields, the required data and basic physics involved is only now emerging from atomic physics research and investigations of the confinement and radial transport processes in plasmas used in fusion research, for example.

9.6.3 Examples of Glow Discharges

In this section we will discuss some examples of glow discharge physics which illustrate points of interest for industrial applications. The first example is shown in figure 9.37, and comes from the cylindrical post magnetron, reported in Vossen and Kern (1978). This figure shows the voltage–current characteristic for cylindrical post magnetrons of varying geometries and sizes. Like other glow discharges, this graph shows a voltage which is almost independent of current density. The trend line through the available data indicates a current density which is proportional to the discharge voltage raised to the ninth power,

$$J = J_0 V^{9.0}. \tag{9.168}$$

This is a characteristic example of the more general power-law relationship given by

$$J = J_0 V^k \tag{9.169}$$
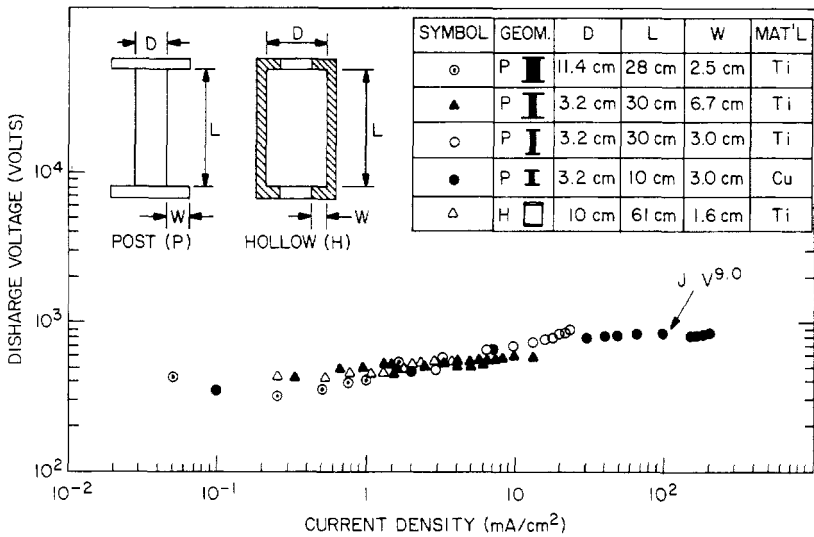
Figure 9.37 The current–voltage characteristic for several cylindrical post magnetrons, as reported by Vossen and Kern (1978).
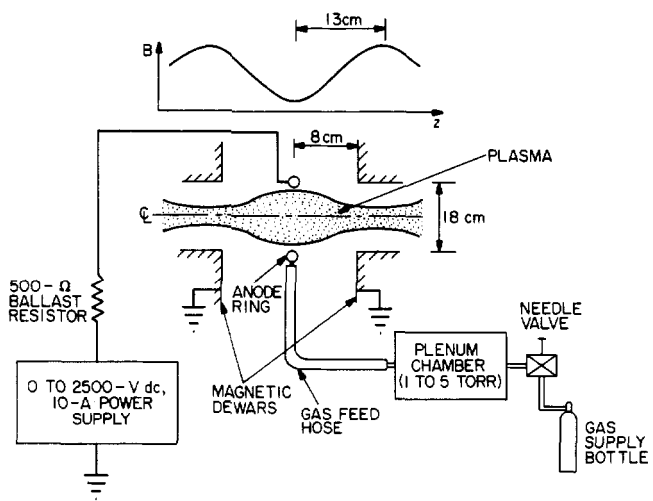
Figure 9.38 Modified Penning discharge with single anode ring geometry. Magnetic induction at midplane 1.0 T; maximum magnetic induction 2.0 T.

where k has been observed to range over the values $2 < k < 12$.

A related example is taken from the modified Penning discharge reported by Roth (1966, 1973), and shown schematically in figure 9.38. Ions leaving the modified Penning discharge were measured with the
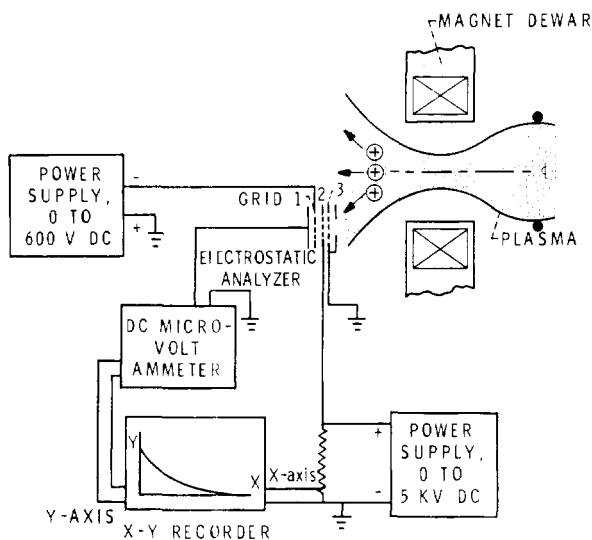
Figure 9.39 Retarding potential energy analyzer used to measure the energy distribution function of ions leaving the modified Penning discharge plasma of figure 9.38.
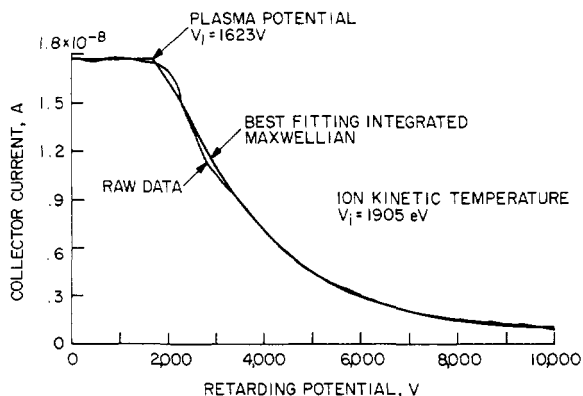
Figure 9.40 Integrated ion energy distribution function from the retarding potential energy analyzer of figure 9.39 (fine line) and the best fitting Maxwellian energy distribution (smooth, heavier line). In this condition, the ion kinetic temperature was approximately 1900 eV, with ions being observed out to energies of 10 keV.

retarding potential energy analyzer shown on figure 9.39. A characteristic example of a Maxwellian ion energy distribution from this discharge is shown in figure 9.40. Here, the best-fitting Maxwellian energy distribution function is shown superimposed on experimental data from
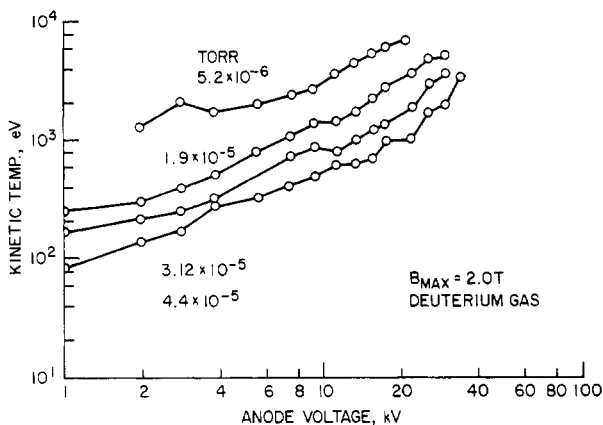
Figure 9.41 Ion kinetic temperature as a function of anode voltage for the modified Penning discharge of figure 9.38 at several background gas pressures of deuterium gas.

the retarding potential energy analyzer. These data indicate that the plasma was floating at a positive potential of 1623 V, and the deuterium ion kinetic temperature was just over 1900 eV. Ions with energies as high as 10 keV were observed in these data, as a result of the magnetoelectric heating discussed previously. The ion kinetic temperature in deuterium is shown as a function of anode voltage for several background gas pressures in figure 9.41. For these data, the modified Penning discharge was run with a magnetic induction of 2 T at the maximum field point, and 1 T at the minimum magnetic field.

The Electric Field Bumpy Torus (EFBT) was a large volume, fusion-related DC glow discharge in which a bumpy toroidal magnetic field provided gross confinement of a toroidal plasma biased to high positive or negative potentials by electrode rings located at one or more midplanes of the toroidal array (Roth 1983). A schematic of one sector of the toroidal plasma and magnet array is shown in figure 9.42. A characteristic current–voltage curve for the EFBT is shown in figure 9.43. This shows two characteristic features of glow discharges, seen often in other contexts. One is the discontinuous *mode transitions* from the high pressure mode, at the upper left, to the low pressure mode at the lower right. In the low pressure mode, the relationship between the current drawn and the anode voltage is approximately $I \propto V^2$. In the high pressure mode, the current–voltage curves are steeper, and $I \propto V^3$. This very different type of electrical discharge (from the cylindrical post magnetron, for example) also exhibits the power-law relationship of equation (9.169) between current and voltage. The discontinuous transition between modes indicated by the dotted lines is often seen
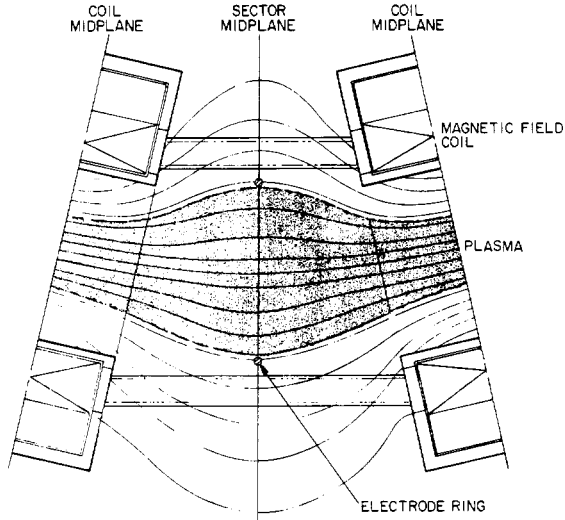
Figure 9.42 One of twelve sectors of the magnetoelectrically contained Electric Field Bumpy Torus plasma. The plasma occupied the region shown by the heavy stippeling. Electrode rings were located at the midplanes of each sector.
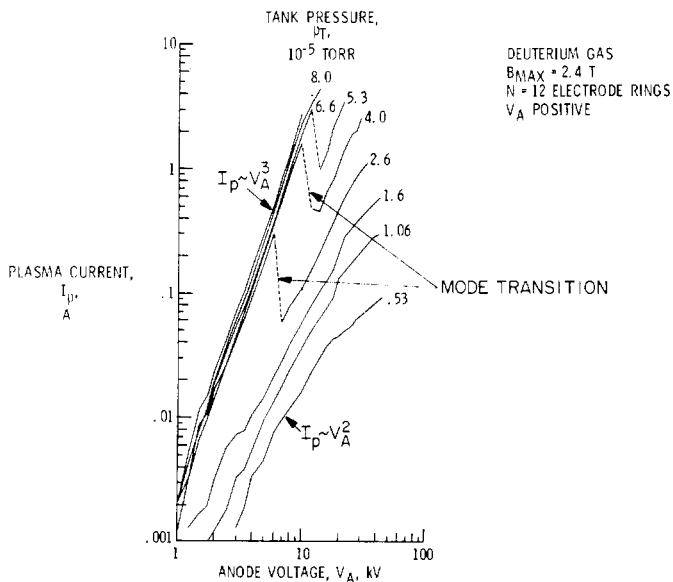
Figure 9.43 Current–voltage curves for the glow discharge plasma in the Electric Field Bumpy Torus. In the high pressure mode, the current is proportional to V_A^3, where V_A is the anode voltage; in the low pressure mode, the current is proportional to V_A^2. Note the mode transitions, shown by the dotted lines.

in industrial glow discharges as well, and sometimes makes it difficult to reproduce operating conditions of interest. Stabilizing such mode transitions is one reason a designer might include a ballast resistor or inductor in a power supply intended for glow discharges.

The electron number density dependence of the two modes of discharge shown in figure 9.43 are very different. Figure 9.44 shows a plot of the electron number density as a function of electrode voltage. The high pressure mode at the upper left has densities far higher than the low pressure mode shown to the lower right. The electron number density in the low pressure mode is far lower, and becomes lower the higher the anode voltage. This indicates that some form of fluctuation-induced transport may be causing loss of plasma. These data also illustrate the very large differences in electron number density which characterize the two modes of operation found in many glow discharges.

9.7 ISSUES IN GLOW DISCHARGE PHYSICS

Before leaving the subject of glow discharges, it is appropriate to point out some of the major areas of ignorance and uncertainty with respect to their operation. The first area is the theory of the current–voltage relation, which, if any such theory existed, might predict the power law relationship between current and voltage given by equation (9.169). At present, no one has any idea what physical process gives rise to this power law relationship, and it has not yet been derived from first principles. It is also not clear why the power-law exponent, k, can vary over values from 2 through 12, for different devices like the cylindrical post magnetron and the Electric Field Bumpy Torus, for example. Clearly, ability to predict this relationship would be of great value in the design of industrial plasma reactors.

Another area of ignorance is the nature of the physical process responsible for the mode transitions shown in figures 9.43 and 9.44. These mode transitions are prevalent in a wide variety of low pressure DC glow discharges. It is evident that entirely different physical processes must be active in the two modes of operation, but, at present, no one knows what these processes are, nor what physical process is responsible for the transition from one mode to the other. Clearly, it would also be very interesting to know this to assist the design of industrial plasma reactors.

The relationship between power input and plasma number density depends sensitively on a knowledge of the physics of radial transport in turbulent plasmas, both magnetized and unmagnetized. The process of radial transport in very quiescent, classical conditions is in some cases adequately predicted by classical diffusion in a magnetic field; when the
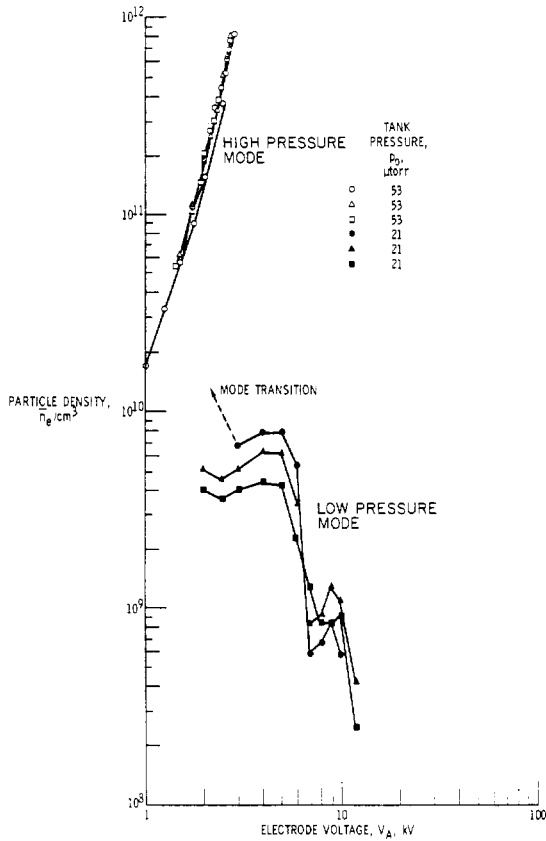
Figure 9.44 The electron number density as a function of electrode voltage in the Electric Field Bumpy Torus plasma. Note the very different functional dependence of the number density on electrode voltage in the two modes, and the large change of densities on either side of the mode transition.

plasma is turbulent, the radial transport rates across the magnetic field are substantially higher than the classical value, but the physics of this process is not well understood, either in fusion or in industrial plasmas.

Another major issue in glow discharges is an understanding of sheath physics. As mentioned previously, available theories of plasma sheaths do not agree well with laboratory measurements in the few cases where theory has been confronted by experiment. Better theories, more detailed experiments, and longer time scale computer simulations will probably be required before theory and experiment on the subject of glow discharge sheaths finally converge.

Finally, a major issue in glow discharges is predicting the electron energy distribution. Particularly at pressures below 1 Torr, the

energy distribution function is often a bi-Maxwellian, two-temperature distribution with relative densities of hot and cold populations which depend on operating conditions. Precise knowledge of the energy distribution function, obtained perhaps by sophisticated Langmuir probing techniques, is necessary to calculate the rates of all the transport coefficients and the inelastic electron collision processes which underlie industrial applications of plasma.

REFERENCES

Abria M 1848 Sur les Lois de L'Induction des Courants par les Courants *Annales de Chimie et de Physique* 7 ser 3, 462–488 (see pages 477–478)

Aston F W 1911 The Distribution of Electric Force in the Crookes Dark Space *Proc. R. Soc. London* A **84** 526–535

Barrett P J and Little P F 1965 Externally Excited Waves in Low-Pressure Plasma Columns *Phys. Rev. Lett.* **14** 356–359

Boenig H V 1988 *Fundamentals of Plasma Chemistry and Technology* (Lancaster, PA: Technomic Publishing Co) ISBN 87762-538-7

Brown S C 1966 *Introducton to Electrical Discharges in Gases* (New York: John Wiley)

Cobine J D 1958 *Gaseous Conductors* (New York: Dover Publications)

Hirsh M N and Oskam H J (ed) 1978 *Gaseous Electronics* vol I *Electrical Discharges* (New York: Academic Press) ISBN 0-12-349701-9

Howatson A M 1976 *An Introduction to Gas Discharges* 2nd edn (Oxford: Pergamon Press) ISBN 0-08-020574-7

Kaufman H R 1961 An Ion Rocket with an Electron-Bombardment Ion Source *NASA Technical Note TND-585* January 1961

—— 1963 The Electron-Bombardment Ion Rocket *Advanced Propulsion Concepts* vol 1 *(Proc. 3rd Symp., October 1962)* (New York: Gordon and Breach)

—— 1965 Performance Correlation for Electron-Bombardment Ion Sources *NASA Technical Note TND-3041* October 1965

Loeb L B 1961 *Basic Processes of Gaseous Electronics* 2nd edn (Berkeley and Los Angeles, CA: University of California Press) LCCCN 55-5196 ch 8

Penning F M 1936 Glow Discharge at Low Pressure Between Coaxial Cylinders in an Axial Magnetic Field *Physica* **3** 873–894

—— 1937 A New Manometer for Low Gas Pressures Between 10^{-3} and 10^{-5} Torr *Physica* **4** 71–75

Penning F M and Moubis J H A 1937 A Neutron Source Without Pumping *Physica* **4** 1190–1199

Roth J R 1966 Modification of Penning Discharge Useful in Plasma Physics Experiments *Rev. Sci. Instrum.* **37** 1100–1101

—— 1967 New Mechanism for Low-Frequency Oscillation in Partially Ionized Gases *Phys. of Fluids* **10** 2712–2714

—— 1969a Experimental Observation of Continuity Equation Oscillations in Slightly Ionized Deuterium, Neon, and Helium Gas *Plasma Phys.* **11** 763–777

Roth J R 1969b Possible Applications of the Continuity-Equation Plasma Oscillation to Pulsars and Other Periodic Astrophysical Phenomena *NASA Technical Note TND-5078* March 1969

—— 1969c Periodic Small-Amplitude Solutions to Volterra's Problem of Conflicting Populations and Their Application to the Plasma Continuity Equations *J. Math. Phys.* **10** 1412–1414

—— 1969d A Theory of Moving Striations Based on the Continuity-Equation Plasma Oscillations *Proc. Ninth Int. Conf. on Phenomena in Ionized Gases (Bucharest, Romania, 1–6 September 1969)* p 464. See also NASA *TMX-52633* September 1969

—— 1973a Hot Ion Production in a Modified Penning Discharge *IEEE Trans. on Plasma Sci.* **1** 34–45

—— 1973b Energy Distribution Functions of Kilovolt Ions in a Modified Penning Discharge *Plasma Phys.* **15** 995–1005

—— 1983 Ion Heating and Containment in an Electric Field Bumpy Torus (EFBT) Plasma *Nucl. Instrum. Methods* **207** 271–299

Schottky W 1924 Diffusion Theory of the Positive Column, *Phys. Zeit.* **25** 635–640

Sugano T (ed) 1985 *Applications of Plasma Processes to VLSI Technology* (New York: John Wiley) ISBN 0-471-86960-0

Vossen J L and Kern W (ed) 1978 *Thin Film Processes* (New York: Academic Press) ISBN 0-12-728250-5

10

DC Electrical Arc Discharges in Gases

The third major regime of industrially important DC electrical discharges is the *arc discharge*, which has been used for illumination and high temperature metals processing for nearly 200 years.

10.1 ARC REGIME

When a DC electrical discharge draws currents of the order of 1 to 10 A at low pressures, it is sometimes difficult to tell whether it is an arc or a glow discharge. An *arc discharge* is defined in terms of its luminosity, current density, and cathode fall voltage. An arc, as opposed to a glow discharge, is highly luminous, especially the *high intensity* thermal *arcs*. Arcs are also characterized by high currents and current densities. Even *low intensity arcs* rarely have total currents less than 1 A. The current densities of arcs range from several amperes per square centimeter to more than a thousand amperes per square centimeter. These current densities contrast with those of glow discharges, in which current densities are seldom more than 50 mA/cm^2. Arcs are also characterized by a relatively small cathode fall voltage, approximately 10 V or less, in the region of high spatial gradients within a few millimeters of the cathode. By contrast, glow discharges typically have a cathode voltage drop greater than 100 V over a distance of more than a centimeter. The total current drawn by an electrical discharge is not definitive, since arcs can be maintained at currents of 1 A or less, whereas glow discharges, if they have sufficiently large electrode surfaces, can draw 10 A or more.

10.1.1 Voltage–Current Characteristic

The voltage–current characteristic of the DC low pressure electrical discharge tube shown on figure 10.1 illustrates the three principal
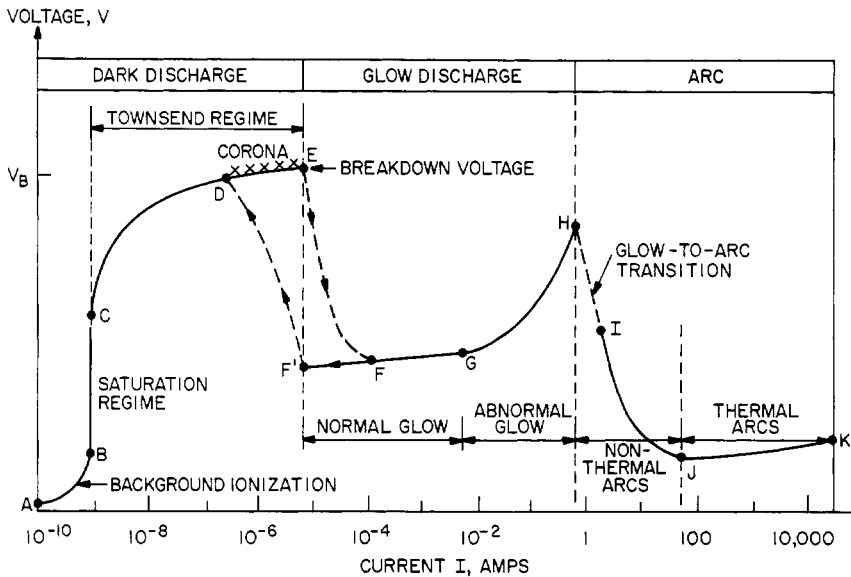
Figure 10.1 Universal voltage–current characteristic of the DC electrical discharge tube.

divisions of the arc regime: These include the *glow-to-arc transition* between points H and I, which is triggered by electron emission from the cathode. This emission results from the high heat loads on the cathode which occur in the high current density regions of the abnormal glow discharge, around the point H on the curve. When the discharge settles down to the point I on the diagram, which is determined by the internal impedance of the DC power supply and its associated circuit, the arc will usually be in the *non-thermal*, low intensity division of the arc regime. This division is characterized by total currents between approximately 1 and 50 A, although non-thermal, low intensity arcs may operate in rare cases outside the limits of this range. This is a region of negative resistance characteristic: i.e. the current–voltage curve has a negative slope in which an increased current results in a decreased voltage. Beyond point J on the diagram, at approximately 20 to 50 A, the arc moves into a division of the arc regime with a nearly flat or slowly rising voltage–current characteristic, which is called the *thermal* or high intensity division of the arc regime, between points J and K in figure 10.1.

10.1.2 Parameter Ranges

Parameter ranges for the non-thermal, low intensity and thermal, high intensity divisions of the arc discharge are shown in table 10.1. We attempt to be specific, because the existing arc literature has a wide

Table 10.1 Plasma parameters of non-thermal (low intensity) and thermal (high intensity) arc discharges.

Plasma parameter	Non-thermal arc	Thermal arc
Equilibrium state	Kinetic	LTE
Electron density, n_e (electrons/m^3)	$10^{20} < n_e < 10^{21}$	$10^{22} < n_e < 10^{25}$
Gas pressure, p (Pa)	$0.1 < p < 10^5$	$10^4 < p < 10^7$
Electron temperature, T_e', (eV)	$0.2 < T_e' < 2.0$	$1.0 < T_e' < 10$
Gas temperature, T_g' (eV)	$0.025 < T_g' < 0.5$	$T_g' = T_e'$
Arc current, I (A)	$1 < I < 50$	$50 < I < 10^4$
E/p (V/m-Torr)	High	Low
IE (kW/cm)	$IE < 1.0$	$IE > 1.0$
Typical cathode emission	Thermonic	Field
Luminous intensity	Bright	Dazzling
Transparency	Transparent	Opaque
Ionization fraction	Indeterminate	Saha equation
Radiation output	Indeterminate	LTE

range of confusing terminology, including different names for the same phenomenon, and the same names for phenomena or divisions of the arc regime which are differently defined by various authors. In the literature what we here call *non-thermal or low intensity arcs* are sometimes called *thermionic*, or *low pressure arcs*, and various authors have slightly different definitions of the relevant division boundary. Also in the literature, *thermal, high intensity arcs* are sometimes called *field emission*, or *high pressure arcs*. At the common boundary of the divisions shown in table 10.1, the distinction between non-thermal and thermal arcs in a particular application may not apply to all of the parameters shown in table 10.1.

The non-thermal, low intensity arcs are difficult to characterize theoretically or to model computationally, because they are in kinetic equilibrium at best, and one cannot assume local thermodynamic equilibrium (LTE), appropriate to thermal, high intensity arcs. Unless an arc is in thermodynamic equilibrium, one cannot confidently analyze either the fraction ionized using the Saha equation, the relative fraction of atoms in excited states, or the radiative transport within the arc on the basis of thermodynamic equilibrium and the Stefan–Boltzmann radiation law. The electron number density of thermal, high intensity arcs is, with rare exceptions, higher than that of non-thermal, low intensity arcs; the gas pressure is not a definitive determinant of the thermal versus non-thermal arc divisions; the values shown in table 10.1 are intended to be representative, and it is possible for arcs operating close to 1 atm not to
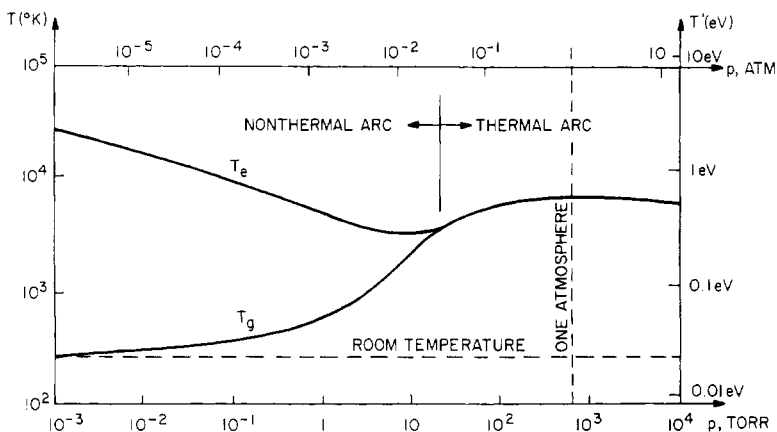
Figure 10.2 The operation of arcs as a function of pressure.

be in local thermodynamic equilibrium. The electron kinetic temperature also is not a definitive characteristic of the arc regime; non-thermal arcs can have electron temperatures ranging over at least an order of magnitude; the electron temperature of thermal, high intensity arcs tends to be of the order of 1 eV at currents of around 50 A or slightly higher, and to increase slowly with power input to approach kinetic temperatures of 10 eV in arcs that dissipate many megawatts per meter of length.

The relationship between the electron kinetic temperature and the gas temperature is a definitive characteristic of the arc division; a requirement of local thermodynamic equilibrium, characteristic of thermal arcs, is that the electron and gas kinetic temperatures be equal; in non-thermal, low intensity arcs, electron–neutral collisions can be infrequent enough that the electron and neutral gas populations are decoupled, and there can be very significant differences in their temperatures. The arc current is not a definitive characteristic of the two divisions; thermal arcs are possible with total currents less than 50 A, as are non-thermal arcs with currents greater than 50 A. Neither the arc current, the E/p ratio, the power dissipated per unit length of the arc, the luminous intensity of the arc, nor the pressure at which it is operated are definitive characteristics of the arc divisions; these parameters can overlap for non-thermal and thermal arcs.

As will be discussed later, non-thermal, low intensity arcs usually require thermionic emission from the cathodes, whereas thermal, high intensity arcs usually operate on field emission. Thermal arcs always are found at high pressures and high gas temperatures, whereas non-thermal arcs can occur at low pressures, i.e. below approximately 500 Pa. Non-thermal arcs also can exist at atmospheric and higher pressures, but at low electron kinetic temperatures. Figure 10.2 shows schematically

the electron and gas kinetic temperatures expected as a function of pressure for an argon discharge. For non-thermal arcs, the electron kinetic temperature is greater than the gas temperature, as a result of the progressive decoupling of the electron and neutral gas populations at lower pressures, where the electron–neutral collision frequency is less. The electron and gas temperatures are virtually the same above a few tens of torr in this example.

10.2 PHENOMENOLOGY OF ELECTRICAL ARCS

The arc regime of electrical discharges was reported by Sir Humphrey Davy in 1808, and was observed in connection with his electrochemical experiments with the large battery bank of the Royal Institution in which many individual wet cells were connected in a series–parallel configuration, allowing the simultaneous generation, for the first time, of large currents at moderately high voltages.

10.2.1 Classical Arc Nomenclature

Until the early 20th century, most arcs were used as lighting devices and operated as non-thermal arcs. This older literature (see Cobine (1958), for example), used terminology slightly different than that of more recent authors. A schematic of such a 'classical' arc is shown at the top of figure 10.3, and a schematic drawing of the axial voltage distribution is shown below. The features of such an arc discharge are as follows, moving from left to right:

(1) The *cathode* is the negative electrode, which, in non-thermal, low intensity arc discharges, usually emits electrons thermionically.

(2) The *cathode spots* are one or more points of plasma attachment of high current density where the cathode material is very hot. The current density in the cathode spots can be on the order of 500 to more than $10\,000$ A/cm^2, and the positive ion current of the order of 100 A. The temperature of the cathode will depend on the type of gas, the electrode material, and the current density, but for atmospheric arcs is typically in the range from 2200 to 3300 K. The cathode spots usually move over the cathode surface with a velocity of the order of meters per second during the operation of an arc discharge. Cathode material is lost by vaporization, since the cathode spots may be at the boiling temperature of the cathode material. While the cathode spots are extremely hot, the temperature of the cathode as a whole is considerably less, as mentioned above. The electron momentum transfer drives the axial convection of neutral gases, which affects the electrodes.
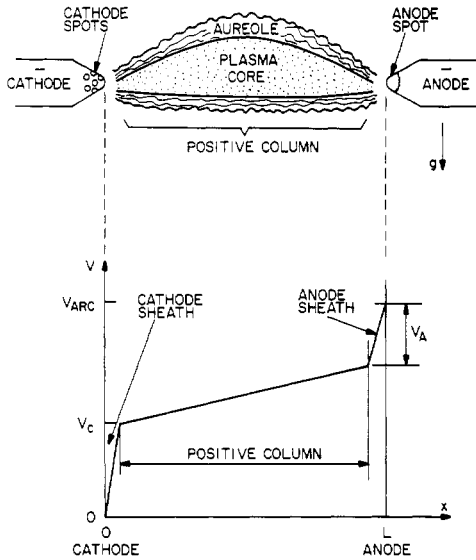
Figure 10.3 A schematic drawing of the visual characteristics and voltage distribution along the axis of an arc discharge.

(3) The *cathode sheath* is located next to the cathode and is usually less than 1 mm thick. It will typically have a voltage drop of 10 V, comparable to the ionization potential of the gas used. This voltage drop is referred to as the *cathode fall*.

(4) The *positive column* contains the bulk of the arc discharge, and occupies nearly all of the axial length of the arc. There is relatively little voltage drop in this region, which visibly can be separated into the two regions indicated at the top of figure 10.3.

(5) The *plasma core* is the bulk of the hot plasma. Most of the gas in this region is dissociated, and for many arcs which operate at pressures of an atmosphere or greater, the plasma core is in thermodynamic equilibrium and radiates like a black body. The temperature of the positive column of an arc discharge depends on the electrode material, the operating gas, and the current density, but typical temperatures for an arc in atmospheric air will range above 5700 K, the surface temperature of the sun.

(6) The *aureole* is a region of flaming gases, not in thermodynamic equilibrium, which surrounds the core, where plasma chemistry can take place.

(7) The *anode sheath* contains a relatively large voltage drop over a short distance, the *anode fall*, comparable to the cathode fall. The anode

fall is comparable to or less than the ionization potential of the gas, and can range from a few volts to ten volts. The electric field in the anode sheath accelerates electrons to the anode spot.

(8) The *anode spot* is usually a single 'hot spot' where the current density is high. Unlike the cathode spots, there is usually only a single spot of larger area and lower current density than the cathode spots. The anode spot forms at a location nearest the arc, and expands backward on the anode with increasing total current.

(9) The *anode* is the electrode which collects the electron current, and, like the cathode, is usually made of a high melting point, refractory metal. At atmospheric pressure, the temperature of the anode is the same or slightly higher than the cathode. The value of the anode temperature depends on the electrode material, the type of gas, the current density, and typically ranges from 2500 to 4200 K for atmospheric arcs operating with carbon, tungsten, copper, or iron electrodes.

10.2.2 Modern Arc Nomenclature

More recent understanding of arcs, subsequent to 1960, has produced the more sophisticated model shown on figure 10.4. This schematic drawing shows the modern nomenclature for the various regions of an arc, along with the accompanying voltage drop along the axis. Starting at the left, the *cathode* emits electrons at very high current densities. For non-thermal, low intensity arcs, this current usually arises from thermionic emission from one or more relatively large, diffuse cathode spots, which move over the surface. The current density in this cathode spot might range from 500 to 10 000 A/cm^2; for thermal, high intensity arcs with field emission, many small *microspots* move over the cathode surface, each with current densities in the range from 10^6 to 10^8 A/cm^2. The *cathode sheath* is comparable to the electron Debye length, $\lambda_{de} \approx 1$–10 μm. The voltage across this sheath is the *cathode fall*, about 10 V in most arcs.

The *cathode region* is a region of potential and density gradients, with an axial extent of perhaps $d_c \approx 1$ mm. Beyond this region, there is a *cathode flow zone* approximately 1 cm in axial extent in which the *cathode jet* is formed, and external neutral gas interacts strongly with the arc column. The cathode jet is a region of high velocity, hot gas which entrains external gas near the cathode, and flows axially with velocities that can reach several hundred meters per second. The cathode jet can reach the anode, and it can, and usually does, greatly increase the heat transfer to the anode. The scouring effect of the cathode jet on the anode also can remove anode material at a rapid rate.. The *arc column* is a region of low axial density gradient and electric fields, and essentially no axial temperature gradients.
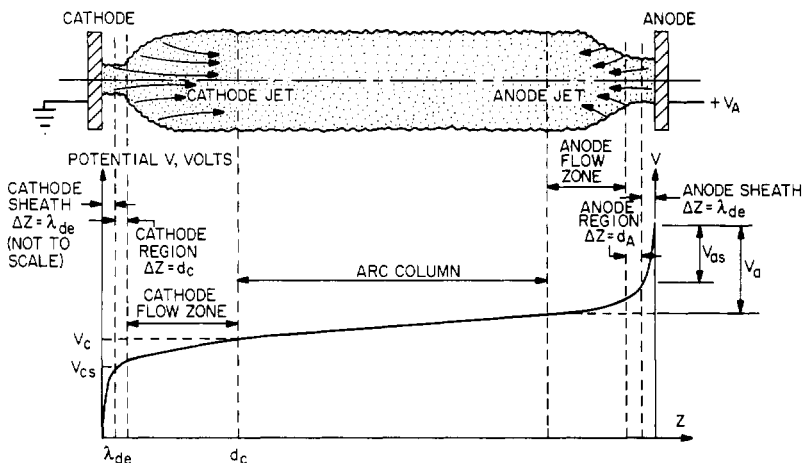
Figure 10.4 Schematic representation of the regions of a linear arc, with the potential distribution in each.

Near the anode, the *anode flow zone*, *anode region* and *anode sheath* are comparable in dimensions to the corresponding cathode region, except that the diameter of the anode attachment spot is usually significantly larger than that of the cathode, leading to a smaller *anode jet* velocity and less prominent anode flow effects. The arc column current density is typically 1000 A/cm^2 in thermal, high intensity arcs, the cathode fall is typically $V_c \approx 10$ V, and the *anode fall*, V_A, is typically equal to the ionization potential of the gas used, from 3 to 13 V.

In arcs, the cathode fall is usually too small for secondary electron emission to play a significant role in electron emission from the cathode. Arcs cannot be sustained without copious emission of electrons from the cathodes, and this is accomplished by two mechanisms: *thermionic emission* and *field emission*, which were examined in Chapter 5.

In low current (approximately 1–10 A) non-thermal, low intensity arcs, the primary electron emission mechanism is sometimes non-self-sustained thermionic emission. In this regime, the cathode must be heated externally in order to bring the cathode surface temperature up to the level where enough electrons are emitted to sustain the arc. In most non-thermal arcs, electrons are emitted from the cathode by self-sustaining thermionic emission, in which the cathode surface is raised to and maintained at electron-emitting temperature by the heat flux from the arc.

Finally, in thermal, high intensity arcs, extremely high currents and current densities are required to maintain the arc, and these are supplied by field emission. In field emission, the cathode temperature is

determined by the characteristics of the heat transfer to the cathode and the cathode cooling mechanism. In order to preserve the electrodes and lengthen the electrode lifetime, the cathode in thermal, high intensity arcs is usually too cool to emit thermionically. Electrons are emitted into the arc by field emission from many small spots *(microspots)*, each with current densities of 10^6–10^8 A/cm^2.

A variety of important phenomena occur at the cathode. The cathode jet discussed above can be very strong, and its effects can reach to and significantly heat the anode. Diffuse attachment of the arc to a significant fraction of the cathode area can result in thermionic current densities of 1000 to 10 000 A/cm^2 at the cathode surface, as the result of emission from a relatively large, incandescent area. Cathode microspots occur in thermal arcs, as the result of field emission from tiny spots which are seen to dance over the cathode surface under close observation. The surface temperature of cathodes in field-emitting thermal arcs can range from near room temperatures to incandescence, and is determined by heat transfer considerations, not by the level of thermionic emission required to maintain the arc. The cathode power deposition can be very large, and water cooling is required.

Similar phenomena occur at the anode. The anode jet is usually significantly less active and of lower velocity than the cathode jet, because of the lesser constriction of the arc, and the larger anode arc radius. Anodes can operate in the *diffuse attachment mode*, in which the current densities can range from 100 to 1000 A/cm^2, and in the so-called *constricted* or *'spot' mode*, in which the current densities reach values from 10^4–10^5 A/cm^2. In most arcs, the anode gets higher heat loads than the cathode. These higher total heat loads can lead to anode burnout, so the anodes of thermal arcs are usually actively cooled. With careful attention to the technological detail of the heat transfer process, heat transfer rates of 5 kW/cm^2 may be achieved. For thermal arcs, the anode fall voltage is usually less than the ionization potential, since the gas is ionized almost exclusively by the Maxwellian electrons in the arc.

10.3 PHYSICAL PROCESSES IN ELECTRICAL ARCS

The understanding of physical processes in arcs began with a classical paper by Tonks and Langmuir (1929), and has reached advanced levels in recent years, particularly for axisymmetric, thermal arcs. More recent texts on arc physics include those by Cobine (1958), Von Engel (1965), Brown (1966), Gross *et al* (1969), Hirsh and Oskam (1978) and Lafferty (1980), for example. Progress has been particularly rapid since 1970 in the computer modeling of high power thermal arcs. In the discussion below, we will not cover the range of computer models currently used
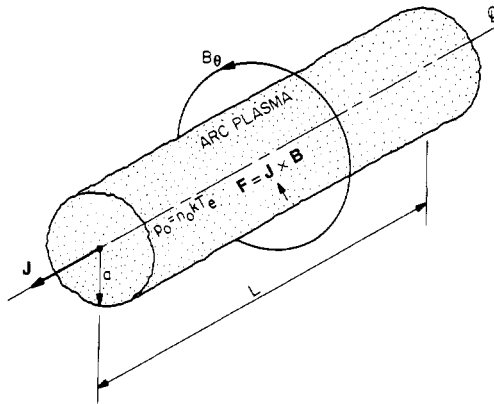
Figure 10.5 Radial body forces on a cylindrical arc plasma of radius $r = a$.

to describe thermal arcs, but will confine ourselves to simple analytical theories which describe some of the most important physical processes and characteristics of industrial arcs.

10.3.1 Body Forces on Arcs

As a result of the high current densities found in typical arcs, large $J \times B$ body forces act on their plasma. A typical geometry for an axisymmetric cylindrical arc is shown in figure 10.5. The arc has a current density $J(r)$. The total current is found by integrating this current density over the radius,

$$I = 2\pi \int_0^a r\, J(r)\, \mathrm{d}r. \tag{10.1}$$

In order to avoid mathematical detail, we will assume that the current density in the arc of figure 10.5 is constant, that is $J(r) = J = \text{constant}$. Under this constraint, the azimuthal magnetic field inside an arc with constant current density is given by

$$B_\theta = \tfrac{1}{2}\mu_0 J_z r \qquad r \leqslant a. \tag{10.2}$$

The body force on the plasma in the arc is therefore

$$\mathbf{F} = \mathbf{J} \times \mathbf{B} = F_r = -\tfrac{1}{2}\mu_0 J_z^2 r \qquad (\text{N/m}^3). \tag{10.3}$$

This body force is radially inward, tending to pinch the arc to a smaller diameter. If the total arc current I is of the order of 10^4 A, the radial body force given by equation (10.3) may be sufficient to balance the kinetic

pressure of the arc, irrespective of any electrode attachment, external gas pressure, or convective stabilizing effects.

A *Bennett pinch* (Willard H Bennett, 1934) is a cylindrical arc which has reached an equilibrium in which the expansionary kinetic pressure of the plasma on axis is balanced by the inward radial body force given by equation (10.3). In most arcs, however, the radial body force given by equation (10.3) is less than the kinetic pressure of the plasma, and other stabilizing mechanisms, including the pressure of the surrounding atmosphere, come into play.

The boundary conditions of interest in analyzing the Bennett pinch can be written with reference to figure 10.5 as

$$B = (0, B_\theta, 0) \qquad\qquad (10.4a)$$

$$J = (0, 0, J_z) \qquad r \leqslant a \qquad (10.4b)$$

$$J = 0 \qquad\qquad r > a. \qquad (10.4c)$$

In the steady state, the balance of forces on the arc is given by

$$\nabla p = J \times B \qquad (10.5)$$

which, for the conditions of equations (10.4) becomes

$$-J_z B_\theta = \frac{dp}{dr}. \qquad (10.6)$$

If we now use Maxwell's equation in the steady state,

$$\nabla \times B = \mu_0 J \qquad (10.7)$$

which is given by, for the geometry of figure 10.5,

$$\frac{1}{r} \frac{d}{dr}(r B_\theta) = \mu_0 J_z. \qquad (10.8)$$

Since the current density J_z is assumed to be constant, equation (10.8) can be integrated along the radius to yield B_θ, given by

$$B_\theta = \begin{cases} \frac{1}{2}\mu_0 J_z r & r \leqslant a \qquad (10.9a) \\ \frac{1}{2}\mu_0 J_z (a^2/r) & r \geqslant a . \qquad (10.9b) \end{cases}$$

The radial pressure distribution inside the arc may be found by substituting equation (10.9a) into equation (10.6) and integrating from the radial position r to the outer boundary of the arc at $r = a$,

$$p(r) = \int_r^a J_z B_\theta \, dr = \left. \frac{1}{4}\mu_0 J_z^2 r^2 \right|_r^a \qquad (10.10)$$
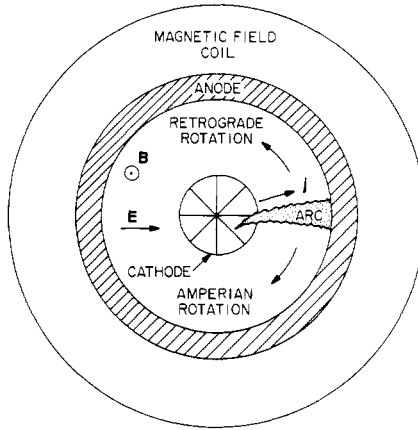
Figure 10.6 Formation of a rotating spoke in a coaxial arc geometry.

which yields, for $r < a$,

$$p(r) = \tfrac{1}{4}\mu_0 J_z^2 (a^2 - r^2) \qquad r \leqslant a. \tag{10.11}$$

The condition for Bennett pinch equilibrium is found in terms of the axial pressure p_0, which is given by, from equation (10.11),

$$p(0) = p_0 = \tfrac{1}{4}\mu_0 J_z^2 a^2. \tag{10.12}$$

Using the relation $I = pa^2 J_z$, equation (10.12) may be rewritten as

$$p_0 = \frac{\mu_0 I^2}{4\pi^2 a^2} \qquad (\text{N/m}^2). \tag{10.13}$$

The equilibrium radius for the Bennett pinch may be found by rearranging equation (10.13),

$$a = \frac{I}{2\pi}\sqrt{\frac{\mu_0}{p_0}} \qquad (\text{m}). \tag{10.14}$$

For an arc with a radius $a = 0.5$ cm, and an axial pressure of 1 atm, $p_0 = 10^5$ N/m^2, a current of $I = 8862$ A is required maintain an equilibrium. The Bennett pinch equilibrium is unstable to sausage and kink instabilities, which are important in magnetic fusion research (see Roth 1986, Chapter 4). Most industrial arcs function below the current required to maintain a Bennett pinch equilibrium, so other stabilizing mechanisms are required.

Arcs are often operated in a coaxial configuration, usually with a cathode on axis, shown schematically in figure 10.6. The 'stabilizing'
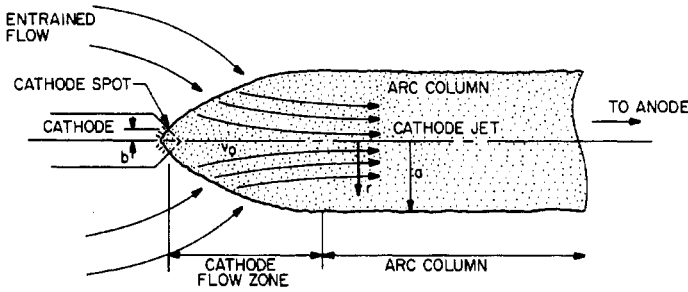
Figure 10.7 Electrode jet formation in the cathode region. The arc column necks down from a radius a in the arc column, to a much smaller radius b at the cathode attachment point.

magnetic induction B is normal to the diagram, and points outward. The arc current density J flows radially. As a result of the *diocotron instability* (see Roth 1986, Chapter 4) perturbations of an initially uniform sheet of plasma between the cathode and anode will result in the 'snowplowing' of the initially uniform plasma into a high density rotating spoke. In thermal arcs, this spoke rotates in the *amperian direction* in response to the force

$$F_m = J \times B \qquad (\text{N/m}^3). \qquad (10.15)$$

This amperian direction of rotation is clockwise in figure 10.6. In some non-thermal, low intensity arcs, the spoke rotates in the *retrograde direction*, opposite to $J \times B$, and the reason for this behavior is not understood. This rotation in coaxial arcs is very important, since the heat loads at the arc root might otherwise melt the electrode material.

10.3.2 Electrode Jet Formation

As indicated in figure 10.7, arcs neck down to a smaller diameter near the electrodes, a defining characteristic of the anode and cathode *flow zones* of the arc. This narrowing down of the arc diameter gives rise to *electrode jets*, which flow *away* from the electrodes. In some ways the electrode jets are a counter-intuitive phenomenon, so it is of interest to analyze their physical mechanism, relying on the previous analysis of the Bennett pinch.

From equation (10.11), the radial pressure profile may be written in terms of the total current I,

$$p(r) = \frac{\mu_0 I^2}{4\pi^2 a^4}(a^2 - r^2) \qquad (\text{N/m}^2). \qquad (10.16)$$

In most arcs, the pressure on axis given by equation (10.16) will be well below the total kinetic pressure of the arc. The axial gradient of this pressure, however, drives the electrode jets. At an axial position in the arc column where the arc radius $r_{max} = a$, the kinetic pressure on the axis of the arc column is given by

$$p_a = \frac{\mu_0 I^2}{4\pi^2 a^2}. \tag{10.17}$$

At the cathode, where the arc diameter constricts to the much smaller radius $r_{max} = b$, the kinetic pressure on axis is larger, and is given by

$$p_b = \frac{\mu_0 I^2}{4\pi^2 b^2}. \tag{10.18}$$

If the radial arc boundary $b \ll a$, then the kinetic pressure p_b at the location b is much greater than the kinetic pressure in the arc column, p_a, so an axial pressure gradient develops, the magnitude of which is

$$\Delta p = p_b - p_a = \frac{\mu_0 I^2}{4\pi^2}\left(\frac{1}{b^2} - \frac{1}{a^2}\right) \approx \frac{\mu_0 I^2}{4\pi^2 b^2}. \tag{10.19}$$

This axial pressure gradient drives neutral gas along the axis away from the electrodes. This pumping action of the axial pressure gradient will then entrain external gas flowing past the electrode.

An estimate can be made of the magnitude of the electrode jet velocity by setting the pressure difference given by equation (10.19) equal to the dynamic (stagnation) pressure which would be produced if the electrode jet stagnated against a flat surface, $\frac{1}{2}\rho v_0^2$, where v_0 is the jet velocity in meters per second, and ρ is the plasma mass density in kilograms per cubic meter,

$$\Delta p \approx \frac{\mu_0 I^2}{4\pi^2 b^2} = p_b = \frac{1}{2}\rho v_0^2 \tag{10.20}$$

Equation (10.20) can be solved to give an estimate of the jet velocity,

$$v_0 \approx \left(\frac{\mu_0 I^2}{2\pi^2 b^2 \rho}\right)^{1/2} = \frac{I}{\pi b}\sqrt{\frac{\mu_0}{2\rho}} \quad \text{(m/s)}. \tag{10.21}$$

The electrode jets are shown schematically on figure 10.4. Their velocity is typically from a few meters per second to several hundred meters per second.

The axial electric field is very high in the electrode sheaths, moderate in the rest of the electrode region within a centimeter or so of the

electrodes, and least in the arc column. The total arc voltage may be written

$$V_1 = V_C + V_A + \int_{d_C}^{L-d_A} E \, dz \qquad (10.22)$$

where V_C and V_A are the cathode and anode falls, respectively. In general, any arc must have a minimum total applied voltage V_1 given by

$$V_1 \geqslant V_C + V_A \qquad (10.23)$$

or it will be extinguished. This relation is important to the design and stabilization of axially segmented arcs.

10.3.3 Radiation From Thermal Arcs

Arc discharges operating at or above 1 atm are often in thermodynamic equilibrium, and thus radiate like a black body. This leads to their utility for lighting devices, and to their being an occupational hazard for ultraviolet radiation when used for industrial processes such as welding. A medium in *thermodynamic equilibrium* is one in which there are no net power flows, and the photon mean free paths are less than the dimensions of the medium. In consequence, the surface of the medium radiates like a black body.

Black bodies emit according to the *Planck radiation law*,

$$\frac{dM_e}{d\lambda} = \frac{2\pi hc^2}{\lambda^5} \frac{1}{\exp(hc/kT\lambda) - 1} \qquad \text{(W/m}^2\text{-m)} \qquad (10.24)$$

where M_e is the *radiant exitance* in watts per square meter, and λ is the wavelength of the radiation in meters. Equation (10.24) leads to a distribution of radiant exitance as a function of wavelength shown schematically on figure 10.8. The radiation goes to zero at very short wavelengths, rises to a maximum, at λ_{max}, and then falls off asymptotically to zero at longer wavelengths. One can determine the wavelength of maximum emission by differentiating equation (10.24), setting the derivative equal to zero, and obtaining

$$\lambda_{max} = \frac{hc}{4.965kT} \qquad \text{(m)}. \qquad (10.25)$$

The sun is a plasma that radiates like a black body at approximately 5700 K. At that temperature, its wavelength of maximum emission is in the middle of the band where the eyes of humans and most other animals are most sensitive, as a result of our eyes having evolved to most efficiently utilize the photon emissions of the sun. At filament
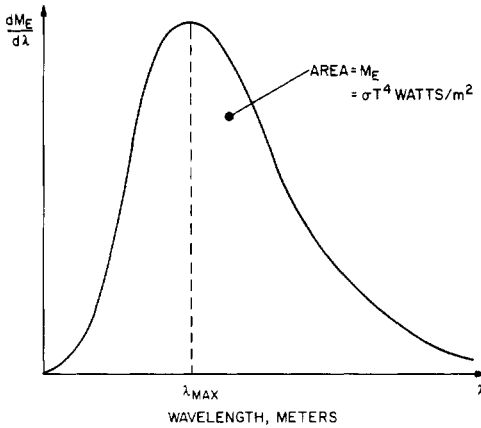
Figure 10.8 The Planck distribution function of radiant exitance, in watts per square meter and per differential wavelength interval, as a function of the emission wavelength in meters.

temperatures of 2500 K, the wavelength of maximum emission of incandescent bulbs is in the infrared, thus wasting most of their photons for lighting purposes. Welding and other arcs typically have electron kinetic temperatures of 1 or 2 eV, between approximately 11 000 and 22 000 K, where the wavelength of maximum emission is in the ultraviolet.

The radiant exitance of an arc, or any other black body, may be found by integrating the area under the curve on figure 10.8,

$$M_e = \varepsilon \int_0^\infty \frac{\mathrm{d}M_e}{\mathrm{d}\lambda} \, \mathrm{d}\lambda \qquad (\text{W/m}^2) \qquad (10.26)$$

where the parameter ε is a *gray body factor* or a *gray body coefficient* which ranges from 0 to 1.0. This accounts for the fact that many arcs and other radiant energy sources do not radiate as effectively as a black body because of surface dirt, turbulence, etc. Substituting equation (10.24) into (10.26) and performing the indicated integration, one obtains the *Stefan–Boltzmann radiation law*,

$$M_e = \varepsilon \frac{2\pi^5 k^4 T^4}{15h^3c^2} = \varepsilon \sigma T^4 \qquad (\text{W/m}^2). \qquad (10.27)$$

The collection of constants denoted by σ is *Stefan's constant*, and is given in the SI system of units by

$$\sigma = \frac{2\pi^5 k^4}{15h^3c^2} = 5.6705 \times 10^{-8} \; \text{W/m}^2\text{-K}^4. \qquad (10.28)$$

Arcs at pressures below 1 atm are often not in thermodynamic equilibrium, but satisfy only the condition of kinetic equilibrium. In such arcs, the electron population can be in kinetic equilibrium and described by a Maxwell–Boltzmann distribution, but if the photon mean free paths are larger than the plasma dimensions, such low intensity, non-thermal arcs cannot radiate like black bodies. Equation (10.27) represents an absolute upper limit on the power radiated from an arc discharge, if it is in thermodynamic or kinetic equilibrium.

10.3.4 Modeling Electrical Arcs

In modeling arcs, the problem is usually approached as an exercise in fluid dynamics, rather than relying upon individual particle equations of motion, or an approach based on the Lorentzian or Krook models. In modeling arcs with the fluid dynamic equations for the conservation of mass, momentum, and energy, it is usually assumed that the arcs are axisymmetric and are not functions of time.

One of the simplest of these models is for the radial power balance of arcs. It is assumed that all heat is generated by Joule heating in the plasma, and that all losses are radial and due to a thermal conductivity κ. This gives a power balance

$$\sigma E^2 = -\nabla \cdot (\kappa \nabla T) \tag{10.29}$$

where σ is the electrical conductivity. If the axial electric field E is constant or a continuous function of the radius r, if there is no axial variation of the arc parameters, and if the temperature T is a function of r only, one can obtain from equation (10.29) the *Elenbaas–Heller equation*,

$$\sigma E^2 = -\frac{1}{r} \frac{d}{dr} \left(r\kappa \frac{dT}{dr} \right). \tag{10.30}$$
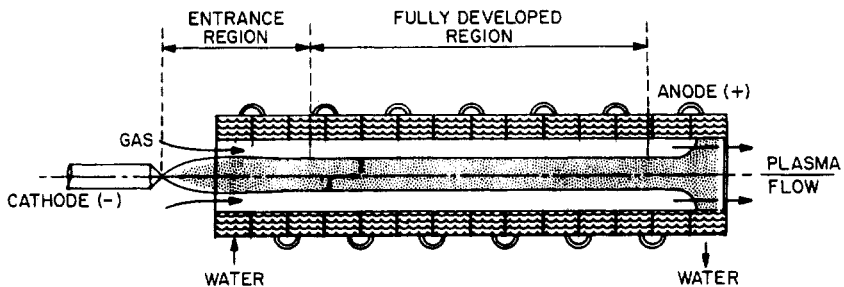
Figure 10.9 Schematic of a wall-stabilized arc discharge studied by Pfender (1978).

Even this simplified equation is very difficult to solve analytically unless further assumptions are made. The *parabolic model* assumes that the electrical conductivity σ and the thermal conductivity κ are not functions of kinetic temperature T or radius (usually, bad assumptions). If it is further assumed that the boundary conditions on temperature are

$$T(r = 0) = T_0 \qquad (10.31a)$$

on the axis, and

$$T(r = a) = T_w \qquad (10.31b)$$

with T_w the wall temperature, the Elenbaaș–Heller equation can be integrated to obtain

$$T_0 = T_w + \frac{\sigma E^2 a^2}{4\kappa}. \qquad (10.32)$$

(a) Enthalpy

(b) Mass Flow

(c) Energy Flux Density

(d) Velocity

(e) Momentum Flux

I = 580 A
ṁ = .00353 kg/s
R = .00635 m
z_0 = 3.50 m
h_∞ = 1.89 x 10⁸ J/kg
ṁ/A = 27.8 kg/sm²
h_∞ṁ/A = 5.29 x 10⁹ W/m²
P_0 = 117 kPa

Figure 10.10 Gas dynamic parameters calculated for the wall-stabilized nitrogen arc shown in figure 10.9, by Pfender (1978).

Figure 10.11 A low pressure vacuum arc operated in hydrogen by Jobes *et al* (1969), diagnosed with the heavy-ion beam probe diagnostic.

This equation and its simplified model contain important truths about arcs; if the edges of an arc are cooled ($\kappa \to 0$), the central temperature of the arc increases in order to maintain the arc equilibrium. This model also predicts a temperature on axis proportional to the arc power dissipation per meter of axial length.

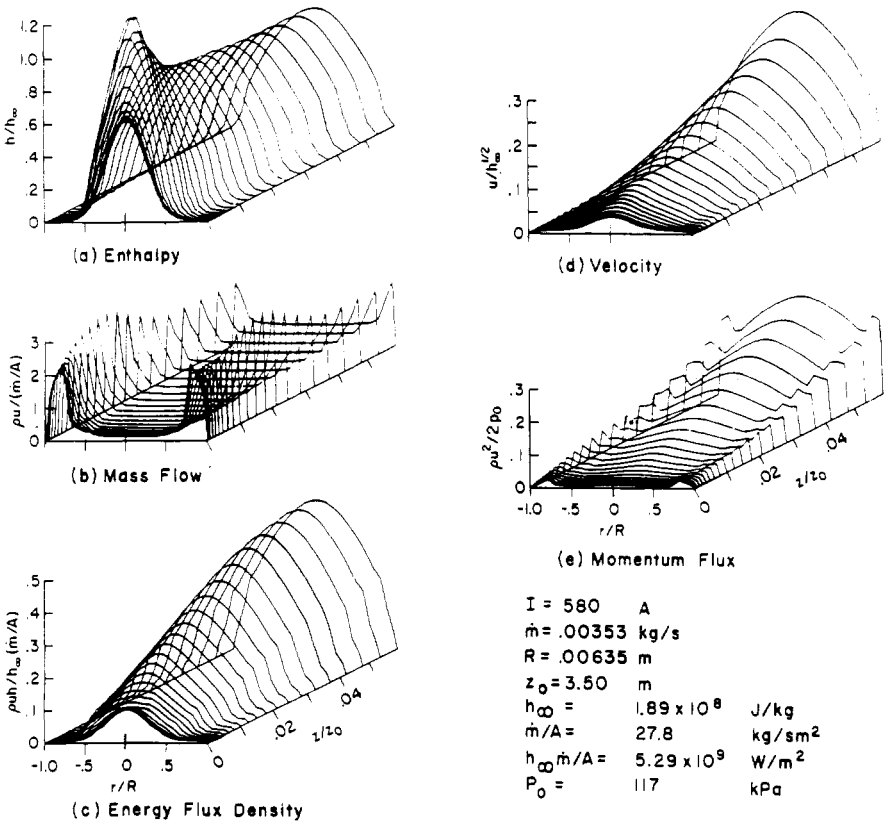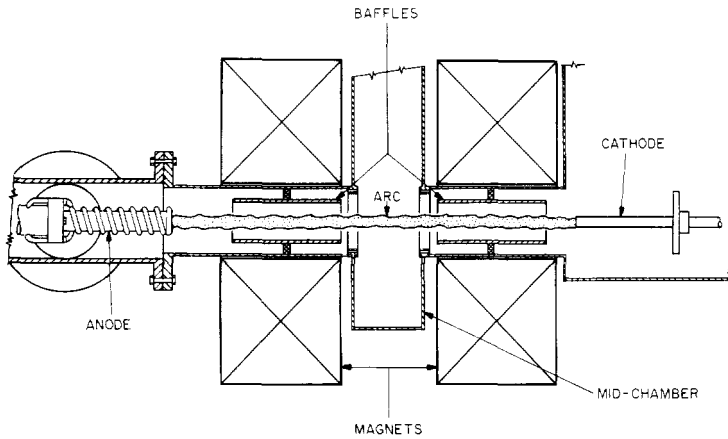More elaborate models have been developed which include black body and line radiation, a functional dependence of σ and κ on the radius and temperature, and gas dynamic effects such as viscosity. This sophistication, however, is purchased at a substantial price in computational difficulty, to the point where most arc models are now the result of computer programs rather than an analytical formalism. As an example, Pfender (1978) developed a computational model of a wall-stabilized arc shown on figure 10.9, and its calculated performance parameters are shown in figure 10.10.

When arc discharges have been studied with the highly sophisticated plasma diagnostic instruments developed for fusion research, time- and space-resolved measurements have revealed very little reason to assume that arcs are either axisymmetric or that their characteristics are independent of time.

In one of the early applications of a fusion diagnostic to a low pressure non-thermal arc, the geometry of which is shown in figure 10.11, the arc was probed with a time- and space-resolved plasma diagnostic method known as heavy ion beam probing (Jobes *et al* 1969). The arc was operated at approximately 1 Torr. The heavy-ion beam probing system was capable of a time resolution of several hundred kilohertz, and a spatial resolution on the order of 1 mm. On figure 10.12 is a contour plot
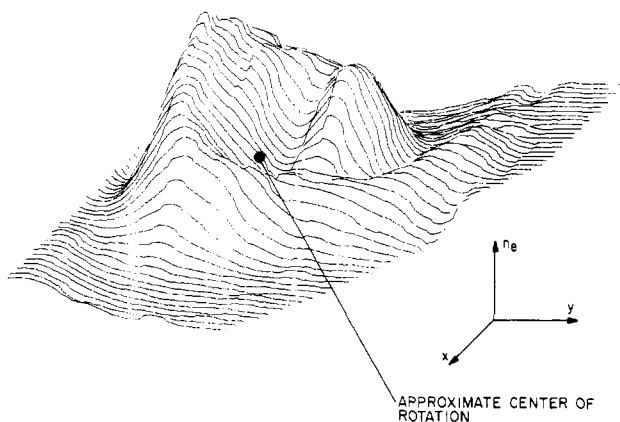
Figure 10.12 A three-dimensional time- and space-resolved plot of the electron number density in the linear, low pressure hydrogen arc shown in figure 10.11. The approximate center of rotation is indicated. The structure shown rotates about this axis with a frequency of 185 kHz.

of the electron number density profile at a particular instant in time. The mountain-like structure shown in this figure was gyrating around a center of rotation indicated on the diagram with a frequency of approximately 185 kHz. Thus, neither the instantaneous appearance of the arc, nor its dynamics were axisymmetric, nor were they independent of time.

It is probably significant that the first and almost the only time that heavy ion beam probing has been applied to a non-thermal, low intensity arc of potential industrial interest, it has been found that many of the common assumptions used to theoretically describe arcs do not apply. Further advances in understanding the physical processes going on in thermal and non-thermal arc discharges probably will require time- and space-resolved measurements and more sophisticated diagnostics and physical modeling, rather than increasingly sophisticated computer models, the input assumptions of which do not reflect the underlying physical reality of arc discharges.

10.4 EXAMPLES OF ARC OPERATION

For the sake of concreteness, we will review the operating characteristics of one non-thermal, low intensity arc and one thermal, high intensity arc which have been reported in the literature. For the non-thermal arc we choose the classic data of Ayrton (1902). These data were taken for a 1 atm non-thermal arc in air with carbon electrodes, in which the electrode
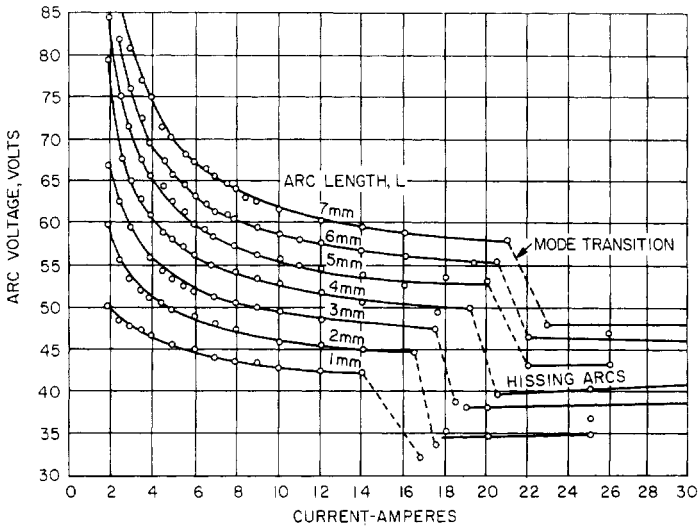
Figure 10.13 The voltage–current characteristic of carbon arcs operated at 1 atm in air, as a function of electrode separation, as reported by Ayrton (1902). Note the negative resistance characteristic on the left, and the mode transition at higher currents.

separation was a parameter. For the thermal arc, we consider the 1 atm argon arc of Eberhart and Seban (1966).

10.4.1 Non-thermal Arc of H Ayrton

A voltage–current relation for carbon arcs in air at 1 atm was published by Mrs Hertha Ayrton in 1902. These data are shown in figure 10.13, with arc length as a parameter (Ayrton 1902, p 177). Note the monotone decreasing, almost hyperbolic nature of the data at low currents, and the transition to the *'hissing' arcs* at high currents, so-called because of the noise they make when operated in the atmosphere. Based on these data, she proposed what has become known as the *Ayrton equation*,

$$V_A = C_1 + C_2 L + \frac{C_3 + C_4 L}{I} \qquad (V) \qquad (10.33)$$

where C_1 through C_4 are constants, L is the arc length, and I is the total arc current (Ayrton 1902, p 186).

Later research by Nottingham (1923) found that for an atmospheric arc of constant length, the voltage–current relation could be described by what has become known as the *Nottingham equation*,

$$V_A = A + \frac{B}{I^n} \qquad (V). \qquad (10.34)$$
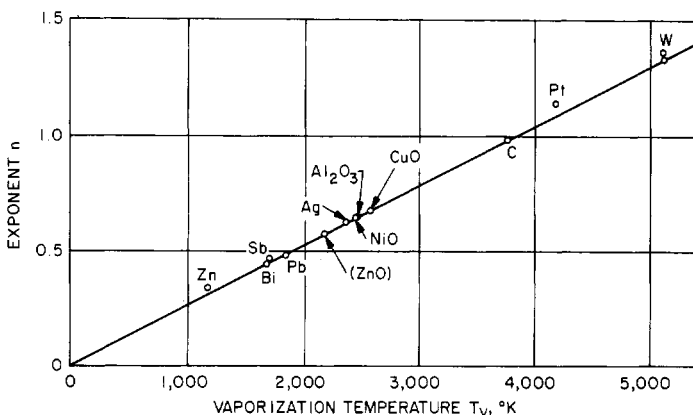
Figure 10.14 The exponent n of the Nottingham correlation, as a function of the vaporization temperature of the anode material.

For many combinations of gases and electrode material, the exponent n appearing the Nottingham equation (10.34) is a linear function of the vaporization temperature of the *anode* material (Nottingham 1926),

$$n = 2.62 \times 10^{-4} T_v \qquad (10.35)$$

where T_v is in kelvin. Data to this effect are shown in figure 10.14, taken from Cobine (1958). Note that for carbon, the exponent $n = 1.0$, consistent with the Ayrton equation (10.33). It is not known why the exponent n should have the linear relationship shown in figure 10.14, nor why the vaporization temperature of the anode is the critical parameter, rather than some property of the cathodes, where the electrons are emitted, as one would intuitively expect. It was later shown by Suits (1934) that this relation does not hold for some arcs.

10.4.2 Axial Electric Field

A key parameter for arc discharges of industrial interest is the total power dissipation, which is closely related to the electric field along the axis in the positive column of the arc. Extensive measurements of the axial electric field as a function arc current, the operating pressure of the arc, and the gas type can be summarized by the phenomenological equation for the axial electric field,

$$E = C_0 \frac{p^m}{I^k} \qquad \text{(V/m)} \qquad (10.36)$$

where the exponents k and m are given in table 10.2. For many gases of interest, including atmospheric air, the axial electric field is a decreasing

Table 10.2 Values of the exponents k (from Suits 1934) and m for an axial electric field, for carbon electrodes at atmospheric pressure in various gases.

Gas	Hg	A	N_2	Air	CO_2	He	H_2O	H_2
k	0.26	0.54	0.60	0.60	0.60	0.73	0.59	0.70
m	—	0.16	0.31	—	—	0.20	—	0.32
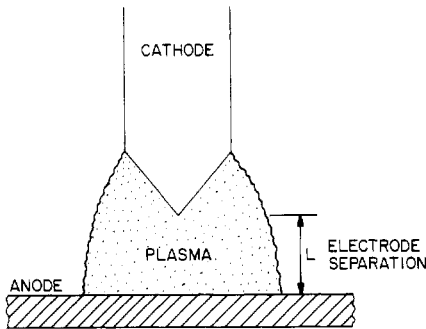
Figure 10.15 Schematic of the thermal arc in argon reported by Eberhart and Seban (1966).

function of arc current. For a particular gas and at a constant current, the electric field usually increases with background pressure. The effect of electrode material on the axial electric field is relatively small.

10.4.3 Thermal Arc of Eberhart and Seban

As an example of a thermal, high intensity arc, we examine the later work of Eberhart and Seban (1966) on an argon arc between a cathode and a planar anode, the geometry of which is shown in figure 10.15. Figure 10.16 shows their data for the power flow fractions of an arc operated in argon between a cathode located 2.54 cm above a grounded anode plane, with the fraction of the input power going to the cathode, into radiation to the walls, and to the anode. The three fractions plotted in figure 10.16 add up to the total at the top of the graph, and the difference between this total and unity represents the errors of measurement. In this case, only a small fraction of the power went into the cathode, more than 60% went into the anode, and approximately 25% appeared in the form of radiation to the walls. The large heat deposition on the anode was due to the cathode jet. This is characteristic of high power thermal arcs, where it is essential to cool the anode because of its relatively large power deposition. In some applications, such as welding, this heat deposition is desirable if the anode is the workpiece.
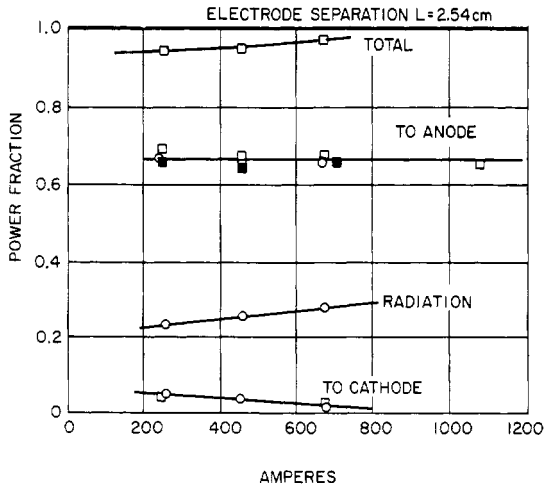
Figure 10.16 Thermal arc data of Eberhart and Seban (1966) showing the fraction of input power of a high intensity, thermal argon arc which is deposited on the cathode and anode, and the fraction appearing as radiation to the walls.
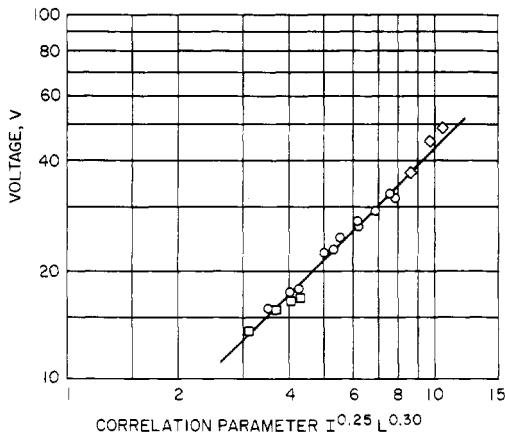
Figure 10.17 A voltage–current correlation found by Eberhart and Seban (1966) for a high intensity, thermal arc in argon. The complete range over which this correlation held was arc lengths from 5 to 31.5 mm; currents from 200 to 2300 A, and power inputs from 4 to 97 kW.

Eberhart and Seban found a phenomenological correlation for the voltage–current characteristic of their arc, which is shown in figure 10.17. They performed experiments for at least three different values of L, the anode-to-cathode separation, and found that the voltage–current relation

could be written as

$$V = 17.1 I^{0.25} L^{0.30} \qquad (V) \qquad (10.37)$$

where I is in amperes and L in meters. This correlation reduced their experimental data to a straight line with a slope of 45° on a log–log plot, as shown in figure 10.17, and, in addition, it correlated the reported data of two other investigators, cited in their paper, who operated other types of thermal arcs. The complete range over which equation (10.37) was found to be valid was $0.5 \leqslant L \leqslant 3.15$ cm; $200 \leqslant I \leqslant 2300$ A; and $4 \leqslant VI \leqslant 97$ kW. Inverting equation (10.37), the current given by this correlation can be written as

$$I = \frac{1.164 \times 10^{-5} V^4}{L^{1.2}}. \qquad (A) \qquad (10.38)$$

This equation indicates a very flat I–V curve in the thermal, high intensity arc division of the arc regime, with the current being proportional to the fourth power of the arc voltage. No theory predicting this functional relationship is available.

10.5 POWER SUPPLIES FOR ELECTRICAL ARCS

10.5.1 Power Supplies

Arcs require for their operation real currents rather than displacement currents, and these currents are provided to the electrodes by either AC or DC power supplies. The power supplies for *AC arcs* are invariably at the supply frequency, either 50 or 60 Hz, although it is possible to sustain arcs at AC frequencies of kilohertz. Except for arcs used in lighting devices, the AC power supplies for industrial thermal arcs typically operate at kilowatt to megawatt levels; may be one or, more usually, three phase; and typically consist of switchgear, step down transformers, and inductors and/or filters to maintain power quality.

Power quality is a major issue with high power AC arcs. If one phase of an AC arc furnace, for example, should fail to strike, this can create electrical disturbances in the distribution network that can affect an entire power grid. Thus, the stability and filtering of AC arcs is a factor of growing importance in these days of more stringent demands on power quality from the electric utilities. AC power supplies for arcs typically cost between 3 and 20 cents per watt, and these specific costs tend to have economies of scale, with a relatively weak inverse dependence on power rating.
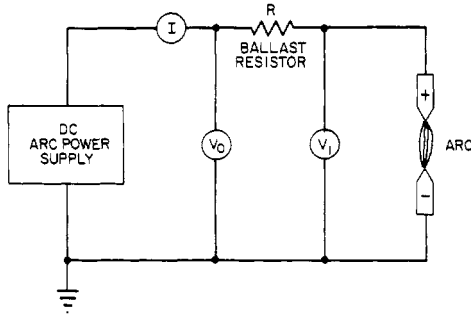
Figure 10.18 Electrical stabilization of non-thermal arcs. The ballast resistor R is sometimes replaced by an inductor to stabilize the arc current.

Typical power levels for DC thermal, high intensity industrial arcs range from kilowatts to tens of kilowatts. Power supplies for such arcs require switchgear, a transformer, a regulator, and rectifiers. Filtering and/or ballasting may be required for stability and/or power quality. Power supplies for DC non-thermal, low intensity arcs require, in addition to the equipment required by thermal arcs, a ballasting circuit for stability, of a kind shown in figure 10.18. The ballasting resistor R is needed to meet the negative resistance characteristic of non-thermal arcs, illustrated by the Aryton data of figure 10.13. Sometimes inductive ballasting is used. The specific cost of electrical power from multi-kilowatt DC power supplies may range from 10 to 50 cents per watt.

10.5.2 Electrical Stabilization of Non-thermal Arcs

Electrical arcs usually require some form of electrical stabilization, either to deal with the negative resistance characteristic of non-thermal, low intensity arcs, or the mode transitions that can occur in all types of arcs. A typical arrangement for non-thermal arcs is the resistive ballasting system shown in figure 10.18. In this circuit, the relation between the power supply voltage V_0 and the voltage across the arc, V_1, is given by

$$V_1 = V_0 - IR. \tag{10.39}$$

A schematic voltage–current relation for a non-thermal arc is shown on figure 10.19, where the quasi-hyperbolic curve of the kind given by the Ayrton correlation is shown as a solid line. The electrical circuit of figure 10.18 yields a *load line* given by the straight line, obtained from equation (10.39),

$$\frac{dV_1}{dI} = -R. \tag{10.40}$$
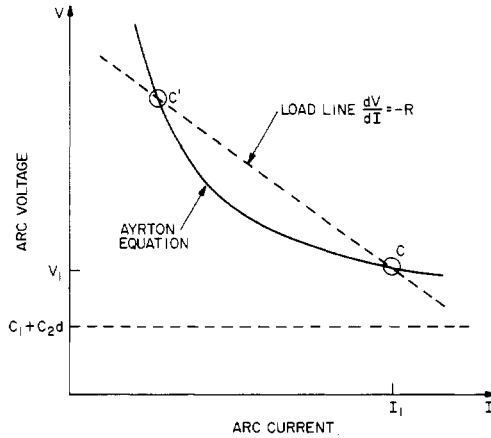
Figure 10.19 Stabilization of non-thermal arcs. The typical voltage–current characteristic is the solid line indicated; the load line of the stabilizing circuit in figure 10.18 usually intersects this in two locations, of which point C is the stable operating point.

Equation (10.40) is shown as the dotted line on figure 10.19. The Ayrton correlation of equation (10.33) will usually intersect this load line at two points, found by setting equation (10.39) and equation (10.33) equal,

$$V_1 = C_1 + C_2 L + \frac{C_3 + C_4 L}{I} = V_0 - IR. \qquad (10.41)$$

This equation has two solutions, I_1, and I_2, which yield the points C and C' on figure 10.19. The point C' is unstable, as a brief intuitive analysis will show. The circuit in figure 10.18 is stable when the *Kaufmann stability criterion* is satisfied; that is, when

$$\frac{dV_1}{dI} + R > 0 \qquad (10.42)$$

or

$$R > \left| \frac{dV_1}{dI} \right|. \qquad (10.43)$$

The condition of equation (10.43) is met at point C, but not at point C'.

10.6 INITIATING MECHANISMS FOR ARCS

Arcs are hard to start because they require either thermionic or field emission. Over the years, a number of initiating mechanisms have been

developed, which can be divided into three major approaches. The first of these is *electrical breakdown*, the process implied by progress on the voltage–current characteristic of figure 10.1 from the point G through the point J. This is a brute force approach, in which the voltage across the electrodes is raised to a high enough value to initiate the glow-to-arc transition. This method of initiating electrical arcs presents a safety hazard with high voltages on the electrodes, and places difficult requirements on the electrical power supply, which must be capable of high initiating voltages as well as the high currents at low voltages required to maintain the arc in the steady state.

The second major initiating mechanism is *'drawing an arc'*, which consists simply of separating electrodes which are initially in contact. This invariably results in high current densities at small asperities or contact points which heat these points locally, and provide the thermionic emission necessary to sustain the arc.

Finally, there are a variety of widely used initiating mechanisms based on *external ionization* of the electrode gap. These include an RF spark, provided, for example, by an induction or tesla coil; an exploding wire between the electrodes which can consist of a carefully placed single wire, or simply a wad of steel wool jammed between the electrodes, a single shot approach; the use of a plasma gun, such as a spark plug for example; the use of ionizing radiation, including alpha and beta emitters; irradiation of the electrodes with ultraviolet, x-rays, or gamma rays; or the irradiation of an electrode with a high energy laser. Arcs may also be initiatied by smaller plasma jets, as might be appropriate for high power gas heaters, where the electrode separation is relatively large; and finally, arcs may be initiated by chemical ionization in a flame, such as provided by a match.

10.7 APPLIED ARC CONFIGURATIONS

In this section, we will discuss various arc configurations which have found industrial use. The linear arcs are usually thermal; other configurations are high power, thermal arcs.

10.7.1 Linear Arcs

We first discuss *linear arcs*, those arcs, usually axisymmetric, which are operated in a substantially linear configuration between two electrodes. Most basic of the linear arcs is the *free-burning arc*, illustrated in both horizonal and vertical configurations in figure 10.20. The primitive horizontal form of arc was first observed by Sir Humphery Davy in the early years of the 19th century. The buoyancy of the hot gases causes a
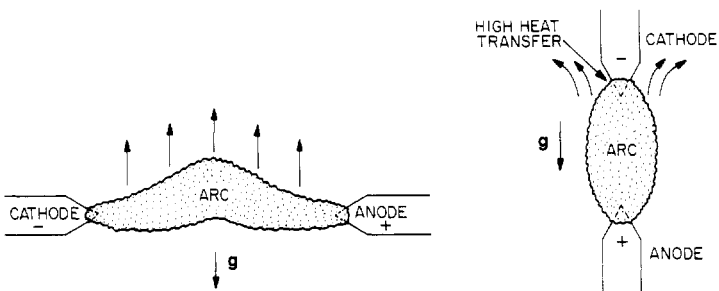
Figure 10.20 Two configurations of the free-burning arc, with horizontal electrode alignment (left) and vertical electrode alignment (right).
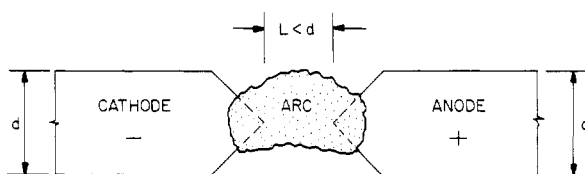
Figure 10.21 The obstructed electrode-stabilized arc.

horizontal linear arc to bow upward, resulting in an arched appearance that gave the 'arc' its name. When the free-burning arc is operated in the vertical configuration, shown on the right of figure 10.20, the cathode is usually operated at the top, in order to better balance the heat loads on the two electrodes. Under the force of gravity, the buoyant hot gases rise and deposit an enhanced heat load on the cathode; to counter this, the cathode is put at the top, so that the heat load due to the cathode jet on the anode will not increase the heat deposition on the upper electrode still further.

On figure 10.21 is shown schematically the *obstructed electrode-stabilized arc*. If the distance between the electrodes is so small that there is no arc column, and the electrode sheath and flow regions touch, the arc is said to be obstructed. Typically, $L \approx 1$ mm in such arcs, but the applied potential between the electrodes, V_1, must be greater than the anode and cathode drops, or the arc will extinguish.

Perhaps the arc most widely used for gas heating is based on the *wall-stabilized arc*, two versions of which are shown in figure 10.22. The geometry of the wall-stabilized arc consists of an axial cathode, and a coaxial hollow anode. This arrangement is normally axisymmetric. The physical mechanism of arc stabilization is based on the Elenbaas–Heller equation (10.32), which states that if an arc is cooled on its edges, the temperature on axis rises. If an initially axisymmetric arc column is perturbed and approaches a coaxial wall as in figure 10.22(a), the edge of the arc will cool, and the temperature of the gas on the axis will
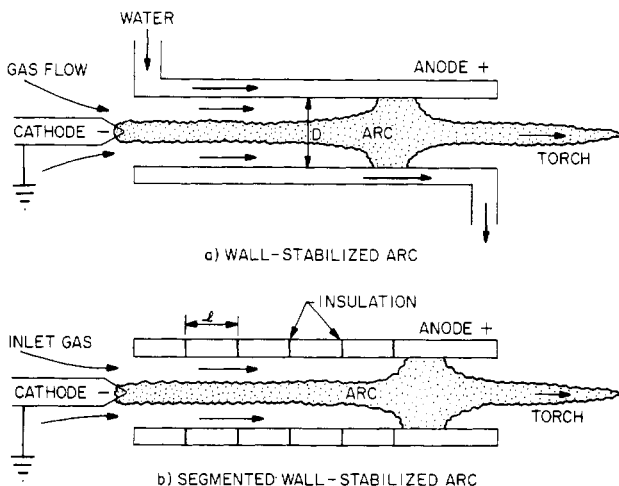
Figure 10.22 Two configurations of the wall-stabilized arc: (a) unitary, coaxial anode; (b) segmented anode, with segments of axial width ℓ.

heat up. The heating up of the gas on the axis will increase the electrical conductivity, and the arc will then be pulled back on axis. In figure 10.22, part of the wall may be an insulating material like quartz if the arc is used for illumination. In high power gas heating applications, the cylindrical anode would be water-cooled.

In the configuration shown in figure 10.22(a), the arc can attach at any point along the anode axis, leading to a potential instability of the axial attachment point, and inadequate heating of the surrounding gas flow if the arc attaches too far toward the cathode. Very often the coaxial gas flow can be used to 'push' the attachment point to the opposite end of the anode cylinder, away from the cathode, but a better-defined arrangement is the *segmented wall-stablized arc* shown in figure 10.22(b). In this form of wall-stabilized arc, the anode walls are again water-cooled, but electrically segmented and isolated to provide a linear decrease of the axial voltage. The axial width of the segments is adjusted so that their length ℓ does not exceed the value necessary to strike an arc from one segment to the next, i.e.

$$\int_0^\ell E \, dz < V_A + V_C. \tag{10.44}$$

If equation (10.44) is satisfied, then any arc striking between the axial segments would be obstructed to such an extent that it could not form in the first place, and this forces the arc to attach to the wider segment at the right-hand end. This arrangement has the advantage of eliminating
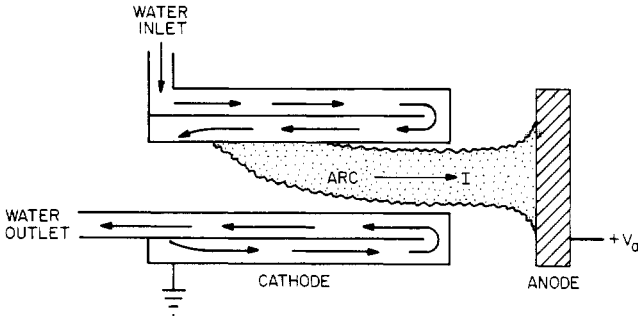
Figure 10.23 The transferred arc configuration, with the arc orginating on the inner wall of a water-cooled hollow cathode structure, and the currrent flowing to an external anode.

any axial instability in the arc position, and also stretches the arc to a length adequate to assure maximum enthalpy addition to the flowing gas passing through the arc. In order for wall-stabilized arcs to be effective, the tube diameter, D, has to be less than the diameter of the arc without the wall in place, i.e. less than the diameter of a free-burning arc of the same power. These wall-stabilized arcs find wide application for gas heating, illumination, and other purposes.

The *transferred arc* with a non-consumable cathode is shown on figure 10.23. This is a relatively recent development in arc technology, intended for high power arcs which operate with cooled, field-emitting cathodes. In such arcs, the electrical circuit is completed only by transferring the arc to an external anode, which might be a tundish or ladle of scrap metal, or some other electrically conducting object to which one wishes to transfer a great deal of energy. This configuration is capable of operating at the multimegawatt level for durations (many hundreds or thousands of hours) that are not possible for thermionically emitting cathodes or uncooled, incandescent cathodes operating in air. Transferred arcs like those in figure 10.23 are coming into increasingly widespread use in the metal melting and refining industry. In these arcs, the arc root shown in figure 10.23 moves over the cathode surface, further reducing the cathode heat load, and increasing the lifetime of the hardware. The object to be heated is used as the anode, since the anode receives the heat deposition from the cathode jet.

Sometimes water cooling of a *wall-stabilized arc* is very difficult, and so an attempt is made to reduce heat transfer problems in wall-stabilized arcs by adopting the *transpiration-stabilized arc* configuration shown in figure 10.24. This is typically a segmented wall-stabilized arc, but instead of introducing the cooling and stabilizing gas coaxially from the end, as in the wall-stabilized arcs discussed previously, the transpiration-
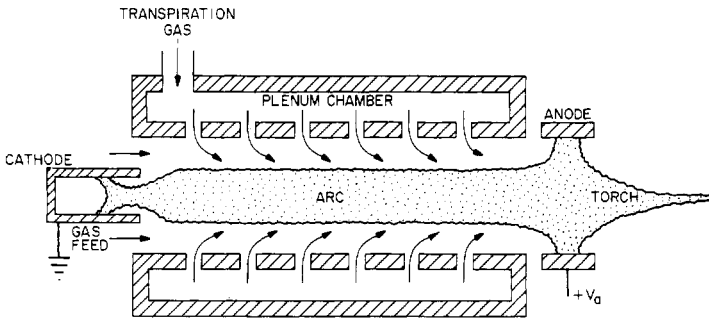
Figure 10.24 The transpiration-stabilized arc, with the arc column maintained in a centered position by radially inward injection of cooling water or gas.
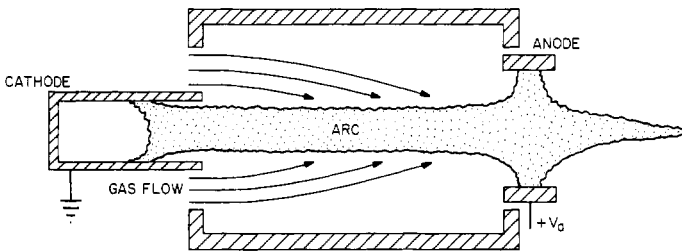
Figure 10.25 The coaxial flow stabilized arc with laminar axial flow of stabilizing gas.

stabilized arc injects additional fluid (which may be a gas or a liquid) through annular slots between the segments, in an attempt to keep the interior segments of the anode cool, and lengthen their lifetime. The transpiration fluid then becomes a part of the working gas incorporated into and heated by the arc.

In these high power arc configurations, the cathode may take any one of a number of forms, of which the solid cathode shown schematically in figure 10.22 is one, the water-cooled hollow cathode shown in figure 10.23 is another, and the hollow cathode configuration shown in figure 10.24 is a third. In the hollow cathode configuration of figure 10.24, the arc attaches to the inner surface of the cathode, where the arc root rotates around the axis. This arrangement generally reduces the heat transfer, improves reliability, and increases the lifetime of the hardware.

Another high power linear arc configuration is the *coaxial flow stabilized arc* shown schematically in figure 10.25. In this case, the anode surface is moved radially far away from the arc, too far to provide wall stabilization. The solid wall which maintains arc stabilization is replaced by a coaxial gas flow along the outer surface of the arc. As long as this
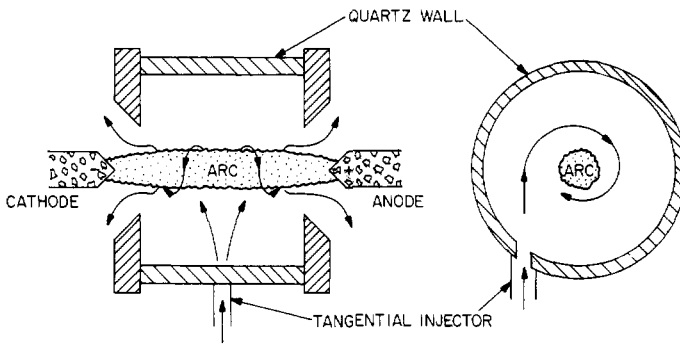
Figure 10.26 The vortex-stabilized arc, in which the arc is kept on axis by a tangentially injected vortex of flowing gas or liquid.
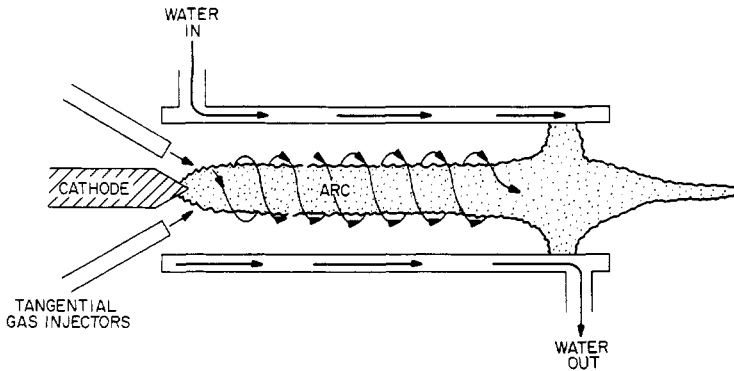
Figure 10.27 An axial vortex-stabilized arc, with tangential gas injectors in the vicinity of the cathode.

coaxial flow remains laminar, the arc will be stabilized, and with greatly reduced concerns about heat transfer to the surrounding wall.

A related linear arc configuration is the *vortex-stabilized arc* shown in figure 10.26. This operates on the same basic principle as the coaxial flow stabilized arc, in that the wall is moved radially far enough away from the arc that it plays little role in stabilizing the arc. The arc instead is stabilized by a vortex gas flow from a tangential injector which cools the edges of the arc and keeps it confined to the axis of the configuration. The fluid used for vortex stabilization may be a liquid or gas, and both have been used when these arcs have been operated as light sources for industrial purposes. The vortex flow is very effective in reducing the heat flux to the wall.

A related variant of the vortex-stabilized arc is shown in figure 10.27. This is an *aerodynamically stabilized arc*, in which the stabilizing gas (or liquid) is injected tangentially near the cathode, in such a way as to
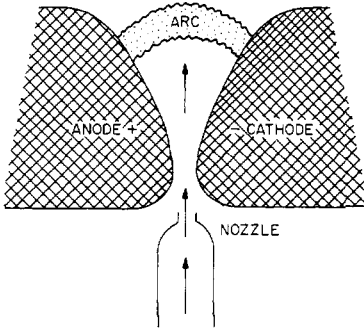
Figure 10.28 The gliding arc, in which an arc strikes across the narrow gap, and rises until its increasing length causes its extinction.
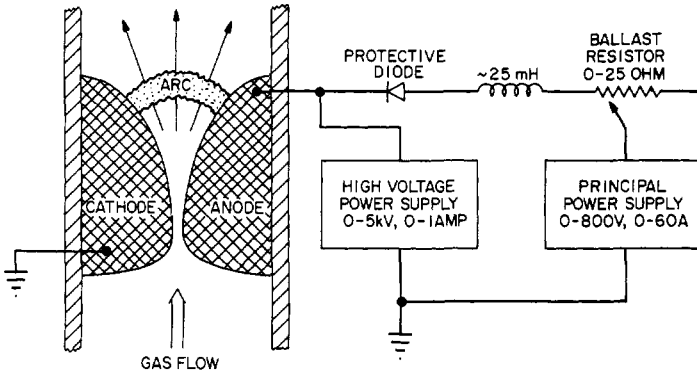
Figure 10.29 The gliding arc power supply, which provides a high voltage to initiate the arc across the narrow gap, and a principal power supply to sustain the arc.

maintain a vortex flow around the periphery of the arc. This flow then cools the arc at its edges, and stabilizes its position on the axis.

10.7.2 Expanding Arcs

Although most high power gas heaters used industrially are based on one of the linear arc configurations discussed above, other important industrial applications including toxic waste disposal, switchgear, and plasma chemistry use *expanding arcs*, of which we will discuss three basic configurations.

The *gliding arc* is used for toxic waste disposal and destructive plasma chemistry. The gliding arc, shown schematically in figure 10.28, consists of a pair of electrodes which extend into and out of the plane of the diagram. These electrodes are energized by the power supply shown in figure 10.29. In operation, a high voltage is maintained across the electrode gap, sufficient to cause electrical breakdown of the gas flowing between the electrodes at the narrowest part of the gap. Once breakdown
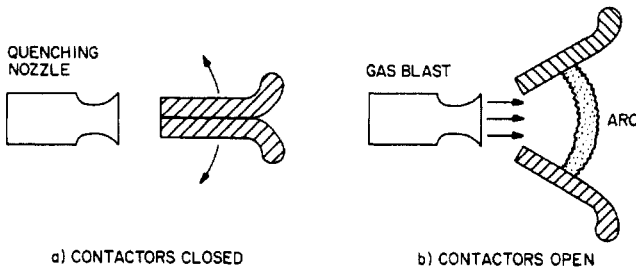
Figure 10.30 Typical switchgear, showing the drawn arc resulting from opening the contacts while a current flows between them.

occurs, the principal power supply provides a high current at a moderate voltage, sufficient to create a powerful arc which expands upward on the hemi-elliptical surfaces of the electrodes, where it lengthens until it can no longer be maintained. At this point, the arc goes out, and the process is repeated. This is a very old arc configuration, first investigated in the 19th century. It is sometimes seen as a *Jacob's ladder* in popular science exhibits. The expanding arc is capable of providing a range of plasma operating parameters which make it of value for various forms of destructive plasma chemistry. Recent work on the gliding arc has been reported by Lesuer *et al* (1990).

A related expanding arc configuration is found in switchgear, one variant of which is shown in figure 10.30. In a typical switchgear application, the contacts shown in figure 10.30(a) start out closed, and are arranged with diverging surfaces, one edge of which is opposite a quenching jet, aimed between the two electrodes. When the contactors open as in figure 10.30(b), an expanding arc is formed which travels along the opening of increasing length, until it reaches a width where the arc can no longer be sustained in the surrounding gas. In many heavy duty switchgear applications, extinction of the arc is promoted by using an electrophilic gas like sulfur hexafluoride, which removes electrons from the arc plasma, and also by cooling the arc with a blast of gas aimed between the open contactors.

Of increasing importance in metal heating and refining applications is the *non-transferred arc* configuration shown schematically in figure 10.31. This configuration consists of a wall-stabilized arc, with a cylindrical cathode and a coaxial anode located in a water-cooled cylindrical configuration. The hollow, coaxial, cylindrical electrodes are separated by an insulator, and an arc is drawn between the inner surface of the cathode and the anode. In order to heat material beyond the anode opening, gas is fed along the axis, which blows the arc out toward the material which is is to be heated. These non-transferred arcs have the advantage that $J \times B$ forces cause the arc roots to rotate
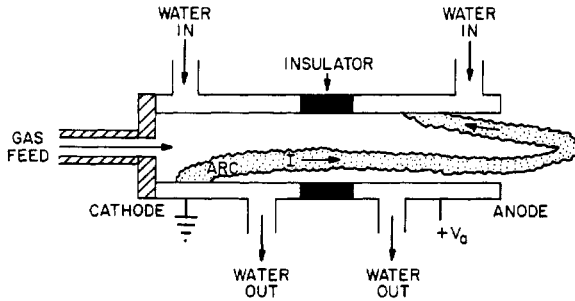
Figure 10.31 The non-transferred arc, in which an arc struck between a coaxial cathode and anode is made to contact external material to which heat is delivered by an axial gas flow.
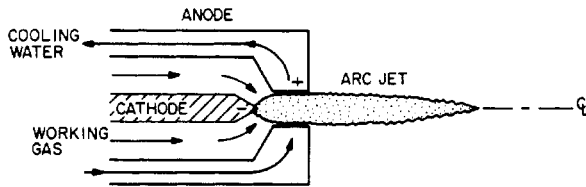
Figure 10.32 The axisymmetric, non-transferred, unmagnetized arc jet, or plasma torch. An arc is struck between the cathode and the coaxial anode, and working gas is heated by passage through the arc region.

around the water-cooled cathode and anode surfaces; they rely wholly on field emission, and the resulting lower cathode and anode surface temperatures permit greater reliability and much longer lifetimes than incandescent graphite electrodes, which previously have been standard in high power arc furnaces, for example.

10.7.3 Rotating Arcs

There are a large variety of coaxial, *rotating arc* configurations in use industrially. The characteristic *axisymmetric non-transferred arc*, also called the *arc jet* or the *plasma torch*, is shown schematically in figure 10.32. This arc consists of an axial cathode, and a water-cooled axisymmetric anode, with a conical gap across which an arc forms in the shape of a rotating spoke. Usually a working gas is fed in coaxially, is heated by the arc, and forms a very high temperature arc jet, often at supersonic velocities, downstream of the nozzle. The *magnetically stabilized rotating arc* is shown in figure 10.33. An axial magnetic field provides $J \times B$ forces which rotate the arc spoke to avoid high local heat loads on the anode. The axial magnetic field is generally used as a supplement to the effects of wall stabilization or aerodynamic stabilization provided by the working gas.
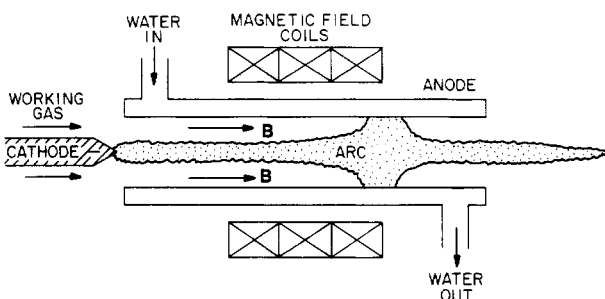
Figure 10.33 The magnetically stabilized arc. In this geometry, additional positional stability is imparted by applying an axial magnetic induction to a wall stabilized, linear arc.
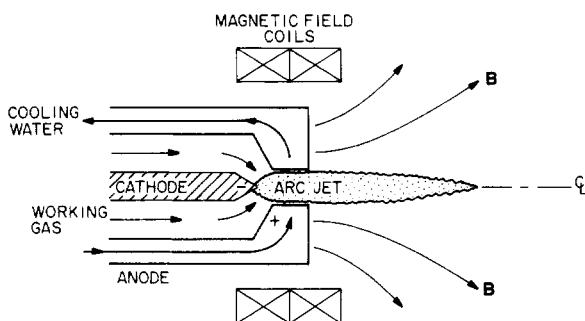
Figure 10.34 The magnetically stabilized plasma torch. The axial magnetic field causes rapid rotation of the arc in the azimuthal direction, thus preventing arc stagnation and damage to the anode or cathode surface.

A very important variant of the magnetically stabilized arc is the *magnetically stabilized plasma torch* shown in figure 10.34. This plasma torch resembles the arc jet shown in figure 10.32, but with an axial magnetic mirror coaxial with the anode so that the magnetic field maximum is near the plane of the arc rotation. A working gas is fed coaxially, passes through the arc, and forms an intense plasma jet downstream of the nozzle. There are many industrial variants of the magnetized plasma torch, including those which are aerodynamically stabilized, vortex-stabilized, wall-stabilized and transpiration-cooled. The plasma torch is used for plasma flame spraying, plasma chemistry, and toxic waste disposal.

The arcs discussed above are all 'high pressure' arcs, usually operating near 1 atm. As discussed in Chapter 6 on ion sources, a class of vacuum or low pressure arcs operate below 10 Torr and are sustained by evaporation of their cathode material. Such arcs have a high ionization fraction, and are used for thin film deposition.

10.8 ISSUES IN ARC PHYSICS

As in other branches of electrical discharge physics, there is a tendency to believe that electrical arcs are well understood, particuarly in view of their long history going back to the year 1806. Unfortunately, many aspects of arc physics are not well understood, and many of these areas of ignorance relate to issues of commerical importance.

One unresolved issue of arc physics is a theory for the voltage–current relation of arcs. Neither the Ayrton correlation for non-thermal, low intensity arcs, nor the correlation of Eberhart and Seban, given by equation (10.37) for high intensity arcs, has been justified analytically, nor have the physical processes responsible for these voltage–current relations been identified. A theoretical explanation of the functional dependences revealed by these correlations would almost certainly require a knowledge of the radial transport of plasma in both magnetized and unmagnetized turbulent media; this is not yet available in the field of fusion research despite intensive effort over 30 years, and so perhaps it is not surprising that a related problem with industrial plasmas has not yet been solved.

Another issue of arc physics is the identification of the physical processes responsible for mode transitions like that shown in Ayrton's data of figure 10.13, and like that seen in high intensity, thermal arcs where spontaneous mode transitions are also observed. The industrial uses of arcs will not be well understood until such time as the physical processes responsible for mode transitions are identified, and the criteria for the onset of mode transitions are understood in a quantitative manner.

A third major issue in arc physics is the physical process responsible for the retrograde rotation of non-thermal arcs, discussed in connection with figure 10.6. This retrograde motion has been widely observed, but the physical mechanism by which the arc rotates in a direction contrary to the $J \times B$ force is not understood.

A fourth major issue in arc physics is an adequate computational modeling of non-thermal arcs. Within limits, the computational modeling of thermal arcs can be said to be understood, with reasonable agreement between theory and experiment in a few cases involving simple monatomic gases such as argon and helium. Whatever success computational modeling has had in arcs arises from the satisfaction of local thermodynamic equilibrium (LTE), which allows the computational model to incorporate the powerful constraints imposed by the Saha equation, and imposed on radiant heat transfer by the Stefan–Boltzmann radiation law. Since non-thermal arcs are not in local thermodynamic equilibrium, the distribution of excited states, the fraction of ionization, and the radiant energy transfer within the arc are not subject to a straighforward analysis.

Finally, radial transport in turbulent arcs, magnetized and unmagnetized, must be better understood, as alluded to above, in order to understand the voltage–current relations of arcs which are actually observed in practice. This issue is related to the broader problem of radial transport in magnetized plasmas, which has been a major stumbling block in the world fusion effort for the last 30 years. At present, it appears likely that fluctuation-induced transport may play a role in arcs and industrial plasmas, as well as in the radial transport of fusion plasmas.

REFERENCES

Ayrton H 1902 *The Electric Arc* The Electrician Printing and Publishing Co. (New York: D Van Nostrand)

Bennett W H 1934 Magnetically Self-Focusing Electron Streams *Phys. Rev.* ser 2 **45** 890–897

Brown S C 1966 *Introduction to Electrical Discharges in Gases* (New York: John Wiley)

Cobine J D 1958 *Gaseous Conductors* (New York: Dover Publications)

Eberhart R C and Seban R A 1966 The Energy Balance for a High Current Argon Arc *Int. J. Heat and Mass Transfer* **9** 939–949

Gross B, Grycz B and Miklossy K 1969 *Plasma Technology* (New York: American Elsevier) LCCCN 68-27535

Hirsh M N and Oskam H J (ed) 1978 *Gaseous Electronics* vol I *Electrical Discharges* (New York: Academic Press) ISBN 0-12-349701-9 (this book contains several chapters on arcs by different authors)

Jobes F C, Marshall J F and Hickok R L 1969 Plasma Density Measurement by Ion-Beam Probing *Phys. Rev. Lett.* **22** 1042–1045

Lafferty J M (ed) 1980 *Vacuum Arcs, Theory and Application* (New York: John Wiley) ISBN 0-471-06506-4

Lesueur H, Czernichowski A and Chapelle J 1990 *Electro-Heating with a Gliding Arc* private communication

Nottingham W B 1923 A New Equation for the Static Characteristic of the Normal Electric Arc *A.I.E.E. Journal* **42** 12–19

Nottingham W B 1926 Normal Arc Characteristic Curves: Dependence on Absolute Temperature of Anode *Phys. Rev.* **28** 764–768

Pfender E 1978 Electric Arcs and Arc Gas Heaters, in: Hirsh M N and Oskam H J (ed) *Gaseous Electronics* vol I *Electrical Discharges* (New York: Academic Press) ISBN 0-12-349701-9 chap 5, pp 291–398

Roth J R 1986 *Introduction to Fusion Energy* (Charlottesville, VA: IBIS Publishing) ISBN 0-935005-07-2

Suits C G 1934 Experiments with Arcs at Atmospheric Pressure *Phys. Rev.* **46** 252–254

Tonks L and Langmuir I 1929 A General Theory of the Plasma of an Arc *Phys. Rev.* **34** 876–922

Von Engel A 1965 *Ionized Gases* 2nd edn (Oxford: Oxford University Press) chap 7

11

Inductive RF Electrical Discharges in Gases

The DC electrical discharges studied in the last three chapters draw a *true current* from the power supply in the form of a flow of ions or electrons to the electrodes, the 'electrical road' of the discharge. The physical processes in such discharges are dominated by the axial DC electric fields. This situation is not greatly changed by the application of a low frequency AC voltage to the electrodes at the power supply frequency of 50 or 60 Hz. The period of the applied frequency is so much longer than the time scale of most physical processes in the plasma that such discharges can be treated as though they were DC, and the phenomenology and theoretical formalism described in the previous three chapters applied.

When the applied frequency becomes high enough, the period of the oscillation will become comparable to the time that it takes electrons or ions, particularly ions, to traverse the sheath between the plasma and the electrodes. At such radio frequencies (RF), the power supply interacts with the plasma almost exclusively by displacement rather than real currents, and entirely different physical processes come into play.

11.1 INTRODUCTION

In industrial applications requiring tens of kilowatts to many megawatts, DC power supplies are available at a cost between ten and fifty cents per watt, whereas RF power supplies characteristically cost from one dollar to five dollars per watt. In spite of the comparatively high cost of RF power relative to DC, there are many industrial applications for which the advantages of RF power outweigh its higher cost. One of the most important advantages of RF power is that it interacts with the

plasma by *displacement currents*, rather than true currents, and thus it can be delivered without the requirement for electrodes in contact with the plasma. The presence of electrodes can be a serious disadvantage in many applications for which control of impurities in the product is an important factor. The absence of current-carrying electrodes in contact with the plasma also tends to improve the reliability, reproducibility, and lifetime of the plasma reactors themselves, and of the products made in them.

11.1.1 Modes of RF Interaction with Plasma

Radio frequency power can interact with plasmas either inductively, capacitively, or quasi-optically, as in microwave–plasma interaction. This and the next two chapters will survey some of the more common industrial methods used to deliver RF power to plasmas using these three coupling methods. This chapter is concerned with inductively coupled RF electrical discharges, in which RF power is transferred by ohmic dissipation of induced RF currents which are caused to flow in the plasma by high frequency transformer action. Chapter 12 covers capacitively coupled RF electrical discharges, in which RF power is transferred to the plasma by the randomization of kinetic energy imparted to the electron population by RF electric fields. Finally, Chapter 13 describes the quasi-optical absorption of RF power at microwave frequencies, above the electron plasma frequency.

11.1.2 Inductive Coupling to Plasma

A relatively small but important class of industrially relevant plasmas is generated by *inductive coupling*. In inductive coupling, the principal linkage between the RF power supply and the plasma is RF currents induced by transformer action in the plasma. The industrially most widely used inductive coupling configuration is shown on figure 11.1. This arrangement characteristically consists of a coil with two to eight turns, wrapped around a (usually) quartz tube, which also serves as a vacuum vessel. Within the tube is a plasma maintained in the steady state by the RF power supplied to the coil. The frequencies used for inductive coupling to plasmas range from below 10 kHz, to as high as 30 MHz or more. The neutral gas pressure in inductively coupled plasmas is usually below 1 atm, ranging perhaps from a few torr to a few hundred torr, although some inductive coupling applications are operated outside this range and even at atmospheric pressure.
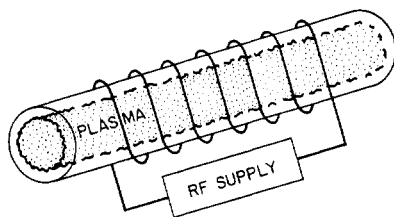
Figure 11.1 Schematic of an inductively coupled RF plasma generator. In a typical arrangement, a coil consisting of two to eight turns is wrapped around a quartz tube, within which a cylindrical plasma is generated at reduced pressure.

11.2 PHENOMENOLOGY OF RF–PLASMA INTERACTIONS

Radio frequency power is coupled to plasma through either an oscillating magnetic field (inductive coupling), an oscillating electric field (capacitive coupling), or both (quasi-optical or microwave coupling). Whether and to what extent these oscillating fields interact with the plasma depend on the frequency of the oscillation, the electron plasma frequency, and the electron collision frequency in the plasma. These parameters determine the electrical conductivity and the energy transfer frequency of the plasma, as well as the plasma skin depth. We now examine these phenomena in greater detail.

11.2.1 Electron Plasma Frequency

In Chapter 4 it was stated that the *electron plasma frequency* plays an important role in determining whether and to what extent an electromagnetic wave will interact with a plasma. The electron plasma frequency is a function of the electron number density and is given by

$$\omega_{pe} = 2\pi \nu_{pe} = \sqrt{\frac{n_e e^2}{\varepsilon_0 m_e}} \qquad \text{(rad/s)}. \qquad (11.1)$$

When the frequency of incident electromagnetic radiation is below this frequency, the inertia of the electrons is low enough for them to respond to the electric field in the incident electromagnetic wave, and the electron therefore can absorb energy from it. This absorbed energy may be converted to heat through collisions, or re-radiated in the form of a reflected electromagnetic wave from the surface of the plasma.

If the frequency of the incident electromagnetic radiation is higher than the electron plasma frequency given by equation (11.1), then the inertia of an electron is too high to allow it to respond fully
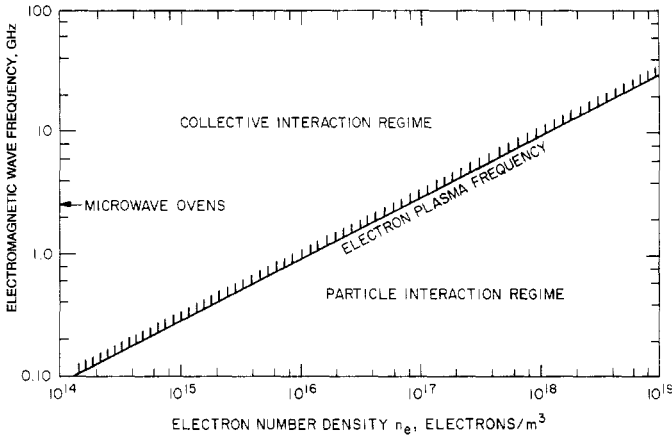
Figure 11.2 The electron plasma frequency, in gigahertz, as a function of the electron number density in electrons per cubic meter. In the particle interaction regime, below the electron plasma frequency, individual electrons can respond to the electric field of the electromagnetic wave; above the electron plasma frequency, the inertia of the individual electrons causes them to respond collectively.

to the incident electromagnetic wave. The electromagnetic wave is then free to propagate through the plasma as a quasi-optical dielectric medium, in which the interaction of the electromagnetic radiation with individual electrons is relatively insignificant, except at the gyro-resonance frequency in magnetized plasmas.

If the natural constants are substituted into equation (11.1), and the frequencies converted to hertz, the requirement that the incident radiation of frequency v_0 be less than the *electron plasma frequency* may be written as

$$v_0 < v_{pe} = 8.980\sqrt{n_e} \text{ Hz} \qquad (11.2)$$

which is a function only of the electron number density, n_e, in electrons per cubic meter. Equation (11.2) is plotted on figure 11.2. Below and to the right is the *particle interaction regime*, in which the incident frequency is low enough for the electrons to respond individually to the electric field of the electromagnetic wave; the *collective interactive regime* or *quasi-optical regime* to the upper left are those frequencies above the electron plasma frequency for which the incident electromagnetic radiation interacts with the plasma as a whole, and for which the electron inertia is too high for the electrons to respond individually.

11.2.2 Critical Number Density

The *critical number density*, which separates the particle interaction regime from the collective interaction regime on figure 11.2, can be found by inverting equation (11.2) to yield

$$n_c = 1.2404 \times 10^{-2} \nu_0^2 \text{ electrons/m}^3. \qquad (11.3)$$

where ν_0 is in hertz.

The incident electromagnetic wave with frequency ν_0 will interact with a plasma collectively if its number density is below the value given by equation (11.3), and will interact relatively strongly with the individual electrons if the number density is above the value shown in equation (11.3). If the number density is above the value given by equation (11.3), the electromagnetic radiation will interact strongly at the surface and be absorbed or reflected there; if the electron number density is less than this value, then the electromagnetic radiation will propagate through the plasma, interacting only relatively weakly with it.

If it is desired to heat a plasma at electron gyroresonance frequency, where electromagnetic radiation is strongly absorbed, the incident radiation must be at the frequency

$$\nu_{ce} = \frac{\omega_{ce}}{2\pi} = \frac{eB}{2\pi m_e} = 2.7992 \times 10^{10} B \text{ Hz} \qquad (11.4)$$
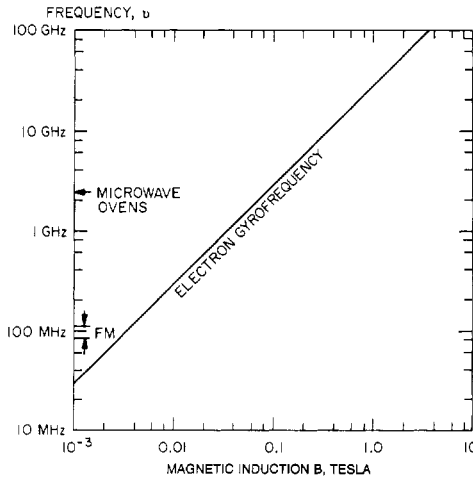
Figure 11.3 Electron gyrofrequency as a function of magnetic induction. This important resonant frequency in magnetized plasmas can be achieved with relatively modest magnetic inductions for frequencies below 10 GHz.
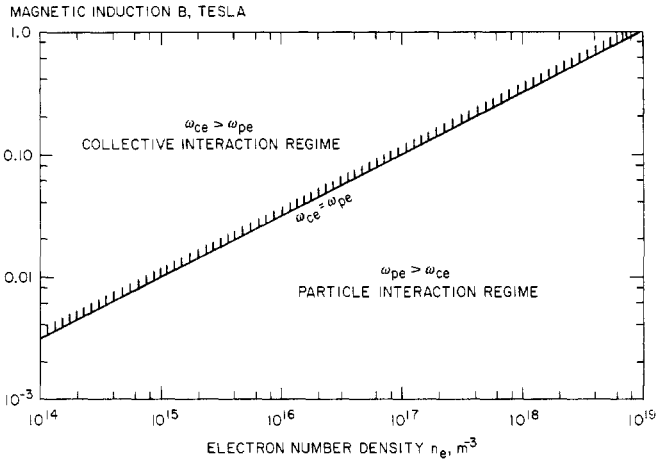
Figure 11.4 The magnetic induction as a function of electron number density indicating the values (straight line) for which the electron cyclotron frequency is equal to the electron plasma frequency. Above the line, the electrons interact collectively with the electromangetic wave; below it their inertia is low enough that they interact individually with the electromagnetic radiation.

where B is in tesla. This electron gyrofrequency is plotted as a function of magnetic induction in figure 11.3. In order to have a strong interaction of the incident electromagnetic radiation at the electron gyrofrequency in a plasma, the frequency of the incident radiation should be greater than the electron plasma frequency,

$$\omega_{ce} = \frac{eB}{m_e} \geqslant \omega_{pe} = \sqrt{\frac{n_e e^2}{\varepsilon_0 m_e}}. \tag{11.5}$$

Squaring both sides of the second and fourth members of equation (11.5) yields a relationship for the electron number density of a plasma subject to electron gyroresonant heating, as a function only of the magnetic induction of the magnetized plasma,

$$n_e \leqslant \frac{\varepsilon_0 B^2}{m_e} = 9.72 \times 10^{18} B^2 \text{ electrons/m}^3. \tag{11.6}$$

The equality in equation (11.6) is plotted in figure 11.4, and this yields two potential operating regimes. The *collective interaction* or *quasi-optical regime*, in which the electron gyrofrequency is greater than the electron plasma frequency, is the case for which incident electromagnetic radiation at the electron gyrofrequency interacts with the plasma as

a collective whole. In this regime, the electromagnetic radiation can penetrate throughout the bulk of the plasma and interact with the electrons at their gyrofrequency. The *particle interaction* or *'overdense' regime*, for which the electron plasma frequency is greater than the electron gyrofrequency, is the regime in which incident electromagnetic radiation interacts strongly with the individual particles at the surface of the plasma. In order to most efficiently heat a plasma at the electron gyrofrequency in the interior of a magnetized plasma, one should operate somewhere to the upper left of the dividing line in figure 11.4, in the collective interaction regime.

11.2.3 Electrical Conductivity and Energy Transfer Frequency

In the discussion prior to equation (4.18) of Chapter 4, we derived the electrical conductivity of an unmagnetized plasma, in siemens per meter, as

$$\sigma_0 = \frac{e^2 n_e}{m_e \, \nu_c} \qquad \text{(S/m)} \qquad (11.7)$$

where the parameter ν_c is the electron collision frequency in hertz. The electrical conductivity of equation (11.7) may be written in terms of the electron plasma frequency of equation (11.1) as

$$\sigma_0 = \frac{\varepsilon_0}{\nu_c} \omega_{pe}^2. \qquad (11.8)$$

In the discussion leading up to equation (9.26) of Chapter 9, it was shown that the energy transfer frequency of an unmagnetized plasma can be written

$$\nu_{*0} = \frac{2\omega_{pe}^2}{\nu_c} \qquad \text{(Hz)}. \qquad (11.9)$$

By comparing equation (11.8) with (11.9), one can write the electrical conductivity of an unmagnetized plasma in terms of the energy transfer frequency as

$$\sigma_0 = \frac{\varepsilon_0}{2} \nu_{*0} \qquad \text{(S/m)}. \qquad (11.10)$$

Thus, the electrical conductivity of an unmagnetized plasma is related to the energy transfer frequency by a fixed constant. Table 11.1 shows some characteristic electrical conductivities for various materials. Also shown in this table are the corresponding characteristic energy transfer frequencies, calculated from equation (11.10).

Table 11.1 Electrical conductivities and energy transfer frequencies of various materials.

Material	Electrical conductivity σ (S/m)	Energy transfer frequency v_* (Hz)
DT fusion plasma, with $T_e = 10$ keV, $Z = 1.5$	1–2×10^9	2.26–4.52×10^{20}
Room temperature copper	10^7–2×10^8	2.26–45.2×10^{18}
Room temperature carbon	3×10^4–10^5	6.8–22.6×10^{15}
Room temperature iron	3×10^4–10^5	6.8–22.6×10^{15}
Argon plasma torch	200–10^4	4.5×10^{13}–2.3×10^{15}
Nitrogen plasma torch	400–2000	9×10^{13}–4.5×10^{14}
Hydrogen plasma torch	100–400	2.3×10^{13}–9×10^{13}
MHD generator plasma	10–100	2.3–23×10^{12}
Saturated salt water	20	4.5×10^{12}
Bakelite	10^{-10}	23
Hard rubber	10^{-16}	2.3×10^{-5}

11.3 SKIN DEPTH OF PLASMA

When a plasma is exposed to RF radiation below the electron plasma frequency, the interaction of the RF energy with the plasma occurs in a *surface interaction layer* in which the RF energy is largely absorbed, reflected, or scattered. This surface interaction layer is called the *skin depth*, and is shown schematically in figure 11.5, which shows a cylindrical plasma of radius a receiving inductively coupled RF power from a coil of radius r_c. The plasma has an electrical conductivity σ and a skin depth (or surface interaction layer) of thickness δ. We now proceed to derive an expression for the skin depth, as a function of the applied frequency ω, and the electrical conductivity of the plasma, σ.
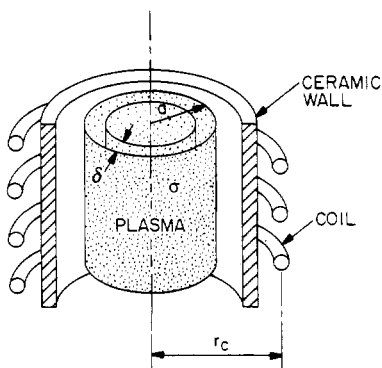
Figure 11.5 A schematic drawing of a cylindrical plasma with electrical conductivity σ, radius a, and skin depth δ, generated by inductive coupling from a coil of radius r_c.
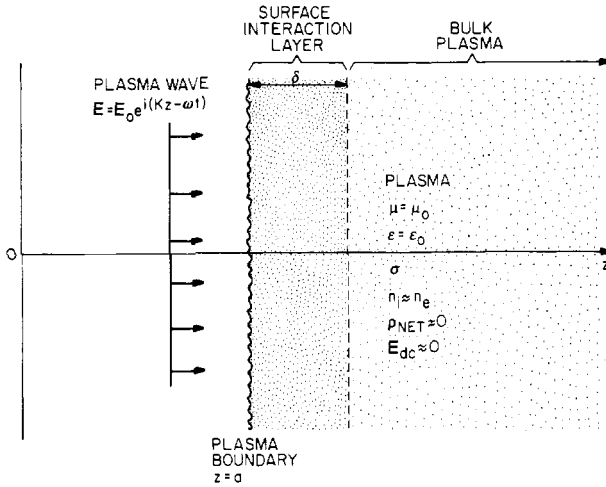
Figure 11.6 A simplified slab model of the plasma shown in figure 11.5. An electromagnetic wave approaching from the left interacts with the surface interaction layer of thickness δ. The plasma is quasi-neutral, has electrical conductivity σ, and no DC electric fields.

11.3.1 Assumed Initial Conditions

We analyze the situation in figure 11.5 by replacing the cylindrical geometry with the plasma slab shown in figure 11.6. This is intended to represent a small section of the cylindrical surface in figure 11.5. An electromagnetic plane wave is assumed to be incident from the left, onto the boundary at $z = a$. The plasma slab has a permittivity and a permeability equal to that of free space, an electrical conductivity σ, and the plasma is assumed to be quasi-neutral with no net charge density, and no DC electric fields. Maxwell's equations which describe this interaction are given by

$$\nabla \cdot E \approx 0 \tag{11.11}$$

$$\nabla \cdot B = 0 \tag{11.12}$$

$$\nabla \times E = -\frac{\partial B}{\partial t} \tag{11.13}$$

and

$$\nabla \times B = \mu_0 J + \mu_0 \varepsilon_0 \frac{\partial E}{\partial t}. \tag{11.14}$$

The current induced by the electromagnetic plane wave in the plasma can be described by Ohm's law,

$$J = \sigma E \quad (\text{A/m}^2) \tag{11.15}$$

where σ is the plasma conductivity. We now take the curl of both sides of equation (11.13), to obtain

$$\nabla \times (\nabla \times \boldsymbol{E}) = -\frac{\partial}{\partial t}(\nabla \times \boldsymbol{B}).$$

(11.16)

Using a vector identity, the left-hand side of equation (11.16) may be written

$$\nabla \times (\nabla \times \boldsymbol{E}) = \nabla(\nabla \cdot \boldsymbol{E}) - \nabla^2 \boldsymbol{E} \sim -\nabla^2 \boldsymbol{E}$$

(11.17)

where we have used equation (11.11), since the plasma is quasi-neutral and free of DC electric fields. Substituting equations (11.14), (11.15), and (11.17) into equation (11.16) yields

$$\nabla^2 \boldsymbol{E} = \mu_0 \sigma \frac{\partial \boldsymbol{E}}{\partial t} + \mu_0 \varepsilon_0 \frac{\partial^2 \boldsymbol{E}}{\partial t^2}.$$

(11.18)

In the one-dimensional geometry of figure 11.6, the Laplacian operator on the left may be rewritten to express equation (11.18) as

$$\frac{\partial^2 E}{\partial z^2} - \mu_0 \sigma \frac{\partial E}{\partial t} - \mu_0 \varepsilon_0 \frac{\partial^2 E}{\partial t^2} = 0.$$

(11.19)

11.3.2 Propagation Constant

The functional dependence of the electric field in the electromagnetic plane wave of figure 11.6 may be written

$$E = E_0 \exp[\mathrm{i}(Kz - \omega t)]$$

(11.20)

where the propagation constant K is given by

$$K \equiv \alpha + \mathrm{i}/\delta.$$

(11.21)

The real part of K represents the oscillation of the electromagnetic field; the imaginary part accounts for damping of the electromagnetic wave in the surface layer of thickness δ. The parameter δ is the *skin depth* of the medium. Substituting equation (11.20) into (11.19), one obtains a dispersion relation for the electromagnetic plane wave in the surface interaction layer,

$$\left(-K^2 + \mathrm{i}\omega\mu_0\sigma + \mu_0\varepsilon_0\omega^2\right) E = 0.$$

(11.22)

In this dispersion relation, the SI constants yield

$$\frac{1}{\varepsilon_0\mu_0} = c^2 \tag{11.23}$$

where c is the velocity of light. Substituting equation (11.21) and (11.23) into (11.22) yields the dispersion relation for the plane electromagnetic wave in the surface interaction layer,

$$K^2 = \left(\alpha + \frac{i}{\delta}\right)^2 = i\frac{\omega\sigma}{c^2\varepsilon_0} + \frac{\omega^2}{c^2}. \tag{11.24}$$

Separating the real and imaginary parts of equation (11.24), one obtains after much algebra, the real part of the propagation constant K,

$$\alpha = \sqrt{\frac{\sigma\mu_0\omega}{2}} \left[\frac{\omega\varepsilon_0}{\sigma} + \sqrt{1 + \left(\frac{\omega\varepsilon_0}{\sigma}\right)^2}\right]^{1/2} \tag{11.25}$$

and an expression for the skin depth δ,

$$\frac{1}{\delta} = \sqrt{\frac{\sigma\mu_0\omega}{2}} \left[\sqrt{1 + \left(\frac{\omega\varepsilon_0}{\sigma}\right)^2} - \frac{\omega\varepsilon_0}{\sigma}\right]^{1/2}. \tag{11.26}$$

11.3.3 Skin Depth

Equation (11.26) is the desired relationship between the skin depth, the electrical conductivity of the medium, and the frequency of the incident RF radiation. In most industrial plasmas, however, the following inequality holds:

$$\frac{\omega\varepsilon_0}{\sigma} = \frac{2\omega}{\nu_{*0}} \ll 1. \tag{11.27}$$

By appealing to equation (11.7) and (11.8), one can write the electrical conductivity appearing in (11.27) as

$$\sigma = \frac{e^2 n_e}{m_e \nu_c} = \frac{\varepsilon_0 \omega_{pe}^2}{\nu_c}. \tag{11.28}$$

Substituting the right-hand member of equation (11.28) into equation (11.27) then reveals that the inequality of (11.27) requires that in the medium,

$$\nu_c\omega \ll \omega_{pe}^2. \tag{11.29}$$

That is, the geometric mean of the collision frequency and the electromagnetic wave frequency in the plasma has to be much less than the electron plasma frequency, a condition that is satisfied in the individual interaction regime in industrial plasmas. Inspection of the very large values of the energy transfer frequency, ν_*, for industrial plasmas in table 11.1 confirms the small magnitude of the left-hand side of equation (11.27).

If equation (11.27) is satisfied in the plasma, then (11.25) for the propagation constant α becomes

$$\alpha \approx \sqrt{\frac{\sigma \mu_0 \omega}{2}} \qquad (\text{m}^{-1}) \qquad (11.30)$$

and the skin depth given by equation (11.26) is approximately equal to

$$\frac{1}{\delta} \approx \sqrt{\frac{\sigma \mu_0 \omega}{2}}. \qquad (11.31)$$

Inverting equation (11.31), the skin depth is

$$\delta = \sqrt{\frac{2}{\sigma \mu_0 \omega}} \qquad (\text{m}). \qquad (11.32)$$

If we substitute the right-hand member of equation (11.28) into (11.32), and express the electron plasma frequency in hertz, then equation (11.32) for the skin depth can be written

$$\delta = \frac{c}{2\pi \nu_{\text{pe}}} \sqrt{\frac{\nu_c}{\pi \nu}}. \qquad (11.33)$$

This equation states that the skin depth is equal to the free space wavelength at the electron plasma frequency, times the square root of the ratio of the collision frequency to the driving frequency, a factor that is often of order unity. Thus, to a first approximation, the skin depth is the distance that an electromagnetic wave propagates into a medium during one period of the electron plasma frequency.

In an inductive coupling geometry similar to that shown in figure 11.5, one can define an *energy coupling parameter*, η_c, which can vary from 0 to 1.0. This energy coupling parameter can be written as

$$\eta_c \equiv \frac{\text{discharge power}}{\text{reactive power}} = f\left(\frac{a}{r_c}, \kappa\right). \qquad (11.34)$$

The energy coupling parameter is a function of the ratio of the plasma radius to the coil radius, and the *coupling parameter*, κ, defined as

$$\kappa \equiv \sqrt{2}\,\frac{a}{\delta}. \tag{11.35}$$

In inductive coupling geometries like that of figure 11.5 (see Boulos *et al* 1994), the energy coupling parameter is a maximum when the value of κ is between approximately 2.0 and 4.0, or when the ratio of plasma radius to skin depth is in the range

$$1.5\delta \leqslant a \leqslant 3\delta. \tag{11.36}$$

Inequality (11.36) implies that electromagnetic radiation is most effectively coupled to a cylindrical plasma when the skin depth is between 1/3 and 2/3 of the plasma radius. It should be noted, however, that satisfying equation (11.36) does not necessarily mean that the plasma will be uniformly heated by the electromagnetic wave. The energy coupling parameter can be close to unity if the electromagnetic radiation is absorbed in a relatively thin surface layer, leaving the interior of the plasma more or less undisturbed. In such a case, efficient coupling can result in a very non-uniform, annular plasma.

The skin depth given by equation (11.32) may be written as

$$\delta = \sqrt{\frac{2m_e}{e^2\mu_0}}\sqrt{\frac{\nu_c}{n_e\omega}}. \tag{11.37}$$

In the SI system of units, the natural constants under the first square root yield

$$\delta = 7.516 \times 10^6 \sqrt{\frac{\nu_c}{n_e\omega}} \qquad \text{(m).} \tag{11.38}$$

Thus, the skin depth for the interaction of electromagnetic radiation with a plasma is proportional to the square root of the electron collision frequency, and inversely proportional to the square root of the electron number density and the driving frequency. In many plasmas of industrial interest, the ratio of the electron collision frequency to the driving frequency is approximately equal to unity. This ratio can be written in terms of the background neutral gas pressure and the driving frequency ν (in hertz),

$$\frac{\nu_c}{\omega} = \frac{n_0\langle\sigma v\rangle}{2\pi\nu} \propto \frac{p}{\nu}. \tag{11.39}$$
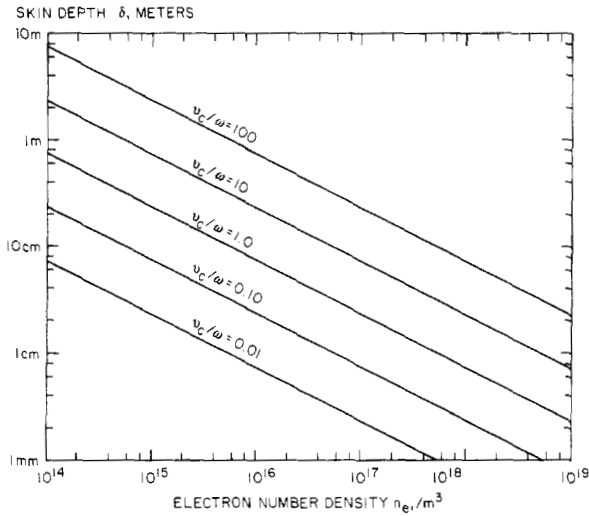
SKIN DEPTH δ, METERS

Figure 11.7 The skin depth δ, in meters, as a function of the electron number density, in electrons per cubic meter, for five values of the ratio of the electron collision frequency ν_c (in hertz), to the frequency ω (in radians per second) of the incident electromagnetic wave.

Equation (11.38) has been plotted in figure 11.7. This shows the skin depth in meters on the ordinate, as a function of the electron number density in electrons per cubic meter plotted on the abscissa. The parameter on the five characteristic lines is the ratio of the electron collision frequency, ν_c, to the driving frequency, ω. When this ratio is approximately equal to unity, this curve predicts that the skin depth of plasmas in the range from 10^{15} to 10^{17} electrons per cubic meter have skin depths from 30 cm to approximately 3 cm, a range which implies that skin depth considerations need to be carefully considered in the design of inductive industrial plasma reactors.

11.4 INDUCTIVE PLASMA TORCH

11.4.1 Torch Characteristics

One of the most widely used industrial plasma sources is the inductively coupled RF plasma torch, a standard configuration of which is illustrated in figure 11.8 (Gross *et al* 1969). The plasma can be started with a pulsed high voltage applied to a starting rod, and maintained by RF power applied to an axisymmetric coil wrapped around the plasma, which is part of an RF tank circuit. The coils and the RF power supplies are essentially identical to those used for the industrial induction heating
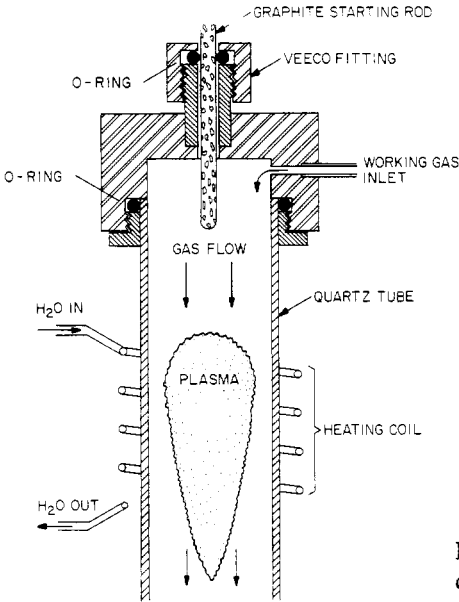
Figure 11.8 A kilowatt-level inductively coupled plasma torch.

of metals, an example of the synergism and conservatism of industrial technology. The heating coil shown schematically in figure 11.8 heats a volume of plasma the diameter of which is approximately half the plasma length. The heating coil is usually water-cooled, and is not in contact with the plasma, thus maintaining plasma purity. The similarity of industrial induction heating and RF plasma generation is suggested by the electrical conductivity data in table 11.1, which gives the electrical conductivity of various materials and gases of industrial interest. The electrical conductivity of argon and nitrogen plasmas is not too different from that of carbon and iron, the usual subject of industrial induction heating operations.

The competing industrial technology to inductively coupled plasma torches is the DC arc jet, indicated in figure 11.9, which also lists some of the characteristics which distinguish the two from each other as sources of plasma or high temperature gas. As compared to the DC arc jet, the inductive plasma torch is capable of treating a larger surface area, with lower gas velocities, which tend not to scour or erode the piece being heated nearly to the extent that an industrial arc jet will do so. In addition, the lack of contact between the plasma and the heating coil in the inductive plasma torch is in contrast with the DC arc jet, in which vaporized and sputtered electrode material usually finds its way into the gas stream to contaminate the hot gases in the arc jet. A further advantage of the inductive plasma torch is that the cross section of the exciting coil, and hence that of the plasma, need not be circular: inductive plasmas with

WORKING GAS   COOLING WATER IN   WORKING GAS   COOLING WATER OUT

H₂O

H₂O

PLASMA   COIL

COAXIAL GAS FLOW

CATHODE

ANODE

JET

INDUCTIVE PLASMA TORCH   ARC JET

10 – 200 m/sec	JET VELOCITY	500 – 150 m/sec
4 – 40 mm	JET DIAMETER	6 – 10 mm
VARIABLE	JET SHAPE	CYLINDRICAL
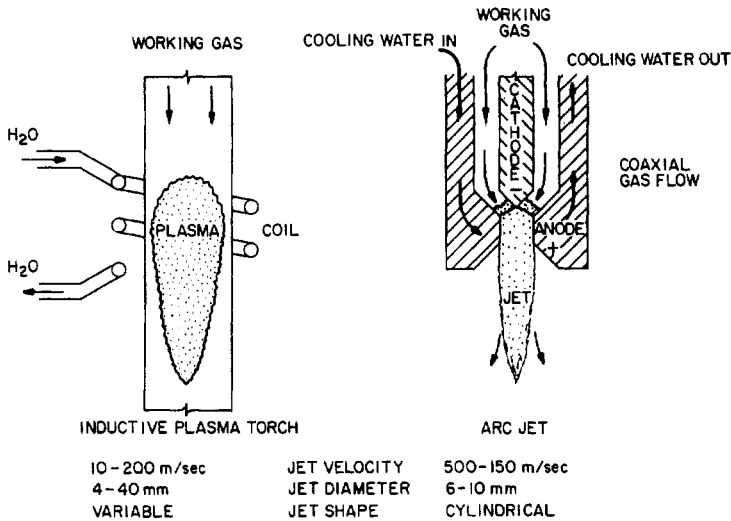
Figure 11.9 A comparison of the characteristics of the inductive plasma torch and the DC arc jet.

non-circular, and even relatively complicated shapes like triangles, have been produced for specific applications.

11.4.2 System Characteristics

A block diagram of a complete inductive RF plasma torch system is shown on figure 11.10. It is usually necessary to have a matching network between the RF power supply and the coil, since the plasma is in most applications a variable load. Subsystems are needed for gas flow control, for ignition of the plasma, and for cooling of the plasma formation volume under the coil. Vacuum pumps, gas handling equipment, and gas treatment facilities are generally needed to cool and detoxify the gases used before being exhausted to the atmosphere. Additional subsystems for the production of fine powders, or the manipulation of flame-sprayed targets, for example, must be added to the schematic on figure 11.10, depending on the specific application of the system.

A schematic drawing of a characteristic power supply used for inductive plasma torches is shown in figure 11.11. Such power supplies are available in unit sizes at least up to 200 kW. These power supplies are relatively inefficient. Approximately 10% of the input AC power is lost in AC to DC conversion; 40% of the input power is lost in the oscillator and tank circuit; and 10–30% of the input power is lost in the coil-plasma coupling process. In a typical application, only 20–40% of the input power is available as plasma enthalpy in the hot gas. Not shown
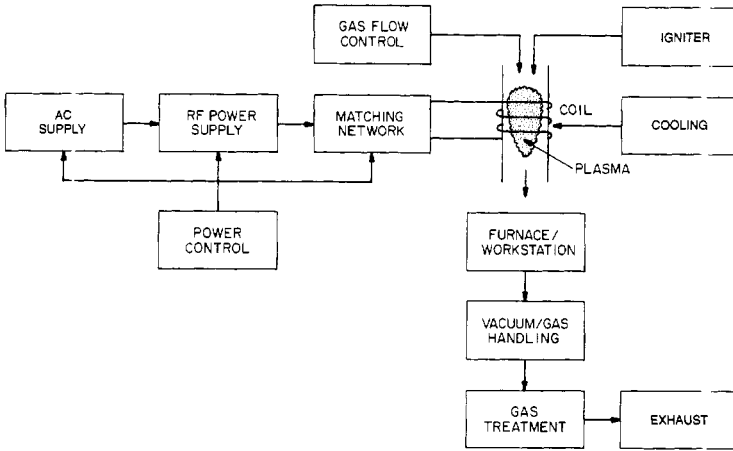
Figure 11.10 A block diagram of an inductively coupled plasma torch system.
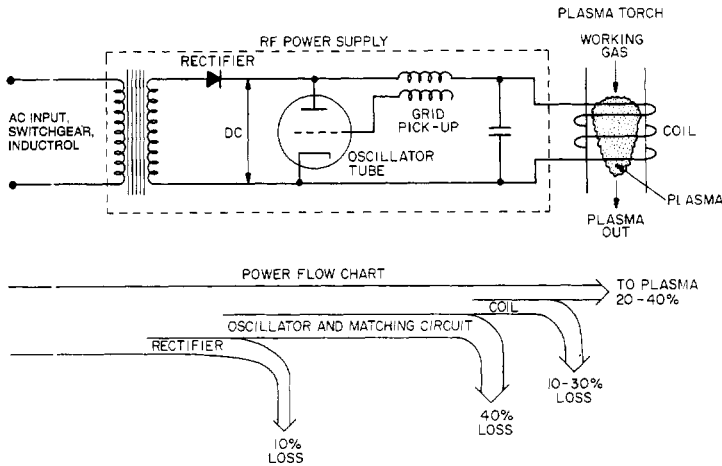
Figure 11.11 A schematic drawing of the RF power supply for an inductively coupled plasma torch, with a power flow chart.

in figure 11.11 is a matching circuit, required when the torch is operated under varying plasma conditions, resulting in a variable RF load.

Inductive RF plasma torches are hard starting, and high voltage initiation is usually required. This can be provided by either an axial electrode, an electrode wire along the axis, or an external Tesla coil brought up to the surface of a dielectric cylinder (usually quartz) separating the excitation coil from the plasma generating volume. These are indicated schematically in figure 11.12.
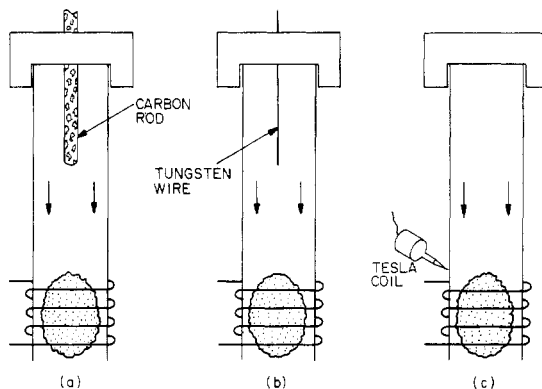
Figure 11.12 Three methods for initiating inductive plasmas. (a) high voltage applied to a carbon rod; (b) high voltage applied to a tungsten wire; and (c) RF high voltage applied by a Tesla coil.

Inductively heated plasmas are often operated in transparent quartz tubes, to avoid the additional heat load from visible radiation which, in these tubes, passes through the walls and is absorbed outside the plasma-generating volume. At relatively low power levels, below perhaps 5 kW, an uncooled wall may be used, and radiant cooling relied upon, as indicated in figure 11.13(a). At higher power levels, it is necessary to cool the walls surrounding the plasma volume. Usually, coaxial or counter-current water cooling is used as shown in figures 11.13(b) and (c), or sometimes coaxial gas flow along the inside surface of the quartz tube is used, as shown in figure 11.13(d).

11.4.3 Operating Regime

The operating regimes of inductive plasma torches are indicated on table 11.2. At VLF and LF frequencies, inductive plasma torches are often operated with a variable frequency; above approximately 500 kHz regulatory and technical requirements enforce a relatively narrow selection of assigned bands for the operation of industrial inductively coupled plasma torches, with 13.56 MHz being a widely used frequency of choice. Power supplies are available with power levels as low as 1 kW, up to 1 MW on an off-the-shelf basis. Many of them operate in the range from 10–30 kW. The overall efficiency of an inductive plasma torch is relatively low, and the efficiency shown in table 11.2 refers to the fraction of the input AC power which actually appears in the enthalpy of the hot gas formed by the inductive plasma. These inductively coupled plasma torches are capable of operating at pressures as low as 10 Torr and as high as 10 atm, but they most commonly operate at or slightly below 1 atm. The gas temperatures can be adjusted to relatively low
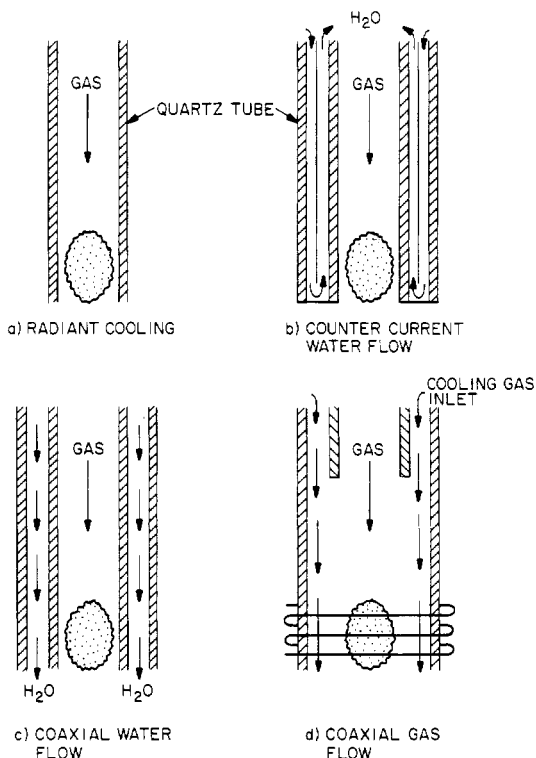
Figure 11.13 Selected cooling configurations for inductive plasma torches. (*a*) Radiant cooling of the plasma through an uncooled quartz tube; (*b*) counter-current water flow; (*c*) coaxial water flow; and (*d*) coaxial gas flow between the plasma and the wall.

Table 11.2 Operating regimes of inductively coupled plasma torches.

Parameter	Low	Characteristic	High
Frequency	10 kHz	13.56 MHz	100 MHz
Power	1 kW	30 kW	1MW
Efficiency	20%	35%	50%
Pressure	10 Torr	1 atm	10 atm
Gas temperature	1000 K	10^4 K	2×10^4 K

values in the exhaust plume, down to 1000 K or even lower by adjusting for a high gas flow rate, but temperatures of the order of 10 000 K and as high as 20 000 K are possible in this form of torch.

Industrial plasma torches produce plasmas that are generally assumed
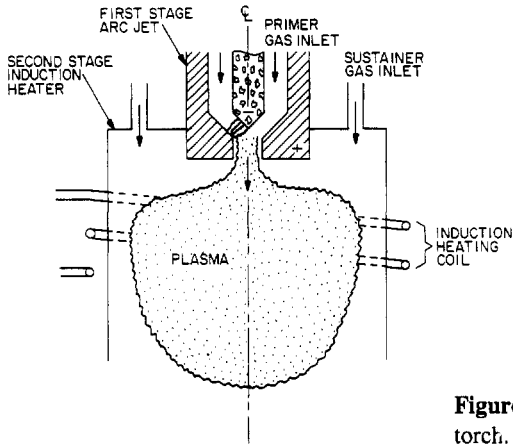
Figure 11.14 The DC–RF hybrid plasma torch.

to be in local thermodynamic equilibrium, allowing computer modeling studies of the plasma properties. These studies have not been adequately supported by detailed experimental measurements of plasma parameters with modern diagnostic methods, but what spectroscopic and other evidence is available, shows moderately good agreement between experiments and the results of computer modeling. It is generally assumed that the electron kinetic temperature and gas temperature in inductive plasma torches are approximately equal, as a consequence of local thermodynamic equilibrium. Inductive plasma torches are usually operated without a static magnetic field to assist confinement, since direct interaction of the plasma with the wall is seldom an issue.

11.4.4 Alternative Inductive Torch Configurations

When operated at high power levels, greater than 10 kW, and at pressures of approximately 1 atm and above, industrial inductive plasma torches are so difficult to start and to run stably that two-stage units are often used, with a smaller 'pilot' unit as the first stage. A schematic of a DC–RF hybrid unit is shown in figure 11.14, in which a DC arc jet is used to supply the plasma for a second stage, higher power inductive RF heating unit. A schematic drawing of a RF–RF hybrid unit is shown in figure 11.15, in which the pilot stage is a smaller inductively coupled RF power supply unit. These hybrid plasma torches characteristically operate at power levels of 50 to 100 kW or even more, where the dimensions of the second-stage, higher-power unit make it difficult to initiate and operate in a stable manner.

11.4.5 Applications of Inductive Plasma Torches

Some of the more important applications of inductively coupled RF
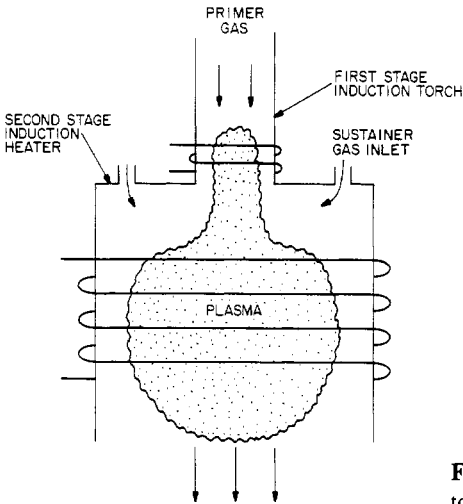
Figure 11.15 The RF–RF hybrid plasma torch.

plasma sources are listed in table 11.3. Many of these applications will be discussed in detail in appropriate chapters of Volume 2 of this work. This table illustrates once again how a particular plasma source can be used for a wide variety of industrial applications. A variety of off-the-shelf units at various power levels are available commercially for these applications.

11.5 OTHER METHODS OF GENERATING INDUCTIVE PLASMAS

All inductive plasma heating methods have in common the induction of high frequency RF currents in the plasma within approximately one skin depth of the plasma surface. These RF currents dissipate by ohmic heating and raise the plasma temperature. In addition to the inductive plasma torch discussed above, other methods of inductive plasma heating which have not yet found widespread industrial application, have been developed in connection with microelectronic plasma processing, and plasma physics and fusion research.

11.5.1 Inductive Parallel Plate Reactors

Within the microelectronics industry, requirements for larger wafer sizes, faster processing times, lower pressure operation, and greater plasma uniformity have stimulated development of new types of plasma reactor, including the *inductive parallel plate reactor* shown in figure 11.16. This reactor was applied to microelectronic plasma processing applications by J H Keller and his colleagues at IBM, Fishkill, NY (Keller 1992).

Table 11.3 Applications of inductive plasma torches.

High purity materials production:
- Silica and other refractories
- Ultrafine powder
- Spherical fine powder
- Refining/purification

High temperature thermal treatment:
- Heat treatment
- Plasma sintering

Surface Treatment:
- Oxidation
- Nitriding

Surface Coating:
- Plasma flame spraying
- Surface coating of powder

Chemical vapor deposition (CVD):
- At atmospheric pressure
- At reduced pressure

Chemical synthesis and processing

Experimental applications:
- Laboratory furnace
- High intensity light source
- Spectroscopic analysis
- Isotope separation
- Ion source
- High power density plasma source

The reactor in figure 11.16 is in most geometrical respects quite similar to a conventional DC or RF capacitive parallel plate reactor. However, in this reactor RF power is applied to a flat spiral inductive coil at the upper surface of the reactor. The coil is separated from the plasma by a quartz or other dielectric insulating plate. The RF currents in the spiral coil induce image currents in the upper surface of the plasma, in an interaction layer approximately equal to the skin depth in thickness. Other important features of this reactor include multipolar permanent magnets around the outer circumference of the plasma, to improve plasma uniformity and plasma confinement and to increase its density, and a DC wafer bias power supply to control the energy of ions impinging on the wafer.

This reactor is capable of operating in the steady state, and producing both uniform plasma and plasma processing results, over wafer diameters
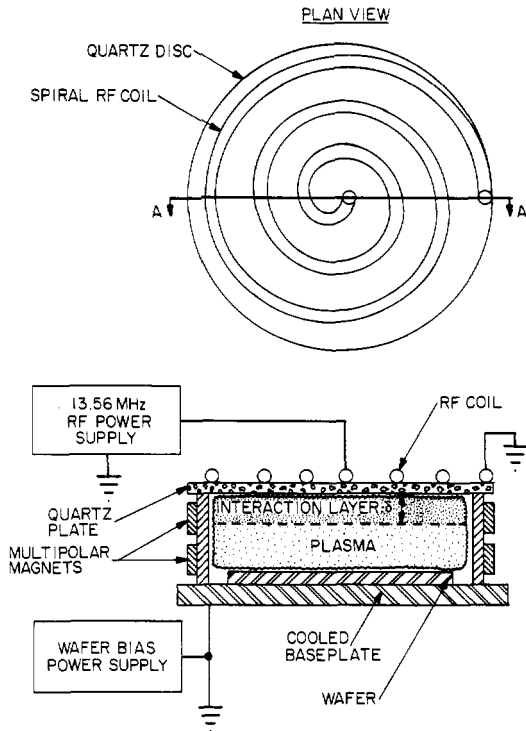
PLAN VIEW

Figure 11.16 Schematic of an inductive parallel plate reactor. Top: plan view showing flat spiral RF coil on top surface of the reactor. Bottom: elevation through section AA' showing cross-section of inductive parallel plate reactor.

of at least 20 cm. Unlike capacitive RF parallel plate reactors, which usually operate at levels of a few hundred watts, the inductive parallel plate reactor has been operated at power levels up to 2 kW. This higher power input has made possible higher than conventional plasma densities, up to 10^{18} electrons/m^3. This reactor has been operated at frequencies ranging from 1 MHz to 40 MHz, but its usual operating frequency is 13.56 MHz. Its operating neutral gas pressure is in the range from 1 to 20 mTorr, far lower than the several hundred mTorr characteristic of capacitive RF parallel plate reactors. These lower pressures are desirable in deposition and etching applications, since they imply longer mean free paths and little scattering of ions or active species before they hit the wafer.

Because of the higher plasma densities possible with this inductive plasma reactor, the flux of ions and other active species on the workpiece is also higher. For example, the IBM group (Keller 1992) has measured 60 mA/cm^2 at 1600 W of power input. This has made possible polymide
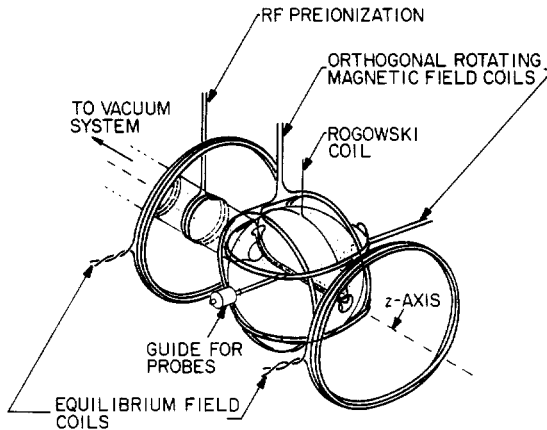
Figure 11.17 A schematic drawing of the coils used in a typical Rotamak plasma generating device, taken from Cottrell *et al* (1991).

etch rates of 1–2 μm per minute, a rate as much as five times that possible with a commerical electron cyclotron resonance (ECR) plasma reactor. The ion energies depend on the DC bias voltage of the wafer, but have ranged over 30 to 400 eV. The unformity of the plasma and of the etching effect compares favorably with other plasma reactors.

11.5.2 Rotamak

A fusion-related heating method which is probably ready for industrial application is the *Rotamak* configuration shown in figure 11.17 (Jones and Hugrass 1981, Hugrass and Grimm 1981, Hugrass *et al* 1981, Hugrass 1982, Hugrass and Jones 1983). The two stationary and orthogonal coils shown in figure 11.17 are energized by two RF sources operating at different phases at the same frequency, typically 1 MHz or higher. This phased excitation of the external coils produces a rotating magnetic induction, successive phases of which are shown in figure 11.18. This rapidly rotating magnetic field generates large plasma currents, thus heating the plasma to densities and temperatures of interest in many industrial applications. A potential advantage of the Rotamak over the inductive plasma torch could be a higher energy transfer efficiency into the plasma, and the ability to raise the plasma to higher electron kinetic temperatures than are possible with the inductive plasma torch.

11.5.3 Inductively Heated Toroidal Plasmas

Another form of inductive coupling is used in fusion research, but has not yet found application in industrial plasmas. This is the ohmic heating of
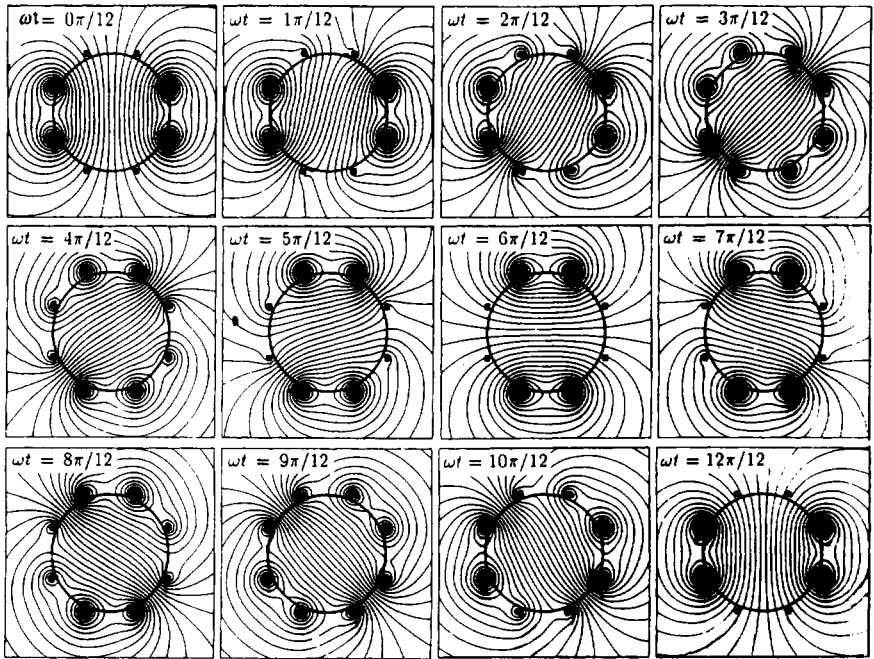
Figure 11.18 Rotating magnetic field lines generated in vacuum by the Rotamak coil assembly shown in figure 11.17. The solid circle indicates the position of the vacuum vessel wall. From Cottrell *et al* (1991).
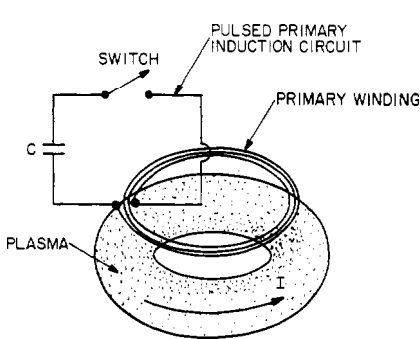
Figure 11.19 Toroidal plasma heating by ohmic losses from a current *I* induced by pulsed primary circuit.
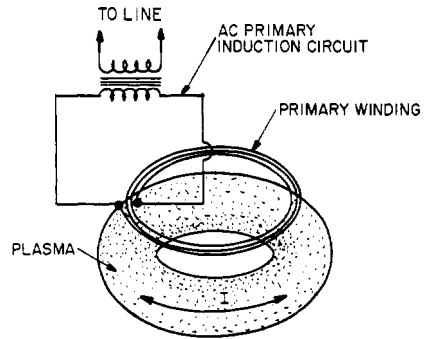
Figure 11.20 Toroidal plasma heated by ohmic losses from an AC current induced by transformer action at 60 Hz.

a toroidal plasma in which the plasma serves as a single-turn secondary of a transformer, as illustrated in the pulsed ohmic heating of a toroidal plasma, in figure 11.19. Large currents are induced in the plasma by transformer action from a ramped current in a pulsed primary induction

circuit. In fusion research, the time scales imposed by the prevailing high electrical conductivity of the plasma do not allow 50 or 60 Hz power to be coupled to the plasma. The potentially interesting generation and heating of a toroidal plasma using 50 or 60 Hz AC energizing a single-turn plasma secondary in a transformer-like arrangement, illustrated in figure 11.20, has not yet found industrial application. Either approach should make possible the generation of large volumes of energetic plasma for industrial purposes.

REFERENCES

Boulos M, Fauchais P and Pfender E 1994 *Thermal Plasma Processing* vol 1 (New York: Plenum Press)

Cottrell G, Jones I R, Lee S and Xu S 1991 An Inexpensive Rotamak Device *Rev. Sci. Instrum.* **62** 1787–1795

Gross B, Grycz B and Miklossy K 1969 *Plasma Technology* (New York: American Elsevier) LCCCN 68-27535

Hugrass W N 1982 Cylindrical Plasma Equilibria Maintained by Means of a Rotating Magnetic Field *J. Plasma Phys.* **28** 369–378

Hugrass W N and Grimm R C 1981 A Numerical Study of the Generation of an Azimuthal Current in a Plasma Cylinder Using a Transverse Rotating Magnetic Field *J. Plasma Phys.* **26** 455–464

Hugrass W N and Jones I R 1983 The Orbits of Electrons and Ions in a Rotating Magnetic Field *J. Plasma Phys.* **29** 155–171

Hugrass W N, Jones I R, and Phillips M G R 1981 An Experimental Investigation of Current Production by Means of Rotating Magnetic Fields *J. Plasma Phys.* **26** 465–480

Jones I R and Hugrass W N 1981 Steady-State Solutions for the Penetration of a Rotating Magnetic Field into a Plasma Column *J. Plasma Phys.* **26** 441–453

Keller J H 1992 Private communication

12

Capacitive RF Electrical Discharges
in Gases

The inductively coupled RF plasma sources discussed in the last chapter rely on large RF currents induced in the outer layers of the plasma, within approximately a skin depth of the surface. The ohmic dissipation of these currents maintains the plasma and heats both the plasma and the background gas. In this chapter, we discuss *capacitively coupled RF plasma sources*, in which the plasma is heated principally by RF electric fields, imposed by a system of (usually) parallel plates between which the plasma is maintained. Such capacitively coupled RF plasma can be at a steady state DC bias above ground if the plasma is in contact with a grounded electrode, or below ground if in electrical contact only with a negative biasing electrode. Such a DC bias voltage can result in real currents flowing to the electrodes, but these real currents play little or no role in the energy transfer process from the RF electric field to the plasma.

12.1 UNMAGNETIZED RF ELECTRICAL DISCHARGES

Most capacitive RF plasma reactors used in industry are unmagnetized, and are operated at frequencies from 1 to 100 MHz, below the electron plasma frequency, where the electrons respond individually to the electromagnetic field. Here, we apply the Lorentzian model to unmagnetized and magnetized plasmas in the individual particle regime, where $\omega < \omega_{pe}$.
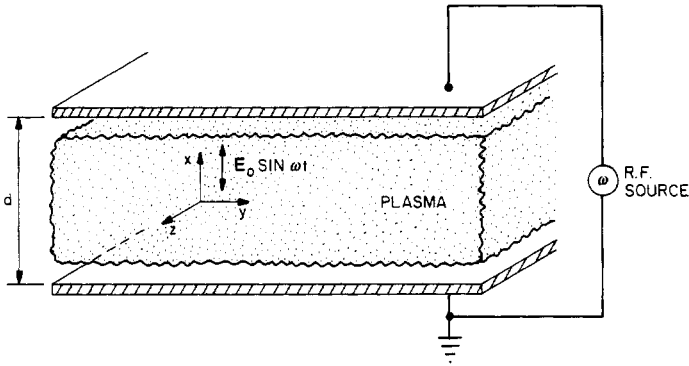
Figure 12.1 The generation of an RF plasma in an unmagnetized, parallel plate plasma reactor with plate separation d and driving frequency ω.

12.1.1 Characteristics of the Theoretical Model

We will now consider the addition of RF power to the *plane parallel plasma reactor* shown in figure 12.1. In this geometry, a plasma slab is generated between two plane parallel electrodes separated by the distance d. An RF voltage with a frequency ω is applied to the plane parallel plates, giving rise to a time-dependent electric field in the x direction given by

$$E = (E_0 \sin \omega t, 0, 0) \qquad (12.1a)$$

and the magnetic field is zero,

$$B = (0, 0, 0). \qquad (12.1b)$$

12.1.2 Coupling of Charges to an Electromagnetic Wave

The force on an individual electron of mass m and charge e is given by

$$F = ma = -mv_c v - eE. \qquad (12.2)$$

The first term on the right-hand side of the equation is the *Lorentz collisional term*, which assumes that the entire momentum of the electron in the direction of the electric field is lost on each collision with the neutral background gas to components at right angles to the electric field. This momentum loss occurs with a frequency v_c. The components of equation (12.2) in the coordinate system of figure 12.1 are

$$m\frac{d^2 x}{dt^2} + mv_c \frac{dx}{dt} = eE_0 \sin \omega t \qquad (12.3)$$

$$m\frac{dv_y}{dt} + mv_c v_y = 0 \qquad (12.4)$$

and

$$m\frac{dv_z}{dt} + mv_c v_z = 0. \tag{12.5}$$

The solutions to equations (12.4) and (12.5) are the relatively trivial ones

$$v_y(t) = v_{y0}\exp(-v_c t) \tag{12.6a}$$

and

$$v_z(t) = v_{z0}\exp(-v_c t). \tag{12.6b}$$

These equations state that any initial velocity the electrons have at time $t = 0$ in the y and z directions will decay with a characteristic time that is the time between collisions. In the x direction, however, where the applied electric field is driving the electron motion, the x position as a function of time is given by

$$x = C_1 \sin \omega t + C_2 \cos \omega t. \tag{12.7}$$

By substituting equation (12.7) into equation (12.3), the constants C_1 and C_2 are found to be

$$C_1 = -\frac{eE_0}{m}\frac{1}{(\omega^2 + v_c^2)} \tag{12.8a}$$

and

$$C_2 = -\frac{v_c eE_0}{\omega m}\frac{1}{(\omega^2 + v_c^2)}. \tag{12.8b}$$

Taking the time derivative of equation (12.7) gives the time-dependent velocity in the x direction,

$$v_x = \omega(C_1 \cos \omega t - C_2 \sin \omega t) \tag{12.9a}$$

or

$$\dot{x} = v_x = -\frac{eE_0\omega}{m(\omega^2 + v_c^2)}\left(\cos \omega t - \frac{v_c}{\omega}\sin \omega t\right). \tag{12.9b}$$

12.1.3 Power Absorbed by the Plasma

We can now calculate the work done on the electron by the electromagnetic field imposed between the plane parallel plates of figure 12.1. The differential work done on the electron is given by

$$dW = -F_e \cdot dx = eE_0 \sin \omega t\, dx. \tag{12.10}$$

Substituting the electrostatic force, eE, yields the right-hand member of equation (12.10). The power in watts delivered to the electron by the electromagnetic field is just

$$p = \frac{\mathrm{d}W}{\mathrm{d}t} = eE_0 \sin \omega t \frac{\mathrm{d}x}{\mathrm{d}t}. \qquad (12.11)$$

Substituting equation (12.9a) for the velocity in the x direction into equation (12.11) yields

$$p = eE_0\omega[C_1 \sin \omega t \cos \omega t - C_2 \sin^2 \omega t] \qquad (\text{W}). \qquad (12.12)$$

If we integrate equation (12.12) over a period of the oscillation, the first term averages to zero, leaving

$$\bar{p} = -\frac{eE_0\omega C_2}{T} \oint_0^T \sin^2 \omega t \, \mathrm{d}(\omega t) = -\frac{eE_0\omega C_2}{2}. \qquad (12.13)$$

Substituting equation (12.8b) into the right-hand member of equation (12.13) gives the total power absorbed by a single electron from the RF electric field,

$$\bar{p} = \frac{e^2 E_0^2}{2m} \frac{\nu_c}{(\omega^2 + \nu_c^2)} \qquad (\text{W/electron}). \qquad (12.14)$$

Since this plasma is in the individual particle regime, one can obtain the total power absorbed per unit volume by multiplying the power absorbed by a single electron in equation (12.14) by the electron number density,

$$\bar{P} = n_e\bar{p} = \frac{n_e e^2 E_0^2}{2m} \frac{\nu_c}{(\omega^2 + \nu_c^2)} \qquad (\text{W/m}^3). \qquad (12.15)$$

This is the total power in watts per cubic meter absorbed by the plasma between the plane parallel plates.

The electrostatic energy of the RF electric field may be written, using equation (12.1a) for the electric field,

$$U = \frac{1}{2}\varepsilon_0 E^2 = \frac{1}{2}\varepsilon_0 E_0^2 \sin^2 \omega t. \qquad (12.16)$$

Integrating the *electrostatic energy* of equation (12.16) over one period of oscillation yields

$$\bar{U} = \frac{1}{2}\varepsilon_0 E_0^2 \frac{1}{T} \oint_0^T \sin^2 \omega t \, \mathrm{d}(\omega t) = \frac{1}{4}\varepsilon_0 E_0^2. \qquad (\text{J/m}^3). \qquad (12.17)$$

The average power delivered by the RF electric field to the plasma given by equation (12.15) can be written, using equation (12.17),

$$\bar{P} = \frac{1}{4}\varepsilon_0 E_0^2 \frac{e^2 n_e}{m\varepsilon_0} \frac{2\nu_c}{(\omega^2 + \nu_c^2)} = \bar{U} \frac{2\omega_{pe}^2 \nu_c}{(\omega^2 + \nu_c^2)} = \bar{U}\nu_*. \qquad (12.18)$$

The energy transfer frequency, ν_*, appearing in equation (12.18), may be defined as

$$\nu_* \equiv \frac{2\omega_{pe}^2 \nu_c}{(\omega^2 + \nu_c^2)} \qquad \text{(Hz)}. \qquad (12.19)$$

The relationship of this energy transfer frequency to the RF electrical conductivity is based upon

$$\bar{P} = \frac{1}{2}\sigma E_0^2 = \sigma \bar{E}^2 \qquad (12.20)$$

where $\bar{E}$ is the rms electric field applied to the plasma. The RF electrical conductivity in equation (12.20) may be written in terms of the energy transfer frequency as

$$\sigma = \frac{\varepsilon_0 \nu_*}{2} = \frac{\varepsilon_0 \omega_{pe}^2 \nu_c}{(\omega^2 + \nu_c^2)}. \qquad \text{(S/m)} \qquad (12.21)$$

This allows the replacement of the electrical conductivity, which is usually identified with the DC flow of real currents, with a parameter which couples the electrostatic energy density (whether DC, AC, or RF) to the electron population of the plasma.

The above anaysis treats electron heating as though it were due solely to their immersion in an RF electric field. Additional mechanisms which can come into play include the production of energetic 'primary' or 'beam' electrons by the transient, RF cathode sheath; and repeated reflection of electrons off the oscillating sheath edge, in which electrons are more likely to gain energy by reflection from a sheath edge moving toward them than away from them. One indicator of the presence of such additional heating mechanisms is a non-Maxwellian electron energy distribution, especially a significant population of hot or monoenergetic electrons.

12.1.4 Constraints on RF Power Coupling

In many industrial applications, it is not possible to vary the applied frequency ω, either because RF power supplies are available only with fixed frequencies or because of the requirement to use certain assigned

frequencies for high power applications, imposed by national regulatory bodies such as the U.S. Federal Communications Commission (FCC). In many experiments, however, the electron collision frequency can be treated as an independent variable by adjusting the gas pressure,

$$\nu_c = n_0 \langle \sigma v \rangle_{es} = p f(T_e). \tag{12.22}$$

In most industrial applications, the electron collision frequency is almost directly proportional to the pressure, and is only a weak function of the electron kinetic temperature.

In order to dissipate the largest possible amount of RF power in the plasma (something which it may be inadvisable to do if this is associated with poor confinement or inefficient plasma generation), one can examine the energy transfer frequency of equation (12.19), and ask under what conditions it is a maximum. If the applied frequency is the variable, the energy transfer frequency is a monotone decreasing function of ω, so equation (12.19) suggests that the largest power dissipation in the plasma will occur with DC operation ($\omega = 0$). If, however, the electron collision frequency ν_c is varied by varying the neutral gas pressure, then the energy transfer frequency has a maximum when its derivative with respect to the electron collision frequency is zero,

$$\frac{d\nu_*}{d\nu_c} = \frac{2\omega_{pe}^2}{(\omega^2 + \nu_c^2)^2}(\omega^2 - \nu_c^2) = 0. \tag{12.23}$$

This maximum occurs when the applied frequency is equal to the electron collision frequency,

$$\omega = \nu_c. \tag{12.24}$$

This yields a maximum energy transfer frequency which is half that of the DC value.

The theory described above for the power dissipation in an unmagnetized RF electrical discharge applies in the individual interaction regime, when the applied frequency is well below the electron plasma frequency. The magnitude of the rms electric field appearing in equations (12.18) and (12.20) would be on the order of tens to hundreds of volts per centimeter for this type of parallel plate RF plasma reactor.

12.2 MAGNETIZED RF ELECTRICAL DISCHARGES

In this section we will consider the RF plasma generation geometry shown in figure 12.2. This is the same as that discussed in the previous section, except that there is now a static magnetic induction parallel to
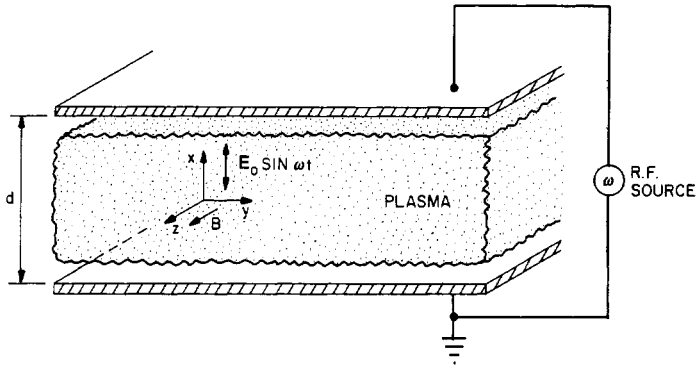
Figure 12.2 The generation of a RF plasma with a driving frequency ω in a parallel plate plasma reactor with plate separation d, and magnetic induction B oriented parallel to the plane of the reactor electrodes.

the z direction; that is, parallel to the planar faces of the generating electrodes. In our discussion of the plasma transport matrix in Chapter 4, the point was made that along the magnetic induction vector, the plasma properties are unchanged from those of an unmagnetized plasma, so there would be very little reason to orient the magnetic induction normal to the parallel plates of the plasma reactor shown in figure 12.2, other than perhaps a slight reduction of plasma losses at the boundary. By orienting the magnetic field parallel to the electrodes, one can reasonably expect to further reduce the ion and electron true current flowing to the electrodes, and increase the relative importance of the displacement currents in the plasma generation and heating process (Tanizuka 1989). It is desirable to do this in many applications, since true ion currents flowing to the electrodes may introduce additional undesirable impurities into the plasma through sputtering and erosion, beyond the sputtering normally associated with RF discharges.

12.2.1 Characteristics of the Theoretical Model

In the geometry of figure 12.2, we consider an electric field in the x direction with maximum amplitude E_0 and a frequency ω given by

$$E = (E_0 \sin \omega t, 0, 0) \qquad (12.25a)$$

and a magnetic induction oriented in the z direction

$$B = (0, 0, B). \qquad (12.25b)$$

We further assume a Lorentzian model for the interaction of the electric and magnetic field with the plasma, in which the plasma electrons lose

all of their momentum in the initial direction on colliding with the neutral background gas. This is expressed by the equation of motion,

$$F = ma = -m\nu_c v - e(v \times B) - eE \qquad (12.26)$$

where the electron mass is m and the electric and magnetic fields are given by equations (12.25a) and (12.25b), respectively.

12.2.2 Coupling of Charges to an Electromagnetic Wave

In the cartesian coordinate system of figure 12.2, the components of the forces acting on an electron are given by

$$m\frac{d^2x}{dt^2} + m\nu_c\frac{dx}{dt} + eB\frac{dy}{dt} = -eE_0 \sin \omega t \qquad (12.27a)$$

$$m\frac{d^2y}{dt^2} + m\nu_c\frac{dy}{dt} - eB\frac{dx}{dt} = 0 \qquad (12.27b)$$

$$m\frac{d^2z}{dt^2} + m\nu_c\frac{dz}{dt} = 0. \qquad (12.27c)$$

Equation (12.27c) can be integrated directly to yield the time-dependent velocity in the z direction,

$$v_z(t) = \frac{dz}{dt} = v_{z0} \exp(-\nu_c t) \qquad (12.28)$$

where v_{z0} is the initial velocity in the z direction. Equation (12.28) can be integrated once more to yield the time-dependent position of the electron in the Lorentzian model,

$$z(t) = z_0 - \frac{v_{z0}}{\nu_c} \exp(-\nu_c t) \qquad (12.29)$$

where z_0 is the initial position of the electron. It is clear that the time-dependent terms of equations (12.28) and (12.29) represent a starting transient which dies away after the RF driving voltage is turned on, so these terms will not be considered further.

By writing the gyrofrequency in the form

$$\omega_c = \frac{eB}{m} \qquad (12.30)$$

we can express equations (12.27a) and (12.27b) in the following way:

$$\frac{d^2x}{dt^2} + \nu_c\frac{dx}{dt} + \omega_c\frac{dy}{dt} = -\frac{eE_0}{m} \sin \omega t \qquad (12.31a)$$

$$\frac{d^2y}{dt^2} + \nu_c\frac{dy}{dt} - \omega_c\frac{dx}{dt} = 0. \qquad (12.31b)$$

We now assume a solution to equations (12.31) of the form

$$x = C_1 \sin \omega t + C_2 \cos \omega t \tag{12.32}$$

$$y = C_3 \sin \omega t + C_4 \cos \omega t \tag{12.33}$$

where the constants C_1 through C_4 are to be determined by the initial conditions. After substituting equations (12.32) and (12.33) into equations (12.31), and much algebra, one obtains the constants

$$C_1 = -\frac{eE_0}{m} \frac{(\omega^2 + v_c^2)[(\omega^2 - \omega_c^2) + v_c^2]}{\omega^2[(\omega^2 - \omega_c^2) + v_c^2]^2 + v_c^2[(\omega^2 + \omega_c^2) + v_c^2]^2} \tag{12.34a}$$

or, in reduced form,

$$C_1 = -\frac{eE_0}{2m\omega}\left[\frac{(\omega + \omega_c)}{(\omega + \omega_c)^2 + v_c^2} + \frac{(\omega - \omega_c)}{(\omega - \omega_c)^2 + v_c^2}\right]. \tag{12.34b}$$

Similarly,

$$C_2 = -\frac{v_c eE_0}{\omega m} \frac{(\omega^2 + v_c^2)[(\omega_c^2 + \omega^2) + v_c^2]}{\omega^2[(\omega^2 - \omega_c^2) + v_c^2]^2 + v_c^2[(\omega_c^2 + \omega^2) + v_c^2]^2} \tag{12.35a}$$

or, in reduced form,

$$C_2 = -\frac{v_c eE_0}{2\omega m}\left[\frac{1}{(\omega + \omega_c)^2 + v_c^2} + \frac{1}{(\omega - \omega_c)^2 + v_c^2}\right]. \tag{12.35b}$$

Also, one obtains

$$C_3 = +\frac{\omega_c(C_1 v_c + C_2\omega)}{(\omega^2 + v_c^2)} \tag{12.36}$$

$$C_4 = -\frac{\omega_c(C_1\omega - C_2 v_c)}{(\omega^2 + v_c^2)}. \tag{12.37}$$

These constants contain the maximum amplitude of the applied electric field E_0, the electron mass m, the driving frequency of the RF power supply ω, the effective electron collision frequency v_c, and the electron gyrofrequency given by equation (12.30).

12.2.3 Power Absorbed by the Plasma

The work done on an individual electron by the electromagnetic field is given by

$$dW = -\boldsymbol{F} \cdot d\boldsymbol{x} = eE_0 \sin \omega t \, dx. \tag{12.38}$$

The power delivered to the electron may be written in terms of equation (12.38) as

$$p = \frac{dW}{dt} = eE_0 \sin \omega t \frac{dx}{dt}$$
$$= eE_0\omega[C_1 \sin \omega t \cos \omega t - C_2 \sin^2 \omega t]. \qquad (12.39)$$

If we now integrate over a period of oscillation of the electromagnetic wave, the first term of equation (12.39) averages to zero, leaving

$$\bar{p} = -\frac{eE_0\omega C_2}{T} \oint_0^T \sin^2 \omega t \, d(\omega t) = -\frac{eE_0\omega C_2}{2}. \qquad (12.40)$$

Substituting equation (12.35b) for the constant C_2, we obtain the power absorbed from the electromagnetic field by a single electron,

$$\bar{p} = \frac{\nu_c e^2 E_0^2}{4m} \left[\frac{1}{(\omega + \omega_c)^2 + \nu_c^2} + \frac{1}{(\omega - \omega_c)^2 + \nu_c^2} \right]. \qquad (12.41)$$

The total average power per unit volume, in this single-particle interaction regime, may be written as

$$\bar{P} = n_e\bar{p} = \frac{1}{4}\varepsilon_0 E_0^2 \times \frac{n_e e^2}{\varepsilon_0 m}$$
$$\times \nu_c \left[\frac{1}{(\omega + \omega_c)^2 + \nu_c^2} + \frac{1}{(\omega - \omega_c)^2 + \nu_c^2} \right] \quad (\text{W/m}^3) \quad (12.42)$$

and is the average power absorbed by a single electron times the electron number density. The terms of equation (12.42) have been grouped in such a way that they include the average energy density of the RF electric field,

$$\bar{U} = \frac{1}{4}\varepsilon_0 E_0^2 \qquad (\text{J/m}^3) \qquad (12.17)$$

and the electron plasma frequency,

$$\omega_{pe}^2 = \frac{n_e e^2}{\varepsilon_0 m}. \qquad (12.43)$$

Substituting these into equation (12.17) yields

$$\bar{P} = \bar{U}\nu_* \qquad (\text{W/m}^3) \qquad (12.44)$$

where the energy transfer frequency for the magnetized plasma may be written as

$$\nu_* = \omega_{pe}^2 \nu_c \left[\frac{1}{(\omega + \omega_c)^2 + \nu_c^2} + \frac{1}{(\omega - \omega_c)^2 + \nu_c^2} \right] \quad \text{(Hz)}. \quad (12.45)$$

The energy transfer frequency in a DC, unmagnetized discharge is given by

$$\nu_{*0} = \frac{2\omega_{pe}^2}{\nu_c} \quad (\omega = \omega_c = 0). \quad (12.46)$$

This can be used to write the energy transfer frequency of equation (12.45) in the form

$$\nu_* = \nu_{*0} \frac{\nu_c^2}{2} \left[\frac{1}{(\omega + \omega_c)^2 + \nu_c^2} + \frac{1}{(\omega - \omega_c)^2 + \nu_c^2} \right]. \quad (12.47)$$

It is of some interest to examine the total power density absorbed by the plasma given by equation (12.42), and its indicator, the energy transfer frequency given by equation (12.45), as functions of the plasma operating regime. In the limit of low collisionality, $\nu_c \ll \omega_c$, equation (12.45) for the energy transfer frequency becomes

$$\nu_* \approx \nu_{*0} \nu_c^2 \left[\frac{(\omega^2 + \omega_c^2)}{(\omega^2 - \omega_c^2)^2} \right] \quad \nu_c \ll \omega_c. \quad (12.48)$$

If, in addition, the gyrofrequency is much greater than the driving frequency ω, equation (12.48) becomes

$$\nu_* \approx \nu_{*0} \frac{\nu_c^2}{\omega_c^2}. \quad (12.49)$$

The energy transfer frequency in this limit would therefore be far below that of a DC reactor with the same electrostatic energy density.

In the opposite limit of high collisionality, in which the collision frequency is far greater than the gyrofrequency, equation (12.45) for the energy transfer frequency becomes

$$\nu_* \approx \nu_{*0} \frac{\nu_c^2}{(\omega^2 + \nu_c^2)} \quad \nu_c \gg \omega_c. \quad (12.50)$$

If, in addition, the collision frequency is much greater than the driving frequency ω, the energy transfer frequency becomes

$$\nu_* \approx \nu_{*0} \quad \nu_c \gg \omega, \omega_c \quad (12.51)$$

which is just that of the unmagnetized DC electrical discharge discussed in Chapter 9.

If, as often happens in industrial applications, the electron gyrofrequency is much greater than either the collision frequency or the driving frequency of the RF power supply, equation (12.45) for the energy transfer frequency becomes

$$\nu_* \approx \nu_{*0} \frac{\nu_c^2}{\omega_c^2} \qquad \omega_c \gg \nu_c, \omega \qquad (12.52)$$

and the energy transfer frequency is again far below the value in a DC discharge.

At the point of gyroresonance, when the driving frequency equals the electron gyrofrequency, the power input to the plasma and the energy transfer frequency behave in a resonant manner, with improved coupling between the electromagnetic field and the plasma electrons. The energy transfer frequency at gyroresonance is given by

$$\nu_* = \nu_{*0} \frac{(2\omega_c^2 + \nu_c^2)}{(4\omega_c^2 + \nu_c^2)} \qquad \omega = \omega_c. \qquad (12.53)$$

If, in addition, the electron gyrofrequency is far greater than the effective collision frequency, as is often the case in ECR sources at low gas pressures, then equation (12.53) becomes

$$\nu_* = \frac{1}{2}\nu_{*0} \qquad \omega = \omega_c \gg \nu_c. \qquad (12.54)$$

This is just one half the power absorption and the energy transfer frequency which one would observe in an unmagnetized DC electrical discharge with the same average electric field strength applied to the plasma.

As in the previous discussion of power coupling to the unmagnetized RF plasma, other electron heating mechanisms can come into play than electron immersion in a RF electric field. These mechanisms are not too likely to be affected by a magnetic induction normal to parallel electrodes, but electron heating may be inhibited by transverse magnetic fields.

12.2.4 Measurement of Effective Collision Frequency

In Section 4.8 of Chapter 4 on the electron collision frequency ν_c, the point was made that the available tabulated data on this parameter are often suspect because the original measurements may have been made with gases contaminated by mercury or other impurities. In addition,

the gases used in a particular industrial application may themselves be contaminated or mixtures for which no tabulated data exist. If a plasma is turbulent, or contains any significant presence of fluctuating electric fields, the electron collision frequency ν_c no longer represents momentum loss due entirely to a binary collisional process with other particles, but instead becomes an *effective collision frequency*. This effective value of ν_c reflects the momentum transfer not only of binary collisions of the electrons, but also of the electron interactions with random, turbulent fluctuating electric fields in the plasma, which also change the electron momentum. For all these reasons, the electron collision frequency ν_c is a very difficult parameter to know accurately in a given experimental situation. This poses a serious problem for the proper understanding of electrical discharge physics, since ν_c plays an essential role in the transport properties of the plasma.

In many industrial situations, it may be easier and more accurate to actually measure the effective collison frequency of the electrons in a particular experimental situation, rather than try to determine the electron collision frequency from tabulated data. In a magnetized plasma in the individual particle regime ($\omega < \omega_{pe}$), such an experimental measurement of the electron collision frequency can be made by measuring the power absorbed as a function of frequency. The full width in frequency of the ECR absorption peak at half the maximum power absorbed by the plasma at electron gyroresonance, is directly related to the electron collision frequency.

Figure 12.3 shows a schematic drawing of the absorbed power as a function of the driving frequency applied between the two plates of a magnetized plasma reactor, such as that shown in figure 12.2. In the vicinity of electron gyroresonance there will be a strong absorption peak, as a result of the resonance in equation (12.42) when $\omega = \omega_c$. This resonant absorption peak is approximately symmetric about the electron gyrofrequency, and the full width of that peak at the half-power point, shown by $2\Delta\omega$ in figure 12.3, can be related to the electron collision frequency. The power transfered at this half-power point is given by

$$\bar{P}_c = \bar{U}\nu_*(\omega = \omega_c) = \bar{U}\nu_{*0}\frac{(2\omega_c^2 + \nu_c^2)}{(4\omega_c^2 + \nu_c^2)} \qquad \omega = \omega_c. \qquad (12.55)$$

This power input can be written in terms of equation (12.45) evaluated at the half-power frequency ω, given by

$$\bar{P}(\omega \pm \Delta\omega) = \frac{1}{2}P_c = \frac{\bar{U}\nu_{*0}}{2}\frac{(2\omega_c^2 + \nu_c^2)}{(4\omega_c^2 + \nu_c^2)}$$

$$= \bar{U}\nu_{*0}\frac{\nu_c^2}{2}\left[\frac{1}{(2\omega_c \pm \Delta\omega)^2 + \nu_c^2} + \frac{1}{(\Delta\omega)^2 + \nu_c^2}\right] \quad (12.56)$$
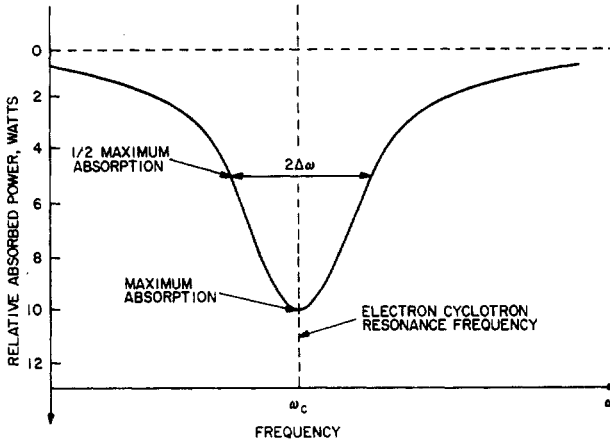
Figure 12.3 A schematic plot of the power absorbed in a magnetized RF plasma in the vicinity of the electron gyroresonance frequency, ω_c. The half width at half the maximum of this absorption curve is equal to the electron collision frequency in the plasma.

where the frequency ω at the half-power point is given by

$$\omega \equiv \omega_c \pm \Delta\omega \qquad (12.57)$$

and $\Delta\omega$ is the half-width of the resonant peak at the electron gyrofrequency, shown schematically in figure 12.3.

Little generality is lost by assuming that the half-power frequency spread $\Delta\omega$ is much less than the electron gyrofrequency ω_c. The half-width of the resonant absorption curve shown in figure 12.3 can then be written in dimensionless form,

$$\delta \equiv \frac{\Delta\omega}{\omega_c} \ll 1. \qquad (12.58)$$

We further assume that the effective collision frequency is far smaller than the electron gyrofrequency, $\nu_c \ll \omega_c$, an assumption which may not be satisfied in some cases of industrial interest, particularly at high neutral gas pressures. With this assumption, however,

$$\varepsilon \equiv \frac{\nu_c}{\omega_c} \ll 1. \qquad (12.59)$$

One can set equation (12.55) equal to equation (12.56), insert equations (12.57) to (12.59) into equation (12.56), and drop small higher-order terms, to show that

$$\frac{(2 + \varepsilon^2)}{(4 + \varepsilon^2)} = \varepsilon^2 \left(\frac{1}{(2 \pm \delta)^2} + \frac{1}{\delta^2 + \varepsilon^2} \right). \qquad (12.60)$$

Neglecting terms of second through fourth order compared to terms of first order or unity, equation (12.60) has the solution

$$\delta \approx \varepsilon \quad \Rightarrow \quad \Delta\omega = \nu_c. \tag{12.61}$$

Thus, in the single particle interaction limit, the half-width of the resonant absorption curve is equal to the effective electron collision frequency, ν_c. This provides a convenient way of measuring the effective electron collision frequency in a magnetized plasma, since the necessary absorption measurements can be made with a network analyzer, and make no assumptions about the electron temperature, the dominance of binary or turbulent collisions, or any of the other assumptions normally required to relate the plasma of interest to the published literature on binary collisions of electrons. A knowledge of the neutral gas pressure is not required to make this measurement. As long as the assumptions made in the above analysis are approximately true, particularly equations (12.58) and (12.59), this procedure allows a direct measurement of the effective collision frequency of the electrons in the actual plasma. This effective electron collision frequency should allow one to calculate, in a direct way, all the transport coefficients of the plasma. For experimental examples, see Roth and Spence (1987) and Spence (1990).

12.2.5 Maximization of RF Power Coupling

As with the unmagnetized plasma in the previous section, it is of interest to examine the conditions under which the power input to the plasma is maximized. This will occur when the energy transfer frequency is a maximum. Equation (12.45) states that the energy transfer frequency is a function of the driving frequency, the effective electron collision frequency, and the electron gyrofrequency. We will now examine the conditions for which the power absorbed is maximized as these variables are independently varied.

Case A: Variable magnetic induction, $B(\omega_c)$. One can obtain the optimum gyrofrequency for RF power coupling to the plasma by examining the maximum of the energy transfer frequency as a function of ω_c. Taking the indicated derivative of equation (12.45), one can show after much algebra that the power input to the plasma is a maximum when

$$\frac{\mathrm{d}\nu_*}{\mathrm{d}\omega_c} = 0 = C_a \nu_c \omega_c [\omega_c^4 + 2(\omega^2 + \nu_c^2)\omega_c^2$$
$$- (3\omega^2 - \nu_c^2)(\omega^2 + \nu_c^2)] \tag{12.62}$$

where C_a is a constant. One solution is a zero gyrofrequency unmagnetized plasma. The more interesting situation in a magnetized

plasma occurs when the gyrofrequency in the square brackets is given by

$$\omega_c^2 = -(\omega^2 + v_c^2) \pm \sqrt{(\omega^2 + v_c^2)^2 + (\omega^2 + v_c^2)(3\omega^2 - v_c^2)}. \quad (12.63)$$

This has real solutions only if

$$\omega \geqslant \frac{v_c}{\sqrt{3}} \quad (12.64)$$

which is a significant constraint on the operating frequency. By factoring out the RF driving frequency from equation (12.63), one obtains

$$\omega_c^2 = \omega^2 \left(1 + \frac{v_c^2}{\omega^2}\right) \left[-1 + \frac{2}{\sqrt{1 + (v_c^2/\omega^2)}}\right]. \quad (12.65)$$

If the ratio of the electron collision frequency to to the driving frequency appearing in equation (12.65) is small, expanding the square root appearing in equation (12.65) under this assumption, one obtains an optimum gyrofrequency given by

$$\omega_{c,\mathrm{opt}} \approx \omega \left(1 - \frac{v_c^4}{\omega^4}\right)^{1/2} \approx \omega. \quad (12.66)$$

Thus, the energy transfer frequency is a maximum when the driving frequency is approximately equal to the electron gyrofrequency, modified by a small factor.

Case B: Variable RF driving frequency, ω. If one wishes to maximize the power coupling to the plasma by varying the driving frequency ω, one must take the variation of equation (12.45),

$$\frac{d v_*}{d\omega} = 0 = C_b v_c \omega [\omega^4 + 2\omega^2(\omega_c^2 + v_c^2) \\ - (\omega_c^2 + v_c^2)(3\omega_c^2 - v_c^2)] \quad (12.67)$$

where C_b is a constant. One solution is the DC discharge, $\omega = 0$. The square bracket in equation (12.67) has real solutions only if

$$\omega_c \gg \frac{v_c}{\sqrt{3}}. \quad (12.68)$$

The square bracket in equation (12.67) is zero when

$$\omega_{\mathrm{opt}}^2 = \omega_c^2 \left(1 + \frac{v_c^2}{\omega_c^2}\right) \left[\frac{2}{\sqrt{1 + (v_c^2/\omega_c^2)}} - 1\right]. \quad (12.69)$$

In the limit for which the effective electron collision frequency is much less than the electron gyrofrequency, equation (12.69) becomes

$$\omega_{\text{opt}} \approx \omega_c \left(1 - \frac{\nu_c^4}{\omega_c^4}\right)^{1/2} \approx \omega_c. \tag{12.70}$$

This shows that if one is free to vary the driving frequency ω, the maximum power input to a magnetized plasma occurs in the vicinity of the electron gyrofrequency. This regime is the basis of the resonant *'helicon' glow discharges*, maintained by feeding RF in at the gyrofrequency to a small helical coil.

Case C: Gas pressure or ν_c variable. Finally, one may have a situation in which the parameter easiest to vary is the background neutral gas pressure, and hence the binary electron collision frequency ν_c. In this case, the optimum power coupling to the plasma occurs when

$$\frac{\mathrm{d}\nu_*}{\mathrm{d}\nu_c} = 0 = C_c 2(\omega^2 + \omega_c^2 + \nu_c^2)[(\omega^2 - \omega_c^2)^2 - \nu_c^4]. \tag{12.71}$$

where C_c is a constant. The optimum collision frequency occurs when the square bracket is zero,

$$\nu_{c,\text{opt}}^2 = (\omega^2 - \omega_c^2). \tag{12.72}$$

In considering the various optimum power coupling conditions derived above, one should keep in mind that the maximum power input to the plasma may not necessarily be the most efficient way to generate the plasma. A maximum power input may mean that the operating condition is very wasteful of power or unusually inefficient. On the other hand, a low energy transfer frequency and low power coupling may indicate a small or negligible interaction of the RF field with the plasma, and hence an uninteresting operating condition. This latter condition is more likely to be prevalent in industrial situations. The constraints discussed above also must satisfy the conditions discussed at the beginning of this section: one must be in the individual particle interaction regime, with the driving frequency, ω, well below the electron plasma frequency; one must be in the regime where the skin depth is large enough to allow significant interaction of the RF electric field with the plasma; and the value of the required maximum RF electric field E_0 must be reasonable. A benefit of using RF plasma generation versus a DC planar plasma reactor geometry is that with RF power, one is able to create and heat the plasma with displacement rather than real currents.

12.2.6 Ion Cyclotron Resonance Heating (ICRH) of Industrial Plasmas

In the field of fusion research, *ion cyclotron resonance heating* (ICRH) has been used successfully to couple tens of megawatts of RF power to the ion population of major experiments, raising their kinetic temperature to levels exceeding 10 keV. It therefore appears appropriate to investigate the utility of (ICRH) for heating industrial plasmas, particularly in contexts where energetic ions or the production of heavy active species is desired. Ion cyclotron resonance heating occurs at the gyrofrequency of an ion of mass M in a magnetic induction B,

$$\omega_{ci} = \frac{eB}{M} \qquad \text{(rad/s)}. \qquad (12.73)$$

For singly-charged argon ions in a magnetic induction of $B = 0.1\,\text{T}$ in a characteristic industrial application, the ion gyrofrequency is only 38 kHz.

In order for ICRH to be possible, the ions must be magnetized, and they must be in the collisionless limit. The requirement that they be magnetized is equivalent to the requirement that the gyroradius be much smaller than the plasma thickness, d,

$$\varepsilon \equiv \frac{R_g}{d} = \frac{M}{eBd} \sqrt{\frac{8eT_i'}{\pi M}} < 1.0. \qquad (12.74)$$

Singly-charged argon ions with kinetic temperatures below 100 eV, are magnetized in magnetic inductions more than 100 mT. A second requirement for ICRH is that ions be in the collisionless limit, in the sense of performing several complete gyrations between collisions. This requirement is met when

$$\theta = \frac{\omega_c}{\nu_c} = \omega_c \tau \gg 1 \qquad (12.75)$$

and τ is the time between collisions. In industrial plasmas, it is very difficult to get the neutral gas pressure low enough, while maintaining a plasma with interesting number densities, for the condition of equation (12.75) to be met.

In addition to the difficulty of achieving collisionless conditions in industrial plasmas, the coupling between the RF electric field and the plasma is weak. This may be seen by writing equation (12.47) in the form

$$\nu_* = \frac{\nu_{*0}}{2} \left[\frac{1}{(\omega/\nu_c + \omega_c/\nu_c)^2 + 1} + \frac{1}{(\omega/\nu_c - \omega_c/\nu_c)^2 + 1} \right]. \qquad (12.76)$$

The term ω/ν_c which appears first in each denominator also appears in the expression for skin depth, and should be large if the RF electric field is to penetrate the plasma. The second term in each denominator is the collisionality. When $\omega/\nu_c \gg 1$ and is dominant, equation (12.76) yields an approximate equality

$$\nu_* \approx \nu_{*0} \left(\frac{\nu_c}{\omega_c} \right)^2 . \qquad (12.77)$$

Thus, the requirement of collisionless conditions ($\omega_c/\nu_c \gg 1$) leads to poor coupling, such that the energy transfer frequency $\nu_* \ll \nu_{*0}$, the latter being characteristic of a DC discharge. Because of the large mass difference between ions and electrons, it is far easier to magnetize the electron population, and hence the successful development of ECR plasma sources for industrial applications.

12.3 THEORY OF RF PLASMA SHEATHS

The entire subject of RF *plasma sheaths* is poorly understood, less well-understood than the DC plasma sheaths discussed in Chapter 9, and is an area under active research at the present time. The approach to understanding RF plasma sheaths which has recently received the most attention is *particle-in-cell computer modeling*. The results of these investigations are not yet in good agreement with experimental observations, perhaps because of the limited ability of the models to span all time scales relevant to a steady-state RF plasma discharge.

12.3.1 Capacitive RF Discharge Model

Consider the parallel plate plasma reactor shown in figure 12.4. In this case, a symmetric, center-tap grounded RF power supply energizes a parallel plate plasma reactor. Shown below is the potential as a function of position and time, with the solid curve presenting the potential distribution at phase angle zero, and the dotted line showing the phase angle π radians out of phase. Because of the symmetric RF connection, the plasma and the sheaths will be symmetric about the midplane of the reactor. The computer modeling studies available at this time indicate that a quasi-neutral plasma with relatively small electric fields and energy dissipation rates will exist in the center of the parallel plate reactor, with oscillating potentials and electric fields to be found in the two sheaths on either side of the plasma.

The power density and electron number density expected in such a parallel plate reactor are indicated schematically in figure 12.5. Because
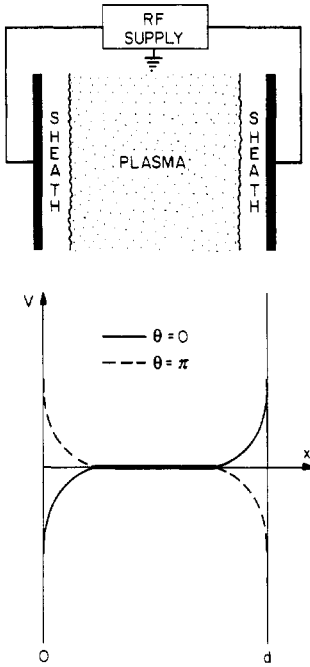
Figure 12.4 Sheaths and potential distribution in a symmetrically driven RF glow discharge at two RF phase angles 180° out of phase.
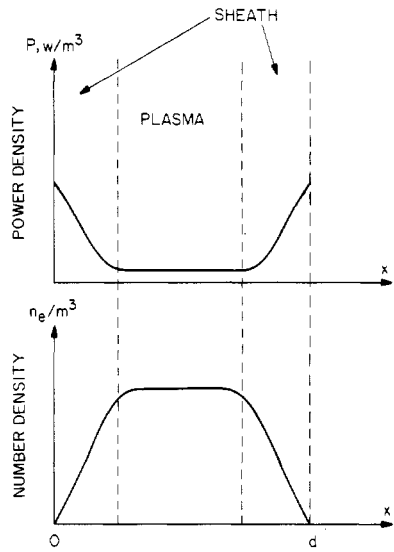
Figure 12.5 Schematic of the power and number density distribution across the symmetrically driven RF discharge of figure 12.4.

the electric fields are so much stronger in the sheaths, it is in that region that the bulk of the RF power is transmitted to the plasma electrons. The electrons, however, oscillate back and forth in the x direction and will carry the velocity which they acquired in the sheath into the interior of the plasma, where it will be dissipated. The electron number densities usually are highest in the center. If the skin depth and the electron neutral mean free paths are not too small, the electron number densities will remain relatively low in the sheaths.

The computer modeling of parallel plate reactor plasmas is a formidable problem for particle-in-cell computer methods, because of the enormous range of time scales which must be spanned in order to properly represent all of the important physical processes which occur in the plasma. In order to follow the gyrorotary motion of the electrons in a magnetic field, or the oscillatory motion of the electrons associated with the electron plasma frequency, it is necessary to follow the electron motion on a scale of picoseconds. As one proceeds to longer time scales, one must include the effects of electron–neutral collisions, the ion and electron particle containment times, the ionization period or the e-folding

time required to build up the plasma density during the breakdown process, the ion gyration frequency, the approach to quasi-neutrality, and finally the equilibration of plasma–wall interaction effects. It is a common observation in the laboratory that after turning on a DC or RF plasma discharge, it often takes many minutes for the plasma and surrounding walls to equilibrate and reach a steady state. At the present time, computer simulations can account for phenomena on the time scale of the electron–neutral collision frequency, but the validity of results on longer time scales is not well established.

From equation (12.42), the rms power dissipated in the plasma may be written using the following three terms:

$$\bar{P} = \frac{1}{4}\varepsilon_0 E_0^2 \times \frac{n_e e^2}{\varepsilon_0 m} \times \nu_c \left[\frac{1}{(\omega + \omega_c)^2 + \nu_c^2} + \frac{1}{(\omega - \omega_c)^2 + \nu_c^2} \right] \quad (\text{W/m}^3).$$
(12.42)

This is the power in watts per cubic meter which the RF electric field is able to couple to the plasma. The last term separated by a multiplication sign in this equation can be characterized as a 'global' term, and contains factors which are approximately time and space independent within the plasma. One variable is the driving frequency of the RF used; the second variable is the electron gyrofrequency, or magnetic induction applied to the discharge, and the third parameter is the electron–neutral collision frequency, values of which are shown for various gases in tables 4.2 and 4.3. This frequency is linearly proportional to the pressure of the background gas. All three of these parameters, driving frequency, gas pressure, and magnetic induction, affect the entire plasma equally, and are independent variables which one can, in principle, adjust from outside the plasma.

The second term separated by multiplication signs on the right-hand side of equation (12.42) is proportional to the electron number density and represents a time- and space-varying term which is smaller in the sheaths than it is in the bulk of the plasma, where the electron number density is higher. One may control the electron number density by adjusting the total power input to the plasma, but the investigator does not have the power deposition represented by this term under complete control, since the plasma will attain a self-consistent solution for the axial number density variation between the plasma proper and the sheath, which will affect this term.

Finally, the first term on the right-hand side of equation (12.42) separated by the multiplication sign represents a time- and space-varying contribution which is almost completely beyond the control of the investigator. This term is also very significant, because the electric field is generally far stronger in the sheaths than it is in the bulk of the quasi-neutral plasma. In general, the plasma will self-consistently adjust the
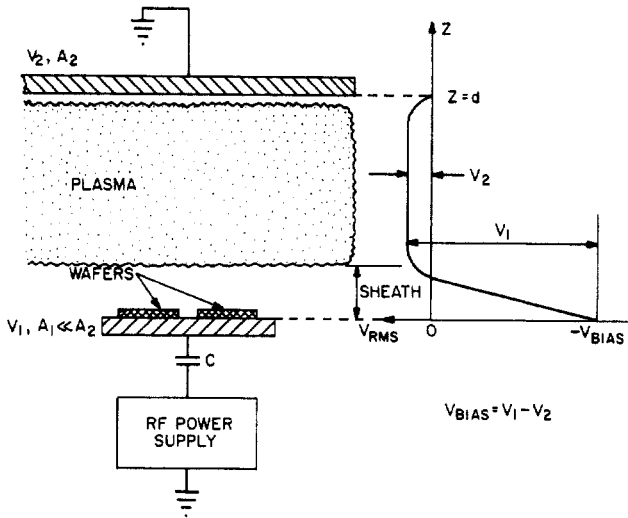
Figure 12.6 A plane parallel RF plasma reactor with electrodes of unequal surface area, and unequal electrode voltage drops.

electric fields in the plasma and in the sheaths, leaving the bulk of the power dissipation to occur in the sheaths. The penetration of the electric fields into the plasma will be controlled by skin depth considerations, and the importance of this term is then an additional reason why the skin depth should not be smaller than the distance between the plates of a parallel plate plasma reactor.

12.3.2 Empirical Scaling of Electrode Voltage Drop

The energy of ions reaching the electrode surfaces is a very important parameter in plasma etching of microelectronic circuits and in some other plasma processing applications. The scaling of the electrode voltage drop which controls this ion energy is therefore an important issue. A characteristic parallel plate RF plasma reactor is shown in figure 12.6. The relationship between the electrode voltage drops V_1 and V_2 and the surface area of the electrodes A_1 and A_2 is given by the empirically derived scaling law

$$\frac{V_1}{V_2} = \left(\frac{A_2}{A_1}\right)^q. \tag{12.78}$$

In *reactive ion etching* (RIE), the parameters V_1 and A_1 refer to the powered electrodes, on which the wafers are located, and V_2 and A_2 refer to the grounded electrodes. Empirical data suggest that the exponent q varies over the range

$$1.0 \leqslant q \leqslant 2.5. \tag{12.79}$$

12.3.3 Theories of Cathode Voltage Drop

Determining the exponent q from first principles is an unresolved theoretical problem in the physics of capacitive RF plasma reactors. The model which gives the best agreement with the empirically determined range of equation (12.79) is that equal real rms ion currents intercept both electrodes. This assumption is clearly true for a symmetric situation with both electrodes powered, but it is less obvious why this should be true of an asymmetric geometry. Assume also that the walls are sufficiently negative with respect to the plasma that the ion current is given by the ion saturation current due to random bombardment.

Adopting this model, consider the electrode voltage drops shown schematically in figure 12.6. The real ion current flowing to electrode number 1 is given by

$$I_1 = A_1 J_1 = A_1 e n_{i1} \bar{v}_{i1} \qquad (12.80)$$

and the real ion current on electrode number 2 is given by

$$I_2 = A_2 J_2 = A_2 e n_{i2} \bar{v}_{i2}. \qquad (12.81)$$

The velocity of an ion after being accelerated through an electrode voltage drop V is given by

$$\bar{v}_i = \sqrt{\frac{2eV}{m_i}}. \qquad (12.82)$$

If the same kind of ions flow to both electrodes, $m_{i1} = m_{i2}$, and if the electron number density is the same at the edge of each sheath (a reasonable assumption if the bulk of the plasma is spatially uniform, a requirement for most plasma processing applications) then, at the edge of the two electrode sheaths, $n_{i1} = n_{i2}$.

If the ion currents given by equations (12.80) and (12.81) are equal, then

$$I_1 = I_2 \qquad (12.83)$$

One can substitute equations (12.80) and (12.81) into equation (12.83) to obtain

$$e A_1 n_{i1} \sqrt{\frac{2eV_1}{m_i}} = e A_2 n_{i2} \sqrt{\frac{2eV_2}{m_i}} \qquad (12.84)$$

which gives the scaling

$$\frac{V_1}{V_2} = \left(\frac{A_2}{A_1}\right)^2 \qquad (12.85)$$

or $q = 2.0$, consistent with the empirical scaling law given by equation (12.79).

Other theories of this electrode voltage drop scaling based on various approximate sheath models do not do as well. One model based on the Child law sheath gives $q = 4.0$, in gross disagreement with observations; another theory based on a constant mean free path model in the sheath gives a value of $q = 2.5$, barely consistent with the extreme limits of the empirical observations. More needs to be done on understanding this important scaling relationship, and on the RF sheath dynamics that can lead to equal real currents flowing to the two parallel plate reactor electrodes of unequal surface areas.

12.4 CAPACITIVELY COUPLED RF PLASMA SOURCES

Capacitively coupled RF plasma sources are well represented among the plasma sources used worldwide in the microelectronic industry, and thus are important to a large industrial market. In microelectronic applications, one wishes to deposit layers (by plasma-assisted chemical vapor deposition or sputtering) or etch patterns on *wafers* which contain many individual microelectronic *chips* (individual integrated circuits).

12.4.1 Electrode Configurations

Uniformity and reproducibility of both the plasma and the etching and deposition processes are key requirements in microelectronic applications. One of the more widely used electrode configurations is illustrated in figure 12.7, the *barrel reactor*, which, in the example illustrated, consists of hemi-cylindrical electrodes outside a glass bell jar. In the barrel reactor, wafers are usually stacked like dishes on a rack along the plasma axis. The wafers float electrically and have low ion bombardment energies.

A related configuration is the *hexagonal reactor* shown in figure 12.8. Here the hexagonal central column has a large number of wafers mounted on each face, and this column forms the powered electrode for most applications. The wafers develop a DC bias which leads to a relatively anisotropic, vertical etch. The space between the hexagonal column and the grounded tank is filled with plasma which must be as uniform as possible. The working gases are usually injected from the top through a shower head-like arrangement, and pumped out the bottom.

Probably the most widely used configuration in the microelectronic industry is the *plane parallel reactor*, shown in figure 12.9. The wafers are usually on the powered electrode of area A_1, and the grounded electrode usually has an area $A_2 > A_1$. The area A_2 is that of the
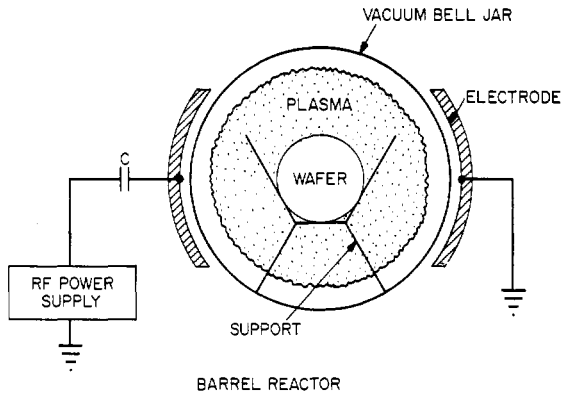
Figure 12.7 A barrel reactor configuration, with capacitively coupled electrodes outside a glass or dielectric vacuum bell jar.
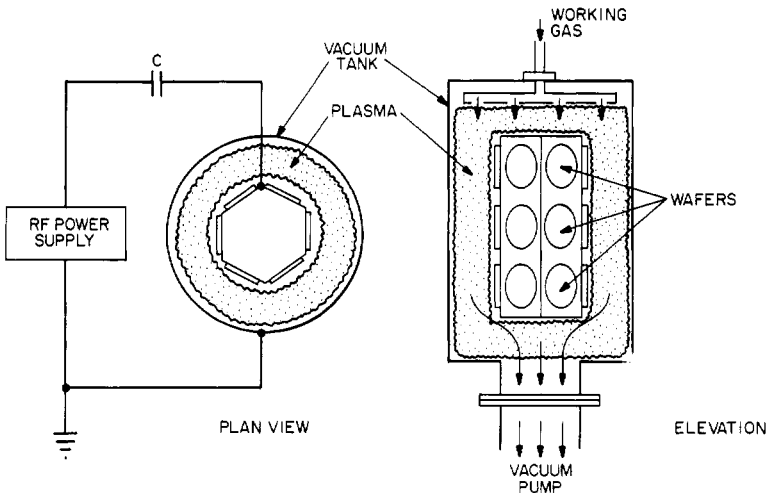
Figure 12.8 A hexagonal reactor configuation operated in the reactive ion etching configuration.

opposite electrode, or sometimes the metallic vacuum tank wall. Various electrode cooling and gas feed arrangements may be used. Sometimes multiple electrodes are used, as shown in figure 12.10. The electrodes can be powered in common, when a large batch of wafers are being treated identically, or they can be powered separately when each batch of wafers is being differently processed.

Other RF plasma reactor configurations which are widely used in industry are the *parallel plate RF magnetron reactor*, and the *planar RF magnetron reactor*. These configurations are essentially identical with their DC counterparts shown on figures 9.32 and 9.33, respectively,
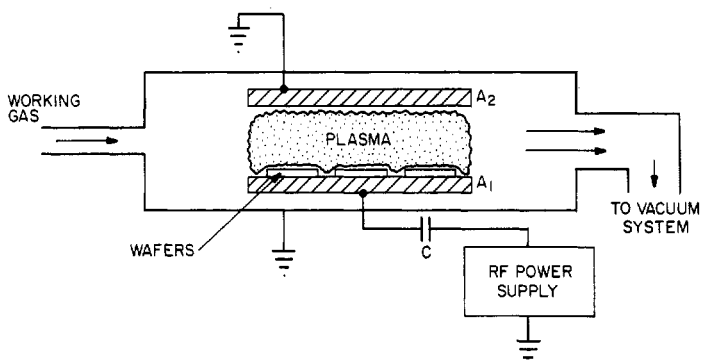
Figure 12.9 A plane parallel capacitively coupled RF plasma reactor operated in the reactive ion etching configuration, with the wafers on the powered electrode.
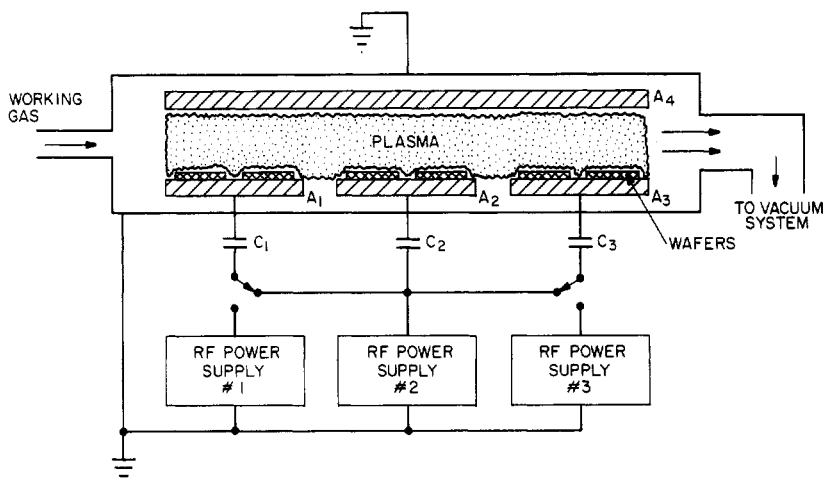
Figure 12.10 A multiple electrode system for parallel plate plasma reactors. Each set of wafers can be processed independently or simultaneously with the other wafers.

except that they are energized with RF typically at 13.56 MHz, for good capacitive coupling through insulating workpieces or wafers. The use of RF allows the plasma to be operated at lower applied voltages than are possible with DC.

Other capacitvely coupled configurations, less widely employed in industry, are sometimes used. Figure 12.11 shows the *end-electrode reactor*, which has been the subject of many computer modeling studies of RF plasmas. In the end electrode reactor, solid metallic electrodes are at
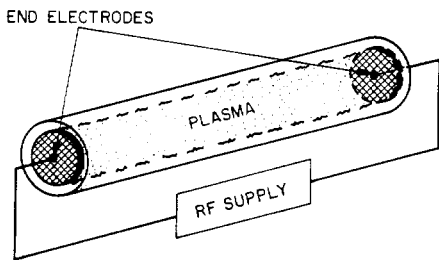
Figure 12.11 End-electrode cylindrical RF capacitively coupled plasma reactor, with end electrodes in contact with the plasma.
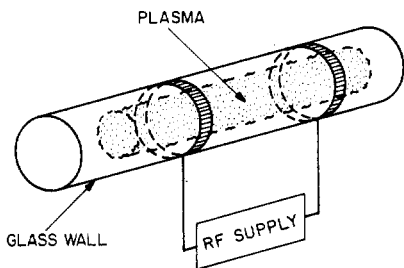
Figure 12.12 Ring-coupled cylindrical RF capacitively coupled plasma reactor, with ring electrodes outside glass wall.

the two ends of a long plasma column and are energized by RF power. The *ring-coupled cylindrical reactor* is shown in figure 12.12, and consists of two metallic rings outside a glass vacuum system energized by RF power. This placement of the electrodes avoids contamination of the plasma with electrode material. The *cylindrical interior electrode reactor* is shown in figure 12.13, and consists of two hemi-cylinders inside the vacuum vessel in direct contact with the plasma. This provides good power coupling, but can result in plasma contamination from electrode material. Finally, the *cylindrical external electrode reactor* is shown in figure 12.14, and is a smaller version of the barrel reactor, with hemi-cylinders outside the glass vacuum system, not in contact with the plasma. This configuration is used to assure plasma purity, a consequence of the lack of electrode contact with the plasma; and also axial uniformity of the plasma.

12.4.2 GEC Reference Cell

As the field of microelectronic deposition and etching evolved, each manufacturer of such equipment, and each laboratory involved in studying deposition and etching by plasma, had their own unique RF power supply circuitry, their own electrode geometry, and their own ensemble of measuring and diagnostic instruments. In order to introduce some standardization in this field, and to be better able to compare results obtained in different laboratories, the American Physical Society's annual Gaseous Electronics Conference proposed what has come to be known as the *Gaseous Electronics Conference (GEC) reference cell* or the *GEC reference research reactor*.
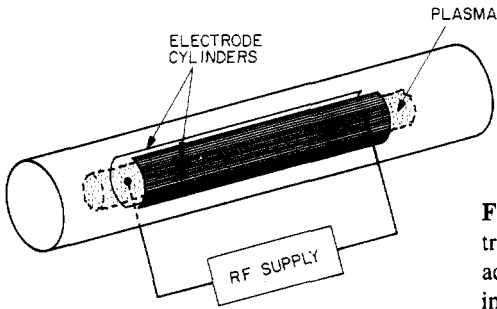
Figure 12.13 Cylindrical interior electrode RF capacitively coupled plasma reactor, with hemi-cylindrical electrodes in contact with the plasma.
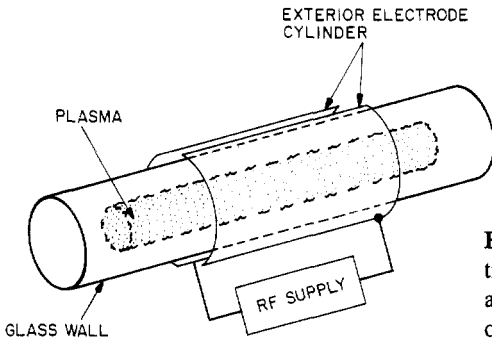
Figure 12.14 Cylindrical external electrode RF capacitively coupled plasma reactor, with hemi-cylindrical electrodes outside glass wall.

The basic configuration of the GEC reference cell is shown in figure 12.15. The vacuum system is made of stainless steel, and contains a pair of axisymmetric disc electrodes 10 cm in diameter, and separated typically by 2.5 cm. The standard RF excitation is 13.56 MHz. The use of RF excitation in the GEC reference cell can present problems in the accurate measurement of the RF power actually delivered to the plasma. In order to facilitate these RF measurements, the equivalent circuit shown in figure 12.16 was adopted for modeling and making electrical measurements. The stray inductance and capacitance are on the left, and the plasma reactor-associated circuit elements are shown to the right. These elements give rise to the impedances indicated on the right-hand side of the diagram.

The standard plasma generated in this device has been diagnosed extensively in order to establish a reference point for use by industrial and other laboratories. A recent example of such diagnostics is that of Bletzinger *et al* (1991), who made microwave interferometric measurements of the integrated plasma number density in the standard GEC reference cell over a wide range of operating conditions. Some of their data are shown in table 12.1. The power shown in this table is that actually delivered to the plasma. The electron densities shown in this table are values averaged across the plasma diameter. In this study, data were taken in both argon and helium. In argon the average electron
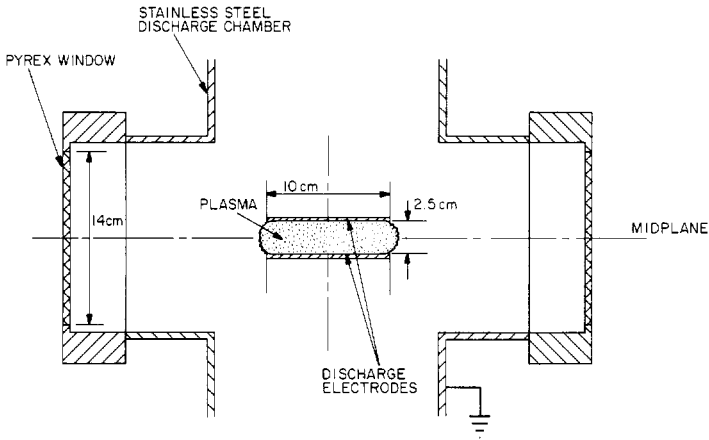
Figure 12.15 A schematic of the GEC standard reference research reactor. The parallel electrodes are axisymmetric about the vertical axis shown.
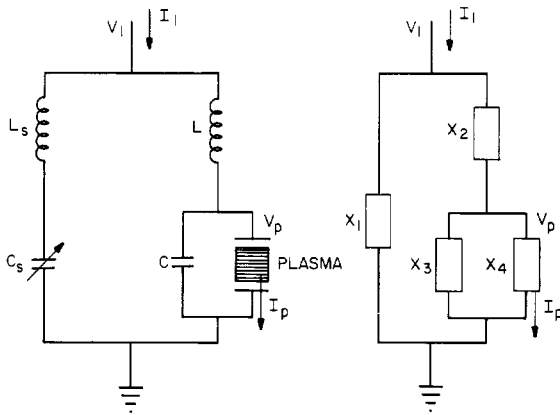
Figure 12.16 Equivalent circuit and circuit elements of the GEC standard reference research reactor.

number density was 2×10^{17} electrons/m^3, with 40 W delivered to the plasma, and in helium the average electron number density was 3×10^{17} electrons/m^3, again with 40 W delivered to the plasma.

Most parallel plate industrial plasma processing reactors are similar to the GEC reference research reactor, without its standardization. This lack of standardization often makes it difficult to know, for example, exactly how much power was applied to a given industrial plasma. This is not just a matter of knowing the phase angle between a sinusoidal voltage and current waveform, but the waveforms—the current waveform particularly—is often non-sinusoidal. To intercompare the power absorbed among commercially available parallel plate reactors, the

Table 12.1 Characteristics of the GEC reference research reactor (from Bletzinger *et al* 1991).

Characteristic	Low value	High value
Power	1 W	100 W
Bias voltage, DC	5 V	250 V
Electron density, n_e	10^{15} electrons/m^3	3×10^{17} electrons/m^3
Gas pressure, p_0	0.10 Torr	1 Torr
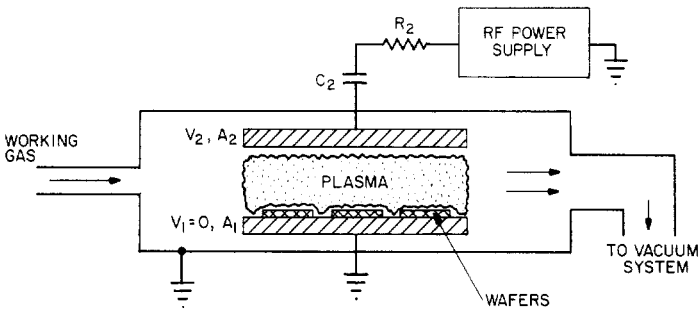
Figure 12.17 A parallel plate RF plasma reactor in the plasma etching (PE) configuration, with wafers on the grounded electrode, and the opposite electrode powered.

electrical characteristics of the RF power supply and of the impedance matching and metering circuit used with a particular research reactor must be known.

12.4.3 System Characteristics

Various arrangements of the RF power supply and electrode connections are used in industrial plasma processing applications, depending upon the particular form of plasma processing desired for a given application. The *plasma etching* (PE) configuration is illustrated schematically in figure 12.17. This configuration consists of wafers or a workpiece mounted on a grounded electrode, with the RF power supply connected to the opposite, powered electrode. This configuation supplies active species, including free radicals, atoms in excited states, and other plasma-related species for etching and/or deposition. This configuration is used when energetic ions are not required.

Perhaps the most commonly used arrangement of power supply and electrodes is the *reactive ion etching* (RIE) configuration, which is shown schematically in figure 12.18. As was indicated in equation (12.78), the
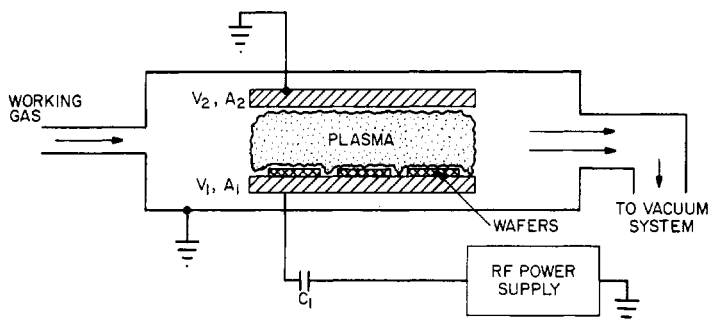
Figure 12.18 A parallel plate RF plasma reactor operated in the reactive ion etching (RIE) configuration, with the wafers mounted on the powered electrode, and the opposite electrode grounded. $V_{bias} \neq 0$, $V_2 = 0$, $A_1 \leqslant A_2$.
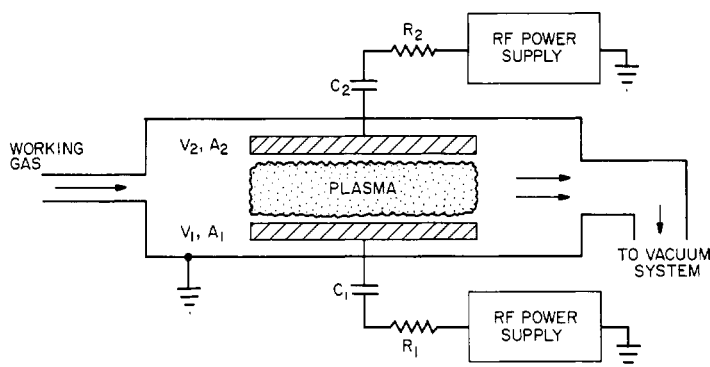
Figure 12.19 A parallel plate RF reactor in the triode etching configuration, with symmetric and asymmetric triode etching. In symmetric operation, the electrode areas are equal, and the RF circuit elements and power supplies are the same for both plates, i.e. $A_1 = A_2$, $R_1 = R_2$, $V_1 = V_2$ and $V_{bias} = 0$, whereas in asymmetric operation $A_1 \neq A_2$, $R_1 \neq R_2$, $V_1 \neq V_2$ and $V_{bias} \neq 0$.

voltage drop across the sheath between the plasma and the powered electrode may be adjusted by changing the ratio of the electrode areas. In the RIE configuration, the wafers are mounted on the powered electrode, and the opposite electrode is grounded. Sometimes the grounded wall of the vacuum tank serves as the opposite, grounded electrode. In this configuration, the electrode voltage drop V_1 can be hundreds of volts if the electrode area ratio is such that $A_1 \ll A_2$, a situation that is desirable for the production of energetic ions incident on the wafer surface.

When it is important to have equal effect on both electrodes, and high ion energies are not important, the *symmetric triode etching* (STE) configuration shown schematically on figure 12.19 is used. This provides
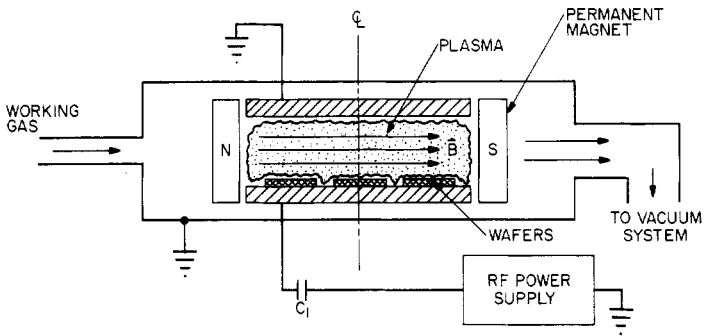
Figure 12.20 A parallel plate RF plasma reactor in the magnetically enhanced reactive ion etching (MERIE) configuration, in which the electrode with the wafers is powered, and a magnetic field is applied parallel to the surface of the electrodes. The magnetic field is rotated with respect to the center line to make the plasma effects more uniform on the wafers.

reactive species to the electrodes and to wafers mounted on them, with relatively low ion fluxes and ion energies. Wafers or workpieces may be mounted on either or both electrodes. The *asymmetric triode etching* (ATE) configuration is sometimes used when fine adjustments in the ion energy are required. This is accomplished by making the circuit elements and sheath electrode areas asymmetrical, and altering the sheath voltage drop above the wafers by manipulation of the external parameters, rather than the electrode area ratios which tend to be fixed by the geometry of the apparatus.

The *magnetically enhanced reactive ion etching* (MERIE) configuration shown schematically on figure 12.20 is used in order to rotate the plasma over the wafers, and thereby average out small asymmetries which might exist in the plasma properties or ion fluxes reaching the surface of the wafers or workpieces to be processed. The magnetic induction is characteristically parallel to the electrodes of parallel plate reactor systems, and may be made mechanically to rotate around the axis of the electrodes, with a relatively low velocity, since only a few revolutions of the magnetic field during a plasma processing run are sufficient to achieve the desired averaging effect.

The magnetic field may be rotated by using the '*rotamagnet*' *configuation*, in which phased modulation of the current in four or more coils surrounding the parallel plate reactor causes the magnetic induction vector to rotate. This is a much slowed-down version of the Rotamak induction heating method discussed in the previous chapter. The rotamagnet configuration has the advantage of not requiring moving parts in the plasma processing vacuum system. The magnetic induction may be produced either by coils or by permanent magnets, and in some

Table 12.2 Operating regime of capacitive plasma reactors used for plasma processing.

Parameter	Low value	Typical value	High value
Frequency	1 kHz	13.56 MHz	100 MHz
Gas pressure	3 mTorr	300 mTorr	5 Torr
Power level	50 W	≈ 200 W	500 W
rms electrode voltage	100 V	≈ 300 V	1000 V
Current density	0.1 mA/cm^2	≈ 3 mA/cm^2	10 mA/cm^2
Electron temperature, T_e	3 eV	≈ 5 eV	8 eV
Electron density, n_e	$10^{15}/m^3$	$\approx 5 \times 10^{15}/m^3$	$3 \times 10^{17}/m^3$
Ion energy, $\mathcal{E}_i$	5 eV	50 eV	500 eV
Electrode separation, d	0.5 cm	4 cm	30 cm

configurations the coils or permanent magnets are mounted on a rotating turntable, and the rotation of the magnetic field achieved by mechanical means.

The RF frequencies used in MERIE configurations like that shown on figure 12.20 are usually so low that the plasma operates far away from electron cyclotron resonance, and ECR heating or power absorption plays little or no role in the operation of the MERIE configurations. If the operating frequency and the value of the magnetic induction are such that the operating frequency is in electron cyclotron resonance anywhere within the plasma volume, the MERIE configuration becomes an *ECR reactor*, which is discussed in Chapter 13.

12.4.4 Operating Regimes

Typical values for the operating regime of capacitively coupled RF parallel plate reactors used for plasma processing are shown in table 12.2, along with extreme limits of each parameter. Their frequency of operation can range from 1 kHz to 100 MHz and more, with 13.56 MHz a widely used value for industrial applications. The gas is at low pressures, where the mean free paths of ions and sputtered atoms are relatively long, and ranges from 3 mTorr to perhaps 5 Torr. The power level is relatively low, ranging from approximately 50 W to 500 W delivered to the plasma. The rms electrode voltage can range from perhaps 100 V to 1000 V, with current densities from below 1 mA/cm^2 to 30 mA/cm^2. The ion energies which reach the 'cathode', usually the powered electrode with the wafers on it, can range up to perhaps 100 eV, values necessary for effective etching of deep trenches. The electrode separations can range from as little as 1 cm to as much as 30 cm in barrel and hexagonal reactors.

12.4.5 Plasma Characteristics

Some of the plasma parameters, including the electron kinetic temperature, number density, and ion energy are listed in table 12.2. Perhaps the most important plasma characteristic of the parallel plate RF reactor for industrial plasma processing applications is the sheath voltage drops, which create energetic ions for etching and sputtering applications. A characteristic RF parallel plate plasma reactor is shown in figure 12.6, with a powered electrode of area A_1 much less than the area A_2 of the wall or opposite electrode. The grounded electrode has a sheath voltage V_2 between the plasma and the grounded electrode, and the powered electrode has a sheath voltage drop V_1. For etching applications it is usually desirable that the powered electrode voltage drop, V_1, be as large as possible. This voltage drop is controlled by the real current density on the electrodes, and hence the area ratio. One electrode is often grounded, and may be the grounded wall of the vacuum tank. In figure 12.6, the potential across the plasma is represented with positive potentials plotted toward the left.

12.5 EXAMPLES OF CAPACITIVE RF PLASMA REACTORS

12.5.1 Mode Transitions in a Chlorine Discharge

The operation of some RF glow discharges, like some DC glow discharges, is subject to *mode transitions*. Examples from a paper by Aydil and Economou (1991), are shown in figures 12.21 and 12.22. These authors describe a 13.56 MHz chlorine glow discharge which was observed to have two stable states: a uniform state, in which the plasma and etching rate were radially uniform over the electrodes, and a 'plasmoid' state, in which a blob of plasma formed between the plates (the 'plasmoid'), and the plasma number density and etching rates were observed to be radially non-uniform.

Figure 12.21(a) shows the ion current density on the electrode as a function of power fed into the parallel plate plasma reactor. These data were taken for a pressure of $p = 0.7$ Torr, an electrode spacing of $d = 2.54$ cm, and a gas flow of 25 standard cm^3/min. Figure 12.21 shows bi-stable operation in two modes. The lower curve represents the uniform plasma. At power inputs above approximately 140 W, the RF glow discharge spontaneously made a transition from point B to C to the plasmoid state, in which it remains unless and until the power level is reduced to approximately 70 W at point E, where it again makes a transition to point F, in the uniform state. This bi-stable operation also affects the median energy of chlorine ions bombarding the wall, as shown in figure 12.21(b), by nearly a factor of 2.
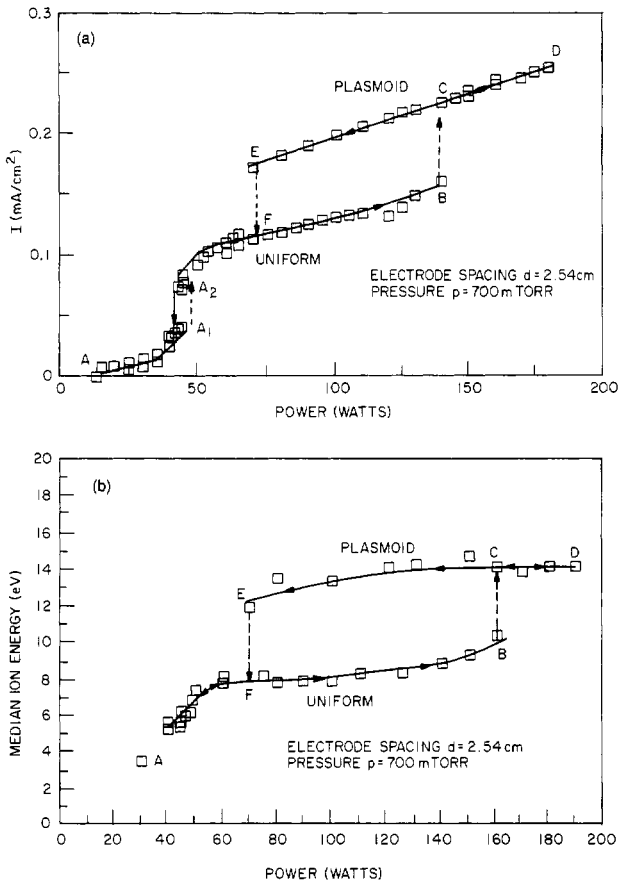
Figure 12.21 (*a*) Mode transitions in a parallel plate chlorine glow discharge. The ion bombardment flux is shown as a function of power for a pressure of 0.7 Torr, 2.54 cm electrode spacing. (*b*) The median ion energy as a function of RF input power, showing the effects of a mode transition, for the same conditions as (*a*). From Aydil and Economou (1991).

The behavior exhibited in figure 12.21 is known mathematically as *catastrophic*, and exhibits the characteristic phenomenon of *hysteresis*, in which plasma parameters, such as the ion flux on the wall and the ion energy, are double-valued for a significant range of power inputs to the plasma. A similar example from the same authors is shown on figure 12.22 for slightly different conditions, in which the power was held constant at 100 W, with $d = 2.54$ cm electrode spacing, but variable pressure. This catastrophic behavior is also apparent when the pressure is an independent variable, with hysteresis and multiply-valued dependent variables.
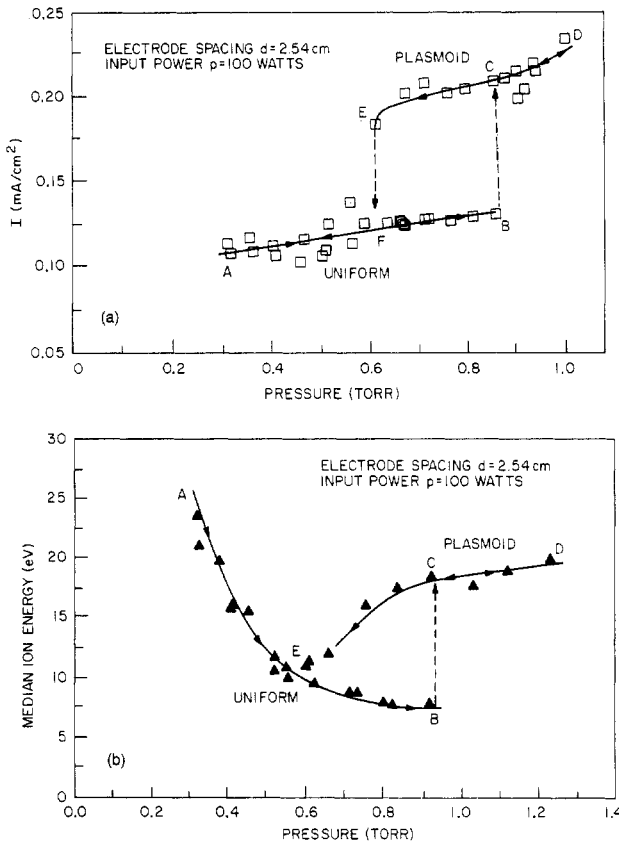
Figure 12.22 (*a*) The ion bombardment flux as a function of gas pressure for a chlorine glow discharge in a parallel plate plasma reactor. The input power was 100 W with a 2.54 cm electrode spacing. The effect of a mode transition is clearly evident. (*b*) Median ion energy as a function of gas pressure for the same conditions as (*a*). From Aydil and Economou (1991).

The mode behavior exhibited in figures 12.21 and 12.22 is very undesirable in industrial applications, not only because a single value of the plasma operating parameters such as the gas pressure or input power can result in one of two ion energies and bombardment fluxes, but also because one of these two bi-stable states is unacceptable for microelectronic applications because it is radially non-uniform and capable of ruining a whole batch of wafers under fabrication. The physical process responsible for these mode transitions has not been identified, and as a result there are no analytical theories predicting the onset and range of this bi-stable behavior; nor are there any empirical correlations which would provide this information.

12.5.2 RF Glow Discharge at 1 atm

A relatively recent development in industrial plasma sources is the production of *RF atmospheric glow discharges* (Kanda *et al* 1991, Roth *et al* 1992). By using high voltage RF excitation at kilohertz frequencies, it is possible to produce a steady-state uniform glow discharge at 1 atm of pressure in air and other gases, thus eliminating the requirement of a vacuum system to expose materials to plasmas.

A schematic of the 1 atm glow discharge plasma reactor system developed at the UTK (University of Tennessee, Knoxville) Plasma Science Laboratory is shown in figure 12.23. The reactor volume is bounded by two plane, parallel plates across which a RF electric field is imposed. This electric field has an amplitude of kilovolts per centimeter, and frequencies in the kilohertz range. The electric fields must be strong enough to electrically break down the gas used, and are much lower for helium and argon than for atmospheric air. The RF frequency must be in the right range, since if it is too low, the discharge will not initiate, and if it is too high, the plasma forms filamentary discharges between the plates. Only in a relatively limited frequency band will the atmospheric glow discharge plasma reactor form a uniform plasma without filamentary discharges.

The parallel electrode plates consitituting the reactor are enclosed in a plexiglass container, indicated in figure 12.23. The principal function of this container is to control the composition of the operating gas used during operation at 1 atm. The reactor has a bare metal median screen, which may be grounded through a current choke, that is located midway between the two parallel electrode plates. This screen provides a rigid surface which supports the material to be treated, and the holes in the screen allow a gas flow from the top half of the plexiglass box to the bottom half. The two parallel electrode plates shown on figure 12.23 are driven by a power amplifier capable of operation from 0 to 10 kV rms, over frequencies from less than 1 kHz to 100 kHz. The gas is sampled from the exhaust line and leaked into a vacuum system with a mass spectrometer. The two copper electrode plates are 21.6 cm square, and the surfaces in contact with the plasma are covered with a 3.2 mm thick Pyrex insulating plate.

The electric fields employed in the 1 atm glow discharge plasma reactor are only a few kilovolts per centimeter, values usually too low to electrically break down the background gas if applied DC. Gases such as helium and argon will break down under such low RF electric fields, however, if the positive ion population is trapped between the two parallel plates, while at the same time the electrons are free to travel to the insulated electrode plates where they recombine or build up a surface charge. The most desirable uniform 1 atm glow discharge plasma is therefore created when the applied frequency of the RF electric field is
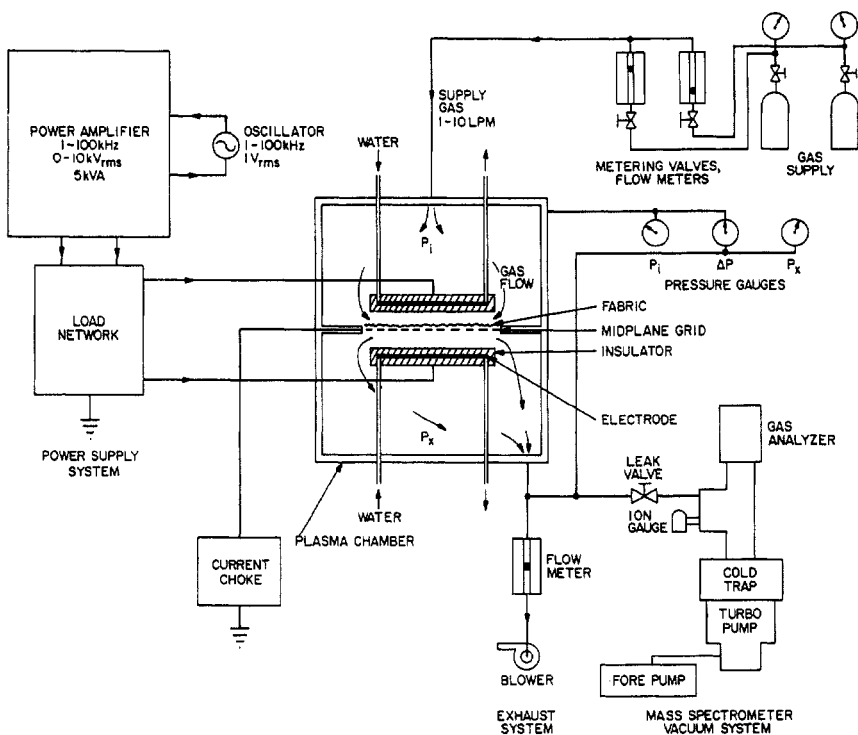
Figure 12.23 A schematic drawing of the 1 atm glow discharge plasma reactor system.

high enough to trap the ions between the median screen and an electrode plate, but not so high that the electrons are also trapped.

If the RF frequency is so low that both the ions and the electrons can reach the boundaries and recombine, the plasma will either not initiate or form a few coarse filamentary discharges between the plates. If the applied frequency is in a narrow band in which the ions oscillate between the median screen and an electrode plate, they do not have time to reach either boundary during a half period of oscillation. If the more mobile electrons are still able to leave the plasma volume and impinge on the boundary surfaces, then the desirable uniform plasma is produced. If the applied RF frequency is still higher so that *both* electrons and ions are trapped in the discharge, then the discharge forms a filamentary plasma.

An approximate theory is available which yields a relationship between the electrode spacing, the rms electrode voltage, and the applied frequency which results in trapping ions but not electrons between the two plates, and produces the desired uniform 1 atm glow discharge plasma. On figure 12.24 is a schematic of the upper chamber of the 1 atm glow discharge plasma reactor. The lower boundary of this space is the midplane screen, the floating potential of which should remain near
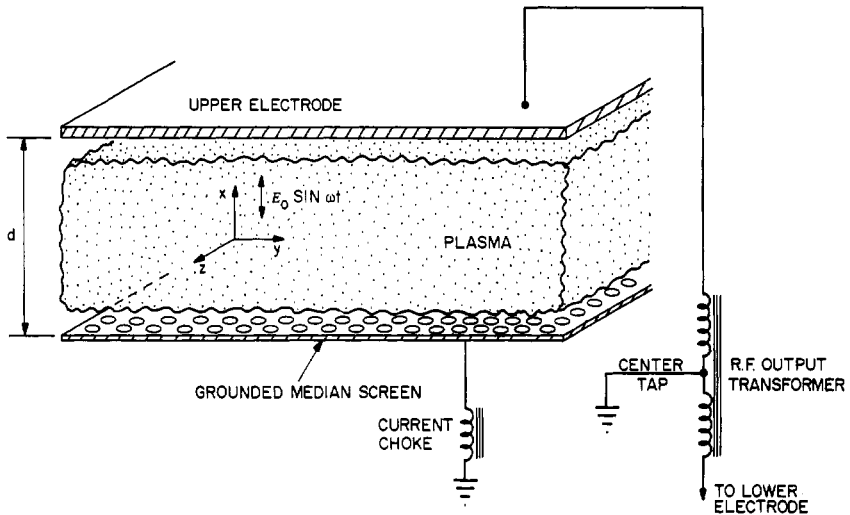
Figure 12.24 A schematic of the 1 atm glow discharge plasma reactor, with RF transformer secondary, the matching network, and the reactor electrodes.

ground if the RF power supply output is connected as a push–pull circuit to the two electrodes with a grounded center tap. In the configuration of figure 12.24, a Cartesian coordinate system is applied as shown, with the applied electric field in the x direction. The maximum amplitude of the electric field between the grounded median screen and the upper electrode is E_0, and the separation of the screen from the electrodes is the distance d. The median screen, with an exposed sample on it, is assumed not to allow ions through the median plane from the upper chamber to the lower, or vice-versa.

The electric field between the electrodes shown on figure 12.24 is given by

$$E = (E_0 \sin \omega t, 0, 0). \tag{12.86}$$

It is assumed that the 1 atm glow discharge operates in a magnetic-field-free plasma. The equation of motion for the ions or electrons in the Lorentzian model is given by

$$F = ma = -mv_c v - eE \tag{12.87}$$

where the first term on the right-hand side is the Lorentzian collision term, according to which the momentum mv is lost with each collision that occurs with a collision frequency v_c. The x component of (12.87) is given by

$$m \frac{d^2 x}{dt^2} + m v_c \frac{dx}{dt} = e E_0 \sin \omega t \tag{12.88}$$

where the electric field E from equation (12.86) has been substituted into the right-hand side of equation (12.87). The general solution to equation (12.88) is

$$x = C_1 \sin \omega t + C_2 \cos \omega t \qquad (12.89)$$

where the constants C_1 and C_2 are given by

$$C_1 = -\frac{eE_0}{m} \frac{1}{(\omega^2 + \nu_c^2)} \qquad (12.90)$$

and

$$C_2 = -\frac{\nu_c e E_0}{\omega m} \frac{1}{(\omega^2 + \nu_c^2)}. \qquad (12.91)$$

The 1 atm helium glow discharge is operated at frequencies between $\omega/2\pi = 1$ and 30 kHz, where, for helium at 1 atm (Anon. 1991), $\nu_{ci} \approx 6.8 \times 10^9$ ion collisions/s, and $\nu_{ce} \approx 1.8 \times 10^{12}$ electron collisions/s. The collision frequency for ions and electrons is much greater than the RF frequency, $\nu_c \gg \omega$. The relation $\nu_c \gg \omega$ for ions and electrons, implies that C_2 is much greater than the constant C_1, or

$$C_2 \approx -\frac{eE_0}{\omega m \nu_c} \gg C_1. \qquad (12.92)$$

The time-dependent position of an ion or an electron in the electric field between the plates is given by substituting equation (12.92) into equation (12.89), to obtain

$$x(t) \approx -\frac{eE_0}{m\omega\nu_c} \cos \omega t \qquad (12.93)$$

The rms displacement of the ion or electron during a half-cycle is given by

$$x_{rms} \approx \frac{2}{\pi} \frac{eE_0}{m\omega\nu_c} \qquad (m). \qquad (12.94)$$

If ν_0 is the driving frequency, in hertz, and V_{rms} is the rms voltage applied to the plates, then the radian RF frequency is given by

$$\omega = 2\pi \nu_0 \qquad (12.95)$$

and the maximum electric field between the plates can be approximated by the maximum voltage V_0 appearing between them,

$$E_0 = \frac{V_0}{d} = \frac{\pi V_{rms}}{2d}. \qquad (12.96)$$

Table 12.3 Characteristic parameter ranges for uniform glow discharge operation of the UTK 1 atm plasma reactor, for various working gases: He; He+1.7%O_2; Ar; Ar+He; Ar+1.7%O_2; air.

Frequency	1–20 kHz
Voltage	1.5–9.5 kV$_{rms}$ plate to plate
Electrode gap, d	0.8–2.5 cm
Pressure	760 +15, −5 Torr
rms power	10–150 W
Power density	4–120 mW/cm^3
Plasma volume	0.7–2.4 liters

If the charge in question moves across the discharge width from the median plane to one of the electrode plates during one full cycle, then we may write

$$x_{rms} \leqslant d/2. \tag{12.97}$$

Equation (12.97) states that the rms displacement of the particle has to be less than half the clear spacing in order to have a build-up of charge between the plates. In the geometry shown in figure 12.24, the distance d is identified with the distance between the grounded median screen and the energized electrode. Substituting equations (12.95) to (12.97) into equation (12.94) yields the relationship

$$\frac{d}{2} \approx \frac{eV_{rms}}{2\pi m \nu_0 \nu_c d}. \tag{12.98}$$

If we now solve for the critical frequency ν_0 above which charge build-up should occur in the plasma volume, we have

$$\nu_0 \approx \frac{eV_{rms}}{\pi m \nu_c d^2} \quad \text{(Hz)} \tag{12.99}$$

In equation (12.99), the collision frequency ν_c is that of ions or electrons, respectively, at 1 atm, and the rms voltage is that which bounds the upper and lower limit of the uniform discharge regime.

The range of parameters over which the 1 atm glow discharge plasma reactor has been operated at the UTK Plasma Science Laboratory is given in table 12.3. The nominal pressure at which this discharge has been operated is 1 atm. The variation of several torr shown in table 12.3 is the pressure differential across the midplane screen. The rms power shown in table 12.3 is the net power delivered to the plasma, less the reactive power which does not appear in the plasma. The total volume of plasma between the two electrode plates is given by

$$S = 0.93d \text{ liters} \tag{12.100}$$
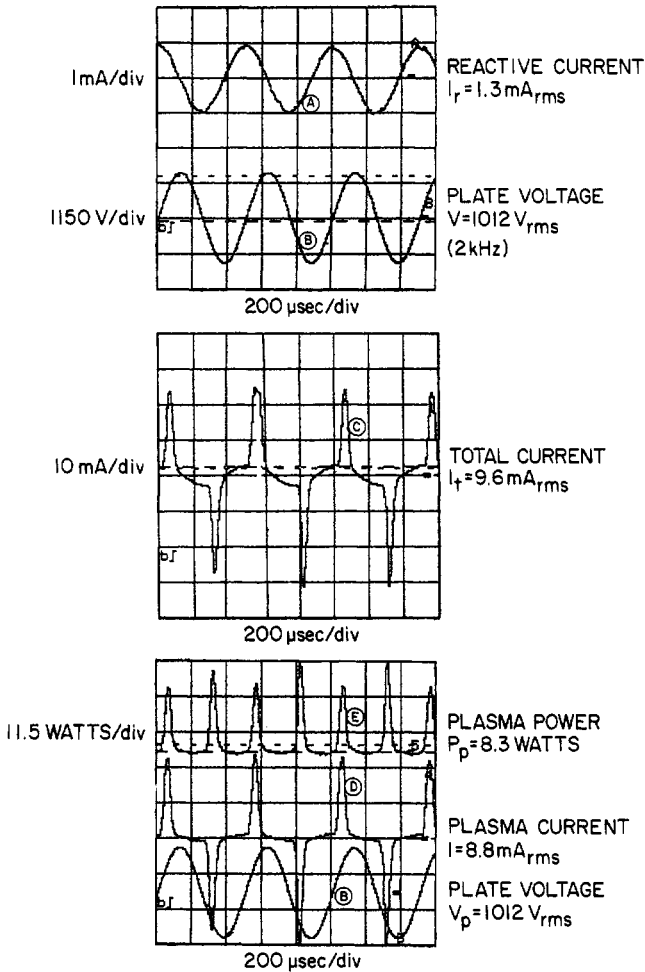
Figure 12.25 Voltage and current waveforms from an operating 1 atm helium glow discharge plasma reactor for a uniform discharge, showing breakdown in the current waveform under conditions of an rms electrode voltage of $V_{rms} = 1.01$ kV, a frequency of $\nu_0 = 2.0$ kHz, and an electrode separation $d = 1.75$ cm.

where d is the separation of a plate from the median screen in centimeters.

Figures 12.25 and 12.26 show two waveforms of voltage and current taken in helium at the same electrode separation and gas flow conditions, but at two different frequencies (Roth *et al* 1993). Figure 12.25 was taken in the uniform glow discharge regime at a frequency of 2.0 kHz, and figure 12.26 was taken in the filamentary discharge regime at a frequency above the uniform plasma operating band at
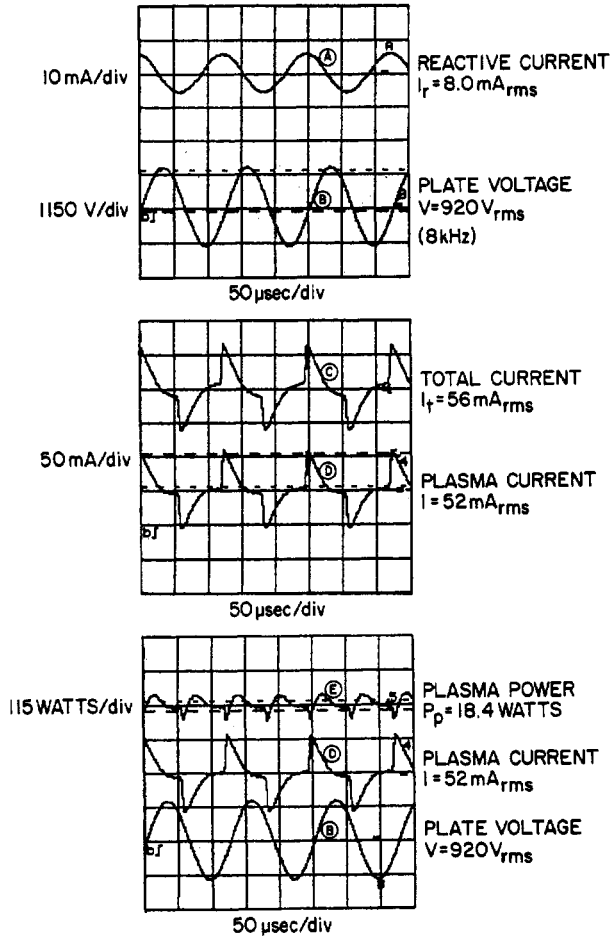
Figure 12.26 Voltage and current waveforms from an operating 1 atm helium glow discharge plasma reactor for a filamentary discharge for operating conditions $V_{rms} = 0.92$ kV; operating frequency $\nu_0 = 8.0$ kHz, and electrode separation $d = 1.75$ cm.

8.0kHz The low internal impedance of the RF power supply results in a voltage waveform (trace B) that is very close to sinusoidal. The total current waveform (trace C) is interrupted by a breakdown of the plasma twice each cycle, once when the voltage is positive, and once when the voltage is negative. Trace A shows the reactive current waveform at the same voltage and operating conditions, but in air, rather than helium. There was no perceptible plasma present in air under these conditions, and the power is completely reactive.
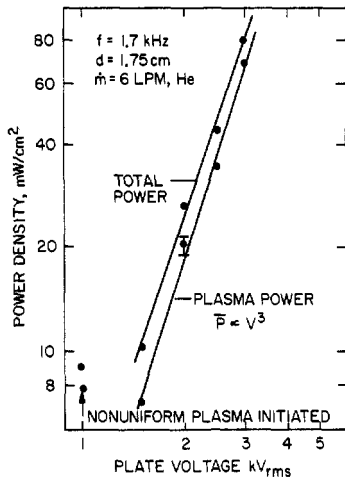
Figure 12.27 Plot of the power density versus the rms electrode voltage for a helium plasma with an electrode separation $d = 1.75$ cm, an operating frequency of $\nu_0 = 1.7$ kHz, and a plasma volume of 1.63 liters. Shown are the plasma power alone on the lower curve, and the total power including the reactive power on the upper curve.
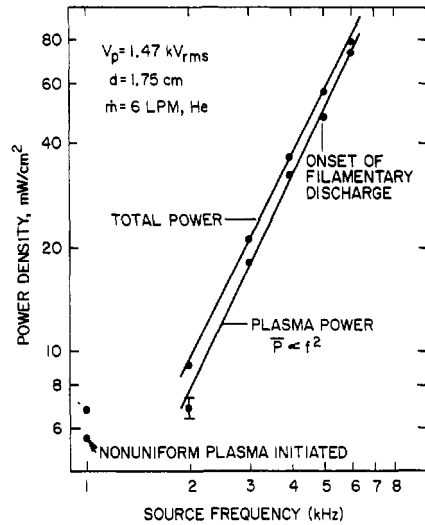
Figure 12.28 A plot of the power density of a helium plasma as a function of RF frequency for an electrode separation $d = 1.75$ cm, an RF electrode voltage $\nu_{rms} = 1.47$ kV, and a total plasma volume of 1.63 liters. The lower curve is the plasma power; the upper curve is the total power including reactive power flowing to the plasma reactor.

This purely reactive current of trace A was subtracted from the total plasma current in trace C, to yield trace D. The instantaneous power deposited in the plasma (trace E) is found by multiplying the excess plasma current above the reactive current (trace D) by the voltage at that point (trace B). The average power is found by integrating over the duration of the pulses shown, and dividing by this duration. It is in this manner that the power and power density into the plasma were calculated for these highly non-sinusoidal current waveforms. Figures 12.25 for the uniform discharge and 12.26 for the filamentary discharge show characteristically different power waveforms in trace E; this is a method of distinguishing the uniform from the filamentary discharge.

The plasma power is of interest because it is proportional to the production rate of active species in the plasma; the reactive power is significant because it determines the required power handling rating of the plasma power supply and associated equipment. The total power is the sum of plasma and reactive power. On figure 12.27 is shown a log–log plot of the plasma and total power density in milliwatts per

cubic centimeter, as functions of the rms voltage applied to the parallel plates. The active plasma volume in figure 12.27 was 1.63 liters, with a separation between the median screen and each plate of $d = 1.75$ cm in a plasma of helium gas. On figure 12.28 is a similar presentation of the power density plotted on log–log coordinates as a function of the frequency. The approximate bound of the uniform plasma discharge regime is shown by the arrow. These data were taken in helium gas for the same plasma volume and electrode separation as figure 12.27.

These developments in the production of DC steady state atmospheric glow discharges at VLF frequencies imply that many industrial surface treatment processes now done in vacuum systems, which are expensive and enforce batch processing, might be done at 1 atm. Possible applications of such atmospheric glow discharges would include antistatic treatment of plastics, improving the wettability of polymers for inks and glue; to change the texture and dye-ability of fabrics; and to promote surface chemical reactions resulting in polymer film formation, etc.

12.6   ISSUES IN CAPACITIVELY COUPLED PLASMA SOURCES

In spite of their widespread use in industry, the capacitively coupled RF plasma sources are not well understood, and important unresolved theoretical problems remain with respect to some industrial applications of these reactors. Some areas of ignorance include:

(1) Better understanding is needed of the sheath physics of RF plasmas. A viable model of the sheath is required which will predict sheath thickness, the voltage drop across the sheath, the ion energies, the power dissipation in the sheath, as well as the real ion and/or electron currents to be expected from the plasma.

(2) The transport and fate of both ions and electrons in the plasma needs to be understood, both in terms of the overall particle balance, and in terms of the detailed physical processes responsible for transport of ions and electrons from the plasma to the electrodes and walls.

(3) The mode transitions to which these RF glow discharges are subject need to be better understood, both in terms of identifying the physical processes responsible for them, and the formulation of an analytical theory which will predict their onset and regimes of stability.

(4) Finally, a theory of the RF parallel plate discharge comprehensive enough to predict the sheath voltage drop and ion energies reaching the electrode surfaces is needed so that ion energies can be tailored to suit the many plasma processing applications for which energetic ions are required.

12.7 APPLICATIONS OF CAPACITIVELY COUPLED REACTORS

Contemporary applications of capacitively coupled RF plasma reactors have been summarized in a recent U.S. National Academy of Sciences report (Anon. 1991). Monographs on the applications of these sources to plasma processing have been written by Baddour and Timmins (1967) and Sugano (1985).

The parallel plate plasma reactors are probably the most widely used plasma reactors in industry. They are utilized for a wide range of applications, both for commercial production purposes, and for laboratory research and development. Parallel plate reactors are used in plasma chemistry; for continuous flow reactors; for studies of surface chemistry, and for the production of chemical reactions involving highly reactive species such as ions, atoms in excited states, or free radicals, or for chemical reactions that require or are facilitated by ultraviolet production from the plasma.

Another widespread area of use is in thin film deposition for microelectronic circuits, where parallel plate plasma reactors are used for plasma-assisted chemical vapor deposition, surface catalysis and surface polymerization, and to promote other forms of surface chemical reactions. The reactive ion etching configuration is widely used for microelectronic etching. Parallel plate plasma reactors are also used to modify the surface of materials exposed to a plasma, for the purpose of changing the adhesion, wettability or antistatic properties of the surface of materials. Finally, parallel plate plasma reactors have been used as an ion source, a general purpose plasma source for research and development applications, and for other purposes.

REFERENCES

Anon. 1991 *Plasma Processing of Materials: Scientific Opportunities and Technological Challenges* (National Academy Press, Washington DC) ISBN 0-309-04597-5

Aydil E S and Economou J 1991 Multiple Steady States in a Radio Frequency Chlorine Glow Discharge *J. Appl. Phys.* **69** 109–114

Baddour R F and Timmins R S (ed) 1967 *The Application of Plasmas to Chemical Processing* (Cambridge, MA: MIT Press) LCCCN 67-17494

Bletzinger P, Garscadden A, Andrews M L, and Cooper D 1991 The Dependence of Integrated Electron Line Density on the Absorbed Power for Different Gases in the GEC RF Standard Plasma Processing Research Reactor *Proc. 1991 IEEE Int. Conf. on Plasma Science, (Williamsburg, VA, 3–5 June 1991)* IEEE Catalog No. 91-CH3037-9, pp 136–137

Kanda N, Kogoma M, Jinno H, Uchiyama H, and Okazaki S 1991 *Proc. 10th Int. Symp. on Plasma Chemistry* vol 3 (International Union of Pure and Applied Chemistry) paper 3.2-20

Roth J R, Laroussi M and Liu C 1992 Experimental Generation of a Steady-State Glow Discharge at Atmospheric Pressure *Proc. 19th IEEE Int. Conf. on Plasma Science, (Tampa, FL, 1–3 June 1992)*

Roth J R and Spence P D 1987 Measurement of the Effective Momentum Collision Frequency in a Turbulent, Weakly Ionized Plasma *Proc. 18th Int. Conf. on Phenomena in Ionized Gases (Swansea, UK)* vol 4 (International Union of Pure and Applied Physics) pp 614–615

Roth J R, Wadsworth L C, Spence P D, Tsai P P-Y and Liu C One atmosphere glow discharge plasma for surface treatment of nonwovens *Proc. 3rd Annual TANDEC Conf. on Meltblowing and Spunbonding Technology (Knoxville, TN, 1–3 November 1993)* (Knoxville, TN: Textiles and Nonwovens Development Center) JN 37996-1950

Spence P D 1990 *A Study of the Effective Electron Collision Frequency in a Weakly Ionized Turbulent Penning Discharge Plasma* PhD Thesis, University of Tennessee, Knoxville, TN

Sugano T (ed) 1985 *Applications of Plasma Processes to VLSI Technology* (New York: John Wiley) ISBN 0-471-86960-0, p 142

Tanizuka N 1989 Plasma Processing Control by a Magnetic Field Crossed to a Sheath Electric Field *Japan. J. Appl. Phys.* **28** 1703–1707

13

Microwave Electrical Discharges in Gases

The interaction of electromagnetic radiation with plasma at microwave frequencies usually occurs in the *collective regime*. In this regime, the radiation interacts with the plasma as a dielectric medium, rather than with the electrons individually, as was the case in the previous chapter. Since the mid-1980's, microwave-generated plasmas have been increasingly used for microelectronic plasma processing and for continuous flow plasma torches and chemical reactors (see the NAS–NRC report *Plasma Processing of Materials* (Anon. 1991)).

13.1 INTRODUCTION

13.1.1 Microwave-Generated Plasma

Microwave-generated plasmas were not studied until after the Second World War, when high power microwave sources became available as the result of research on radio-assisted detection and ranging (radar) and communications systems. This research produced a variety of kilowatt-level microwave sources capable of operating in the steady-state or in a pulsed mode. Early work on microwave-generated plasmas was conducted at the Research Laboratory of Electronics at MIT, at the Polytechnic University of New York, at the University of California's Berkeley campus, as well as other locations. Much of this microwave plasma research was motivated by an attempt to extend the power and range of radar systems at sea level to high altitude and lower pressure, but some research was also motivated by the unique characteristics of microwave-generated plasmas.

Microwave-generated plasmas generally have a higher electron kinetic temperature than is found in DC or low frequency RF-generated plasmas, typically ranging from 5 to 15 eV, rather than the 1 or 2 eV characteristic of the latter discharges. If microwave power is available at the kilowatt level, the electron number density in microwave-generated plasmas can approach the critical number density determined by the electron plasma frequency. This number density is 7×10^{16} electrons/m^3 at a frequency of 2.45 GHz, a typical frequency for microwave discharge. Microwave-generated plasmas can be operated over a wide range of gas pressures, ranging from atmospheric pressure, down to 10^{-6} Torr for some ECR microwave discharges. Unmagnetized microwave discharges are usually operated at pressures from 10 mTorr to 1 atm, and magnetized ECR microwave discharges generally operate at lower pressures, from 10 mTorr down to a few μTorr.

Because of their higher electron kinetic temperatures and lower pressures, microwave discharges are capable of providing a higher fraction of ionization and dissociation than DC or low frequency RF discharges—an important advantage in many plasma chemical applications. Microwave plasmas do not have a high voltage sheath, with its accompanying ion sputtering of the wall. Microwave discharges are operated with no internal electrodes, thus reducing sputtering and contamination of the plasma from electrode materials. Microwave discharges also can remain stable over a wide range of background gas pressures, relative to DC or low frequency RF discharges.

Microwave-generated plasmas have found many industrial uses, particularly since the early 1980's. Microwave plasmas are widely used as sources of continuous and spectral line radiation in the ultraviolet and visible regions of the spectrum. Microwave-generated plasmas are also used as sources of plasma-related active species, such as ions, free radicals, excited atoms, and dissociated neutral species, a function promoted by the relatively high electron kinetic temperature of microwave discharges. Microwave discharges have been used to provide a lasing medium, and to pump lasers. Microwave discharges are used in the initial phases of controlled fusion experiments to generate steady-state, relatively high density plasmas which are confined and heated to conditions of fusion interest by other means. Finally, microwave generated plasmas have found increasing use in the production of industrial plasmas, both for continuous flow plasma–chemical reactors, and for electron cyclotron resonance (ECR) generated plasmas for microelectronic plasma processing applications.

13.1.2 Microwave Frequency Regime

There is no consensus in the scientific literature on a precise definition of the 'microwave' portion of the electromagnetic spectrum. It is generally

understood to include the upper part of the *ultra high frequency* (UHF) portion of the electromagnetic spectrum between wavelengths of 30 and 10 cm; the *super high frequency* (SHF) portion of the spectrum between wavelengths of 10 cm and 1 cm; and the *extremely high frequency* (EHF) portion of the electromagnetic spectrum between 1 cm and 1 mm. Although this definition would extend as low as 1 GHz where the wavelength is 30 cm, current common usage designates the 'microwave' region of the electromagnetic spectrum from a wavelength of 30 cm down to wavelengths of 1 mm, at 300 GHz, at the boundary of the infrared portion of the electromagnetic spectrum, which starts at a wavelength of 1 mm.

Microwave sources and circuit components are most available and least expensive at the frequency $\nu = 2.45$ GHz, for which the free space wavelength is $\lambda = 12.24$ cm. This is the frequency of choice for the vast majority of microwave plasma reactors, although hardware is available in other frequency bands, such as 915 MHz. Nearly all microwave technology was originally developed for radar and communications applications, so therefore microwave hardware is less available in those frequency bands with high atmospheric water vapor absorption, indicated in figure 13.1. These absorption frequencies, relatively useless for communications or radar, should logically be the ultimate choice for high power industrial plasma heating applications, but this has not yet happened. Hardware for communications and radar purposes is most available in the following transmission bands, shown in figure 13.1:

$$0.4 \leqslant \nu \leqslant 20 \text{ GHz}$$
$$27 \leqslant \nu \leqslant 40 \text{ GHz}$$
$$75 \leqslant \nu \leqslant 110 \text{ GHz}$$
$$\nu \approx 125 \text{ GHz}.$$

Nearly all current applications of microwaves for industrial plasma production use two frequencies: $\nu = 2.45$ GHz, and $\nu = 0.915$ GHz.

13.1.3 Microwave Plasma Reactor Configurations

Probably one of the most used microwave plasma generation configurations is the *waveguide coupled reactor* shown in figure 13.2. In this configuration, microwave power is fed into a tapered resonator which surrounds a quartz or other dielectric tube, containing the working gas or reactants at low pressure. Intense axial electric fields at the microwave frequency are set up in the region where the tapered resonator surrounds the plasma, and this causes the gas to break down and the plasma to be maintained. These are generally medium power applications involving hundreds of watts to many kilowatts, and so it is usually necessary to
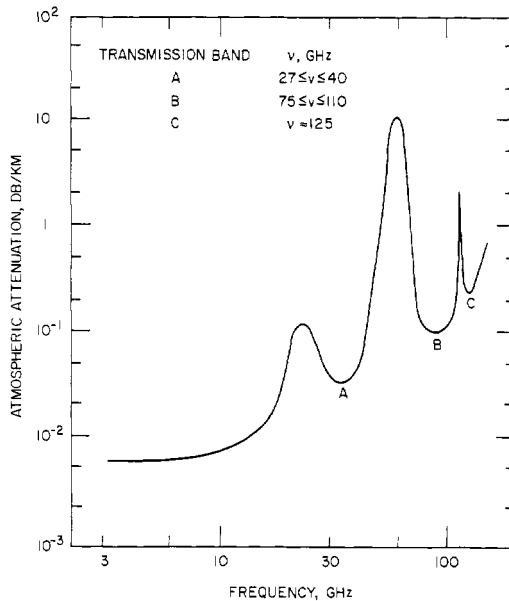
Figure 13.1 The attenuation, in decibels per kilometer, in atmospheric air as a function of frequency in the microwave portion of the spectrum. Major transmission bands are indicated.

cool the quartz tube. This arrangement allows the microwave power to be coupled to the plasma in a simple way, minimizing the impedance matching problems associated with feeding the microwave power from atmospheric pressure into a low pressure vacuum system. When used as a plasma–chemical reactor, the configuration shown in figure 13.2 can be operated in a continuous flow mode.

Another type of microwave plasma reactor is the resonant or *multimode cavity reactor* shown in figure 13.3. In this reactor, microwave power is fed through a window separating the waveguide, which is normally at atmospheric pressure, from the vacuum system. If the impedance matching is good, one can feed many kilowatts of RF power in the steady state into an evacuated cavity operated at low pressure, which contains a working gas from which one wishes to form a plasma. At 2.45 GHz, the free space wavelength of the radiation is $\lambda_0 = 12.24$ cm. In a *resonant cavity reactor*, this relatively small wavelength leads to modal patterns in the electromagnetic field in the cavity, when the cavity radius and length are comparable to, or small multiples of the wavelength.

In order to decrease the surface-to-volume ratio and thereby improve confinement, as well as to avoid the formation of electromagnetic modal
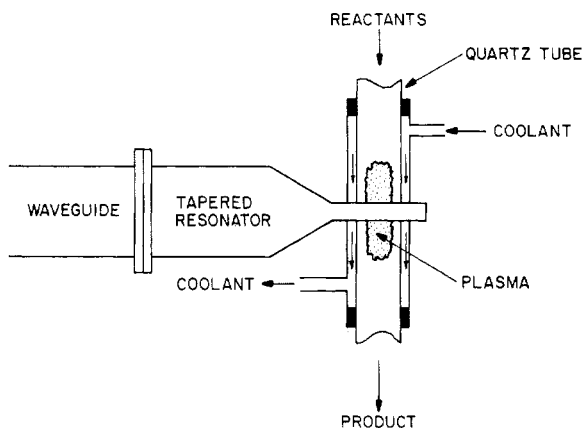
Figure 13.2 The waveguide coupled plasma reactor, used for coupling microwave power fed from the left by the waveguide, to a plasma generated in a cooled quartz tube maintained at lower pressure.

RESONANT CAVITY: $R \approx \lambda_0$; $d \approx \lambda_0$
MULTIMODE CAVITY: $R \gg \lambda_0$; $d \gg \lambda_0$
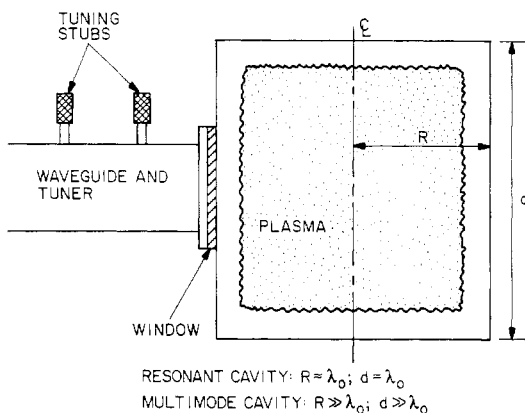
Figure 13.3 A schematic of a cylindrical cavity microwave plasma reactor. The plasma is at reduced pressure, necessitating a vacuum window for microwave power transmission. If the dimensions of the cavity are comparable to the free space wavelength, it is a resonant cavity; if its dimensions are much larger than the free space wavelength, it is a multimode cavity.

structures in the plasma volume, one may use a multimode cavity reactor like that shown in figure 13.3, in which the radius and length of the multimode cavity are sufficiently larger than the free space wavelength that modal patterns do not develop, and the microwave power is spread uniformly throughout the cavity volume, thus improving the chances of obtaining a uniform plasma.
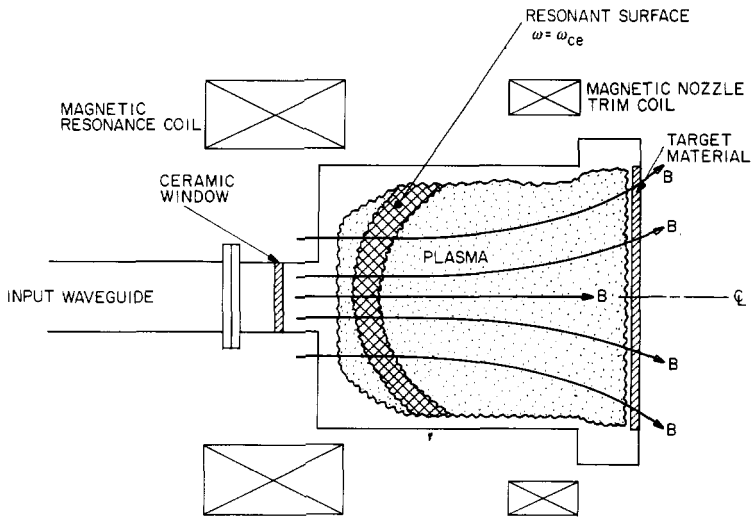
Figure 13.4 A schematic drawing of the electron cyclotron resonance (ECR) plasma reactor. In this configuration, microwave power is fed into the vacuum system through a ceramic window, and generates a plasma at the resonant surface where the external magnetic field produces electron cyclotron resonance at the frequency of the incoming microwave power. The plasma thus created on the resonance surface is guided along the magnetic field to the target material on the right.

In the last decade, industrial applications of ECR plasma reactors have developed in the field of plasma processing, using a configuration similar to that shown in figure 13.4. In this geometry, an ECR plasma is generated in a diverging magnetic field. Microwave power is fed into the geometry through a strong magnetic field generated by a surrounding coil. After passing through an impedance-matched ceramic window, as shown in figure 13.4, the microwave radiation propagates along a diverging magnetic field until it reaches a resonant surface, at which the electron cyclotron frequency in the magnetic field is equal to the frequency of the microwave input power. At that point, the feed gas will break down, and the plasma will absorb the input microwave power very strongly. The plasma generated by strong absorption at the resonant surface will continue to flow along the magnetic field lines until it interacts with a target downstream. A complete theoretical understanding of the interaction of the microwave power with a magnetized plasma below the electron plasma frequency is very involved, but ray tracing computer software is available as a spinoff of the magnetic fusion program.

13.1.4 Characteristics of Microwave Plasma Reactors

Microwave plasma reactors—and especially ECR microwave reactors—have found widespread application in microelectronic plasma processing and other industrial uses because they offer several present and potential advantages over DC and RF glow discharge reactors. Potential advantages include a large, uniform volume of plasma, desirable in plasma ion implantation and the processing of large microelectronic wafers; spatial uniformity, desirable in the above applications and in virtually all plasma processing applications; ability to operate at low pressure (below 10 mTorr), desirable when vertical etching and sputter coating are required in plasma processing; and high plasma number density, desirable when high densities or fluxes of active species are required for rapid thin film deposition, etching, or continuous flow plasma reactors, for example. At present, it is much more difficult and expensive to make ECR microwave plasmas uniform over a large surface area than RF glow discharge plasmas.

13.2 ELECTROMAGNETIC PROPAGATION IN THE COLLECTIVE REGIME

In previous chapters, we confined ourselves to studying the interaction of electromagnetic radiation with plasmas in the individual particle regime, in which the frequency of the RF electric field is less than the electron plasma frequency. In this regime, the individual electrons respond to the RF electric field, and the electron–electromagnetic field interaction is described adequately by a simple equation of motion in the form of Newton's law. This individual particle regime has, until the recent past, been adequate to describe nearly all plasma-related industrial applications of RF power, since the driving frequencies have been well below the electron plasma frequency.

In recent years, however, the availability of relatively inexpensive, high power microwave tubes has led to the introduction of plasma generation and heating methods, the frequencies of which are at or above the electron plasma frequency, in the collective interaction regime. In this regime, it is necessary not only to account for the dynamics of the electron with Newton's law, but also to incorporate Maxwell's equations, in order to describe the collective interactions of the electromagnetic wave with the plasma as a whole. These collective interactions are described by *cold plasma theory*, a field of research which has been greatly elaborated since its introduction in the late 1920's to describe the interaction of radio transmissions with the ionosphere, which is magnetized by the earth's magnetic field. Cold plasma theory is too rich and varied a subject to develop here from first principles; we will

adopt the notation, conventions, and some of the results of cold plasma theory developed by Heald and Wharton (1965).

13.2.1 Characteristics of the Theoretical Model

The equation of motion for an electron acted on by an electromagnetic wave may be written

$$F = m\frac{dv}{dt} = -eE - v_c mv - e(v \times B) \tag{13.1}$$

where m is the electron mass, v_c is the effective momentum collision frequency of the electrons, E is the electric field of the electromagnetic wave plus the effects of the surrounding plasma, and B is the static background magnetic field, when present. In the collective regime, equation (13.1) is not sufficient to describe the interaction of the electromagnetic wave with the plasma. One must also take into account Maxwell's equations, as given in equations (11.11)–(11.14). The electron motion described by equation (13.1) is linked to Maxwell's equations through the electric field E and through the electron collision frequency, which appears in the expression for the electrical conductivity in equation (11.14). The magnetic field of the electromagnetic wave is sufficiently small that it need not be taken into account in the magnetic body force term at the far right of equation (13.1).

The solution to equation (13.1) combined with Maxwell's equations can be expressed in the form of a *propagation equation* given by

$$I(z, t) = I_0 \exp(-\alpha z) \exp[j(\omega t - kz)] \tag{13.2}$$

where I_0 is the initial intensity normally incident on a plane slab in the direction z. The other parameters appearing in equation (13.2) are

$$\omega = 2\pi v \tag{13.3a}$$
$$k = 2\pi/\lambda \tag{13.3b}$$
$$\alpha = 1/\delta \tag{13.3c}$$

where the angular frequency ω is related to the frequency in hertz in equation (13.3a), the wavenumber k is given in terms of the free space wavelength in the plasma by equation (13.3b), and the attenuation coefficient α is related to the skin depth δ by equation (13.3c).

13.2.2 The Propagation Equation

Following Heald and Wharton (1965), it is often useful to define a *complex refractive index*

$$\bar{\mu} = \mu - j\chi \tag{13.4}$$

where μ is a positive definite quantity, the *real refractive index*, and χ is the *attenuation index*, with j the square root of -1. The parameter μ measures how much the electromagnetic wave is slowed down in the medium, relative to propagation in a vacuum, and the parameter χ measures how much the wave is attenuated. The relationship between the attenuation index χ and the *attenuation coefficient* α is given by

$$\alpha = \frac{\omega}{c}\chi. \tag{13.5}$$

The *propagation constant* β is related to the real refractive index μ by

$$\beta = \frac{\omega}{c}\mu. \tag{13.6}$$

13.2.3 Propagation in an Unmagnetized Plasma

Heald and Wharton describe the propagation of an electromagnetic wave in an isotropic, unmagnetized plasma in terms of the real index of refraction,

$$\mu = \left\{ \frac{1}{2}\left(1 - \frac{\omega_{pe}^2}{\omega^2 + \nu_c^2}\right) \right.$$
$$\left. + \frac{1}{2}\left[\left(1 - \frac{\omega_{pe}^2}{\omega^2 + \nu_c^2}\right)^2 + \frac{\nu_c^2}{\omega^2}\left(\frac{\omega_{pe}^2}{\omega^2 + \nu_c^2}\right)^2\right]^{1/2} \right\}^{1/2} \tag{13.7}$$

and the attenuation index,

$$\chi = \left\{ -\frac{1}{2}\left(1 - \frac{\omega_{pe}^2}{\omega^2 + \nu_c^2}\right) \right.$$
$$\left. + \frac{1}{2}\left[\left(1 - \frac{\omega_{pe}^2}{\omega^2 + \nu_c^2}\right)^2 + \frac{\nu_c^2}{\omega^2}\left(\frac{\omega_{pe}^2}{\omega^2 + \nu_c^2}\right)^2\right]^{1/2} \right\}^{1/2} \tag{13.8}$$

where ω_{pe} is the electron plasma frequency of equation (4.63), and ν_c is the electron–neutral collision frequency. Equation (13.8) illustrates the physical linkage between collisions (ν_c) and attenuation (χ). As the collision frequency becomes insignificant compared to the applied frequency ($\nu_c \ll \omega$), the attenuation index goes to zero. Without collisions ($\nu_c = 0$), equation (13.8) for χ is zero.

Plasmas encountered in industrial applications rarely have sharp boundaries, and such boundaries tend unrealistically to enhance the
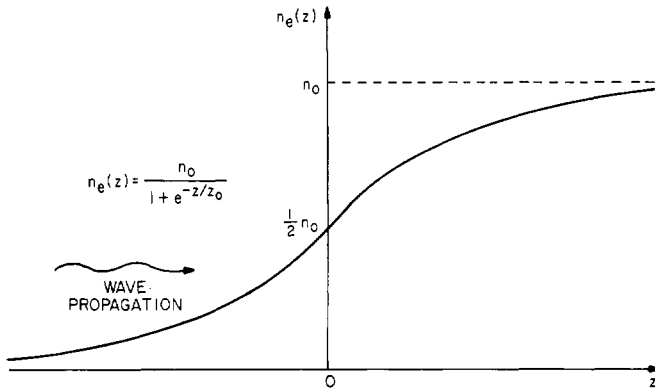
Figure 13.5 A schematic drawing of the Epstein profile, used to model an electron number density increase from zero at the far left, to n_0 at the far right.

reflected and scattered incident microwave power. In order to model a more realistic gradient of plasma number density, the *Epstein profile* is often assumed. The Epstein profile is described mathematically by

$$n_{\mathrm{e}}(z) = \frac{n_0}{1 + \exp(-z/z_0)}. \tag{13.9}$$

This function is plotted in figure 13.5. The limiting values of the electron number density for the Epstein profile are given by

$$n_{\mathrm{e}}(z = -\infty) = 0 \tag{13.10a}$$

$$n_{\mathrm{e}}(z = 0) = n_0/2 \tag{13.10b}$$

$$n_{\mathrm{e}}(z = +\infty) = n_0. \tag{13.10c}$$

The electromagnetic radiation propagates from the far left, where the electron number density is 0. The electron number density builds up to a value of $n_0/2$ at the position $z = 0$, and finally reaches the value n_0 at $z = +\infty$. The gradient scale length z_0 can be adjusted to model a very steep or a very shallow gradient. It is a characteristic of the Epstein profile that the slab of plasma between $-z_1$ and $+z_1$ has a total density given by

$$\int_{-z_1}^{z_1} n_{\mathrm{e}}(z)\,\mathrm{d}z = n_0 z_1 \qquad \text{(electrons/m}^2\text{)}. \tag{13.11}$$

13.2.4 Propagation in a Magnetized Plasma

We now consider the case in which an electromagnetic plane wave propagates at an angle θ to the magnetic induction B in an infinite,
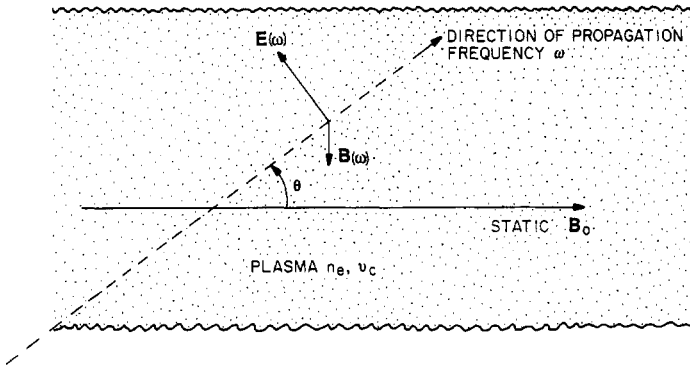
Figure 13.6 The propagation of an electromagnetic wave of frequency ω through a magnetized plasma with number density n_e and electron collision frequency ν_c, at an angle θ with respect to the magnetic induction.

homogeneous plasma, as shown in figure 13.6. The plasma has a constant number density n_e, and a collision frequency ν_c. The frequency ω of the propagating plane wave may be greater or less than the electron plasma frequency.

The complex index of refraction for the situation shown in figure 13.6 is given by *Appleton's equation*,

$$\bar{\mu}^2 = (\mu - j\chi)^2$$

$$= 1 - \frac{\omega_{pe}^2/\omega^2}{C_1 \pm C_2^{1/2}} \qquad (13.12)$$

where j is the square root of -1 and the constants are given by

$$C_1 = 1 - j\frac{\nu_c}{\omega} - \frac{(\omega_c^2/\omega^2)\sin^2\theta}{2\left[1 - (\omega_{pe}^2/\omega^2) - j\nu_c/\omega\right]} \qquad (13.13)$$

$$C_2 = \frac{(\omega_c^4/\omega^4)\sin^4\theta}{4\left[1 - (\omega_{pe}^2/\omega^2) - j\nu_c/\omega\right]^2} + \frac{\omega_c^2}{\omega^2}\cos^2\theta \qquad (13.14)$$

where ω_c is the electron gyrofrequency in the magnetic induction B, given by

$$\omega_c = \frac{eB}{m_e}. \qquad (3.18)$$

Equation (13.12) contains the angle θ as a parameter, which describes the most general case.
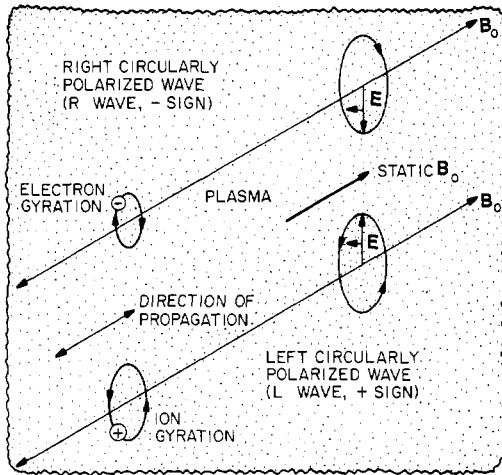
Figure 13.7 The polarization convention for parallel propagation of electromagnetic radiation in a magnetized plasma with $\theta = 0$. In the right circularly polarized wave, the electric field rotates in the direction of the electron gyration. In the left circularly polarized wave, the electric field rotates in the direction of ion gyration.

Two special cases of equation (13.12) are commonly encountered. The first of these occurs when the electromagnetic plane wave propagates along the magnetic field (*parallel propagation*), such that the angle $\theta = 0$. This case is illustrated in figure 13.7. The electric field of the electromagnetic wave can rotate either in the direction in which an electron gyrates around the magnetic field, the *right circularly polarized wave*, or *R-wave*; or in the opposite direction, the *left circularly polarized wave* or *L-wave*, the direction in which an ion would gyrate around the magnetic induction.

The real part of the complex dielectric constant for $\theta = 0$ is given by

$$\mu_{\mathrm{L,R}} = \left\{ \frac{1}{2}\left(1 - \frac{\omega_{\mathrm{pe}}^2(\omega \pm \omega_{\mathrm{c}})}{\omega\left[(\omega \pm \omega_{\mathrm{c}})^2 + \nu_{\mathrm{c}}^2\right]} \right) \right.$$
$$+ \frac{1}{2}\left[\left(1 - \frac{\omega_{\mathrm{pe}}^2(\omega \pm \omega_{\mathrm{c}})}{\omega\left[(\omega \pm \omega_{\mathrm{c}})^2 + \nu_{\mathrm{c}}^2\right]} \right)^2 \right.$$
$$\left. \left. + \left(\frac{\omega_{\mathrm{pe}}^2 \nu_{\mathrm{c}}}{\omega\left[(\omega \pm \omega_{\mathrm{c}})^2 + \nu_{\mathrm{c}}^2\right]} \right)^2 \right]^{1/2} \right\}^{1/2} \qquad (13.15)$$

where the subscripts L and R refer respectively to the left circularly polarized wave (+) and to the right circularly polarized wave (−).
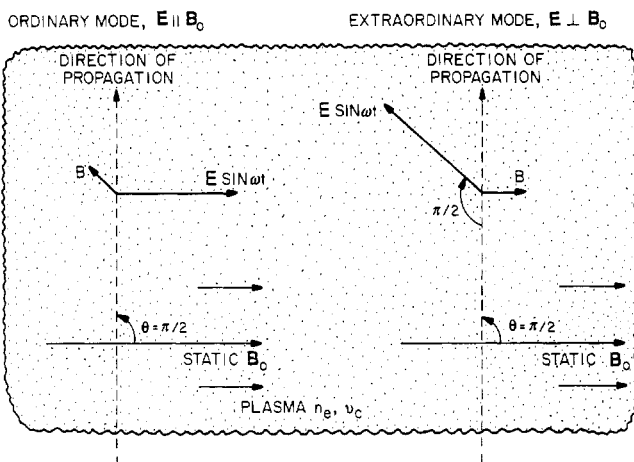
Figure 13.8   The 'mode' convention for the propagation of electromagnetic radiation. The electric field is parallel to the background magnetic induction in the ordinary mode. In the extraordinary mode, the electric field is perpendicular to the background magnetic field.

The attenuation index from the complex dielectric constant is given by

$$\chi_{L,R} = \left\{ -\frac{1}{2}\left(1 - \frac{\omega_{pe}^2(\omega \pm \omega_c)}{\omega[(\omega \pm \omega_c)^2 + \nu_c^2]} \right) \right.$$
$$+ \frac{1}{2}\left[\left(1 - \frac{\omega_{pe}^2(\omega \pm \omega_c)}{\omega\left[(\omega \pm \omega_c)^2 + \nu_c^2\right]} \right)^2 \right.$$
$$\left. \left. + \left(\frac{\nu_c \omega_{pe}^2}{\omega\left[(\omega \pm \omega_c)^2 + \nu_c^2\right]} \right)^2 \right]^{1/2} \right\}^{1/2} \tag{13.16}$$

where the subscripts L and R have the same significance for the left and right polarized wave, respectively. As in the unmagnetized case, the attenuation coefficient χ goes to zero as the collision frequency ν_c becomes small compared to the driving frequency ω, $\nu_c \ll \omega_0$. If the collision frequency is zero, there is no attenuation.

Another common situation occurs when the electromagnetic wave propagates perpendicular to the magnetic induction (*perpendicular propagation*), such that $\theta = \pi/2$. The '*mode' convention* which describes propagation perpendicular to B is illustrated schematically in figure 13.8. Here a plane electromagnetic wave propagates through a plasma from the bottom to the top of the diagram, perpendicular to the static magnetic induction B, with the propagation angle $\theta = \pi/2$.

If the electric field of the propagating wave is parallel to the magnetic induction, this is called the *ordinary mode*. This is shown on the left diagram of figure 13.8. If the electric field of the electromagnetic wave is at right angles to B, shown schematically on the right diagram in figure 13.8, this geometry is referred to as the *extraordinary mode* with the electric field of the wave perpendicular to the background magnetic field.

For propagation perpendicular to the magnetic field, the ordinary mode with $\theta = \pi/2$ gives a complex dielectric constant equal to

$$\bar{\mu}_{\text{ord}}^2 = (\mu_{\text{ord}} - j\chi_{\text{ord}})^2$$

$$= 1 - \frac{\omega_{\text{pe}}^2/\omega^2}{1 - (j\nu_{\text{c}}/\omega)}. \tag{13.17}$$

The significant feature of the ordinary wave is that its dielectric constant in equation (13.17) is not a function of the magnetic induction, which would express itself through the gyrofrequency ω_{c}. Solving for the real and imaginary parts of equation (13.17) yields the real part of the ordinary mode dielectric constant,

$$\mu_{\text{ord}} = \left\{ \frac{[(\omega^2 + \nu_{\text{c}}^2) - \omega_{\text{pe}}^2]}{2(\omega^2 + \nu_{\text{c}}^2)} \left[1 + \sqrt{1 + \frac{\nu_{\text{c}}^2 \omega_{\text{pe}}^4}{\omega^2[(\omega^2 + \nu_{\text{c}}^2) - \omega_{\text{pe}}^2]^2}} \right] \right\}^{1/2} \tag{13.18}$$

and the attenuation index for the ordinary mode given by

$$\chi_{\text{ord}} = \left\{ \frac{[(\omega^2 + \nu_{\text{c}}^2) - \omega_{\text{pe}}^2]}{2(\omega^2 + \nu_{\text{c}}^2)} \left[-1 + \sqrt{1 + \frac{\nu_{\text{c}}^2 \omega_{\text{pe}}^4}{\omega^2[(\omega^2 + \nu_{\text{c}}^2) - \omega_{\text{pe}}^2]^2}} \right] \right\}^{1/2}. \tag{13.19}$$

Comparison with equations (13.7) and (13.8) shows that these parameters are exactly the same as those of an unmagnetized plasma. Thus, the ordinary mode in a magnetized plasma propagates with the same real dielectric constant and attenuation index as it would in an unmagnetized plasma.

For the extraordinary mode of propagation, with $\theta = \pi/2$ and the electric field of the electromagnetic wave perpendicular to B, the real part of the complex dielectric constant is given by

$$\mu_{\text{ex}} = \sqrt{\frac{L + (L^2 + M^2)^{1/2}}{2}} \tag{13.20}$$

and the attenuation index for the extraordinary mode is given by

$$\chi_{\text{ex}} = \sqrt{\frac{-L + (L^2 + M^2)^{1/2}}{2}} \tag{13.21}$$

where the parameters L and M are defined as

$$L \equiv \left\{ 1 - \frac{\omega_{pe}^2[(\omega^2 - \omega_{pe}^2)(\omega^2 - \omega_{pe}^2 - \omega_c^2) + \nu_c^2\omega^2]}{\omega^2(\omega^2 - \omega_{pe}^2 - \omega_c^2 - \nu_c^2)^2 + \nu_c^2(2\omega^2 - \omega_{pe}^2)^2} \right\} \quad (13.22)$$

and

$$M \equiv \left\{ \frac{\nu_c\omega_{pe}^2[\omega_{pe}^4 + \omega^2(\omega^2 - 2\omega_{pe}^2 + \omega_c^2 + \nu_c^2)]}{\omega[\omega^2(\omega^2 - \omega_{pe}^2 - \omega_c^2 - \nu_c^2)^2 + \nu_c^2(2\omega^2 - \omega_{pe}^2)^2]} \right\}. \quad (13.23)$$

These expressions for the real dielectric constant and the attenuation index are a complicated function of four variables; the driving frequency ω; the electron plasma frequency (or electron number density) ω_{pe}; the electron cyclotron frequency (or magnetic induction), ω_c; and the electron collision frequency, ν_c. Parametric plots of the real dielectric constant and the attenuation index may be found in standard references, such as Heald and Wharton (1965) and in Stix (1962).

13.2.5 Experimental Examples

In order to provide examples of the analytical theory summarized above, two numerical examples are shown in figures 13.9 and 13.10, for the signal attenuation and phase angle as functions of electromagnetic wave frequency ν for plasma parameters characteristic of some experiments in the author's laboratory. The two curves shown in each of figures 13.9 and 13.10 were calculated by Spence (1990) for extraordinary mode propagation across the 12 cm diameter of a cylindrical plasma column in which the electron cyclotron frequency was $\nu_{ce} = 4$ GHz, and the electron plasma frequency was $\nu_{pe} = 1.0$ GHz.

These two curves have a resonance displaced from the electron gyrofrequency by about 130 MHz. This resonance is close to the upper hybrid frequency ν_{uh}, given by

$$\nu_{uh} = \sqrt{\nu_{ce}^2 + \nu_{pe}^2}. \quad (13.24)$$

The two curves shown on each of figures 13.9 and 13.10 were for electron collision frequencies at 20 MHz (1), and 40 MHz (2). The calculations shown in figures 13.9 and 13.10 were based on cold plasma theory and Appleton's equation, as discussed above.

These results indicate large attenuations in the vicinity of the upper hybrid frequency, an important characteristic of ECR heating. The two curves in figure 13.9 also illustrate the fact that in the vicinity of ν_{uh}, the attenuation becomes *greater* at *lower* collision frequencies, as a result of
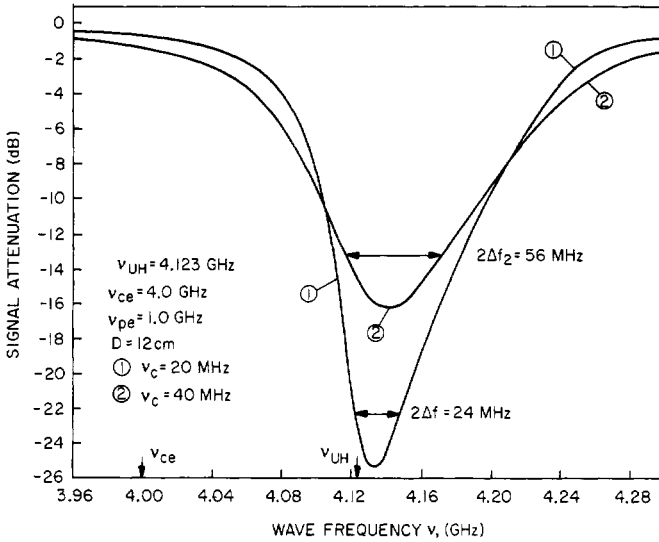
Figure 13.9 The signal attenuation for extraordinary propagation, calculated for a slab plasma of thickness 12 cm, with an electron plasma frequency of 1 GHz, an electron cyclotron frequency of 4 GHz, and two electron collision frequencies, (1) $\nu_c = 20$ MHz and (2) $\nu_c = 40$ MHz.
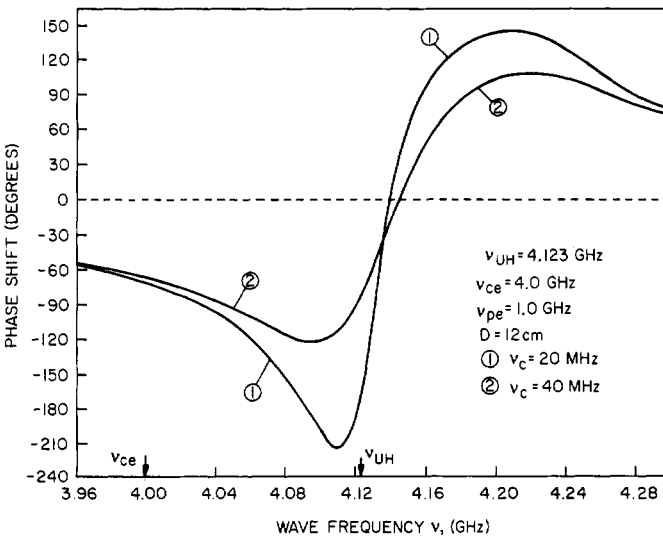
Figure 13.10 The phase shift of electromagnetic radiation for the conditions of figure 13.9 in the vicinity of electron cyclotron resonance. Note the reversal in phase of the electromagnetic wave as it passes through resonance.
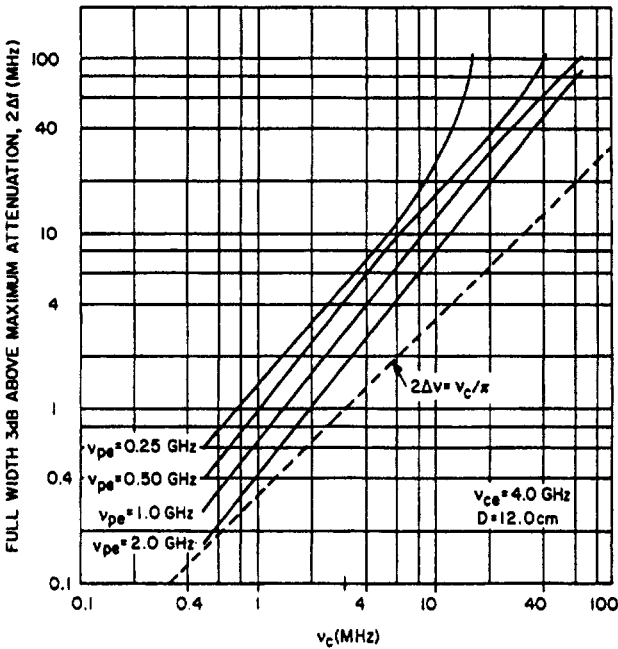
Figure 13.11 The full width 3 dB above the maximum attenuation as a function of the electron collision frequency, as calculated from cold plasma theory. The dotted line shows the simple approximation appropriate to the single-particle regime; the four solid curves were calculated in the manner of figure 13.9 from cold plasma theory for a cylindrical plasma slab 12 cm thick with an electron cyclotron frequency of 4 GHz. The parameter on these four curves is the electron plasma frequency.

cyclotron damping, the ability of the electrons to acquire more energy, achieve larger gyro radii, and fall across a larger potential difference per cycle if they collide less frequently. The full width at half maximum is indicated by the arrows, 3 dB below the maximum. Figure 13.10 shows the phase angle of the electromagnetic radiation as it goes through resonance, exhibiting the reversal in phase of driven, resonant systems.

As indicated in figure 13.9, the relationship between the half-width of the resonant absorption curve and the electron collision frequency is no longer one to one, as it was for the single-interaction result examined earlier (Roth and Spence 1987, Spence 1990). Calculations of the resonant curves have been made by Spence (1990) who found that the full width at half-maximum was a function not only of the electron collision frequency ν_c, but also of the electron plasma frequency. These curves are shown in figure 13.11, along with a dotted line which represents the previously obtained result for the single-interaction regime, $\Delta\omega = \nu_c$.

When the electromagnetic wave interacted with only single electrons in a magnetized plasma, it was shown that the collison frequency was equal to the half-width of the resonant absorption curve at the half-power point, given by

$$\nu_c = \Delta\omega = 2\pi\,\Delta\nu. \tag{13.25}$$

In terms of the frequency in hertz, the full width at half-maximum is given by

$$2\Delta\nu = \frac{\nu_c}{\pi} \quad \text{(Hz)}. \tag{13.26}$$

This equation has been plotted as the dotted line in figure 13.11, and represents a lower bound on the full width at half-maximum actually to be expected in a plasma where the frequency of propagation is above the electron plasma frequency. The curves shown in figure 13.11 allow one to measure the full width at half-maximum of the absorption peak near ν_{uh}, and from this obtain an experimental measurement of the electron collision frequency, ν_c in the collective interaction regime.

Finally, a number of experimental measurements were made of the attenuation of a cylindrical plasma column, using a network analyzer as shown schematically in figure 13.12. With this instrument, it is possible to launch an electromagnetic wave through the plasma and feed the received signal back to the network analyzer. This allows one to directly measure, among other things, the attenuation due to the plasma as a function of frequency, and the phase angle of the transmitted radiation, also as a function of frequency. Characteristic experimental data are shown in figure 13.13. Figure 13.13(a) shows the attenuation in the vicinity of the upper hybrid frequency, in this case approximately 33 dB at the maximum attenuation. Figure 13.13(b) shows the phase angle going through the resonance point, including the reversal associated with the resonant peak. This reversal occurs as the result of the inertia of the electrons. Below the resonant frequency, the electrons are in phase with the driving electromagnetic radiation, and above it they are out of phase.

13.3 MICROWAVE BREAKDOWN OF GASES

In this section, we will discuss the physical processes responsible for generating plasma as the result of applying microwave power, and the *microwave breakdown* of gases.

13.3.1 Breakdown Parameters

The breakdown of a gas by microwave radiation occurs when the rms value of the microwave electric field reaches the *breakdown electric field*
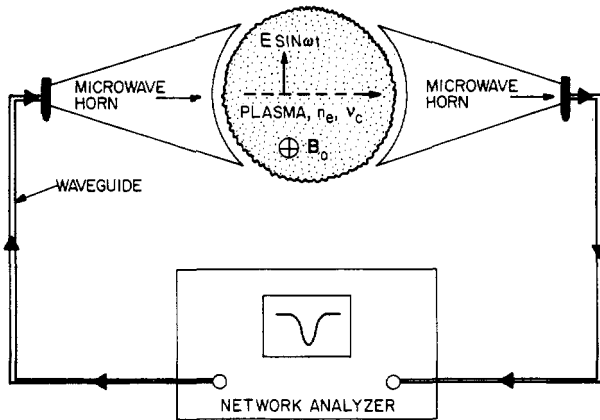
Figure 13.12 Experimental arrangement for measuring the attenuation of a cylindrical plasma in the vicinity of the electron cyclotron frequency. Microwave power is fed from a network analyzer into the left-hand horn, propagates across the cylindrical plasma into the right-hand horn, and is fed back into the network analyzer where the attenuation and phase angles are measured as a function of frequency.
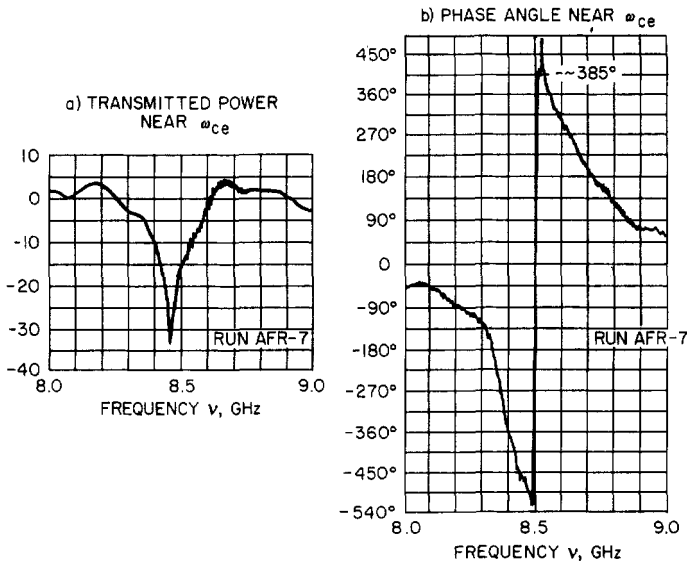
Figure 13.13 Experimental measurements of the transmitted power and the phase angle of the radiation near the electron cyclotron frequency made with the experimental set-up shown in figure 13.12. Approximately 30 dB of attenuation were measured near resonance, with a significant change in phase angle as the plasma passed through its resonant frequency shown on the right.

given by

$$E_b = E_{0b}/\sqrt{2} = \tilde{E} \qquad (V/m) \qquad (13.27)$$

where E_b is the rms breakdown electric field, E_{0b} is the peak electric field of the electromagnetic radiation, and the tilda over the electric field indicates an rms value.

In order to remove the effect of the applied frequency ω, it is useful to define an approximately frequency-independent *effective electric field* which is related to the actual electric field E, given by

$$E_{eff}^2 = \tilde{E}^2 \frac{\nu_c^2}{\omega^2 + \nu_c^2} \qquad (13.28)$$

which is the value appropriate to a collisional, unmagnetized plasma. If the microwave discharge is in a magnetic induction with electron gyrofrequency ω_c, and has an excitation frequency ω, the effective electric field which removes the effects of both the microwave frequency and the magnetic field with its resonance at ω_c, is given by

$$E_{eff}^2 = \tilde{E}^2 \frac{\nu_c^2}{2} \left[\frac{1}{(\omega + \omega_c)^2 + \nu_c^2} + \frac{1}{(\omega - \omega_c)^2 + \nu_c^2} \right] \qquad (13.29)$$

where $\tilde{E}$ is the rms electric field of the electromagnetic radiation. These effective electric fields may or may not be identified with the breakdown electric field indicated in equation (13.27).

In this chapter it is necessary to discuss concurrently the free-space wavelength of the microwave radiation, and the mean free path of the electrons, both usually designated by the greek lower case lambda. To avoid confusion, we use λ for the free-space wavelength, and ℓ for the electron mean free path.

The *free-space wavelength* of the microwave radiation is given by

$$\lambda = \frac{c}{\nu} = \frac{2\pi c}{\omega} \qquad (m) \qquad (13.30)$$

where ν is the frequency in hertz, ω is the frequency in radians per second, and c is the speed of light in vacuum.

Another parameter important to microwave breakdown of a gas is the *electron mean free path*, ℓ,

$$\ell = \frac{\bar{v}_e}{\nu_c} = \frac{\bar{v}_e}{n_0 \langle \sigma v \rangle_c} \sim \frac{f(T_e)}{p} \qquad (m) \qquad (13.31)$$

which is equal to the electron mean thermal velocity, divided by the product of the neutral number density and the reaction rate coefficient.

The reaction rate coefficient contains the collision cross section averaged over a Maxwellian distribution of electron velocities. As indicated in equation (13.31), the mean free path is proportional to a (usually) slowly varying function of electron kinetic temperature, divided by the background neutral gas pressure. Another critical parameter for the microwave breakdown of a gas is the *ionization potential* of the gas, which determines the energy the electrons must have to produce ionization. A final parameter which is important in determining the microwave breakdown of gases is the *characteristic diffusion length*, Λ, which is the characteristic distance over which a particle must diffuse in order to be lost from the plasma.

A requirement for the generation of a microwave discharge is that the electromagnetic field have an rms electric field greater than the breakdown value, which can be written in the following functional form:

$$E_b = E(\lambda, V_i, \ell, \Lambda) \qquad (V/m) \qquad (13.32)$$

where E_b is the breakdown electric field, λ is the free space wavelength, V_i is the ionization potential of the gas in electronvolts, ℓ is the electron mean free path in meters, and Λ is the *characteristic diffusion length*. These five variables contain only two independent dimensions: length, and voltage (electronvolts have the dimension of voltage). With five variables and two independent dimensions, Buckingham's Pi theorem (Buckingham 1914, Bridgman 1963, and Samaras 1971) states that three dimensionless variables are sufficient to describe the relationship implied by equation (13.32).

Two possible sets of three such dimensionless variables which may be written are, following MacDonald (1966),

$$\frac{E\Lambda}{V_i}, \frac{\lambda}{\ell}, \frac{\Lambda}{\ell} \qquad (13.33a)$$

or

$$\frac{E\lambda}{V_i}, \frac{E\ell}{V_i}, \frac{\lambda}{\Lambda}. \qquad (13.33b)$$

An implication of equation (13.32) and Buckingham's Pi theorem is that it requires a three-dimensional surface to specify the RF and microwave breakdown conditions of a gas; the axes describing these three-dimensional surfaces would be the dimensionless parameters specified in equation (13.33a) or (13.33b). Radio frequency breakdown of a gas is therefore more difficult to describe parametrically than DC breakdown, for which λ is not necessary and only a two-dimensional graph is required, in the form of the universal Paschen curve.

The dimensionless parameters specified in equation (13.33a) and (13.33b) are often not convenient, and therefore common practice in

the field of microwave discharges has come to use so-called 'proper' variables. These *proper variables* are based on the fact that the mean free path of the electrons in a neutral gas is inversely proportional to the gas pressure, as implied by equation (13.31),

$$\ell \sim \frac{1}{p} \tag{13.34a}$$

and that, for a given gas, the ionization potential is a constant,

$$V_i \approx \text{constant.} \tag{13.34b}$$

The use of relations (13.34a) (13.34b) in the dimensionless ratios of equation (13.33) leads to the following dimensional *proper variables*,

$$E\Lambda, \; p\lambda, \; p\Lambda \tag{13.35a}$$

and

$$E\lambda, \; E/p, \; \lambda/\Lambda. \tag{13.35b}$$

It is these parameters which are usually used in the literature of microwave breakdown of gases.

13.3.2 Breakdown in Unmagnetized Plasma

In an unmagnetized microwave discharge, the continuity equation for the electron population may be written

$$\frac{\partial n_e}{\partial t} = P - A - \nabla \cdot \Gamma. \tag{13.36}$$

P is the electron production rate by ionization, and is given by

$$P = n_e \nu_i = n_e n_0 \langle \sigma \upsilon \rangle_{\text{ne}} \qquad (\text{electrons/m}^3\text{-s}) \tag{13.37}$$

where ν_i is the ionization frequency, and the Maxwellian averaged ionization rate coefficient has been used in the right-hand member of the equation. The electrons may be lost by attachment to the neutral gas, at a rate which is given by

$$A = n_e \nu_a = n_e n_0 \langle \sigma \upsilon \rangle_a \qquad (\text{electrons/m}^3\text{-s}) \tag{13.38}$$

where ν_a is the attachment frequency. The final divergence term in equation (13.36) may be written in terms of a time- and space-averaged

$$1/\Lambda^2 = (\pi/d)^2 \qquad \text{PLASMA}$$

O   d   z
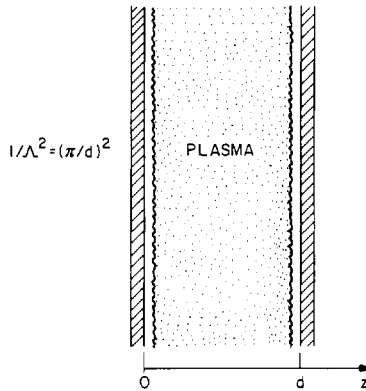
Figure 13.14 The effective diffusion length of a plasma slab of width d.

diffusion coefficient D and the electron number density, using *Fick's Law of Diffusion*,

$$\Gamma = -D\nabla n_e. \tag{13.39}$$

If equations (13.37)–(13.39) are substituted into equation (13.36), the equation of continuity becomes

$$\frac{\partial n_e}{\partial t} = n_e (v_i - v_a) + D\nabla^2 n_e. \tag{13.40}$$

We now divide equation (13.40) by the electron number density, and perform a separation of variables, to obtain

$$\frac{1}{n_e}\frac{\partial n_e}{\partial t} - (v_i - v_a) = \frac{D\nabla^2 n_e}{n_e} = -\frac{D}{\Lambda^2}. \tag{13.41}$$

The first member of equation (13.41) is assumed to be independent of position, and the second member is assumed to be independent of time. Under this separation of variables, the first two members of equation (13.41) are equal to a constant, which we take to be the diffusion coefficient divided by the square of the characteristic diffusion length Λ, the spatial eigenvalue for the problem.

The two right-hand members of equation (13.41) may be written in the form

$$\nabla^2 n_e + \frac{n_e}{\Lambda^2} = 0. \tag{13.42}$$

In the slab plasma of thickness d shown in figure 13.14, a solution to equation (13.42) for the electron number density is

$$n_e = n_{e0}\sin\frac{\pi z}{d} \tag{13.43}$$
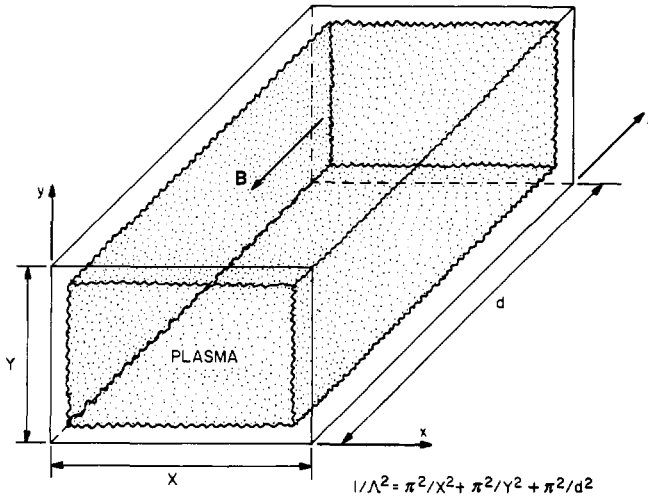
Figure 13.15 The effective diffusion length of a rectangular plasma slab with dimensions X, Y, and thickness d in the z direction.

where n_{e0} is the maximum density at the center of the slab. Substituting equation (13.43) into equation (13.42) yields the characteristic diffusion length for this geometry,

$$\frac{1}{\Lambda^2} = \frac{\pi^2}{d^2}. \tag{13.44}$$

In a Cartesian coordinate system, a rectangular prismatic plasma like that shown in figure 13.15 has a solution for the electron number density given by

$$n_e = n_{e0} \sin \frac{\pi x}{X} \sin \frac{\pi y}{Y} \sin \frac{\pi z}{d} \tag{13.45}$$

where n_{e0} is the maximum electron number density in the middle of the plasma. The characteristic diffusion length is found by substituting equation (13.45) into (13.42), to yield

$$\frac{1}{\Lambda^2} = \left(\frac{\pi}{X}\right)^2 + \left(\frac{\pi}{Y}\right)^2 + \left(\frac{\pi}{d}\right)^2 \tag{13.46}$$

where d is the thickness of the plasma in the z direction, and X and Y are its dimensions in the x and y directions, respectively. If this rectangular plasma has a magnetic induction in the z direction, diffusion in the x and y direction is reduced, effectively increasing the dimensions of the plasma normal to $\mathbf{B}$. With a magnetic field along the axis of the rectangular plasma in figure 13.15, the characteristic diffusion length is given by

$$\frac{1}{\Lambda^2} = \left(\frac{1}{X^2} + \frac{1}{Y^2}\right) \frac{\pi^2 \nu_c^2}{\nu_c^2 + \omega_c^2} + \frac{\pi^2}{d^2}. \tag{13.47}$$

$1/\Lambda^2 = (2.405/R)^2 + (\pi/d)^2$
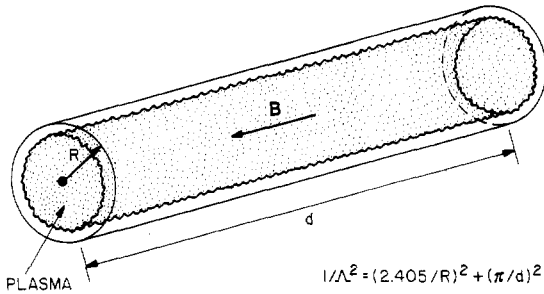
Figure 13.16 The effective diffusion length of a cylindrical plasma of radius R and axial length d, with an axial magnetic induction B.

In a cylindrical plasma of radius R shown in figure 13.16, a solution to equation (13.42) for the electron number density is given by

$$n_e = n_{e0} \sin \frac{\pi z}{d} J_0 \left(\frac{2.405 r}{R} \right). \tag{13.48}$$

J_0 is the zero-order Bessel function, and n_{e0} is the maximum electron number density along the axis of the plasma. Substituting equation (13.48) into equation (13.42) yields the characteristic diffusion length for the cylindrical geometry,

$$\frac{1}{\Lambda^2} = \left(\frac{\pi}{d} \right)^2 + \left(\frac{2.405}{R} \right)^2. \tag{13.49}$$

If a magentic induction is applied along the axis of the cylindrical plasma, the radial diffusion is reduced, and the effective radius increases, giving rise to a characteristic diffusion length for the magnetized cylindrical plasma of

$$\frac{1}{\Lambda^2} = \left(\frac{2.405}{R} \right)^2 \frac{v_c^2}{v_c^2 + \omega_c^2} + \frac{\pi^2}{d^2}. \tag{13.50}$$

In the cylindrical plasma, the presence of a magnetic field increases the effective radius of the plasma across which the particles have to diffuse. This increased effective radius is given by

$$R_{\text{eff}} = R \sqrt{1 + \frac{\omega_c^2}{v_c^2}}. \tag{13.51}$$

and a similar relationship applies to the transverse dimensions of the rectangular plasma in figure 13.15.

Substituting equation (13.42) into equation (13.40) yields the transformed continuity equation,

$$\frac{\partial n_e}{\partial t} = \left(\nu_i - \nu_a - \frac{D}{\Lambda^2} \right) n_e. \tag{13.52}$$

In the steady state, the time derivative on the left is zero, yielding a condition for a steady-state equilibrium,

$$(\nu_i - \nu_a) = \frac{D}{\Lambda^2}. \tag{13.53}$$

When the electron number density is time dependent, as it is during the process of microwave breakdown, a solution to equation (13.52) is given by

$$n_e = n_{e0} \exp \left[\left(\nu_i - \nu_a - \frac{D}{\Lambda^2} \right) t \right]. \tag{13.54}$$

In the absence of attachment, this equation becomes

$$\approx n_{e0} \exp \left[\left(\nu_i - \frac{D}{\Lambda^2} \right) t \right]. \tag{13.55}$$

Equations (13.54) and (13.55) predict an exponentially increasing electron number density during microwave breakdown. This exponentiation of the electron number density will begin when the argument of the exponential becomes even slightly positive. The *breakdown condition* occurs when the argument of the exponential in equations (13.54) or (13.55) is equal to zero, which, in the absence of attachment, yields the breakdown condition

$$\nu_i = \frac{D}{\Lambda^2}. \tag{13.56}$$

This is equivalent in microwave discharges to the Townsend breakdown condition discussed for dark DC electrical discharges.

Having derived the microwave breakdown condition of equation (13.56), we are now in a position to estimate the breakdown electric field in the high and low pressure limits. We first consider the high pressure, collision-dominated limit, for which the collision frequency, ν_c, is much greater than the driving RF frequency ω. In the high pressure limit of a Lorentzian plasma, the electron will lose in a single collision all of the kinetic energy in the direction of the electric field which it gained between collisions. In order to break down the gas, an individual electron must absorb enough energy from the electric field, between collisions, to ionize the background neutral gas. The power absorbed by a *single*

electron in an RF electric field with the frequency ω is given by the following modification of equation (12.14),

$$p = \frac{e^2 E_0^2}{2 m \nu_c} \left(\frac{\nu_c^2}{\nu_c^2 + \omega^2} \right) \qquad (W). \qquad (13.57)$$

The energy absorbed from the RF electric field by the electron between collisions is given by multiplying the power of equation (13.57) by the time, τ_c, between collisions,

$$E_a = p \tau_c = \frac{p}{\nu_c} = \frac{e^2 E_0^2}{2 m \nu_c^2} \left(\frac{\nu_c^2}{\nu_c^2 + \omega^2} \right) \qquad (J). \qquad (13.58)$$

At high pressures, when $\nu_c \gg \omega$, equation (13.58) becomes equivalent to

$$E_a \approx \frac{e^2 E_0^2}{2 m \nu_c^2} \qquad \nu_c \gg \omega. \qquad (13.59)$$

This energy acquired from the RF electric field must go into ionizing the gas, in order to to maintain the discharge in the steady state.

The process of transferring the energy of an electron to neutral particles is very inefficient because of their large mass difference. It has been shown (McDaniel 1964) that the fraction of the ionization energy imparted by an electron of mass m to neutral particles of mass M is given by

$$E_c = \frac{2 m M e V_i}{(m + M)^2} \approx \frac{2 m e V_i}{M} \qquad M \gg m. \qquad (13.60)$$

To maintain the discharge, the electrons must reach the ionization energy V_i, and the energy absorbed by the electron from the electric field between collisions, given by equation (13.59), must be equal to or greater than the energy imparted by the same electron to the neutral particles of mass M, given by equation (13.60). Equating (13.59) and (13.60), one obtains

$$E_a \approx \frac{e^2 E_{0c}^2}{2 m \nu_c^2} = E_c = \frac{2 m e V_i}{M}. \qquad (13.61)$$

The rms value of the critical electric field for breakdown may be found by solving equation (13.61), to obtain

$$\tilde{E}_c = \frac{E_{0c}}{\sqrt{2}} = m \nu_c \sqrt{\frac{2 V_i}{e M}} \approx C_1 p. \qquad (13.62)$$

Thus, at high gas pressures in the collisional limit, the breakdown electric field is directly proportional to the neutral gas pressure, since the

collision frequency for the electrons is a linear function of pressure for most gases.

At the opposite, collisionless limit at low pressures, for which the driving frequency is much greater than the collision frequency, all the input power goes into ionization, since the electron will presumably have enough time to acquire energy at least equal to the ionization potential, V_i of the neutral gas. If all of the input power goes into ionization, the input power may be written

$$p = \nu_i e V_i \quad \text{(W)}. \tag{13.63}$$

Solving equation (13.63) for the ionization frequency, and substituting equation (12.14) for the RF power input into an unmagnetized plasma, one obtains

$$\nu_i = \frac{p}{eV_i} = \frac{eE_{0c}^2}{2mV_i\nu_c}\left(\frac{\nu_c^2}{\nu_c^2 + \omega^2}\right). \tag{13.64}$$

In the collisionless limit for which $\omega \gg \nu_c$, equation (13.64) becomes

$$\nu_i \approx \frac{eE_{0c}^2\nu_c}{2mV_i\omega^2} = \frac{D}{\Lambda^2}. \tag{13.65}$$

The last member of equation (13.65) has been obtained from the breakdown condition, equation (13.56).

The diffusion coefficient appearing in equation (13.65) may be written using the kinetic theory results discussed in Chapter 2, equation (2.36):

$$D = \frac{1}{3}\ell\bar{v} = \frac{\bar{v}^2}{3\nu_c} = \frac{8eT_e'}{3\pi\nu_c m} \tag{13.66}$$

where $\bar{v}$ is the mean thermal velocity and T_e' is a characteristic energy, in eV, of the electron population. Substituting equation (13.66) into the breakdown condition of equation (13.56) yields the ionization frequency

$$\nu_i = \frac{8eT_e'}{3\pi\nu_c m\Lambda^2}. \tag{13.67}$$

Equating the ionization frequency from equation (13.65) to that from kinetic theory arguments in equation (13.67), one obtains

$$\frac{eE_{0c}^2\nu_c}{2mV_i\omega^2} = \frac{8eT_e'}{3\pi m\nu_c\Lambda^2}. \tag{13.68}$$

Solving equation (13.68) for the rms breakdown electric field yields

$$\tilde{E}_c = \frac{E_{0c}}{\sqrt{2}} = \frac{4c}{\nu_c\lambda\Lambda}\sqrt{\frac{2\pi V_i T_e'}{3}} \tag{13.69}$$
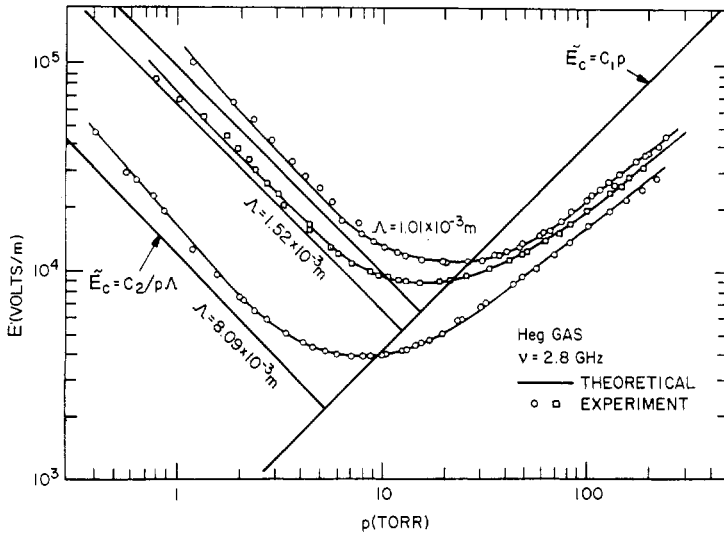
Figure 13.17 The microwave breakdown electric field as a function of the pressure in torr for Heg gas at a frequency of 2.8 GHz. The theoretical comparison drawn through the experimental points is taken from MacDonald (1966). The solid straight lines are based on the approximations given in equations (13.62) and (13.70).

where the driving frequency ω has been written in terms of the speed of light divided by the free space wavelength of the radiation. Because the electron collision frequency in the denominator is proportional to the neutral gas pressure, the rms breakdown electric field may be written

$$\tilde{E}_c \sim \frac{C_2}{\Lambda p}. \tag{13.70}$$

This equation predicts an inverse dependence on background neutral gas pressure in the long mean free path, collisionless regime.

It is of interest to compare the theoretical relationships discussed above with experimental data. Good sources of such data are MacDonald (1966) and MacDonald and Tetenbaum (1978). The best agreement between theory and experiment has been obtained for helium with a small admixture of mercury, Heg gas, in which all inelastic collisions are ionizing collisions with mercury at the metastable energy level of helium, 19.8 eV. On figure 13.17 is plotted some experimental data (with a detailed theoretical comparison) for the critical breakdown electric field in Heg gas, as a function of the background gas pressure, from MacDonald (1966). These data were taken at 2.8 GHz, for three values of the characteristic diffusion length shown as a parameter on the curves.

The experimental data show a characteristic behavior expected from the functional dependences indicated in equations (13.62) and (13.70); an inverse dependence on pressure at low pressures, and a direct linear proportionality to pressure at high pressures. The minimum in the experimental data occurs when the physical processes which are dominant at either limit of the pressure range are of equal effect. The microwave breakdown curves are sometimes less smooth than that of figure 13.17, as the result of excitation and other inelastic processees, but the general shape tends to hold true of all gases. These curves are the high frequency analog of the Paschen curve for DC discharges, just as equation (13.56) for the breakdown criterion is the analog of the Townsend criterion of equation (8.136). The solid line through the experimental data in figure 13.17 is the prediction of a detailed theoretical model (MacDonald 1966).

It is of interest to compare these experimental data for Heg gas with the relatively crude analysis which led to equations (13.62) and (13.70). In evaluating these expressions for the critical electric field, one needs the collision frequency as a function of pressure for the gases involved. For two of the principal gases encountered in microwave discharges, MacDonald and Tetenbaum (1978) give for helium gas,

$$\nu_c = 2.37 \times 10^9 \, p(\text{Torr}) \qquad (\text{Hz}) \qquad (13.71a)$$

while Brown (1966) gives for air,

$$\nu_c = 5.3 \times 10^9 \, p(\text{Torr}) \qquad (\text{Hz}). \qquad (13.71b)$$

The collision frequencies for other gases are given in table 4.3, from Vidmar (1991). For the above two gases, and over the ranges of electron temperature commonly encountered, these collision frequencies are virtually independent of electron kinetic temperature and other plasma-related parameters.

Since the collision frequency of an electron in Heg gas is determined by the dominant helium background gas, equation (13.71a) can be used to provide a quantitative estimate of the collision frequency required in equations (13.62) and (13.70). If we use an ionization potential of $V_i = 19.8$ eV for Heg gas, since this metastable state is responsible for ionizing the trace amount of mercury in the gas, the constant C_1 appearing in equation (13.62) can be evaluated and is

$$C_1 = 416 \text{ V/m-Torr}. \qquad (13.72)$$

Similarly, the constant C_2 can be evaluated on the additional assumption that the thermal energy, T_e', of the electrons is half the ionization potential of 19.8 eV. This assumption yields

$$C_2 = 95.8 \text{ V/m-Torr}. \qquad (13.73)$$

If the constants C_1 and C_2 are used in conjunction with equations (13.62) and (13.70), the dependence of the mean breakdown electric field can be plotted as the heavy straight lines in figure 13.17 for Heg gas. This crude theory is in relatively good agreement with the experimental data, both as to magnitude, and the functional dependence on pressure, although it is clear that the required magnitude of the electric field is lower than that predicted by equation (13.62) at high pressures by a factor of approximately 3 in the highly collisional regime.

By equating equation (13.62) to equation (13.69), one may obtain a condition for the minimum of the microwave breakdown curve, corresponding to the Paschen minimum for DC electrical discharges, given by

$$m v_c \sqrt{\frac{2V_i}{eM}} = \frac{4c}{v_c \lambda \Lambda} \sqrt{\frac{2\pi V_i T_e'}{3}}. \qquad (13.74)$$

Solving this equation for the collision frequency at the minimum breakdown electric field, one obtains

$$v_{c,\text{min}} = 2\sqrt{\frac{v}{m\Lambda}} \left(\frac{\pi M e T_e'}{3}\right)^{1/4}. \qquad (13.75)$$

From this minimum collision frequency, using empirically determined expressions like equations (13.71a) and (13.71b), one can obtain the pressure at which a gas may be most readily broken down. The minimum
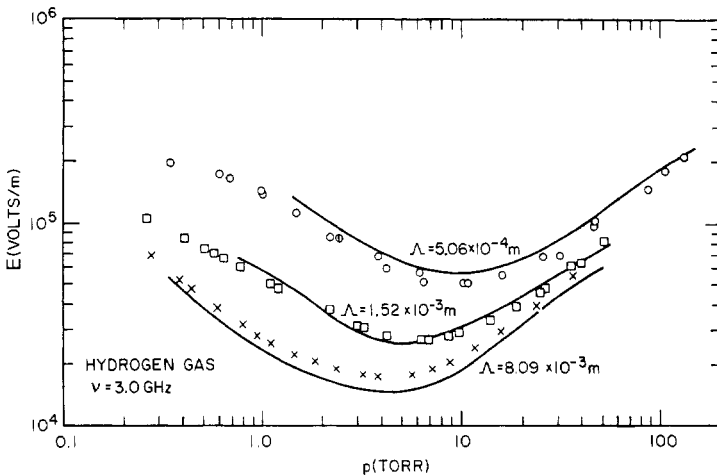
Figure 13.18 Experimental data on microwave breakdown in hydrogen gas at a frequency of 3.0 GHz for three values of the effective diffusion length, taken from MacDonald and Brown (1948).
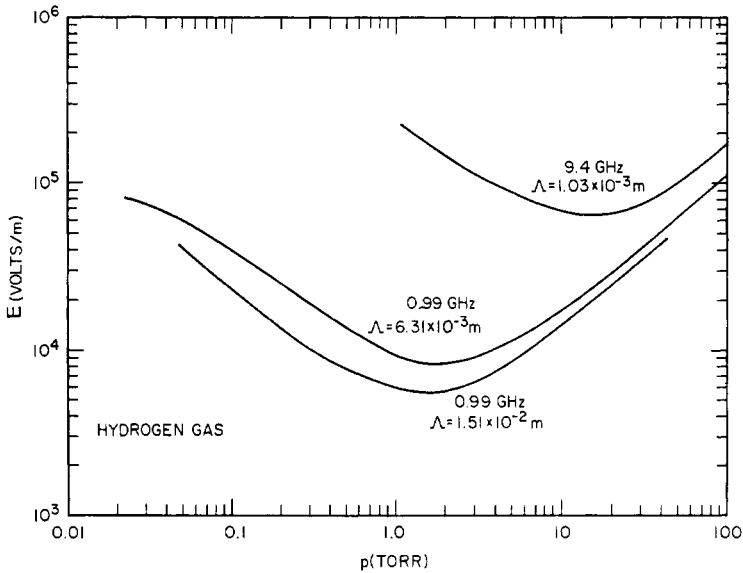
Figure 13.19 The breakdown microwave electric field, from MacDonald (1966), as a function of the pressure in torr for microwave frequencies of 0.99 and 9.4 GHz, and two values of the effective diffusion length, Λ, in hydrogen gas.

breakdown electric field can be obtained by substituting equation (13.75) into either equation (13.62) or equation (13.70), to obtain,

$$\tilde{E}_{c,min} = m\nu_{c,min}\sqrt{\frac{2V_i}{eM}}.\qquad(13.76)$$

Substituting equation (13.75) into equation (13.76), one obtains the minimum value of the microwave breakdown electric field, given by

$$\tilde{E}_{c,min} = 2\sqrt{\frac{2\nu V_i m}{e\Lambda M}}\left(\frac{\pi M e T'_e}{3}\right)^{1/4}.\qquad(13.77)$$

This minimum breakdown electric field is a function of: the free space wavelength (or the microwave frequency ν); the ionization potential of the gas, V_i; the effective diffusion length Λ; the electron and ion masses; and the mean thermal energy of the electron population.

Much data have been taken concerning the microwave breakdown properties of various gases, particularly the noble gases helium, neon, argon, krypton, and xenon, since their collisional cross sections (and hence their electron–neutral collision frequencies) are relatively
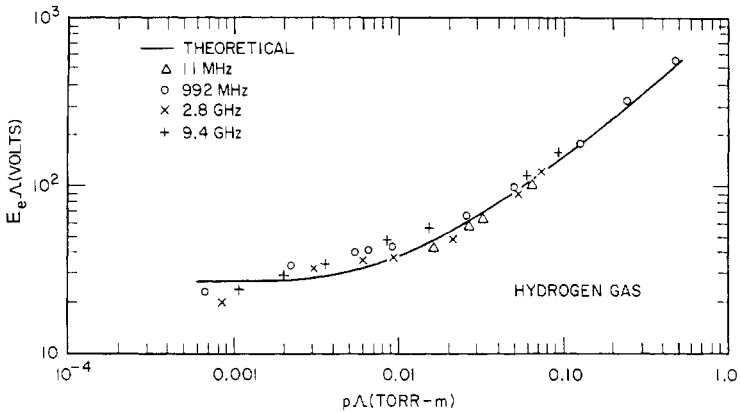
Figure 13.20 The product of pressure in torr and the effective diffusion length for hydrogen gas. The data from several frequencies fall along a common curve when plotted as a function of these proper variables. Data from MacDonald (1966).
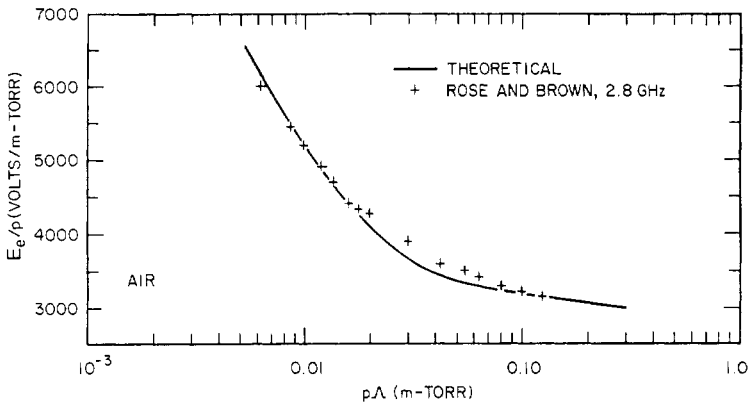
Figure 13.21 Effective breakdown electric field as a function of proper variables for air, from Rose and Brown (1957).

independent of electron kinetic temperature. Much attention also has been given to the microwave breakdown properties of air, because of the importance of such data to the operation of radar and high frequency communication systems in the atmosphere, particularly at high altitudes.

In figure 13.18 are shown some experimental data for the breakdown electric field at 3.0 GHz in hydrogen gas, for three values of the effective diffusion length Λ, taken from MacDonald and Brown (1949). Figure 13.19, from MacDonald (1966), illustrates the effect of varying the microwave frequency by a factor of 10 on the microwave breakdown of hydrogen gas. The lower frequencies tend to break down at lower

pressures and lower electric field strengths. Figure 13.20, also from McDonald (1966) illustrates how, for hydrogen gas, the use of proper variables can allow one to plot breakdown data over a wide range of frequencies on the same graph. The ordinate is plotted in terms of the effective electric field given by equation (13.28). In figure 13.20, the breakdown of hydrogen at frequencies from 11 MHz to 9.4 GHz—nearly a factor of 1000—is adequately described by the same breakdown theory, even at frequencies in the individual particle, capacitive RF discharge regime. There exists an extensive literature on high frequency and microwave breakdown of gases, which has been summarized by MacDonald (1966), and by MacDonald and Tetenbaum (1978).

13.3.3 Breakdown With Attachment

Several gases of industrial interest, including air, chlorine, and sulfur hexafluoride, exhibit the phenomenon of *attachment*, whereby electrons in the gas will attach themselves to a molecule of the background gas. This process is exemplified by electron attachment to oxygen in air,

$$e + O_2 \rightarrow O_2^-. \tag{13.78}$$

When electron attachment is present, it represents a process in addition to diffusion to the walls which is responsible for electron loss. From equation (13.54), the breakdown condition when attachment is present is given by

$$\nu_i = \nu_a + \frac{D_e}{\Lambda^2} \tag{13.79}$$

where the ionization frequency ν_i, or the attachment frequency ν_a, or their difference, must be determined experimentally. On figure 13.21 are shown the effective breakdown electric field, plotted in units of E/p against the product $p\Lambda$ for air. A theory developed by Rose and Brown (1957) is compared with some of their own experimental data in this figure, in which the effective electric field on the ordinate is given by equation (13.28).

13.3.4 Steady-State Microwave Discharges

Once a gas breaks down, the diffusion coefficent is no longer the free electron diffusion value D_e, but becomes smaller than this, due to ambipolar electric fields which tend to keep the electrons electrostatically confined in the plasma. This electrostatic containment greatly reduces the ionization frequency required to maintain the ionization of the plasma, compared to the electric field required to break down the gas in the first place. This lessened requirement for microwave electric field strength
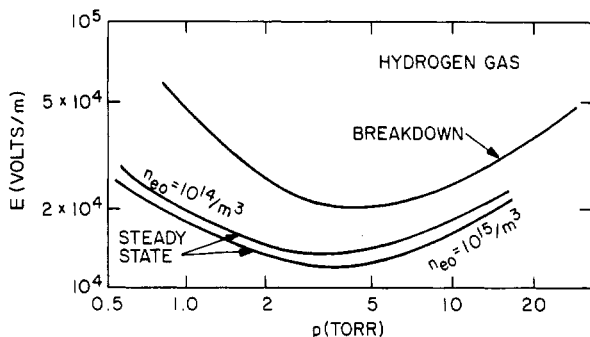
Figure 13.22 The steady-state and breakdown microwave electric field for hydrogen gas as a function of pressure in torr, taken from Brown (1966).
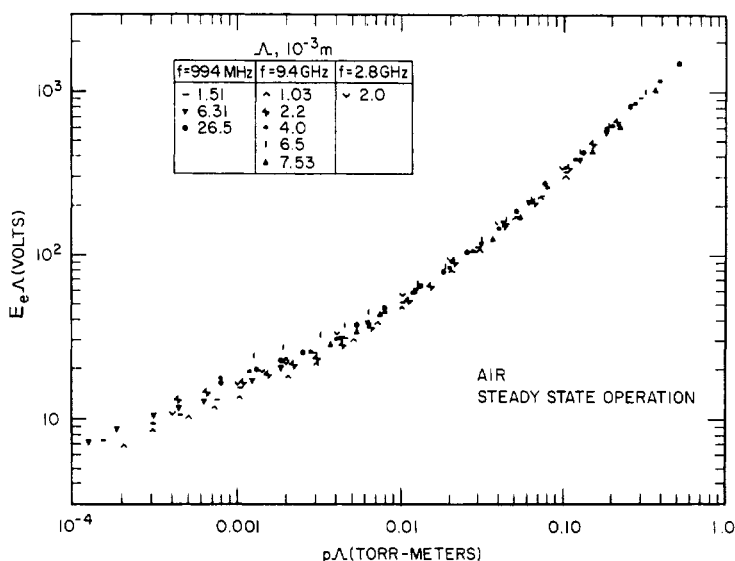
Figure 13.23 Data from MacDonald *et al* (1963) for steady state microwave discharges in air, plotted in proper variables for a range of effective diffusion lengths and microwave frequencies.

is illustrated by some data published by Brown (1966) which is shown in figure 13.22 for hydrogen gas. The upper curve is the electric field required for breakdown; the lower two curves are the electric fields required to maintain a steady-state microwave discharge in hydrogen at the maximum electron number densities indicated on the two curves. In this case, the required electric field is approximately a factor of three or four less than that of breakdown to maintain the steady state, and the minimum of the breakdown curve has been shifted to lower pressures by

a factor of approximately two.

If the ambipolar diffusion coefficient D_a is dominant in the steady-state, then equation (13.54) can be written

$$n_e = n_{e0} \exp\left[\left(\nu_i - \nu_a - \frac{D_a}{\Lambda^2}\right)t\right].$$ (13.80)

The condition required to maintain a steady state in the discharge is that the argument of the exponential is equal to zero,

$$(\nu_i - \nu_a) = \frac{D_a}{\Lambda^2}.$$ (13.81)

Using equation (4.104) for the ambipolar diffusion coefficient, and Einstein's relation between the diffusion coefficients and mobilities of ions and electrons, the relationship between the ambipolar and electron diffusion coefficients is given by

$$D_a \approx \frac{D_i T_e}{D_e T_i}\left(\frac{T_i}{T_e} + 1\right)D_e \approx \frac{\mu_i}{\mu_e}D_e.$$ (13.82)

In typical microwave discharges, the ion kinetic temperature is far less than the electron kinetic temperature, and the ion mobility is much less than that of the electrons because of its higher mass. Under these conditions, the steady-state breakdown condition combining equation (13.81) and the right-hand member of equation (13.82) becomes

$$(\nu_i - \nu_a) \approx \frac{\mu_i}{\mu_e}\frac{D_e}{\Lambda^2}.$$ (13.83)

The data of Brown (1966) in figure 13.22 indicates that the effect of ambipolarity on the breakdown condition is not as large as equation (13.83) predicts, but it does result in a significant decrease in the electric field required to maintain the discharge, as compared with the electric field required to break the gas down initially.

In figure 13.23 are shown the product of the effective electric field of equation (13.28) and the characteristic diffusion length Λ plotted against the product of the pressure and the characteristic diffusion length for air in steady-state operation, taken from the work of McDonald *et al* (1963). These data show that using the effective electric field, and plotting the data in terms of 'proper' parameters, reduces a wide variety of data taken at three different frequencies and a variety of characteristic diffusion lengths to a single plot.
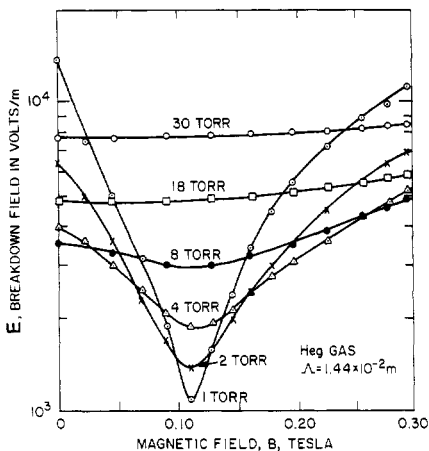
Figure 13.24 Data taken from the experiments of Lax *et al* (1950), showing the breakdown electric field in Heg gas as a function of magnetic induction for several pressures. The resonance near the electron cyclotron frequency is evident at low pressures.
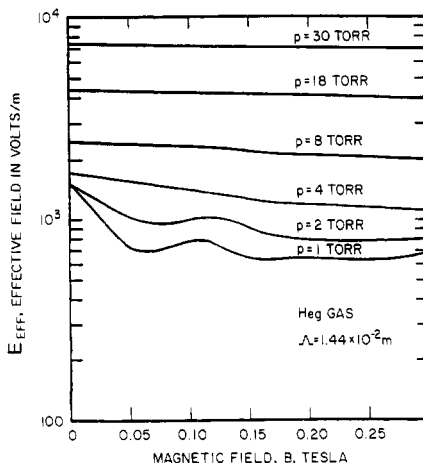
Figure 13.25 The data of figure 13.24, plotted in terms of the effective electric field, from Lax *et al* (1950).

13.3.5 Breakdown in Magnetized Plasmas

When a magnetic field is present, microwave breakdown proceeds much the same as in unmagnetized plasmas, with the exception of a large decrease of microwave electric field in the vicinity of the electron gyrofrequency. The frequency dependence (ω) and the magnetic field dependence (ω_c) of the breakdown electric field can be removed by using the effective electric field given by equation (13.29),

$$E_{eff}^2 = E^2 \frac{\nu_c^2}{2} \left[\frac{1}{(\omega + \omega_c)^2 + \nu_c^2} + \frac{1}{(\omega - \omega_c)^2 + \nu_c^2} \right]. \qquad (13.29)$$

A classic example of the breakdown electric field in Heg gas with an effective diffusion length of $\Lambda = 1.44 \times 10^{-2}$ m is shown in figure 13.24 from the experiments of Lax *et al* (1950). Figure 13.24 shows the characteristic resonant structure, with the electric field required to break down the gas showing a minimum near the electron gyrofrequency. This minimum breakdown field becomes smaller, the lower the background gas pressure and fewer the collisions. On figure 13.25 is shown the result of using the effective electric field of equation (13.29) to plot the data. Here, the effects of the magnetic field are almost removed, leaving the expected effect of background pressure only.

13.4 ECR MICROWAVE PLASMA SOURCES

The electron cyclotron resonant (ECR) microwave plasma sources are a well-established misnomer, since the resonance in question is much closer to the *upper hybrid frequency*

$$\omega_{uh} = \sqrt{\omega_{ce}^2 + \omega_{pe}^2} \qquad (13.84)$$

than to the electron gyrofrequency,

$$\omega_{ce} = \frac{eB}{m_e} \qquad (13.85)$$

These sources are characterized by a magnetized plasma somewhere within which the electron cyclotron frequency (or the upper hybrid frequency) is in resonance with the microwave excitation frequency. Electron cyclotron resonance heating of plasmas was originally developed in the field of fusion research, and has been applied to plasma processing applications since the mid 1980's.

13.4.1   Characteristics of ECR Plasmas

In Chapters 9 and 12, it was shown that the power input to a magnetized plasma in the individual particle regime has a sharp maximum near the electron cyclotron resonance frequency, given by

$$\nu_{ec} = \frac{eB}{2\pi m_e} = 27.9922B \text{ GHz.} \qquad (13.86)$$

This frequency is plotted as a function of the magnetic induction in tesla in figure 13.26. For the widely used industrial frequency of 2.45 GHz, a magnetic induction of 87.5 mT is required. This magnetic induction is within easy reach of low power DC electromagnets or permanent magnets.

In electron cyclotron resonance plasma heating, a *resonant surface* forms where the supply frequency ν_0 is approximately equal to the ECR frequency,

$$\nu_0 \approx \nu_{ec} < \nu_{uh}. \qquad (13.87)$$

For plasmas of significant density, the resonant frequency is equal to the *upper hybrid frequency*

$$\nu_0 \approx \nu_{uh} = \sqrt{\nu_{ec}^2 + \nu_{ep}^2}. \qquad (13.88)$$

At the resonant surface defined by equation (13.88), the input of significant power ($P > 500$ W) can result in electron number densities
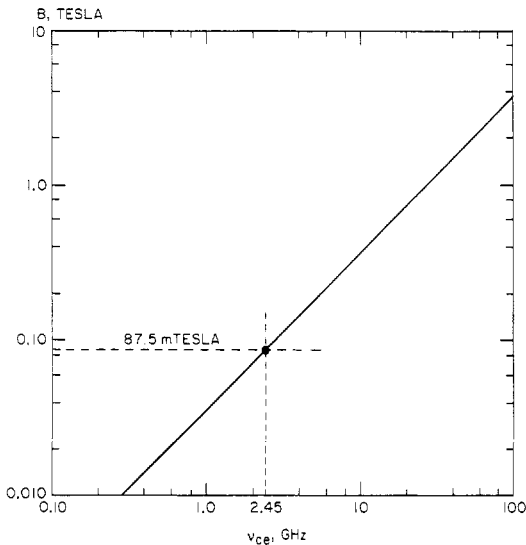
Figure 13.26 Electron cyclotron resonance in magnetized plasmas. The electron cyclotron frequency is plotted as a function of magnetic induction in tesla.

equal to or exceeding the critical density for reflection, given by equations (4.65) and (4.66),

$$n_c = \frac{4\pi m_e \varepsilon_0}{e^2} \nu_0^2 = 1.2404 \times 10^{-2} \nu_0^2 \text{ electrons/m}^3 \qquad (13.89)$$

where ν_0 is in hertz. For $\nu_0 = 2.45$ GHz , the critical number density is 7.45×10^{16} electrons/m^3. Equation (13.89) is plotted in figure 13.27 as the solid line.

ECR plasma sources generally provide plasmas that are somewhere to the left of the critical density line; however, ECR plasmas may have electron number densities greater than the critical density in and near the resonant zone. Such plasmas are called *overdense*. Plasmas generated by ECR may be as much as a factor of 10 or more times denser than the electron number densities generated by non-resonant RF power.

Microwave power sources are easy to modulate. A magnetron is typically turned on and off many times a second to control the average power; this is how the power is adjusted in domestic microwave ovens. Some plasma processing applications, including deposition and etching, benefit from pulsed application of microwave power. While the mechanism responsible is not well understood, it has been speculated that pulsing the microwave power on and off allows surface contaminants and the reaction products of surface chemical reactions to leave the surface between individual pulses of microwave power.
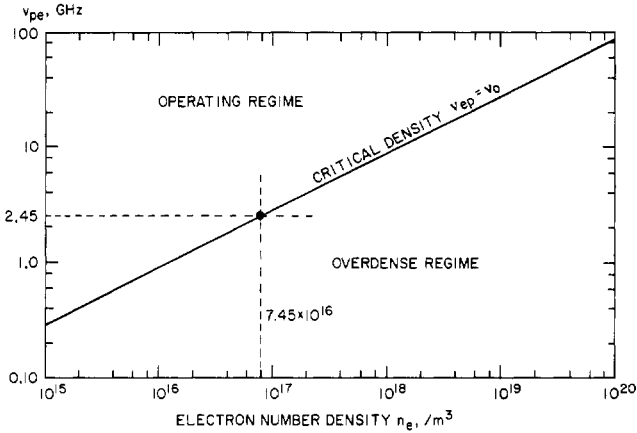
Figure 13.27 The electron plasma frequency plotted as a function of electron number density. Overdense plasmas are those below and to the right of the critical density.
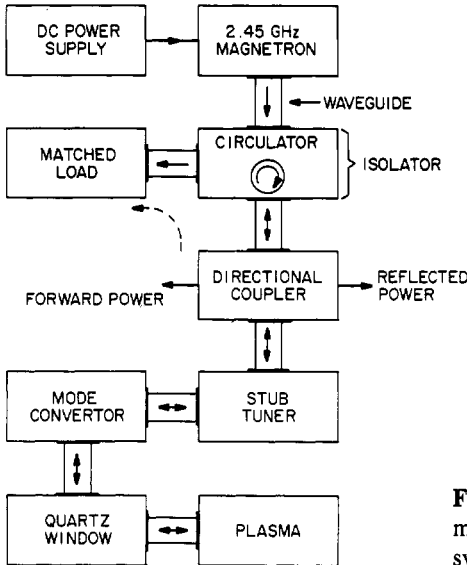
Figure 13.28 A schematic drawing of the major components of an ECR microwave system.

13.4.2 ECR Microwave Systems

A typical ECR microwave system is shown in figure 13.28. The individual components include:

(1) The *DC Power Supply and Magnetron* is available off-the-shelf, at a conventional 2.45 GHz, in the form of commercial microwave ovens at power ratings of approximately 400 W up to 1 kW, and is available

from equipment vendors at power ratings from 1 kW to 10 kW.

(2) *The Circulator/Matched Load* isolates the magnetron from the variable plasma load. It functions like a one-way valve for microwave power, allowing it to circulate from the magnetron source to the plasma, but diverting the reflected microwave power to a matched load where it is absorbed.

(3) *The Directional Coupler* consists of microwave circuit elements which allow measurement of the forward power to the load, and the microwave power reflected from the load back to the source. The difference in these two power flows is either absorbed by the plasma, or dissipated in the rest of the system.

(4) *The Stub Tuner* is used to minimize the reflected power, while maximizing the forward power absorbed by the load.

(5) *A Mode Convertor* is sometimes used to symmetrize the electric field of the microwaves, in order to produce a symmetric, uniform plasma, or to convert from a rectangular to a cylindrical waveguide.

(6) *The Quartz Window* is used to separate the air at atmospheric pressure in the waveguide from the vacuum in which the plasma is generated.

(7) *The Cavity Plasma* is usually a variable load, and depends on the plasma operating parameters. Its variable RF impedance is compensated for by adjusting the stub tuner, and this is sometimes done automatically by a feedback control system connected to the forward and reverse power measuring system.

13.4.3 Immersed ECR System

The *immersed ECR systems* are those in which a relatively small plasma is immersed in a microwave cavity or waveguide located in a magnetic field which contains a region in which the electrons are in gyroresonance with the microwave frequency. A widely used version of the immersed ECR system, now available off-the-shelf, is shown schematically in figure 13.29. Microwave power at 2.45 GHz is generated by a magnetron, and propagates through microwave matching and power monitoring circuits, to a transition section and mode convertor in which the microwave radiation in the rectangular waveguide is converted to a symmetric mode in a cylindrical waveguide. The cylindrical waveguide contains a re-entrant quartz tube which serves as the vacuum boundary between the waveguide, at atmospheric pressure, and the high vacuum plasma generating region. The re-entrant quartz tube is located in the bore of an axisymmetric magnetic field coil which generates a magnetic field with a resonant surface on the axis of the tube.
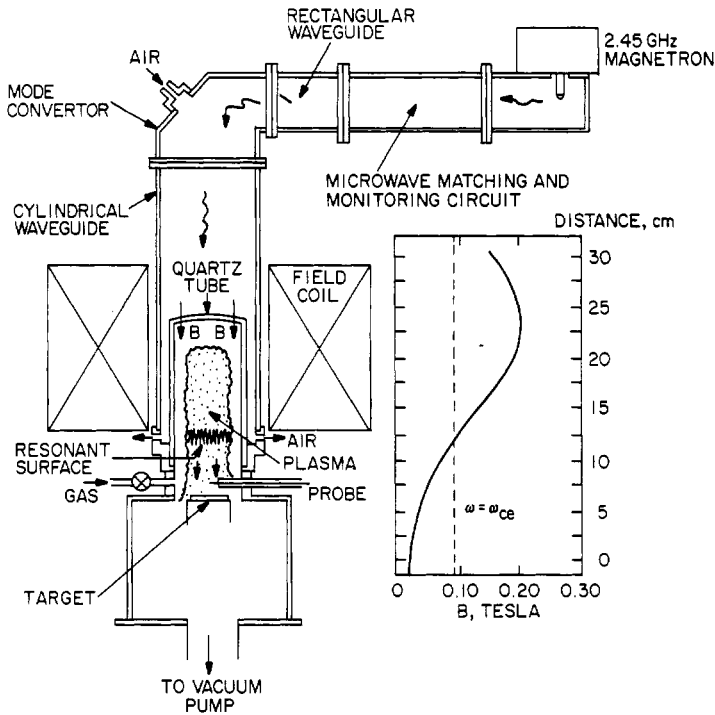
Figure 13.29 An immersed ECR plasma source. Microwaves are propagated along the waveguide, through a quartz vacuum wall, and are absorbed at the resonant surface to generate a steady state plasma.

The current in the magnetic field coil can be adjusted to move the resonant surface along the tube axis. Atmospheric air is introduced into the waveguide, and flows coaxially on the outside of the quartz tube, thus cooling it during operation. Usually, the plasma created at the resonant surface flows along diverging magnetic field lines in a magnetic nozzle before hitting the target. The background neutral gas pressure in the plasma generating region may be below 1 mTorr, and the electron number densities near the resonant surface are typically at or above the critical number density. Using this arrangement, the immersed ECR system can provide high particle fluxes on targets for diamond or other thin film deposition, and the ions in the plasma flux can also be used for etching.

13.4.4 Distributed ECR System

The *distributed electron cyclotron resonance system*, also available commercially, consists typically of a large cavity into which microwaves are introduced. A magnetic field, either near the cavity walls or
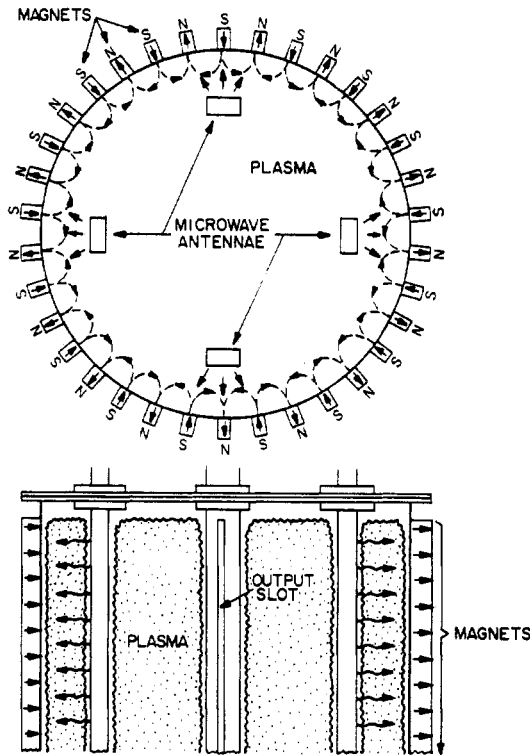
Figure 13.30 A distributed ECR plasma source. Microwave radiation is distributed in a large cavity by antennae, and is absorbed by the plasma at the ECR resonant surface near the tank boundary.

throughout the entire cavity volume, provides a resonant surface at the microwave frequency (Namura *et al* 1992). In the system shown schematically in figure 13.30, microwave power is introduced by four antennae or slotted waveguides into a large diameter vacuum tank with multipolar magnets on its boundary. These multipolar magnets are strong enough to create a cylindrical resonant surface just inside the inner wall of the vacuum tank, where microwave power introduced by the antennae is strongly absorbed. This distributed absorption of the microwave power is capable of filling the entire vacuum tank with plasma. The multipolar magnetic field at the tank boundary can serve a double function, not only to provide a resonant surface for ECR absorption of the microwave power, but also to improve the confinement of the plasma and keep it away from the vacuum tank wall where it would recombine and be lost.

Table 13.1 Characteristics of ECR microwave plasmas and RF parallel plate capacitively coupled plasma sources.

| Parameter | ECR microwave plasmas | | | RF sources |
	High value	Low value	Typical value	Typical value
Plasma diameter (cm)	30	5	10	10
Plasma length (cm)	100	10	20	5
Frequency (GHz)	10	0.9	2.45	13.56 MHz
Power (W)	2000	200	500	200
Neutral gas pressure (mTorr)	100	0.02	0.40	75
Electron kinetic temperature, T_e' (eV)	15	5	10	5
Electron density, n_e (electrons/m^3)	5×10^{18}	10^{16}	10^{17}	10^{16}
Ion bombardment energy (eV)	50	10	30	100

13.4.5 ECR Source/Plasma Characteristics

ECR microwave plasma sources for industrial applications are a relatively recent development. To illustrate why these sources have been preferred over parallel plate RF glow discharges for many industrial applications, the range of ECR plasma parameters is compared on table 13.1 with corresponding characteristic values for parallel plate capacitively coupled plasma sources. The microwave sources can provide plasmas with dimensions at least as large as the parallel plate capacitively coupled reactor. Unlike parallel plate reactors, however, the distributed ECR plasma sources have the capability of filling very large volumes with plasma of moderately high density, a major advantage for the processing of large microelectronic wafers, 20 or 30 cm in diameter.

The difference in power requirements and RF frequency are not by themselves major factors in choosing between the two approaches to the production of plasma. The very low pressures at which the ECR plasma sources can operate, however, can be an important advantage, where long mean free paths are desired in order to achieve vertical etching, or where low background pressures are desired to maintain low levels of contamination in the system being processed. The generally higher electron number densities possible with microwave plasma sources, approximately a factor of 10 higher than with parallel plate RF glow discharges, generally result in higher ion fluxes and shorter processing times, a major advantage in some applications.

13.4.6 Applications

Relative to capacitively coupled parallel plate reactors, ECR microwave plasma sources have the following potential advantages:

(1) Lower neutral gas pressure, and longer ion and neutral mean free paths. This can be an important advantage when vertical etching is required.

(2) A higher fraction ionized, and hence a surface flux with a much higher proportion of active species such as ions, atoms in excited states, or free radicals.

(3) Higher electron density, which results in higher ion surface fluxes and shorter processing times.

Some relative disadvantages of ECR microwave plasma sources include:

(1) Lower ion bombardment energies.

(2) Less control of the bombarding ion energy, if biasing is not used.

(3) Difficulty in tuning up and achieving efficient coupling betweent the microwave source and an ECR plasma, since the plasma is a variable load, and microwave systems tend to require iterative adjustments to produce optimum operating conditions.

(4) The ECR system is much more difficult and expensive to make uniform over a large area than RF parallel plate glow discharges.

(5) ECR technology is generally more expensive than DC or RF glow discharge reactor technology.

ECR plasma sources have already found application to thin film deposition (diamond deposition), etching of microelectronic circuits, and various forms of surface treatment.

13.5 NON-RESONANT MICROWAVE PLASMA SOURCES

Non-resonant microwave plasmas use microwave power to break down and maintain a plasma, under conditions for which the magnetic induction is zero, or for which no resonant surface exists in the plasma volume. The pressure and number density regimes for non-resonant microwave plasmas are not too different from inductive plasma reactors for high power ($P > 2$ kW) operation.

13.5.1 Continuous Flow Reactors

Microwave continuous flow reactors are used as plasma–chemical reactors, and for plasma–chemical processes requiring ultraviolet
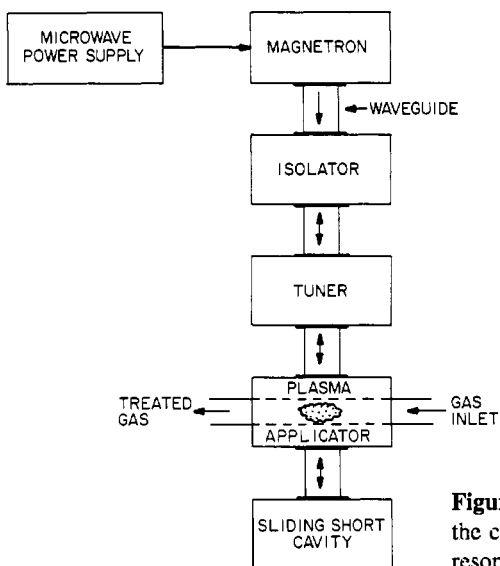
Figure 13.31 A schematic drawing of the components of a continuous flow non-resonant microwave plasma source.

radiation or such chemically active species as ions, atoms in excited states, or free radicals. Microwave heated continuous flow reactors can also be used to provide a plasma torch-like flow, similar to inductive plasma torches.

A characteristic microwave system for continuous flow reactors is shown schematically in figure 13.31. The power levels used industrially range from 100 W to 2 kW, but some high power units are capable of operating at 1 atm, and use up to 50 kW of power. The tuner, applicator, and sliding short are usually a single section of rectangular waveguide. The frequency used is almost invariably 2.45 or 0.9 GHz, usually the former.

The usual arrangement for coupling microwave power to the gas is shown schematically in figure 13.32. A cylindrical quartz or alumina tube passes through a microwave waveguide, where the axis of the cylindrical tube is aligned with the electric field of the radiation propagating in the waveguide. Sometimes the waveguide is pinched down to a small thickness, as in figure 13.32(*b*), to intensify the electric field. The high axial electric fields break down the gas flowing through the tube, thus providing a continuous flow of hot gas in a non-resonant plasma. The quartz or alumina tube serves as the vacuum boundary for low pressure operation.

At high powers ($p > 10$ kW), this form of microwave plasma reactor can be operated at pressures up to 1 atmosphere. The approximate range of operating parameters of the continuous flow non-resonant microwave reactors is shown on table 13.2. At high powers, these reactors
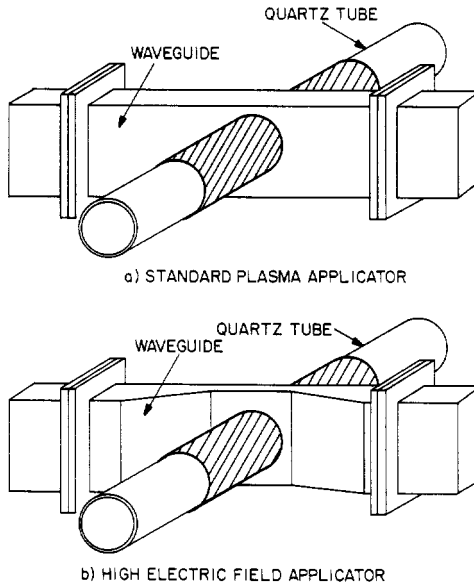
Figure 13.32 Two designs of microwave applicator for a low power continuous flow plasma reactor. (*a*) Standard configuration. (*b*) High electric field configuration.

Table 13.2 Operating parameters of continuous flow non-resonant microwave plasma reactors.

Parameter	Low value	High value
Gas pressure (Torr)	10	760
Power level (kW)	0.20	50
Frequency (GHz)	0.915	2.45
Gas kinetic temperature (eV)	0.10	≈ 1.0
Electron kinetic temperature (eV)	0.50	6.0
Electron density, n_e (electrons/m^3)	10^{15}	10^{19}

can produce gas kinetic temperatures and electron number densities comparable to those produced by DC arc jets and high power inductive plasma torches.

13.5.2 The Microwave Plasma Torch

This relatively new concept, published by Mitsuda *et al* (1989), is shown schematically in figure 13.33. The *microwave plasma torch* consists of microwave power delivered by a rectangular waveguide through a quartz
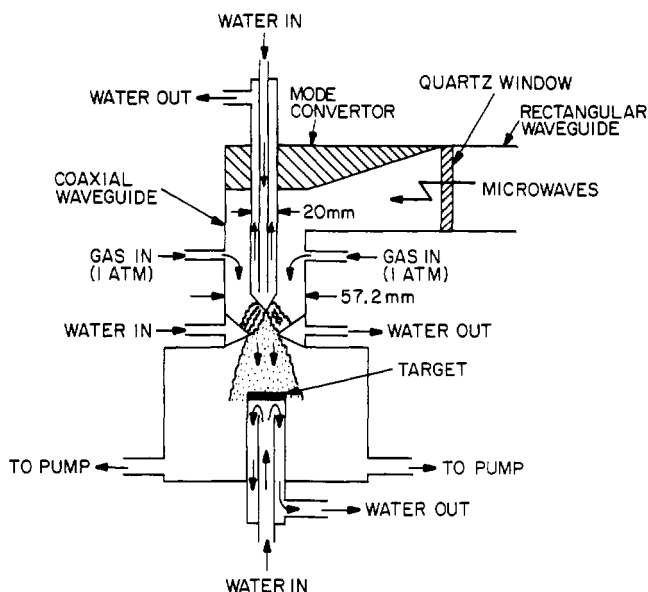
Figure 13.33 The microwave plasma torch, as developed by Mitsuda *et al* (1989).

window into an impedance-matching mode convertor which couples the microwave power to a coaxial waveguide. The center conductor of the coaxial waveguide forms one electrode of an arc jet-like configuration, and the other electrode comprises an annular flange on the outer coaxial electrode. When 2 kW of microwave power at 2.45 GHz is applied, the working gas, hydrogen, is broken down and forms a plasma torch, driven by microwave energy. A rotating arc, similar to that which forms in a DC arc jet, was struck in the working gas between the center electrode and the outer coaxial electrode. The plasma from this microwave plasma torch was used by Mitsuda *et al* for diamond film deposition at a much faster rate than was possible with other types of plasma source.

13.5.3 Distributed, Non-resonant Microwave Plasma

With growing interest in microelectronic wafers 20 or 30 cm in diameter, interest has arisen in large volume, uniform plasmas. Distributed, non-resonant plasma sources capable of producing such plasmas are not available off the shelf; here we describe the Microwave Plasma Facility (MPF) which has been developed and operated at the University of Tennessee, Knoxville (UTK) Plasma Science Laboratory (Spence *et al* 1991, Kamath and Roth 1992). Figure 13.34 shows this facility as a whole. The stainless steel vacuum tank is 1 m high and 50 cm in diameter.
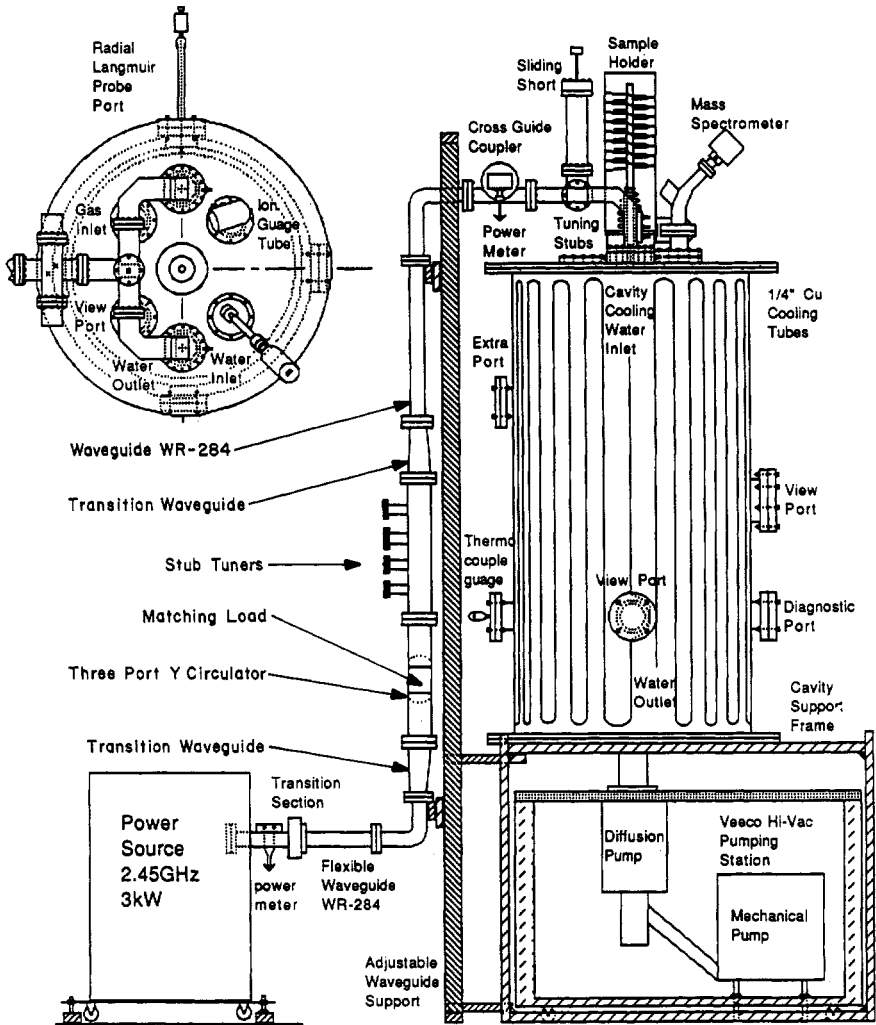
Figure 13.34 The UTK Microwave Plasma Facility (MPF).

Vacuum pumping is at the bottom, high voltage and microwave inputs are at the top, for safety. A 3 kW, 2.45 GHz magnetron-based source is at the lower left. Power takeoffs for monitoring forward and reverse power are shown. To minimize electrical breakdown at the microwave window, the power flux was divided in half by a tee in the waveguide, and the power equalized in the two distribution arms by a sliding short and tuning stubs on each of the two arms. The observation ports on the side of the tank were covered with screen on the inside, to minimize microwave leakage.

Table 13.3 Parameters of the UTK Microwave Plasma Facility (MPF).

Parameter	High value	Low value	Typical value
Plasma diameter (cm)	—	—	50
Plasma length (cm)	—	—	100
Microwave frequency GHz	—	—	2.45
Microwave power (W)	2500	500	1500
Nitrogen gas pressure (mTorr)	120	10	20
Electron kinetic temperature, T_e' (eV)	12	6	8
Electron density, n_e (electrons/m^3)	6.7×10^{16}	1.0×10^{16}	4.0×10^{16}

Data were taken on the plasma characteristics of this facility with and without multipolar permanent magnets in place on the outer surface of the vacuum tank. The magnetic field strength was approximately 30 mT near the inner surface of the tank, well below electron cyclotron resonance. To assess the effect of the multipolar magnets on confining the plasma, radial and axial traverses of the plasma were made with a Langmuir probe at about 1.7 kW of net microwave power input to the plasma. Such traverses were made both without the permanent magnets on the outer surface of the vacuum vessel, and with them in place. It was found that, with both magnetized and unmagnetized boundaries, the plasma was uniform over about 70% of its volume. It was also found by comparing the plasma electron number density before and after applying the magnets at the same power input level, that the density increased by a factor of about 1.7 when the magnets were placed on the walls, providing additional plasma confinement. The operating characteristics of this facility are shown on table 13.3. The electron number densities observed are slightly below the cutoff density of 7.45×10^{16} electrons/m^3.

An advantage of non-resonant, distributed microwave plasma sources like the MPF is good volumetric uniformity. In the MPF, approximately 70% of the 200 liter volume of the vacuum tank contained a plasma the number density of which varied by less than 10%. Distributed microwave sources also should be capable of good planar uniformity; they use a familiar plasma generating technology, 2.45 GHz microwave power; they are capable of providing high electron number densities and large plasma fluxes; and they can provide very large volumes of plasma, a total of approximately 200 liters in the case of the MPF just discussed.

Some disadvantages of the non-resonant distributed microwave plasma sources include the necessity of operating at relatively high background

neutral gas pressures, in the range from 10 mTorr to 120 mTorr; and, like all microwave systems, the lack of a relatively direct control on the plasma-wall voltage drop and of control of the energy of the ions which hit the walls surrounding the plasma.

REFERENCES

Anon. 1991 *Plasma Processing of Materials: Scientific Opportunities and Technological Challenges* (Washington, DC: National Academy Press) ISBN 0-309-04597-5.

Bridgman W 1963 *Dimensional Analysis* (New Haven, CT: Yale University Press)

Brown S C 1966 *Introduction to Electrical Discharges in Gases* (New York: John Wiley)

Buckingham E 1914 On Physically Similar Systems: Illustrations of the Use of Dimensional Equations *Phys. Rev.* Ser. 2 **4** 345–376

Heald M A and Wharton C B 1965 *Plasma Diagnostics with Microwaves* (New York: John Wiley)

Kamath S G and Roth J R 1992 Stabilization and Performance Enhancement of a Large Volume, Unmagnetized Microwave Plasma Facility (MPF) *Proc. 1992 IEEE Int. Conf. on Plasma Science* IEEE Catalog No. 92 TH0460-6, p 170

Lax B, Allis W P and Brown S C 1950 The Effect of Magnetic Field on The Breakdown of Gases at Microwave Frequencies *J. Appl. Phys.* **21** 1297–1304

MacDonald A D 1966 *Microwave Breakdown in Gases* (New York: John Wiley) LCCCN 66-22841

MacDonald A D and Brown S C 1949 High Frequency Gas Discharge Breakdown in Hydrogen *Phys. Rev.* **76** 1634–1639

MacDonald A D, Gaskell D U and Gitterman H N 1963 Microwave Breakdown in Air, Oxygen, and Nitrogen *Phys. Rev.* **130** 1841–1850

MacDonald A D and Tetenbaum S J 1978 High Frequency and Microwave Discharges, in: Hirsh M N and Oskam H J (ed) *Gaseous Electronics* vol 1 *Electrical Discharges* (New York: Academic Press) ISBN 0-12-349701-9 chap 3

McDaniel E W 1964 *Collision Phenomena In Ionized Gases* (New York: John Wiley) LCCCN 64-13219 p 19

Mitsuda Y, Yoshida T and Akashi K 1989 Development of a New Microwave Plasma Torch and its Application to Diamond Synthesis *Rev. Sci. Instrum.* **60** 249–252

Namura T, Arikata I, Fukumasa O, Kubo M and Itatani R 1992 Effects of Permanent Magnet Arrangements and Antenna Locations on the Generation of Multicusp Electron Cyclotron Resonance Plasma *Rev. Sci. Instrum.* **63** 21–30

Rose D J and Brown S C 1957 Microwave Gas Discharge Breakdown in Air, Nitrogen and Oxygen *J. Appl. Phys.* **28** 561–63

Roth J R and Spence P D 1987 Measurement of the Effective Momentum Collision Frequency in a Turbulent, Weakly Ionized Plasma. *Proc. 18th Int. Conf. on Phenomena in Ionized Gases (Swansea, UK)* vol 4 (International Union of Pure and Applied Physics) pp 614–615

Samaras D G 1971 *Theory of Ion Flow Dynamics* (New York: Dover Publications)

Spence P D 1990 *A Study of the Effective Electron Collision Frequency in a Weakly Ionized Turbulent Penning Discharge Plasma* PhD Thesis University of Tennessee, Knoxville, TN

Spence P D, Keebler P F, Freeland M S and Roth J R 1991 A Large-Volume, Uniform, Unmagnetized Microwave Plasma Facility (MPF) for Industrial Plasma Processing Applications *Proc. Workshop on Industrial Plasma Applications and Engineering Problems, 10th Int. Symp. on Plasma Chemistry (10 August 1991, Bochum, Germany)* (International Union of Pure and Applied Chemistry)

Stix Thomas H 1962 *The Theory of Plasma Waves* (New York: McGraw-Hill) LCCN 62-17376

Sugano T (ed) 1985 *Applications of Plasma Processes to VLSI Technology* (New York: John Wiley) ISBN 0-471-86960-0

Vidmar R J 1991 *Plasma Cloaking: Air Chemistry, Broadband Absorption, and Plasma Generation* Final Report, SRI Project 8656 (Menlo Park, CA: SRI International)

Appendix A

Nomenclature

LATIN SYMBOLS

A	Area (m^2)
	Arbitrary constant
	Nuclear mass number
	Richardson emission constant (A/m^2-K^2)
a	Plasma or electrode radius (m)
	Similarity scaling factor
B, $\boldsymbol{B}$	Magnetic induction: scalar, vector quantities (T)
B	Arbitrary constant
b	Distance, radius (m)
C	Arbitrary constant
	Fowler–Nordheim constant (A/V^2)
C_v	Specific heat capacity (J/kg-K)
c	Speed of light, 2.998×10^8 m/s
D	Arbitrary constant
	Diffusion coefficient (m^2/s)
	Fowler–Nordheim constant (V/m)
	Displacement vector
	Beam diameter (m)
$\boldsymbol{D}$	Diffusion matrix
d	Distance (m)
E, $\boldsymbol{E}$	Electric field intensity: scalar, vector quantities (V/m)
E	Incomplete elliptic integral
$\mathcal{E}$	Energy (J)
$\mathcal{E}'$	Energy (eV)

e	Electronic charge, 1.602×10^{-19} C
F, $\boldsymbol{F}$	Force: scalar, vector quantities (N)
F	Body force (N/m^3)
	Form factor
	Incomplete elliptic integral
	Ionization fraction
f, $\boldsymbol{f}$	Force per particle: scalar, vector quantities (N)
f	Particle distribution function
g	Gravitational acceleration (m/s^2)
	Statistical weight of atomic state
H	Magnetic field strength (A/m)
h	Planck's constant, 6.626×10^{-34} J-s
I	Electric current (A)
	Luminous intensity, power flux (W/m^2)
J, $\boldsymbol{J}$	Electric current density: scalar, vector quantities (A/m^2)
J	Bessel function
$\mathcal{J}$	Relativistic dimensionless current density
K	Complete elliptic integral
	Wave number (m^{-1})
	Dimensionless wave number
k	Boltzmann's constant, 1.380×10^{-23} J/K
	Exponent
	Wave number (m^{-1})
L	Distance, separation (m)
	Density scale length (m)
	Inductance (H)
	Extraordinary wave parameter, equation (13.22)
l	Length (m)
	Electron mean free path (m)
M	Extraordinary wave parameter, equation (13.23)
	Magnetic moment (J/T)
M_e	Radiant exitance (W/m^2)
m	Particle mass (kg)
	Exponent
	Surface roughness factor
N	Number of events, etc
	Dimensionless electron number density
N_A	Avogadro's number, 6.023×10^{26} /kg-mole
n	Number density (particles/m^3)
P	Total power (W)
	Power flux (W/m^2)
P, p	Power density (W/m^3)
p	Pressure (Pa or N/m^2)
$\mathcal{P}$	Perveance (A/V$^{3/2}$)

Q	Charge (C)
q	Charge, a signed quantity (C)
	Parametric exponent
r	Radial coordinate (m)
R	Radius of curvature (m)
	Reaction rate (reactions/m^3-s)
	Radius of gyration (m)
	Resistance (Ω)
S	Source rate (particles/m^3-s)
	Sheath thickness
	Power flux (W/m^2)
s	Distance along trajectory (m)
T	Kinetic temperature (K)
	Time duration (s)
	Dimensionless time
T'	Kinetic temperature (eV)
$\mathbf{T}$	Transport matrix
t	Time (s)
U	Work (J)
	Potential, stored energy (J)
V	Volume (m^3)
	Potential (V)
V^*	Effective ionization potential (eV)
$v, \boldsymbol{v}$	Speed: scalar, vector quantities (m/s)
W	Energy or work done (J)
	Dimensionless frequency
w	Particle kinetic energy (J)
X	Dimensionless value of pd
x	Cartesian coordinate (m)
Y	Dimensionless potential
y	Cartesian coordinate (m)
z	Cartesian coordinate (m)
Z	Ionic charge number

GREEK SYMBOLS

α	Attenuation coefficient
	Radius ratio, equation (8.102)
	Townsend's first ionization coefficient (ion–electron pairs/m)
β	Relativistic velocity ratio, v/c
	Dimensionless cylindrical diode parameter

β (cont.)	Propagation constant
	Dimensionless ion drift velocity
	Townsend's second ionization coefficient
Γ, $\boldsymbol{\Gamma}$	Particle flux: scalar, vector quantities (particles/m²-s)
γ	Ratio of specific heats
	Relativistic parameter
	Dimensionless neutral drift velocity
	Secondary electron emission coefficient (electrons/ion)
Δ	Small increment of quantity prefixed
δ	Direction cosine
	Small departure
	Atmospheric density factor, equation (8.105)
	Grid geometry ratio, equation (8.49)
	Ionization fraction
	Skin depth (m)
ε_0	Permittivity of free space, 8.854×10^{-12} F/m
ε	Emissivity of a plasma
	Small parameter
	Dimensionless energy
	Sputtering yield (atoms/ion)
η	Resistivity (Ω-m)
	Amplitude modulation factor
	Energy cost of ion–electron pair (eV)
	Energy coupling parameter, equation (11.34)
	Efficiency
	Coefficient of viscosity (N-s/m³)
θ	Angle with respect to magnetic field (rad)
	Azimuthal angle (rad)
	Vertex half-angle of escape cone
κ	Thermal conductivity (W/m-K)
Λ	Argument of Coulomb logarithm
	Characteristic diffusion length (m)
λ	Debye shielding length (m)
	Wavelength (m)
	Mean free path (m)
μ, $\boldsymbol{\mu}$	Mobility: scalar, tensor quantities (C-s/kg)
	Magnetic moment (J/T)
	Index of refraction (real)
μ_0	Permeability of free space, $4\pi \times 10^{-7}$ H/m
ν	Frequency of an event/particle (Hz)
ν_c	Collision frequency/particle (Hz)
ν_i	Ionization frequency/particle (Hz)
ξ	Dimensionless distance, equation (3.165b)
π	3.14159

ρ	Charge density (C/m^3)
	Dimensionless radial parameter, equation (3.196a)
	Mass density (kg/m^3)
	Resistivity (Ω-m)
σ	Cross section (m^2)
	Electrical conductivity ($S/m \equiv mho/m$)
	Stefan–Boltzmann constant, 5.671×10^{-8} W/m^2-K
	Surface charge density (C/m^2)
$\langle \sigma v \rangle$	Reaction rate coefficient (m^3/s)
τ	Characteristic time (s)
	Particle containment time (s)
ϕ	Potential (V)
	Angle of rotation (rad)
	Magnetic flux (Wb)
	Maximum allowable power flux (W/m^2)
	Dimensionless potential
χ	'Child' coefficient, equation (3.144)
	Attenuation index
Ω	Solid angle (rad)
ω	Angular frequency (rad/s)
	Relativistic parameter, equation (3.175)
ω_p	Plasma frequency (rad/s)

SUBSCRIPTS

0	Neutral gas
	At rest value
	Outside surface value
	Free space value
	Axial value
	Maximum value
	Initial value
A	Ambipolar value
A, a	Anode
B	Bohm value
B, b	Breakdown
b	Beam value
	Outer radius
c	Critical
	Cathode region
	Gyrofrequency
	Collision

c (cont.)	Centrifugal
	Child-law critical current
	Charged particle
cl	Classical
d	Deflection
	Relating to Debye length
	Relating to electrical discharge
	Relating to particle drift
eff	Effective value
E	Electric field
	Efficiency
$\mathcal{E}$	Energy
ex	External
	Extraordinary wave
e	Electrons
f	Filament
	Final value
	Floating valve
g	Gravitational
	Radius of gyration
	Relating to gas
H	Heating
	Hall direction
i	Ions
	Ionization
	Injection
in	Inside
L	Left circularly polarized
	Load
lim	Limiting value
m	Magnetic
	Most probable value
mob	Mobility
max	Maximum value
min	Minimum value
n	Neutral gas
ne	Electron–neutral ionization
op	Operating
oh	Ohmic heating
ord	Ordinary wave
out	Outside
P	Pedersen direction
p	Plasma
	Proton

p (cont.)	Particles
R	Right circularly polarized
r	Radial
	Relativistic
rms	Root mean square value
S	Standing
	Source
s	Sheath
	Surface value
	Species
sc	Space charge
T	Trapping
t, tot	Total
uh	Upper hybrid
v	Volume, constant volume
w	Pertaining to kinetic energy
	Wall, wall value
x	Cartesian direction
y	Cartesian direction
z	Cartesian direction
$\parallel$	Parallel to magnetic field
$\perp$	Perpendicular to magnetic field
*	Associated with energy transfer frequency
1	Perturbed value

SUPERSCRIPTS

′ (prime)	Indicates energy $\mathcal{E}'$, kinetic temperature T' and pressure p' in non-SI units
	Derivative
	Moving coordinate system
	Value per unit axial length
*	Associated with eV/ion

OTHER NOTATION

⟨ ⟩	Implies averaging over a Maxwellian distribution for the quantity between angle brackets
—	Mean value, as in $\bar{E}$, $\bar{p}$, etc

Appendix B

Physical Constants

c	Velocity of light	2.998×10^{8} m/s
e	Electronic charge	1.602×10^{-19} C
m_e	mass of an electron	9.109×10^{-31} kg
e/m_e	Electron charge to mass ratio	1.759×10^{11} C/kg
	Electron rest mass	0.511 MeV
m_p	Mass of a proton	1.673×10^{-27} kg
e/m_p	Proton charge to mass ratio	9.564×10^{7} C/kg
	Proton rest mass	938.21 MeV
m_p/m_e	Proton to electron mass ratio	1836
h	Planck's constant	6.626×10^{-34} J s
k	Boltzmann's constant ($k = R/N_A$)	1.381×10^{-23} J/K
N_A	Avogadro's number	6.022×10^{26} /kg-mole
σ	Stefan–Boltzmann constant	5.671×10^{-8} J/m^2-s-K^4
g	Standard gravity	9.807 m/s^2
ε_0	Permittivity of free space	8.854×10^{-12} F/m
μ_0	Permeability of free space	$4\pi \times 10^{-7}$ H/m
R	Molar gas constant	8.315 J/K-mol

Appendix C

Units and Conversion Factors

This appendix lists the quantities and units that are relevant to plasma physics and engineering. All units are SI except those marked with an asterisk (*). The following quantities have their own named units.

Quantity	Name	Symbol	Equivalent units
Mass	kilogram	kg	
Length	meter	m	
Time	second	s	
Temperature	kelvin	K	
	*electronvolt	eV	11604 K
Electrical current	ampere	A	C/s
Amount of substance	mole	mol	*kg-mole
Plane angle	radian	rad	
Frequency	hertz	Hz	/s
Force	newton	N	$m\text{-}kg/s^2$
Energy	joule	J	N-m
	*electronvolt	eV	
Power	watt	W	$J/s \equiv V\text{-}A$
Pressure	pascal	Pa	N/m^2
	*torr	Torr	*mm Hg
	*standard atmosphere	atm	
Electric charge	coulomb	C	A-s
Electric potential, voltage	volt	V	$J/C \equiv W/A$
Electric resistance	ohm	Ω	V/A
Electric conductance	siemens	S	$A/V \equiv /\Omega \equiv$ *mho
Capacitance	farad	F	C/V
Magnetic flux	weber	Wb	V-s
Magnetic induction	tesla	T	Wb/m^2
Inductance	henry	H	Wb/A

The following quantities are expressed in terms of the units listed above.

Quantity	Name	Symbol
Area, cross section	square meter	m^2
Volume	cubic meter	m^3
Mass density	kilogram per cubic meter	Kg/m^3
Velocity	meter per second	m/s
Acceleration	meter per second squared	m/s^2
Wave number	per meter	$/m$
Electric current density	ampere per square meter	A/m^2
Electric field strength	volt per meter	V/m
Power flux	watt per square meter	W/m^2
Power density	watt per cubic meter	W/m^3
Resistivity	ohm meter	Ω-m
Electrical conductivity	siemens per meter	S/m
Magnetic field strength	ampere per meter	A/m
Magnetic moment	joule per tesla	J/T
Permittivity	farad per meter	F/m
Permeability	henry per meter	H/m
Mobility	coulomb second per kilogram	C-s/kg
Specific heat capacity	joule per kilogram kelvin	J/kg-K
Thermal conductivity	watt per meter kelvin	W/m-K
Angular frequency	radian per second	rad/s
Plasma frequency	radian per second	rad/s
Number density	particles per cubic meter	$particles/m^3$

CONVERSION FACTORS

Energy
pages 56, 57

$1\ eV = 1.602 \times 10^{-19}\ J$
$\mathcal{E}(J) = e\mathcal{E}'(eV)$

Temperature
page 40

$1\ eV = e/k = 11\,604\ K$
$kT(K) = eT'(eV)$

Pressure
pages 34, 35

1 atm = 760 Torr = 101 325 Pa
1 Torr = 101 325/760 Pa

Conversion formulas for neutral particle density (in $particles/m^3$) and pressure (in Pa, Torr and atm) are given in Appendix D.

Appendix D

Useful Formulas

SI units are used except as indicated. The kinetic temperatures T', T'_e and T'_i are in electronvolts throughout, whereas T is in kelvin; m_e, m_i and m_p are the electron, ion and proton masses, respectively; n_e and n_i are the electron and ion number densities, respectively; B is the magnetic induction, e is the electronic charge; Z is the charge of an ion; and $A \approx m_i/m_p$ is the atomic mass number and is approximately the ratio of ion to proton mass.

FREQUENCIES

Electron cyclotron (or gyro) frequency:

$$v_{ce} \equiv \frac{eB}{2\pi m_e} = 28.00B \qquad \text{(Ghz)} \tag{D.1}$$

Ion cyclotron (or gyro-) frequency:

$$v_{ci} \equiv \frac{ZeB}{2\pi m_i} = 15.22\frac{ZB}{A} \qquad \text{(Mhz)} \tag{D.2}$$

Electron plasma frequency:

$$v_{pe} \equiv \frac{1}{2\pi}\left(\frac{n_e e^2}{\varepsilon_0 m_e}\right)^{1/2} = 8.980(n_e)^{1/2} \quad \text{(Hz)} \tag{D.3}$$

Ion plasma frequency:

$$v_{pi} \equiv \frac{1}{2\pi}\left(\frac{n_i Z^2 e^2}{\varepsilon_0 m_i}\right)^{1/2} = 0.2095Z\left(\frac{n_i}{A}\right)^{1/2} \qquad \text{(Hz)} \tag{D.4}$$

CHARACTERISTIC LENGTHS

Electron Debye length:

$$\lambda_{de} \equiv \left(\frac{\varepsilon_0 T'}{n_e e}\right)^{1/2} = 7434 \left(\frac{T'}{n_e}\right)^{1/2} \quad \text{(m)} \qquad \text{(D.5)}$$

Electron gyroradius (based on mean thermal velocity):

$$r_{ge} \equiv \frac{m_e v_e}{eB} = \frac{1}{B}\left(\frac{8m_e T'_e}{\pi e}\right)^{1/2} = 3.805 \times 10^{-6}\frac{(T'_e)^{1/2}}{B} \quad \text{(m)} \quad \text{(D.6)}$$

Ion gyroradius (based on mean thermal velocity):

$$r_{gi} \equiv \frac{m_i v_i}{ZeB} = \frac{1}{ZB}\left(\frac{8m_p A T'_i}{\pi e}\right)^{1/2} = 1.632 \times 10^{-4}\frac{(A T'_i)^{1/2}}{ZB} \quad \text{(m)}$$
$$\text{(D.7)}$$

VELOCITIES

Electron mean thermal velocity:

$$v_e \equiv \left(\frac{8e T'_e}{\pi m_e}\right)^{1/2} = 6.693 \times 10^5 (T'_e)^{1/2} \quad \text{(m/s)} \qquad \text{(D.8)}$$

Ion mean thermal velocity:

$$v_i \equiv \left(\frac{8e T'_i}{\pi m_i}\right)^{1/2} = 1.561 \times 10^4 \left(\frac{T'_i}{A}\right)^{1/2} \quad \text{(m/s)} \qquad \text{(D.9)}$$

NUMBER DENSITY/PRESSURE CONVERSIONS

At 300 K, the number density of a neutral gas, as derived from equation (2.3), is given by differing conversion formulas, depending on the units in which the pressure is given:

$$n \equiv P/kT \qquad \qquad \text{(2.3)}$$
$$= 2.415 \times 10^{20} p(\text{Pa}) \qquad (\text{atoms/m}^3) \qquad \text{(D.10)}$$
$$= 2.447 \times 10^{25} p'(\text{atm}) \qquad (\text{atoms/m}^3) \qquad \text{(D.11)}$$
$$= 3.220 \times 10^{22} p'(\text{Torr}) \qquad (\text{atoms/m}^3) \qquad \text{(D.12)}$$
$$= 3.220 \times 10^{16} p'(\text{Torr}) \qquad (\text{atoms/cm}^3). \qquad \text{(D.13)}$$